A thermodynamic approach to modelling pre- and post-localisation behaviour of partially saturated soils for failure analysis using the Smoothed Particle Hydrodynamics

A Thesis submitted for the degree of Doctor of Philosophy

School of Civil, Environmental & Mining Engineering, The University of Adelaide

by

Dat Gia Phan

April 2021

A thermodynamic approach to modelling pre- and post-localisation behaviour of partially saturated soils for failure analysis using the Smoothed Particle Hydrodynamics

A Thesis submitted for the degree of Doctor of Philosophy

by

Dat Gia Phan

School of Civil, Environmental & Mining Engineering,

The University of Adelaide, Australia

April 2021

Abstract

Geotechnical failures usually involve changes in the state of partially saturated soils under different loading and saturation regimes resulting in significant differences in its nonlinear responses observed in experiments. The macro inelastic behaviour of partially saturated soils is intrinsically linked to the coupled mechanical and hydraulic dissipations governed by the interaction between frictional sliding, grain rearrangement and ruptures of liquid bridges and their redistributions at the grain contacts. This nature of the grain scale interaction leads to strong coupling between plastic strains and irrecoverable degree of saturation as two key internal variables in thermodynamics-based continuum modelling of partially saturated soils. This thesis focuses on the development of a new generic thermo-mechanical approach reflecting these underlying mechanisms in modelling the coupled hydro-mechanical behaviour of unsaturated soils. A generic form of dissipation potential is developed in this study to capture the interdependence of thermodynamic forces, internal variables and their rates. The proposed dissipation potential allows the derivation of constitutive models possessing a unique yield surface dependent on both stress and suction, and two evolutions rules for irrecoverable saturation and plastic strain, both of which share the same "plastic" multiplier. This feature automatically guarantees simultaneous activation and evolution of both hydraulic and mechanical yielding responses, reflecting the inseparable nature of grain-scale hydro-mechanical interactions and their effects on macro behaviour. It makes the current approach distinct from other thermodynamics-based approaches where multiple yield functions are usually needed as a consequence of adding more internal variables and a decoupling of dissipative stresses from all the rates of internal variables.

The potential of the proposed generic approach is elucidated through a specific constitutive model for partially saturated soils. Two explicitly defined free energy and dissipation potentials are used for the formulation of a thermodynamically consistent critical state model encapsulating a path-dependent

water retention curve. The model is able to naturally capture the interdependence between wetting-drying and loading-unloading paths without having to use a separate Soil Water Characteristic Curve (SWCC) for inelastic behaviour, as usually found in existing unsaturated soil models. The benefit of this approach is the reduction in the number of parameters and the identification and calibration of all parameters based on standard tests. Extensive analyses of coupled hydro-mechanical dissipation characteristics and experimental validation show the capabilities of the model and the advantages of the proposed thermodynamics-based approach.

Hydro-mechanical coupling is also a crucial element in modelling localised failures in the form of shear banding and size effects commonly observed in partially saturated soils, given the dependence of the onset and orientation of localisation bands on material properties and different hydromechanical conditions. Deformation and saturation in such cases are inhomogeneous, with irreversible behaviours taking place inside the shear band, while the zone outside it usually undergoes reversible processes, invalidating the classical homogenous assumption implicitly adopted in all existing continuum models for partially saturated soils. This characteristic, along with properties of the mesoscale shear band (inclination, thickness) and specimen size, is essentially incorporated into a thermodynamics-based approach for localised behaviour of partially saturated soils. In this double-scale approach, enrichment terms for both kinematics and degree of saturation are used to take into account strong variations of strain and saturation degree outside and inside the shear band. The proposed formulation automatically leads to a size-dependent constitutive structure capable of describing the transition correctly from diffuse to localised stages of deformation. A bifurcation criterion taking into account a wide range of loading-unloading and wetting-drying paths is used to determine the onset of localisation and orientation of the localisation band. The promising features of the proposed double-scale formulation are illustrated using a model based on critical state soil mechanics and data in suction-controlled triaxial tests.

The developed generic thermodynamics-based approach and models are used in a mixed formulation for flow through partially saturated porous media. The governing equations are implemented in a numerical code based on the Smoothed Particle Hydrodynamics (SPH) for the solutions of Boundary Value Problems involving partially saturated porous media. The adoption of the above-proposed thermodynamics-based model allows a better reflection of the intrinsic behavioural mechanisms of partially saturated soils at the constitutive level, where the inseparable relationship between plasticity and hydraulic irreversibility is captured. This distinguishes the current approach from other existing SPH studies for flow through partially saturated porous media. The performance of the SPH approach is investigated through a range of numerical examples of Boundary Value Problems under various loading and saturation conditions.

Declaration

I, Dat G. Phan, certify that this work contains no material which has been accepted for the award of any other degree or diploma in my name, in any university or other tertiary institution and, to the best of my knowledge and belief, contains no material previously published or written by another person, except where due reference has been made in the text. In addition, I certify that no part of this work will, in the future, be used in a submission in my name, for any other degree or diploma in any university or other tertiary institution without the prior approval of the University of Adelaide and where applicable, any partner institution responsible for the joint-award of this degree.

I acknowledge that copyright of published works contained within this thesis resides with the copyright holder(s) of those works.

I also give permission for the digital version of my thesis to be made available on the web, via the University's digital research repository, the Library Search and also through web search engines, unless permission has been granted by the University to restrict access for a period of time. I acknowledge the support I have received for my research through the provision of an Australian Government Research Training Program Scholarship.

April 13th 2021

Dat G. Phan

Acknowledgements

Foremost, I would like to express my sincerest gratitude to my principal advisor, Associate Professor Giang D. Nguyen, for giving me the privilege to research under his invaluable guidance. I am forever indebted to him since his effort has facilitated both the advancement of my research and the establishment of my career. Most of what I have in research so far is from him. He is a great mentor where his patience, enthusiasm, immense knowledge, vision, sincerity and motivation have deeply inspired me. I also would like to express my deep and sincere gratitude to my associate supervisor Associate Professor Ha H. Bui (Monash University), for his generous support, dedication and valuable advice for my research work. Especially, my thanks go to him for allowing me to use his SPH code with some developments by Associate Professor Giang D. Nguyen. I am also very grateful to Dr Terry Bennett, another my co-advisor, for his invaluable assistance and support for providing insightful comments for improving my research skills. It is my great honour to study under the guidance of these three supervisors.

I am also grateful to comments from Professor Antonio Gens (Technical University of Catalonia, Spain) and an anonymous examiner.

The financial support (the Adelaide Graduate Research scholarship) from the University of Adelaide is greatly appreciated. I am also very thankful to Associate Professor Giang D. Nguyen for providing several months of scholarship top-ups from Australian Research Council grants (FT140100408 and DP170103793).

I much appreciate the Ho Chi Minh City University of Architecture (Vietnam) for direct and indirect supports throughout the years of my PhD.

My sincere thanks also go to Ms Julie Mayo for her dedicated assistance in some academic-related activities organized by the Faculty of Engineering Computer and Math Sciences. To all of my friends in Adelaide and teammates in the soccer club of Adelaide Uni SC White which made my life here more pleasant and joyful.

My special gratitude goes to my parents, parents-in-law and family, who have been a great source of motivation and encouragement during the course of my DPhil study. Finally, I would like to say thank to my wife, Y, for her love, endurance, sacrifice and understanding during my study. We share the blessing of having a wonderful daughter who became the centre of our universe.

List of publications

Phan, DG, Nguyen, GD, Bui, HH & Bennett, T 2021 ‘Constitutive modelling of partially saturated soils: Hydro-mechanical coupling in a generic thermodynamics-based formulation’, *International Journal of Plasticity,* vol 136 (https://doi.org/10.1016/j.ijplas.2020.102821).

Phan, DG, Nguyen, GD, Bui, HH & Bennett, T 2020 ‘A thermodynamics-based formulation for coupled hydro-mechanical behaviour of unsaturated soils’, The 16th International Association for Computer Methods and Advances in Geomechanics, IACMAG 2021, Turin May 5th-8th (https://doi.org/10.1007/978-3-030-64514-4_53)

Table of Contents

Chapter 3. Hydro-mechanical coupling of partially saturated soils: governing equations and a generic thermodynamic approach to constitutive modelling

Chapter 4. A thermodynamics-based critical state model for partially saturated soils

Chapter 5. Meso-macro connection in a mechanism-based approach to constitutive modelling of unsaturated soils under the drained shearing condition

Chapter 6. Analysis of failure using the Smoothed Particle Hydrodynamics

Chapter 7. Conclusion and future research

List of symbols (*only the most frequently used symbols are listed*)

β	parameter governing the coupling between saturation and volumetric deformation upon yielding
p_b	parameter controlling the stored irreversible hydraulic energy
ζ	empirical constant
ξ	parameter controlling the maximum soil stiffness
$\bar{\xi}$	parameter controlling the maximum soil stiffness
κ	elastic index
κ_h	parameter controlling the amount of reversible energy stored in the water menisci
κ_s	elastic stiffness parameter for changes in suction
k_{unsat}	scalar relative permeability coefficient in the partially saturated regime
K_{sat}	saturated hydraulic conductivity
$\bar{\kappa}$	the slope of URL in the $v: \ln\bar{p}$ plane for saturated conditions
k_s	constant controlling the apparent cohesion
λ	the slope of NCL in the $\ln v: \ln p'$ plane for saturated conditions
N	reference specific volumes of NCL under the saturated condition
Γ	reference specific volumes of CSL under the saturated condition
$\bar{\lambda}$	the slope of NCL in the $v: \ln\bar{p}$ plane for saturated conditions
λ_s	stiffness parameter for changes in suction for virgin states of the soil
λ'	hardening parameter
λ_{us}	stiffness parameter for partially saturated conditions
μ	parameter controlling the change of soil stiffness with modified suction
$\bar{\mu}$	parameter controlling the change of soil stiffness with suction
μ'	function controlling the size of the yield surface and the dilation behaviour
c'	function controlling the size of the yield surface and the dilation behaviour
μ'_0	parameter of the classical Drucker-Prager yield criterion
c'_0	parameter of the classical Drucker-Prager yield criterion
η_c	parameters of the classical Drucker-Prager yield criterion
c'_m	parameter controlling the hydraulic effects on inelastic behaviour
ω_μ	parameter controlling the hydraulic effects on inelastic behaviour
ω_c	parameter controlling the hydraulic effects on inelastic behaviour
α	parameter governing the strength of the material and non-associativity of the flow rules

r	spacing ratio
γ	parameter controlling the non-associated flow rule
M	slope of CSL
f	volume fraction
h	the thickness of the shear band
H'	effective size
ϱ	Poisson's ratio
E	Young modulus
G	shear moduli
g	gravity acceleration constant
p_u	unity pressure
p'_R	parameter controlling the yield curve
p'_{c0}	the initial yield pressure under isotropic compression at the fully saturated condition
$\bar{p}_R$	parameter controlling the yield curve
p_{at}	atmospheric pressure
ϕ_{wsat}	the saturated volumetric water content
ϕ_{wres}	residual volumetric water content
Ψ	Helmholtz specific free energy
$\widetilde{W}$	rate of work input
$\tilde{\Gamma}$	infinitesimal work supplied to the solid skeleton
Ψ^{i}	Helmholtz specific free energy outside the shear band
Ψ^{o}	Helmholtz specific free energy inside the shear band
$\widetilde{\Phi}$	dissipation potential
$\widetilde{\Phi}_v$	volumetric part of the total dissipation rate
$\widetilde{\Phi}_s$	shear part of the total dissipation rate
$\widetilde{\Phi}_h$	hydraulic part of the total dissipation rate
ϕ_1^v	first-order homogeneous functions of $\dot{\varepsilon}_v^{\mathrm{p}}$
ϕ^s	the first-order homogeneous function of $\dot{\varepsilon}_s^{\mathrm{p}}$
ϕ^h	the first-order homogeneous function of $-\dot{S}_r^{\mathrm{p}}$
ϕ_2^v	first-order homogeneous functions of $\dot{\varepsilon}_v^{p}$
φ^v	first-order homogeneous functions of $\dot{\varepsilon}_v^{\mathrm{p}}$
φ^s	the first-order homogeneous function of $\dot{\varepsilon}_s^{\mathrm{p}}$

φ^h	the first-order homogeneous function of $-\dot{S}_r^{\mathrm{p}}$
A'	general functions dependent on stresses and suction
B'	general functions dependent on stresses and suction
C'	general functions dependent on stresses and suction
A	functions governing the behaviour of the model
B	functions governing the behaviour of the model
C_1	kinematic constraint equation
C_2	kinematic constraint equation
a_1	dimensionless coefficient governing dissipative micromechanical mechanisms
a_2	dimensionless coefficient governing dissipative micromechanical mechanisms
a_3	dimensionless coefficient governing dissipative micromechanical mechanisms
b_1	dimensionless coefficient governing dissipative micromechanical mechanisms
b_2	dimensionless coefficient governing dissipative micromechanical mechanisms
b_3	dimensionless coefficient governing dissipative micromechanical mechanisms
Λ_1	Lagrangian kinematic multiplier
Λ_2	Lagrangian kinematic multiplier
θ	temperature
η	entropy
u'	specific internal energy
ϑ_k	heat supply to a volume element
y^*	yield function in generalised stress space (χ_v, χ_s, and χ_h)
y	yield function in true stress space (p', q, and s^*)
y^n	loading function in true stress space at n state
y^{new}	new loading function in true stress space
y^{trial}	trial loading function in true stress space
$y_{(SI)}$	Suction-Increase yield surface
$y_{(LC)}$	Loading-Collapse yield surface
λ_p	non-negative plasticity-like multiplier
$\lambda_{p(LC)}$	the non-negative plasticity-like multiplier of the Loading-Collapse yield surface
$\lambda_{p(SI)}$	the non-negative plasticity-like multiplier of the Suction-Increase yield surface
R_v	volumetric dissipation ratio
R_s	shear dissipation ratio
R_h	hydraulic dissipation ratio

Λ_{ijkl}	terms of the tangent stiffness tensor expressed in terms of σ'_{ij} and s^*
$\bar{\Lambda}_{ijkl}$	terms of the tangent stiffness tensor expressed in terms of $\bar{\sigma}_{ij}$ and s
$\bar{\Lambda}^{\mathrm{i}}_{ijkl}$	terms of the tangent stiffness tensor expressed in terms of $\bar{\sigma}^{\mathrm{i}}_{ij}$ and s^{i}
Π_{ij}	terms of the tangent stiffness tensor expressed in terms of σ'_{ij} and s^*
$\bar{\Pi}_{ij}$	terms of the tangent stiffness tensor expressed in terms of $\bar{\sigma}_{ij}$ and s
$\bar{\Pi}^{\mathrm{i}}_{ij}$	terms of the tangent stiffness tensor expressed in terms of $\bar{\sigma}^{\mathrm{i}}_{ij}$ and s^{i}
C_{ik}	localisation or acoustic tensor
Ω_{kl}	terms of the tangent stiffness tensor expressed in terms of σ'_{ij} and s^*
$\bar{\Omega}_{kl}$	terms of the tangent stiffness tensor expressed in terms of $\bar{\sigma}_{ij}$ and s
$\bar{\Omega}^{\mathrm{i}}_{kl}$	terms of the tangent stiffness tensor expressed in terms of $\bar{\sigma}^{\mathrm{i}}_{ij}$ and s^{i}
D_{ijkl}	homogeneous tangent stiffness
D^{e}_{ijkl}	pressure-dependent elastic stiffness tensor
D^{en}_{ijkl}	secant elastic stiffness evaluated at state n
D^{o}_{ijkl}	tangent stiffness tensor outside the shear band
D^{i}_{ijkl}	tangent stiffness tensor inside the shear band
D^{T}_{pqmn}	macro tangent stiffness tensor
M_{kl}	term of the “plastic” multiplier
H	term of the “plastic” multiplier
Υ	terms of the tangent stiffness tensor expressed in terms of σ'_{ij} and s^*
$\bar{\Upsilon}$	terms of the tangent stiffness tensor expressed in terms of $\bar{\sigma}_{ij}$ and s
$\bar{\Upsilon}^{\mathrm{i}}$	terms of the tangent stiffness tensor expressed in terms of $\bar{\sigma}^{\mathrm{i}}_{ij}$ and s^{i}
δ_{ij}	Kronecker delta
$\bar{n}_i$	the outward unit normal vector on a surface
χ	effective stress parameter
σ_{ij}	total stress
σ^{o}_{ij}	total stress outside the shear band
σ^{i}_{ij}	total stress inside the shear band
$\sigma'^{\mathrm{i}}_{ij}$	effective stress inside the shear band
$\bar{\sigma}_{ij}$	net stress
σ'_{ij}	effective stress
$\sigma'^{\,n}_{ij}$	effective stress at step n

$\bar{\sigma}_{ij}^{n}$	net stress at step n
$\bar{\sigma}_{ij}^{s}$	partial stresses of solid constituent
$\bar{\sigma}_{ij}^{w}$	partial stresses of water constituent
$\bar{\sigma}_{ij}^{a}$	partial stresses of air constituent
σ_{ij}^{s}	intrinsic stress of soil skeleton
σ_{v}'	Bishop's effective vertical stress
$\bar{\sigma}_{v}$	net vertical stress
$\sigma_{ij}'^{\mathrm{trial}}$	trial effective stress
$\sigma_{ij}'^{\mathrm{corrt}}$	corrective effective stress
B_i	body force of the mass
q	shear stress
q^{i}	shear stress inside the shear band
q_{CSL}	shear stress at the critical state
$\bar{p}$	net mean stress
$p_{c(us)}'$	the yield pressure under isotropic compression at the partially saturated condition
$\bar{p}_0$	initial net mean stress
p^{a}	intrinsic pore pressure acting on air constituent
p^{w}	intrinsic pore pressure acting on water constituent
p_0'	Initial Bishop's effective mean stress
p_c'	pre-consolidation stress at the saturated condition
$\bar{p}_{co}$	the initial yield pressure under isotropic compression at the fully saturated condition
p_{CSL}'	effective mean stress at the critical state
p'^{trial}	trial effective mean stress
p'^{corrt}	corrective effective mean stress
p'^{n}	effective mean stress at step n
p'	Bishop's effective mean stress
$\bar{p}^{n}$	net mean stress at step n
R_i^{s}	the viscous drag force acting on the solid phase
R_i^{w}	the viscous drag force acting on the water phase
$\bar{t}_i$	traction vector
$\bar{t}_i^{\mathrm{o}}$	traction vector outside the shear band
$\bar{t}_i^{\mathrm{i}}$	traction vector inside the shear band

$\bar{r}_i$	residual traction vector
res	residual vector
$\mathrm{res}^{\mathrm{new}}$	new residual vector
$\mathrm{res}^{\mathrm{previous}}$	previous residual vector
$\bar{r}_i^{\mathrm{new}}$	residual traction vector at the new state
$\bar{r}_i^{\mathrm{previous}}$	residual traction vector at the previous state
s	matric suction
s_0	initial matric suction
s^{i}	suction inside the shear band
s^{o}	suction outside the shear band
s_c	hardening parameter of the suction increase yield locus
s_{c0}	the initial hardening parameter of the suction increase yield locus
s_e	air entry value
s^*	modified suction
s_0^*	initial modified suction
$s^{*\mathrm{i}}$	modified suction inside the shear band
$s^{*\mathrm{o}}$	modified suction outside the shear band
s^n	matric suction at step n
s^{*n}	modified suction at step n
$s^{*\mathrm{trial}}$	trial modified suction
$s^{*\mathrm{corrt}}$	corrective modified suction
χ_s	shear dissipative generalised stresses
χ_h	hydraulic dissipative generalised stresses
χ_v	volumetric dissipative generalised stresses
$\bar{\chi}_v$	thermodynamic conjugates of volumetric plastic strain rate $\dot{\varepsilon}_v^{\mathrm{p}}$
$\bar{\chi}_s$	thermodynamic conjugates of shear plastic strain rate $\dot{\varepsilon}_s^{\mathrm{p}}$
$\bar{\chi}_h$	thermodynamic conjugates of irrecoverable saturation rate $-\dot{S}_r^{\mathrm{p}}$
χ_{ij}	dissipative generalised stress tensor
ϕ	Eulerian porosity
ϕ_0	initial Lagrangian porosity
ϕ^n	Lagrangian porosity at step n
$\bar{\phi}$	Lagrangian porosity
ϕ_w	Eulerian volumetric water content

$\bar{\phi}_w$	Lagrangian volumetric water content
$\bar{\phi}_w^{\mathrm{o}}$	Lagrangian volumetric water content outside the shear band
$\bar{\phi}_w^{\mathrm{i}}$	Lagrangian volumetric water content inside the shear band
w	gravimetric water content
φ	the angle between the normal to the localisation band and the vertical axis
ω	the azimuthal angle in the 23-plane from the 2-axis
ς^s	the volume fraction of solid phase
ς^a	the volume fraction of air phase
ς^w	the volume fraction of water phase
ε_v	total volumetric strain
$\varepsilon_v^{\mathrm{p}}$	plastic volumetric strain
$\varepsilon_{ij}^{\mathrm{p}}$	plastic strain tensor
$\varepsilon_s^{\mathrm{ip}}$	plastic shear strain outside the shear band
$\varepsilon_v^{\mathrm{ip}}$	plastic volumetric strain inside the shear band
ε_s	total shear strain
$\varepsilon_s^{\mathrm{p}}$	plastic shear strain
ε_p	accumulated plastic strain
ε_{ij}	total strain tensor
$\varepsilon_{v(LC)}^{\mathrm{p}}$	plastic volumetric strain associated with the Loading-Collapse yield surface
$\varepsilon_{v(SI)}^{\mathrm{p}}$	plastic volumetric strain associated with the Suction-Increase yield surface
$\varepsilon_{ij}^{\mathrm{i}}$	strain tensor inside the shear band
$\varepsilon_{ij}^{\mathrm{o}}$	strain tensor outside the shear band
$\varepsilon_{kl}^{\mathrm{ip}}$	plastic strain tensor inside the shear band
q_i^{ws}	Darcy's volume flux
ρ	the average mass density of the mixture
$\bar{\rho}^s$	the partial mass density of solid constituent
$\bar{\rho}^w$	the partial mass density of water constituent
$\bar{\rho}^a$	the partial mass density of air constituent
ρ^s	the intrinsic mass density of solid constituent
ρ^a	the intrinsic mass density of air constituent
ρ^w	the intrinsic mass density of water constituent
S_r^{p}	irreversible saturation degree

S_r^{ip}	irreversible saturation degree inside the shear band
S_r	total saturation degree
S_{r0}	total saturation degree at the initial state
S_r^{o}	total saturation degree outside the shear band
S_r^{i}	total saturation degree inside the shear band
S_r^n	total saturation degree at step n
u_k	the relative velocity between two faces of the localisation band
v	specific volume
v_0	initial specific volume
V_0	initial total volume
V	total volume
V^s	solid volume
V^a	air volume
V^w	water volume
V^p	pore volume
ψ^a	field variable of particle a
ψ^b	field variable of particle b
ψ^{ba}	relative values of a field variable between particle a and particle b
$\psi^{boundary}$	field variable of boundary particle
l	smoothing length
$\sigma_{ij}'^b$	effective stress of particle b
$\psi^{prescribed}$	prescribed field variable of boundary particle
$\sigma_{ij}'^{boundary}$	effective stress of boundary particle
Ω'	interpolation domain
$Л_{ij}^a$	rotation of the local artificial stress tensor to their principal values for particle a
$Л_{ij}^b$	rotation of the local artificial stress tensor to their principal values for particle b
f_n^{ab}	repulsive force
$Д_{ij}^{ab}$	artificial viscosity
C_s	coefficient of consolidation
L_c	width of the soil column
H_c	height of soil column
m^s	mass of the solid phase
$s^{boundary}$	the suction of boundary particle

$s^{prescribed}$	prescribed suction of boundary particle
$v_i^{s,boundary}$	the solid velocity of boundary particle
$v_i^{s,prescribed}$	the prescribed solid velocity of boundary particle
t	real time
$\bar{t}$	dimensionless time
t_f	time to failure
x_i	spatial coordinate
${x_i}^a$	the spatial coordinate of particle a
${x_i}^b$	the spatial coordinate of particle b
${x_i}^{ab}$	distance between particles
v_i^s	the velocity of the solid phase
v_i^w	the velocity of the water phase
v_i^{ws}	Darcy seepage velocity
$(v_i^s)^a$	the velocity of the solid phase of particle a
$(v_i^s)^b$	the velocity of the solid phase of particle b
$(v_i^s)^{ba}$	the relative velocity of solid-phase between particle a and particle b
W^{ab}	smoothing function of an interpolation domain

Chapter 1. Introduction

1.1. Background

Partially saturated soil is defined as a three-phase media consisting of a deformable soil skeleton and two fluid phases (water, air). It is a state of the soil (Gens et al., 2006; Sheng, 2011) falling within the range between the dry and saturated conditions, dependent on how much fluid is in pores of porous media. The majority of soil structures are constructed in soils well above the groundwater table, which usually are partially saturated over their entire service life (Wheeler & Sivakumar, 1995; Vanapalli et al., 1999). Thus, unsaturated soil mechanics is usually related to a variety of issues in industries, such as mining (e.g. hydromechanical processes of heap leach materials, mine tailings, mineral products such as coal, stored mine wastes, geo-covers placed on mine wastes on rehabilitation), geo-environmental engineering (e.g. thermal-hydro-mechanical process of deep geological storage or disposal for the long-term confinement of heat-emitting, high-level nuclear waste) and geotechnical engineering. To illustrate how significant unsaturated soil mechanics is in geotechnical engineering, the three most frequently encountered problems involving partially saturated soils in Australia are discussed as follows:

Foundation and pavement design/construction: Expansive and collapsible soils pose one of the most problematic issues geotechnical engineers have to face. In this concern, Australia is one of the countries with the broadest coverage of expansive soils. According to investigations, they cover 20 per cent of the total area of the Australian surface soils (Richards et al., 1983). Given this, Australia is amongst the nations most affected by geotechnical problems related to this kind of soil, with damage associated with residential buildings and traffic infrastructure, which is estimated at millions of AU dollars annually (Li et al., 2014; Pupazzoni, 2020; Goetze, 2020), as can be seen in examples provided in Figure 1.1 and 1.2. Expansive or collapsible soils can be regarded as a particular form of partially saturated soils with the coupled hydromechanical characteristics. The practical analysis revealed that the failure mechanism of building footing and road structures on such soils is related to the occurrence and evolution of cracking due to excessive structure settlements as a result of soil movements in response to the wetting/drying process under the impact of the external environment (Li & Guo, 2017). Despite this, most conventional foundation or pavement practices are mainly based on fully saturated soil mechanics in which the influence of hydraulic behaviour is usually neglected for simplicity (Vanapalli & Oh, 2010). This conservative approach may lead to incorrect interpretation of failure and the lack of the efficiency and cost-effectiveness of design or construction procedures. Therefore, intensifying research activities in unsaturated soils mechanics and expanding

the application thereof to the practices of residential construction projects is incredibly significant in Australia.

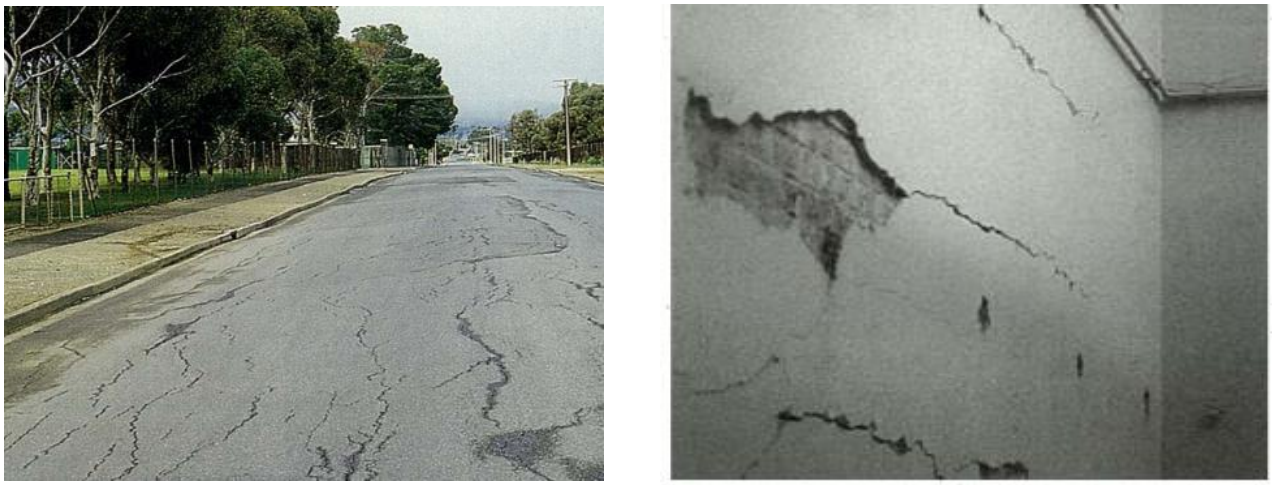

(a) (b)

Figure 1.1. (a) A cracked road in Adelaide, Australia (b) A cracked wall of the South Australia Art Gallery, Adelaide, Australia (Considine et al., 1984).

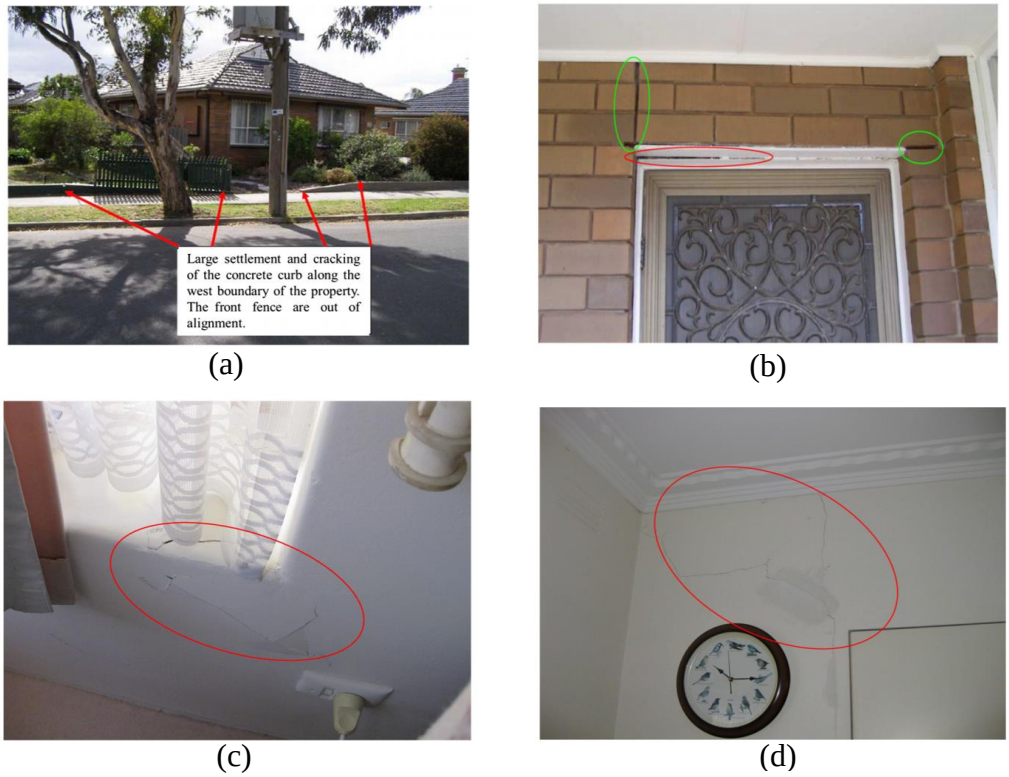

(a) (b)

(c) (d)

Figure 1.2. (a) Large settlement and cracking of the concrete curb (b) Distortion above the front entry door (c) Crack on the interior wall above the doorway to the kitchen (d) Cracking below a window of a bedroom of a residential building in a southwest suburb of Melbourne, Australia (Li & Guo, 2017).

Rainfall-induced landslide: Landslides have become increasingly severe and frequent in Australia among the other most frequent natural hazards, leading to serious safety problems and substantial economic losses (Buscarnera, 2010). For instance, Leiba (2013) has documented reports of at least 138 people killed and 114 others injured by 114 different landslides from 1842 to 2011; approximately 370 buildings destroyed or damaged by 83 slope failure events; 300 other landslides during the 2000-2011 period, causing severe disruptions or damages to strategic infrastructure (roads, railways, bridges) as seen in Figure 1.3 - all of which are estimated to cost approximately $82 million AU dollars throughout the period between 1842 and 2011 in Australia. Furthermore, as reported in the Australian Building Codes Board (ABCB), the Australian Geomechanics Society (2015, p.5) claims that "*The most common cause of landslides in Australia is water infiltration*". These statistics can be a serious wake-up call for the Australian geomechanics community to devote increasing attention to the issues of rainfall-induced landslides. Most importantly, the triggering of rainfall-induced landslides is closely linked to the failure mechanisms of unsaturated soils. A piece of evidence points strongly to this conclusion that the decrease of suction and surface-tension effect due to the wetting process under heavy rainfalls is responsible for the swelling heave and the loss of shear strength that trigger geostructural collapses. Therefore, putting forward a serious attempt to improve the understanding of the behaviour of unsaturated soils is a worthwhile contribution to the development of hazard assessment methodologies pertinent to rainfall-induced landslides.

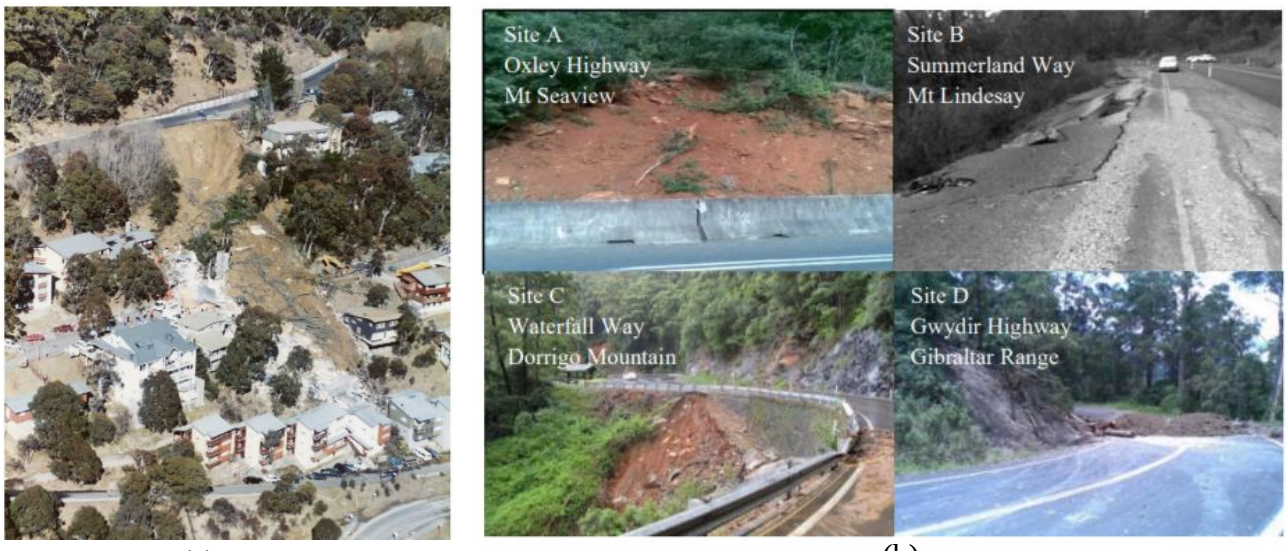

(a) (b)

Figure 1.3. (a) Thredbo landslide (Leventhal & Kotze, 2008) (b) Typical landslides in Northern New South Wales, Australia (Ravindran et al., 2019)

Embankment dam engineering: Australia occupies the world's driest inhabited continent, with a great susceptibility to drought. As a drought-affected country, acknowledging the severe devastation of droughts on the landscape, the agricultural economy and personal lives, the Australian Government

has been considering building more and more small earth dams. These dams are known as water supply reservoirs, as one of the essential drought mitigation actions in such harsh conditions. The safety of dams is dependent on the changes of water content and pore-water pressure due to the potential seepage through the structure of the dams (see an example in Figure 1.4) and the compaction of the soil as fill material in both construction and operation stages. All these features should be investigated and interpreted using unsaturated soils mechanics.

Figure 1.4. Talgai dam leak in Southern Queensland, Australia (Bavas et al., 2020)

Given the importance of unsaturated soil mechanics, the behaviour of partially saturated soils has received significant attention recently across fundamental and practical levels (Gens et al., 2006; Zhou et al., 2018; Hu et al., 2014). Despite some successes, obtaining an adequate understanding of their behavioural features, associated with the complicated interactions between the various phases (solid, water, air), is still challenging in the field of computational geomechanics (Sheng, 2011), leading to over-or under-engineering in geotechnical practices. In particular, it is neither straightforward convincingly demonstrated how the coupled hydro-mechanical behavioural features of various loading and hydraulic paths are coherently incorporated into a constitutive framework, consistent with the nature of physical thermodynamics or how it is adequately solved using computational methods. The existing numerical approaches are, therefore, for the most part, not rigorous and somewhat incomplete to reflect the actual failure mechanisms of partially saturated soils. That could hinder the development of state-of-the-art numerical techniques for facilitating a better prediction of geotechnical hazards.

1.2. Aims and Scope

Failure mechanisms of geohazards have been extensively investigated and elucidated in a wide range of laboratory tests on partially saturated soils, ranging from the microscopic scale (e.g. X-ray computed tomography, Scanning Electron Microscopy images, Mercury Intrusion Porosimetry) to the macroscopic scale (e.g. isotropic compression, direct shear, triaxial shear). These experiments

reflect essential features of the coupled hydro-mechanical behaviour under different loading and saturation conditions, such as irreversible swelling/shrinkage upon wetting/drying, load/deformation-dependency of capillary irreversibility, together with effects of hydraulic irreversibility on shear strength, stiffness, and dilation. A constitutive modelling and numerical method being able to predict the soil behaviour under a wide range of both mechanical loading and saturation conditions is required for the prediction of geotechnical failure involving partially saturated soils to improve the safety and cost-efficiency of geotechnical designs and construction. This is a challenge given the complex and coupled hydro-mechanical interactions at the grain scale that intrinsically govern the macro inelastic responses.

In line with the goal mentioned above, this thesis focuses on a new generic thermodynamics-based approach which is developed as a versatile means to connect all essential characteristics of partially saturated soil behaviour under a wide variety of both loading/unloading and wetting/drying conditions. It aims to bring benefits in achieving a good balance between simplicity, number of parameters and performance in the derived constitutive models. Fundamentally, this thesis attempts to provide a more rigorous way to capture the coupled mechanical and hydraulic dissipations produced by the grain scale interaction between particle rearrangements due to frictional sliding and rupture of water menisci. In thermodynamics-based continuum modelling, these coupled grain-scale processes can be represented by plastic strains and an irrecoverable degree of saturation. Due to the nature of the grain-scale interaction, the thermodynamic forces associated with these internal variables should be dependent on their rates, in addition to stress and suction. In reflecting on this mechanism, a generic form of dissipation potential or some kinematic constraint equations are pursued to result in a single yield surface and two flow rules with a single “plastic” multiplier, encapsulating the strong coupling between plastic strains and irrecoverable degree of saturation. This automatically leads to simultaneous activation of both hydraulic and mechanical dissipative mechanisms upon yielding, and hence different hydro-mechanical responses in wetting-drying and loading-unloading paths. The proposed formulation allows quantifying the amounts of hydraulic and mechanical energy dissipations while always guaranteeing the thermodynamic admissibility of the derived models. It is noted that explicit representations of grain-scale details are missing in the model, given the proposed approach is based on continuum mechanics interpreted as the averaged behaviour over a particular volume element. Only the effects of grain-scale mechanisms appear at the continuum scale through the use of two internal variables. This continuum-based approach, despite still being phenomenological, is computationally efficient and hence will allow modelling practical geotechnical engineering problems with reasonable computational costs when implemented in a powerful computational platform for the solutions of Boundary Value Problems (BVPs).

On the basis of the proposed general approach, a specific thermo-mechanical framework is systematically constructed to describe the inter-dependence between mechanical and hydraulic yielding responses in conditions of homogeneous deformation at a material scale, with emphasis on the concept of the critical state. The basis of this framework is the isotropic compression interaction between volumetric and hydraulic energy dissipations, which are vanished to make room for the shear dissipation occupying the total dissipation at the critical state. The whole model, formulated under the infinitesimal strain assumption, is derived from two explicitly defined free energy and dissipation potentials to address a range of experimental features obtained from drained and undrained tests, warranting a smooth transition between different regimes/responses (e.g. saturated and partially saturated, isotropic compression and triaxial shear, hardening and softening). This model provides a path-dependent hydraulic response, reflecting the nature of the hydro-mechanical interactions at the grain scale while eliminating the use of a separate Soil Water Characteristic Curve (SWCC). The benefits are the reduction in the number of parameters in conjunction with the identification and calibration of all model parameters from standard tests. In this model, it is assumed that the partially saturated soil behaves isotropically in both cases of recoverable and irrecoverable deformation/saturation, although it is acknowledged that the behaviour of wet granular materials is realistically anisotropic due to highly inhomogeneous textures due to the effects of liquid bridges.

Hydro-mechanical coupling is also indispensable for the localised failure, which induces strong non-homogeneous deformation and fluid distribution within a variably saturated soil structure, leading to the size-dependent constitutive behaviour and breaking down the classical homogeneous assumption. Experimental observations in several triaxial shearing tests on partially saturated soils indicate that the onset and orientation of localisation bands in partially saturated soils are intrinsically dependent upon different mechanical loading and saturation conditions, besides material properties. The localisation band splits the soil specimen into two separate zones (inside and outside this band), where they behave very differently under the condition of total stress equilibrium with strong variations in strain and saturation degree. This requires an adequate description of the constitutive model to handle the transition from diffuse to localised modes, with an appropriate hydromechanical bifurcation criterion for partially saturated soils. In response to this concern, details on inclination and thickness of the shear band and specimen size will be embedded into the proposed generic formulation to establish a two-scale framework for addressing the lack of coupled hydro-mechanical effects of strain localisation in the existing continuum models. In this framework, the tangent stiffness with cross-coupling terms always guarantees hydro-mechanical coupling upon yielding, facilitating the bifurcation analysis for the onset of localisation and corresponding orientation of shear bands under different hydromechanical conditions. The introduction of features related to sizes of the shear band

and specimen in the constitutive relations benefits it to give more correct predictions of the mixed material-structural response and size effects of partially saturated soils. It is noted that this framework is only to capture essential characteristics of the macro behaviour observed in triaxial shear tests under drained conditions while temporarily ignoring undrained conditions. Besides, this thesis only investigates localised failures under the forms of a single tabular shear band, which is assumed to remain unchanged, while issues related to the multiple localisation bands are outside the scope of the present thesis.

To investigate hydromechanical coupling issues in solving BVPs, a new mathematical framework of the coupled flow deformation process is developed. It encompasses the aforementioned homogeneous constitutive relationships and a mixed form of the governing conservation laws for three-phase porous media based on the mixture theory. It is assumed that this framework is only applicable for modelling laminar flow, thus paving the way for the appropriate use of Darcy's law. The obtained formulation implemented in a Smoothed Particle Hydrodynamics (SPH) code (Bui et al., 2008) for the Boundary Value Problems solutions. The use of SPH, a mesh-free method, allows tackling failures involving large deformations in geotechnical engineering (Bui et al., 2008; 2011) and avoiding mesh distortion issues usually encountered in Finite Element (FE) simulations involving large deformations. The proposed SPH-based approach results in a simple, highly efficient and relatively inexpensive computation framework that do not impair the advanced performance in predicting geotechnical failures when subjected to diverse hydromechanical external forces and mixed-boundary conditions (e.g. infiltration-induce slope instability, bearing capacity of partially saturated soils under shallow foundations,). In comparison with existing numerical methods for porous media, the current method inherits advanced features of the above-described generic thermodynamic approach and its derived constitutive models, inspired by the strong hydro-mechanical coupling at the grain scale, allowing for a better representation of responses of each material point. Solving all balance laws through a single set of Lagrangian particles in SPH and updating stress-like variables based on a unique hydromechanical yield locus bring an effective solution in simplifying the computational procedure. Noting that the focus of the current SPH-based approach is on improving the performance at the constitutive level to better reflect the intrinsic failure mechanisms of partially saturated soils and not on algorithms for more accurate numerical simulations of BVPs. Therefore, simple and proven algorithms (Bui et al., 2008; Bui & Fukagawa, 2011) make the numerical implementation adequate and acceptable in simulating essential behavioural features instead of pursuing high-performance algorithms.

1.3. Outline of the thesis

To address aims and scopes, this thesis is organised into seven Chapters, proceeding from generic to specific formulations, homogeneous to inhomogeneous deformation conditions and material to structural scales to provide a thorough picture of modelling partially saturated porous media. After the significance, aims, scope and outline of this thesis in this Chapter, the contents of the six other successive chapters are briefly summarised as follows:

Chapter 2 is to undertake a literature review for providing background and outstanding issues on the problems under consideration relevant to aims and scope, as mentioned in Chapter 1. This chapter first provides a comprehensive review on salient features of the fully coupled hydro-mechanical behaviour of partially saturated soils at the continuum level observed in different suction-controlled and water content-controlled tests. It is followed by an analysis of hydromechanical dissipative mechanisms drawn from both micro-scale reasoning and experiments. These physical observations are then used as a basis for a comparative analysis to weigh the pros and cons of existing continuum models for partially saturated soils. Another emphasis of this literature review is placed on Boundary Values Problems involving partially saturated soils for computational geomechanics. This makes an overview of recent improvements in numerical approaches (e.g. SPH, FEM, Generalised Interpolation Material Point Method (GIMPM) for predicting geotechnical failure with the focus on constitutive models for partially saturated soils. This Chapter also discusses the current progress existing studies made towards addressing the hydromechanical effects on strain localisation, which are discussed after a brief review of essential characteristics related to how the onset and evolution of shear bands are dependent on different loading and hydraulic paths and vice versa. At the end of this Chapter, several discussions are made to gain an overall picture of both advantages and limitations of previous studies, motivating the development of a new computational approach for modelling coupled hydro-mechanical responses of partially saturated soils at both material and structural levels.

The aim of **Chapter 3** is to provide a generalised framework of coupled flow deformation processes, opening the path for more extensive theoretical developments in the successive chapters of this thesis. In this framework, to describe the three-phase transport in unsaturated porous media, the mixture theory is used to furnish field equations of kinematic variables (e.g. porosity, saturation degree, solid velocity, Darcy seepage velocity) after reviewing relevant basic concepts and assumptions. These equations are coupled with the novel homogeneous constitutive law (e.g. stress-strain, SWCC) of a generic thermodynamics-based model based on a full coupling between plasticity and hydraulic irreversibility using mechanisms at the microscale for physical interpretations. General formulations

of the tangent stiffness tensor and semi-implicit stress return algorithm of the proposed constitutive model are then constructed.

In **Chapter 4**, following the proposed general formulation in Chapter 3, a particular constitutive model for unsaturated soils is suggested and investigated to indicate good potentials of the generic approach in balancing simplicity and predictive performance. In the course of the formulation development of this model, new specific forms of free energy and dissipation potentials are assumed, taking into account some essential critical-state-based features of suction-and water content-controlled experiments at low stresses. A systematic procedure is employed to construct a Modified Cam-Clay family yield surface and corresponding flow rules. Dissipation properties follow this to investigate the thermodynamic admissibility and coupling level between plasticity and hydraulic irreversibility. This chapter then describes the numerical implementation algorithms and their verification. The parameter identification and determination are presented in the next part of the Chapter, followed by the validation and demonstration of the capabilities of the proposed model in performing fully coupled hydro-mechanical behaviour from a wide range of stress/suction paths and testing conditions. The advantages of this model, compared to a well-established one, the Barcelona Basic Model (Alonso et al., 1990), are also highlighted.

Chapter 5 is devoted to developing a double-scale approach describing localised failure mechanisms of partially saturated soils for an inhomogeneous representative volume element (RVE) under drained conditions. This Chapter starts with general fundamental relationships with the evolving thickness of the localisation band. It is derived by using generic expressions of Helmholtz energy and dissipation potentials of a new thermo-mechanical approach based on kinematic enhancements accounting for the difference in the hydromechanical response outside and inside the shear band. This is succeeded by the formulation of a specific two-scale constitutive model through specifications of both energy and dissipation potentials inspired from experimental observations of suction-controlled triaxial tests based on the homogeneous model developed in Chapter 4. This framework is then applied to the construction of macro constitutive structures for a volume element containing a shear band, covering a physically meaningful transition of responses over the two regimes: homogeneous inelastic deformation, onset of localisation and post-localisation. The Chapter then moves on to describe the numerical algorithms for detecting the discontinuous bifurcation condition and modelling the post-localisation behaviour of the generic model. A numerical verification is then provided before giving several numerical examples to analyse and validate the performance of the derived specific model.

Chapter 6 is concerned with the development of SPH formulation and algorithms for the simulations of BVPs involving coupling between fluid flow and deformation fields in porous media employing

the generic three-phase flow framework and formulations in Chapter 3. Particular forms of Darcy seepage velocity, saturation degree rate, solid velocity rate, strain rate and porosity rate are first summarised based on expressions provided in Chapter 3. This is followed by formulations of two specific hydromechanical constitutive laws based on Drucker-Prager and Modified Cam-Clay yield criteria, where their behavioural features are briefly discussed. The developed multi-phase flow framework is then used for the formulations of the SPH approximation for the solutions of field equations in the temporal and spatial domains. Key features (e.g. time integration, stress return algorithm, boundary treatments) are presented in the implementation procedure of the proposed numerical approach and accuracy is then verified by several examples. Towards the end of this Chapter, the performances of this SPH-based approach in predicting failures of partially saturated soils are elucidated through BVPs under different loading and hydraulic conditions and validated against several sets of experimental data.

Finally provided in **Chapter 7** are a summary and conclusions on the most salient contributions of the present numerical approach. Limitations of this study are then identified, and several recommendations are made for potential future lines of research for further improvements.

Chapter 2. Literature review

2.1. Introduction

A better understanding of how unsaturated soils behave in constitutive modelling at the material level will help to improve the safety and cost-efficiency of geotechnical designs and construction. This process is central to any numerical simulation in geotechnical engineering projects as it captures mechanisms of soil collapse. In recent decades, there have been numerous studies of experimental, constitutive models and computational methods at different levels of complexity and applicability to advance knowledge of the response of partially saturated soils. In an attempt to assess the current progress of these existing studies, in this Chapter, a comprehensive review, focusing on constitutive models for partially saturated soils, is carried out to address two critical aspects of the aims of this thesis (see Chapter 1) as follows:

Intrinsic mechanisms behind the hydromechanical behaviour of soil in constitutive modelling of partially saturated soils: Concerning this aspect, data from several experimental tests are discussed to highlight important behavioural features of partially saturated soils under different stress paths and hydraulic states at both particle and material scales. This is to emphasize that the nonlinear behaviour of unsaturated soils is governed by the fully coupled hydro-mechanical dissipation phenomenon due to the irrecoverable movement of particles and fluids, which serves as a benchmark for reviewing the performance of existing constitutive models. In this review, instead of examining several models on a case-by-case basis, these models are grouped and assessed in relation to the underlying mechanisms governing the responses of partially saturated soils, with a focus on plasticity theory and thermodynamics-based formulation at the continuum level. This review leads to the conclusion that the underlying hydromechanical dissipation mechanism is usually accounted for in existing constitutive models by using separate evolution rules for plastic deformation and saturation, linked with two yield conditions for stress and suction. This is not sufficient to account for the hydro-mechanical coupling and hence considered as an outstanding issue. The conclusion provides a basis for the development of a new thermo-mechanical approach to constitutive modelling of partially saturated soils that allows the use of a single yield surface, incorporating the effects of both stress and suction.

BVPs of partially saturated soils: In response to this problem, the limitations of existing numerical methods in predicting failure mechanisms of partially saturated soils for BVPs are also discussed, highlighting the lack of an adequate hydromechanical model for capturing different responses in

wetting-drying and loading-unloading paths at the material level despite its importance in capturing failure mechanisms. The primary purpose of this review is to give a background for the development of a new SPH method, possessing the advantages of SPH in addressing mesh-distortion and computationally expensive problems encountered in FEM and IGMPM, respectively, for predicting fully coupled solid deformation-fluid flow in partially saturated deformable porous media.

Additionally, a review of several experimental results is provided to interpret localised failure mechanisms of partially saturated soils briefly. Given these mechanism features, this chapter analyses several existing continuum models to examine whether they can adequately reflect the onset of localisation and post-localisation responses under different hydromechanical conditions. Through this review, it can be found that the effect of thickness/orientation of shear bands and their dependence on irreversible saturation in the modelling of partially saturated soils has been missing in the literature, despite its importance in governing post-localisation behaviour. This serves as a motivation for the development of a new constitutive model for partially saturated soils, possessing two scales of hydro-mechanical responses (meso and macro), in this study.

2.2. The behaviour of partially unsaturated soils

2.2.1. Macro behaviour

Experimental observations under different loading and hydraulic paths

The behaviour of partially saturated soils has been investigated extensively in a range of constant net stress wetting/drying (Cunningham et al., 2003; Tarantino, 2009; Sharma, 1998; Raveendiraraj, 2009), constant suction triaxial (Alonso, 1987; Cui & Delage, 1996; Wheeler & Sivakumar, 1995; Chen, 2007; Macari et al., 2003), constant water content triaxial (Thu et al., 2006; Marinho et al., 2016; Rahardjo et al., 2004; Maleki & Bayat, 2012; Li, 2015; Zhang, 2016) and constant suction direct shear tests (Hossain & Yin, 2010; 2015). Through the experimental results observed in these tests, several vital behavioural features of partially saturated soils can be discussed, as follows:

Hydraulic path: The water retention behaviour (or SWCC) is represented by the constitutive relationship between the saturation degree (S_r) (or volumetric water content, ϕ_w) and suction (s), which varies across three different regimes of water saturation (capillary, funicular, and pendular). As can be seen in Figure 2.1a, the pendular regime involves very low levels of saturation degree, while the capillary regime is related to the residual state of saturation degree at $S_r \approx 1$. The transition between pendular and capillary regimes is reflected through the funicular regime by a sharp change in saturation degree. In the literature, to describe the unique reversible link between suction and saturation degree, different mathematical expressions are proposed (Brooks & Corey, 1964; van

Genuchten, 1980; Fredlund & Xing, 1994), without accounting for the mechanical history, as compared in Figure 2.1b and written in the following forms:

$$S_r = [1 + (a_v s)^{n_v}]^{-m_v} \text{ (van Genuchten, 1980)} \tag{2.1}$$

$$\begin{cases} S_r = 1 & s < s_e \\ S_r = \left(\frac{s_e}{s}\right)^{\lambda_b} & s > s_e \end{cases} \text{ (Brooks \& Corey, 1964)} \tag{2.2}$$

$$S_r = \left[ln\left(2.71828 + \left(\frac{s}{a_f}\right)^{n_f}\right)\right]^{-m_f} \text{ (Fredlund \& Xing, 1994)} \tag{2.3}$$

where a_v, n_v, m_v, λ_b, a_f, n_f, m_f are the material parameters and s_e is the air entry value.

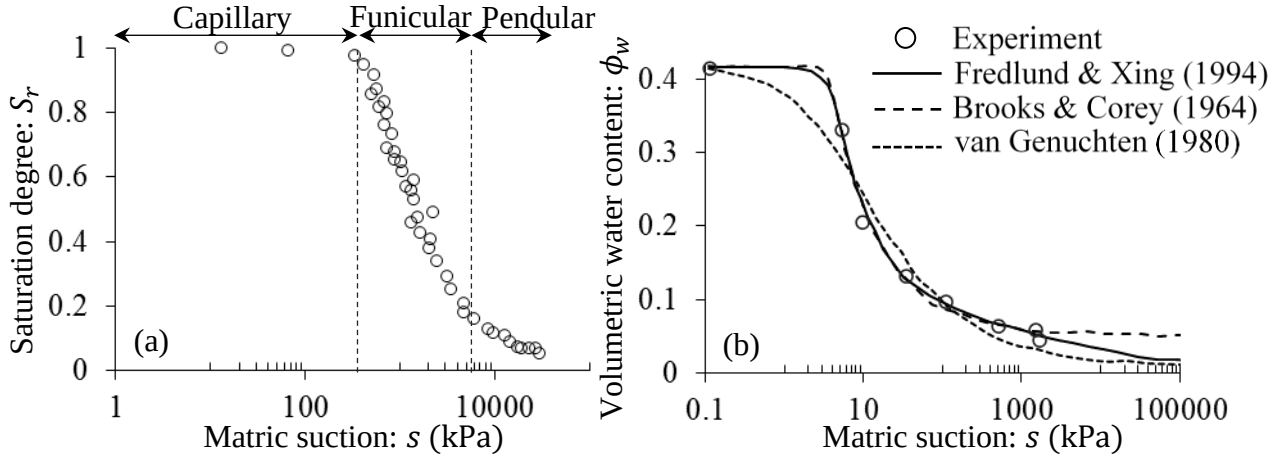

Figure 2.1. (a) Soil-water characteristic curve under a constant net stress test on clayey silt (after Cunningham et al., 2003) (b) Comparison of one set of soil-water characteristic curve data fitted using various models for a silty loam soil (after Sillers & Fredlund, 2001)

However, the SWCC of a soil sample is experimentally observed not to be unique due to its dependence on changes in stress (see Figure 2.2a) and volume (see Figure 2.2b) (Vanapalli et al., 1999; Tarantino, 2009; Miller et al., 2008; Mbonimpa et al., 2006; Masin, 2010). In this case, for example, Gallipoli et al. (2003) added void ratio (e) to the form (van Genuchten, 1980), as given in Eq. (2.4), to capture the shifting of the water retention curve along the axis of suction governed by the volume change as follows:

$$S_r = \left[1 + \left(a_g e^{b_g} s\right)^{n_g}\right]^{-m_g} \tag{2.4}$$

where a_g, b_g, n_g and m_g are material parameters.

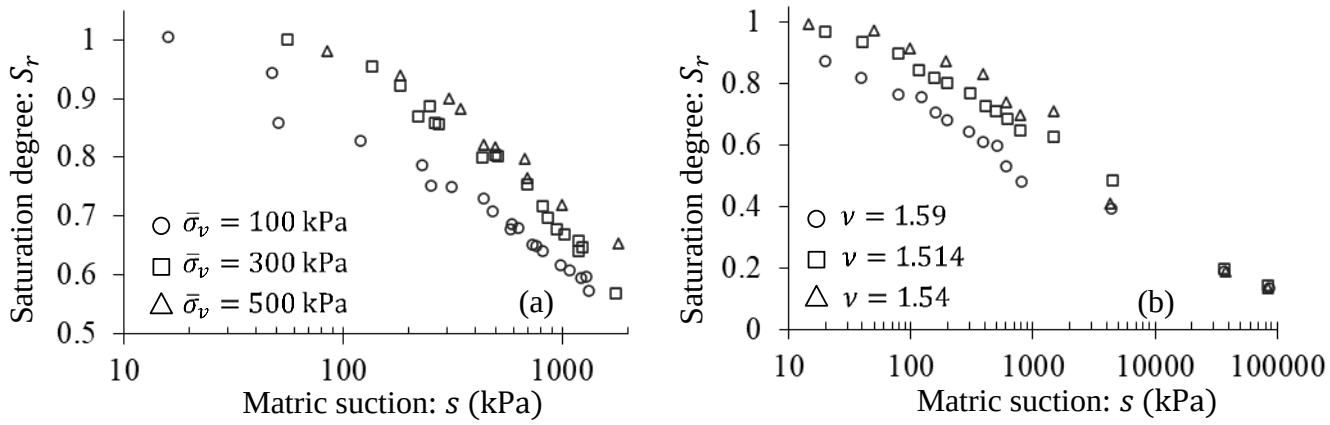

Figure 2.2. Water retention curves (a) at different vertical stresses (after Tarantino, 2009) (b) at different specific volumes (after Vanapalli et al., 1999)

Furthermore, Figures 2.3a and 2.3b illustrate that a sample of partially saturated soil can exhibit the same level of suction at more than two different saturation degrees of wetting and drying paths, reflecting the irreversible characteristic of the hydraulic response (Sharma, 1998; Tarantino, 2009). Also observed in Figures 2.3a and 2.3b is the irrecoverable change in volume during wetting-drying cycles. This feature is one of the indicators of the interdependence between plasticity and capillary irreversibility. The wetting-drying difference in SWCC is accounted for in several hydraulic models in the literature (Li, 2005; Nuth & Laloui, 2008). For instance, Nuth & Laloui (2008) proposed a hydraulic yield criterion based on an elastoplastic analogy between mechanical consolidation and the retention curve, as illustrated in Figure 2.4.

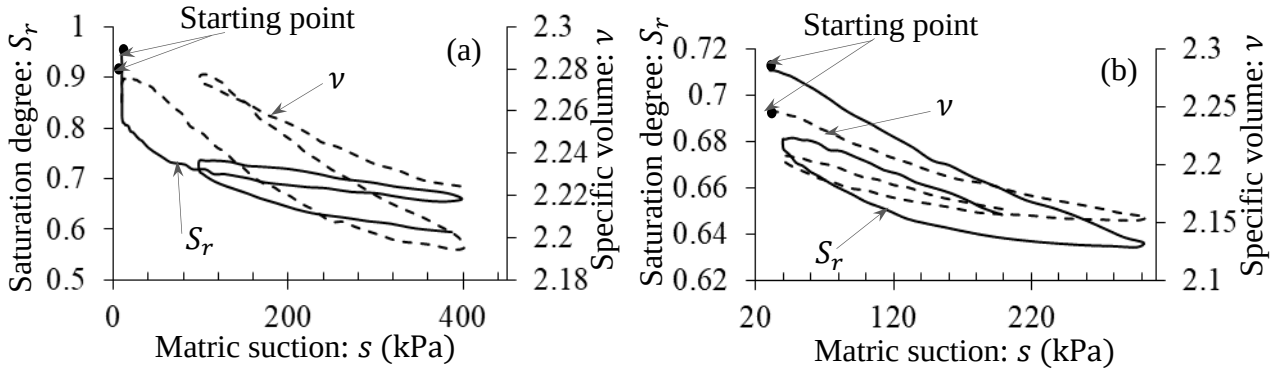

Figure 2.3. The wetting-drying difference in water retention curves under constant net stress tests (a) at $\bar{p} = 20$ kPa (after Sharma, 1998) (b) at $\bar{p} = 10$ kPa (after Raveendiraraj, 2009)

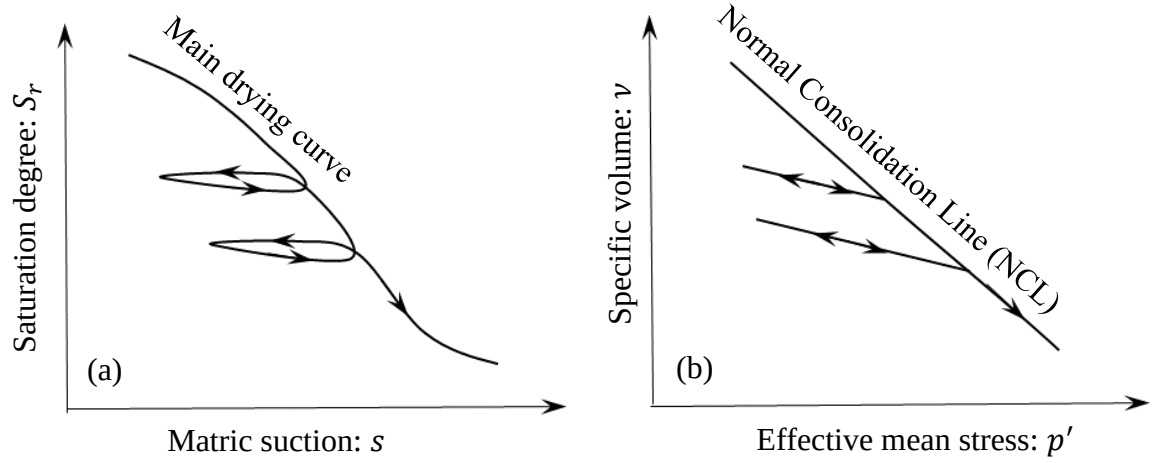

Figure 2.4. The analogy between (a) mechanical consolidation plasticity and (b) hydraulic irreversibility (Nuth & Laloui, 2008)

Isotropic compression path: The data in Figures 2.5-2.6 demonstrate experimentally observed responses of soils in isotropic compression tests at different suction levels. In particular, at each level of suction, the stress path is at first reversible in both mechanical and hydraulic responses. In this stage, no profound change in the slope of the Normal Compression Line (NCL) is observed over the suction range. Once the stress path reaches the initial yield point, irreversible changes in both the specific volume and saturation degree activate and develop simultaneously (see Figures 2.5-2.6). During this yielding stage, the initial yield stress is observed to increase if the suction gets higher (see Figure 2.7). NCL shifts with suction where the compression index was found to decrease (Alonso, 1987; Alonso et al., 1990; Cui & Delage, 1996; Zhang & Lytton, 2009; Zhan, 2003) (see Figure 2.5) or increase (Wheeler & Sivakumar, 1995; Matsuoka et al., 2002; Sun et al., 2000; 2004) (see Figure 2.6) with increasing suction. Figures 2.5-2.6 show that the degree of saturation is raised during compression, despite the constant suction. This, in turn, increases the compressibility of the soil. These observations are clear signs of coupled hydro-mechanical responses.

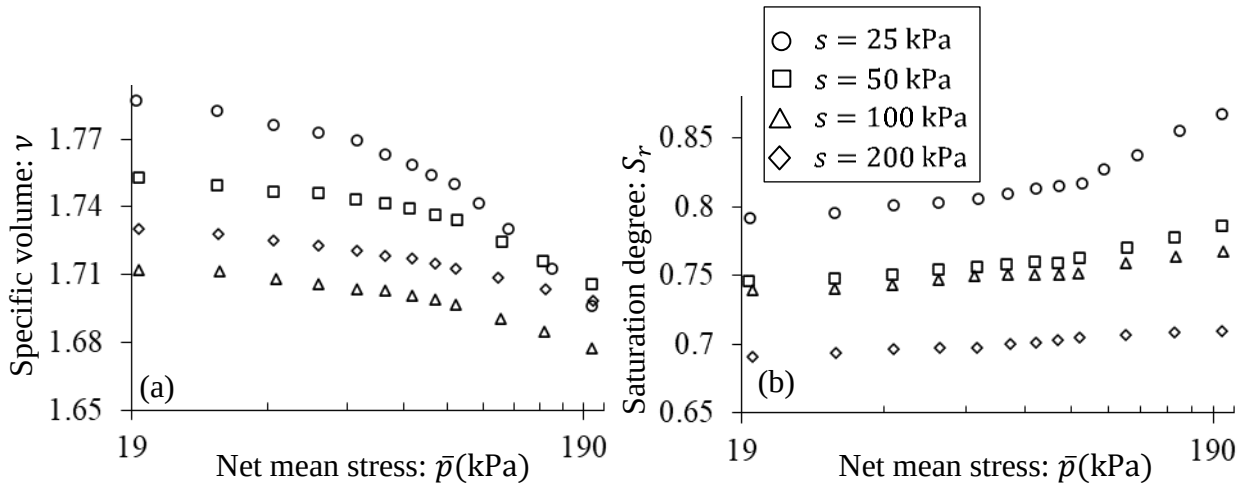

Figure 2.5. Drained isotropic compression test of the compacted partially saturated expansive clay (after Zhan, 2003)

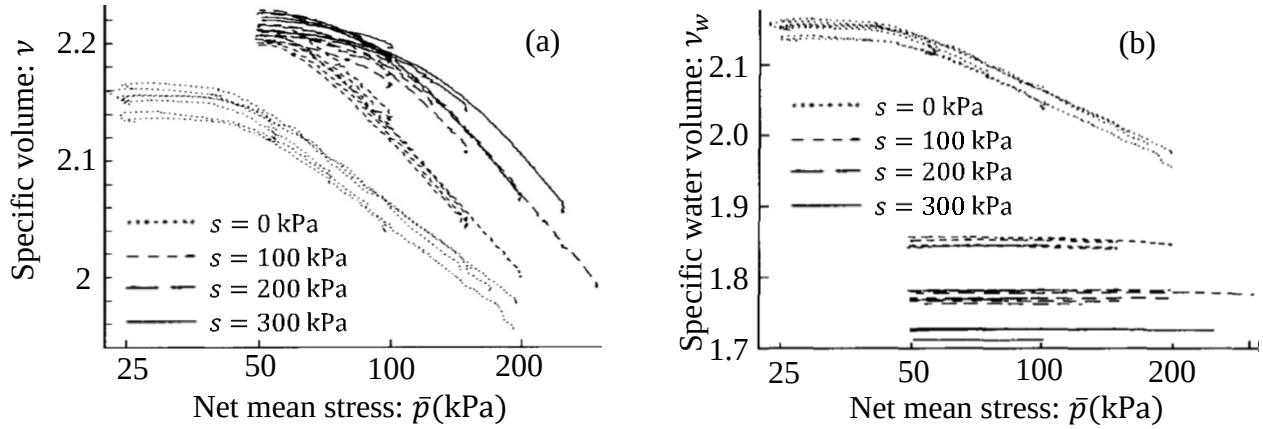

Figure 2.6. Drained isotropic compression test of the compacted speswhite kaolin (after Wheeler & Sivakumar, 1995)

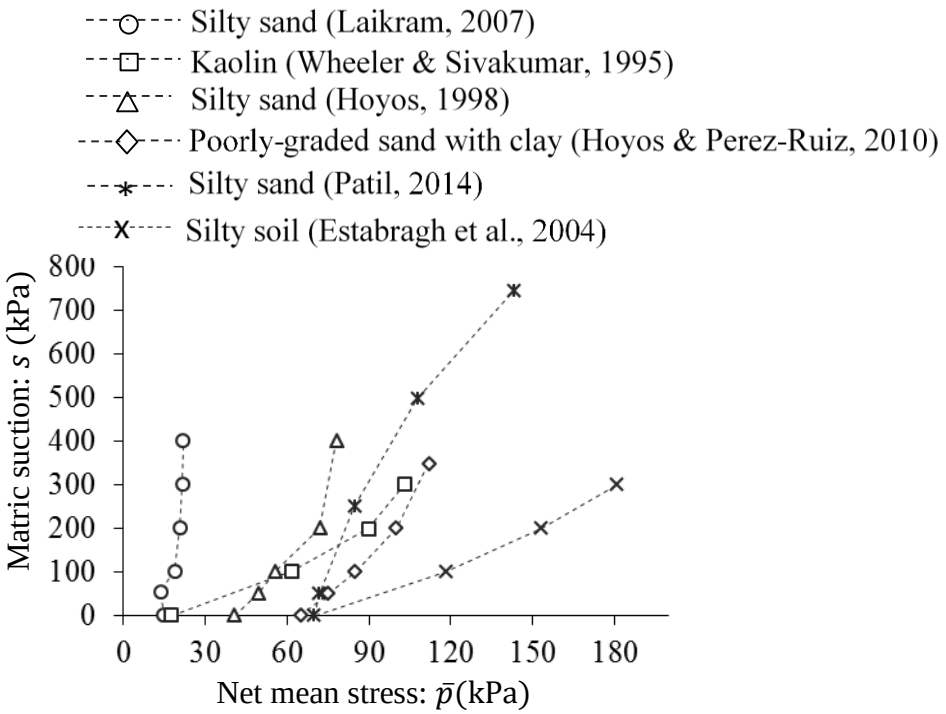

Figure 2.7. Comparison of different yield curves in the $\bar{p}$: s space for different soil compaction conditions

Next, experimental data of the undrained isotropic compression test at different levels of gravimetric water content (w) are investigated. As illustrated in Figure 2.8, the slope of NCL becomes steeper and more curved away from the initial yield point if the gravimetric water content increases. Decreases in suction and saturation degree are observed during loading, and they are more profound at the lower levels of gravimetric water content. Besides, Figure 2.9 reveals that there is a concurrent occurrence between the plastic volumetric strain and the irrecoverable saturation degree when both loading and wetting paths reach the yielding regime. From this point on, both NCL and SWCC exhibit the same yield points at any instant during further isotropic loading, reflecting the non-uniqueness and wetting-drying difference of SWCC induced by the loading-unloading process.

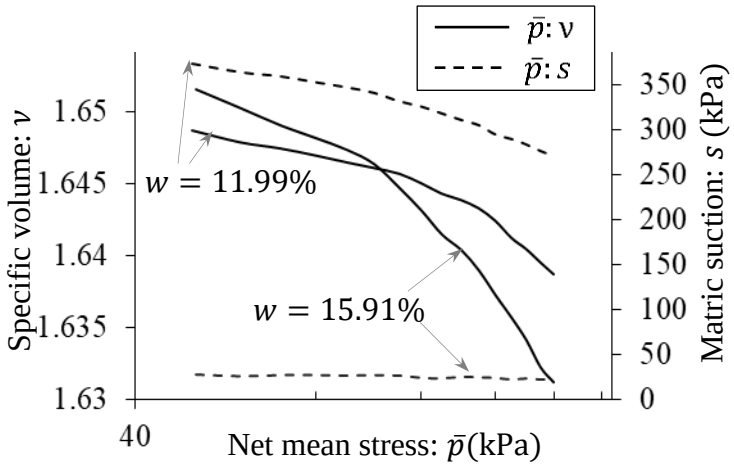

Figure 2.8. Undrained isotropic compression tests on the mixture of Fairbanks silt and Kaolin clay (after Li, 2015)

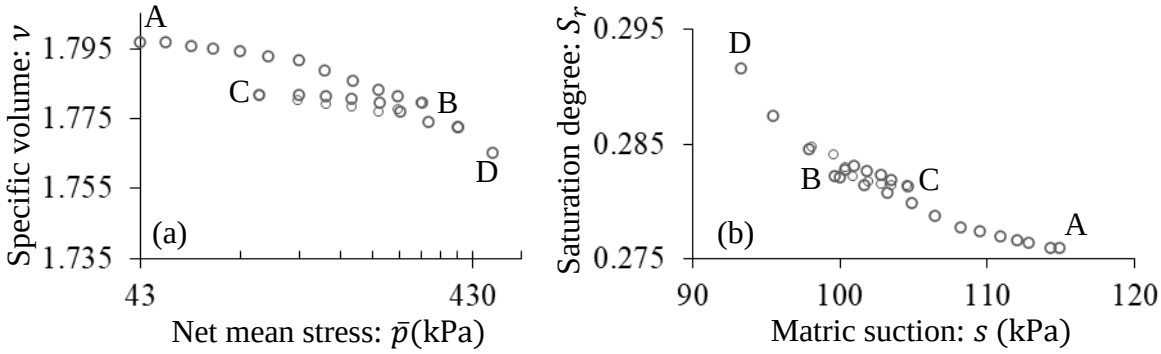

Figure 2.9. ABCD loading paths in undrained isotropic compression tests on Fairbanks silt at $w =$ 8.3% (after Zhang, 2016) (a) $\bar{p} - \nu$ (b) $s - S_r$

Shearing path: The plots presented in Figure 2.10 depict the experimental trend of shear response drawn from triaxial compression tests at different levels of suction and gravimetric water content. As can be seen, the sheared sample first experiences a negligible nonlinear response that can usually be considered as elastic behaviour, where a rapid increase in shear stress, volumetric strain and saturation degree is observed. This elastic stage is ongoing until the stress paths reach the initial yield points. The next stage involves the softening/hardening response with the activation and development of irrecoverable changes in the strain and saturation degree. Figure 2.11a illustrates that the yield loci expand with increasing suction in both $\bar{p}: q$ and $p': q$ spaces, indicating that the increase in suction results in a growth in the shear resistance of partially saturated soils. A gradual transition between hardening, perfect plasticity and softening responses under different suctions are demonstrated in Figure 2.10. The more dilative response is observed at lower suctions (see Figure 2.10a) and higher

gravimetric water contents (see Figure 2.10b). The capillary effect on dilation is also shown in Figure 2.11b, where the dilatancy ratio becomes greater with decreasing suction.

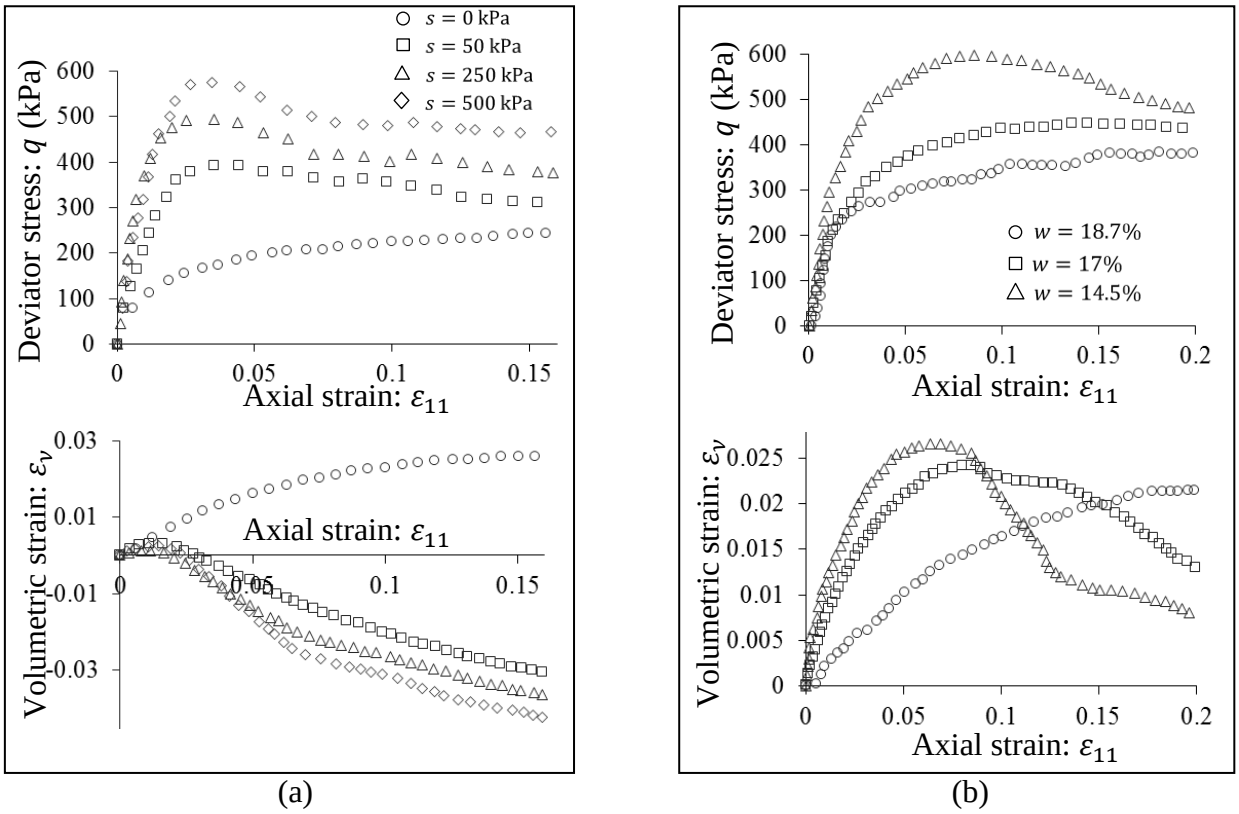

Figure 2.10. (a) Drained triaxial compression tests on compacted silty sand at $\bar{\sigma}_{33} = 100$ kPa (after Patil, 2014) (b) Undrained triaxial compression tests on residual sandy clay at $\bar{\sigma}_{33} = 150$ kPa (after Toll & Ong, 2003)

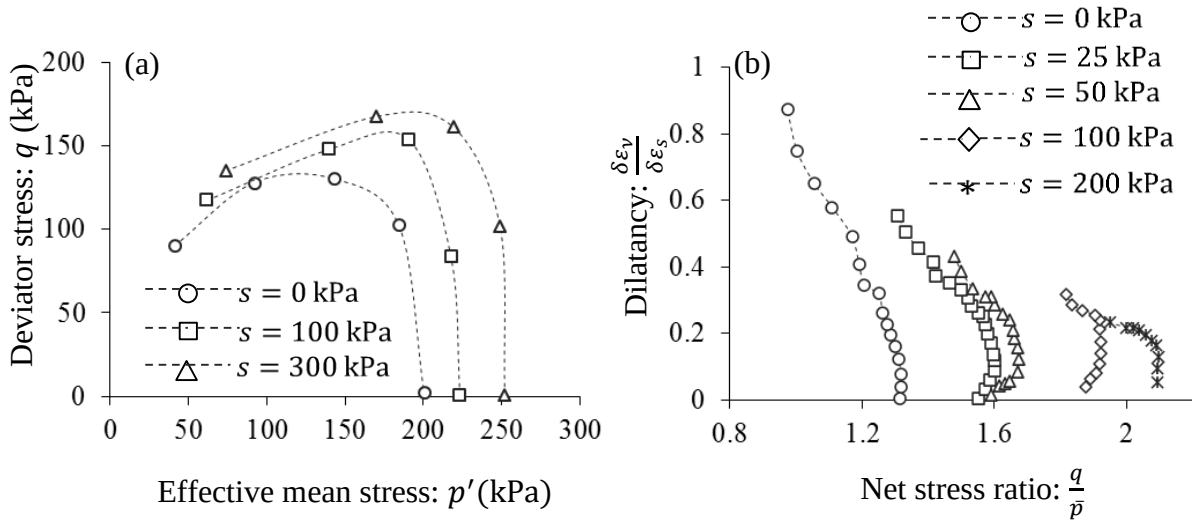

Figure 2.11. (a) Yield points at different suction levels (after Uchaipichat, 2005; Uchaipichat & Khalili, 2009) (b) Effects of suction on dilation in suction-controlled triaxial compression test on compacted Zaoyang clay at $\bar{\sigma}_{33} = 50$ kPa (after Chen, 2007)

At the end of the shearing process, changes in shear stress, volumetric strain and saturation degree/volumetric water strain become progressively slower until approaching the steady state, whilst the shear strain keeps changing, reflecting the critical state of partially saturated soils (see Figure 2.10). This is of great concern, given its importance for understanding the ultimate behaviour of the post-failure stage. With that in mind, the last periods have triggered numerous studies on the critical state of unsaturated soils, based upon the analysis of a large number of shear test results at the macro-level, which sometimes give rise to a heated debate about the constraints for the critical state, along with the existence and uniqueness/non-uniqueness of the critical state line. Most prominently, many, such as Zhao (2014), Chen (2007), D'Onza et al. (2011), Chiu (2002), Al-Sharrad (2013) and Toll & Ong (2003), agree that the increments of shear strength, volumetric strain, and notably saturation degree, are around zero, whilst the shear strain keeps changing at the ultimate state. This is related to the existence and uniqueness of the Critical State Line in $\bar{p}: q$ or $p': q$ space (see Figure 2.12) and Critical State Plane (CSP) in the $\bar{p}: q: s$ space (see Figure 2.13), with a constant slope regardless of the variations in suction (Sivakumar, 1993; Wheeler & Sivakumar, 1995; Lloret, 2011; Al-Sharrad, 2013; Tarantino, 2007). Suction only has effects on the upward shift in the position of CSL through creating tensile strength/cohesion for partially saturated soils, as shown in Figure 2.12a. They are then verified theoretically within the thermodynamic-based frameworks suggested by Zhao et al. (2014) and Li (2007). One must bear in mind that this is just one stand-point of particular concern: there are others about the nature of the steady state of partially saturated soils. Nevertheless, this viewpoint can be considered to be of sufficient significance, since it is suggested by a majority of experimental works on unsaturated soils with some theoretical clarifications and has advantages of simplicity and convenience, in the context of difficulties in defining actual critical state conditions for boned soils (Toll & Ong, 2003).

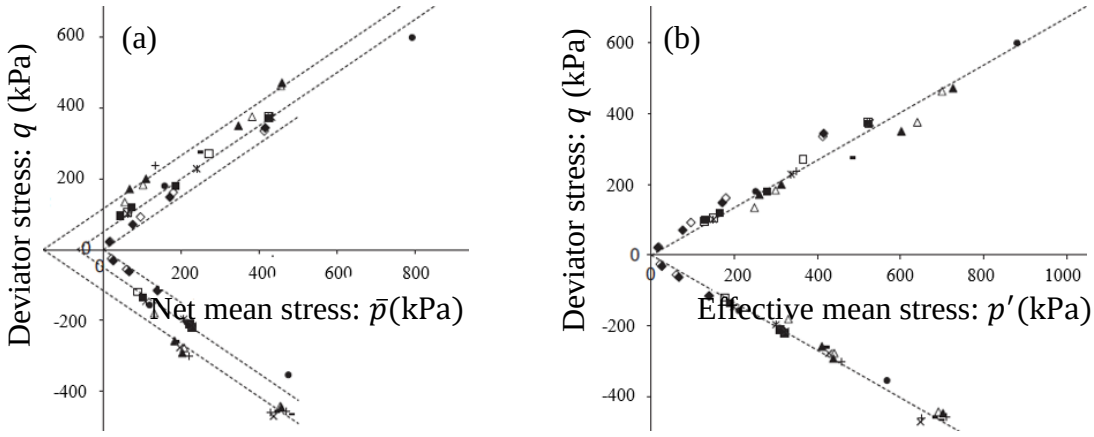

Figure 2.12. Critical state lines from suction-controlled triaxial tests (after Al-Sharrad et al., 2017) (a) in $\bar{p}$: q plane (b) in p': q plane

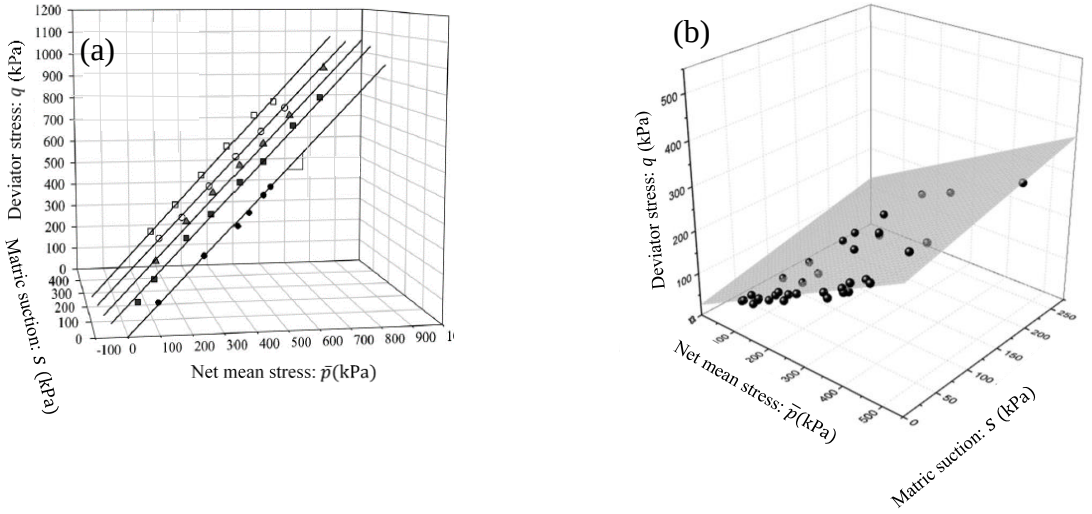

Figure. 2.13. Critical state planes in $\bar{p}$: q: s space from (a) drained triaxial tests (after Thu, 2006) (b) water content-controlled triaxial tests (after Marinho et al., 2016)

Summary of the coupling behaviour from the test at the continuum level

Given the experimental observations in different hydraulic and loading cases, it can be said that hydro-mechanical coupling is part of the intrinsic nature of unsaturated soil behaviour. It is reflected at the continuum level through the interactions between SWCC (hydro-) and stress-strain (mechanical) relationships. The results of these studies primarily reveal the dependence of strength and deformation characteristics on suction. In particular, when increases in suction do occur, the shear strength (Vaunat et al., 2007; Toyota et al., 2001), yield limit (Alonso et al., 1990; Wheeler & Sivakumar, 1995; Cui & Delage, 1996) and dilatancy (Ng & Zhou, 2005; Cui & Delage, 1996) increase; whereas the elastoplastic stiffness (Alonso, 1987; Alonso et al., 1990; Cui & Delage, 1996; Zhang & Lytton, 2009; Charlier et al., 1997; Geiser et al., 2000) decreases or increases (Wheeler & Sivakumar, 1995; Matsuoka et al., 2002; Sun et al., 2000; 2004), while the contribution of suction on the change in

elastic stiffness is generally minor, or even negligible (Alonso et al., 1990; Cui & Delage, 1996). All of the features described above are underpinned by the volume change behaviour related to swelling in the wetting process (suction decrease) and shrinkage in the drying process (suction increase), which is one of the most fundamental properties of unsaturated soils, according to Sheng et al. (2008). Accordingly, the equations of volume change, usually the equations of the normal compression line and loading/unloading line, reveal an essential basis for theory development of unsaturated soil mechanics, not only because they provide information on the constitutive relationship but also because they matter for the hardening laws. In this sense, through the experimental results obtained, there have been many attempts to propose different formulas for the volume variation. Many of them, such as Alonso et al. (1990), Fredlund & Rahardjo (1993) and Sheng et al. (2008), postulate that the normal compression line tends to shift with suction in the logarithmic mean stress-specific volume space. Although these results generate good predictions, there are still growing concerns about their inadequacies related to the role of the saturation degree under constant suction conditions, leading to several debates. For example, some studies (Sun et al., 2010; Zhou et al., 2012) show that the degree of saturation is raised during compression, despite the constant suction. This, in turn, increases the compressibility of the soil. In identical values of net stress, suction and volume, two soil samples may produce different degrees of saturation: the reason being that there are differences in the numbers of voids filled with bulk water and influenced by meniscus water. The two specimens are, therefore, distinct from each other in terms of the inter-particle contact forces, as a result of which their mechanical responses are not the same. Such evidence indicates the important role of saturation degree in understanding the behaviour of unsaturated soils. To address this, the influence of saturation change on the stress-strain response has been studied both theoretically and experimentally by several authors, such as Gallipoli et al. (2003), Wheeler et al. (2003), Sun et al. (2010). These studies found that there are also considerable changes in the texture of the granular material, characterized by comprising the volumetric strain, shear strength, yield stress, soil stiffness and dilatancy due to variations in the degree of saturation, corresponding with suction along the SWCC curve. Furthermore, the stiffnesses in geomaterials are different between drying and wetting paths at the same saturation. Drawing on the above discussions, both suction and saturation degree usually link together in SWCC and have considerable effects on the mechanical responses of unsaturated soils. Thus, it can be seen that water retention behaviour plays a fundamental role when studying the actual mechanism of wetting/drying-induced collapses in soil mechanics.

On the other hand, the effect of hydraulic behaviour on the mechanical strength is governed by several factors associated with the stress state (Nuth & Laloui, 2008; Masin, 2010; Uchaipichat, 2010; Miller et al., 2008), volume change (Gallipoli et al., 2003; Vanapalli et al., 1999; Pham, 2005; Nuth & Laloui,

2008) and soil density (Tarantino, 2009; Masin, 2010; Simms & Yanful, 2004; Mbonimpa et al., 2006; Sun et al., 2007). A range of those studies agree that the volume change (volumetric strain, porosity, and void ratio) during loading and unloading cause shifting of the water retention curve along the axis of suction. This can be explained by the observation that the specific volume variation modifies the dimensions of voids and connecting passageways between voids. A change of suction is henceforth required to be compatible with a given degree of saturation. To better gauge this coupling mechanism, Wheeler et al. (2003) suggest that only the irreversible part of the volumetric strain affects the translation of the primary drying and primary curve. The wetting-drying difference in SWCC, through the appearance of irrecoverable saturation, should be another matter of considerable concern for an in-depth understanding of how partially saturated soils behave. Regarding this, McNamara (2014) states that "Less mechanical energy is required to make dry soil wet than to make that wet soil dry". In light of the information gathered through these discussions, the interactive relationship between the hydraulic and mechanical processes must be the key to understanding the actual behaviour of unsaturated soils.

2.2.2. Micromechanical insights

In partially saturated soils, the distributions of sizes/shapes of both grains (Blonquist Jr et al., 2006; Heinse et al., 2007) and fluid pores (Gili & Alonso, 2002; Revil & Cathles, 1999) characterise soil properties. The interfaces between the three phases are governed by the grain surface profiles, their hydrophilicity and thermodynamic characteristics (Blake & Haynes, 1969; Bachmann et al., 2003; Goebel et al., 2004; Lourenco et al., 2012; Russell & Buzzi, 2012). Therefore, the above-described experimental features of hydro-mechanical coupling at the continuum level are intrinsically linked to the grain-scale phenomena related to grain arrangement and liquid-bridge distribution, which can be discussed with the focus on granular materials and water menisci as below:

Grain-scale properties of liquid bridges

Fluid pressures and surface tension, changes that occur with the variation of water content during the wetting/drying processes, have long been recognized as fundamental factors of the unsaturated soil condition for understanding the failure mechanisms of soils. They produce the capillary forces exerted by water menisci and affect the grain-to-grain contact behaviour. The behavioural mechanism of liquid bridges and air-water interfaces on the soil skeleton is considered as a debonding action upon wetting and a bonding action due to any suction increase. Soil grains are pulled together by the contractile films at interfaces between the wetting and non-wetting phases of these liquid bridges (see Figure 2.14). Furthermore, a specimen of partially saturated soils can be subjected to the same value of suction at more than two different saturation degrees of wetting and drying curves, reflecting their

dependence on the hydraulic history of responses. This phenomenon is the key feature of SWCC and attributed to geometric or ink-bottle effects, entrapment of a non-wetting phase and the shrinking and swelling of pores (Gan et al., 2013; Morrow, 1975; Tindall et al., 1999; Lappalainen et al., 2009; Pereira & Arson, 2013), and variations in contact angles during wetting and drying (Gan et al., 2013). The nature of this yielding hydraulic response lies in the irreversible movement of air-water interfaces and rate-independent hysteresis of the contact angle, which can be demonstrated through the difference in morphology of the water phase between drying and wetting processes at the same saturation degree, as seen in the experimental example in Figure 2.15. The here-mentioned microstructural phenomenon can be regarded as the physical mechanism of the irrecoverable wetting/drying process, associated with the irreversible changes of saturation at the macro-scale, as mentioned by Wheeler et al. (2003).

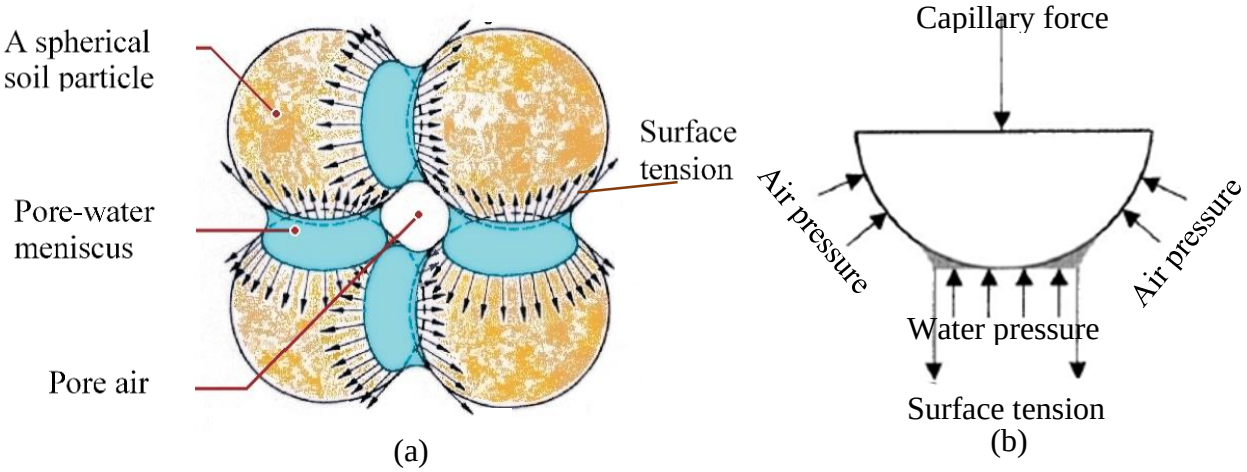

Figure 2.14. (a) Illustration of water meniscus between contacting spheres (Farouk et al., 2004) (b) Free body diagram for evaluating interparticle forces between two spheres (Bozkurt et al., 2017)

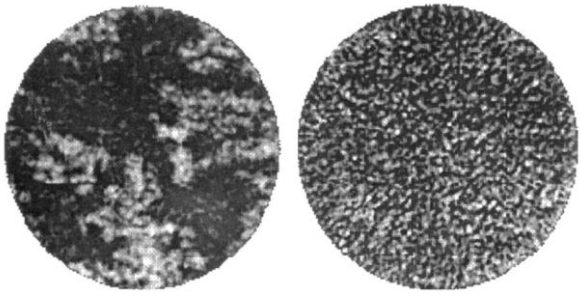

Figure 2.15. CT images of moisture distribution in the unsaturated Estaillades limestone at saturation of 92% (a) prepared by drying (b) prepared by wetting (after Cadoret et al., 1998).

Grain-scale properties of soil skeletons

Mechanical yielding behaviour is attributable to the rearrangement of particles through the sliding/rolling contact, leading to plastic strain (an internal mechanical variable) (Collins, 2005; Li, 2007). Soil skeleton stress is the stress at inter-particle contacts, playing a fundamental role in governing deformation and failure of partially saturated soils. Experimental observations in several microstructural testing techniques (X-ray computed tomography (Moscariello et al., 2016; Manahiloh & Meehan, 2017; Higo et al., 2013), Scanning Electron Microscopy images (Louati et al., 2015; 2017), and Mercury Intrusion Porosimetry (Romero & Simms, 2008)) suggest that the soil skeleton stress of partially saturated soils is linked with the frictional and capillary forces of grain-to-grain contacts. The frictional force (repulsive) stems from the sliding between grains, while the capillary force (attractive) is induced by fluid pressures (air and water) and surface tensions of water meniscuses around the particle contact points (see Figure 2.14). The capillary force serves as an internal tensioning/cohesion to maintain the stability of the soil structure by raising the strength and stiffness of the soil skeleton. It is accommodated by the morphology of the water phase, which is very different in the three saturation regimes (pendular, funicular, and capillary) (see Figure 2.16) (Louati et al., 2017; Wang et al., 2017). In particular, the water phase in the pendular regime is formed into isolated liquid bridges between pairs of grains. In the funicular state, liquid clusters between more than two grains are constructed through the coalescence of water bridges. The capillary regime exhibits a continuous water phase with small air bubbles. In the literature, there have been many attempts to propose mathematical expressions of the attractive capillary force between two idealized particles (spheres) for the pendular regime (Taibi et al., 2009; Cho & Santamaria, 2001; Chateau et al., 2002; Hicher & Chang, 2007; Farouk et al., 2004; Likos & Lu, 2004) and three idealized particles for the funicular regime (Wang et al., 2017), accounting for the effects of the separation distance between the particles and water-air-solid contact angles on liquid volumes (see Figure 2.17).

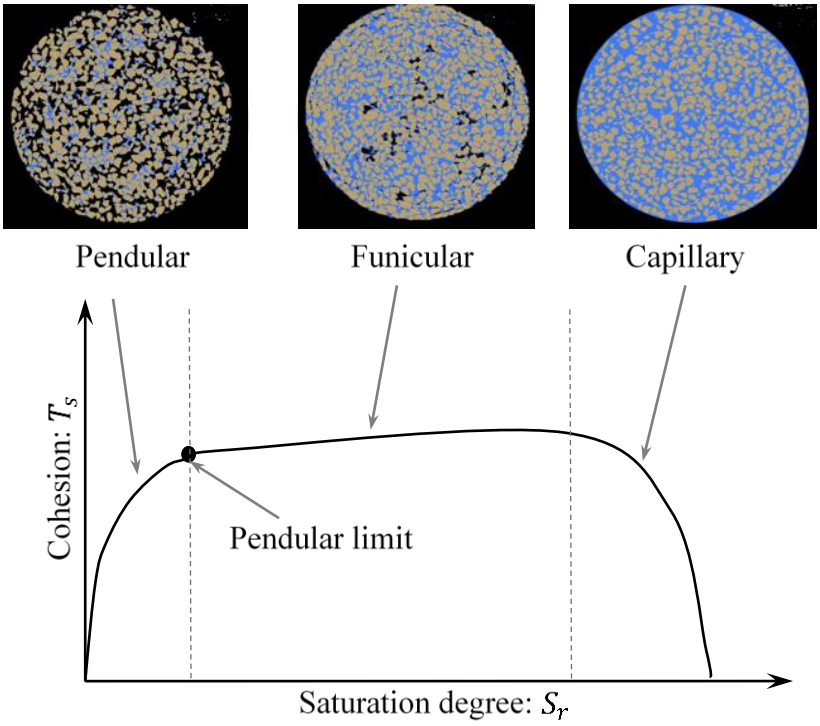

Figure 2.16. Liquid bridge distribution and cohesion in different saturation regimes (water in light blue, the air in black and solid in light brown) (Wang et al., 2017)

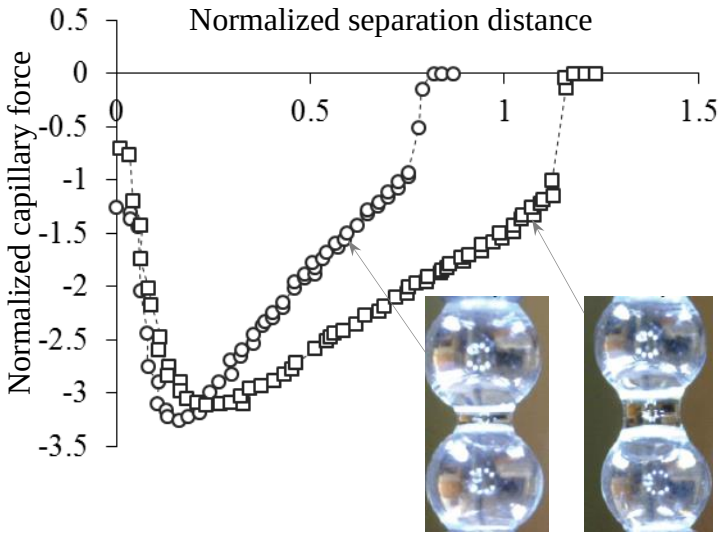

Figure 2.17. Effects of separation distance and meniscus volume between particles on capillary force (Bozkurt et al., 2017)

Grain-scale mechanisms of hydromechanical coupling

For partially saturated soils, the reversible responses of the mechanical part are produced by the elastically compressed grains, which can recover to their previous states upon unloading (Collins, 2005), while that of the hydraulic part stems from the reversible movement of the air-water interfaces

or water meniscuses against the rewetting/redrying cycle (Wheeler et al., 2003). Furthermore, it is worth noting that, due to the heterogeneous structure of unsaturated soils, not all of such elastically compressed particles and elastically wetted/dried meniscuses return to their previous states since many of them can be trapped within the compacted grain (Collins, 2005) and liquid bridge networks (Wei & Dewoolkar, 2006) during reloading and rewetting/redrying, respectively. In this situation, their recovery modes (expanding and giving up stored elastic energies) can only take place if there are simultaneous rearrangements of the grains and redistribution of the water meniscuses in the surrounding area. It proves that the irreversible changes of strain and saturation degree can cause trapped elastic energies, known as stored plastic or frozen/locked energies (Collins, 2005; Collins & Kelly, 2002). Collins (2005) states that such locked energies are considered to be scalars or "memory parameters", and these induce the hydromechanical hardening effect (Li, 2007) (see Figure 2.18). In particular, in the family of critical-state-based models, they have a crucial role in generating the dilatancy, which can be explained by the "sawtooth" analogy. Despite such understandings of the real presence of stored plastic energies, it can be assumed, for simplicity, that the concept of locked energy is irrelevant to this study. Additionally, the coupling in the reversible regime is very slight, such that this study can consider it as a minor feature to account for in the prediction of the current model. For instance, many experimental data show that the soil stiffness of elastic behaviour associated with the slope of the unloading-loading line in the specific volume–mean stress space is independent or inconsiderably dependent on the change of suction (Alonso et al., 1990; Wheeler & Sivakumar, 1995; Cui & Delage, 1996).

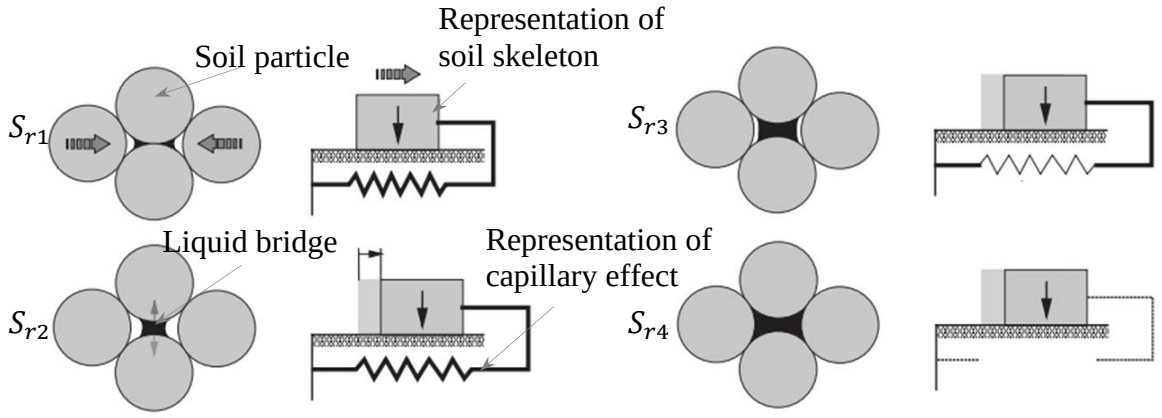

Figure 2.18. The change in coupling effect of capillary-related locked energy in soil skeleton with saturation degree ($S_{r1} < S_{r2} < S_{r3} < S_{r4}$) (after Li, 2007)

A strong coupling between mechanical and hydraulic responses is intrinsically observed in the inelastic stage. It can be physically demonstrated that such a coupled hydro-mechanical mechanism can be highlighted in the coupled dissipative process triggered by internal structural changes of soil

particles and pore fluids pertaining to mechanical and hydraulic responses, respectively. These two grain-scale phenomena activate and develop simultaneously and have mutual effects on each other (Li, 2007; Hu et al., 2015; Wheeler et al., 2003). For example, during the wetting/drying process, the redistribution of water menisci induces changes of capillary forces between grains and hence their inter-particle contact forces, leading to the rearrangement of particles that are usually represented in continuum modelling by plastic deformation. They have effects on the average stress acting on the soil skeleton and the cementing effect on the soil packing where their air-water interfaces with surface tensions and specific interface areas are in the nature of the grain-to-grain contacts of porous media. The pore water pressure in the meniscus water rings induces the additional normal force at inter-particle contacts, reducing the possibility of slippage at the inter-particle contacts. Under mechanical loadings, the movement of particles triggers the imbibition/drainage of pore throats and rupture of fluid bridges (see Figure 2.20). This rupture of liquid bridges, as an irrecoverable process, results in changes of macro suction and saturation. To micro-mechanically illustrate this, the irreversibility of the porosity change, associated with the movement of particles in the porous packing, triggers local instabilities to be propagated to the fluid interfaces. Consequently, instantaneous jumps between stable configurations give rise to a discontinuous process of fluid phases, including imbibition/drainage of pore throats/bodies and bridge rupture. Additionally, this phenomenon of grain rearrangement itself makes a significant contribution to varying capillary pressures, which are mainly dependent on inter-particle distances, which elongate during the volumetric dilation and shortening processes during the volumetric contraction. Alongside this, the difference in such capillary forces enables liquid bridges to redistribute. As a result, the suction-saturation curve is different in wetting and drying, as experimentally observed in several experiments (see Figure 2.3). In the light of the information gathered through these discussions, the two dissipations of plastic strain and irreversible saturation degree, associated with yielding, activate and develop simultaneously (see Figure 2.19). These two have effects on one another during the loading or saturation processes. This is the central mechanism for the fully coupled hydro-mechanical response. It should be of great concern, given its importance to understanding the realistic yielding behaviour of partially saturated soils in continuum theory.

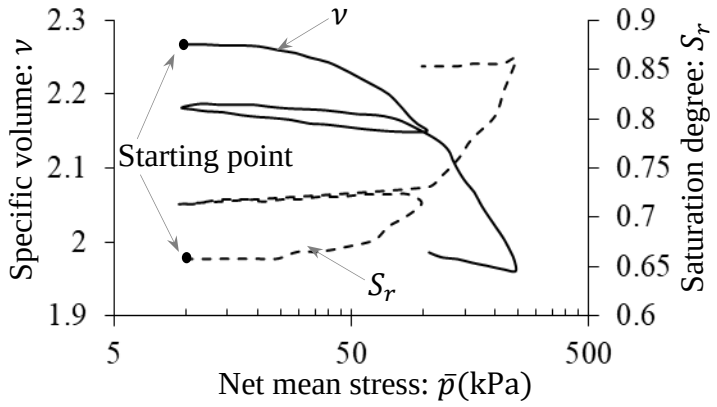

Figure 2.19. The loading-unloading difference in NCL of drained isotropic compression test of the highly expansive clays at $s = 200$ kPa (after Sharma, 1998)

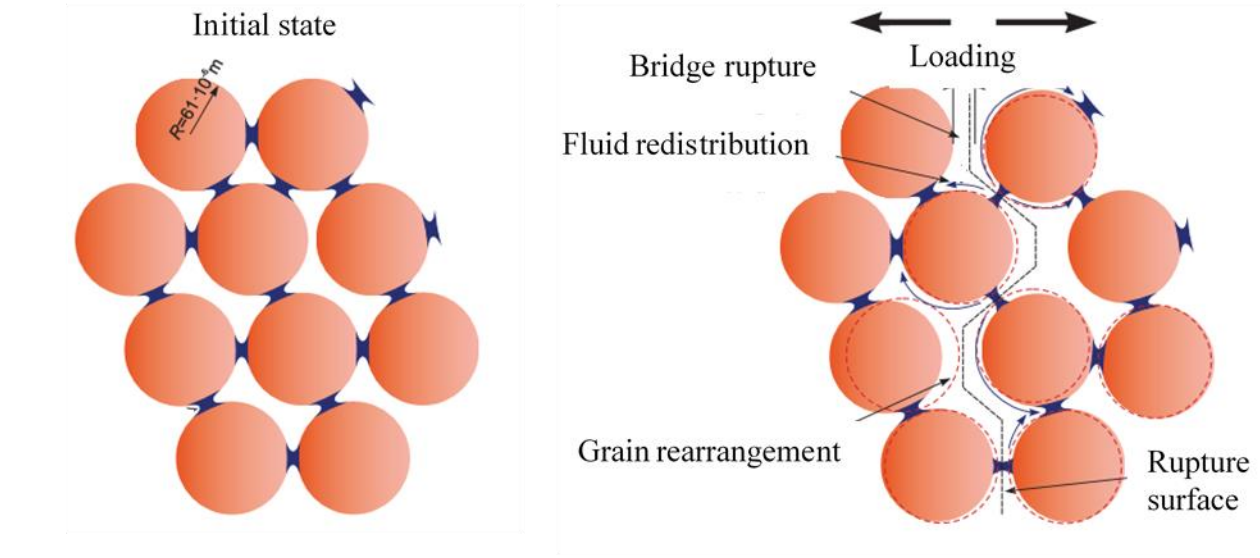

Figure 2.20. Interaction between grain rearrangement and liquid bridge redistribution in the granular medium during loading (after Bianchi et al., 2016)

2.2.3. Requirements in continuum modelling of partially saturated soils

As discussed earlier, the overall response of partially saturated soils is dependent on the state of the solid skeleton, how the water and air phases are connected, and the way internal forces interact along these interfaces at the microscopic scale. From the aspects of constitutive modelling, the material behaviour at the microscopic level can be reflected simply by the representative macroscopic variables and their evolutions during loading and wetting/drying for computational processes. In continuum modelling, an approximate manner is used to capture the microscopically observed mechanisms of partially saturated soils, where details of the model are required to satisfy the rigorous

link between experimental observation at the continuum level and the micromechanical nature of the interactions of all constituents (soil skeleton, and fluids) to reduce ad hoc assumptions.

In principle, the underlying micromechanical forces can be characterized by a few representative macroscopic stress-like variables in continuum modelling. Effective stress and suction can be interpreted as important and widely-used stress-like variables at the continuum level for specifying the responses of each constituent in the overall behaviour of partially saturated soils. Physically, the effective stress here can be understood as the stress at the inter-particle contacts, related to the deformation and failure of the soil skeleton, and governed by both the external load and contact-level capillary action. From the micromechanical point of view, there must be two contributions to the capillarity of the average skeleton stress, including suction and surface tension forces along the contours between the grains and liquid bridges (Wan et al., 2014; Li, 2003; Likos, 2014), both of which affect the form of Bishop's effective stress parameter χ. The latter still needs further investigation (Likos, 2014) and is not always taken into account in constitutive modelling (Gallipoli et al., 2003; Hu et al., 2014). There have been attempts at phenomenological expressions of the effective stress parameter χ, which can be represented as either a function of the saturation degree (e.g. Hassanizadeh & Gray, 1990; Muraleetharan & Wei, 1999) or the air-entry value (Khalili & Khabbaz, 1998), to capture the transition between fully and partially saturated states. Despite their usefulness being demonstrated in Russell & Khalili (2006), Khalili et al. (2008), Loret & Khalili (2002), extensive research on the micromechanical aspects for better forms of Bishop's effective stress parameter χ is still needed (Wan et al., 2014; Li, 2003). This research is, therefore, not covered within the scope of this study. On the other hand, internal fluid pressures at the micro-scale can be represented by the modified suction representing the hydraulic conductivity of bulk fluids, where porosity is accommodated to demonstrate the explicit effect of volumetric changes on the saturation processes. These stress-like variables are work conjugate with the strain-like variables (e.g. strain and saturation degree) to generate a certain amount of work input associated with a change in the state of a system (Houlsby, 1997).

All the underlying micro-mechanisms of deformation and saturation can be encompassed in constitutive modelling in an indirect way by means of macroscopic irreversible quantities. These quantities are regarded as internal variables and corresponding internal forces of the energy dissipation processes to record the history of changes of the state variables within a system. In principle, an infinite number of internal variables can be used in the constitutive equations to replicate accurately the evolution of microstructural processes for the realistic behaviour of partially saturated soils. Nevertheless, only a few internal variables are selected in practice for simplicity to give reasonable approximations to the real response. For example, movements and reorganisations of soil

grains are usually represented by the plastic strain tensor to encapsulate the history of inelastic deformation or mechanical dissipation in many existing plasticity models for solids. Within three-phase porous media, the moisture/fluid pore redistribution, induced by the formation and breakage of water meniscuses, takes place to produce the yielding hydraulic responses. In this case, the irreversible saturation degree can be selected as an additional internal variable to identify the essential mechanisms of saturation and hydraulic energy dissipation, capturing the process of local structural rearrangements related to the change of moisture distribution. The strong coupling between hydraulic irreversibility and plasticity gives rise to the existence of a single yield function, controlling the simultaneous evolution of all internal variables to facilitate the simulation of material behaviour under a wide range of loading and hydraulic cases. This is a crucial requirement for constitutive modelling of partially saturated soils to reflect the coupled hydro-mechanical grain-scale processes associated with the interdependence of mechanical and hydraulic internal forces and their dependence on all internal variables, in addition to effective stress and suction. To illustrate, experimental data indicate that there is a concurrent occurrence between the plastic volumetric strain and the irrecoverable degree of saturation changes when the stress paths reach the yield curve (Zhang & Lyttom, 2012). In other words, they exhibit the same yield points at any instant (see Figure 2.9). Closely linked to these findings is the actual existence of the unique yield locus, the embodiment of a material's behaviour, for both state processes of volume and saturation changes in unsaturated soils (Delage & Graham 1996; Sivakumar & Doran, 2000; Zhang & Lyttom, 2012). Drawing on the above discussions, the water retention curve (e.g. the suction-saturation degree relationship) and the inseparable nature of plasticity and hydraulic irreversibility in the energy loss play a fundamental role in studying the actual mechanism of collapses in unsaturated soil mechanics. This feature is the focus of this thesis. It sets out the challenges ahead in the development of constitutive modelling of partially saturated soils. Against that background, the following section briefly reviews whether the existing frameworks are adequate.

2.3. Constitutive modelling of partially saturated soils

The above key characteristics of partially saturated soil behaviour should be reflected in a constitutive model to capture the transition between partially- and fully-saturated conditions (Zhou & Sheng, 2009; Sheng, 2011). At a glimpse, it is found that a countless number of continuum models for partially saturated soils exist in the literature and can be grouped into several categories, each of which corresponds to a particular choice of stress variables. Among them, there are two most prominent groups of elastoplastic models, one that is generated by the pair of net stress and suction (Alonso et al., 1990; Wheeler & Sivakumar, 1995; Cui & Delage, 1996; Sheng et al., 2008), and another one based on the average skeleton stress (Bolzon et al., 1996; Loret & Khalili, 2002; Sheng et al., 2004;

Sun et al., 2007; Tamagnini & Pastor, 2004). It is undeniable that the latter choice can capture the transition between unsaturated and saturated states at a material point level thanks to the reflection of variations in saturation degree, while the former cannot. Despite all the disputes, several authors (Houlsby, 1997; Coussy et al., 2010) have reached one radical consensus: that both are just inadequate approximations of the much more complex behaviour of unsaturated soils. In such a case, two other stress-like variables, namely, the effective stress and modified suction (the product between porosity and suction), have instead been chosen to be work conjugate to the changes of strain and saturation degree, respectively, on the basis of the equation of energy input in multiphase porous media, as suggested by Houlsby (1997). Such a conjugate pair of variables then constitutes the prerequisite theoretical foundations for the development of several other models for unsaturated soils, proposed by Wheeler et al. (2003), Buscarnera & Nova (2009) and Li (2007). It should be noted that any form of stress variables is geared towards the ultimate goal of understanding the coupling of the hydraulic and mechanical behaviour of partially saturated soils.

2.3.1. Model without saturation degree

On the basis of such choices of stress-strain variables, existing models of unsaturated soils can more or less address the experimental observations outlined in Section 2.2.1. The effects of suction on the stress-strain relationships have been addressed in several papers (e.g. Alonso et al., 1990 (see Figure 2.21); Wheeler & Sivakumar, 1995; Cui & Delage, 1996; Sun et al., 2000; Stropeit et al., 2008; Blatz & Graham, 2003; Macari et al., 2003; Farias et al., 2006; Solowski & Sloan, 2015). The fundamental characteristics of these frameworks are the enhancement of classical critical state models, taking into account the evolution of the pre-consolidation pressure with increasing matric suction. In particular, suction was used in the loading-collapse yield function and volume equations to capture plastic compression under the effects of suction. This approach is able to capture several important behavioural features of unsaturated soils. For example, the effects of suction on soil stiffness observed in suction-controlled tests are reproduced reasonably effectively by these models. These bring several significant advantages for unsaturated mechanics by representing several stress paths related to independent stress state variables (e.g. net stress and suction) in a simple way. They allow the model to capture the collapse mechanism of wetting-induced swelling and the increase of shear strength with suction. This is linked to the influence of suction on the yield limit, where the shape of the yield surface is influenced by the suction change and where the increase of suction widens the size of the yield surface (see Figure 2.21). However, the link between the suction and degree of saturation was missing in these models, making it hard to reproduce the dependence of model responses on different saturation regimes (capillary in fully saturated conditions, funicular at high saturations, and pendular at low saturations), although SWCC is indicated as being an indispensable component for partially

saturated soils to capture the realistic responses of partially saturated soils. To illustrate this, the relative area associated with water and air pressures is dependent on the saturation degree, affecting the number and intensity of capillary-induced inter-particle forces at the microscopic scale. Therefore, constitutive models with suction alone for hydraulic responses are inadequate to describe realistic mechanisms of unsaturated soils. Furthermore, these models are not capable of capturing the transition between saturated and unsaturated states due to the lack of saturation degree effects. To address this, Zhou et al. (2012) and Zhou & Sheng (2015) used an NCL with a soil compression index varying with the effective degree of saturation, while Alonso et al. (2013) proposed an NCL dependent on both the suction and saturation degrees. Wheeler et al. (2003), Tamagnini (2004), Xie & Shao (2006) and Buscarnera & Nova (2009) suggested different hardening constitutive laws governing the coexistence of the strain and saturation rates. These studies demonstrate that both the suction and saturation degrees play an indispensable role in modelling the wetting/drying-induced collapses of partially saturated soils.

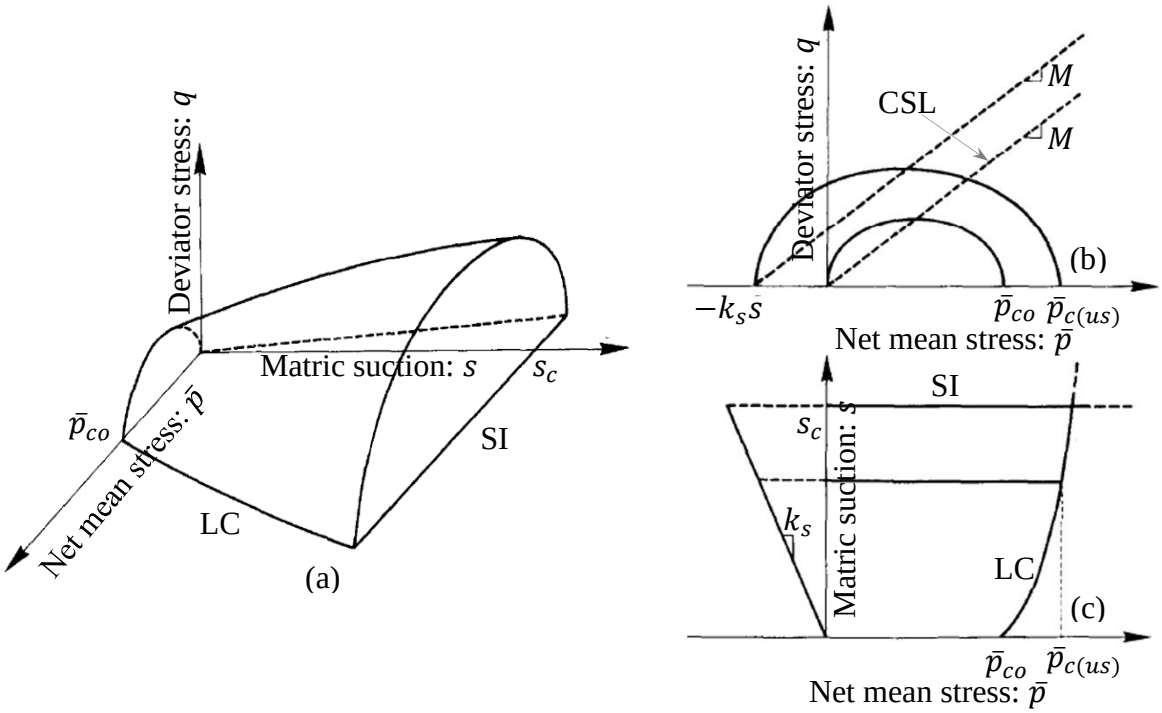

Figure 2.21. Yield surfaces of BBM model (Alonso et al., 1990) in (a) $(\bar{p}, q, s)$ space, (b) $(\bar{p}, q)$ space and (c) $(\bar{p}, s)$ space

2.3.2. Model with SWCC

The use of an SWCC, independent of the volumetric behaviour, has been the focus in several models (Thu et al., 2007; Zhou & Sheng, 2009; Russell & Khalili, 2006; Kohler & Hofstetter, 2007; Wong et al., 2010) to reflect the effects of the degree of saturation and suction on mechanical behaviour.

For example, Russell & Khalili (2006) proposed a unified constitutive model for unsaturated soils presented through critical state bounding surface plasticity theory, using the concepts of effective stress for unsaturated granular materials. Zhou & Sheng (2009) extend the SFG model (Sheng et al., 2008) to provide a consistent presentation of the dependence of yield stress, shear strength, dilation and volume change behaviour of partially saturated soils on suction to capture extensive experimental data for describing the volume change during drying under constant stresses, volume change during constant suction isotropic compression tests and shear strength during direct suction-controlled shear and triaxial compression tests. In general, all of these models are effective to demonstrate how a volumetric collapse phenomenon, due to hydraulic debonding/bonding effects, can be described by constitutive models in different saturation regimes. The transition between partially and fully saturated conditions is naturally captured by this model thanks to the use of the saturation degree. However, all of them (Thu et al., 2007; Zhou & Sheng, 2009; Russell & Khalili, 2006; Kohler & Hofstetter, 2007; Wong et al., 2010) only take into account the one-way interaction, commonly encompassing the effects of hydraulic behaviour on the stress-strain relationship and, as such, are considered to be at the level of partial coupling. They neglect the non-uniqueness of SWCC observed and addressed in several other papers (Nuth & Laloui, 2008; Miller et al., 2008, Gallipoli et al., 2003; Vanapalli et al., 1999; Tarantino, 2009; Masin, 2010; Mbonimpa et al., 2006). In other words, the key point of these models lies in the mainstreaming of the suction and saturation degree into the function of yield surface to capture plastic compression due to the wetting-induced collapse behaviour over different saturation regimes, but without any consideration of the mechanical impacts on the hydraulic response. Regardless of whether these mainstreaming approaches are rigorous or not, the ignorance of the stress/strain-dependent SWCC is a notable demerit of these frameworks and constitutes a significant impediment to an adequate understanding of the realistic response of unsaturated soils with the simultaneous processes of deformation and saturation because the degree of saturation increases with the void ratio, even when the value of the suction is constant. Furthermore, although the identification and determination of the model parameters are widely regarded as serving an essential role in determining the model's applicability and predictive ability, the selection of the input data in existing models of unsaturated soils is generally arbitrary and has unclear links with the testing procedures applied.

Other models employing an SWCC dependent on volume change to have stronger interactions between the hydraulic and mechanical responses have also been proposed (e.g. Buscarnera, 2010; Buscarnera & Nova, 2009). In this type of model, Bishop's stress, with the effects of both suction and saturation, is used as a stress-like variable for the mechanical part. Meanwhile, the modified suction is used as a hydraulic stress-like variable to demonstrate the influence of porosity on the saturation-

suction relationship in representing the mechanical effect of hydraulic behaviour for unsaturated soils. The appealing feature of this class of models is the introduction of a coupled hydromechanical form of elastoplastic stiffness matrix, allowing for a shifting SWCC with volume change. These models have proven successful in taking the concurrent existence of hydraulic effects towards mechanical changes and vice versa into consideration in constitutive formulations. These models provide good results on stress state changes under hydraulic paths in the net and skeleton stress space where different key behavioural features are reasonably captured, such as the dependency of strain on the stress–suction path, accumulation of expansion and compression strain during suction cycles at different confining stresses, and the effects of suction on dilatancy. Despite their successes in taking into account hydro-mechanical coupling in the constitutive behaviour of partially saturated soils, the difference in wetting and drying paths was not taken into account in these models. The irreversible degree of saturation was missing in these models, thus hindering them from reproducing the macro behaviour generated by the interactions between grain contact sliding and capillary irreversibility at the grain scale, as discussed earlier. Furthermore, the model parameters have not carefully been identified and determined during model development, leading to somewhat arbitrary choices of model parameters.

2.3.3. The model with wetting-drying differences in SWCC

In order to remedy deficiencies associated with hydro-mechanical coupling in the approaches mentioned above, several alternative models are proposed. More complete representations of water retention behaviour, taking into account the irreversibility between the wetting and drying processes, have been successfully presented in several fully coupled hydro-mechanical models (e.g. Gallipoli et al., 2003; Loret & Khalili, 2000; 2002; Wheeler et al., 2003; Hu et al., 2014; Khalili et al., 2008; Muraleetharan et al., 2009; Liu & Muraleetharan, 2012; Sheng et al., 2008; Sun et al., 2007; 2010; Sun & Sun, 2012; Zhou et al., 2012; 2018; Zhou & Sheng, 2015; Lloret-Cabot et al., 2017; Ghorbani et al., 2018; Gholizadeh & Latifi, 2018; Bruno & Gallipoli, 2019; Kodikara et al., 2020). Some of these models are briefly presented below in two groups (i) Model without internal hydraulic variables (e.g. irreversible saturation) and (ii) Model with internal hydraulic variables (e.g. irreversible saturation).

Without using the internal hydraulic variable

In Khalili et al. (2008), the effective stress principle with the effective stress parameter defined as a function of suction, air entry and air expulsion suction values are used for quantifying the contribution of suction to the stress on a solid skeleton, taking into account the effects of hysteresis due to wetting and drying. A novel constitutive formulation is derived, with the hydromechanical coupling described

through the combination of the governing equations for seepage flow and the bounding surface plasticity model for elastoplastic deformation behaviour. These two components are linked together through plastic hardening, taking into account the effect of suction and the effective stress equation. This model presents the explicit effect of mechanical behaviour on a separate SWCC by shifting the primary drying and primary wetting curves to the right due to density through the function of air entry and air expulsion suction values, which are explicitly dependent on the change in density. On the other hand, Zhou et al. (2012), (2018) and Zhou & Sheng (2015) propose a new volume change equation, accounting for the stress and degree of saturation, to better represent the nonlinear variation of soil compressibility in the case of constant suction. In this sense, the soil compression index is dependent on the effective degree of saturation interpolated from its compressibility at the fully saturated state. An alternative approach for simulating the wetting-drying difference and its coupling with plasticity is then suggested, allowing users to calculate the effective degree of saturation under different complicated mechanical and hydraulic paths. From the proposed equation of volume change, a loading-collapse yield surface dependent on the effective degree of saturation and Bishop's effective stress is derived to simulate plastic behaviour under the effects of saturation degree, which are different between drying and wetting paths. In general, these models are assessed to be adequate, robust and effective in reproducing many important behavioural features of partially saturated soils, such as the effects of volume change on wetting-drying differences in SWCC, transitions between softening and hardening, the soaking-induced deviator strain when the stress ratio is kept constant, the dependence of compressive and dilative volume changes on both wetting/drying and shearing, and changes in the saturation degree owing to both wetting/drying and shearing in different tests (e.g. drying–wetting cycle tests, isotropic and triaxial loading tests and undrained cyclic triaxial tests). However, the concern here is that they adopt a separate law of hydraulic hysteresis, in which each drying and wetting path possesses different parameters, as a result of neglecting internal hydraulic variables for reflecting the formation and/or breakage of water menisci. This hinders these models from presenting the hydraulic dissipation properties of partially saturated soils, which are very important to capture the mechanisms of hydromechanical coupling inspired by the interdependence between pore fluid redistribution and grain rearrangement at the grain scale, as previously discussed. These models are hence not capable of modelling the simultaneous activation and development between yield stress and suction in a wide range of loading and saturation conditions, which are usually observed in experiments.

Using the internal hydraulic variable

Several other models use an additional variable for hydraulic irreversibility as a potential way to represent the effects of wetting-drying differences in modelling responses of partially saturated soils.

For example, Muraleetharan et al. (2009), Liu & Muraleetharan (2012), Ghasemzadeh et al. (2017) and Ghasemzadeh & Amiri (2013) used the evolution of the irrecoverable volume fraction of water and hysteresis within the framework of classical isotropic cyclic plasticity to describe the nature of hydraulic irreversibility. In this group of models, the conjugated stress-strain variables for both hydro and mechanical responses are proposed where the bounding surface plasticity concept is used to derive a hysteretic model for SWCCs. The incorporation of the bounding surface plasticity concept enables simulation of different complex hydromechanical responses of partially saturated soils under multiple cycles of wetting and drying, or multiple cycles of loading and unloading. While the hydromechanical hysteresis and accumulation of permanent deformation during repetitive loading cycles are described by the concept of bounding surface plasticity, a separate law for hydraulic hysteresis, requiring different sets of parameters for drying and wetting paths, is still required in these models to capture the wetting-drying differences in behaviour (see Figure 2.22). Furthermore, the identification and calibration of several parameters in these models (e.g. Liu & Muraleetharan, 2012) is a challenge for their applications. In particular, these models need many parameters, some of which possess unclear physical meanings, to gain insight into the behavioural mechanism of hydromechanical coupling in partially saturated porous media.

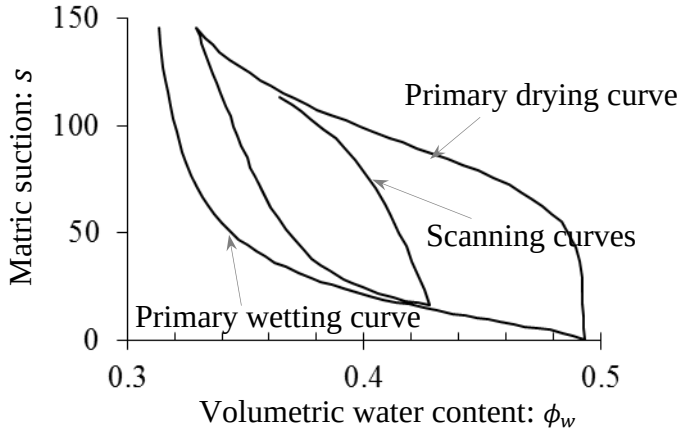

Note:

Primary wetting curve: $\phi_w = \frac{\phi_{wsat}+\phi_{wres}\left(\frac{s}{f_1}\right)^{d1}}{1+\left(\frac{s}{f_1}\right)^{d1}}$

Primary drying curve: $\phi_w = \frac{\phi_{wsat}+\phi_{wres}\left(\frac{s}{f_2}\right)^{d2}}{1+\left(\frac{s}{f_2}\right)^{d2}}$

where ϕ_{wsat} is the saturated volumetric water content; ϕ_{wres} is the residual volumetric water content at very high suction; f_1, d_1, f_2, d_2 are material parameters

Figure 2.22. Separate law of soil-water characteristic curve in the model of Muraleetharan et al. (2009)

Irreversible saturation is incorporated into hydro-mechanical coupling in some other models (e.g. Wheeler et al., 2003; Sheng et al., 2004; Lloret-Cabot et al., 2017), requiring the use of multiple yield surfaces (see Figure 2.23 and 2.24), e.g. one mechanical (Loading Collapse; LC) and two hydraulic (Suction Increase/Decrease; SI/SD, usually as horizontal straight lines) with complicated treatments for the coupled evolutions of all yield functions (Wheeler et al., 2003; Sheng et al., 2004). For instance, Wheeler et al. (2003) introduce the equations of the irreversible increments of strain and saturation degree with the coupling parameters controlling the path traced by the corner between yield curves in the mean stress-modified suction-volumetric strain space and the mean stress-modified suction-saturation degree space, to reflect the coupled movements of the various yield curves. Thanks to this technique, the effect of irreversible changes of degree of saturation on the stress-strain behaviour and the influence of plastic volumetric strains on SWCC are accounted for, indicating the ability of these models to reflect realistic mechanisms of full hydromechanical coupling. As a result, these fully coupled models can capture several essential features of coupled hydro-mechanical behaviour under different loading and saturation conditions, such as irreversible swelling/shrinkage upon wetting/drying, load/deformation-dependency of capillary hysteresis, together with the effects of hydraulic hysteresis on shear strength, stiffness, and dilation, which are validated through extensive variations of the experimental conditions (suction-controlled isotropic loading and soaking tests, undrained isotropic compression tests, suction-controlled triaxial tests, and undrained triaxial tests). Despite some successes in using internal hydraulic variables (the irrecoverable volume fraction or saturation degree) to capture the interaction between wetting-drying differences and plasticity, these models are generated based on weakly-coupled forms through the interconnections of multiple separate yielding surfaces. Owing to the discretization of the yield functions, the activation and/or evolution of the energy-dissipation phenomena, induced by both grain rearrangements and water-meniscus redistributions, are highly unlikely to be concurrent. This is inconsistent with what occurred during the irreversible changes of partially saturated soils, as mentioned earlier. It poses a significant obstacle to actualizing the coupled hydro-mechanical evolutions in the size, shape and position of these distinct yield surfaces to be compatible with those observed in laboratory tests. Thus, the dependence of all internal forces on stress, suction, plastic strain and irrecoverable saturation and their rates cannot be described in this model, leading to a weak hydromechanical coupling and hence hindering it from faithfully capturing the actual behaviour of partially saturated soils. To further illustrate by experimental evidence, Delage & Graham (1996) and Tang & Graham (2002) found that LC and SI/SD should merge into a single yield locus to capture the micromechanical nature of coupled hydro-mechanical yielding. This issue has been investigated through a combination of drained isotropic compression and drying tests by Sivakumar & Doran (2000) (see Figure 2.25b) and the extended Barcelona Basic model of Pedroso & Farias (2011). On the other hand, net stress-controlled

experiments by Thu et al. (2007) and Sivakumar & Doran (2000) showed that these widely adopted horizontal straight lines for SI/SD are not reasonable (see Figure 2.25) despite their usefulness in constitutive modelling, as discussed in several papers (e.g. Delage & Graham, 1996; Robles & Elorza, 2002; Tang & Graham, 2002; Zhang et al., 2009). Another inadequacy of these models principally revolves around the methodology, in which the mathematically defined yielding surfaces and flow rules are determined without full thermodynamic consistency, despite their usefulness in some applications. No specific link between the dissipation rate and the stress state (or yielding condition) in the inelastic regime is provided in the models mentioned above, requiring the use of many ad hoc assumptions in the model formulation.

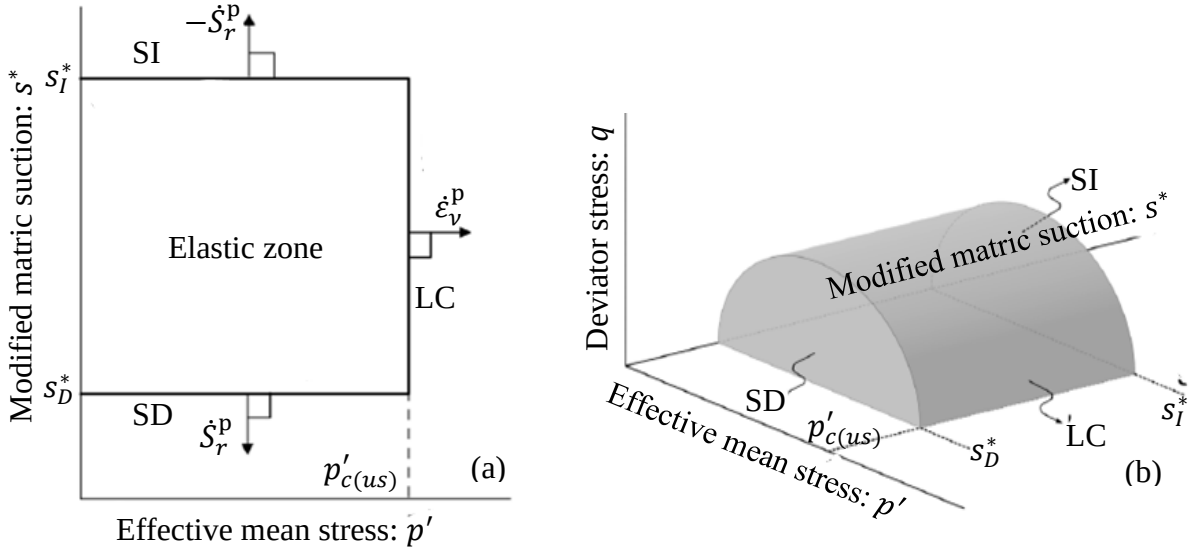

Note:

Loading Collapse (LC) yield curve:	$q^2 - M^2 p'\left(p'_{c(us)} - p'\right) \leq 0$
Suction Increase (SI) yield curve:	$s^* - s_I^* \leq 0$
Suction Decrease (SD) yield curve:	$s_D^* - s^* \leq 0$

Figure 2.23. Yield surfaces of the model of Wheeler et al. (2003) in (a) (p', s^*) space, (b) (p', q, s^*) space

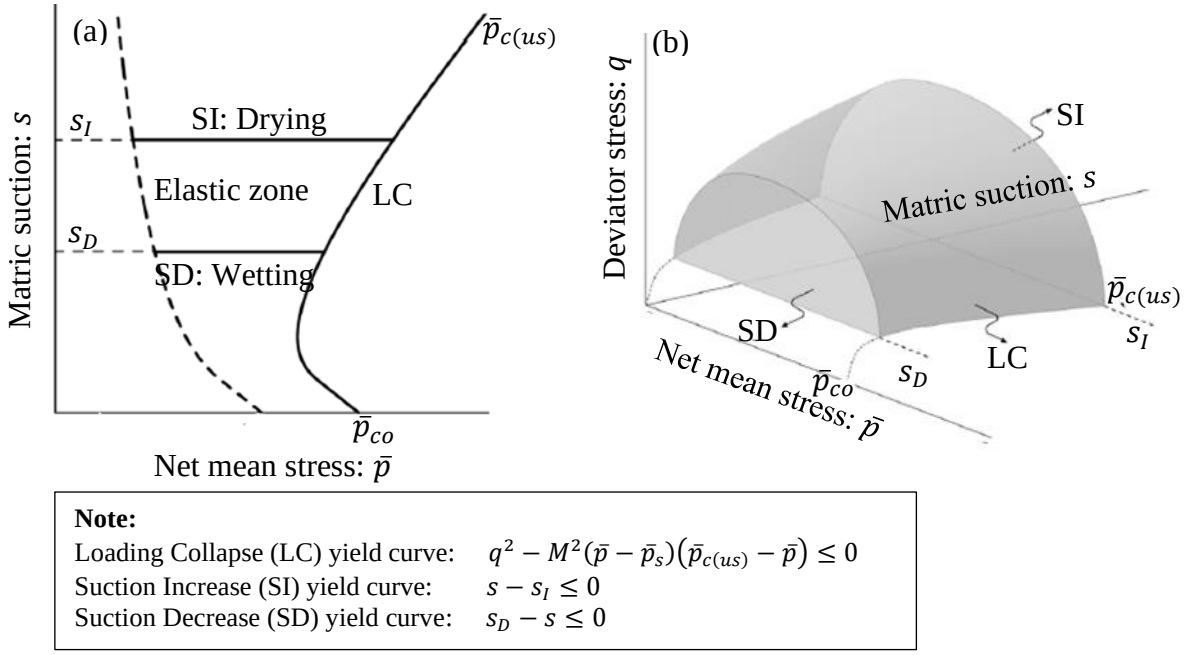

Note:

Loading Collapse (LC) yield curve: $q^2 - M^2(\bar{p} - \bar{p}_s)(\bar{p}_{c(us)} - \bar{p}) \leq 0$

Suction Increase (SI) yield curve: $s - s_I \leq 0$

Suction Decrease (SD) yield curve: $s_D - s \leq 0$

Figure 2.24. Yield surfaces of the SFG model (Sheng et al., 2008) in (a) $(\bar{p}, s)$ space, (b) $(\bar{p}, q, s)$ space

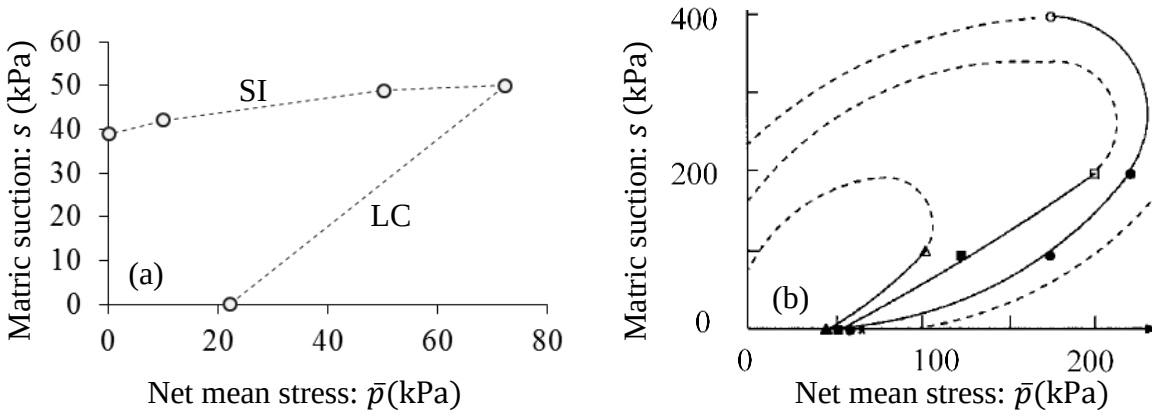

Figure 2.25. Experimental results of yield curves in the $\bar{p}$: s plane (a) Thu (2006) (b) Sivakumar & Doran (2000)

2.3.4. Thermodynamics-based model for unsaturated soils

In principle, the essential components of a constitutive model can be established separately without defining the connection between the dissipation properties and the yield criterion of materials. The requirement for thermodynamic admissibility is a necessary, but not sufficient, condition for constitutive modelling, as it can be applied retrospectively after completing the derivation of the model formulation. The key advantage of such developments is that all essential behavioural characteristics of geomaterials in general, and unsaturated soils in particular, can be rigorously

incorporated in a thermodynamics-based model, while the number of arbitrary assumptions and model parameters can be reduced without compromising the model's performance (e.g. Collins & Hilder, 2002; Einav, 2007; Buscarnera & Einav, 2012). A thermodynamics-based approach can help constitutive models to understand the nature of microscopic work and the microscopic forces involved in a complex system, where the state of a system is dependent on both the instantaneous values of the state variables and the previous history of these variables. The success of such approaches to constitutive modelling has been demonstrated for a wide range of engineering materials (Buscarnera & Einav, 2012; Liu et al., 2018; Zhang, Z, 2017; Balieu & Kringos, 2015; Nguyen et al., 2015; Lai et al., 2016; Al-Rub & Darabi, 2012; Darabi et al., 2018). For soils, the relationship between continuum theory and the thermodynamic framework can be found in well-known critical state models such as Cam-Clay and Modified Cam-Clay by Roscoe & Burland (1968) and Schofield & Wroth (1968). Although the key methodology of these classical model developments is experimental analysis to determine elastoplastic features, including the function of the yield surface, constitutive stress-strain relationship, hardening law and flow rule, all of these can be interpreted in thermodynamics-based formulations. In this sense, some authors (Collins & Houlsby, 1997; Houlsby & Puzrin, 2000; Collins & Kelly, 2002) revisit such critical state models regarding the thermodynamic concept in a more rigorous way. Through these works, they demonstrate the generality and promising features of explicit application of thermodynamics laws to soil modelling but only when applied to dry and fully saturated soils where the mechanical behaviour related to the stress-strain conjugate is the sole focus of thermodynamic discussions. It will be a different matter in the case of unsaturated soils, where thermodynamic laws must comply with the coupled hydromechanical behaviour.

The development of thermodynamic-based approaches to constitutive modelling of partially saturated soils has attracted considerable attention over the last 15 years (Sheng et al., 2004; Tamagnini & Pastor, 2004; Uchaipichat, 2005; Santagiuliana & Schrefler, 2006; Li, 2007; Coussy et al., 2010; Buscarnera & Einav, 2012; Dangla & Pereira, 2014; Hu et al., 2015; Lei et al., 2016). Yet, the papers remain still too few, given the demands of theoretical improvements in unsaturated soil mechanics. Despite the attempts and successes, full coupling between plasticity and hydraulic irreversibility has usually not been adequate in previous thermodynamics-based approaches. In particular, the hydraulic dissipation attributed to the irrecoverable change of saturation degree is overlooked in Tamagnini & Pastor (2004), Uchaipichat (2005), Coussy et al. (2010), Buscarnera & Einav (2012), Dangla & Pereira (2014) and Lei et al. (2016). Consequently, these models cannot naturally capture different responses under wetting and drying paths. Furthermore, the investigation of their associated hydro-mechanical dissipation properties is essential yet often overlooked or inadequate in some existing so-

called thermodynamic-based models. The proof for thermodynamic admissibility (non-negativeness of the dissipation rate function) is frequently missing in several approaches. That is responsible for the inadequate details of thermodynamic admissibility and strong coupling between plasticity and hydraulic hysteresis in unsaturated soils. Additionally, despite bringing the usefulness, the use of multiple yield surfaces in several models (Sheng et al., 2004; Santagiuliana & Schrefler, 2006; Hu et al., 2015) does not reflect the inseparable nature of hydro-mechanical interactions at the grain scale, given the dissipative stresses are not dependent on the rates of all internal variables. This is because the dissipation potential in these approaches is decomposed into two additive parts (e.g. mechanical and hydraulic) which are homogeneous first order in the rate of a corresponding internal variable, leading to the so-called weak coupling between plastic strain and irreversible saturation.

2.4. Boundary Values Problems involving partially saturated soils

The development of a robust computational platform with an advanced theoretical framework of porous media is essential for predicting geohazards. In this sense, FEM, one of the most prevailing mesh-based techniques in geotechnical engineering, has increasingly become a powerful tool for simulating the coupled dynamic flow-deformation response of partially saturated soils. For example, in recent years, numerous studies on FEM have been undertaken ranging over different applications for unsaturated soils such as bearing capacity of foundation (Kim, 2000; Tang & Taiebat, 2015; Mehndiratta & A, Sawant, 2017; Ng & Small, 2000; Song & Borja, 2014); compressed air support in tunnelling (Nagel & Meschke, 2010); unsaturated slope stability under the effects of rainfall and water level fluctuation (Xiong et al., 2019; Hamdhan & Schweiger, 2013; Griffiths & Lu, 2005; Oh & Lu, 2015; Johari & Talebi, 2019; Oka et al., 2010; Callari & Abati, 2009; Huang & Jia, 2009); rainfall-induced landslides (Leshchinsky et al., 2015; Jeong et al., 2017); unsupported vertical cuts on unsaturated sand (Song & Borja, 2014); and liquefaction of unsaturated sand (Bian et al., 2017; Zhang & Muraleetharan, 2018). Although fruitful results in establishing numerical simulations pertaining to the full hydromechanical interaction have been obtained in these existing studies, they have limitations associated with severe mesh distortion issues compromising solution accuracy in modelling large deformations (see Figure 2.26). To avoid the mesh-distortion issues encountered with the use of FEM, Particle Finite Element Method (Oñate et al., 2004; Idelsohn et al., 2004) was introduced based on the combination of FEM and an efficient remeshing procedure given the fixed nodes of the previous mesh. Nevertheless, this method requires ad-hoc techniques to recover boundaries during the remeshing process. In addition, GIMPM (Bardenhagen & Kober, 2004), an extension of the Material Point Method (MPM), has gained attention over recent years for predicting coupled flow deformation processes in partially saturated soils (Yerro, 2015; Yerro et al., 2015; Wang et al., 2018; Alonso et al., 2015; Lei et al., 2020; Bandara et al., 2016; Vardon et al., 2017). In this

method, the computational domain is based on both the mesh and the particle. Despite the benefits that GIMPM brings in capturing large plastic deformation of unsaturated soils, it is often computationally expensive due to the use of high dimensional shape functions (Soga et al., 2016). In computational geomechanics, SPH, a particle-based method, has already been proven successful in avoiding the issue of large-deformation grid distortion encountered in FEM and is computationally cheaper than IGMPM (Bui, 2007; Bui et al., 2011; Bui & Nguyen, 2017; Bui & Fukagawa, 2011; Nonoyama et al., 2015; Zhao, 2019). Despite these advantages, there is a shortage of studies (Bui & Nguyen, 2017; Fadaei-Kermani et al., 2019; Zhao, 2019) exploring and examining the application of SPH for capturing the response of partially saturated soils. SPH is therefore lagging behind FEM and MPM in handling coupled solid deformation-fluid flow in deformable porous media. For these reasons, the SPH method is used to investigate the behaviour of geotechnical failures numerically under unsaturated conditions in this thesis, focusing on the constitutive models used to represent the coupled hydro-mechanical response.

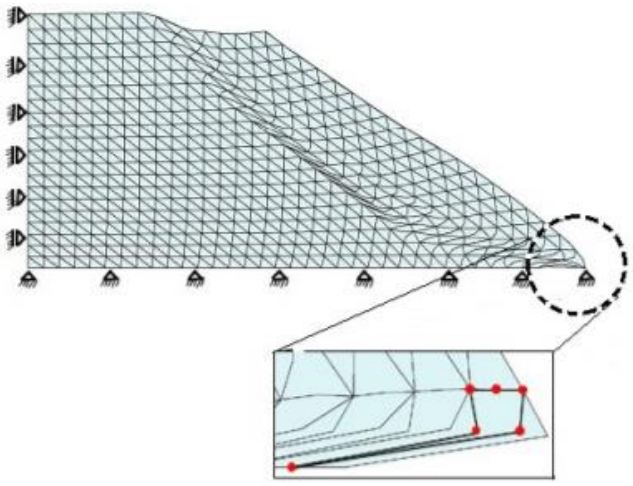

Figure 2.26. Example of extreme mesh distortion using FEM to simulate deformation problems (Rohe & Vermeer, 2014)

2.4.1. Constitutive modelling of partially saturated soils implemented in BVPs

The coupled flow deformation problem is of importance in geotechnical engineering, involving complicated fluid flow patterns and large deformations of the solid phase due to the complex multiphase interactions in unsaturated porous media under different loading and saturation conditions. In this case, the matric suction (or saturation degree) and its dependence on volume change in different wetting-drying paths are one of the salient, fundamental factors controlling the failure mechanisms of partially saturated soils that have been observed in various field studies. For instance, the decrease in suction due to the wetting process under heavy rainfalls is responsible for

the swelling heave and the loss of shear strength that trigger and govern geostructural collapses (Jeong et al., 2017; Yang et al., 2020; Ng et al., 2003; Xie et al., 2020). On the other hand, the drying process results in the desiccation shrinkage and cracking of expansive soils when suction increases (Jiang et al., 2018; Abdujauwad et al., 1998; Li & Guo, 2017; Caunce, 2010; Dessouky et al., 2015). Furthermore, under external loading, the localisation bands in the post-localisation stage, defined by the concentration of plastic strain, become a fluid flow barrier or fluid pathway, inducing the redistribution of liquids associated with the wetting-drying difference inside these bands (Song, 2014). The results of these field tests are consistent with the experimental observations made in a wide range of laboratory tests for partially saturated soils, such as the bearing capacity of shallow foundations (Shwan, 2015; Alabdullah, 2010) and the stability of slopes (Okura et al., 2002; Schnellmann et al., 2010; Lee et al., 2011; Kim et al., 2018; Ahmadi-adli et al., 2017; Xie et al., 2020; Xiong et al., 2018; 2019). Given these structural failure mechanisms of partially saturated soils in field and laboratory tests, a proper representation of the wetting-drying difference in SWCC and its interdependence with inelastic deformation should be an essential requirement for numerical modelling of coupled flow–deformation problems. The success and reliability of numerical simulations are mainly dependent on material models that represent constitutive relationships between the applied, or in-situ, stresses/fluid pressures and the resultant deformations/saturations (or vice versa) for soils of several known material properties. Thus, in this review, the attention in this thesis is drawn to the hydromechanical coupling in constitutive models for simulating the coupled flow deformation problem of partially saturated soils in existing BVPs. It is a concern that constitutive modelling for unsaturated soils in BVPs will generally be considered to be adequate if its physical arguments can address a sufficient number of experimental mechanisms, as outlined above. Moreover, when developing a continuum model, attention needs to be paid to warranting the simplicity of the numerical implementation and high flexibility in analysing BVPs at a structural level.

To address coupled flow deformation problems of partially saturated soils, many conventional geotechnical engineering practices/designs (e.g. Sheng et al., 2003; Xiong et al., 2014; Bandara et al., 2016; Lei et al., 2020; Wang et al., 2018) are predominantly based on classical models, themselves based on saturated soil mechanics (e.g. Modified Camclay or Drucker Prager) in which the influence of hydraulic behaviour is neglected in constitutive relationships for the sake of simplicity. In this approach, a separate function of SWCC is used as an additional function to compute the suction from the saturation degree and vice versa, where it does not interact with the stress-strain relationship, to describe the behaviour at the material point. The results of these works demonstrate that these methods are relatively efficient and able to capture the simple interaction between failure responses

and seepage flows under several loading and hydraulic processes thanks to the hydromechanical coupling recognised in the mixing mass and momentum conservation laws of three phases. To be more specific, the effects of fluid transport on the stiffness reduction and localised failure reflected in the onset and development of inelastic strain and yield stresses can be handled. However, in principle, the underlying mechanism of failure of partially saturated soils, which is the significant dependence of properties of the soil skeleton (e.g. strength and deformation) on the saturation condition at both material levels are ignored in these simulations, hindering them from correctly predicting the realistic behaviour of the material. This is due to the lack of appropriate hardening laws reflecting the dependence of the yield strength of hydraulic variables (e.g. the suction or saturation degree).

Although simple saturated soil models can still provide satisfactory results in some loading and saturation cases, the constitutive formulations of stress-strain and suction-saturation degree relationships for the behaviour of material points in BVPs in rigorous theoretical formulations are essential for describing the macroscopic behaviour of materials. In this sense, in recent years, more studies have been turning their attention to the potential of constitutive models of unsaturated soils implemented in numerical methods (e.g. FEM, MPM and SPH) as a critical component to simulate the failure mechanism of three-phase porous media accurately. In general, the vast majority of these models focused on the incorporation of hydraulic factors (e.g. the suction and saturation degree) into hardening laws to better reflect the reduction in shear strengths due to the transition from unsaturated to saturated conditions. For example, the Barcelona Basic Model (BBM) given by Alonso et al. (1990) is implemented in FEM by Rutqvist et al. (2011), Li et al. (1999), Abed & Vermeer (2004) to include the effect of suction on the yielding behaviour at the material point. The adoption of two separate loading functions (e.g. LC and SI) in BBM model causes certain difficulties for their computational implementation in terms of correlating these separate surfaces with the experimentally obtained data and its evolution to failure (Pedroso & Farias, 2011). They are, perhaps, the indefinite gradients in the flow rule in the case of stress paths passing through discontinuous intersections between separate yield surfaces, on the one hand, and cumbersome/complicated manipulations in checking and determining the activation of coupled hydro-mechanical yielding states on the other. Furthermore, a Cam-clay yield model is extended in Oka et al. (2010) by modifying an isotropic yield pressure with the influence of both saturation degree and suction to present the expansion of a yield surface with saturation processes. In Zhao (2019), an SPH method is enhanced for modelling the coupled multiphase flow in deformable porous media, based on the Lagrangian particle discretization of soil-water-air coupled governing equations (Oka et al., 2010). In this approach, simple suction, dependent on the Mohr-Coulomb softening model given by Yerro (2015) for MPM, is used to describe the plastic

behaviour of soils under hydraulic effects, going with a separate SWCC in the classical van Genuchten form (van Genuchten, 1980). It can be said that these approaches are capable of performing the change of soil stiffness and yield stresses with suction and saturation degree. These approaches can reproduce vital features of wetting-induced collapse behaviour of partially saturated soils due to the degradation of soil strengths, which are validated through extensive experimental tests (e.g. water infiltration tests and rainfall-induced slope failures). However, they are unable to capture the non-uniqueness and wetting-drying difference of SWCC at the constitutive level.

In addressing this issue, Ghorbani et al. (2018) and Tamagnini (2005) improve FEM to account for the effect of hydraulic hysteresis in a constitutive model for partially saturated soils. In these two models, a Modified Cam-clay model is extended using an LC yield surface dependent on the change of the plastic volumetric strain and saturation degree, along with a water retention curve accounting for the hydraulic hysteresis. These studies provided good numerical results, highlighting its success in predicting the realistic behaviour of unsaturated soils with the effect of hydraulic hysteresis on failure mechanisms. Nonetheless, they use a separate SWCC with the primary drying and wetting curves defined by various parameters. The irreversible saturation degree associated with the coupled hydro-mechanical dissipation mechanism is missing in these models, making them hard to use to describe the intrinsic nature of the wetting-drying difference and its interdependence with inelastic deformation, as discussed earlier.

2.4.2. Localised failure

One of the most indispensable features during the investigation on BVPs is the effect of strain localisation on structural behaviour in the post-localisation stage. Strain localisation involves the inception and propagation of shear dilation/compaction bands, characterized by thickness and inclination angle (see Figure 2.27). It is found ubiquitously as a critical precursor to geomaterial failures (Peric et al., 2014). In this context, much attention has been given over the past few decades to studying this phenomenon on fully saturated soils (e.g. Muhlhaus & Vardoulakis, 1987; Muhlhaus, 1986; Vardoulakis, 1989; Nova, 1989, 1994; Darve, 1994; 1996; Darve et al., 1986, 2004; Desrues & Viggiani, 2004; Daouadji et al., 2010; Loret & Rizzi, 1999; Mallikarachchi & Soga, 2019; Guo & Stolle, 2013; Nguyen & Bui, 2020). However, in practice, the fully saturated state is rarely reached in most geotechnical structures throughout the entire life of the service (Wheeler & Sivakumar, 1995; Vanapalli et al., 1999). Responses of partially saturated soils under different loading and hydraulic conditions are usually recognised in geohazards. Therefore, localisation of deformation at a partially saturated condition is of fundamental significance for understanding the failure mechanism of soils.

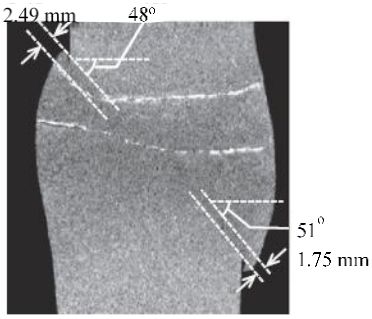

Figure 2.27. Thickness and inclination of a shear band of triaxial shear test on partially saturated dense Toyoura sand (Higo et al., 2013)

Localised failure: lab-scale observation

Localised failure's importance can be seen from several examples at a structural scale, such as failure of a tunnel during the drainage process of underground excavation, a rainfall-induced landslide, or the instability of dam abutments affected by the phreatic surface (Callari et al., 2010). Given the localised failure of partially saturated soils are an indispensable mechanism of soil collapse, its behaviour at material scale has been studied extensively in several triaxial (Patil et al., 2017; Kasangaki, 2012; Cui & Delage, 1996; Cunningham et al., 2003; Higo et al., 2011; 2013) and biaxial (Cruz et al., 2012; Alabdullah, 2010) tests. The experimental evidence suggests that partially saturated soils exhibit a localised stage of deformation after a homogeneous (diffuse) stage of deformation and wetting process (Cunningham et al., 2003; Higo et al., 2011; 2013). It is indicated through observations of a rapid reduction of shear strength, volumetric strain and saturation degree beyond the bifurcation (see Figure 2.28). Such stress losses and water retention capability degrades always come with the formation of shear bands whose onset (discontinuous bifurcation) is usually triggered at around the pre-peak (Song, 2014) or post-peak (Higo et al., 2011; 2013) moment of shear strength and where the width is roughly five times the mean grain size d_{50} (Kido et al., 2017).

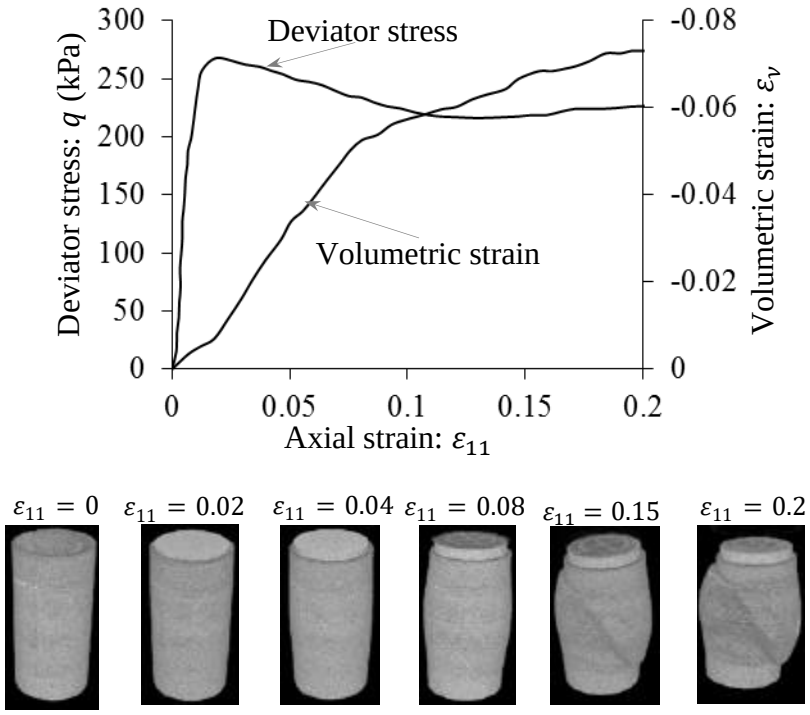

Figure 2.28. Evolution of shear band and softening response of triaxial shear test on partially saturated dense Toyoura sand (Higo et al., 2013)

As can be seen in Figures 2.29 and 2.30, localisation bands are observed to be more apparent, and their inclination angles increase, reflecting higher brittleness in conjunction with stronger dilatancy/strain-softening when suction increases (Patil et al., 2017; Kasangaki, 2012; Cunningham et al., 2003; Alabdullah, 2010). All of the features mentioned above are governed by the intrinsic nature of hydro-mechanical coupling due to the interactions between the grain rearrangement and liquid-bridge redistribution. In particular, solid deformation induces a change in the topology of the pore space, which varies the transport properties (i.e., permeability) and storage capacities (i.e., water retention law) of the fluid flow. On the other hand, wetting/drying processes lead to a variation in the capillary force on particles at their point of contact and hence their effective stress, manifesting the change in soil stiffness and brittleness. These micro-scale mechanisms must be used to obtain constraints on the interactions of internal variables, reflected in the dependence of all internal forces associated with plastic strains and irrecoverable saturation on stress, suction and plastic strain alongside irrecoverable saturation and their rates inside the localisation band.

(a) (b)

Figure 2.29. Patterns of localised failure at (a) partially saturated state (b) fully saturated state (Marinho et al., 2016)

$s = 50$ kPa $s = 250$ kPa $s = 500$ kPa $s = 750$ kPa

Figure 2.30. Effects of suction on the localized failure of drained triaxial compression tests at $\bar{\sigma}_{33} = 300$ kPa (a) $s = 50$ kPa (b) $s = 250$ kPa (c) $s = 500$ kPa (d) $s = 750$ kPa (Patil et al., 2017)

In addition, these experiments show that the changes of strain, porosity and saturation degree inside the localisation zone are predominant compared to those of the surrounding zone in the localised stage (Kido et al., 2017; Higo et al., 2011). In such cases, microstructural changes governing irrecoverable behaviour largely (or fully) take place inside the localisation region (see Figure 2.31). This suggests that the material outside this region usually undergoes insignificant deformation and saturation compared with that inside the shear band. This feature is consistent with the numerical results of strain and saturation degree distributions from finite element simulations of the plane-strain compression test in Song & Borja (2014) (see Figure 2.32). Thus, the overall response must be subject to the inhomogeneous mode of deformation and hydraulic fields over the whole Representative Volume Element (REV) once localised failure takes place.

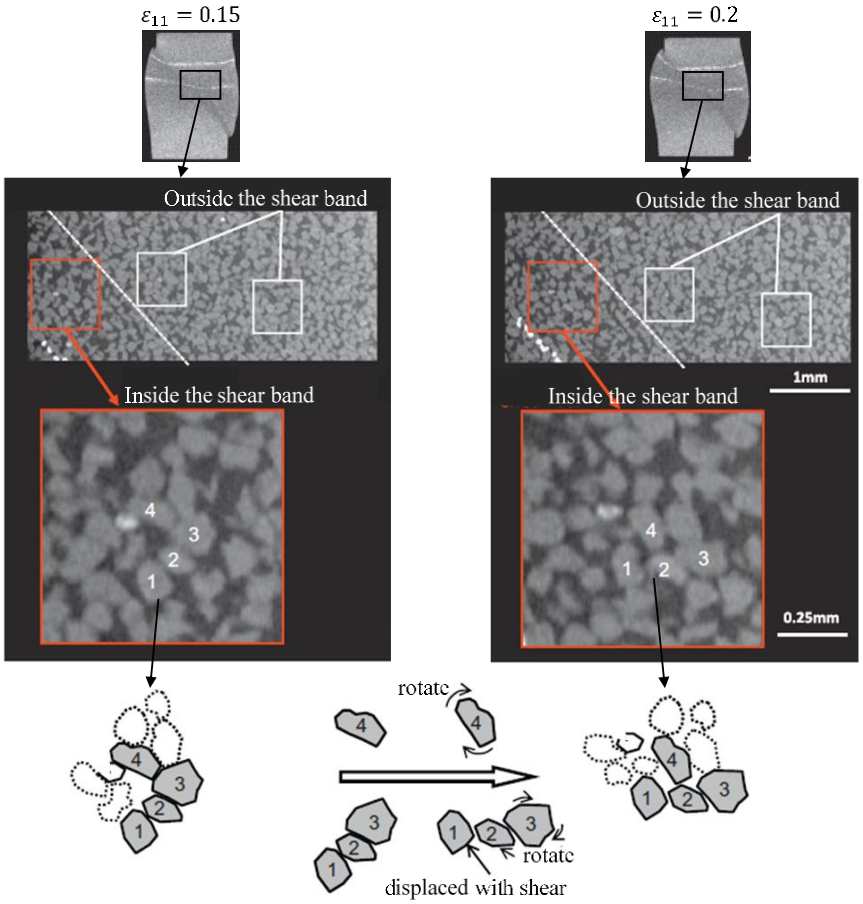

Figure 2.31. The microstructural change observed outside and inside the shear bands during shearing from $\varepsilon_{11} = 0.15$ to $\varepsilon_{11} = 0.2$ (Higo et al., 2013)

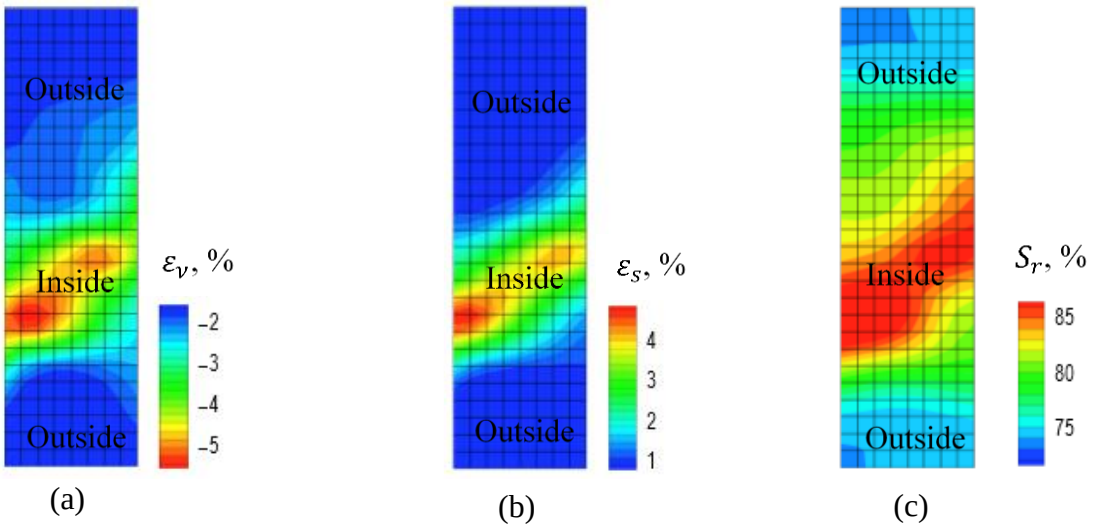

Figure 2.32. FE contours of (a) volumetric strain (b) shear strain (c) saturation degree in a rectangular soil sample of the plane-strain compression test (Song, 2014).

In addition, when localised failure does take place, the overall experimental curves of stress-strain and suction-saturation degree relationships are generally considered to be not unique, to represent the behaviour of soils and their tendency to vary depending on the specimen size due to their mixed material-structural properties (see Figure 2.33). It is defined as the effect of the characteristic structure size on the post-peak load-displacement response and the strength of the structure where the 'statistical size effect' and 'deterministic size effect' are considered (Nguyen & Bui, 2020). In particular, the statistical size effect is used to describe the variations in strength due to the probability that the presence of flaws and defects increases with the size of the structure, while the deterministic size effect is associated with the change in the post-peak load-displacement response and stress redistributions induced by the formation and propagation of localisation bands. This indicates that the size effect is crucial when using a constitutive model to predict a structural response, as well as during the development of a constitutive model (Nguyen & Bui, 2020).

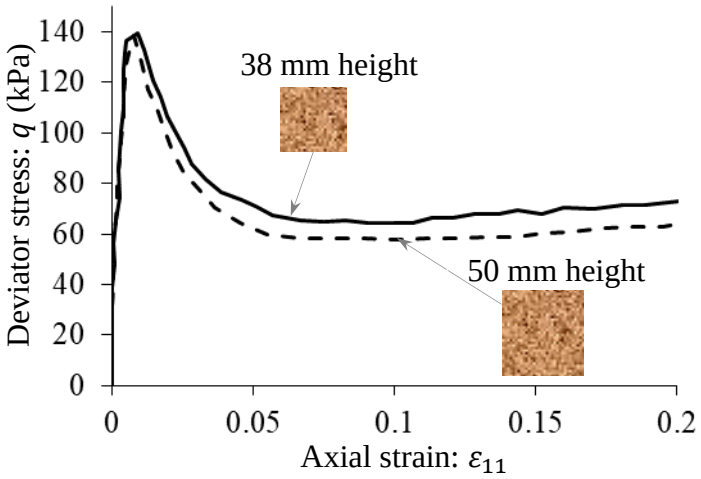

Figure 2.33. Size effects in undrained triaxial compression tests on fully saturated uniformly-graded Ottawa sand at $\bar{\sigma}_{33} = 300$ kPa (after Omar & Sadrekarimi, 2015) using specimens with a 38 mm and 50 mm height.

Numerical modelling of partially saturated soils involving localised failure

Given the above observation, the coupled hydro-mechanical behaviour, taking into account strain localisation, should be addressed in theoretical frameworks to account for the transition from a diffuse to a localised mode and the associated size effects in different saturation regimes. The development of such frameworks remains hugely few, although there has been a wide range of advanced constitutive models for partially saturated soils in the literature (e.g. Hu et al., 2014; Khalili et al., 2008; Sheng et al., 2008; Wheeler et al., 2003; Zhou et al., 2012ab; 2018; Zhou & Sheng, 2015; Muraleetharan et al., 2009).

Bifurcation: All recent works only attempt to provide solutions for the localization detection of partially saturated soils at the material level. Some bifurcation criteria for partially saturated soils have been introduced for analysing the bifurcation of homogeneous stress-like fields into non-unique stress-like states as a consequence of non-unique deformation and saturation fields. These bifurcation criteria are used to set an upper limit to soil stability. For instance, Buscarnera & Nova (2011) employed the second-order work concept (which becomes negative) as a discontinuous bifurcation criterion to investigate the wetting/drying-induced instability in triaxial testing (see Figure 2.34). In this approach, on the basis of work input (Houlsby, 1997), effective stress and modified suction can also be chosen as stress-like variables to conjugate with the stress and saturation degree as train-like variables for explaining the conceptual links between Hill's stability criterion (e.g. the second-order work concept) and the notion of test controllability of unsaturated soils. This condition can be applied to any specific constitutive model to check the stability conditions based on the hydro-mechanical response retrieved from laboratory tests. In this approach, the onset of localised failure is observed to occur exactly at the peak stress (see Figure 2.34), although acoustic emission measurements and microstructural observations (Higo et al., 2011; 2013) commonly indicate that the onset of localisation occurs somewhere in the vicinity of the peak stress (e.g. the pre-and post-peak stress). Furthermore, this approach is unable to capture the orientation of the failure plane at the bifurcation point. For soils, consideration of the formation and propagation of shear bands is needed in these models because these bands cause material separation and then the soil collapses. Miss-predicting the orientation of the localisation band in constitutive modelling leads to incorrect predictions of the localised failure. In Schiava & Etse (2006), the discontinuous bifurcation theory of Rudnicki & Rice (1975) (the zero or negative determinant of the acoustic tensor) has been developed to detect the activation of the shear band, considering the suction-dependent inclination angle but without the soil-water characteristic curve (SWCC) to reproduce the transition between the saturation regimes (see Figure 2.35). SWCC is taken into consideration in the discontinuous bifurcation condition in Borja (2004), in which both the suction and the saturation degree are incorporated into the tangent stiffness tensor of an extended Modified Cam-Clay model, and its first zero eigenvalues are investigated to detect the limit point bifurcation and determine the inclination of the shear bands under both undrained and drained conditions of partially saturated soils. Regardless of the advantages it offers, the non-uniqueness of water retention behaviour (Nuth & Laloui, 2008; Gallipoli et al., 2003; Vanapalli et al., 1999; Tarantino, 2009) is neglected in this framework, thus hindering its ability to reflect the effects of mechanical deformation on hydraulic responses. Peric et al. (2014) and Song et al. (2018) suggest analytical solutions using more complete localisation criteria where the dependence of SWCC on the volume change can be addressed. The obtained solutions are then incorporated into the bounding surface plasticity model for partially saturated soils (Khalili et al., 2008) to detect the

inception and computing orientation of strain localization with critical hardening moduli in the case of constant water content and drained loadings. The solutions take into account the simultaneous fluid flow and their complex interactions with the solid skeleton. They can collapse to that for fully saturated porous materials to capture the transition between fully and partially saturated conditions. Nevertheless, these two approaches are not yet capable of capturing the wetting-drying difference in generating the onset of localisation. They neglect the effect of hydraulic internal variables related to the intrinsic mechanism for the tight interaction between grain rearrangement and liquid redistribution behind the macro response of unsaturated soils inside localisation bands at the moment of bifurcation.

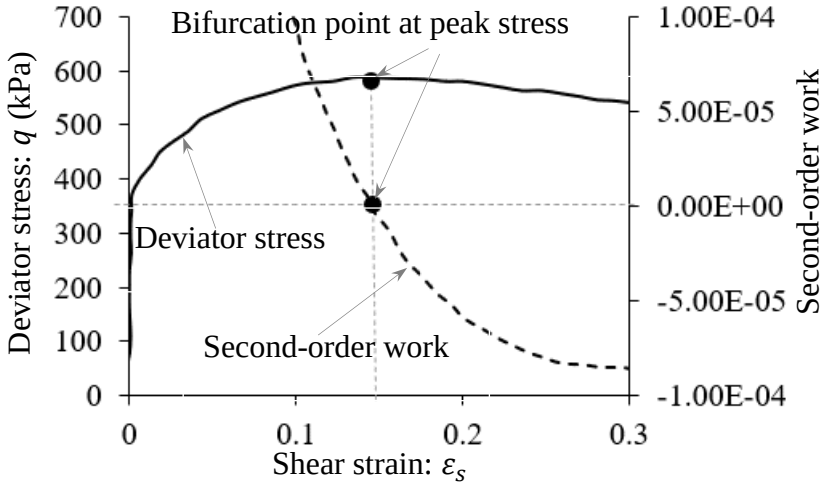

Figure 2.34. The onset of instability predicted by the second-order work (after Buscarnera & Mihalache, 2014)

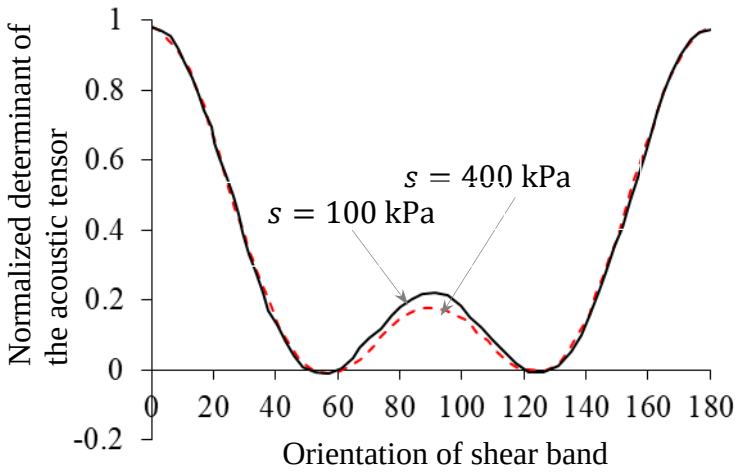

Figure 2.35. The onset of instability predicted by the discontinuous bifurcation theory of Rudnicki & Rice (1975) (after Schiava & Etse, 2006)

Post-localisation behaviour: None of the existing constitutive models is able to describe the post-localisation behaviour of partially saturated soils correctly. This is owing to their assumption of homogeneous deformation through the adoption of a single set of strain and saturation degree measurements for the whole REV crossed by a shear band. They neglect details about the size of the shear band and the evolution of the material behaviour inside it. Consequently, their performance fails to give a correct description of the size-dependent responses induced by localised failures, leading to mathematical ill-posedness of the boundary value problems in numerical simulations at a structural level (Oliver et al., 1999; 2012). To illustrate this, owing to the inhomogeneity within a structure induced by the localisation, the uniqueness of fields (stress, fluid pressure, strain, and saturation degree) is lost, resulting in physically meaningless continuum definitions or measures of stress-like and strain-like variables of the whole RVE and hence the variation of the results in accordance with the spatial discretisation mesh size due to the interaction between material and structural properties (see Figure 2.36).

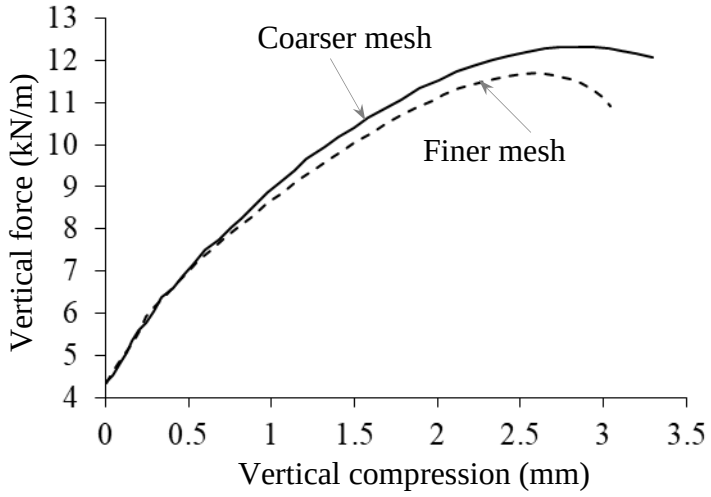

Figure 2.36. Mesh sensitivity in the FEM simulation of the partially saturated silica-concrete sand specimen subjected to vertical compression in plane strain test (after Song, 2014)

To describe the post-localisation behaviour of partially saturated soils, several attempts have been made concerning numerical treatments of size effects. In particular, Callari et al. (2010) adopted enhancements to the discretisation of partially saturated poroplastic solids using a multi-scale framework, which involves the response of the strong discontinuity (the Strong Discontinuity Approach). There have been other higher-order continuum theories, such as the Cosserat continuum (Li, 2015), non-local/gradient (Mroginski et al., 2011; Menon & Song, 2019; Song & Khalili, 2019), and viscoplasticity (Ehlers et al., 2004; Zhang & Schrefler, 2004), using an extra parameter of length scale associated with the width of the localisation band to regularise BVPs. The fundamental principle

of these methods is to allow the preservation of the ellipticity of the governing partial differential equations (PDEs) in the post-localisation stage, hence eliminating the spatial discretisation dependency. These approaches can all adequately tackle the scale effect and guarantee meaningful convergence of numerical solutions upon discretisation refinement. Despite some successes in tackling the effects of strain localisation, these treatments are relatively phenomenological, failing to address the underlying mechanisms of localised failure in partially saturated soils. On the other hand, these regularisations are usually applied ad hoc after the formulation of a constitutive level, while the performance and calibration of the model are usually carried out without taking into account localisation. This is an inconsistency that has been overlooked in the literature, not only in constitutive modelling of partially saturated soils but also in a wide range of geomaterials. This is due to the mixing of the material behaviour and numerical techniques for BVPs, used to analyse the inhomogeneous deformation. Such a mixing always requires the inseparability of the parameter identification/calibration and solutions of BVPs. It leads to difficulties in performing model calibration and validation at a material scale in these enriched models, making their application in practice a challenge. Additionally, their base constitutive relationships for partially saturated soils are inadequate to capture the micromechanical nature of coupled hydro-mechanical yielding, in which different responses under wetting and drying paths are not accounted for.

2.5. Summary and discussions

The above literature review is summarized, and several vital motivations are briefly discussed in terms of the following three aspects:

2.5.1. Constitutive model for partially saturated soils

Macro behaviour is governed by the coupled hydro-mechanical mechanism due to the interaction between the two grain-scale phenomena, (i) grain sliding and rearrangement, and (ii) ruptures of liquid bridges and their redistributions. These grain-scale phenomena result in observable hydro-mechanical coupling at the continuum level that has been extensively investigated in several net stress constant, suction-controlled and constant water content triaxial tests. In particular, when the suction increases (or the saturation degree decreases), the shear strength, yield limit and dilatancy increase. SWCC is not unique and is dependent on histories of both deformation and saturation. Furthermore, these experimental findings are somehow related to the existence and uniqueness of CSL with an independent slope in the coupled hydro-mechanical spaces defined by deviatoric stress, mean stress, suction, specific volume and saturation degree. All of the features described above lead to dependence on mechanical and hydraulic thermodynamic forces on both of their rates, in addition to stress and

suction. In this sense, constitutive models should possess only a single yield surface with two evolution rules to better represent the effects of hydro-mechanical coupling in a rigorous way.

There have been several attempts and successes in developing constitutive models for unsaturated soils to capture these experimentally observed characteristics over the last 30 years. In particular, the suction-dependent mechanical responses have been investigated in many models without SWCC (e.g. Alonso et al., 1990; Wheeler & Sivakumar, 1995; Cui & Delage, 1996; Sun et al., 2000). In some others (Thu et al., 2007; Zhou & Sheng, 2009; Russell & Khalili, 2006), the hydraulic influence through SWCC is added to distinguish the effects of different saturation regimes on the mechanical behaviour, but the effects of mechanical behaviour on hydraulic responses were not accounted for in these models. The non-uniqueness of SWCC has been well recognised and was taken into account in Buscarnera & Nova (2011). However, these studies neglect the wetting-drying difference in the behaviour, which has been successfully addressed in several other models (e.g. Wheeler et al., 2003; Khalili et al., 2008; Muraleetharan et al., 2009). For example, Muraleetharan et al. (2009) adopt a separate law of hydraulic hysteresis in which each drying and wetting path possesses different parameters, while others (e.g. Wheeler et al., 2003) employ the multiple yield surface. Nevertheless, the micromechanical nature of coupled hydro-mechanical yielding should be represented by a unique yield locus. Furthermore, several net stress-controlled experiments indicate the irrationality of horizontal straight lines for the SI/SD curves adopted in these models. The thermodynamic-based approaches to constitutive modelling of partially saturated soils have recently been brought to the attention of several studies. They bring benefits in minimizing the number of arbitrary assumptions and model parameters. Despite some successes, the inadequacy in capturing the full coupling between plasticity and hydraulic irreversibility can be seen in these existing studies. For instance, hydraulic dissipation is overlooked in some models (Tamagnini & Pastor, 2004; Uchaipichat, 2005; Coussy et al., 2010; Buscarnera & Einav, 2012; Dangla & Pereira, 2014; Lei et al., 2016). The use of multiple yield surfaces in existing models does not naturally reflect the inseparable nature of the hydro-mechanical coupling because they use a decoupling of dissipative stresses from all the rates of internal variables (Sheng et al., 2004; Santagiuliana & Schrefler, 2006; Hu et al., 2015). There also remain a limited number of experimentally validated and operational models derived from thermodynamics. Full coupling between plasticity and hydraulic irreversibility and their associated hydro-mechanical dissipation properties have not usually been explored at length in previous thermodynamics-based models. Furthermore, a good balance between the rigour, simplicity, number of parameters and performance in the derived constitutive models has not always been the case in the existing models.

In a bid to address the above challenges, a more rigorous thermodynamics-based constitutive model is needed to reflect better the experimentally observed influences of deformation on the water

retention curve and vice versa in the mixed mode of loading and saturation conditions. In this sense, central to this development is the dependence of all thermodynamic forces on stress, suction, plastic strain and irrecoverable saturation and their rates, inspired by the inseparable nature of the interaction between frictional sliding, grain rearrangement and ruptures of liquid bridges and their redistributions at the grain contacts. Attention also needs to be paid to obtaining a good balance between several factors (rigour, simplicity, number of parameters and performance). Towards this aim, a framework, derived from strongly and generically based fundamentals, is put forward to reproduce the experimentally observed influences of mechanical deformation on SWCC and vice versa, systematically and consistently, in a mixed mode of loading and hydraulic conditions. The full coupling between dissipative mechanisms of plastic deformation and hydraulic irreversibility can be investigated rigorously by using a unified thermodynamically admissible approach: whereby a single loading function can be established to capture the simultaneous activation and development of both mechanical and hydraulic yielding adequately at any instant, with the coupled evolution laws for plastic strain and irreversible saturation rates sharing a unique plastic multiplier. Beneficially, the coupled changes in the shape/size of this yielding surface can naturally reflect the cross-interaction hardening laws in a smooth transition between saturated and unsaturated conditions. Thanks to such a systematic approach being taken, the new model will provide a small and manageable number of identifiable parameters that all have explicit physical meanings. This model will be adequately validated with a broader range and larger number of loading and hydraulic conditions obtained from experiments (e.g. suction-, water content- and net stress-controlled experiments) when compared with existing thermodynamic-based modelling of unsaturated soils. Going hand in hand with this, also provided will be a corresponding calibration method, possessing a close and consistent connection with the laboratory procedures and data associated therewith, for identifying the physically-based parameters.

2.5.2. BVPs for partially saturated soils

Regarding BVPs, this thesis focuses on two aspects, including the constitutive model for partially saturated soils implemented in BVPs and strain localisation due to their importance in understanding the realistic mechanisms of soil failure. These are summarized along with corresponding motivations as follows.

Constitutive model for partially saturated soils implemented in BVPs

The coupled flow deformation problem of partially saturated soils involves complex seepage flow patterns and large deformations of the solid phase under the various loading and saturation conditions observed in many field and laboratory tests in the literature. To solve these coupled hydro-mechanical

BVPs, the SPH technique is proven more advantageous than FEM in tackling mesh distortion issues and GIMPM in reducing computational cost when simulating large-deformation problems (Bui & Nguyen, 2017). Nevertheless, there has been not much attention paid to the development of SPH for simulating the coupled flow deformation problems of partially saturated soils. On the other hand, the constitutive model is a vital component for the accuracy and robustness of numerical simulations when predicting realistic phenomena of soil collapse. Nevertheless, most of the existing numerical approaches for partially saturated soils adopt several models with plastic strain as the only internal variable representing the effects of microstructural changes, neglecting micro-scale mechanisms associated with irreversible saturation to reflect wetting-drying differences in SWCC. None of them can describe the dependence of all internal forces on stress, suction and internal variables, which restricts the model's capability to capture faithfully the actual response of partially saturated soils associated with the strong interaction between plasticity and hydraulic irreversibility under a wide range of stress paths and testing conditions.

Given this review, further SPH developments for partially saturated soils are still needed to incorporate an additional hydraulic internal variable (e.g. the irreversible saturation degree), taking into account the effects of underlying mechanisms of hydromechanical coupling that cannot be captured by plastic strain alone. Within the SPH approach in this thesis, the proposed single yield surface model for unsaturated soils is used to show how each SPH particle responds in the case of the coupled hydro-mechanical large-deformation condition, where the interaction between the SPH particles is described by a mixed form of governing equations of three phases. It is expected to be simplified, reliable and economical for applications that involve fundamental mechanisms of unsaturated soils.

Strain localisation of partially saturated soils

Hydro-mechanical coupling makes a substantial contribution to the localized failure behaviour of partially saturated soils. This postulation is drawn from the ubiquitous observation of a very rapid reduction of the shear strength beyond the peak in many triaxial shear tests of unsaturated soils. This significant loss of stress always comes with the formation of shear bands, characterised by inclination and thickness. The experimental evidence illustrates that partially saturated soils are more brittle at higher levels of suction, where shear bands get clearer with an increase in the inclination angle. It is intrinsically linked to energy dissipation, which is entirely governed by the rearrangement (sliding and rotation) of soil grains and the disruption of water meniscuses associated with inelastic material behaviour, irreversible deformation and saturation occurring inside the localisation band. The material outside the band usually behaves reversibly in both mechanical and hydraulic processes

because of the negligible microstructural changes. This difference in deformation and saturation between the localisation band and the surrounding material induces the size effect observed in experiments.

To address strain localisation in partially saturated soils, several attempts have been made to provide solutions for detecting the onset of localized failure in partially saturated soils (Buscarnera & Nova, 2011; Schiava & Etse, 2006; Borja et al., 2004; Peric et al., 2014; Song et al., 2018). Nonetheless, none of them addresses the hydraulic irreversibility of SWCC in governing the coupled hydro-mechanical discontinuous bifurcation condition. Furthermore, localisation of deformation in the form of shear bands leads to the breakdown of the assumption of homogenous deformation of classical continuum models for partially saturated soils due to the considerable variations in the strain and saturation degree across the shear band. In this sense, traditional continuum models are unable to capture localised failure of soils correctly because they ignore the effects of inclination, thickness and the evolution of the shear band in constitutive equations, leading to ill-posed boundary value problems and discretisation-dependent numerical solutions. On the other hand, existing enrichment approaches (e.g. non-local and gradient dependent regularizations) and discretization-based enhancements, although having reached a mature state of development, are usually mixed with the numerical methods for solving boundary value problems. As a consequence, the analysis of localised failures and size effects always have to depend on the analysis of boundary value problems. These approaches are also complicated to implement in a numerical code and/or computationally expensive for broad applications in engineering design.

The above analysis has demonstrated the need to develop better models for describing strain localisation of partially saturated soils, taking into account the interdependence between mechanical and hydraulic yielding responses. In this sense, this study follows a new line of development in which the size and orientation of the shear band are embedded directly in the constitutive structure of coupled hydro-mechanical models to naturally describe the localised failure mechanism of partially saturated soils at the material level. A physically meaningful transition between homogeneous inelastic deformation, the onset of localisation and localised deformation is captured through a rigorous thermodynamics-based two-scale approach (Nguyen & Bui, 2020) for partially saturated soils, accounting for the interdependence between loading-unloading and wetting-drying differences.

Chapter 3. Hydro-mechanical coupling of partially saturated soils: governing equations and a generic thermodynamic approach to constitutive modelling

3.1. Introduction

The main objective of this Chapter is to present a generalized framework accounting for the most fundamental features of the coupling between the matrix of porous material and fluid flow in partially saturated soils, aiming to strike a good balance between rigour and simplicity in formulations. It forms a basis for the developments of specific models in the later chapters.

In this framework, basic concepts of Biot's three-phase continuum mixture theory are first reviewed before presenting how mass and momentum conservation laws for individual phases of the mixture can be derived from the Reynolds transport theorem. These governing equations of the separate phases are combined to construct a generic seepage flow model for partially saturated soils in a simple mixed form of essential field variables (e.g. porosity, saturation degree, solid velocity, Darcy seepage velocity) following the motion of the solid skeleton. The distinct feature of this framework lies in the development of a generic thermodynamics-based approach for a hydromechanical constitutive relationship (stress-strain and suction-saturation degree) inspired from the inseparable nature of grain rearrangement and liquid-bridge redistribution at the microscale, compared to existing ones. Such intrinsic micro-scale mechanisms are used to obtain constraints on the interactions between plastic strains (internal mechanical variable) and irrecoverable saturation (internal hydraulic variable) at the macro scale, reflected in the dependence of all thermodynamic forces on stress and suction. These required characteristics for constitutive models are the outcomes of the review and assessment of the behaviour of partially saturated soils at both macro and grain scales in the previous Chapter. All these appear in a generic special form of the dissipation potential or kinematic constraint equations, leading to a single yield function dependent on stress and suction and two flow rules with a single "plastic" multiplier. In inelastic behaviour, any change in irrecoverable saturation automatically leads to plastic deformation, and vice versa, given a single yield surface plastic multiplier. The above features are different from unsaturated models in the literature that possess more than one yield surface and hence more than one "plastic" multipliers. The proposed approach brings benefits in minimizing the number of arbitrary assumptions and parameters. Following the thermomechanical formulation, this chapter preliminarily addresses the computational aspect of the proposed model where tangent stiffness tensor and semi-implicit stress return algorithm are presented in generic forms.

3.2. Seepage flow model

The properties of seepage flow depend on the microstructure of the pores related to fluid pressures in different saturation regimes and its interactions with the behaviour of deformable soil skeleton represented through effective stresses and deformation fields (Lewis & Schrefler, 1998). In principle, an uncoupled hydrological approach can be used for analysing problems of unsaturated soils where a non-deformable body of soil skeleton can be assumed to derive the continuity equations of seepage flow (Richard, 1992; Li & Cameron, 1996; Sheng et al., 2003). Several essential fields of fluid phases (e.g. seepage velocity, saturation degree, suction) obtained from these simplified equations are then used as inputs and incorporated into the mechanical equations for the solid displacements (e.g. solid velocity, porosity, stress, strain) to simulate the effect of fluid transports on the mechanical response. Despite the simplicity and some successes, this approach lacks the consistency between the continuity equations of fluid phases in the case of a rigid soil skeleton and the mechanical equations for a deformable medium. As a result, it is unable to describe the effect of volume change over time on the variation of seepage flow, leading to the inaccuracy in capturing important mechanisms of coupled deformation-flow processes. On the other hand, the coupled hydro-mechanical seepage flow model (Alonso et al., 1988; Thomas & He, 1995; Loret & Khalili, 2000; Sheng et al., 2003; Borja, 2004) is conceptually more rigorous, complete and accurate in simulating the coupling between deformation and fluid transport within the deformable body of partially saturated soils. This is due to the fact that both hydraulic and mechanical properties of material inspired from the coupling between grain and liquid dynamics can be approximately quantified through a system of governing equations derived from a series of basic balance laws in three-phase porous media without assumptions about fluid transports in the rigid soil skeleton. These governing equations are simultaneously solved and rigorously linked together through appropriate laws representing the interaction between three phases (e.g. seepage forces, mixture theory). Thus, this approach, a mainstream in modelling seepage flow and deformation of unsaturated soils (Sheng et al., 2003), will be applied and studied in this section.

3.2.1. Basic concepts of the mixture theory

This section is to present several vital basic principles and concepts of Biot's mixture theory (Biot, 1941; Zienkiewicz et al., 1990). In the mixture theory, partially saturated porous media are made up of three constituents (soil, water, air) as described by the superposition in Figure 3.1, where each of them is assumed to be continuous and occupy every material point in the space at any arbitrary time instant. In principle, a microscopic quantity over volume and area of a REV is integrated and averaged to determine the averaged macroscopic quantities (Lewis & Schrefler, 1998), which are summarized as follows.

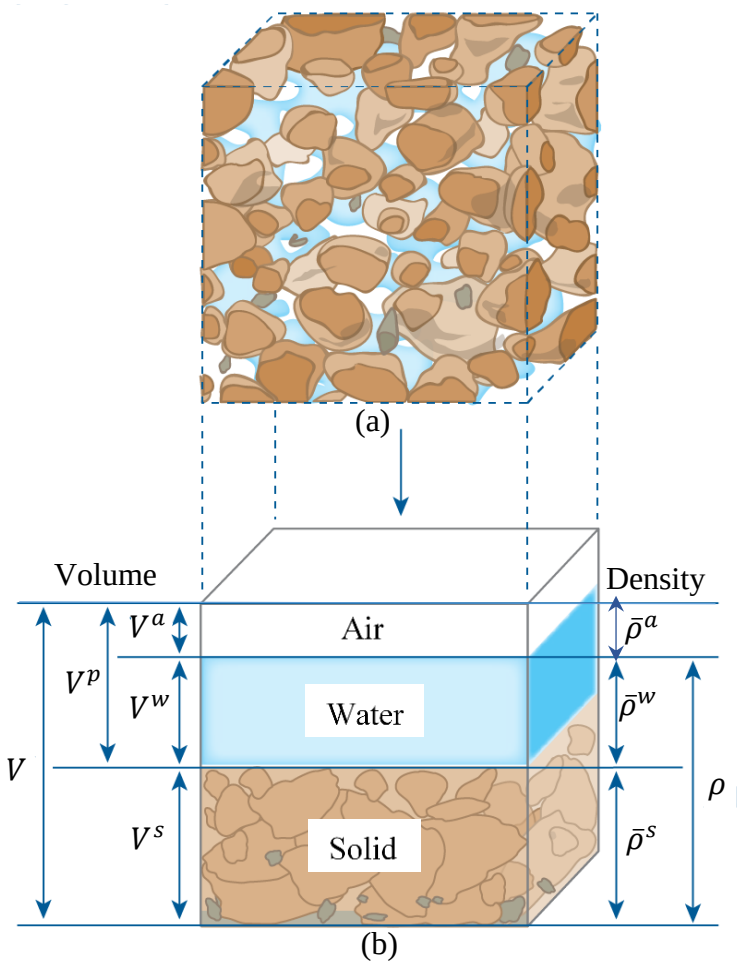

Figure 3.1. Continuum approximation of partially saturated porous media (a) Unsaturated porous media (b) Phases (after Selker & Or, 2018)

Volume fractions

The concept of volume fraction is fundamental for the mixture theory (Mills, 1966; Morland, 1972). As can be seen in Figure 3.1, its basis is the current total volume V (superimposed continua) defined as the sum of the partial volumes $V^{\varkappa}$:

$$V = V^s + V^w + V^a \tag{3.1}$$

and the pore volume (V^p) which is defined as:

$$V^p = V^w + V^a \tag{3.2}$$

in which the superscript $\varkappa$ is used to denote the constituent where "$\varkappa$" stands for "s" for solid or "w" for water or "a" for air.

From Eqs. (3.1) and (3.2), Eulerian porosity ϕ can be defined as a variable related to the current volume V as:

$$\phi = \frac{V^p}{V} \tag{3.3}$$

In addition, a Lagrangian porosity $\bar{\phi}$ is introduced denoting the ratio between the current pore volume V_p and the initial volume V_0:

$$\bar{\phi} = \frac{V^p}{V_0} \tag{3.4}$$

Saturation degree S_r is given by:

$$S_r = \frac{V^w}{V^p} \tag{3.5}$$

Eqs. (3.1-3.5) allow writing the volume $V^\varkappa$ occupied by the $\varkappa$ phase as follows:

$$V^w = \phi S_r V = \bar{\phi} S_r V_0 \tag{3.6}$$

$$V^a = \phi(1 - S_r)V = \bar{\phi}(1 - S_r)V_0 \tag{3.7}$$

$$V^s = (1 - \phi)V \tag{3.8}$$

The volume fraction $\varsigma^\varkappa$ of phase $\varkappa$ is written in the following forms:

$$\varsigma^w = \frac{V^w}{V} = \phi S_r \tag{3.9}$$

$$\varsigma^a = \frac{V^a}{V} = \phi(1 - S_r) \tag{3.10}$$

$$\varsigma^s = \frac{V^s}{V} = 1 - \phi \tag{3.11}$$

which satisfy the closure condition:

$$\varsigma^w + \varsigma^a + \varsigma^s = 1 \tag{3.12}$$

Density of mixture

The average mass density of the mixture ρ is defined by the following expression:

$$\rho = \bar{\rho}^s + \bar{\rho}^w + \bar{\rho}^a = \varsigma^s \rho^s + \varsigma^w \rho^w + \varsigma^a \rho^a \tag{3.13}$$

where $\bar{\rho}^\varkappa = \varsigma^\varkappa \rho^\varkappa$ is the partial mass density and $\rho^\varkappa$ is the intrinsic mass density of constituent $\varkappa$.

Definition of the effective and partial stresses of the fluid-solid mixture theory

The total stress tensor σ_{ij} of the three-phase mixture is made up by the sum of partial stresses $\bar{\sigma}_{ij}^\varkappa$, being of the form:

$$\sigma_{ij} = \bar{\sigma}_{ij}^s + \bar{\sigma}_{ij}^w + \bar{\sigma}_{ij}^a = \varsigma^s \sigma_{ij}^s + \varsigma^w(-p^w)\delta_{ij} + \varsigma^a(-p^a)\delta_{ij} \tag{3.14}$$

where σ_{ij}^{s} is the intrinsic stress of soil skeleton; p^w and p^a denote intrinsic pore pressures acting on water and air constituents; δ_{ij} is the Kronecker delta. Physically, Eq. (3.14) can be interpreted using the sum of averaged microscopic stress tensor at the microscale (Lewis & Schrefler, 1998; Lu, 2008).

The matric suction is defined as (see Figure 3.2):

$$s = p^a - p^w \tag{3.15}$$

The definition of net stress tensor reads:

$$\bar{\sigma}_{ij} = \sigma_{ij} - p^a \delta_{ij} \tag{3.16}$$

In Eqs. (3.15) & (3.16), while σ_{ij} serves as the external stress provided during the loading process, fluid pressures of air and water phases can be experimentally measured through different testing techniques such as axis-translation Technique (Fredlund, 1989), suction Probe (Ridley & Burland,1993), time-domain reflectometry (Topp et al., 1980), electrical conductivity sensors (Skinner et al., 1997), thermal conductivity sensor (Phene et al., 1971; Lee & Fredlund, 1984; Fredlund & Wong, 1989), in-contact filter paper technique (McKeen, 1980; Chandler & Gutierez, 1986; Chandler et al., 1992; Houston et al., 1994; Fredlund et al., 1995; Ridley, 1995; Leong et al., 2002). The effective stress in this model takes the Bishop's form, as commonly used in many papers on constitutive modelling of unsaturated soils (Wheeler et al., 2003; Sheng et al., 2004; Houlsby, 1997; Coussy et al., 2010) (see Figure 3.3). Its Cauchy form can be expressed as:

$$\sigma'_{ij} = \bar{\sigma}_{ij} + S_r s \delta_{ij} \tag{3.17}$$

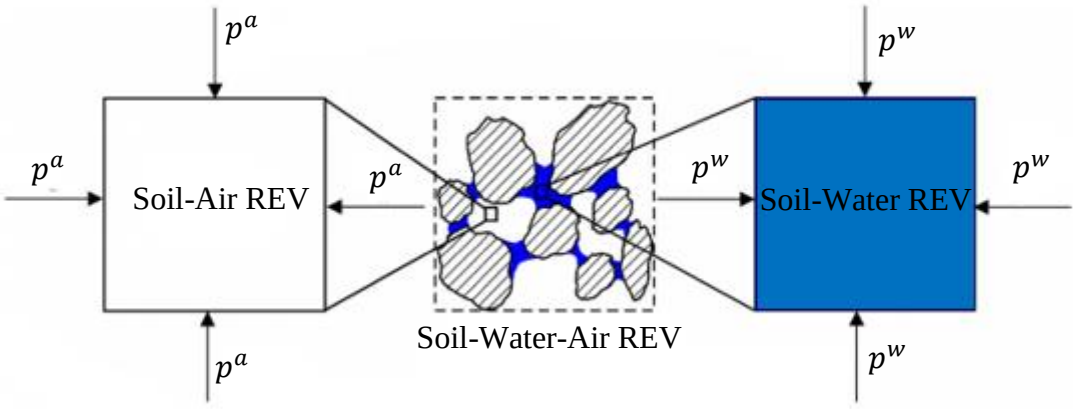

Figure 3.2. Illustration of scale definition difference among air-water-solid REV, soil water REV, and soil air REV where air-water-solid REV include air-water-solid system, soil water REV, and soil air REV involving only pore or subpore scale (Lu, 2008).

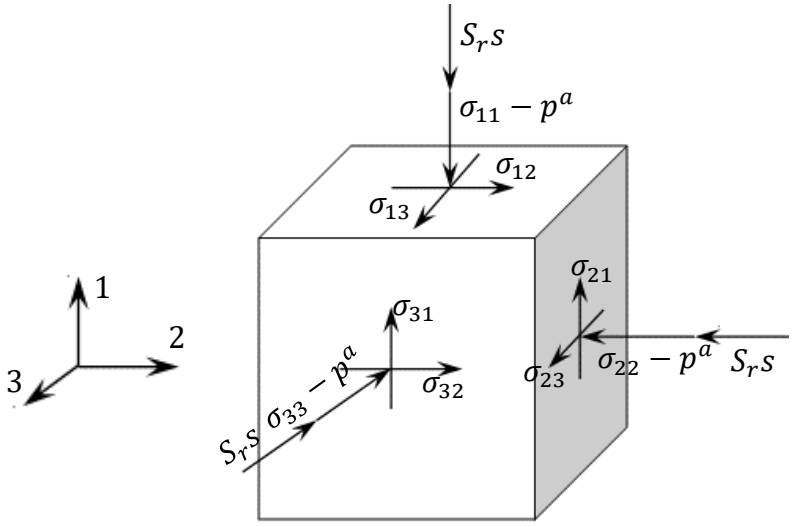

Figure 3.3. Schematic representation of stress components for air-water-solid REV of partially saturated soils based on Bishop's effective stress (Lu, 2008).

Kinematics

The material (or Lagrangian) time derivative of a field variable $\psi(x_i, t)$ following the motion of the $\varkappa$-constituent is given by the following expressions ("$\varkappa$" stands for "s" (solid) or "w" (water)):

$$\frac{D^s\psi}{Dt} = \frac{\partial\psi}{\partial t} + v_i^s \frac{\partial\psi}{\partial x_i} \tag{3.18}$$

$$\frac{D^w\psi}{Dt} = \frac{\partial\psi}{\partial t} + v_i^w \frac{\partial\psi}{\partial x_i} \tag{3.19}$$

where $v_i^{\varkappa}$ is the velocity of phase $\varkappa$, $\frac{\partial\psi}{\partial t}$ is the Eulerian time derivative representing the time rate of change of the field variable $\psi(x_i, t)$ at a fixed point within a reference coordinate system. It is noted that $\frac{D^{\varkappa}\psi}{Dt}$ is a scalar operator which can be used either for a scalar quantity or a vector quantity (Lewis & Schrefler, 1998).

Combining Eqs. (3.18) and (3.19) gives:

$$\frac{D^w\psi}{Dt} = \frac{D^s\psi}{Dt} + (v_i^w - v_i^s)\frac{\partial\psi}{\partial x_i} = \frac{D^s\psi}{Dt} + v_i^{ws}\frac{\partial\psi}{\partial x_i} \tag{3.20}$$

with $v_i^{ws} = v_i^w - v_i^s$

Balance laws

The balance laws for individual constituents can be derived from the Reynolds transport theorem (Takatsu, 2017; Haltas & Ulusoy, 2015) given in the following form:

$$\frac{d^{\varkappa}}{dt}\int_{V^{\varkappa}(t)}\psi dV^{\varkappa}=\int_{V^{\varkappa}(t)}\left[\frac{\partial\psi}{\partial t}+\frac{\partial(\psi v_i^{\varkappa})}{\partial x_i}\right]dV^{\varkappa} \tag{3.21}$$

Mass balance

Since the mass exchange between phases is assumed to be negligible, the mass balance of each phase can be expressed using the transport theorem for a material volume $V^{\varkappa}(t)$ as follows:

$$\frac{d^{\varkappa}}{dt}\int_{V^{\varkappa}(t)}\bar{\rho}^{\varkappa}dV^{\varkappa}=\int_{V^{\varkappa}(t)}\left[\frac{\partial\bar{\rho}^{\varkappa}}{\partial t}+\frac{\partial(\bar{\rho}^{\varkappa}v_i^{\varkappa})}{\partial x_i}\right]dV^{\varkappa}=0 \tag{3.22}$$

Eq. (3.22) can be rewritten as:

$$\frac{d^{\varkappa}}{dt}\int_{V^{\varkappa}(t)}\bar{\rho}^{\varkappa}dV^{\varkappa}=\int_{V^{\varkappa}(t)}\left[\frac{\partial\bar{\rho}^{\varkappa}}{\partial t}+v_i^{\varkappa}\frac{\partial\bar{\rho}^{\varkappa}}{\partial x_i}+\bar{\rho}^{\varkappa}\frac{\partial v_i^{\varkappa}}{\partial x_i}\right]dV^{\varkappa}=0 \tag{3.23}$$

It is noted that the volume $V^{\varkappa}(t)$ is arbitrary, and the integrals of both sides of Eq. (3.23) are equal. By applying the Gauss theorem for Eq. (3.23), the following expression can be obtained:

$$\frac{\partial\bar{\rho}^{\varkappa}}{\partial t}+v_i^{\varkappa}\frac{\partial\bar{\rho}^{\varkappa}}{\partial x_i}+\bar{\rho}^{\varkappa}\frac{\partial v_i^{\varkappa}}{\partial x_i}=0 \tag{3.24}$$

From Eqs. (3.18-3.19) and (3.24), the conservation of mass of each constituent is given by the following form:

$$\frac{D^{\varkappa}\bar{\rho}^{\varkappa}}{Dt}=-\bar{\rho}^{\varkappa}\frac{\partial v_i^{\varkappa}}{\partial x_i} \tag{3.25}$$

Linear momentum balance

The momentum of a constituent is conservative in the sense that the momentum change is equal to the total external force on its volume. This is reflected through the following form:

$$\frac{d}{dt}\int_{V^{\varkappa}(t)}\bar{\rho}^{\varkappa}v_i^{\varkappa}dV^{\varkappa}=\int_{S^{\varkappa}(t)}\left(\bar{\sigma}_{ij}^{\varkappa}\bar{n}_j\right)dS^{\varkappa}+\int_{V^{\varkappa}(t)}\bar{\rho}^{\varkappa}B_i dV^{\varkappa}+\int_{V^{\varkappa}(t)}R_i^{\varkappa}dV^{\varkappa} \tag{3.26}$$

In the above expression, $\bar{\sigma}_{ij}^{\varkappa}\bar{n}_j$ represents the partial traction force acting on the surface area $dS^{\varkappa}$ of volume $V^{\varkappa}$ with $\bar{n}_j$ being the outward unit normal vector on this surface, B_i is the body force of the mass $\bar{\rho}^{\varkappa}dV^{\varkappa}$ induced by the gravity acceleration constant g and $R_i^{\varkappa}$ denotes the viscous drag force acting on the $\varkappa$-phase.

The Reynolds transport theorem in Eq. (3.21) is adopted for the term on the left-hand side of Eq. (3.26), leading to:

$$\frac{d^{\varkappa}}{dt}\int_{V^{\varkappa}(t)}\bar{\rho}^{\varkappa}v_i^{\varkappa}dV^{\varkappa}=\int_{V^{\varkappa}(t)}\left[\frac{\partial(\bar{\rho}^{\varkappa}v_i^{\varkappa})}{\partial t}+\frac{\partial(\bar{\rho}^{\varkappa}v_i^{\varkappa}v_i^{\varkappa})}{\partial x_i}\right]dV^{\varkappa} \tag{3.27}$$

which then gives:

$$\frac{d^{\varkappa}}{dt}\int_{V^{\varkappa}(t)}\bar{\rho}^{\varkappa}v_i^{\varkappa}dV^{\varkappa}=\int_{V^{\varkappa}(t)}\left[v_i^{\varkappa}\left(\frac{\partial\bar{\rho}^{\varkappa}}{\partial t}+v_i^{\varkappa}\frac{\partial\bar{\rho}^{\varkappa}}{\partial x_i}\right)+\bar{\rho}^{\varkappa}\left(\frac{\partial v_i^{\varkappa}}{\partial t}+v_i^{\varkappa}\frac{\partial v_i^{\varkappa}}{\partial x_i}\right)+\bar{\rho}^{\varkappa}v_i^{\varkappa}\frac{\partial v_i^{\varkappa}}{\partial x_i}\right]dV^{\varkappa} \tag{3.28}$$

By adopting Eqs. (3.18-3.19), Eq. (3.28) becomes:

$$\frac{d^{\varkappa}}{dt}\int_{V^{\varkappa}(t)}\bar{\rho}^{\varkappa}v_i^{\varkappa}dV^{\varkappa}=\int_{V^{\varkappa}(t)}\left(v_i^{\varkappa}\frac{D^{\varkappa}\bar{\rho}^{\varkappa}}{Dt}+\bar{\rho}^{\varkappa}\frac{D^{\varkappa}v_i^{\varkappa}}{Dt}+\bar{\rho}^{\varkappa}v_i^{\varkappa}\frac{\partial v_i^{\varkappa}}{\partial x_i}\right)dV^{\varkappa} \tag{3.29}$$

Substitution of Eq. (3.25) into Eq. (3.29) gives the expression:

$$\frac{d^{\varkappa}}{dt}\int_{V^{\varkappa}(t)}\bar{\rho}^{\varkappa}v_i^{\varkappa}dV^{\varkappa}=\int_{V^{\varkappa}(t)}\left(\bar{\rho}^{\varkappa}\frac{D^{\varkappa}v_i^{\varkappa}}{Dt}\right)dV^{\varkappa} \tag{3.30}$$

From Eqs. (3.26) and (3.30), the balance of linear momentum for phase $\varkappa$ can be written using the Gauss theorem as follows:

$$\bar{\rho}^{\varkappa}\frac{D^{\varkappa}v_i^{\varkappa}}{Dt}=\frac{\partial\bar{\sigma}_{ij}^{\varkappa}}{\partial x_j}+\bar{\rho}^{\varkappa}B_i+R_i^{\varkappa} \tag{3.31}$$

The linear momentum balance in Eq. (3.31) can be then used to derive formulations of seepage flow velocity and solid velocity in porous media.

3.2.2. Governing equations

Due to interactions between different phases in a wide range of loading and saturation cases, the behaviour of three-phase porous media is usually complicated (Bear, 2018). It is incredibly complex and costly to account for every physical detail related to these interactions in the numerical framework, requiring a significant number of material parameters (Sheng et al., 2003). Thus, assumptions are essential and unavoidable for the development of a theoretical model, which should be required to strike a balance between rigour, performance and simplicity to describe necessary behavioural features of unsaturated soils for specific purposes and to make the theoretical framework more accessible to practical engineering (Sheng et al., 2003). In principle, from basic balance laws, different frameworks can be derived, depending on what the set of assumptions is used to eliminate the irrelevant and redundant features for a certain focus at hand. In this sense, given principle governing equations in Eqs. (3.25) and (3.31), mathematical modelling of the coupled hydro-mechanical seepage flow within partially saturated soils is formulated in this section quantifying change rates of seepage force, solid velocity, porosity and saturation degree in coordinates with respect to the motion of the solid phase. Several common assumptions adopted during the derivation procedure of this model are shown and discussed as follows:

(i) No mass, entropy and internal energy exchanges among constituents (Zienkiewicz, 1982; Lewis & Schrefler, 1998; Bui & Nguyen, 2017).

(ii) Isothermal process: The temperature of the system is constant where the thermal effects are neglected. Particularly, heat conduction, vapour diffusion, heat convection, latent heat transfer induced by the change of water phase (e.g. evaporation, condensation) inside the pores and relevant thermal fields are not taken into account in this model (Zienkiewicz, 1982; Lewis & Schrefler, 1998; Borja & White, 2010).

(iii) Neglecting the air phase: The mobility of the air phase is larger than that of the water phase in the case of the same condition (e.g. both fluids have similar relative permeabilities) (Zienkiewicz, 1982). As a result, any pressure difference in the air constituent can be equilibrated far faster than that in the water constituent (Zienkiewicz, 1982). Furthermore, the pressure acting on the air phase can usually be set to zero (e.g. atmospheric) for shallow, non-dynamic solid deformation where the pore air remains passive due to its connection with the atmosphere (Borja & White, 2010; Song & Borja, 2014; Tamagnini, 2005; Sheng et al., 2003). The mass of air can reasonably be assumed to be relatively small and hence ignored (Borja & White, 2010; Song & Borja, 2014; Tamagnini, 2005; Sheng et al., 2003). These assumptions lead to an elimination of equations associated with the flow of air from the system of governing equations (Zienkiewicz, 1982).

(iv) Constant solid and water densities: Without loss of generality, all phases of porous media are assumed to be incompressible (Borja & White, 2010; Bear, 2018; Tamagnini, 2005; Sheng et al., 2003; Song & Borja, 2014; Zienkiewicz, 1982) where densities remain unchanged and are considered as model parameters. This is a realistic and common assumption for many geotechnical applications (Borja & White, 2010).

(v) Neglecting the gradient of porosity and saturation degree: This assumption implies that the changes of volume fractions with the location within the soil body are sufficiently small and was used by Lewis & Schrefler (1998), Oka et al. (2010) to derive the formulation for simulating the motion of fluids. It is acknowledged that this simplifying assumption is somewhat inconsistent with what takes place within the soil structure when the localised failure occurs with a strong discontinuity in deformation and saturation fields (see review in Chapter 2). However, this is not covered in the scope of the current study for the sake of simplicity.

(vi) Neglecting the inertia force of water phase and macroscopic viscous effects: The seepage flow is laminar in the case of low velocities in which fluid particles follow smooth paths in layers with little or no lateral mixing between these layers. Therefore, the acceleration of the water phase and macroscopic viscous effects are considered to be sufficiently inconsiderable (Zienkiewicz, 1982; Lewis & Schrefler, 1998; Borja & White, 2010). This assumption facilitates the derivation of Darcy's law.

Seepage forces

Apart from stress and suction, the seepage force is another indispensable variable for describing coupled solid deformation-fluid flow in partially saturated deformable porous media. For Darcy's law, seepage force is considered as one of the main components in governing the overall rate of energy loss associated with the friction at the interphase between water and solid (Zienkiewicz, 1982; Bear, 1972; Lewis & Schrefler, 1998). It can be adopted in whatever form being able to reproduce mechanisms of the fluid transport effectively. In this sense, because of being already verified and validated to be sufficiently robust in many existing simulation models for unsaturated soils, the viscous drag force is of the simple form (Oka et al., 2010; Zienkiewicz, 1982; Borja & White, 2010):

$$R_i^w = -\frac{\phi S_r \rho^w g}{k_{unsat} K_{sat}} \phi S_r v_i^{ws} \tag{3.32}$$

In the above expression, K_{sat} is the saturated hydraulic conductivity, and k_{unsat} is a scalar relative permeability coefficient in the partially saturated regime dependent at least on saturation degree. They are dependent on the geometric characteristics of the pores (e.g. volumetric fraction, capillary effects, fluid-fluid momentum exchange terms) (Zienkiewicz, 1982; Lewis & Schrefler, 1998) and possess significant effects on the velocity of the infiltration process. In the literature, K_{sat} and k_{unsat} can be determined for a given pore geometry through Stokes equations of REV (Valdes-Parada et al., 2009). Alternatively, standardised laboratory or field experiments (e.g. constant head permeameter tests, parallel capillary tubes) were used to propose different empirical or semi-empirical forms of k_{unsat} (Ergun 1952; Carman, 1956; Gardner, 1958; Childs & Collis-George, 1950; Irmay, 1954; Corey, 1957; Brooks & Corey, 1964; Mualem, 1976; van Genuchten, 1980; Hillel, 1971). Among them, the simple relationship between k_{unsat} and S_r given by Hillel (1971) is selected in this study due to its simplicity in the formulation, implementation and parameter identification (Yerro, 2015), taking the following form:

$$k_{unsat} = (S_r)^{\zeta} \tag{3.33}$$

with ζ being an empirical constant that lies in the interval of 2-4 (Yerro, 2015). As can be seen, the relative permeability varies between 0 and 1, reflecting the transition between fully and partially saturated conditions. It can be seen in Eq. (3.33) that the current hydraulic conductivity is explicitly independent from several mechanical field quantities (porosity, stress), that may be inadequate for describing the behaviour of the post-failure flow. Nonetheless, the present form of seepage force is acknowledged just as a relatively simple example to demonstrate the applicability of the proposed generic framework in capturing the hydro-mechanical coupling of partially saturated soils in an

acceptable manner. More comprehensive forms of seepage forces can be considered in my future works.

Darcy seepage velocity

To derive Darcy seepage velocity, this formulation can start with the linear momentum balance of water constituent, which is expressed based on Eq. (3.31) as follows:

$$\bar{\rho}^w \frac{D^w v_i^w}{Dt} = \frac{\partial \bar{\sigma}_{ij}^w}{\partial x_j} + \bar{\rho}^w B_i + R_i^w \tag{3.34}$$

If $p^a = 0$ (assumption iii) then Eq. (3.15) result in:

$$s = -p^w \tag{3.35}$$

Substituting $\bar{\rho}^w = \phi S_r \rho^w$, $\bar{\sigma}_{ij}^w = \phi S_r(-p^w)\delta_{ij}$ (see Eqs. (3.13-3.14)) and Eq. (3.35) into Eq. (3.34) and assuming $\frac{\partial(\phi S_r)}{\partial x_j} = 0$ (assumption v), one gets:

$$\phi S_r \rho^w \frac{D^w v_i^w}{Dt} = \phi S_r \left(\frac{\partial s}{\partial x_j}\delta_{ij} + \rho^w B_i\right) + R_i^w \tag{3.36}$$

If $\frac{D^w v_i^w}{Dt} = 0$ is assumed (assumption vi), then the seepage force can be determined as:

$$R_i^w = -\phi S_r \left(\frac{\partial s}{\partial x_j}\delta_{ij} + \rho^w B_i\right) \tag{3.37}$$

Eq. (3.37) is an extended Darcy's law describing the energy dissipation due to the relative motion between solid and fluid phases in partially saturated soils. Darcy seepage velocity is to describe the relative velocity between moving water and solid phases ($v_i^{ws} = v_i^w - v_i^s$). Comparing Eqs. (3.37) and (3.32), one obtains:

$$\frac{\phi S_r \rho^w g}{k_{unsat} K_{sat}} \phi S_r v_i^{ws} = \phi S_r \left(\frac{\partial s}{\partial x_j}\delta_{ij} + \rho^w B_i\right) \tag{3.38}$$

After rearranging the above expression, Darcy's seepage velocity can be obtained as follows:

$$v_i^{ws} = \frac{k_{unsat} K_{sat}}{\phi S_r g}\left(\frac{1}{\rho^w}\frac{\partial s}{\partial x_j}\delta_{ij} + B_i\right) \tag{3.39}$$

As can be seen in Eq. (3.39), v_i^{ws} is an apparent velocity through the bulk of porous media proportional to permeability coefficients and hydraulic gradient for predicting the travel time of fluid flow. This law is only valid for the slow flow of a macroscopically inviscid fluid through partially saturated soils (Lewis & Schrefler, 1998). Porosity is explicitly taken into consideration in this velocity, reflecting the effect of solid deformation on the wetting/drying processes. It is noted that

Darcy's seepage velocity is different from and greater than the discharge velocity (or Darcy's volume flux) q_i^{ws} which is considered for a total cross-sectional area within porous media in the form of $q_i^{ws} = \phi S_r v_i^{ws}$. This velocity is written in the form of volume-averaged relative velocity measured from experiments (Lewis & Schrefler, 1998).

Solid velocity rate and strain rate tensor

Solid velocity and strain are considered as the mechanical field variables of soil skeleton, a representation of deformation and failure of the solid phase. Based on Eq. (3.31), the form of momentum balance for the solid phase can be expressed as follows:

$$\bar{\rho}^s \frac{D^s v_i^s}{Dt} = \frac{\partial \bar{\sigma}_{ij}^s}{\partial x_j} + \bar{\rho}^s B_i + R_i^s \tag{3.40}$$

Substitution of $(1-\phi)\rho^s$ in place of $\bar{\rho}^s$ (from Eq. (3.13)) and $(\sigma_{ij} - \phi S_r s \delta_{ij})$ in place of $\bar{\sigma}_{ij}^s$ (from Eq. (3.14) with $p^a = 0$) in Eq. (3.40) leads to:

$$\frac{D^s v_i^s}{Dt} = \frac{1}{(1-\phi)\rho^s} \frac{\partial(\sigma_{ij} - \phi S_r s \delta_{ij})}{\partial x_j} + B_i + \frac{1}{(1-\phi)\rho^s} R_i^s \tag{3.41}$$

Due to the assumption of $\frac{\partial(\phi S_r)}{\partial x_j} = 0$ (assumption v), Eq. (3.41) can be rewritten as:

$$\frac{D^s v_i^s}{Dt} = \frac{1}{(1-\phi)\rho^s} \frac{\partial \sigma_{ij}}{\partial x_j} - \frac{\phi S_r}{(1-\phi)\rho^s} \frac{\partial s}{\partial x_j} \delta_{ij} + B_i + \frac{1}{(1-\phi)\rho^s} R_i^s \tag{3.42}$$

On the other hands, the balance of momentum must satisfy the following constraint:

$$R_k^s + R_k^w = 0 \tag{3.43}$$

Using constraint in Eq. (3.43) and substituting Eq. (3.37) into Eq. (3.43) results in:

$$R_i^s = -R_i^w = \phi S_r \left(\frac{\partial s}{\partial x_j} \delta_{ij} + \rho^w B_i \right) \tag{3.44}$$

The final form of solid velocity rate can be derived by substituting Eq. (3.44) into Eq. (3.42), so obtaining:

$$\frac{D^s v_i^s}{Dt} = \frac{1}{(1-\phi)\rho^s} \frac{\partial \sigma_{ij}}{\partial x_j} + \frac{[(1-\phi)\rho^s + \phi S_r \rho^w]}{(1-\phi)\rho^s} B_i \tag{3.45}$$

Ignoring the density of air phase (assumption iii), Eq. (3.13) yields:

$$\rho = \bar{\rho}^s + \bar{\rho}^w = (1-\phi)\rho^s + \phi S_r \rho^w \tag{3.46}$$

Therefore, Eq. (3.45) can be rewritten as:

$$\frac{D^s v_i^s}{Dt} = \frac{1}{(1-\phi)\rho^s}\left(\frac{\partial \sigma_{ij}}{\partial x_j} + \rho B_i\right) \tag{3.47}$$

To further derive the rate of solid velocity, the form of the total stress is used where it can be formulated directly from the definition of Bishop's effective stress (see Eq. (3.17)) as:

$$\sigma_{ij} = \sigma'_{ij} - S_r s \delta_{ij} \tag{3.48}$$

Bishop's effective stress will be further discussed in Section 3.3.

Substituting Eq. (3.48) into Eq. (3.47) gives:

$$\frac{D^s v_i^s}{Dt} = \frac{1}{(1-\phi)\rho^s}\left[\frac{\partial\left(\sigma'_{ij} - S_r s \delta_{ij}\right)}{\partial x_j} + \rho B_i\right] \tag{3.49}$$

If one assumes $\frac{\partial S_r}{\partial x_j} = 0$ (assumption v), the solid acceleration in Eq. (3.49) simplifies to the form:

$$\frac{D^s v_i^s}{Dt} = \frac{1}{(1-\phi)\rho^s}\left(\frac{\partial \sigma'_{ij}}{\partial x_j} - S_r \frac{\partial s}{\partial x_j}\delta_{ij} + \rho B_i\right) \tag{3.50}$$

According to Eq. (3.50), the velocity rate of solid phase within porous media is governed not only by effective stress but also by suction and saturation degree. It reflects the capacity of this approach in capturing the influence of the fluid infiltration process on the soil displacement within deformable three-phase porous media. Eq. (3.50) is used to update the solid velocity, which allows this framework to compute the strain rate tensor given as below:

$$\frac{D^s \varepsilon_{ij}}{Dt} = \frac{1}{2}\left(\frac{\partial v_i^s}{\partial x_j} + \frac{\partial v_j^s}{\partial x_i}\right) \tag{3.51}$$

Combining Eqs. (3.50) and (3.51) reveals that, in a porous medium domain, the perturbation of the total/external stress and fluid pressures produced by fluid motion, or by loading the porous medium domain, the stress on soil skeleton varies, causing its displacement and distortion (Lewis & Schrefler, 1998). This means that the solid matrix of partially saturated soils is "strained" due to the hydromechanical coupling. In the case of small strain, the strain rate tensor is the combination of two components: shear/deviatoric strain representing the change in the shape of the structure (i.e. changes in angles, sliding) and volumetric strain defining the relative change in volume of the solid body (i.e. no changes in angles, no sliding).

Porosity rate

From Eq. (3.25), the mass conservation of the solid constituent takes the following form:

$$\frac{D^s \overline{\rho}^s}{Dt} = -\bar{\rho}^s \frac{\partial v_i^s}{\partial x_i} \tag{3.52}$$

After substituting $\bar{\rho}^s = (1-\phi)\rho^s$ into Eq. (3.52), the following expression is obtained:

$$\frac{D^s[(1-\phi)\rho^s]}{Dt} = -[(1-\phi)\rho^s]\frac{\partial v_i^s}{\partial x_i} \tag{3.53}$$

Taking $\rho^s = const$ (assumption iv), Eq. (3.53) can be rewritten as:

$$\frac{D^s\phi}{Dt} = (1-\phi)\frac{\partial v_i^s}{\partial x_i} \tag{3.54}$$

Eq. (3.54) represents the reciprocity between incremental forms of porosity and volumetric strain (e.g. $\frac{\partial v_i^s}{\partial x_i}$) thanks to the assumption of incompressible soil skeleton. This form is analogous to that used by Buscarnera (2010).

Saturation degree

Using Eq. (3.25), the mass balance for the water phase takes the following form:

$$\frac{D^w\bar{\rho}^w}{Dt} = -\bar{\rho}^w\frac{\partial v_i^w}{\partial x_i} \tag{3.55}$$

or

$$\frac{D^w(\phi S_r\rho^w)}{Dt} = -(\phi S_r\rho^w)\frac{\partial v_i^w}{\partial x_i} \tag{3.56}$$

From Eq. (3.56), using the assumption of $\rho^w = const$ (assumption iv) facilitates the following relation:

$$S_r\frac{D^w\phi}{Dt} + \phi\frac{D^wS_r}{Dt} = -\phi S_r\frac{\partial v_i^w}{\partial x_i} \tag{3.57}$$

By applying Eq. (3.20) for ϕ and S_r while eliminating convective terms ($\frac{\partial\phi}{\partial x_j}$, $\frac{\partial S_r}{\partial x_j}$) (assumption v), $\frac{D^w\phi}{Dt} = \frac{D^s\phi}{Dt}$ and $\frac{D^wS_r}{Dt} = \frac{D^sS_r}{Dt}$ are obtained, allowing Eq. (3.57) to be rewritten as follows:

$$S_r\frac{D^s\phi}{Dt} + \phi\frac{D^sS_r}{Dt} = -\phi S_r\frac{\partial v_i^w}{\partial x_i} \tag{3.58}$$

from which and Eq. (3.54), the saturation rate can be given by the following equation:

$$\frac{D^sS_r}{Dt} = -S_r\frac{\partial v_i^{ws}}{\partial x_i} - \frac{S_r}{\phi}\frac{\partial v_i^s}{\partial x_i} \tag{3.59}$$

In order to further derive the rate of saturation degree, Eq. (3.39) is substituted into Eq. (3.59), resulting in the form below:

$$\frac{D^s S_r}{Dt} = -S_r \frac{\partial\left[\frac{k_{unsat}K_{sat}}{g\phi S_r}\left(\frac{1}{\rho^w}\frac{\partial s}{\partial x_j}\delta_{ij}+B_i\right)\right]}{\partial x_i} - \frac{S_r}{\phi}\frac{\partial v_i^s}{\partial x_i} \tag{3.60}$$

By assuming $\frac{\partial S_r}{\partial x_j} = 0$ and $\frac{\partial \phi}{\partial x_j} = 0$ (assumption v), the rate for the degree of saturation reduces to the following:

$$\frac{D^s S_r}{Dt} = -\frac{k_{unsat}K_{sat}}{g\rho^w\phi}\frac{\partial^2 s}{\partial x_i \partial x_j}\delta_{ij} - \frac{S_r}{\phi}\frac{\partial v_i^s}{\partial x_i} \tag{3.61}$$

The above expression of saturation rate is analogous to that used by Borja & White (2010), Tamagnini (2005), Sheng et al. (2003) for partially saturated soils. The change in water volume, in this case, is produced by the second-order suction gradient and the first-order solid velocity gradient, apart from the inclusion of porosity and saturation degree. It is consistent with the physical phenomenon that when the deformation of the binary phase medium is triggered, the compression of the soil skeleton leads to the movement of fluid through the pores.

Summary on governing equations

As can be seen, there are seven variables in this coupled flow-deformation problem, including: v_i^{ws}, S_r, v_i^s, ε_{ij}, ϕ, σ'_{ij} and s, requiring a system of seven corresponding equations in the mathematical principle. Among them, v_i^{ws}, S_r, v_i^s, ε_{ij} and ϕ are determined by Eqs. (3.39), (3.50), (3.51), (3.54) and (3.61), which can be rewritten as follows:

$$v_i^{ws} = \frac{k_{unsat}K_{sat}}{\phi S_r g}\left(\frac{1}{\rho^w}\frac{\partial s}{\partial x_j}\delta_{ij} + B_i\right) \tag{3.62}$$

$$\frac{D^s S_r}{Dt} = -\frac{k_{unsat}K_{sat}}{g\rho^w\phi}\frac{\partial^2 s}{\partial x_i \partial x_j}\delta_{ij} - \frac{S_r}{\phi}\frac{\partial v_i^s}{\partial x_i} \tag{3.63}$$

$$\frac{D^s v_i^s}{Dt} = \frac{1}{(1-\phi)\rho^s}\left(\frac{\partial \sigma'_{ij}}{\partial x_j} - S_r\frac{\partial s}{\partial x_j}\delta_{ij} + \rho B_i\right) \tag{3.64}$$

$$\frac{D^s \varepsilon_{ij}}{Dt} = \frac{1}{2}\left(\frac{\partial v_i^s}{\partial x_j} + \frac{\partial v_j^s}{\partial x_i}\right) \tag{3.65}$$

$$\frac{D^s \phi}{Dt} = (1-\phi)\frac{\partial v_i^s}{\partial x_i} \tag{3.66}$$

Among the equations mentioned above, Eqs. (3.62) and (3.63) are to present the expressions of hydraulic field variables, including Darcy seepage velocity and saturation degree representing the fluid transport through porous media. In this seepage flow model, the motion of the fluid phases is described in terms of mass-averaged velocities relative to the moving solid, where the evolution of hydraulic field variables can be expressed with reference to those of the corresponding soil skeleton

thanks to the use of relative velocities and kinematics in porous media theory (Lewis & Schrefler, 1998).

To complete this coupled dynamic flow-deformation response of partially saturated soils, two more constitutive equations for linking effective stress σ'_{ij} and suction s with the above-described equations are needed. In this case, increments of strain and saturation given by governing equations in Eqs. (3.63) and (3.64-3.65) can serve as inputs to return increments of stress and suction as outputs through appropriate constitutive models (e.g. stress-strain, SWCC). It is well known that constitutive models are to simulate the behaviour of materials and are an important element for any analysis within the continuum mechanics framework, that is the focus of this thesis. Without proper constitutive laws (e.g. stress-strain, suction-saturation), numerical methods for modelling coupled flow-deformation processes in three-phase porous media find it hard to adequately reproduce mechanisms of failure due to the interaction between irreversible deformation and fluid transport in the inelastic regime under a wide range of loading and saturation conditions. As discussed in Chapter 2, for unsaturated soils, constitutive models are required to consider the intrinsic interaction between grain rearrangements and liquid-bridge redistributions at the grain scale, reflected in the simultaneous activation and evolution of mechanical and hydraulic yielding responses observed at the continuum level. This nature requires the interdependence of mechanical and hydraulic internal forces and their dependence on all internal variables (e.g. plastic strain, irreversible saturation), in addition to effective stress and suction, leading to a single yield locus governed by a unique "plastic" multiplier with two flow rules. A constitutive model that miss-predicts this micromechanical nature of coupled hydro-mechanical yielding behaviour may give unreasonable predictions and unphysical results of the realistic hydromechanical process of unsaturated soils in different loading and hydraulic cases. However, the importance of the determination of this coupling mechanism is not always recognised in existing constitutive modelling of partially saturated soils where multiple yield surfaces (Wheeler et al., 2003; Sheng et al., 2008) and separate laws of SWCC with different parameter sets for wetting and drying paths (Khalili et al., 2008; Zhou et al., 2012ab; 2018 and Zhou & Sheng, 2015) are usually used despite significant benefits that they bring in matching a wide range of experimental data. Furthermore, the violation of thermodynamics laws maybe not guaranteed in these models, and the crucial properties of energy dissipation are not always addressed in the literature to interpret failure mechanisms of partially saturated soils. Without recourse to thermodynamic principles, constructions of many existing models for partially saturated soils are sometimes not rigorous and arbitrary through incoherent combinations of different theories. These requirements need to be addressed to move towards the aim of establishing better constitutive models in more rigorous ways to describe the coupled hydro-mechanical mechanisms of unsaturated soils, focusing on stress-strain and suction-

saturation degree relationships. The next section will be dedicated to this feature and is the emphasis of this thesis.

3.3. Constitutive relationship

As discussed beforehand in Chapter 2, the inelastic behaviour of partially saturated soils is experimentally observed in the interdependence between loading-unloading and wetting-drying differences. It is intrinsically linked to the inseparability of mechanical and hydraulic dissipations produced by the interaction between the rearrangements of particles and water meniscuses. This observable behaviour of partially saturated soils requires coupling between internal variables representing the hydro-mechanical behaviour in constitutive modelling. A generic thermodynamic approach is described in this section under assumptions of rate-independent and homogeneous deformation to serve as a basis for the interaction between the mechanical and hydraulic responses represented by plastic strain and irrecoverable saturation, respectively. The inseparable nature of this interaction will be reflected in the proposed approach through the interdependence of plastic strain and irrecoverable saturation where a single yield surface in stress-suction space with two evolution rules for plastic strains and irrecoverable saturation is derived from two new forms of free energy and dissipation potentials in different ways. The proposed formulation has the advantage of being able to naturally perform a bi-directional interaction between mechanical and hydraulic yielding responses at any instant with a small number of parameters.

3.3.1. A generalized thermodynamics-based formulation

State variables

The first step in the development of this framework involves the proper choice of stress and strain variables. It is admitted that at least two stress/strain-like variables must be needed to capture the concurrent existence of both the mechanical (stress-strain relationship) and hydraulic (SWCC) responses, that is the first-and necessary condition to guarantee the success of the fully-coupled hydro-mechanical model predictions for unsaturated soils (Buscarnera & Nova, 2009). Addressing this, several existing models choose the net stress and suction in conjugation with the Cauchy strain and saturation degree (Sheng et al., 2004) or water ratio strain (Vaunat et al., 2000; Buisson & Wheeler, 2000) as they are at an advantage in allowing for convenient implementations of Finite Element Method (FEM) using normally total stresses (Sheng et al., 2004) and simple representations of stress paths from experimental data (Gallipoli et al., 2018). However, such choices are somehow improper regarding the thermo-mechanical considerations. According to Houlsby (1997) and Coussy et al. (2010), these stress-like and strain-like variables can be arbitrarily selected in different ways,

but provided that these are work conjugate to guarantee the theoretical rigour and thermodynamic consistency of the entire formulation in continuum models. Under such conditions, the proper form of work input will serve as a fundamental basis to plausibly identify energy conjugated stress/strain variables for continuum modelling. Recognizing the importance of that matter, there have been numerous studies and attempts to make progress on the closed-form expression of work input for unsaturated soils, such as works of Houlsby (1997), Gray et al. (2009), Li (2007) and Coussy et al. (2010). In general, they indeed share many similar features in the work-input form and relevant variables, and the controversy among them mainly revolves around the energy of the air-water interface. It is essential to take into account the effect of the fluid interface in the expression of energy input and then the constitutive framework. However, this research point of view is considered beyond the scope of this thesis and will be addressed in future works. Instead, the form of work input, without the surface tension or other terms related to the fluid interface, as suggested by Coussy et al. (2010), is employed in this study for simplicity and convenience in model development where its derivation can be reviewed as follows.

Water V^w and air V^a volumes take the following forms:

$$V^w = V_0 \bar{\phi} S_r \tag{3.67}$$

$$V^a = V_0 \bar{\phi} (1 - S_r) \tag{3.68}$$

Water and air volume rates are then written as:

$$\dot{V}^w = V_0 \left(S_r \dot{\bar{\phi}} + \bar{\phi} \dot{S}_r \right) \tag{3.69}$$

$$\dot{V}^a = V_0 \left[(1 - S_r) \dot{\bar{\phi}} - \bar{\phi} \dot{S}_r \right] \tag{3.70}$$

If the soil is assumed to be incompressible, the following expression can be written:

$$\dot{\bar{\phi}} = -\dot{\varepsilon}_v \tag{3.71}$$

where ε_v is volumetric strain.

The infinitesimal work $\tilde{\Gamma}$ supplied to the solid skeleton can be expressed as:

$$\tilde{\Gamma} = -p\dot{V} + p^w \dot{V}^w + p^a \dot{V}^a \tag{3.72}$$

with p denoting the total mean stress.

Substituting Eqs (3.69-3.70) into Eq. (3.72), Eq. (3.72) yields:

$$\dot{\Gamma} = -p\dot{V} + p^w V_0 \left(-S_r \dot{\varepsilon}_v + \bar{\phi} \dot{S}_r \right) + p^a V_0 \left[-(1 - S_r) \dot{\varepsilon}_v - \bar{\phi} \dot{S}_r \right] \tag{3.73}$$

Dividing Eq. (3.73) by V_0, the work input $\widetilde{W}$ can be obtained as follows:

$$\widetilde{W} = \frac{\dot{I}}{V_o} = -p\frac{\dot{V}}{V_o} + p^w\left(-S_r\dot{\varepsilon}_v + \bar{\phi}\dot{S}_r\right) + p^a\left[-(1-S_r)\dot{\varepsilon}_v - \bar{\phi}\dot{S}_r\right] \tag{3.74}$$

Thanks to $\dot{\varepsilon}_v = -\frac{\dot{V}}{V_o}$, Eq. (3.74) is rewritten as:

$$\widetilde{W} = [p - p^a + S_r(p^a - p^w)]\dot{\varepsilon}_v + \bar{\phi}(p^a - p^w)\left(-\dot{S}_r\right) \tag{3.75}$$

or,

$$\widetilde{W} = (\bar{p} + S_r s)\dot{\varepsilon}_v + \bar{\phi}s\left(-\dot{S}_r\right) \tag{3.76}$$

Eq. (3.76) can be extended to the form for triaxial stress conditions. Thus, the rate of work input can be expressed as:

$$\widetilde{W} = (\bar{p} + S_r s)\dot{\varepsilon}_v + q\dot{\varepsilon}_s + \bar{\phi}s\left(-\dot{S}_r\right) = p'\dot{\varepsilon}_v + q\dot{\varepsilon}_s + s^*\left(-\dot{S}_r\right) \tag{3.77}$$

where $\bar{p}, p', q, s^*, \varepsilon_v$ and ε_s are the net mean stress, effective mean stress, shear stress, modified suction, volumetric strain and shear strain, respectively. It can be seen that the modified suction, $s^* = s\bar{\phi}$ with porosity explicitly representing the effect of volumetric changes on the hydraulic conductivity of the bulk fluid, is used as a conjugate of the strain-like variable $-\dot{S}_r$, according to Houlsby (1997), Coussy et al. (2010) and Buscarnera & Einav (2012). It agrees with Lu (2008) and Vaunat et al. (2000) that suction can be considered a stress-like variable. Under geotechnical sign convention (compression positive) and assumption of incompressible solid grains, the volumetric strain can be expressed as $\varepsilon_v = \bar{\phi}_0 - \bar{\phi}$, with $\bar{\phi}_0$ being the initial porosity. The triaxial stresses (p', q) and triaxial strains $(\varepsilon_v, \varepsilon_s)$ can be expressed in terms of Cauchy stress $\left(\sigma'_{ij}\right)$ and strain tensors $\left(\varepsilon_{ij}\right)$, respectively.

$$p' = -\frac{1}{3}\sigma'_{kk} \qquad q = \sqrt{\frac{3}{2}\left(\sigma'_{ij} - \frac{1}{3}\sigma'_{kk}\delta_{ij}\right)\left(\sigma'_{ij} - \frac{1}{3}\sigma'_{kk}\delta_{ij}\right)} \tag{3.78}$$

$$\varepsilon_v = \varepsilon_{kk} \qquad \varepsilon_s = \sqrt{\frac{2}{3}\left(\varepsilon_{ij} - \frac{1}{3}\varepsilon_v\delta_{ij}\right)\left(\varepsilon_{ij} - \frac{1}{3}\varepsilon_v\delta_{ij}\right)} \tag{3.79}$$

The limitation of the work input (Eq. (3.77)) is acknowledged in neglecting the work due to moving air-fluid interface in a partially saturated volume element, as explained in Houlsby (1997), the consequence of which is the simplest form of Bishop's effective stress parameter, $\chi = S_r$. As discussed earlier in Chapter 2, the effective stress here can be understood as the stress at inter-particle contacts related to the deformation and failure of the soil skeleton, governed by both external load and contact-level capillary action. There have been attempts to make progress on the closed-form expression of effective stress $(p' = \bar{p} + \chi s)$ for unsaturated soils. These studies mainly revolve

around the form of effective stress parameter χ which can be a function of saturation degree (e.g. Hassanizadeh & Gray, 1990; Muraleetharan & Wei, 1999) or air-entry value (Khalili & Khabbaz, 1998) to reproduce the fully-partially saturated transition. Nevertheless, the effect of air-entry value in the effective stress considered to be beyond the scope of this thesis despite its robustness demonstrated in Russell & Khalili (2006), Khalili et al. (2008), Loret & Khalili (2002). On the other hand, it is acknowledged that there must be two contributions on the capillarity of the average skeleton stress, including suction and surface tension forces along the contours between grains and liquid bridges (Wan et al., 2014; Li, 2003; Likos, 2014). The latter still needs further investigations (Likos, 2014) and hence is not always taken into account in constitutive modelling (Gallipoli et al., 2003; Hu et al., 2014). This research is, therefore, not covered within the scope of this study. To address this problem, the micro-mechanical approach (Nicot & Darve, 2005) can be adopted to infer the global response of a granular soil from its local properties with the grain interaction and liquid-bridge distribution, using the statistical description of the fabrics for a force-displacement model.

Fundamental relations

For the isothermal process with the temperature θ, the first law of thermodynamics reads (Houlsby & Puzrin, 2000; Nguyen, 2005):

$$\widetilde{W} + \vartheta_{k,k} = \dot{u}' \tag{3.80}$$

where u' is the specific internal energy, $\vartheta_{k,k}$ is the heat supply to a volume element.

The second law of thermodynamics is of the following form:

$$\dot{\eta} \geq -\left(\frac{\vartheta_k}{\theta}\right)_{,k} = -\left(\frac{\vartheta_{k,k}}{\theta} - \frac{\vartheta_k \theta_{,k}}{\theta^2}\right) \tag{3.81}$$

with η denoting the entropy and $\frac{\vartheta_k}{\theta}$ being the entropy flux. Eq. (3.81) can be expanded as follows:

$$\theta\dot{\eta} + \vartheta_{k,k} - \frac{\vartheta_k \theta_{,k}}{\theta} \geq 0 \tag{3.82}$$

From Eq. (3.82), the dissipation function $\widetilde{\Phi}$ including mechanical ($\theta\dot{\eta} + \vartheta_{k,k}$) and thermal ($-\frac{\vartheta_k \theta_{,k}}{\theta}$) dissipations can be written in the following form:

$$\widetilde{\Phi} = \theta\dot{\eta} + \vartheta_{k,k} - \frac{\vartheta_k \theta_{,k}}{\theta} \geq 0 \tag{3.83}$$

The tilde symbol "~" is used here to indicate the path-dependent nature of the work input and dissipation; only their rates can be defined.

In the case that the thermal dissipation is negligible, Eq. (3.83) then writes:

$$\vartheta_{k,k} = \theta\dot{\eta} - \widetilde{\Phi} \tag{3.84}$$

From Eqs. (3.84) and (3.80), the following equation can be obtained:

$$\widetilde{\Phi} = \widetilde{W} + \theta\dot{\eta} - \dot{u}' \geq 0 \tag{3.85}$$

where the Helmholtz specific free energy Ψ is defined as:

$$\Psi = u' - \theta\eta \tag{3.86}$$

Making differentiation of Eq. (3.86), the rate of internal energy then yields:

$$\dot{u}' = \dot{\Psi} + \theta\dot{\eta} + \dot{\theta}\eta \tag{3.87}$$

From Eqs. (3.87) and (3.85), under isothermal conditions, the energy balance is of the form:

$$\widetilde{W} = \dot{\Psi} + \widetilde{\Phi} \tag{3.88}$$

For a thermodynamics-based approach, a few internal variables are used to represent the evolution of the complicated underlying physics of micro-scale mechanisms. The appropriate selection of internal variables and their interactions is important in a consistent thermodynamics-based approach to enable the model to have a sound physical basis. For partially saturated soils, the energy dissipation reflects the inseparable nature of the interaction between frictional sliding, grain rearrangement and ruptures of liquid bridges and their redistributions at the grain contacts. In particular, grain-scale frictional sliding leads to rupture of liquid bridges and hence the change of saturation; on the other hand, change of liquid bridges leads to change of grain-scale frictional resistance and hence macro shear strength of the material. These coupled hydro-mechanical processes lead to the irreversible deformation and saturation observed at the macro scale. In constitutive modelling of partially saturated soils, the use of irrecoverable saturation degree S_r^{p} has also been adopted in some papers (Wheeler et al., 2003; Li, 2007a; Hu et al., 2015). These irreversible strains and strain-like variable (volumetric plastic strain $\varepsilon_v^{\mathrm{p}}$, and deviatoric plastic strain $\varepsilon_s^{\mathrm{p}}$ and irrecoverable saturation degree S_r^{p}) govern the dissipation and hence are used as internal variables controlling the behaviour of the proposed partially saturated soil model. The Helmholtz free energy can assume the following general form:

$$\Psi = \Psi\left(\varepsilon_v, \varepsilon_s, -S_r, \varepsilon_v^{\mathrm{p}}, \varepsilon_s^{\mathrm{p}}, -S_r^{\mathrm{p}}\right) \tag{3.89}$$

Therefore, its rate is:

$$\dot{\Psi} = \frac{\partial\Psi}{\partial\varepsilon_v}\dot{\varepsilon}_v + \frac{\partial\Psi}{\partial\varepsilon_s}\dot{\varepsilon}_s + \frac{\partial\Psi}{\partial(-S_r)}\left(-\dot{S}_r\right) + \frac{\partial\Psi}{\partial\varepsilon_v^{\mathrm{p}}}\dot{\varepsilon}_v^{\mathrm{p}} + \frac{\partial\Psi}{\partial\varepsilon_s^{\mathrm{p}}}\dot{\varepsilon}_s^{\mathrm{p}} + \frac{\partial\Psi}{\partial(-S_r^{\mathrm{p}})}\left(-\dot{S}_r^{\mathrm{p}}\right) \tag{3.90}$$

By substituting Eq. (3.90) into Eq. (3.88), the following expression can be obtained:

$$\widetilde{W} = \frac{\partial \Psi}{\partial \varepsilon_v}\dot{\varepsilon}_v + \frac{\partial \Psi}{\partial \varepsilon_s}\dot{\varepsilon}_s + \frac{\partial \Psi}{\partial(-s_r)}\left(-\dot{S}_r\right) + \frac{\partial \Psi}{\partial \varepsilon_v^{\mathrm{p}}}\dot{\varepsilon}_v^{\mathrm{p}} + \frac{\partial \Psi}{\partial \varepsilon_s^{\mathrm{p}}}\dot{\varepsilon}_s^{\mathrm{p}} + \frac{\partial \Psi}{\partial(-s_r^{\mathrm{p}})}\left(-\dot{S}_r^{\mathrm{p}}\right) + \widetilde{\Phi} \tag{3.91}$$

Comparing Eq. (3.91) with Eq. (3.77), the following fundamental relationships are obtained:

$$p' = \frac{\partial \Psi}{\partial \varepsilon_v} \tag{3.92}$$

$$q = \frac{\partial \Psi}{\partial \varepsilon_s} \tag{3.93}$$

$$s^* = \frac{\partial \Psi}{\partial(-S_r)} \tag{3.94}$$

and

$$\widetilde{\Phi} = -\frac{\partial \Psi}{\partial \varepsilon_v^{\mathrm{p}}}\dot{\varepsilon}_v^{\mathrm{p}} - \frac{\partial \Psi}{\partial \varepsilon_s^{\mathrm{p}}}\dot{\varepsilon}_s^{\mathrm{p}} - \frac{\partial \Psi}{\partial(-s_r^{\mathrm{p}})}\left(-\dot{S}_r^{\mathrm{p}}\right) = \bar{\chi}_v\dot{\varepsilon}_v^{\mathrm{p}} + \bar{\chi}_s\dot{\varepsilon}_s^{\mathrm{p}} + \bar{\chi}_h\left(-\dot{S}_r^{\mathrm{p}}\right) \tag{3.95}$$

in which the generalised stresses $\bar{\chi}_v = -\frac{\partial \Psi}{\partial \varepsilon_v^{\mathrm{p}}}$, $\bar{\chi}_s = -\frac{\partial \Psi}{\partial \varepsilon_s^{\mathrm{p}}}$ and $\bar{\chi}_h = -\frac{\partial \Psi}{\partial(-s_r^{\mathrm{p}})}$ are the thermodynamic conjugates to the volumetric plastic strain $\varepsilon_v^{\mathrm{p}}$, shear plastic strain $\varepsilon_s^{\mathrm{p}}$ and irrecoverable saturation degree $-S_r^{\mathrm{p}}$, respectively.

For rate-independent behaviour (Houlsby & Puzrin, 2000), the dissipation is a homogeneous function of order one in terms of $\dot{\varepsilon}_v^{\mathrm{p}}$, $\dot{\varepsilon}_s^{\mathrm{p}}$ and $-\dot{S}_r^{\mathrm{p}}$:

$$\widetilde{\Phi} = \frac{\partial \widetilde{\Phi}}{\partial \dot{\varepsilon}_v^{\mathrm{p}}}\dot{\varepsilon}_v^{\mathrm{p}} + \frac{\partial \widetilde{\Phi}}{\partial \dot{\varepsilon}_s^{\mathrm{p}}}\dot{\varepsilon}_s^{\mathrm{p}} + \frac{\partial \widetilde{\Phi}}{\partial(-\dot{s}_r^{\mathrm{p}})}\left(-\dot{S}_r^{\mathrm{p}}\right) = \chi_v\dot{\varepsilon}_v^{\mathrm{p}} + \chi_s\dot{\varepsilon}_s^{\mathrm{p}} + \chi_h\left(-\dot{S}_r^{\mathrm{p}}\right) \tag{3.96}$$

where χ_v, χ_s and χ_h are volumetric, shear and hydraulic dissipative generalised stresses, respectively. Comparing Eq. (3.96) with Eq. (3.95), a form of Ziegler's orthogonality condition (Ziegler, 1983; Houlsby & Puzin, 2000; Puzrin & Houlsby, 2001) can be obtained:

$$\chi_v = \bar{\chi}_v \tag{3.97}$$

$$\chi_s = \bar{\chi}_s \tag{3.98}$$

$$\chi_h = \bar{\chi}_h \tag{3.99}$$

Dissipation function, loading function and evolution laws

Making an explicit link between loading function/evolution laws and dissipation potential by performing the degenerate Legendre transformation is a central principle and advantage of the thermodynamics-based framework (Collins & Houlsby, 1997; Houlsby & Puzrin, 2007). In general, for rate-independent models, the dissipation potential $\widetilde{\Phi}$ can assume any form that is first-order homogeneous in the rates of internal variables provided the thermodynamic admissibility is met. It is noted that explicit representations of grain-scale details are missing in this model, given the proposed approach is based on continuum mechanics. It will be addressed in future works to move towards a

better model where micromechanics-based approaches (e.g. Nguyen & Gan, 2014; Bignonnet et al., 2016; Fang et al., 2017; Nicot & Darve, 2007; Yin et al., 2009) can be adopted. In this paper, microscale mechanisms are used only to obtain constraints on the interactions of internal variables, reflected in the dependence of all thermodynamic forces on stress, suction, plastic strain and irrecoverable saturation and their rates. The inseparable nature of the grain scale hydro-mechanical coupling described earlier requires that χ_v, χ_s, and χ_h be dependent on stress, suction, all internal variables and their rates representing the dissipative processes. Mathematically they can be written as (i stands for v, s, or h):

$$\chi_i = \chi_i\left(p, q, s^*, \dot{\varepsilon}_v^{\mathrm{p}}, \dot{\varepsilon}_s^{\mathrm{p}}, \dot{S}_r^{\mathrm{p}}\right) \tag{3.100}$$

Although a decoupling of χ_i from all the rates of internal variables can be used to simplify the formulation as can be seen in several thermodynamics-based models in the literature (Sheng et al., 2004; Li, 2007; Hu et al., 2015; Santagiuliana & Schrefler, 2006), this decoupling at this level leads to the employment of different loading functions to describe the interactions between different dissipative processes. Instead, a tighter coupling between these processes is pursued in this study. To address it, two generic approaches associated with dissipation function can be adopted to derive a single loading function and corresponding evolution laws to encapsulate the tight connection of plastic strains and irrecoverable saturation, including a special form of dissipation potential and constraints. Both approaches can allow dissipative stresses to be intrinsically dependent on each other and all internal variables, aside from their interactions through the constitutive relationships. They are presented as follows.

A special form of dissipation potential

In this approach, a special form of first-order homogeneous dissipation potential (Collins & Houlsby, 1997; Collins & Kelly, 2002; Collins & Hilder, 2002; Collins, 2003; Einav et al., 2007) is used to obtain the required form of generalised dissipative stresses in Eq. (3.100). This generic form of dissipation potential has been used successfully in modelling dissipative processes involving more than one dissipative mechanisms. Examples include coupling plastic strains with breakage (Einav, 2007ab; Nguyen & Einav, 2009) and damage with plastic strains (Nguyen et al., 2012; Guiamatsia & Nguyen, 2012; Mir et al., 2018). The dissipation potential takes the following generic form:

$$\widetilde{\Phi} = \sqrt{(\phi_1^v)^2 + (\phi^s)^2 + (\phi^h)^2} + \phi_2^v \tag{3.101}$$

In the above expression, ϕ_1^v, and ϕ_2^v are first-order homogeneous functions of $\dot{\varepsilon}_v^{\mathrm{p}}$; they are required for the introduction of dilation behaviour in the model. Functions ϕ^s, and ϕ^h are first-order homogeneous with respect to $\dot{\varepsilon}_s^{\mathrm{p}}$, and $\dot{S}_r^{\mathrm{p}}$, respectively. The specific expressions of these functions

(ϕ_1^v, ϕ_2^v, ϕ^s, and ϕ^h) govern the behaviour of the constitutive model and will be presented in the next chapters.

The generalised dissipative stresses take the following generic forms:

$$\chi_v = \frac{\partial \widetilde{\Phi}}{\partial \dot{\varepsilon}_v^{\mathrm{p}}} = \frac{\partial \widetilde{\Phi}}{\partial \phi_1^v}\frac{\partial \phi_1^v}{\partial \dot{\varepsilon}_v^{\mathrm{p}}} + \frac{\partial \widetilde{\Phi}}{\partial \phi_2^v}\frac{\partial \phi_2^v}{\partial \dot{\varepsilon}_v^{\mathrm{p}}} = \frac{\phi_1^v}{\sqrt{(\phi_1^v)^2+(\phi^s)^2+(\phi^h)^2}}\frac{\partial \phi_1^v}{\partial \dot{\varepsilon}_v^{\mathrm{p}}} + \frac{\partial \phi_2^v}{\partial \dot{\varepsilon}_v^{\mathrm{p}}} \tag{3.102}$$

$$\chi_s = \frac{\partial \widetilde{\Phi}}{\partial \dot{\varepsilon}_s^{\mathrm{p}}} = \frac{\partial \widetilde{\Phi}}{\partial \phi^s}\frac{\partial \phi^s}{\partial \dot{\varepsilon}_s^{\mathrm{p}}} = \frac{\phi^s}{\sqrt{(\phi_1^v)^2+(\phi^s)^2+(\phi^h)^2}}\frac{\partial \phi^s}{\partial \dot{\varepsilon}_s^{\mathrm{p}}} \tag{3.103}$$

$$\chi_h = \frac{\partial \widetilde{\Phi}}{\partial (-\dot{S}_r^{\mathrm{p}})} = \frac{\partial \widetilde{\Phi}}{\partial \phi^h}\frac{\partial \phi^h}{\partial (-\dot{S}_r^{\mathrm{p}})} = \frac{\phi^h}{\sqrt{(\phi_1^v)^2+(\phi^s)^2+(\phi^h)^2}}\frac{\partial \phi^h}{\partial (-\dot{S}_r^{\mathrm{p}})} \tag{3.104}$$

Thanks to the properties of first-order homogeneous functions, the following equation can be deduced from Eqs. (3.102-3.104):

$$\chi_v \dot{\varepsilon}_v^{\mathrm{p}} + \chi_s \dot{\varepsilon}_s^{\mathrm{p}} + \chi_h\left(-\dot{S}_r^{\mathrm{p}}\right) = \widetilde{\Phi} \tag{3.105}$$

Thus, the dissipation rate function in Eq. (3.101) can be written as follows:

$$\widetilde{\Phi} = \widetilde{\Phi}_v + \widetilde{\Phi}_s + \widetilde{\Phi}_h \tag{3.106}$$

where $\widetilde{\Phi}_v = \chi_v \dot{\varepsilon}_v^{\mathrm{p}}$, $\widetilde{\Phi}_s = \chi_s \dot{\varepsilon}_s^{\mathrm{p}}$ and $\widetilde{\Phi}_h = \chi_h\left(-\dot{S}_r^{\mathrm{p}}\right)$ are denoted as volumetric, shear and hydraulic parts of the total dissipation rate, respectively. The above properties allow the investigation of dissipation characteristics of any partially saturated models derived from this proposed generic framework, given the explicitly defined dissipation potential (see Eq. (3.101)). This will be illustrated in Chapter 4.

As can be seen in Eqs. (3.102-3.104), all generalised dissipative stresses χ_i are dependent on all rates of internal variables, $\dot{\varepsilon}_v^{\mathrm{p}}$, $\dot{\varepsilon}_s^{\mathrm{p}}$, and $-\dot{S}_r^{\mathrm{p}}$. Thanks to this, the degenerate Legendre transformation of the dissipation potential (Puzrin & Houlsby, 2001) leads to a single yield function y^* in generalised stress space (χ_v, χ_s, and χ_h):

$$y^* = \frac{\left(\chi_v - \frac{\partial \phi_2^v}{\partial \dot{\varepsilon}_v^{\mathrm{p}}}\right)^2}{\left(\frac{\partial \phi_1^v}{\partial \dot{\varepsilon}_v^{\mathrm{p}}}\right)^2} + \frac{(\chi_s)^2}{\left(\frac{\partial \phi^s}{\partial \dot{\varepsilon}_s^{\mathrm{p}}}\right)^2} + \frac{(\chi_h)^2}{\left(\frac{\partial \phi^h}{\partial (-\dot{S}_r^{\mathrm{p}})}\right)^2} - 1 \leq 0 \tag{3.107}$$

Eq. (3.107) represents an ellipsoid, as shown in Figure 3.4. The role of y^* is similar to that of a plastic potential in classical plasticity theory. Three evolution laws (or flow rules) for the rates of plastic strains and irreversible saturation rates, sharing a single multiplier $\dot{\lambda}_p$ can then be expressed as:

$$\dot{\varepsilon}_v^{\mathrm{p}} = \dot{\lambda}_p \frac{\partial y^*}{\partial \chi_v} = \dot{\lambda}_p \frac{2\left(\chi_v - \frac{\partial \phi_2^v}{\partial \dot{\varepsilon}_v^{\mathrm{p}}}\right)}{\left(\frac{\partial \phi_1^v}{\partial \dot{\varepsilon}_v^{\mathrm{p}}}\right)^2} \tag{3.108}$$

$$\dot{\varepsilon}_s^{\mathrm{p}} = \dot{\lambda}_p \frac{\partial y^*}{\partial \chi_s} = \dot{\lambda}_p \frac{2\chi_s}{\left(\frac{\partial \phi^s}{\partial \dot{\varepsilon}_s^{\mathrm{p}}}\right)^2} \tag{3.109}$$

$$-\dot{S}_r^{\mathrm{p}} = \dot{\lambda}_p \frac{\partial y^*}{\partial \chi_h} = \dot{\lambda}_p \frac{2\chi_h}{\left(\frac{\partial \phi^h}{\partial\left(-\dot{S}_r^{\mathrm{p}}\right)}\right)^2} \tag{3.110}$$

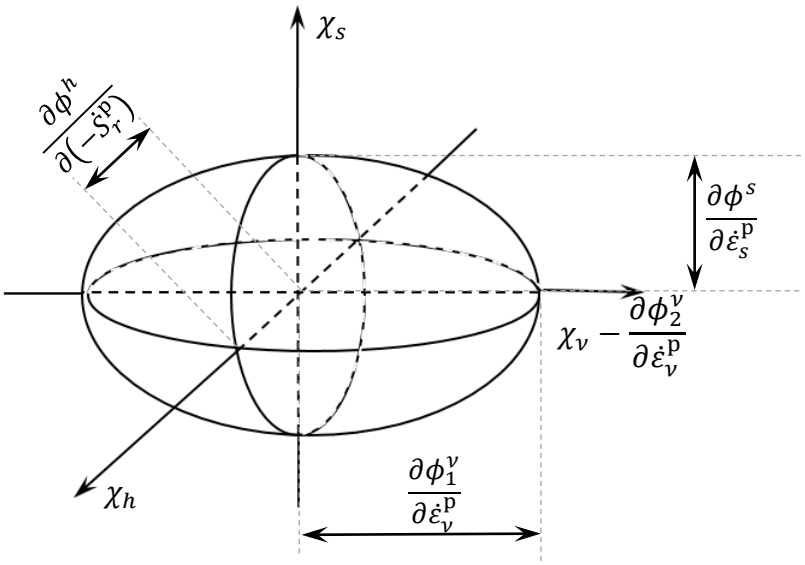

Figure 3.4. Geometric representation of yield potential in dissipative stress space for the approach of "using a specifical form of dissipation potential."

Using the orthogonality conditions in the forms $\chi_v = \bar{\chi}_v = -\frac{\partial \Psi}{\partial \varepsilon_v^{\mathrm{p}}}$, $\chi_s = \bar{\chi}_s = -\frac{\partial \Psi}{\partial \varepsilon_s^{\mathrm{p}}}$, and $\chi_h = \bar{\chi}_h = -\frac{\partial \Psi}{\partial\left(-S_r^{\mathrm{p}}\right)}$, the generic yield surface y in true stress space can be obtained as:

$$y\left(p', q, s^*, \varepsilon_v^{\mathrm{p}}, \varepsilon_s^{\mathrm{p}}, -S_r^{\mathrm{p}}\right) = \frac{\left(-\frac{\partial \Psi}{\partial \varepsilon_v^{\mathrm{p}}} - \frac{\partial \phi_2^v}{\partial \dot{\varepsilon}_v^{\mathrm{p}}}\right)^2}{\left(\frac{\partial \phi_1^v}{\partial \dot{\varepsilon}_v^{\mathrm{p}}}\right)^2} + \frac{\left(-\frac{\partial \Psi}{\partial \varepsilon_s^{\mathrm{p}}}\right)^2}{\left(\frac{\partial \phi^s}{\partial \dot{\varepsilon}_s^{\mathrm{p}}}\right)^2} + \frac{\left(-\frac{\partial \Psi}{\partial\left(-S_r^{\mathrm{p}}\right)}\right)^2}{\left(\frac{\partial \phi^h}{\partial\left(-\dot{S}_r^{\mathrm{p}}\right)}\right)^2} - 1 \leq 0 \tag{3.111}$$

Eqs. (3.92-3.94) and (3.107-3.111) present a generic form of thermodynamic-based models for partially saturated soils. The specifications of functions ϕ_1^v, ϕ_2^v, ϕ^s, and ϕ^h complete the definition of a specific model. This coupling allows capturing the simultaneous activation and development of both mechanical and hydraulic yielding at any instant without requiring arbitrary and complicated treatments, in comparison with the use of multiple yield surfaces and plastic multipliers (e.g. Wheeler et al., 2003; Sheng et al., 2004; Santagiuliana & Schrefler, 2006). The specifications of both energy

and dissipation potentials to formulate a specific constitutive model for partially saturated soils will be described in Chapter 4.

Using kinematic constraint equations

In an alternative way, the interdependent and inseparable evolutions of mechanical and hydraulic dissipative processes reflecting underlying grain-scale hydromechanical mechanisms can be incorporated into the model formulation through another approach by means of constraint equations. In this approach, dissipation potential takes the form set out below:

$$\widetilde{\Phi} = \varphi^{v}\dot{\varepsilon}_{v}^{\mathrm{p}} + \varphi^{s}\dot{\varepsilon}_{s}^{\mathrm{p}} + \varphi^{h}\left(-\dot{S}_{r}^{\mathrm{p}}\right) \geq 0 \tag{3.112}$$

In the above expression, functions φ^{v}, ϕ^{s}, and ϕ^{h} are first-order homogeneous with respect to $\dot{\varepsilon}_{v}^{\mathrm{p}}$, $\dot{\varepsilon}_{s}^{\mathrm{p}}$, and $\dot{S}_{r}^{\mathrm{p}}$, respectively. Eq. (3.112) can be understood as a weak form of coupled hydro-mechanical dissipation function because the interaction between χ_{v}, χ_{s} and χ_{h} is only valid in the constitutive equations. In a thermodynamic form of weak coupling, two separate yield surfaces, one for controlling the evolution rule of plasticity and one for controlling that of capillarity, can be derived from Eq. (3.112). Noting that the non-negative plastic-type multipliers of each are distinct. Such a weak approach can be found in several existing thermodynamic-based frameworks of Sheng et al. (2004), Santagiuliana & Schrefler (2006) and Hu et al. (2015), where the non-negative value of every additive part within the dissipation function is stringently required to warrant the compliance with the second laws of thermodynamic.

In this framework, to reflect kinematic interdependencies between three internal variables $\dot{\varepsilon}_{v}^{\mathrm{p}}$, $\dot{\varepsilon}_{s}^{\mathrm{p}}$, and $\dot{S}_{r}^{\mathrm{p}}$, two following kinematic constraint equations (C_1, C_2) are introduced:

$$C_1 = B'\dot{\varepsilon}_{v}^{\mathrm{p}} + A'\dot{\varepsilon}_{s}^{\mathrm{p}} = 0 \tag{3.113}$$

$$C_2 = C'\dot{\varepsilon}_{v}^{\mathrm{p}} + A'\left(-\dot{S}_{r}^{\mathrm{p}}\right) = 0 \tag{3.114}$$

where A', B' and C' are general functions dependent on stresses and suction (e.g. p',q,s^{*}) to capture the interdependence between internal variables. As can be seen in Eqs. (3.113-3.114), kinematic constraint equations are also homogeneous first-order functions in terms of the rates of internal variables. Thanks to zero values, they can be used to supplement the dissipation potential to obtain an equivalent dissipation function using the standard method of Lagrangian multipliers (Houlsby & Puzrin, 2000; Nguyen & Bui, 2020) as follows:

$$\widetilde{\Phi} = \widetilde{\Phi} + \Lambda_1 C_1 + \Lambda_2 C_2 = \varphi^{v}\dot{\varepsilon}_{v}^{\mathrm{p}} + \varphi^{s}\dot{\varepsilon}_{s}^{\mathrm{p}} + \varphi^{h}\left(-\dot{S}_{r}^{\mathrm{p}}\right) + \Lambda_1\left(B'\dot{\varepsilon}_{v}^{\mathrm{p}} + A'\dot{\varepsilon}_{s}^{\mathrm{p}}\right) + \Lambda_2\left[C'\dot{\varepsilon}_{v}^{\mathrm{p}} + A'\left(-\dot{S}_{r}^{\mathrm{p}}\right)\right] \geq 0 \tag{3.115}$$

in which Λ_1 and Λ_2 are Lagrangian kinematic multipliers. Using Eqs. (3.115) and (3.96), generalized dissipative stresses take the following forms:

$$\chi_v = \frac{\partial \tilde{\Phi}}{\partial \dot{\varepsilon}_v^{\mathrm{p}}} = \varphi^v + B'\Lambda_1 + C'\Lambda_2 \tag{3.116}$$

$$\chi_s = \frac{\partial \tilde{\Phi}}{\partial \dot{\varepsilon}_s^{\mathrm{p}}} = \varphi^s + \Lambda_1 A' \tag{3.117}$$

$$\chi_h = \frac{\partial \tilde{\Phi}}{\partial (-\dot{s}_r^{\mathrm{p}})} = \varphi^h + \Lambda_2 A' \tag{3.118}$$

By combining Eqs. (3.116-3.118), the loading function in the dissipative stress space y^* is obtained:

$$\chi_v = \varphi^v + \frac{B'}{A'}(\chi_s - \varphi^s) + \frac{C'}{A'}(\chi_h - \varphi^h) \tag{3.119}$$

As can be seen in Eq. (3.119), all generalised dissipative stresses χ_i are interdependent and dependent on all rates of internal variables, $\dot{\varepsilon}_v^{\mathrm{p}}$, $\dot{\varepsilon}_s^{\mathrm{p}}$, and $-\dot{S}_r^{\mathrm{p}}$. Thanks to this, a single yield function y^* in generalised stress space (χ_v, χ_s, and χ_h) can be obtained from Eq. (3.119) as:

$$y^* = A'\chi_v - B'\chi_s - C'\chi_h - A'\varphi^v + B'\varphi^s + C'\varphi^h \leq 0 \tag{3.120}$$

Of numerous existing models for partially saturated soils, none suggests a general yield function of the linear surface, including the hydraulic component as such, as shown in Figure 3.5. By taking its derivatives with respect to χ_v, χ_s and χ_h, the associated flow rules in the space of dissipative stresses, sharing a single non-negative plastic-type multiplier, can be cast in the following formats to capture the initiation and evolution of plastic strain-like variables and their couplings at the same instant of the failure process. Along with this, the final expressions for the coupled hydro-mechanical flow rules are hence obtained as follows:

$$\dot{\varepsilon}_v^{\mathrm{p}} = \dot{\lambda}_p \frac{\partial y^*}{\partial \chi_v} = \dot{\lambda}_p A' \tag{3.121}$$

$$\dot{\varepsilon}_s^{\mathrm{p}} = \dot{\lambda}_p \frac{\partial y^*}{\partial \chi_s} = -\dot{\lambda}_p B' \tag{3.122}$$

$$-\dot{S}_r^{\mathrm{p}} = \dot{\lambda}_p \frac{\partial y^*}{\partial \chi_h} = -\dot{\lambda}_p C' \tag{3.123}$$

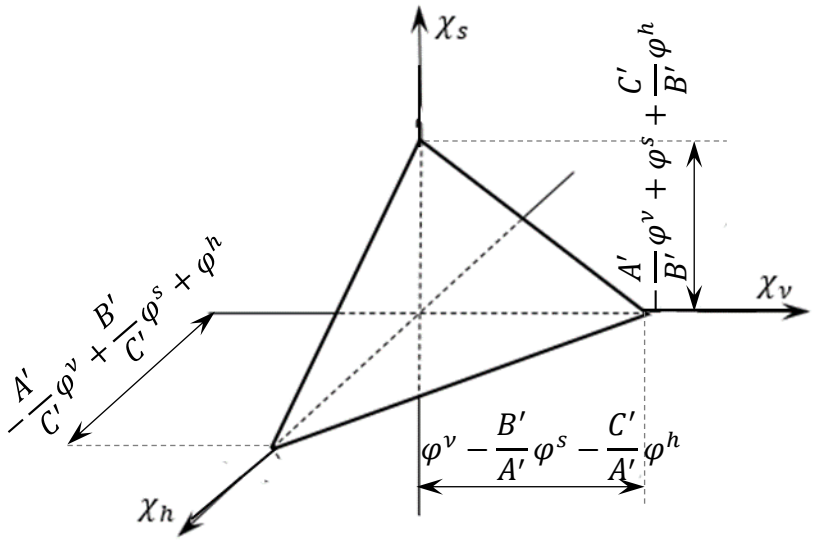

Figure 3.5. Geometric representation of yield potential in dissipative stress space for the approach of "using constraint equations."

Substituting the orthogonality conditions in the forms $\chi_v = \bar{\chi}_v = -\frac{\partial \Psi}{\partial \varepsilon_v^{\mathrm{p}}}$, $\chi_s = \bar{\chi}_s = -\frac{\partial \Psi}{\partial \varepsilon_s^{\mathrm{p}}}$, and $\chi_h = \bar{\chi}_h = -\frac{\partial \Psi}{\partial(-s_r^{\mathrm{p}})}$ (see Eqs. (3.95) and (3.97-3.99)) into Eq. (3.120), the following yield surface y in true stress space can be obtained as follows:

$$y\left(p', q, s^*, \varepsilon_v^{\mathrm{p}}, \varepsilon_s^{\mathrm{p}}, -S_r^{\mathrm{p}}\right) = A'\left(-\frac{\partial \Psi}{\partial \varepsilon_v^{\mathrm{p}}}\right) - B'\left(-\frac{\partial \Psi}{\partial \varepsilon_s^{\mathrm{p}}}\right) - C'\left[-\frac{\partial \Psi}{\partial(-s_r^{\mathrm{p}})}\right] - A'\varphi^v + B'\varphi^s + C'\varphi^h \leq 0 \tag{3.124}$$

Eqs. (3.92-3.94) and (3.120-3.124) can be understood as another generic form of thermodynamic-based models for unsaturated soils using kinematic constraint equations. It is of particular advantage for describing a great variety of physical responses through a wide range of yield conditions and evolution rules, thanks to the flexibility of selecting functions $A', B', C', \varphi^v, \varphi^s$ and φ^h.

Summary and comparison of two thermodynamic approaches for dissipation potential, loading function and flow rules

As discussed earlier in Chapter 2, based on physical observations on the tight interaction between mechanical and hydraulic processes at both continuum and grain levels, it is essential to establish a constitutive model for partially saturated soils with a single yield locus governed by a unique "plastic" multiplier with two flow rules. It is a consequence of the interdependence of thermodynamic forces and their dependence on all internal variables, in addition to effective stress and suction. This feature can be handled through two thermodynamics-based approaches: using a special form of dissipation

potential (see Eqs. (3.101-3.111)) and using constraint equations (see Eqs. (3.115-3.124)). A comparison between the two proposed thermodynamic approaches is carried out to analyse their similarity and difference. For this purpose, the following table summarises the model description derived from such approaches, pointing out several criteria (i) Helmholtz free energy (ii) Dissipation function (iii) True stresses (iv) Thermodynamic forces (v) Yield function in generalised stress space (vi) Yield function in true stress space (vii) Evolution rules.

Table 3.1. Comparison of the model description between approaches of "using a special form of dissipation potential" and "using constraint equations".

Using a special form of dissipation potential	**Using constrain equations**
(i) Helmholtz free energy	
$\Psi = \Psi\left(\varepsilon_v, \varepsilon_s, -S_r, \varepsilon_v^{\mathrm{p}}, \varepsilon_s^{\mathrm{p}}, -S_r^{\mathrm{p}}\right)$	$\Psi = \Psi\left(\varepsilon_v, \varepsilon_s, -S_r, \varepsilon_v^{\mathrm{p}}, \varepsilon_s^{\mathrm{p}}, -S_r^{\mathrm{p}}\right)$
(ii) Dissipation function	
$\widetilde{\Phi} = \sqrt{(\phi_1^v)^2 + (\phi^s)^2 + (\phi^h)^2} + \phi_2^v$	$\widetilde{\Phi} = \varphi^v \dot{\varepsilon}_v^{\mathrm{p}} + \varphi^s \dot{\varepsilon}_s^{\mathrm{p}} + \varphi^h\left(-\dot{S}_r^{\mathrm{p}}\right) + \Lambda_1 C_1 + \Lambda_2 C_2 \geq 0$ $C_1 = B'\dot{\varepsilon}_v^{\mathrm{p}} + A'\dot{\varepsilon}_s^{\mathrm{p}} = 0$ $C_2 = C'\dot{\varepsilon}_v^{\mathrm{p}} + A'\left(-\dot{S}_r^{\mathrm{p}}\right) = 0$
(iii) True stresses	
$p' = \frac{\partial \Psi}{\partial \varepsilon_v}$ $q = \frac{\partial \Psi}{\partial \varepsilon_s}$ $s^* = \frac{\partial \Psi}{\partial(-S_r)}$	$p' = \frac{\partial \Psi}{\partial \varepsilon_v}$ $q = \frac{\partial \Psi}{\partial \varepsilon_s}$ $s^* = \frac{\partial \Psi}{\partial(-S_r)}$
(iv) Thermodynamic forces	
$\chi_v = \frac{\partial \widetilde{\Phi}}{\partial \dot{\varepsilon}_v^{\mathrm{p}}} = \frac{\phi_1^v}{\sqrt{(\phi_1^v)^2 + (\phi^s)^2 + (\phi^h)^2}} \frac{\partial \phi_1^v}{\partial \dot{\varepsilon}_v^{\mathrm{p}}} + \frac{\partial \phi_2^v}{\partial \dot{\varepsilon}_v^{\mathrm{p}}}$ $\chi_s = \frac{\partial \widetilde{\Phi}}{\partial \dot{\varepsilon}_s^{\mathrm{p}}} = \frac{\phi^s}{\sqrt{(\phi_1^v)^2 + (\phi^s)^2 + (\phi^h)^2}} \frac{\partial \phi^s}{\partial \dot{\varepsilon}_s^{\mathrm{p}}}$	$\chi_v = \frac{\partial \widetilde{\Phi}}{\partial \dot{\varepsilon}_v^{\mathrm{p}}} = \varphi^v + B'\Lambda_1 + C'\Lambda_2$ $\chi_s = \frac{\partial \widetilde{\Phi}}{\partial \dot{\varepsilon}_s^{\mathrm{p}}} = \varphi^s + \Lambda_1 A'$ $\chi_h = \frac{\partial \widetilde{\Phi}}{\partial(-\dot{S}_r^{\mathrm{p}})} = \varphi^h + \Lambda_2 A'$

$\chi_h = \frac{\partial \widetilde{\Phi}}{\partial(-\dot{S}_r^{\mathrm{p}})} = \frac{\phi^h}{\sqrt{(\phi_1^v)^2+(\phi^s)^2+(\phi^h)^2}} \frac{\partial \phi^h}{\partial(-\dot{S}_r^{\mathrm{p}})}$	
(v) Yield function in generalised stress space	
$y^* = \frac{\left(\chi_v - \frac{\partial \phi_2^v}{\partial \dot{\varepsilon}_v^{\mathrm{p}}}\right)^2}{\left(\frac{\partial \phi_1^v}{\partial \dot{\varepsilon}_v^{\mathrm{p}}}\right)^2} + \frac{(\chi_s)^2}{\left(\frac{\partial \phi^s}{\partial \dot{\varepsilon}_s^{\mathrm{p}}}\right)^2} + \frac{(\chi_h)^2}{\left(\frac{\partial \phi^h}{\partial(-\dot{S}_r^{\mathrm{p}})}\right)^2} - 1 \leq 0$	$y^* = A'\chi_v - B'\chi_s - C'\chi_h - A'\varphi^v + B'\varphi^s + C'\varphi^h \leq 0$
(vi) Yield function in true stress space	
$y = \frac{\left(-\frac{\partial \Psi}{\partial \varepsilon_v^{\mathrm{p}}} - \frac{\partial \phi_2^v}{\partial \dot{\varepsilon}_v^{\mathrm{p}}}\right)^2}{\left(\frac{\partial \phi_1^v}{\partial \dot{\varepsilon}_v^{\mathrm{p}}}\right)^2} + \frac{\left(-\frac{\partial \Psi}{\partial \varepsilon_s^{\mathrm{p}}}\right)^2}{\left(\frac{\partial \phi^s}{\partial \dot{\varepsilon}_s^{\mathrm{p}}}\right)^2} + \frac{\left(-\frac{\partial \Psi}{\partial(-S_r^{\mathrm{p}})}\right)^2}{\left(\frac{\partial \phi^h}{\partial(-\dot{S}_r^{\mathrm{p}})}\right)^2} - 1 \leq 0$	$y = A'\left(-\frac{\partial \Psi}{\partial \varepsilon_v^{\mathrm{p}}}\right) - B'\left(-\frac{\partial \Psi}{\partial \varepsilon_s^{\mathrm{p}}}\right) - C'\left[-\frac{\partial \Psi}{\partial(-S_r^{\mathrm{p}})}\right] - A'\varphi^v + B'\varphi^s + C'\varphi^h \leq 0$
(vii) Evolution rules	
$\dot{\varepsilon}_v^{\mathrm{p}} = \dot{\lambda}_p \frac{\partial y^*}{\partial \chi_v} = \dot{\lambda}_p \frac{2\left(\chi_v - \frac{\partial \phi_2^v}{\partial \dot{\varepsilon}_v^{\mathrm{p}}}\right)}{\left(\frac{\partial \phi_1^v}{\partial \dot{\varepsilon}_v^{\mathrm{p}}}\right)^2}$ $\dot{\varepsilon}_s^{\mathrm{p}} = \dot{\lambda}_p \frac{\partial y^*}{\partial \chi_s} = \dot{\lambda}_p \frac{2\chi_s}{\left(\frac{\partial \phi^s}{\partial \dot{\varepsilon}_s^{\mathrm{p}}}\right)^2}$ $-\dot{S}_r^{\mathrm{p}} = \dot{\lambda}_p \frac{\partial y^*}{\partial \chi_h} = \dot{\lambda}_p \frac{2\chi_h}{\left(\frac{\partial \phi^h}{\partial(-\dot{S}_r^{\mathrm{p}})}\right)^2}$	$\dot{\varepsilon}_v^{\mathrm{p}} = \dot{\lambda}_p \frac{\partial y^*}{\partial \chi_v} = \dot{\lambda}_p A'$ $\dot{\varepsilon}_s^{\mathrm{p}} = \dot{\lambda}_p \frac{\partial y^*}{\partial \chi_s} = -\dot{\lambda}_p B'$ $-\dot{S}_r^{\mathrm{p}} = \dot{\lambda}_p \frac{\partial y^*}{\partial \chi_h} = -\dot{\lambda}_p C'$

As can be seen, these two methods have the same expression of Helmholtz free energy, leading to similar forms of true stresses and constitutive relationships. The main distinction between the two lies in the form of dissipation potential and the way how they result in essential properties of the hydromechanical coupling. To be more specific, in the approach of "using a special form of dissipation potential", the interdependence of thermodynamic forces and internal variables can be produced through the mathematical properties of derivatives of the square root ($\sqrt{(\phi_1^v)^2 + (\phi^s)^2 + (\phi^h)^2}$). Alternatively, multiple kinematic constraint equations of internal variables ($C_1 = B'\dot{\varepsilon}_v^{\mathrm{p}} + A'\dot{\varepsilon}_s^{\mathrm{p}} = 0$, $C_2 = C'\dot{\varepsilon}_v^{\mathrm{p}} + A'\left(-\dot{S}_r^{\mathrm{p}}\right) = 0$) are incorporated into the standard form of dissipation potential based on the mathematical method of Lagrangian multipliers (Λ_1, Λ_2) to manipulate these dependent relationships for the approach of "using constraints". This leads to the

difference in the form/shape of generic loading function in generalised stress space between these approaches where "ellipsoid" is for "using a special form of dissipation potential" and "linear surface" is for "using constraint equations". Although the proposed approaches are different in the generic mathematical expressions, they are expected to derive the same specific models meeting thermodynamic admissibility and possessing similar dissipation properties through appropriate and consistent detailed formulations of ϕ_1^v, ϕ_2^v, ϕ^s, and ϕ^h for the solution of "using a special form of dissipation potential" and A', B', C', φ^v, φ^s and φ^h for the solution of "using constraint equations". This feature is one of the outstanding findings regarding the thermodynamic theory for partially saturated soils in this thesis that cannot be seen in existing studies. Its potential will be elucidated in specific models presented in Chapter 4 and Appendix A.

3.3.2. Coupled hydro-mechanical tangent stiffness tensor

A consistent tangent stiffness matrix linking stress-like variables and strain-like variables at the material level is one of the indispensable components in the numerical implementation of the constitutive model. In the case of unsaturated soils models, the tangent stiffness matrix is used to represent both incremental stress-strain and suction-saturation degree relationships and serve as an explicit indicator of the interaction between mechanical and hydraulic processes in the inelastic regime. For the purpose of formulation derivation of the tangent stiffness, several essential formulations of the generic model based on two approaches (e.g. a special form of dissipation potential, constraints) are first shown in tensorial forms. In particular, the tensorial stress-strain and suction-saturation relationships can be derived from Eqs. (3.92-3.94) as follows:

$$\sigma'_{ij} = \frac{\partial \Psi}{\partial \varepsilon_{ij}} \tag{3.125}$$

$$s^* = \frac{\partial \Psi}{\partial(-S_r)} \tag{3.126}$$

From Eqs. (3.108-3.111) and (3.121-3.124), the yield function and evolution rules are of the following generic forms for both approaches:

$$y = y\left(p', q, s^*, \varepsilon_v^{\mathrm{p}}, \varepsilon_s^{\mathrm{p}}, -S_r^{\mathrm{p}}\right) \tag{3.127}$$

$$\dot{\varepsilon}_{ij}^{\mathrm{p}} = \dot{\lambda}_p \frac{\partial y^*}{\partial \chi_{ij}} = \dot{\lambda}_p \left(\frac{\partial y^*}{\partial \chi_v}\frac{\partial \chi_v}{\partial \chi_{ij}} + \frac{\partial y^*}{\partial \chi_s}\frac{\partial \chi_s}{\partial \chi_{ij}}\right) \tag{3.128}$$

$$-\dot{S}_r^{\mathrm{p}} = \dot{\lambda}_p \frac{\partial y^*}{\partial \chi_h} \tag{3.129}$$

where ε_{ij} is total strain tensor and $\varepsilon_{ij}^{\mathrm{p}}$ is the plastic strain tensor. It is noted that the generic form of yield surface in Eq. (3.127) is obtained thanks to the use of Eqs. (3.111) and (3.124) where $-\frac{\partial \Psi}{\partial \varepsilon_v^{\mathrm{p}}}$,

$-\frac{\partial \Psi}{\partial \varepsilon_s^{\mathrm{p}}}$ and $-\frac{\partial \Psi}{\partial(-S_r^{\mathrm{p}})}$ are functions of true stresses (p', q, s^*) and internal variables $(\varepsilon_v^{\mathrm{p}}, \varepsilon_s^{\mathrm{p}}, -S_r^{\mathrm{p}})$ while Eq. (3.128) is the combination of Eqs. (3.108-3.109) or (3.121-3.122).

From Eqs. (3.125-3.126), using an assumption of $\frac{\partial^2 \Psi}{\partial \varepsilon_{ij} \partial \varepsilon_{kl}} = -\frac{\partial^2 \Psi}{\partial \varepsilon_{ij} \partial \varepsilon_{kl}^{\mathrm{p}}}$, $\frac{\partial^2 \Psi}{\partial \varepsilon_{ij} \partial(-S_r)} = -\frac{\partial^2 \Psi}{\partial \varepsilon_{ij} \partial(-S_r^{\mathrm{p}})}$, $\frac{\partial^2 \Psi}{\partial(-S_r) \partial \varepsilon_{kl}} = -\frac{\partial^2 \Psi}{\partial(-S_r) \partial \varepsilon_{kl}^{\mathrm{p}}}$, $\frac{\partial^2 \Psi}{\partial(-S_r)^2} = -\frac{\partial^2 \Psi}{\partial(-S_r) \partial(-S_r^{\mathrm{p}})}$, the incremental forms of the effective stress tensor $\dot{\sigma}_{ij}'$ and modified suction $\dot{s}^*$ can be described as:

$$\dot{\sigma}_{ij}' = \frac{\partial^2 \Psi}{\partial \varepsilon_{ij} \partial \varepsilon_{kl}} \left(\dot{\varepsilon}_{kl} - \dot{\varepsilon}_{kl}^{\mathrm{p}}\right) + \frac{\partial^2 \Psi}{\partial \varepsilon_{ij} \partial(-S_r)} \left[\left(-\dot{S}_r\right) - \left(-\dot{S}_r^{\mathrm{p}}\right)\right] \tag{3.130}$$

$$\dot{s}^* = \frac{\partial^2 \Psi}{\partial(-S_r) \partial \varepsilon_{kl}} \left(\dot{\varepsilon}_{kl} - \dot{\varepsilon}_{kl}^{\mathrm{p}}\right) + \frac{\partial^2 \Psi}{\partial(-S_r)^2} \left[\left(-\dot{S}_r\right) - \left(-\dot{S}_r^{\mathrm{p}}\right)\right] \tag{3.131}$$

Using the yield function in Eq. (3.127), the consistency condition can be written as:

$$\dot{y} = \frac{\partial y}{\partial \sigma_{ij}'} \dot{\sigma}_{ij}' + \frac{\partial y}{\partial s^*} \dot{s}^* + \frac{\partial y}{\partial \varepsilon_{ij}^{\mathrm{p}}} \dot{\varepsilon}_{ij}^{\mathrm{p}} + \frac{\partial y}{\partial(-S_r^{\mathrm{p}})} \left(-\dot{S}_r^{\mathrm{p}}\right) = 0 \tag{3.132}$$

Substituting Eqs. (3.128-3.131) into Eq. (3.132) leads to:

$$\frac{\partial y}{\partial \sigma_{ij}'} \frac{\partial^2 \Psi}{\partial \varepsilon_{ij} \partial \varepsilon_{kl}} \left(\dot{\varepsilon}_{kl} - \dot{\lambda}_p \frac{\partial y^*}{\partial \chi_{kl}}\right) + \frac{\partial y}{\partial \sigma_{ij}'} \frac{\partial^2 \Psi}{\partial \varepsilon_{ij} \partial(-S_r)} \left[\left(-\dot{S}_r\right) - \dot{\lambda}_p \frac{\partial y^*}{\partial \chi_h}\right] + \frac{\partial y}{\partial s^*} \frac{\partial^2 \Psi}{\partial(-S_r) \partial \varepsilon_{kl}} \left(\dot{\varepsilon}_{kl} - \dot{\lambda}_p \frac{\partial y^*}{\partial \chi_{kl}}\right) +$$

$$\frac{\partial y}{\partial s^*} \frac{\partial^2 \Psi}{\partial(-S_r)^2} \left[\left(-\dot{S}_r\right) - \dot{\lambda}_p \frac{\partial y^*}{\partial \chi_h}\right] + \frac{\partial y}{\partial \varepsilon_{ij}^{\mathrm{p}}} \dot{\lambda}_p \frac{\partial y^*}{\partial \chi_{ij}} + \frac{\partial y}{\partial(-\dot{S}_r^{\mathrm{p}})} \dot{\lambda}_p \frac{\partial y^*}{\partial \chi_h} = 0 \tag{3.133}$$

Given $\dot{\varepsilon}_{kl}$ and $\dot{S}_r$, the multiplier $\dot{\lambda}_p$ can be obtained from Eq. (3.133) in the following form:

$$\dot{\lambda}_p = M_{kl} \dot{\varepsilon}_{kl} + H\left(-\dot{S}_r\right) \tag{3.134}$$

where

$$M_{kl} = \frac{\frac{\partial^2 \Psi}{\partial \varepsilon_{ij} \partial \varepsilon_{kl} \partial \sigma_{ij}'} \frac{\partial y}{\partial} + \frac{\partial^2 \Psi}{\partial(-S_r) \partial \varepsilon_{kl} \partial s^*}}{\left(\frac{\partial^2 \Psi}{\partial \varepsilon_{ij} \partial \varepsilon_{kl} \partial \chi_{kl}} \frac{\partial y^*}{\partial} + \frac{\partial^2 \Psi}{\partial \varepsilon_{ij} \partial(-S_r) \partial \chi_h} \frac{\partial y^*}{\partial}\right) \frac{\partial y}{\partial \sigma_{ij}'} + \left(\frac{\partial^2 \Psi}{\partial(-S_r) \partial \varepsilon_{kl} \partial \chi_{kl}} \frac{\partial y^*}{\partial} + \frac{\partial^2 \Psi}{\partial(-S_r)^2 \partial \chi_h} \frac{\partial y^*}{\partial}\right) \frac{\partial y}{\partial s^*} - \frac{\partial y^*}{\partial \chi_{ij}} \frac{\partial y}{\partial \varepsilon_{ij}^{\mathrm{p}}} - \frac{\partial y^*}{\partial \chi_h} \frac{\partial y}{\partial(-S_r^{\mathrm{p}})}} \tag{3.135}$$

$$H = \frac{\frac{\partial^2 \Psi}{\partial \varepsilon_{ij} \partial(-S_r) \partial \sigma_{ij}'} \frac{\partial y}{\partial} + \frac{\partial^2 \Psi}{\partial(-S_r)^2 \partial s^*}}{\left(\frac{\partial^2 \Psi}{\partial \varepsilon_{ij} \partial \varepsilon_{kl} \partial \chi_{kl}} \frac{\partial y^*}{\partial} + \frac{\partial^2 \Psi}{\partial \varepsilon_{ij} \partial(-S_r) \partial \chi_h} \frac{\partial y^*}{\partial}\right) \frac{\partial y}{\partial \sigma_{ij}'} + \left(\frac{\partial^2 \Psi}{\partial(-S_r) \partial \varepsilon_{kl} \partial \chi_{kl}} \frac{\partial y^*}{\partial} + \frac{\partial^2 \Psi}{\partial(-S_r)^2 \partial \chi_h} \frac{\partial y^*}{\partial}\right) \frac{\partial y}{\partial s^*} - \frac{\partial y^*}{\partial \chi_{ij}} \frac{\partial y}{\partial \varepsilon_{ij}^{\mathrm{p}}} - \frac{\partial y^*}{\partial \chi_h} \frac{\partial y}{\partial(-S_r^{\mathrm{p}})}} \tag{3.136}$$

By substituting Eq. (3.134) into Eqs. (3.130-3.131), the incremental coupled hydro-mechanical relationships can be written as:

$$\dot{\sigma}_{ij}' = \frac{\partial^2 \Psi}{\partial \varepsilon_{ij} \partial \varepsilon_{kl}} \left\{\dot{\varepsilon}_{kl} - \left[M_{kl} \dot{\varepsilon}_{kl} + H\left(-\dot{S}_r\right)\right] \frac{\partial y^*}{\partial \chi_{kl}}\right\} + \frac{\partial^2 \Psi}{\partial \varepsilon_{ij} \partial(-S_r)} \left\{\left(-\dot{S}_r\right) - \left[M_{kl} \dot{\varepsilon}_{kl} + H\left(-\dot{S}_r\right)\right] \frac{\partial y^*}{\partial \chi_h}\right\} \tag{3.137}$$

$$\dot{s}^* = \frac{\partial^2\Psi}{\partial(-S_r)\partial\varepsilon_{kl}}\left\{\dot{\varepsilon}_{kl} - \left[M_{kl}\dot{\varepsilon}_{kl} + H\left(-\dot{S}_r\right)\right]\frac{\partial y^*}{\partial\chi_{kl}}\right\} + \frac{\partial^2\Psi}{\partial(-S_r)^2}\left\{\left(-\dot{S}_r\right) - \left[M_{kl}\dot{\varepsilon}_{kl} + H\left(-\dot{S}_r\right)\right]\frac{\partial y^*}{\partial\chi_h}\right\} \tag{3.138}$$

Eqs. (3.137-3.138) can be rewritten as:

$$\dot{\sigma}'_{ij} = \left[\frac{\partial^2\Psi}{\partial\varepsilon_{ij}\partial\varepsilon_{kl}}\left(1 - M_{kl}\frac{\partial y^*}{\partial\chi_{kl}}\right) - \frac{\partial^2\Psi}{\partial\varepsilon_{ij}\partial(-S_r)}M_{kl}\frac{\partial y^*}{\partial\chi_h}\right]\dot{\varepsilon}_{kl} + \left[\frac{\partial^2\Psi}{\partial\varepsilon_{ij}\partial(-S_r)}\left(1 - H\frac{\partial y^*}{\partial\chi_h}\right) - \frac{\partial^2\Psi}{\partial\varepsilon_{ij}\partial\varepsilon_{kl}}H\frac{\partial y^*}{\partial\chi_{kl}}\right]\left(-\dot{S}_r\right) = \Lambda_{ijkl}\dot{\varepsilon}_{kl} + \Pi_{ij}\left(-\dot{S}_r\right) \tag{3.139}$$

$$\dot{s}^* = \left[\frac{\partial^2\Psi}{\partial(-S_r)\partial\varepsilon_{kl}}\left(1 - M_{kl}\frac{\partial y^*}{\partial\chi_{kl}}\right) - \frac{\partial^2\Psi}{\partial(-S_r)^2}M_{kl}\frac{\partial y^*}{\partial\chi_h}\right]\dot{\varepsilon}_{kl} + \left[\frac{\partial^2\Psi}{\partial(-S_r)^2}\left(1 - H\frac{\partial y^*}{\partial\chi_h}\right) - \frac{\partial^2\Psi}{\partial(-S_r)\partial\varepsilon_{kl}}H\frac{\partial y^*}{\partial\chi_{kl}}\right]\left(-\dot{S}_r\right) = \Omega_{kl}\,\dot{\varepsilon}_{kl} + \Upsilon\left(-\dot{S}_r\right) \tag{3.140}$$

in which $\Lambda_{ijkl}, \Pi_{ij}, \Omega_{kl}$ and Υ are terms of the tangent stiffness tensor expressed in terms of σ'_{ij} and s^*:

$$\Lambda_{ijkl} = \frac{\partial^2\Psi}{\partial\varepsilon_{ij}\partial\varepsilon_{kl}}\left(1 - M_{kl}\frac{\partial y^*}{\partial\chi_{kl}}\right) - \frac{\partial^2\Psi}{\partial\varepsilon_{ij}\partial(-S_r)}M_{kl} \tag{3.141}$$

$$\Pi_{ij} = \frac{\partial^2\Psi}{\partial\varepsilon_{ij}\partial(-S_r)}\left(1 - H\frac{\partial y^*}{\partial\chi_h}\right) - \frac{\partial^2\Psi}{\partial\varepsilon_{ij}\partial\varepsilon_{kl}}H\frac{\partial y^*}{\partial\chi_{kl}} \tag{3.142}$$

$$\Omega_{kl} = \frac{\partial^2\Psi}{\partial(-S_r)\partial\varepsilon_{kl}}\left(1 - M_{kl}\frac{\partial y^*}{\partial\chi_{kl}}\right) - \frac{\partial^2\Psi}{\partial(-S_r)^2}M_{kl}\frac{\partial y^*}{\partial\chi_h} \tag{3.143}$$

$$\Upsilon = \frac{\partial^2\Psi}{\partial(-S_r)^2}\left(1 - H\frac{\partial y^*}{\partial\chi_h}\right) - \frac{\partial^2\Psi}{\partial(-S_r)\partial\varepsilon_{kl}}H\frac{\partial y^*}{\partial\chi_{kl}} \tag{3.144}$$

The expressions of constitutive relationship in Eqs. (3.139-3.140) can be presented in the form of the Voigt notations as follows:

$$\begin{pmatrix}\dot{\sigma}'_{11}\\ \dot{\sigma}'_{22}\\ \dot{\sigma}'_{33}\\ \dot{\sigma}'_{12}\\ \dot{\sigma}'_{23}\\ \dot{\sigma}'_{31}\\ \dot{s}^*\end{pmatrix} = \begin{bmatrix}\Lambda_{1111} & \Lambda_{1122} & \Lambda_{1133} & \Lambda_{1112} & \Lambda_{1123} & \Lambda_{1131} & \Pi_{11}\\ \Lambda_{2211} & \Lambda_{2222} & \Lambda_{2233} & \Lambda_{2212} & \Lambda_{2223} & \Lambda_{2231} & \Pi_{22}\\ \Lambda_{3311} & \Lambda_{3322} & \Lambda_{3333} & \Lambda_{3312} & \Lambda_{3323} & \Lambda_{3331} & \Pi_{33}\\ \Lambda_{1211} & \Lambda_{1222} & \Lambda_{1233} & \Lambda_{1212} & \Lambda_{1223} & \Lambda_{1231} & \Pi_{12}\\ \Lambda_{2311} & \Lambda_{2322} & \Lambda_{2333} & \Lambda_{2312} & \Lambda_{2323} & \Lambda_{2331} & \Pi_{23}\\ \Lambda_{3111} & \Lambda_{3122} & \Lambda_{3133} & \Lambda_{3112} & \Lambda_{3123} & \Lambda_{3131} & \Pi_{31}\\ \Omega_{11} & \Omega_{22} & \Omega_{33} & \Omega_{12} & \Omega_{23} & \Omega_{31} & \Upsilon\end{bmatrix}\begin{pmatrix}\dot{\varepsilon}_{11}\\ \dot{\varepsilon}_{22}\\ \dot{\varepsilon}_{33}\\ \dot{\varepsilon}_{12}\\ \dot{\varepsilon}_{23}\\ \dot{\varepsilon}_{31}\\ -\dot{S}_r\end{pmatrix} \tag{3.145}$$

As can be seen in Eqs. (3.139-3.140) (or alternatively, Eq. (3.145)), the cross-coupling terms Π_{ij}, and Ω_{kl} indicate the inter-dependence between mechanical and hydraulic responses. As a consequence, the water retention curve (or SWCC; Eq. (3.140)) generated by the model (not imposed like any other existing ones) is path-dependent, governed by both states (stress and suction) and hydro-mechanical loading paths. This path-dependence nature of both mechanical and hydraulic responses induces different responses under wetting/drying and mechanical loading conditions, reflecting the inseparable nature of the coupling rooting from grain-scale interactions. With cross-coupling terms,

the hydro-mechanical coupling is always guaranteed by the tangent stiffness upon yielding, enabling the proposed model to describe the simultaneous activation and development of plasticity and hydraulic irreversibility under any condition of loading and saturation. These are the key characteristics of the proposed model that are advanced from existing models in the literature possessing multiple yield surfaces and thus multiple "plastic" multipliers as a result of adding more internal variables, as presented in Chapter 2. Due to a decoupling of dissipative stresses from all the rates of internal variables, the inseparable nature of the hydro-mechanical coupling cannot be naturally reflected by the adoption of more than one yield surfaces and corresponding forms of tangent stiffness in such existing models.

3.3.3. Semi-implicit stress return algorithm for the behaviour in the homogeneous stage

The semi-implicit stress return algorithm is employed in this constitutive model for the stress and suction update, given the input total strain $\Delta\varepsilon_{kl}$ and saturation degree $(-\Delta S_r)$ increments. This method is to compute and correct trial stress back onto the yield surface if it is located outside the yield surface (Crisfield, 1993). As illustrated in Figure 3.6, in the first step of this algorithm, the values of effective stress $\left(\sigma_{ij}^{\prime\mathrm{trial}}\right)$ and modified suction $\left(s^{*\mathrm{trial}}\right)$ at trial state (see Figure 3.6) are calculated from the effective stress tensor $\left(\sigma_{ij}^{\prime n}\right)$ and modified suction (s^{*n}) at step n, respectively.

$$\sigma_{ij}^{\prime\mathrm{trial}} = \sigma_{ij}^{\prime n} + \Delta\sigma_{ij}^{\prime\mathrm{trial}} = \sigma_{ij}^{\prime n} + \frac{\partial^2\Psi^n}{\partial\varepsilon_{ij}\partial\varepsilon_{kl}}\Delta\varepsilon_{kl} + \frac{\partial^2\Psi^n}{\partial\varepsilon_{ij}\partial(-S_r)}(-\Delta S_r) \tag{3.146}$$

$$s^{*\mathrm{trial}} = s^{*n} + \Delta s^{*\mathrm{trial}} = s^{*n} + \frac{\partial^2\Psi^n}{\partial(-S_r)\partial\varepsilon_{kl}}\Delta\varepsilon_{kl} + \frac{\partial^2\Psi^n}{\partial(-S_r)^2}(-\Delta S_r) \tag{3.147}$$

in which $\frac{\partial^2\Psi^n}{\partial\varepsilon_{ij}\partial\varepsilon_{kl}}$, $\frac{\partial^2\Psi^n}{\partial\varepsilon_{ij}\partial(-S_r)}$, $\frac{\partial^2\Psi^n}{\partial(-S_r)\partial\varepsilon_{kl}}$ and $\frac{\partial^2\Psi^n}{\partial(-S_r)^2}$ denote terms of the secant elastic stiffness evaluated at state n.

If yielding takes place, e.g. $y^{\mathrm{trial}}\left(\sigma_{ij}^{\prime\mathrm{trial}}, s^{*\mathrm{trial}}, p_c^{\prime}\right) > 0$ (see Figure 3.6), a first-order Taylor expansion is applied to the yield function at trial point B (see Figure 3.6), resulting in

$$y^{\mathrm{new}} = y^{\mathrm{trial}} + \Delta\sigma_{ij}^{\prime\mathrm{corrt}}\frac{\partial y}{\partial\sigma_{ij}^{\prime}}\bigg|^{\mathrm{trial}} + \Delta s^{*\mathrm{corrt}}\frac{\partial y}{\partial s^{*}}\bigg|^{\mathrm{trial}} + \Delta\varepsilon_{ij}^{\mathrm{p}}\frac{\partial y}{\partial\varepsilon_{ij}^{\mathrm{p}}}\bigg|^{\mathrm{trial}} + \left(-\Delta S_r^{\mathrm{p}}\right)\frac{\partial y}{\partial(-S_r^{\mathrm{p}})}\bigg|^{\mathrm{trial}} \tag{3.148}$$

where $\Delta\sigma_{ij}^{\prime\mathrm{corrt}}$ and $\Delta s^{*\mathrm{corrt}}$ (see Figure 3.6) are the corrective terms to effective stress tensor and modified suction, respectively, in the following form, given $\Delta\varepsilon_{kl}$ and $(-\Delta S_r)$ have been applied to move from points A to B (see Figure 3.6):

$$\Delta\sigma_{ij}^{\prime\mathrm{corrt}} = \sigma_{ij}^{\prime n+1} - \sigma_{ij}^{\prime\mathrm{trial}} = -\frac{\partial^2\Psi^n}{\partial\varepsilon_{ij}\partial\varepsilon_{kl}}\Delta\varepsilon_{kl}^{\mathrm{p}} - \frac{\partial^2\Psi^n}{\partial\varepsilon_{ij}\partial(-S_r)}\left(-\Delta S_r^{\mathrm{p}}\right) \tag{3.149}$$

$$\Delta s^{*\mathrm{corrt}} = s^{*n+1} - s^{*\mathrm{trial}} = -\frac{\partial^2 \Psi^n}{\partial(-S_r)\partial\varepsilon_{kl}}\Delta\varepsilon_{kl}^{\mathrm{p}} - \frac{\partial^2 \Psi^n}{\partial(-S_r)^2}\left(-\Delta S_r^{\mathrm{p}}\right) \tag{3.150}$$

With the use of flow rules in Eqs. (3.128) and (3.129), the substitution of Eqs. (3.149-3.150) into Eq. (3.148) leads to:

$$y^{\mathrm{new}} = y^{\mathrm{trial}} - \Delta\lambda_p \left(\frac{\partial^2 \Psi^n}{\partial\varepsilon_{ij}\partial\varepsilon_{kl}}\frac{\partial y^*}{\partial\chi_{kl}} + \frac{\partial^2 \Psi^n}{\partial\varepsilon_{ij}\partial(-S_r)}\frac{\partial y^*}{\partial\chi_h}\right)\frac{\partial y}{\partial\sigma'_{ij}}\Bigg|^{\mathrm{trial}} - \Delta\lambda_p \left(\frac{\partial^2 \Psi^n}{\partial(-S_r)\partial\varepsilon_{kl}}\frac{\partial y^*}{\partial\chi_{kl}} + \frac{\partial^2 \Psi^n}{\partial(-S_r)^2}\frac{\partial y^*}{\partial\chi_h}\right)\frac{\partial y}{\partial s^*}\Bigg|^{\mathrm{trial}} + \Delta\lambda_p \frac{\partial y^*}{\partial\chi_{ij}}\frac{\partial y}{\partial\varepsilon_{ij}^{\mathrm{p}}}\Bigg|^{\mathrm{trial}} + \Delta\lambda_p \frac{\partial y^*}{\partial\chi_h}\frac{\partial y}{\partial\left(-S_r^{\mathrm{p}}\right)}\Bigg|^{\mathrm{trial}} \tag{3.151}$$

Enforcing the yield condition $y^{\mathrm{new}} = 0$ results in the plasticity multiplier $\Delta\lambda_p$ as:

$$\Delta\lambda_p = \frac{y^{\mathrm{trial}}}{\left(\frac{\partial^2\Psi}{\partial\varepsilon_{ij}\partial\varepsilon_{kl}}\frac{\partial y^*}{\partial\chi_{kl}} + \frac{\partial^2\Psi}{\partial\varepsilon_{ij}\partial(-S_r)}\frac{\partial y^*}{\partial\chi_h}\right)\frac{\partial y}{\partial\sigma'_{ij}}\Bigg|^{\mathrm{trial}} + \left(\frac{\partial^2\Psi}{\partial(-S_r)\partial\varepsilon_{kl}}\frac{\partial y^*}{\partial\chi_{kl}} + \frac{\partial^2\Psi}{\partial(-S_r)^2}\frac{\partial y^*}{\partial\chi_h}\right)\frac{\partial y}{\partial s^*}\Bigg|^{\mathrm{trial}} - \frac{\partial y^*}{\partial\chi_{ij}}\frac{\partial y}{\partial\varepsilon_{ij}^{\mathrm{p}}}\Bigg|^{\mathrm{trial}} - \frac{\partial y^*}{\partial\chi_h}\frac{\partial y}{\partial\left(-S_r^{\mathrm{p}}\right)}\Bigg|^{\mathrm{trial}}} \tag{3.152}$$

Once $\Delta\lambda_p$ is obtained, the new increments of effective stress tensor ($\Delta\sigma'_{ij}$) and modified suction (Δs^*) can be obtained as follows:

$$\Delta\sigma'_{ij} = \Delta\sigma'^{\mathrm{trial}}_{ij} + \Delta\sigma'^{\mathrm{corrt}}_{ij} \tag{3.153}$$

$$\Delta s^* = \Delta s^{*\mathrm{trial}} + \Delta s^{*\mathrm{corrt}} \tag{3.154}$$

These increments are then used to update the effective stress tensors and modified suction, or alternatively net stress tensor and matric suction:

$$\sigma'^{n+1}_{ij} = \sigma'^{n}_{ij} + \Delta\sigma'_{ij} \tag{3.155}$$

$$s^{*n+1} = s^{*n} + \Delta s^* \tag{3.156}$$

$$\bar{\sigma}^{n+1}_{ij} = \sigma'^{n+1}_{ij} - S_r^{n+1} s^{n+1}\delta_{ij} \tag{3.157}$$

$$s^{n+1} = \frac{s^{*n+1}}{\bar{\phi}^{n+1}} \tag{3.158}$$

where $\bar{\phi}^{n+1}$ and S_r^{n+1} are updated porosity and saturation degree, respectively.

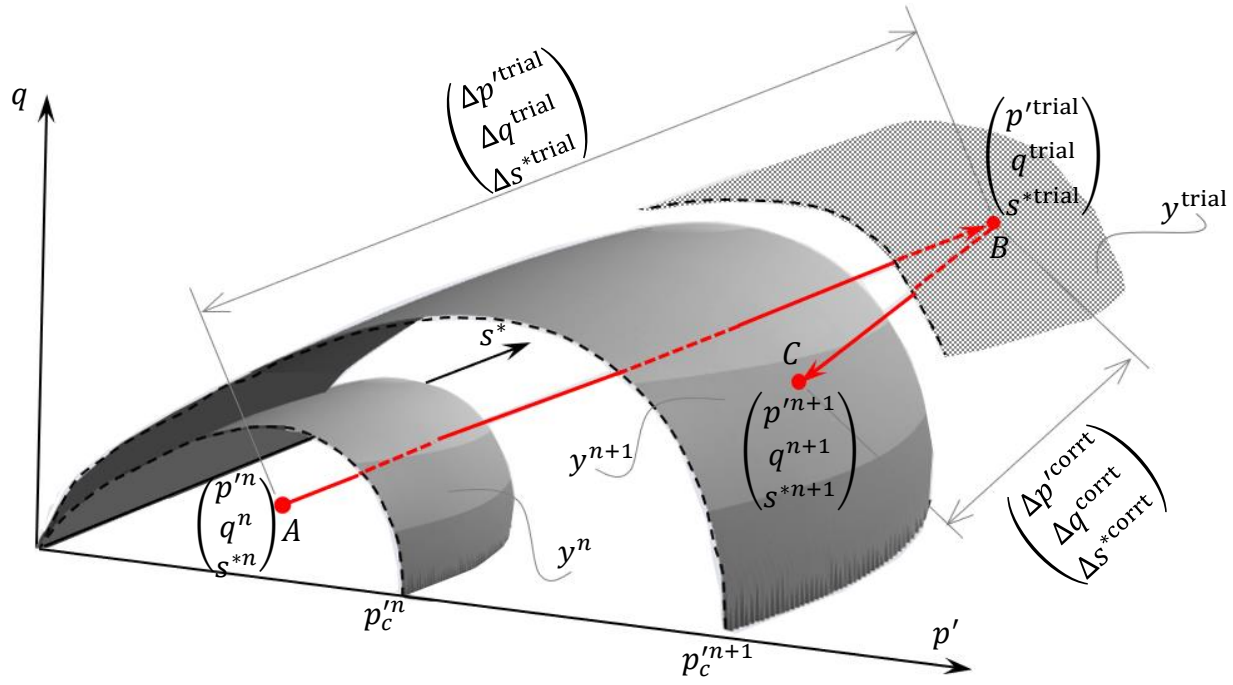

Figure 3.6. Schematic representation of the stress update algorithm in three-dimensional space.

3.4. Closure

This chapter focuses on the development of a generic coupled hydro-mechanical framework, identifying key fundamentals to develop specific models for partially saturated soils in successive Chapters of this thesis. The formulations in this framework are rigorous, generic and well structured, hence bringing benefit in reducing the number of parameters and arbitrary assumptions. With the use of the mixture theory, a mixed form of field variables (e.g. seepage force, solid velocity, porosity, saturation degree) is derived from the combination of mass and momentum conservation laws of all constituents of the mixture to reflect the coupled solid deformation-fluid laminar flow within three-phase porous media in respect to the motion of solid skeleton. To complete this framework, additional constitutive relationships between stress-like (stress, suction) and strain-like (strain, saturation degree) variables are provided through a generic thermodynamics-based approach with the focus on the nature of the interaction between grain contact sliding and capillary irreversibility at the grain scale. The novelty of this approach is the incorporation of the irreversible degree of saturation and its strong coupling with plastic strain in a special form of dissipation potential or constraint equations. It leads to a single yield function with different evolution rules for plastic strains and irrecoverable saturation degree without requiring a separate SWCC and different sets of parameters for drying and wetting paths. This feature is a numerical advantage as a hydro-mechanical coupling in the inelastic regime is always automatically guaranteed. The proposed approach allows addressing the lack of hydraulic

dissipation and interdependence of thermodynamic forces in some earlier models for partially saturated soils where multiple yield functions are usually needed due to the lack of micro-mechanical insights about the inseparable nature of grain rearrangements and liquid redistributions as discussed in Chapter 2.

It is noted that the current model does not explicitly incorporate details associated with underlying micro-mechanisms, although their importance to understanding proper responses of partially saturated soils. The focus of this paper is the continuum modelling based on observations at the macroscale. Microscopic mechanisms are used here only as a means to obtain constraints on the interactions of internal variables in the continuum models, in particular their inter-dependency in energy dissipation at the continuum scale. Furthermore, the current approach has not yet accounted for the effects of localised deformation where no details on orientation and thickness of the shear band are incorporated into the constitutive equations that will be addressed in Chapter 5.

Chapter 4. A thermodynamics-based critical state model for partially saturated soils

4.1. Introduction

A critical state model is described in this section following the generic formulation in Chapter 3 to serve as an example to indicate its promising performances in simulating suction- and water content-controlled tests at low stresses without the transition to void closure and pressurised saturation. This chapter aims for the establishment of a rigorous thermodynamics-based approach that leads to a good balance between rigour, simplicity, number of parameters and performance in the derived constitutive models. In this model, two free energy and dissipation potentials are explicitly defined, reflecting the energy transformation between isotropic compression (e.g. volumetric and hydraulic energy dissipations occupy the total dissipation) and critical states (e.g. shear dissipation occupies the total dissipation) in both drained and undrained triaxial shear tests. Given these two potentials, the proposed thermodynamic formulation is used as a versatile means to connect all essential behavioural characteristics of partially saturated soils, resulting in a single yield surface in stress-suction space and two evolution rules for plastic strains and irrecoverable saturation with a single "plastic" multiplier. This is thanks to the inter-dependence of mechanical and hydraulic dissipations in the proposed dissipation potential, providing smooth transitions from fully to partially saturated states and from contraction to dilation responses under homogeneous deformation conditions. This coupling naturally induces the effects of mechanical behaviour on the saturation-suction relationship. As a result, models derived from this approach possess an implicitly defined SWCC dependent on the volumetric behaviour, reflecting the hydro-mechanical interactions at the grain scale. This is consistent with suggestions in Wheeler et al. (2003), based on both micro-mechanical reasoning and experiments (e.g. Sharma, 1998; Gallipoli et al., 2003), that the irreversible part of the volumetric strain, arising from the mechanical energy lost due to slippage at inter-particle contacts, results in the translation of the water retention curve. The proposed thermodynamic formulation also helps minimise the number of parameters required while not compromising the performance of the derived models. The obtained model, formulated under infinitesimal strain assumption, possesses a small number of identifiable parameters, which have clear physical meanings and can be calibrated from standard tests on partially saturated soils. The model performance is assessed and validated against a range of experiments on partially saturated soils.

The outline of this chapter is as follows. In section 4.2, the formulation of a critical state thermo-mechanical model for partially saturated soils is described where two approaches of "using a special

form of dissipation potential" and "using constraint equations" are presented. This is followed by its dissipation properties. Section 4.3 describes the numerical implementation algorithms and their verification. The parameter identification and determination are presented in Section 4.4, followed by the validation and demonstration of the capabilities of the proposed model in Section 4.5.

4.2. Model formulation

This section is to present a rigorous and systematic procedure for deriving the specific formulation of a thermodynamics-based critical state model for partially saturated soils based on the generic approach developed beforehand in Chapter 3.

4.2.1. Helmholtz specific energy potential and constitutive relationships

The Helmholtz specific energy potential can be assumed of the following form:

$$\Psi = \overbrace{\kappa p_0' \exp\left[\frac{(\varepsilon_v - \varepsilon_v^{\mathrm{p}})}{\kappa}\right]}^{Volumetric\ part} + \overbrace{\frac{3}{2}G\left(\varepsilon_s - \varepsilon_s^{\mathrm{p}}\right)^2}^{Shear\ part} + \overbrace{\kappa_h(p_u + s_0^*)\exp\left\{\frac{S_{r0} + [(-S_r) - (-S_r^{\mathrm{p}})]}{\kappa_h}\right\} - [(-S_r) - (-S_r^{\mathrm{p}})]p_u + (-S_r^{\mathrm{p}})p_b}^{Hydraulic\ part} \tag{4.1}$$

where κ is the elastic index controlling the pressure-dependent elastic behaviour of the model; G is the shear moduli; κ_h is to control the amount of reversible energy stored in the water menisci (Buscarnera & Einav, 2012); $p_u = 1$ kPa is to make the unit consistent and p_b is a parameter controlling the stored irreversible hydraulic energy. Initial values of p', s^* and S_r are denoted as p_0', s_0^* and S_{r0} , respectively.

Eq. (4.1) indicates that the Helmholtz free energy is a combination of stored energies induced by both mechanical and hydraulic processes. They are produced by the compressed grains, which can recover to their previous states (Collins, 2005) and the reversible movement of the air-water interfaces (Wheeler et al., 2003). The last term of Eq. (4.1), $(-S_r^{\mathrm{p}})p_b$, represents the irrecoverable hydraulic energy that is stored in the volume element, reflecting the entrapment of fluid menisci in the heterogeneous structure during wetting-drying processes (Wei & Dewoolkar, 2006). It is noted that the Helmholtz free energy potential is of phenomenological form, and the elastic behaviour does not possess strong hydro-mechanical coupling, given the focus on the dissipation properties and inelastic behaviour.

Using Eqs. (3.92-3.94) and (4.1), the true stresses are:

$$p' = \frac{\partial \Psi}{\partial \varepsilon_v} = p'_0 \exp\left[\frac{(\varepsilon_v - \varepsilon_v^{\mathrm{p}})}{\kappa}\right] \tag{4.2}$$

$$q = \frac{\partial \Psi}{\partial \varepsilon_s} = 3G\left(\varepsilon_s - \varepsilon_s^{\mathrm{p}}\right) \tag{4.3}$$

$$s^* = \frac{\partial \Psi}{\partial(-S_r)} = (p_u + s_0^*) \exp\left\{\frac{S_{r0} + [(-S_r) - (-S_r^{\mathrm{p}})]}{\kappa_h}\right\} - p_u \tag{4.4}$$

The generalised stresses can also be obtained from the Helmholtz free energy potential in Eq. (4.1) as:

$$\bar{\chi}_v = -\frac{\partial \Psi}{\partial \varepsilon_v^{\mathrm{p}}} = p'_0 \exp\left[\frac{(\varepsilon_v - \varepsilon_v^{\mathrm{p}})}{\kappa}\right] = p' \tag{4.5}$$

$$\bar{\chi}_s = -\frac{\partial \Psi}{\partial \varepsilon_s^{\mathrm{p}}} = 3G\left(\varepsilon_s - \varepsilon_s^{\mathrm{p}}\right) = q \tag{4.6}$$

$$\bar{\chi}_h = -\frac{\partial \Psi}{\partial(-S_r^{\mathrm{p}})} = (p_u + s_0^*) \exp\left\{\frac{S_{r0} + [(-S_r) - (-S_r^{\mathrm{p}})]}{\kappa_h}\right\} - p_u - p_b = s^* - p_b \tag{4.7}$$

Eq. (4.2) implies the pressure-dependent elastic soil bulk employing a linear relationship between $\ln\nu$ and $\ln p'$ (Butterfield, 1979; Hashiguchi, 1995; Callari et al., 1998; Collins & Kelly, 2002). In an alternative way, the elastic moduli of soils can be assumed to be independent on pressure for simplicity without compromising the model performance, that will be further explored in the next chapters. Since $s^* = s\bar{\phi}$, and $\varepsilon_v = \phi_0 - \bar{\phi}$ (Chapter 3) hydraulic effects on the elastic stiffness are accounted for in the (p', s) space. However, these effects are usually considered insignificant and can be neglected (Alonso et al., 1990; Sheng et al., 2004). Eqs. (4.2 & 4.4) can be expanded to forms of net mean stress and suction to expose the interaction between NCL and SWCC as:

$$\bar{p} + S_r s = (\bar{p}_0 + S_{r0} s_0) \exp\left[\frac{(\varepsilon_v - \varepsilon_v^{\mathrm{p}})}{\kappa}\right] \tag{4.8}$$

$$\bar{\phi} s = \left\{(p_u + \phi_0 s_0) \exp\left\{\frac{S_{r0} + [(-S_r) - (-S_r^{\mathrm{p}})]}{\kappa_h}\right\} - p_u\right\} \tag{4.9}$$

where $\bar{p}_0$ and s_0 are initial values of mean net stress and suction. From Eqs. (4.8 & 4.9), the net mean stress and suction can be expressed as:

$$\bar{p} = (\bar{p}_0 + S_{r0} s_0) \exp\left[\frac{(\varepsilon_v - \varepsilon_v^{\mathrm{p}})}{\kappa}\right] - \frac{S_r}{\bar{\phi}}\left\{(p_u + \phi_0 s_0) \exp\left\{\frac{S_{r0} + [(-S_r) - (-S_r^{\mathrm{p}})]}{\kappa_h}\right\} - p_u\right\} \tag{4.10}$$

$$s = \frac{1}{\bar{\phi}}\left\{(p_u + \phi_0 s_0) \exp\left\{\frac{S_{r0} + [(-S_r) - (-S_r^{\mathrm{p}})]}{\kappa_h}\right\} - p_u\right\} \tag{4.11}$$

As can be seen in Eqs. (4.10) and (4.11), both suction and saturation have an influence on the change of net stress and hence the elastic stiffness.

4.2.2. Dissipation potential, yield function and flow rules

Chapter 3 provides two different approaches (using a special form of dissipation potential, using constraint equations) to construct yield function and evolution rules from the dissipation potential. Although these two methods are somewhat different in the mathematical formulation, they have one thing in common: A strong coupling between irrecoverable changes of strain and saturation degree is governed by a unique yield surface of both stress and suction associated with a single "plastic" multiplier of two flow rules, as a result of the dependence of generalised stresses on others and the rate of all internal variables. Their potential can be indicated through the following systematic procedure for constructing a specific critical state yield criterion for partially saturated soils.

Using a special form of dissipation potential

(i) Generic formulation

In this approach, the nature of grain-scale interactions leads to the proposal of a suitable form of dissipation potential that reflects the hydro-mechanical coupling in the inelastic behaviour of unsaturated soils. From Eq. (3.101), the special form of dissipation potential can be rewritten as:

$$\widetilde{\Phi} = \sqrt{(\phi_1^v)^2 + (\phi^s)^2 + (\phi^h)^2} + \phi_2^v \tag{4.12}$$

which results in a single yield function y^* in generalised stress space (χ_v, χ_s, and χ_h) (see details on how to obtain them in Chapter 3):

$$y^* = \frac{\left(\chi_v - \frac{\partial \phi_2^v}{\partial \dot{\varepsilon}_v^{\mathrm{p}}}\right)^2}{\left(\frac{\partial \phi_1^v}{\partial \dot{\varepsilon}_v^{\mathrm{p}}}\right)^2} + \frac{(\chi_s)^2}{\left(\frac{\partial \phi^s}{\partial \dot{\varepsilon}_s^{\mathrm{p}}}\right)^2} + \frac{(\chi_h)^2}{\left(\frac{\partial \phi^h}{\partial \left(-\dot{S}_r^{\mathrm{p}}\right)}\right)^2} - 1 \leq 0 \tag{4.13}$$

and flow rules for three internal variables take the following generic forms:

$$\dot{\varepsilon}_v^{\mathrm{p}} = \dot{\lambda}_p \frac{\partial y^*}{\partial \chi_v} = \dot{\lambda}_p \frac{2\left(\chi_v - \frac{\partial \phi_2^v}{\partial \dot{\varepsilon}_v^{\mathrm{p}}}\right)}{\left(\frac{\partial \phi_1^v}{\partial \dot{\varepsilon}_v^{\mathrm{p}}}\right)^2} \tag{4.14}$$

$$\dot{\varepsilon}_s^{\mathrm{p}} = \dot{\lambda}_p \frac{\partial y^*}{\partial \chi_s} = \dot{\lambda}_p \frac{2\chi_s}{\left(\frac{\partial \phi^s}{\partial \dot{\varepsilon}_s^{\mathrm{p}}}\right)^2} \tag{4.15}$$

$$-\dot{S}_r^{\mathrm{p}} = \dot{\lambda}_p \frac{\partial y^*}{\partial \chi_h} = \dot{\lambda}_p \frac{2\chi_h}{\left(\frac{\partial \phi^h}{\partial \left(-\dot{S}_r^{\mathrm{p}}\right)}\right)^2} \tag{4.16}$$

(ii) Specific form of dissipation potential

Functions ϕ_1^v, ϕ_2^v, ϕ^s and ϕ^h in the dissipation potential (see Eq. (4.12)) take the below specific forms:

$$\phi_1^v = \frac{1}{\sqrt{\exp[-\beta(1-S_r)]}} A\dot{\varepsilon}_v^{\mathrm{p}} \tag{4.17}$$

$$\phi_2^v = \frac{p'_{c(us)}}{r}\dot{\varepsilon}_v^{\mathrm{p}} \tag{4.18}$$

$$\phi^s = B\dot{\varepsilon}_s^{\mathrm{p}} \tag{4.19}$$

$$\phi^h = \frac{1}{\sqrt{1-\exp[-\beta(1-S_r)]}} \frac{(s^*-p_b)}{\left(p'-\frac{p'_{c(us)}}{r}\right)}\left(-\dot{S}_r^{\mathrm{p}}\right)A \tag{4.20}$$

The dimensionless parameter β ($0 < \beta \leq 1$) is used to govern the coupling between saturation and volumetric deformation upon yielding. Its role will be elaborated in Sections 4.4 and 4.5.1. Parameter r is defined as "spacing ratio" in the range of 1.5-∞ to control the dilatancy (Crouch et al., 1994; Yu, 1998; Collins & Hilder, 2002; Lai et al., 2016). Noting in these formulations above that $p'_{c(us)}$ is considered as the main component in governing the overall rate of energy loss associated with the slippage at inter-particle or inter-packet contacts under the effect of meniscus water rings, thus justifying the name hardening function. The evolving threshold pressure $p'_{c(us)}$ can take different forms of evolution laws based on experimentally observed responses at low stresses (e.g. Alonso et al., 1990; Wheeler et al., 2003; Sheng et al., 2008; Tamagnini, 2004; Khalili et al., 2008) or high stresses (Mun & McCartney, 2017; Loret & Khalili, 2002; Alonso et al., 2013; Zhou et al., 2018). A relatively simple law is presented in this study to reproduce experimental trends at low pressures; any other forms can be used given the generic thermodynamic framework proposed in this study. In particular, the form of the employed hardening law is selected based on several experimental observations on NCL in (p', v) of drained isotropic compression tests (e.g. Zhan, 2003; Mun & McCartney, 2017). In this case, function $p'_{c(us)}$ is expressed as a function of s^* and $\varepsilon_v^{\mathrm{p}}$:

$$p'_{c(us)} = p'_R\left(\frac{p'_c}{p'_R}\right)^{\frac{\lambda-\kappa}{\lambda_{us}-\kappa}} = p'_R\left[\frac{p'_{c0}\exp\left(\frac{\varepsilon_v^{\mathrm{p}}}{\lambda-\kappa}\right)}{p'_R}\right]^{\frac{\lambda-\kappa}{\lambda[(1-\xi)\exp(-\mu s^*)+\xi]-\kappa}} \tag{4.21}$$

The above evolution law is based on the combination of pre-consolidation effective mean pressure for saturated conditions (Collins & Hilder, 2002),

$$p'_c = p'_{c0}\exp\left[\varepsilon_v^{\mathrm{p}}/(\lambda-\kappa)\right] \tag{4.22}$$

and stiffness parameter for partially saturated conditions,

$$\lambda_{us} = \lambda[(1-\xi)\exp(-\mu s^*) + \xi] \tag{4.23}$$

with λ representing the slope of the virgin compression line in the $\ln v : \ln p'$ plane for saturated conditions; p'_{c0} is the initial yield pressure under isotropic compression at fully saturated condition; p'_R denotes the stress parameter controlling the yield curve; ξ is a dimensionless parameter controlling the maximum soil stiffness, and μ is a constant related to the change of soil stiffness with modified suction.

As demonstrated in Figures 4.1-4.2, the hardening law in Eqs. (4.21-4.23) results in good agreement with experimental data. It is similar to the wetting-induced hardening law proposed in Alonso et al. (1990), which has been shown to be adequate in several models for partially saturated soils (e.g. Alonso et al., 1990; Bolzon et al., 1996; Cui & Delage, 1996; Al-Sharrad, 2013; Sun & Sun, 2012; Macari et al., 2003). However, it is acknowledged that only volume change responses at low stresses were investigated in such cases. Therefore, the hardening law represented by Eqs. (4.21-4.23) is not suitable or even invalid for modelling responses of partially saturated soils under high-stress levels (Khalili & Nguyen, personal communication, 29th Nov. 2019), including the transition to void closure and pressurised saturation (Mun & McCartney, 2015; 2017). Figure 4.1 shows the responses and the performance of the model using the hardening law (Eqs. (4.21-4.23)) in such cases. The current study also acknowledges several limitations of drained tests for determining yield curves (Zhang & Li, 2011; Zhang, 2016) and so the inadequacy of the proposed hardening laws in capturing yielding behaviour under more complicated stress paths (Loret & Khalili, 2002).

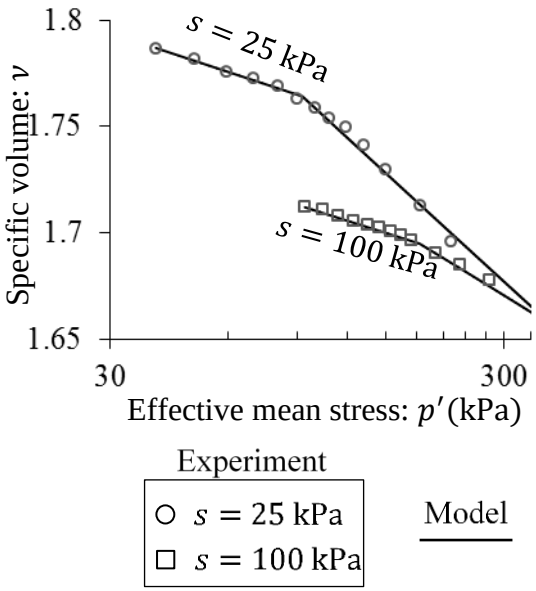

Figure 4.1. NCL in (p', v) of drained isotropic compression test of the compacted partially saturated expansive clay at $s = 25\ kPa$ and $s = 100\ kPa$ (after Zhan, 2003); $\kappa = 0.015$, $\lambda = 0.05$,$p'_{c0} = 80\ kPa$, $p'_R = 50\ kPa$, $\mu = 0.025\ kPa^{-1}$, $\xi = 0.3$

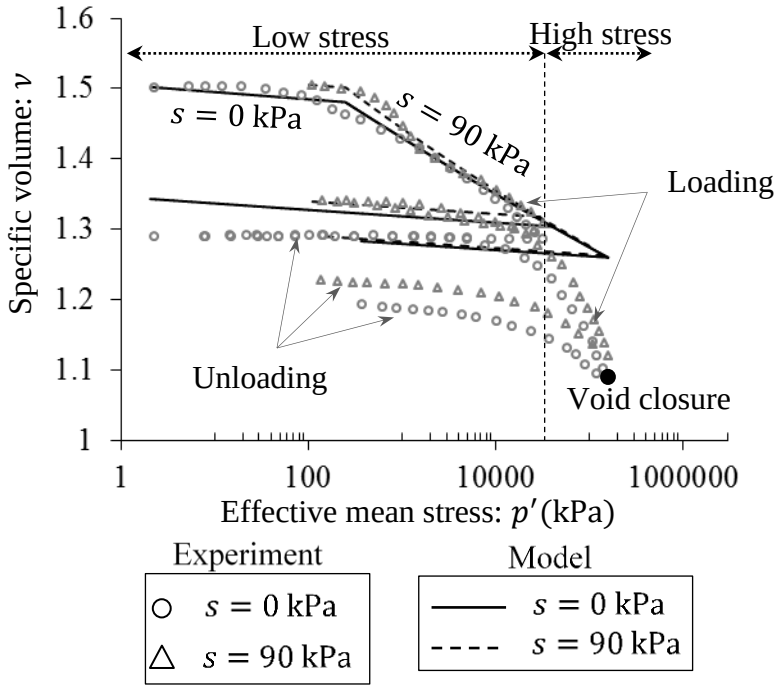

Figure 4.2. NCL in (p', v) of drained isotropic compression test of the Boulder clay at $s = 0\ kPa$ and $s = 90\ kPa$ (after Mun & McCartney, 2017); $\kappa = 0.003$,$\lambda = 0.025$, $p'_{c0} = 250\ kPa$, $p'_R = 300\ kPa$, $\mu = -0.005\ kPa^{-1}$, $\xi = 0.05$

(iii) Derivation of yield surface and flow rules

Using Eqs. (4.17-4.20), the yield function in dissipative stress space (Eq. (4.13)) can be obtained as:

$$y^* = \frac{\left(\chi_v - \frac{p'_{c(us)}}{r}\right)^2}{\left[\frac{1}{\sqrt{\exp[-\beta(1-S_r)]}}A\right]^2} + \frac{(\chi_s)^2}{(B)^2} + \frac{(\chi_h)^2}{\left[\frac{1}{\sqrt{1-\exp[-\beta(1-S_r)]}}\frac{(s^*-p_b)}{\left(p' - \frac{p'_{c(us)}}{r}\right)}A\right]^2} - 1 \leq 0 \tag{4.24}$$

Using Eqs. (3.97-3.99), (4.5-4.7) and the orthogonality conditions in the forms $\chi_v = \bar{\chi}_v = p'$, $\chi_s = \bar{\chi}_s = q$, and $\chi_h = \bar{\chi}_h = s^* - p_b$, the yield surface y in true stress space can be obtained as:

$$y = \frac{\left(p' - \frac{p'_{c(us)}}{r}\right)^2}{A^2} + \frac{(q)^2}{B^2} - 1 \leq 0 \tag{4.25}$$

which governs the following evolution rules:

$$\dot{\varepsilon}_v^{\mathrm{p}} = \dot{\lambda}_p \frac{2\left(p' - \frac{p'_{c(us)}}{r}\right)}{A^2} \exp[-\beta(1-S_r)] \tag{4.26}$$

$$\dot{\varepsilon}_s^{\mathrm{p}} = \dot{\lambda}_p \frac{\partial y^*}{\partial \chi_s} = \dot{\lambda}_p \frac{2q}{B^2} \tag{4.27}$$

$$-\dot{S}_r^{\mathrm{p}} = \dot{\lambda}_p \frac{\partial y^*}{\partial \chi_h} = \dot{\lambda}_p \frac{2\left(p' - \frac{p'_{c(us)}}{r}\right)^2}{(s^*-p_b)A^2}\{1 - \exp[-\beta(1-S_r)]\} \tag{4.28}$$

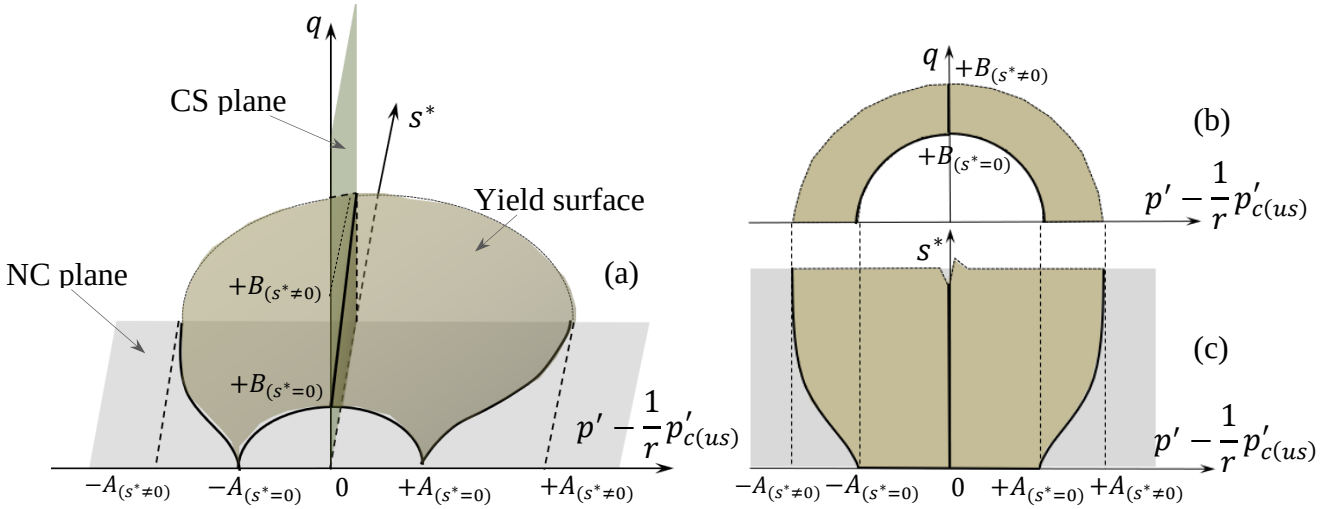

Figure 4.3. Yield surface in (a) $\left(p' - \frac{p'_{c(us)}}{r}, q, s^*\right)$ space, (b) $\left(p' - \frac{p'_{c(us)}}{r}, q\right)$ space and (c) $\left(p' - \frac{p'_{c(us)}}{r}, s^*\right)$ space

As can be seen in Figure 4.3, in the $(p' - p'_{c(us)}/r, q)$ plane, the yield function in Eq. (4.25) is the upper half of an ellipse of radii A and B. The change of its shape towards increasing s^* reflects the effect of suction on shear strength. The ellipse axes coincide with the normal consolidation line (NCL) when $\dot{\varepsilon}_v^{\mathrm{p}} = 0$ and critical state line (CSL) when $\dot{\varepsilon}_s^{\mathrm{p}} = 0$, respectively.

Functions A and B in Eqs. (4.17), (4.19-4.20) and then (4.25) govern the behaviour of the model. A systematic procedure (Collins, 2003; Collins & Hilder, 2002) is conducted to determine their specific forms. This procedure first investigates the dependence of functions A and B on stress-like variables, based on details given in Eqs. (3.102-3.104) and (4.12-4.28).

From Eqs. (3.102-3.103), the following expressions can be written:

$$\chi_v - \frac{\partial \phi_2^v}{\partial \dot{\varepsilon}_v^{\mathrm{p}}} = \frac{\phi_1^v}{\tilde{\Phi} - \phi_2^v} \frac{\partial \phi_1^v}{\partial \dot{\varepsilon}_v^{\mathrm{p}}} \tag{4.29}$$

$$\chi_s = \frac{\phi^s}{\tilde{\Phi} - \phi_2^v} \frac{\partial \phi^s}{\partial \dot{\varepsilon}_s^{\mathrm{p}}} \tag{4.30}$$

Substituting Eqs. (4.17-4.19) into Eqs. (4.29-4.30) yields:

$$\chi_v - \frac{p'_{c(us)}}{r} = \frac{A^2 \dot{\varepsilon}_v^{\mathrm{p}}}{\tilde{\Phi} - \frac{p'_{c(us)}}{r} \dot{\varepsilon}_v^{\mathrm{p}}} \frac{1}{\exp[-\beta(1 - S_r)]} \tag{4.31}$$

$$\chi_s = \frac{B^2 \dot{\varepsilon}_s^{\mathrm{p}}}{\tilde{\Phi} - \frac{p'_{c(us)}}{r} \dot{\varepsilon}_v^{\mathrm{p}}} \tag{4.32}$$

Invoking Eqs. (3.97-3.99), (3.105-3.106) and (4.5-4.7), Eqs. (4.31-4.32) become:

$$p' - \frac{p'_{c(us)}}{r} = \frac{A^2 \dot{\varepsilon}_v^{\mathrm{p}}}{\left(p' - \frac{p'_{c(us)}}{r}\right) \dot{\varepsilon}_v^{\mathrm{p}} + q \dot{\varepsilon}_s^{\mathrm{p}} + (s^* - p_b)(-\dot{S}_r^{\mathrm{p}})} \frac{1}{\exp[-\beta(1 - S_r)]} \tag{4.33}$$

$$q = \frac{B^2 \dot{\varepsilon}_s^{\mathrm{p}}}{\left(p' - \frac{p'_{c(us)}}{r}\right) \dot{\varepsilon}_v^{\mathrm{p}} + q \dot{\varepsilon}_s^{\mathrm{p}} + (s^* - p_b)(-\dot{S}_r^{\mathrm{p}})} \tag{4.34}$$

The relationship between $-\dot{S}_r^{\mathrm{p}}$ and $\dot{\varepsilon}_v^{\mathrm{p}}$ can be derived from flow rules in Eqs. (4.26) and (4.28) as follows:

$$(s^* - p_b)\left(-\dot{S}_r^{\mathrm{p}}\right) = \frac{1 - \exp[-\beta(1 - S_r)]}{\exp[-\beta(1 - S_r)]} \left(p' - \frac{1}{r} p'_{c(us)}\right) \dot{\varepsilon}_v^{\mathrm{p}} \tag{4.35}$$

Substitution of Eq. (4.35) into Eqs. (4.33-4.34), with some mathematical arrangements, one obtains the following functions for A and B:

$$A = \pm\sqrt{\frac{\exp[-\beta(1-S_r)]\left(p'-\frac{p'_{c(us)}}{r}\right)\left[\left(p'-\frac{p'_{c(us)}}{r}\right)\frac{1}{\exp[-\beta(1-S_r)]}\dot{\varepsilon}_v^{\mathrm{p}}+q\dot{\varepsilon}_s^{\mathrm{p}}\right]}{\dot{\varepsilon}_v^{\mathrm{p}}}} \tag{4.36}$$

$$B = \pm\sqrt{\frac{q\left[\left(p'-\frac{p'_{c(us)}}{r}\right)\frac{1}{\exp[-\beta(1-S_r)]}\dot{\varepsilon}_v^{\mathrm{p}}+q\dot{\varepsilon}_s^{\mathrm{p}}\right]}{\dot{\varepsilon}_s^{\mathrm{p}}}} \tag{4.37}$$

Based on Eq. (4.36), the stress derivatives of the function A are written as follows:

$$\frac{\partial A}{\partial p'} = \frac{\left[2\left(p'-\frac{p'_{c(us)}}{r}\right)\dot{\varepsilon}_v^{\mathrm{p}}\right]+\exp[-\beta(1-S_r)]q\dot{\varepsilon}_s^{\mathrm{p}}}{2A\dot{\varepsilon}_v^{\mathrm{p}}} \tag{4.38}$$

$$\frac{\partial A}{\partial q} = \frac{\exp[-\beta(1-S_r)]\left(p'-\frac{p'_{c(us)}}{r}\right)\dot{\varepsilon}_s^{\mathrm{p}}}{2A\dot{\varepsilon}_v^{\mathrm{p}}} \tag{4.39}$$

$$\frac{\partial A}{\partial p'_{c(us)}} = \frac{2\left(-\frac{1}{r}\right)\left(p'-\frac{p'_{c(us)}}{r}\right)\dot{\varepsilon}_v^{\mathrm{p}}+\left(-\frac{1}{r}\right)\exp[-\beta(1-S_r)]q\dot{\varepsilon}_s^{\mathrm{p}}}{2A\dot{\varepsilon}_v^{\mathrm{p}}} \tag{4.40}$$

With Eqs. (4.38-4.40), the following form can be expressed as:

$$\frac{\partial A}{\partial p'}p' + \frac{\partial A}{\partial q}q + \frac{\partial A}{\partial p'_{c(us)}}p'_{c(us)} = \frac{\left[2\left(p'-\frac{p'_{c(us)}}{r}\right)p'\dot{\varepsilon}_v^{\mathrm{p}}\right]+\exp[-\beta(1-S_r)]p'q\dot{\varepsilon}_s^{\mathrm{p}}}{2A\dot{\varepsilon}_v^{\mathrm{p}}} + \frac{\exp[-\beta(1-S_r)]\left(p'-\frac{p'_{c(us)}}{r}\right)q\dot{\varepsilon}_s^{\mathrm{p}}}{2A\dot{\varepsilon}_v^{\mathrm{p}}} + \frac{2\left(-\frac{1}{r}\right)\left(p'-\frac{p'_{c(us)}}{r}\right)p'_{c(us)}\dot{\varepsilon}_v^{\mathrm{p}}+\left(-\frac{1}{r}\right)\exp[-\beta(1-S_r)]qp'_{c(us)}\dot{\varepsilon}_s^{\mathrm{p}}}{2A\dot{\varepsilon}_v^{\mathrm{p}}} \tag{4.41}$$

Or,

$$\frac{\partial A}{\partial p'}p' + \frac{\partial A}{\partial q}q + \frac{\partial A}{\partial p'_{c(us)}}p'_{c(us)} = \frac{2\exp[-\beta(1-S_r)]\left(p'-\frac{p'_{c(us)}}{r}\right)\left[\left(p'-\frac{p'_{c(us)}}{r}\right)\frac{1}{\exp[-\beta(1-S_r)]}\dot{\varepsilon}_v^{\mathrm{p}}+q\dot{\varepsilon}_s^{\mathrm{p}}\right]}{2A\dot{\varepsilon}_v^{\mathrm{p}}} = A \tag{4.42}$$

Similarly, the following form can be obtained:

$$\frac{\partial B}{\partial p'}p' + \frac{\partial B}{\partial q}q + \frac{\partial B}{\partial p'_{c(us)}}p'_{c(us)} = B \tag{4.43}$$

Eqs. (4.42-4.43) indicate that A and B must be homogeneous functions of degree one in terms of the three defining effective stress variables p', q and $p'_{c(us)}$. For simplicity, they are assumed to be in linear forms (Collins & Hilder, 2002):

$$A = a_1p' + a_2q + a_3p'_{c(us)} \tag{4.44}$$

$$B = b_1p' + b_2q + b_3p'_{c(us)} \tag{4.45}$$

where $a_1, a_2, a_3, b_1, b_2, b_3$ are dimensionless coefficients governing dissipative micromechanical mechanisms. To determine them, the yielding behaviour of the wet granular material under isotropic

compression and decompression is examined where $\dot{\varepsilon}_s^{\mathrm{p}} = 0$ or $q = 0$. In this case, Eq. (4.44) can be reduced to the following expression:

$$p' - \frac{1}{r}p'_{c(us)} = \pm A = \pm\left[a_1 p' + a_3 p'_{c(us)}\right] \tag{4.46}$$

In Eq. (4.46), $p' = p'_{c(us)}$ for the plus sign of the yielding compression and $p' = 0$ for the minus sign of the yielding expansion (see Figure 4.3). Employing this, a_1 and a_3 can be deduced from Eq. (4.46) that:

$$a_1 = 1 - \frac{2}{r} \text{ and } a_3 = \frac{1}{r} \tag{4.47}$$

The coefficient a_2 is determined to be zero by assuming similarity between deviatoric extension and compression (Uchaipichat, 2005; Collins, 2003). Therefore:

$$A = \left(1 - \frac{2}{r}\right)p' + \frac{1}{r}p'_{c(us)} \tag{4.48}$$

Parameters b_1, b_2, b_3 can be identified by examining the yielding response at the critical state where the volumetric strain and saturation degree remain constant (Zhao et al., 2014; Chen, 2007). With $\dot{\varepsilon}_v^{\mathrm{p}} = 0$, if p'_{CSL} and q_{CSL} respectively denote the effective mean and shear stresses at the critical state, Eqs. (4.25) and (4.26) are therefore simplified as $(q_{CSL})^2 = B^2$ and $p'_{CSL} = \frac{1}{r}p'_{c(us)}$. With the use of Eq. (4.45), these equations lead to:

$$(q_{CSL})^2 = [b_1(p'_{CSL}) + b_2(q_{CSL}) + b_3 r(p'_{CSL})]^2 \tag{4.49}$$

So,

$$q_{CSL} = \pm\frac{(b_1 + b_3 r)p'_{CSL}}{(1 - b_2)} \tag{4.50}$$

Suppose that the compressive (positive) and extensive (negative) shear stresses in Eq. (4.50) are similar. Consequently, b_2 is null (Uchaipichat, 2005; Collins, 2003). Furthermore, the uniqueness of CSL with a constant slope M in the p': q plane is assumed (Russell & Khalili, 2006; Khalili et al., 2008). In this sense, Eq. (4.50) provides that:

$$\frac{q_{CSL}}{p'_{CSL}} = M = b_1 + b_3 r \tag{4.51}$$

The dimensionless parameter α $(0 < \alpha \leq 1)$ is now introduced to enable Eq. (4.51) to give:

$$b_1 = (1 - \alpha)M \text{ and } b_3 = \frac{\alpha}{r}M \tag{4.52}$$

Consequently,

$$B = (1-\alpha)Mp' + \frac{\alpha}{r}Mp'_{c(us)} \tag{4.53}$$

in which α is a parameter governing the strength of the material and non-associativity of the flow rules via the tear-drop shape and convexity near the origin of the yield surface.

In summary, from Eqs. (4.48) and (4.53), functions A and B are first-order homogeneous in terms of p' and $p'_{c(us)}$ and take the following forms:

$$A = \left(1-\frac{2}{r}\right)p' + \frac{1}{r}p'_{c(us)} \tag{4.54}$$

$$B = (1-\alpha)Mp' + \frac{\alpha}{r}Mp'_{c(us)} \tag{4.55}$$

For completeness, with obtained functions A and B, the final form of yield surface is expressed as:

$$y = \frac{\left(p'-\frac{p'_{c(us)}}{r}\right)^2}{A^2} + \frac{(q)^2}{B^2} - 1 = \frac{\left(p'-\frac{1}{r}p'_{c(us)}\right)^2}{\left[\left(1-\frac{2}{r}\right)p'+\frac{1}{r}p'_{c(us)}\right]^2} + \frac{q^2}{\left[(1-\alpha)p'+\frac{\alpha}{r}p'_{c(us)}\right]^2 M^2} - 1 \leq 0 \tag{4.56}$$

In conjunction with this yield surface, the evolution rules in Eqs. (4.26-4.28) now become:

$$\dot{\varepsilon}_v^{\mathrm{p}} = \dot{\lambda}_p \frac{\partial y^*}{\partial \chi_v} = \dot{\lambda}_p \frac{2\left(p'-\frac{p'_{c(us)}}{r}\right)}{A^2}\exp[-\beta(1-S_r)] = \dot{\lambda}_p \frac{2\left(p'-\frac{1}{r}p'_{c(us)}\right)}{\left[\left(1-\frac{2}{r}\right)p'+\frac{1}{r}p'_{c(us)}\right]^2}\exp[-\beta(1-S_r)] \tag{4.57}$$

$$\dot{\varepsilon}_s^{\mathrm{p}} = \dot{\lambda}_p \frac{\partial y^*}{\partial \chi_s} = \dot{\lambda}_p \frac{2q}{B^2} = \dot{\lambda}_p \frac{2q}{\left[(1-\alpha)p'+\frac{\alpha}{r}p'_{c(us)}\right]^2 M^2} \tag{4.58}$$

$$-\dot{S}_r^{\mathrm{p}} = \dot{\lambda}_p \frac{\partial y^*}{\partial \chi_h} = \dot{\lambda}_p \frac{2\left(p'-\frac{p'_{c(us)}}{r}\right)^2}{(s^*-p_b)A^2}\{1-\exp[-\beta(1-S_r)]\} = \dot{\lambda}_p \frac{2\left(p'-\frac{1}{r}p'_{c(us)}\right)^2}{(s^*-p_b)\left[\left(1-\frac{2}{r}\right)p'+\frac{1}{r}p'_{c(us)}\right]^2}\big[1-$$

$$\exp[-\beta(1-S_r)]\big] \tag{4.59}$$

Using constraint equations

(i) Generic formulation

As shown beforehand in Eq. (3.115) of Chapter 3, the dissipation potential can be supplemented by kinematic constraint equations using Lagrangian multipliers as:

$$\widetilde{\Phi} = \varphi^v\dot{\varepsilon}_v^{\mathrm{p}} + \varphi^s\dot{\varepsilon}_s^{\mathrm{p}} + \varphi^h\left(-\dot{S}_r^{\mathrm{p}}\right) + \Lambda_1\left(B'\dot{\varepsilon}_v^{\mathrm{p}} + A'\dot{\varepsilon}_s^{\mathrm{p}}\right) + \Lambda_2\left[C'\dot{\varepsilon}_v^{\mathrm{p}} + A'\left(-\dot{S}_r^{\mathrm{p}}\right)\right] \geq 0 \tag{4.60}$$

As a result of this, a unique yield function y^* dependent on all thermodynamic forces (χ_v, χ_s, and χ_h) can be established (see Eq. (3.120)) as:

$$y^* = A'\chi_v - B'\chi_s - C'\chi_h - A'\varphi^v + B'\varphi^s + C'\varphi^h \leq 0 \tag{4.61}$$

which goes with flow rules of internal variables taking the following generic forms (see Eqs. (3.121-3.123):

$$\dot{\varepsilon}_v^{\mathrm{p}} = \dot{\lambda}_p \frac{\partial y^*}{\partial \chi_v} = \dot{\lambda}_p A' \tag{4.62}$$

$$\dot{\varepsilon}_s^{\mathrm{p}} = \dot{\lambda}_p \frac{\partial y^*}{\partial \chi_s} = -\dot{\lambda}_p B' \tag{4.63}$$

$$-\dot{S}_r^{\mathrm{p}} = \dot{\lambda}_p \frac{\partial y^*}{\partial \chi_h} = -\dot{\lambda}_p C' \tag{4.64}$$

(ii) Specific form of dissipation potential and kinematic constraint equations

Taking $A', B', C', \varphi^v, \varphi^s$ and φ^h as functions of p', q and $p'_{c(us)}$ to govern the contribution of each individual dissipative mechanism in the total dissipation rate, with A', B', φ^v and φ^s representing the particle rearrangements and C', φ^h representing the liquid bridge redistribution, their specific expressions can be assumed as:

$$\varphi^v = \frac{p'_{c(us)}}{r} \tag{4.65}$$

$$\varphi^h = 0 \tag{4.66}$$

$$\varphi^s = \frac{\left[(1-\alpha)p' + \frac{\alpha}{r}p'_{c(us)}\right]^2 M^2}{q} \tag{4.67}$$

$$A' = \frac{2\left(p' - \frac{1}{r}p'_{c(us)}\right)}{\left[\left(1-\frac{2}{r}\right)p' + \frac{1}{r}p'_{c(us)}\right]^2} \exp[-\beta(1-S_r)] \tag{4.68}$$

$$B' = -\frac{2q}{\left[(1-\alpha)p' + \frac{\alpha}{r}p'_{c(us)}\right]^2 M^2} \tag{4.69}$$

$$C' = -\frac{2\left(p' - \frac{1}{r}p'_{c(us)}\right)^2}{(s^* - p_b)\left[\left(1-\frac{2}{r}\right)p' + \frac{1}{r}p'_{c(us)}\right]^2}\left[1 - \exp[-\beta(1-S_r)]\right] \tag{4.70}$$

(iii) Derivation of yield surface and flow rules

Substitution of Eqs. (4.65-4.70) into Eq. (4.61) leads to:

$$y^* = \frac{2\left(p' - \frac{1}{r}p'_{c(us)}\right)}{\left[\left(1-\frac{2}{r}\right)p' + \frac{1}{r}p'_{c(us)}\right]^2} \exp[-\beta(1-S_r)]\chi_v + \frac{2q}{\left[(1-\alpha)p' + \frac{\alpha}{r}p'_{c(us)}\right]^2 M^2}\chi_s + \frac{2\left(p' - \frac{1}{r}p'_{c(us)}\right)^2}{(s^* - p_b)\left[\left(1-\frac{2}{r}\right)p' + \frac{1}{r}p'_{c(us)}\right]^2}\Big[1 - \exp[-\beta(1-S_r)]\Big]\chi_h - \frac{2\left(p' - \frac{1}{r}p'_{c(us)}\right)}{\left[\left(1-\frac{2}{r}\right)p' + \frac{1}{r}p'_{c(us)}\right]^2} \exp[-\beta(1-S_r)]\frac{p'_{c(us)}}{r} - \frac{2q}{\left[(1-\alpha)p' + \frac{\alpha}{r}p'_{c(us)}\right]^2 M^2}\frac{\left[(1-\alpha)p' + \frac{\alpha}{r}p'_{c(us)}\right]^2 M^2}{q} \leq 0 \tag{4.71}$$

By substituting the orthogonality conditions with $\chi_v = \bar{\chi}_v = p'$, $\chi_s = \bar{\chi}_s = q$, and $\chi_h = \bar{\chi}_h = s^* - p_b$ into Eq. (4.71), the yield surface in true stress space can be established as:

$$y = \frac{2\left(p' - \frac{1}{r}p'_{c(us)}\right)}{\left[\left(1-\frac{2}{r}\right)p' + \frac{1}{r}p'_{c(us)}\right]^2}\exp[-\beta(1-S_r)]p' + \frac{2q}{\left[(1-\alpha)p' + \frac{\alpha}{r}p'_{c(us)}\right]^2 M^2}q + \frac{2\left(p' - \frac{1}{r}p'_{c(us)}\right)^2}{(s^* - p_b)\left[\left(1-\frac{2}{r}\right)p' + \frac{1}{r}p'_{c(us)}\right]^2}\left[1 - \exp[-\beta(1-S_r)]\right](s^* - p_b) - \frac{2\left(p' - \frac{1}{r}p'_{c(us)}\right)}{\left[\left(1-\frac{2}{r}\right)p' + \frac{1}{r}p'_{c(us)}\right]^2}\exp[-\beta(1-S_r)]\frac{p'_{c(us)}}{r} - \frac{2q}{\left[(1-\alpha)p' + \frac{\alpha}{r}p'_{c(us)}\right]^2 M^2}\frac{\left[(1-\alpha)p' + \frac{\alpha}{r}p'_{c(us)}\right]^2 M^2}{q} \leq 0 \quad (4.72)$$

After some mathematical manipulations in Eq. (4.72), a single yield surface dependent on stresses and suction can be obtained as:

$$y = \frac{\left(p' - \frac{1}{r}p'_{c(us)}\right)^2}{\left[\left(1-\frac{2}{r}\right)p' + \frac{1}{r}p'_{c(us)}\right]^2} + \frac{q^2}{\left[(1-\alpha)p' + \frac{\alpha}{r}p'_{c(us)}\right]^2 M^2} - 1 \leq 0 \quad (4.73)$$

Along with this, the expressions for the coupled hydro-mechanical flow rules are hence obtained as follows:

$$\dot{\varepsilon}_v^{\mathrm{p}} = \dot{\lambda}_p \frac{\partial y^*}{\partial \chi_v} = \dot{\lambda}_p A' = \dot{\lambda}_p \frac{2\left(p' - \frac{1}{r}p'_{c(us)}\right)}{\left[\left(1-\frac{2}{r}\right)p' + \frac{1}{r}p'_{c(us)}\right]^2}\exp[-\beta(1-S_r)] \quad (4.74)$$

$$\dot{\varepsilon}_s^{\mathrm{p}} = \dot{\lambda}_p \frac{\partial y^*}{\partial \chi_s} = -\dot{\lambda}_p B' = \dot{\lambda}_p \frac{2q}{\left[(1-\alpha)p' + \frac{\alpha}{r}p'_{c(us)}\right]^2 M^2} \quad (4.75)$$

$$-\dot{S}_r^{\mathrm{p}} = \dot{\lambda}_p \frac{\partial y^*}{\partial \chi_h} = -\dot{\lambda}_p C' = \dot{\lambda}_p \frac{2\left(p' - \frac{1}{r}p'_{c(us)}\right)^2}{(s^* - p_b)\left[\left(1-\frac{2}{r}\right)p' + \frac{1}{r}p'_{c(us)}\right]^2}\left[1 - \exp[-\beta(1-S_r)]\right] \quad (4.76)$$

Summary and discussion

It can be found that two approaches allow constructing the same formulations of yield surface and evolutions rules which are summarised below (Eqs. (4.56-4.59) and Eqs. (4.73-4.76)):

$$y = \frac{\left(p' - \frac{1}{r}p'_{c(us)}\right)^2}{\left[\left(1-\frac{2}{r}\right)p' + \frac{1}{r}p'_{c(us)}\right]^2} + \frac{q^2}{\left[(1-\alpha)p' + \frac{\alpha}{r}p'_{c(us)}\right]^2 M^2} - 1 \leq 0 \quad (4.77)$$

$$\dot{\varepsilon}_v^{\mathrm{p}} = \dot{\lambda}_p \frac{\partial y^*}{\partial \chi_v} = \dot{\lambda}_p \frac{2\left(p' - \frac{1}{r}p'_{c(us)}\right)}{\left[\left(1-\frac{2}{r}\right)p' + \frac{1}{r}p'_{c(us)}\right]^2}\exp[-\beta(1-S_r)] \quad (4.78)$$

$$\dot{\varepsilon}_s^{\mathrm{p}} = \dot{\lambda}_p \frac{\partial y^*}{\partial \chi_s} = \dot{\lambda}_p \frac{2q}{\left[(1-\alpha)p' + \frac{\alpha}{r}p'_{c(us)}\right]^2 M^2} \quad (4.79)$$

$$-\dot{S}_r^{\mathrm{p}} = \dot{\lambda}_p \frac{\partial y^*}{\partial \chi_h} = \dot{\lambda}_p \frac{2\left(p' - \frac{1}{r}p'_{c(us)}\right)^2}{(s^* - p_b)\left[\left(1-\frac{2}{r}\right)p' + \frac{1}{r}p'_{c(us)}\right]^2}\left[1 - \exp[-\beta(1-S_r)]\right] \quad (4.80)$$

As can be seen in Eqs. (4.78-4.80), the activation and evolution of both plastic deformation and irrecoverable saturation takes place simultaneously, given the same multiplier $\dot{\lambda}_p$, reflecting the

inseparable nature of the hydro-mechanical coupling at the grain scale (Zhang & Lytton, 2009ab; Delage & Graham, 1996; Tang & Graham, 2002). In particular, the inelastic volumetric response (see Eq. (4.78)) and evolution of irrecoverable saturation (see Eq. (4.80)) take into account the coupled hydro-mechanical effects through stresses, volumetric plastic strain, suction and saturation.

The proposed yield surface (see Figures 4.4 & 4.5) is identical with the Modified Cam-Clay (MCC; see Collins, 2003) model for $r = 2$ and $\alpha = 1$ under saturated condition ($s^* = 0$ and $S_r = 1$), allowing a smooth transition between saturated and partially saturated conditions. The shape of the yield locus reflects the experimental observations of suction-controlled or water content-controlled tests for partially saturated soils: (i) tear-drop shape of the yield surface (see Figures 4.4b & 4.5b); (ii) increasing effective yield pressure with modified suction (see Figures 4.4c & 4.5c), and (iii) apparent cohesion thanks to $S_r s$ (Jommi, 2000).

Furthermore, it can be said that outstanding features of volumetric response are addressed by the evolution rules in a comprehensive manner, taking into account all physics of dilation and contraction under the effect of capillarity. In accordance with principles of critical state soil models, the geometric interactions among stress paths, critical state line and initial yield curve in the p': q plane help the current model identify whether the geomaterials are dilative or contractive. For example, according to Eq. (4.78), with $p' < \frac{1}{r} p'_{c(us)}$ in relation to shear tests of dense soils and relatively high confining stresses, the phenomenon of dilatancy is triggered when the stress path meets the critical state line before it intersects the initial yield loci. Such geometric interactions rely significantly on saturation degree and suction in partially saturated soils, meaning the dependence of dilatancy on SWCC can be effectively generated by this model. On the other hand, this model can deal with mechanisms of hydraulic irreversibility through the evolution rule of irrecoverable saturation degree in Eq. (4.80) where p' and $p'_{c(us)}$ have certain contributions.

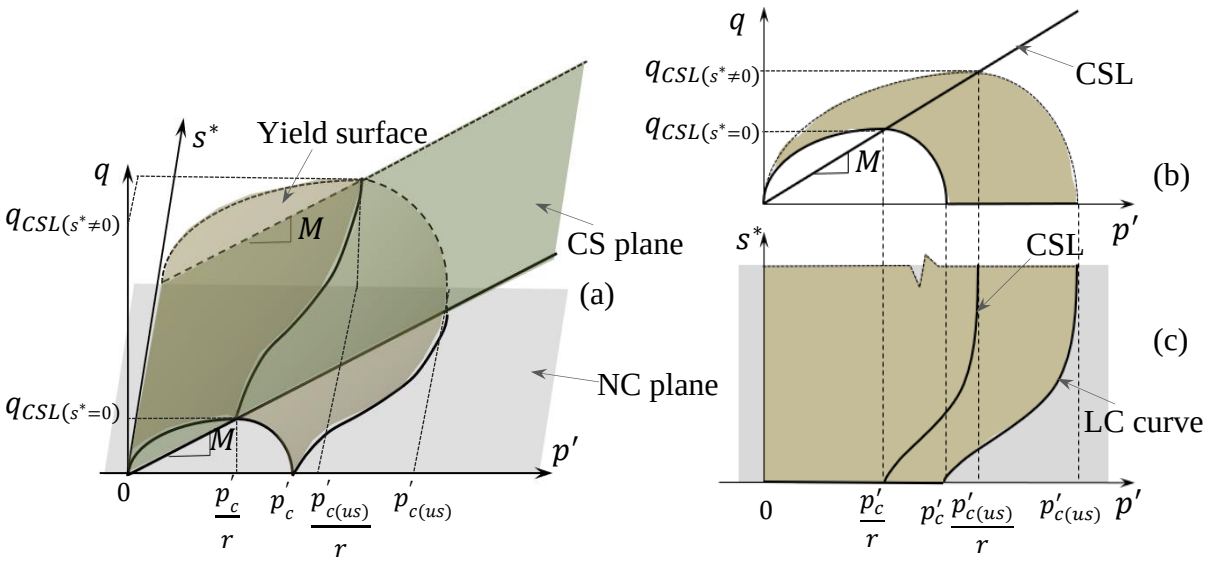

Figure 4.4. Yield surface (a) in (p', q, s^*) space; (b) front view (c) top view

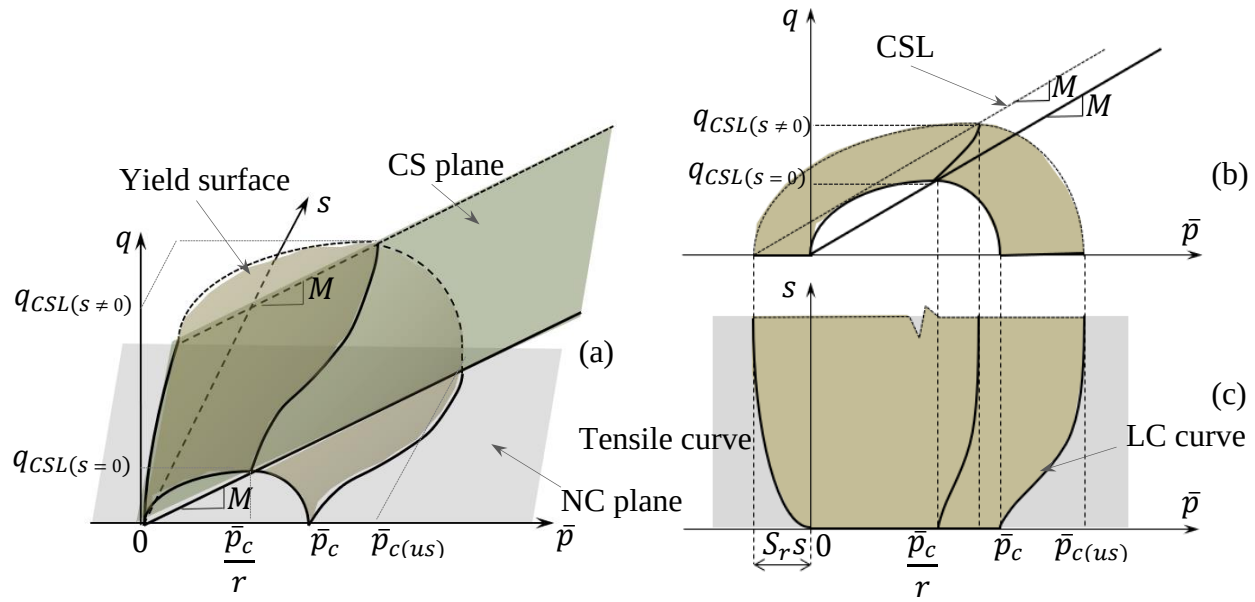

Figure 4.5. Yield surface (a) in $(\bar{p}, q, s)$ space; (b) front view (c) top view

The above-mentioned features make the proposed approach different from other critical-state-based models for partially saturated soils. For example, a comparison between the proposed model and BBM (Alonso et al., 1990) is carried out regarding the model description. This comparison is briefly summarized in Table 4.1. As can be seen, the differences between them are pointed out based on different criteria (i) Methodology (ii) SWCC (iii) Stress-like variables (iv) Strain-like variables (v) Cohesion (vi) Yield surface (vii) Flow rules (viii) Hardening law.

Table 4.1. Comparison of the model description between the present model and BBM.

Barcelona Basic Model (BBM) (see Table 4.2 for further details)	**Present model**
(i) Methodology	
Conventional elastoplastic approach	Thermodynamic-based approach
(ii) SWCC (wetting/drying difference, volume-dependent SWCC)	
No	Yes
(iii) Stress-like variables	
Net stress: $\bar{\sigma}_{ij}$ ($\bar{p}$ and q) Suction: s	Effective stress: σ'_{ij} ($p'$and q) Modified suction: s^*
(iv) Strain-like variables	
Strain: ε_{ij}	Strain: ε_{ij} Saturation degree: S_r
(v) Cohesion	
$k_s s$	$S_r s$
(vi) Yield surface	
$y_{(LC)} = q^2 - M^2(\bar{p} + k_s s)\left(\bar{p}_{c(us)} - \bar{p}\right) \leq 0$ $y_{(SI)} = s - s_c \leq 0$	$y = \frac{\left(p' - \frac{1}{r}p'_{c(us)}\right)^2}{\left[\left(1-\frac{2}{r}\right)p' + \frac{1}{r}p'_{c(us)}\right]^2} + \frac{q^2}{\left[(1-\alpha)p' + \frac{\alpha}{r}p'_{c(us)}\right]^2 M^2} - 1 \leq 0$
(vii) Flow rules	
$\dot{\varepsilon}_v^{\mathrm{p}} = \dot{\varepsilon}_{v(LC)}^{\mathrm{p}} + \dot{\varepsilon}_{v(SI)}^{\mathrm{p}} = \dot{\lambda}_{p(LC)} M^2\left(2\bar{p} + k_s s - \bar{p}_{c(us)}\right) + \dot{\lambda}_{p(SI)}$ $\dot{\varepsilon}_s^{\mathrm{p}} = \dot{\lambda}_{p(LC)} 2\gamma q$	$\dot{\varepsilon}_v^{\mathrm{p}} = \dot{\lambda}_p \frac{\partial y^*}{\partial \chi_v} = \dot{\lambda}_p \frac{2\left(p' - \frac{1}{r}p'_{c(us)}\right)}{\left[\left(1-\frac{2}{r}\right)p' + \frac{1}{r}p'_{c(us)}\right]^2} \exp[-\beta(1 - S_r)]$ $\dot{\varepsilon}_s^{\mathrm{p}} = \dot{\lambda}_p \frac{\partial y^*}{\partial \chi_s} = \dot{\lambda}_p \frac{2q}{\left[(1-\alpha)p' + \frac{\alpha}{r}p'_{c(us)}\right]^2 M^2}$ $-\dot{S}_r^{\mathrm{p}} = \dot{\lambda}_p \frac{\partial y^*}{\partial \chi_h} = \dot{\lambda}_p \frac{2\left(p' - \frac{1}{r}p'_{c(us)}\right)^2}{(s^* - p_b)\left[\left(1-\frac{2}{r}\right)p' + \frac{1}{r}p'_{c(us)}\right]^2} \left[1 - \exp[-\beta(1 - S_r)]\right]$
(viii) Hardening law	

$\bar{p}_{c(us)} = \bar{p}_R \left[\frac{\bar{p}_{co} \exp\left(\frac{v\varepsilon_{v(LC)}^{p}}{\bar{\lambda}-\bar{\kappa}} \right)}{\bar{p}_R} \right]^{\frac{\bar{\lambda}-\bar{\kappa}}{\bar{\lambda}[(1-\bar{\xi})\exp(-\bar{\mu}s)+\bar{\xi}]-\bar{\kappa}}}$	$p'_{c(us)} = p'_R \left[\frac{p'_{c0} \exp\left(\frac{\varepsilon_v^{p}}{\lambda-\kappa} \right)}{p'_R} \right]^{\frac{\lambda-\kappa}{\lambda[(1-\xi)\exp(-\mu s^*)+\xi]-\kappa}}$
$s_c = (s_{c0} + p_{at}) \exp\left(\frac{v\varepsilon_{v(SI)}^{p}}{\lambda_s-\kappa_s} \right) - p_{at}$	

Table 4.2. Definitions of parameters and variables of BBM (Alonso et al., 1990).

k_s	constant controlling the apparent cohesion
$\bar{\kappa}$	the slope of URL in the v: ln$\bar{p}$ plane for saturated conditions
$\bar{\lambda}$	the slope of NCL in the v: ln$\bar{p}$ plane for saturated conditions
κ_s	elastic stiffness parameter for changes in suction
λ_s	stiffness parameter for changes in suction for virgin states of the soil
γ	parameter controlling the non-associated flow rule
$\bar{\mu}$	parameter controlling the change of soil stiffness with suction
$\bar{\xi}$	parameter controlling the maximum soil stiffness
$\bar{p}_R$	parameter controlling the yield curve
p_{at}	atmospheric pressure
$\bar{p}_{c(us)}$	the yield pressure under isotropic compression at the partially saturated condition
$\bar{p}_{c0}$	the initial yield pressure under isotropic compression at the fully saturated condition
s_c	hardening parameter of the suction increase yield locus
s_{c0}	the initial hardening parameter of the suction increase yield locus
$y_{(LC)}$	Loading-Collapse yield surface
$y_{(SI)}$	Suction-Increase yield surface
$\varepsilon_{v(LC)}^{p}$	plastic volumetric strain associated with the Loading-Collapse yield surface
$\varepsilon_{v(SI)}^{p}$	plastic volumetric strain associated with the Suction-Increase yield surface
$\dot{\lambda}_{p(LC)}$	the non-negative plasticity-like multiplier of the Loading-Collapse yield surface
$\dot{\lambda}_{p(SI)}$	the non-negative plasticity-like multiplier of the Suction-Increase yield surface

As can be seen in the table above, the proposed model has a few notable advances compared to the BBM (i) Thermomechanical rigour (ii) A single yield surface (iii) Saturation degree (iv) inherent SWCC as an integral part of the model (v) Fully coupled hydro-mechanical response taking into account the volume-dependent SWCC (vi) Non-linear increase in cohesion with $S_r s$ (vii)

wetting/drying difference. These features are associated with some main distinctions between the two in terms of parameters as follows: (i) In hardening laws of the current model, parameters κ, λ, p_R' , μ and ξ are used for effective stress and modified suction. Therefore, their effects on responses of the proposed model are different from those of the BBM. (ii) r and α are adopted in the present model to provide a more extensive/flexible yielding behaviour in comparison with the BBM. In particular, they allow constructing the tear-drop shape of the yield surface to mimic a wide variety of experimentally observed initial shear yield surface. (iii) In the BBM, parameter k_s is used to describe the linear increase in cohesion with suction. Instead, the term $S_r s$ in Bishop's effective stress is to describe the non-linear relationship between cohesion and suction in the current model. (iv) Additional parameters κ_h, β and p_b for SWCC are needed for this model, which cannot be found in the BBM. With the above-mentioned advances, the present model yields better predictions of the ε_s: q and ε_s: ε_v responses in suction-controlled triaxial shearing test on Speswhite Kaolin at $s = 200$ kPa and $\bar{\sigma}_{33} = 75$ kPa (Raveendiraraj, 2009), as compared to the BBM (see Figure 4.6). Additionally, Figure 4.6b demonstrates the ability of the proposed approach to capture the increase in saturation degree during shearing, which cannot be predicted by the BBM. Nevertheless, the limitation associated with an abrupt change in the stress-strain curve (see Figure 4.6a) is acknowledged. It is noted that the conventional approach of the stress return algorithm is adopted in the current work for the purpose of describing the predictive capacity of the proposed model. This limitation can be addressed in my future works using the sub-loading surface approach (Salomoni & Fincato, 2012) to reproduce the smooth transition between elastic to plastic regimes.

To further highlight the advanced features of the current model, in future works, it can be compared to performances of more recently developed models for partially saturated soils such as Wheeler et al. (2003), Khalili et al. (2008), Sheng et al. (2008).

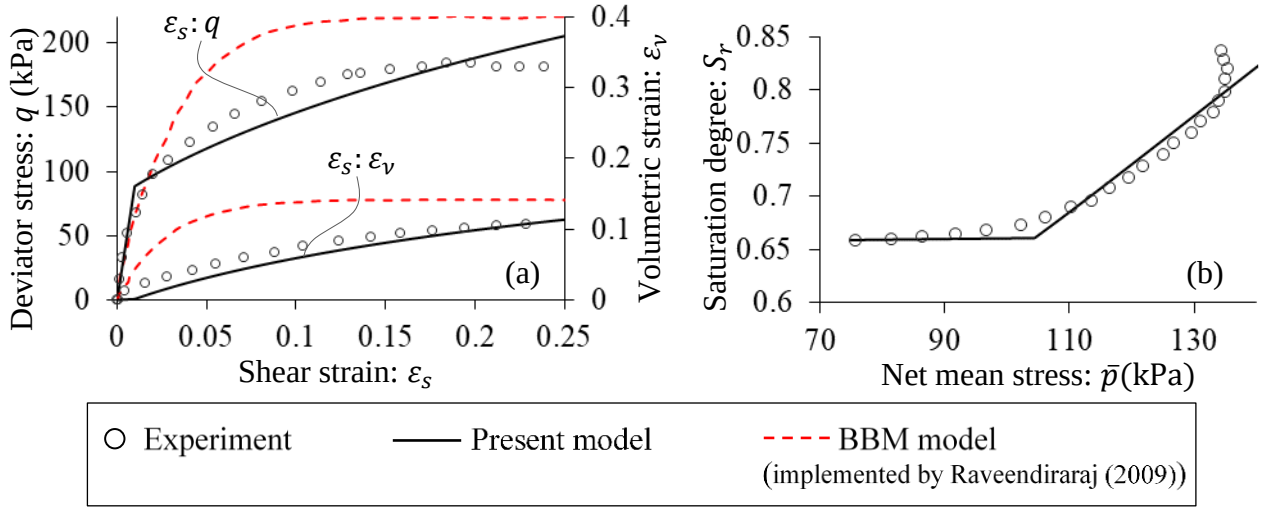

Figure 4.6. Drained triaxial compression tests on Speswhite Kaolin at $s = 200\ kPa$ and $\bar{\sigma}_{33} = 75\ kPa$ (after Raveendiraraj, 2009) (a) $\varepsilon_s - q$, $\varepsilon_s - \varepsilon_v$ (b) $\bar{p} - S_r$; $\kappa = 0.01$; $\lambda = 0.3$; $M = 0.889$; $G = 3000\ kPa$; $\kappa_h = 0.75$; $p'_R = 120\ kPa$; $\mu = 0.06\ kPa^{-1}$; $\xi = 0.6$; $p'_{c0} = 200\ kPa$; $r = 2.5$; $\alpha = 0.7$; $\beta = 0.005$; $p_b = 70\ kPa$

On the other hand, thanks to the use of the systematic thermomechanical approach, the proposed model has a well-defined structure with a small number of parameters (13 parameters). To highlight this advantage, a comparison of the number of parameters in existing coupled hydro-mechanical models for partially saturated soils is shown in the following table.

Table 4.3. Comparison of the number of parameters in existing coupled hydro-mechanical models.

Model	Number of parameters
Khalili et al. (2008) "A fully coupled flow deformation model for cyclic analysis of unsaturated soils including hydraulic and mechanical hysteresis."	17
Hu et al. (2015) "A coupled stress-strain and hydraulic hysteresis model for unsaturated soils: Thermodynamic analysis and model evaluation."	16
Liu & Muraleetharan (2011) "Coupled Hydro-Mechanical Elastoplastic Constitutive Model for Unsaturated Sands and Silts"	32
Ghasemzadeh et al. (2017) "Elastoplastic model for hydro-mechanical behaviour of unsaturated soils."	18

Gholizadeh & Latifi (2018) "A coupled hydro-mechanical constitutive model for unsaturated frictional and cohesive soil."	21
Sun & Sun (2012) "Coupled modelling of hydro-mechanical behaviour of unsaturated compacted expansive soils."	13
Muraleetharan et al. (2009) "An elastoplastic framework for coupling hydraulic and mechanical behaviour of unsaturated soils."	12 (isotropic behaviour only)
Bruno & Gallipoli (2019) "A coupled hydromechanical bounding surface model predicting the hysteretic behaviour of unsaturated soils."	12 (isotropic behaviour only)

However, for the sake of simplicity, it is assumed that the partially saturated soil behaves isotropically in both cases of recoverable and irrecoverable deformation/saturation, although the behaviour of wet granular materials can be anisotropic because of highly inhomogeneous textures due to the effects of liquid bridges. It is also acknowledged that the proposed model can still be improved to capture the transition between fully and partially saturated states with the effects of air-entry suction (Sheng, 2011; Sheng et al., 2008; Khalili et al., 2008; Loret & Khalili, 2000; 2002), to have closed-shape yield surface (Thu et al., 2007b; Sivakumars & Doran, 2000; Delage & Graham, 1996; Tang & Graham, 2002), to predict yielding behaviour of more complex experimental loading paths (Loret & Khalili, 2000; 2002), and to simulate NCL with pressurized saturation and the transition to full-void closure at high stresses (Mun & McCartney, 2015; 2017; Zhou et al., 2018). Furthermore, with some sets of parameters, the convexity of the LC loading surface is not assured. It is not a physical matter since the thermodynamic admissibility in this framework is always guaranteed. Nonetheless, this issue should be avoided if possible during calibration to minimise numerical errors in implementations. In order to sidestep these problems, a general approach should be focused on the enhancement of Helmholtz free energy and dissipation potentials, taking into account relevant physical features drawn from experimental observations.

4.2.3. Dissipation properties

Based on the review in Chapter 2, it is found that full coupling between plasticity and hydraulic irreversibility and their associated hydro-mechanical dissipation properties are usually not explored at length in previous thermodynamics-based approaches. In other words, the investigation of the bi-directional hydro-mechanical dissipation properties (positiveness) is essential yet often overlooked or inadequate in such models. That is responsible for uncertain details on the thermodynamic admissibility and full coupling between plasticity and hydraulic irreversibility. Therefore, studying

the dissipation properties of the proposed model in this section is essential and significant, distinguishing it from others in the literature.

Using Eq. (3.106) and Eqs. (4.78-4.80), the dissipations due to plastic volumetric deformation, plastic shear deformation and irrecoverable saturation can be expressed as:

$$\widetilde{\Phi}_v = \chi_v \dot{\varepsilon}_v^{\mathrm{p}} = p' \dot{\varepsilon}_v^{\mathrm{p}} = \dot{\lambda}_p \frac{2p'\left(p' - \frac{1}{r}p'_{c(us)}\right)}{\left[\left(1-\frac{2}{r}\right)p' + \frac{1}{r}p'_{c(us)}\right]^2} \exp[-\beta(1-S_r)] \tag{4.81}$$

$$\widetilde{\Phi}_s = \chi_s \dot{\varepsilon}_s^{\mathrm{p}} = q \dot{\varepsilon}_s^{\mathrm{p}} = \dot{\lambda}_p \frac{2q^2}{\left[(1-\alpha)p' + \frac{\alpha}{r}p'_{c(us)}\right]^2 M^2} \tag{4.82}$$

$$\widetilde{\Phi}_h = \chi_h\left(-\dot{S}_r^{\mathrm{p}}\right) = (s^* - p_b)\left(-\dot{S}_r^{\mathrm{p}}\right) = \dot{\lambda}_p \frac{2\left(p' - \frac{1}{r}p'_{c(us)}\right)^2}{\left[\left(1-\frac{2}{r}\right)p' + \frac{1}{r}p'_{c(us)}\right]^2} \{1 - \exp[-\beta(1-S_r)]\} \tag{4.83}$$

Utilising Eq. (4.77) and Eqs. (4.81-4.83) allows expressing Eq. (3.106) in the following form:

$$\widetilde{\Phi} = \widetilde{\Phi}_v + \widetilde{\Phi}_s + \widetilde{\Phi}_h = 2\dot{\lambda}_p \left\{1 + \frac{\frac{1}{r}p'_{c(us)}\left(p' - \frac{1}{r}p'_{c(us)}\right)}{\left[\left(1-\frac{2}{r}\right)p' + \frac{1}{r}p'_{c(us)}\right]^2} \exp[-\beta(1-S_r)]\right\} \tag{4.84}$$

Since $\exp[-\beta(1-S_r)] \leq 1$, the following relation can be written:

$$\widetilde{\Phi} \geq 2\dot{\lambda}_p \left\{\frac{\left[\left(1-\frac{2}{r}\right)p'\right]^2 + \left(3-\frac{4}{r}\right)\frac{1}{r}p'p'_{c(us)}}{\left[\left(1-\frac{2}{r}\right)p' + \frac{1}{r}p'_{c(us)}\right]^2}\right\} \exp[-\beta(1-S_r)] \tag{4.85}$$

Given $r \geq 1.5$, the numerator of the bracketed expression in Eq. (4.85) is always positive, and hence the positiveness of the total dissipation is always guaranteed. However, due to dilation, $\widetilde{\Phi}_v$ can admit negative values, while $\widetilde{\Phi}_s$ and $\widetilde{\Phi}_h$ are always positive. From Eqs. (4.81-4.85), the dissipation ratios $\mathrm{R}_v, \mathrm{R}_s, \mathrm{R}_h$ between $\widetilde{\Phi}_v, \widetilde{\Phi}_s, \widetilde{\Phi}_h$ and $\widetilde{\Phi}$ can be expressed as:

$$\mathrm{R}_v = \frac{\widetilde{\Phi}_v}{\widetilde{\Phi}} = \frac{p'\left(p' - \frac{1}{r}p'_{c(us)}\right)\exp[-\beta(1-S_r)]}{\left[\left(1-\frac{2}{r}\right)p' + \frac{1}{r}p'_{c(us)}\right]^2 + \frac{1}{r}p'_{c(us)}\left(p' - \frac{1}{r}p'_{c(us)}\right)\exp[-\beta(1-S_r)]} \tag{4.86}$$

$$\mathrm{R}_s = \frac{\widetilde{\Phi}_s}{\widetilde{\Phi}} = \frac{\left[\left(1-\frac{2}{r}\right)p' + \frac{1}{r}p'_{c(us)}\right]^2 - \left(p' - \frac{1}{r}p'_{c(us)}\right)^2}{\left[\left(1-\frac{2}{r}\right)p' + \frac{1}{r}p'_{c(us)}\right]^2 + \frac{1}{r}p'_{c(us)}\left(p' - \frac{1}{r}p'_{c(us)}\right)\exp[-\beta(1-S_r)]} \tag{4.87}$$

$$\mathrm{R}_h = \frac{\widetilde{\Phi}_h}{\widetilde{\Phi}} = \frac{\left(p' - \frac{1}{r}p'_{c(us)}\right)^2[1-\exp[-\beta(1-S_r)]]}{\left[\left(1-\frac{2}{r}\right)p' + \frac{1}{r}p'_{c(us)}\right]^2 + \frac{1}{r}p'_{c(us)}\left(p' - \frac{1}{r}p'_{c(us)}\right)\exp[-\beta(1-S_r)]} \tag{4.88}$$

For $S_r = 1$, $\mathrm{R}_h = 0$ indicates purely mechanical dissipation under saturated condition. At the critical state where $p' = p'_{c(us)}/r$, volumetric and hydraulic energy dissipations totally vanish, reflecting the fact that the total energy dissipation is fully governed by only the sliding of soil grains. These dissipation properties will be further illustrated using experimental data later in Section 4.5.3.

4.3. Numerical implementation

A specific numerical implementation algorithm of the proposed model is briefly presented in this section, following the generic formulations in Section 3.3.2 and 3.3.3 of Chapter 3. For implementation purpose, the model descriptions can be summarised and rewritten in tensorial form as follows.

The stress-strain and suction-saturation relationships:

$$p' = p'_0 \exp\left[\frac{(\varepsilon_v - \varepsilon_v^{\mathrm{p}})}{\kappa}\right] \tag{4.89}$$

$$q = 3G\left(\varepsilon_s - \varepsilon_s^{\mathrm{p}}\right) \tag{4.90}$$

$$s^* = (p_u + s_0^*) \exp\left\{\frac{S_{r0} + [(-S_r) - (-S_r^{\mathrm{p}})]}{\kappa_h}\right\} - p_u \tag{4.91}$$

The yield function and evolution rules:

$$y = \frac{\left(p' - \frac{1}{r}p'_{c(us)}\right)^2}{\left[\left(1-\frac{2}{r}\right)p' + \frac{1}{r}p'_{c(us)}\right]^2} + \frac{q^2}{\left[(1-\alpha)p' + \frac{\alpha}{r}p'_{c(us)}\right]^2 M^2} - 1 \leq 0 \tag{4.92}$$

$$\dot{\varepsilon}_{ij}^{\mathrm{p}} = \dot{\lambda}_p \frac{\partial y^*}{\partial \chi_{ij}} = \dot{\lambda}_p \left(\frac{\partial y^*}{\partial \chi_v}\frac{\partial \chi_v}{\partial \chi_{ij}} + \frac{\partial y^*}{\partial \chi_s}\frac{\partial \chi_s}{\partial \chi_{ij}}\right) \tag{4.93}$$

$$-\dot{S}_r^{\mathrm{p}} = \dot{\lambda}_p \frac{\partial y^*}{\partial \chi_h} = \dot{\lambda}_p \frac{2\left(p' - \frac{1}{r}p'_{c(us)}\right)^2}{(s^* - p_b)\left[\left(1-\frac{2}{r}\right)p' + \frac{1}{r}p'_{c(us)}\right]^2}\left[1 - \exp[-\beta(1 - S_r)]\right] \tag{4.94}$$

where $p'_{c(us)}$ has been defined in Eqs. (4.21-4.23), and $\chi_v = p'$, $\chi_s = q$, $\chi_h = s^* - p_b$, and $\frac{\partial y^*}{\partial \chi_v}$ and $\frac{\partial y^*}{\partial \chi_s}$ are in Eqs. (4.78-4.79).

4.3.1. Coupled hydro-mechanical tangent stiffness tensor

The incremental forms of the effective stress tensor $\dot{\sigma}'_{ij}$ and modified suction $\dot{s}^*$ can be derived from Eqs. (4.89-4.91) as follows:

$$\dot{\sigma}'_{ij} = D^e_{ijkl}\left(\dot{\varepsilon}_{kl} - \dot{\varepsilon}_{kl}^{\mathrm{p}}\right) = \left[\left(\frac{p'}{\kappa} - \frac{2}{3}G\right)\delta_{ij}\delta_{kl} + G\left(\delta_{ik}\delta_{jl} + \delta_{il}\delta_{jk}\right)\right]\left(\dot{\varepsilon}_{kl} - \dot{\varepsilon}_{kl}^{\mathrm{p}}\right) \tag{4.95}$$

$$\dot{s}^* = \frac{(s^* + p_u)}{\kappa_h}\left[\left(-\dot{S}_r\right) - \left(-\dot{S}_r^{\mathrm{p}}\right)\right] \tag{4.96}$$

where $\varepsilon_{kl}^{\mathrm{p}}$ is the plastic strain tensor and $D^e_{ijkl} = \left(\frac{p'}{\kappa} - \frac{2}{3}G\right)\delta_{ij}\delta_{kl} + G\left(\delta_{ik}\delta_{jl} + \delta_{il}\delta_{jk}\right)$ is the pressure-dependent elastic stiffness tensor.

The consistency condition of the yield function in Eq. (4.92) is written as:

$$\dot{y} = \frac{\partial y}{\partial \sigma'_{ij}}\dot{\sigma}'_{ij} + \frac{\partial y}{\partial p'_{c(us)}}\dot{p}'_{c(us)} = \frac{\partial y}{\partial \sigma'_{ij}}\dot{\sigma}'_{ij} + \frac{\partial y}{\partial p'_{c(us)}}\frac{\partial p'_{c(us)}}{\partial s^*}\dot{s}^* + \frac{\partial y}{\partial p'_{c(us)}}\frac{\partial p'_{c(us)}}{\partial p'_c}\frac{\partial p'_c}{\partial \varepsilon_v^{\mathrm{p}}}\dot{\varepsilon}_v^{\mathrm{p}} = 0 \tag{4.97}$$

where explicit forms of $\frac{\partial y}{\partial \sigma'_{ij}}$, $\frac{\partial y}{\partial p'_{c(us)}}$, $\frac{\partial p'_{c(us)}}{\partial p'_c}$ and $\frac{\partial p'_{c(us)}}{\partial s^*}$ are detailed as follows.

The derivatives of the yield function in Eq. (4.92) with respect to effective stress takes the following explicit form:

$$\frac{\partial y}{\partial \sigma'_{ij}} = \frac{\partial y}{\partial p'}\frac{\partial p'}{\partial \sigma'_{ij}} + \frac{\partial y}{\partial q}\frac{\partial q}{\partial \sigma'_{ij}} \tag{4.98}$$

in which

$$\frac{\partial y}{\partial p'} = \frac{2\left(p' - \frac{1}{r}p'_{c(us)}\right)}{\left[\left(1-\frac{2}{r}\right)p' + \frac{1}{r}p'_{c(us)}\right]^2} - \frac{2\left(1-\frac{2}{r}\right)\left(p' - \frac{1}{r}p'_{c(us)}\right)^2}{\left[\left(1-\frac{2}{r}\right)p' + \frac{1}{r}p'_{c(us)}\right]^3} - \frac{2(1-\alpha)q^2}{\left[(1-\alpha)p' + \frac{\alpha}{r}p'_{c(us)}\right]^3 M^2} \tag{4.99}$$

$$\frac{\partial y}{\partial q} = \frac{2q}{\left[(1-\alpha)p' + \frac{\alpha}{r}p'_{c(us)}\right]^2 M^2} \tag{4.100}$$

$\frac{\partial y}{\partial p'_{c(us)}}$ is written as follows:

$$\frac{\partial y}{\partial p'_{c(us)}} = \frac{2\left(-\frac{1}{r}\right)\left(p' - \frac{1}{r}p'_{c(us)}\right)}{\left[\left(1-\frac{2}{r}\right)p' + \frac{1}{r}p'_{c(us)}\right]^2} - \frac{2\left(\frac{1}{r}\right)\left(p' - \frac{1}{r}p'_{c(us)}\right)^2}{\left[\left(1-\frac{2}{r}\right)p' + \frac{1}{r}p'_{c(us)}\right]^3} - \frac{2\left(\frac{\alpha}{r}\right)q^2}{\left[(1-\alpha)p' + \frac{\alpha}{r}p'_{c(us)}\right]^3 M^2} \tag{4.101}$$

From Eqs. (4.21-4.23), the derivative of $p'_{c(us)}$ with respect to p'_c and s^* are expressed as:

$$\frac{\partial p'_{c(us)}}{\partial p'_c} = \left[\frac{\lambda-\kappa}{\lambda\left((1-\xi)\exp(-\mu s^*)+\xi\right)-\kappa}\right]\left(\frac{p'_c}{p'_R}\right)^{\frac{\lambda-\lambda\left((1-\xi)\exp(-\mu s^*)+\xi\right)}{\lambda\left((1-\xi)\exp(-\mu s^*)+\xi\right)-\kappa}} \tag{4.102}$$

$$\frac{\partial p'_{c(us)}}{\partial s^*} = p'_R\left(\frac{p'_c}{p'_R}\right)^{\frac{\lambda-\kappa}{\lambda\left((1-\xi)\exp(-\mu s^*)+\xi\right)-\kappa}} \ln\left(\frac{p'_c}{p'_R}\right)\frac{(\lambda-\kappa)\lambda(1-\xi)\mu\exp(-\mu s^*)}{\left[\lambda\left((1-\xi)\exp(-\mu s^*)+\xi\right)-\kappa\right]^2} \tag{4.103}$$

From Eqs. (4.93-4.97), the incremental coupled hydro-mechanical relationships can be obtained as follows:

$$\dot{\sigma}'_{ij} = D^e_{ijkl}\left\{\dot{\varepsilon}_{kl} - \left[M_{kl}\dot{\varepsilon}_{kl} + H\left(-\dot{S}_r\right)\right]\frac{\partial y^*}{\partial \chi_{kl}}\right\} \tag{4.104}$$

$$\dot{s}^* = \frac{(s^*+p_u)}{\kappa_h}\left\{\left(-\dot{S}_r\right) - \left[M_{kl}\dot{\varepsilon}_{kl} + H\left(-\dot{S}_r\right)\right]\frac{\partial y^*}{\partial \chi_h}\right\} \tag{4.105}$$

where

$$M_{kl} = \frac{D^e_{ijkl}\frac{\partial y}{\partial \sigma'_{ij}}}{\left(\frac{\partial y}{\partial \sigma'_{ij}}\right)^T D^e_{ijkl}\frac{\partial y^*}{\partial \chi_{kl}} + \frac{\partial y}{\partial p'_{c(us)}}\frac{\partial p'_{c(us)}}{\partial s^*}\frac{(s^*+p_u)}{\kappa_h}\frac{\partial y^*}{\partial \chi_h} - \frac{\partial y}{\partial p'_{c(us)}}\frac{\partial p'_{c(us)}}{\partial p'_c}\frac{p'_c}{(\lambda-\kappa)}\frac{\partial y^*}{\partial \chi_v}} \tag{4.106}$$

$$H = \frac{\frac{(s^*+p_u)}{\kappa_h}\frac{\partial y}{\partial p'_{c(us)}}\frac{\partial p'_{c(us)}}{\partial s^*}}{\left(\frac{\partial y}{\partial \sigma'_{ij}}\right)^T D^e_{ijkl}\frac{\partial y^*}{\partial \chi_{kl}} + \frac{\partial y}{\partial p'_{c(us)}}\frac{\partial p'_{c(us)}}{\partial s^*}\frac{(s^*+p_u)}{\kappa_h}\frac{\partial y^*}{\partial \chi_h} - \frac{\partial y}{\partial p'_{c(us)}}\frac{\partial p'_{c(us)}}{\partial p'_c}\frac{p'_c}{(\lambda-\kappa)}\frac{\partial y^*}{\partial \chi_v}} \tag{4.107}$$

Eqs. (4.104-4.105) can be rewritten as:

$$\dot{\sigma}'_{ij} = \left[D^e_{ijkl}\left(1 - M_{kl}\frac{\partial y^*}{\partial \chi_{kl}}\right)\right]\dot{\varepsilon}_{kl} + \left(-D^e_{ijkl}H\frac{\partial y^*}{\partial \chi_{kl}}\right)\left(-\dot{S}_r\right) = \Lambda_{ijkl}\dot{\varepsilon}_{kl} + \Pi_{ij}\left(-\dot{S}_r\right) \tag{4.108}$$

$$\dot{s}^* = \left[-\frac{(s^*+p_u)}{\kappa_h}\frac{\partial y^*}{\partial \chi_h}M_{kl}\right]\dot{\varepsilon}_{kl} + \left[\frac{(s^*+p_u)}{\kappa_h}\left(1 - H\frac{\partial y^*}{\partial \chi_h}\right)\right]\left(-\dot{S}_r\right) = \Omega_{kl}\,\dot{\varepsilon}_{kl} + \Upsilon\left(-\dot{S}_r\right) \tag{4.109}$$

in which

$$\Lambda_{ijkl} = D^e_{ijkl}\left(1 - M_{kl}\frac{\partial y^*}{\partial \chi_{kl}}\right) \tag{4.110}$$

$$\Pi_{ij} = -D^e_{ijkl}H\frac{\partial y^*}{\partial \chi_{kl}} \tag{4.111}$$

$$\Omega_{kl} = -\frac{(s^*+p_u)}{\kappa_h}\frac{\partial y^*}{\partial \chi_h}M_{kl} \tag{4.112}$$

$$\Upsilon = \frac{(s^*+p_u)}{\kappa_h}\left(1 - H\frac{\partial y^*}{\partial \chi_h}\right) \tag{4.113}$$

Alternatively, the above incremental coupled hydro-mechanical relationships in Eqs. (4.108-4.109) can also be expressed in terms of net stress $\bar{\sigma}_{ij}$ and suction s. To do that, the constitutive relationships Eqs. (4.95-4.96) can be rewritten using Bishop's effective stress ($\sigma'_{ij} = \bar{\sigma}_{ij} + S_r s\delta_{ij}$) and modified suction ($s^* = s\bar{\phi}$), as:

$$\dot{\bar{\sigma}}_{ij} = \dot{\sigma}'_{ij} - s\dot{S}_r\delta_{ij} - S_r\dot{s}\delta_{ij} \tag{4.114}$$

$$\dot{s} = \frac{1}{\bar{\phi}}\left(\dot{s}^* - s\dot{\bar{\phi}}\right) = \frac{1}{\bar{\phi}}\left(\dot{s}^* + s\delta_{kl}\dot{\varepsilon}_{kl}\right) \tag{4.115}$$

Substituting Eqs. (4.108-4.109) in the above equations, $\dot{\bar{\sigma}}_{ij}$ and $\dot{s}$ can be obtained as:

$$\dot{\bar{\sigma}}_{ij} = \left[\Lambda_{ijkl} - \frac{S_r\delta_{ij}\left(\bar{\Omega}_{kl}+s\delta_{kl}\right)}{\bar{\phi}}\right]\dot{\varepsilon}_{kl} + \left[\Pi_{ij} + \left(s - \frac{S_r\Upsilon}{\bar{\phi}}\right)\delta_{ij}\right]\left(-\dot{S}_r\right) = \bar{\Lambda}_{ijkl}\dot{\varepsilon}_{kl} + \bar{\Pi}_{ij}\left(-\dot{S}_r\right) \tag{4.116}$$

$$\dot{s} = \left[\frac{(\Omega_{kl}+s\delta_{kl})}{\bar{\phi}}\right]\dot{\varepsilon}_{kl} + \left(\frac{\Upsilon}{\bar{\phi}}\right)\left(-\dot{S}_r\right) = \bar{\Omega}_{kl}\,\dot{\varepsilon}_{kl} + \bar{\Upsilon}\left(-\dot{S}_r\right) \tag{4.117}$$

with $\bar{\Lambda}_{ijkl} = \Lambda_{ijkl} - \frac{S_r\delta_{ij}\left(\bar{\Omega}_{kl}+s\delta_{kl}\right)}{\bar{\phi}}$; $\bar{\Pi}_{ij} = \Pi_{ij} + \left(s - \frac{S_r\Upsilon}{\bar{\phi}}\right)\delta_{ij}$; $\bar{\Omega}_{kl} = \frac{(\Omega_{kl}+s\delta_{kl})}{\bar{\phi}}$ and $\bar{\Upsilon} = \frac{\Upsilon}{\bar{\phi}}$ expressed in terms of net stress $\bar{\sigma}_{ij}$ and suction s.

4.3.2. Semi-implicit stress return algorithm

The increments of trial effective stress $\left(\sigma_{ij}^{\prime\mathrm{trial}}\right)$ and trial modified suction $\left(s^{*\mathrm{trial}}\right)$ can be of the following forms:

$$\Delta\sigma_{ij}^{\prime\mathrm{trial}} = D_{ijkl}^{en}\Delta\varepsilon_{kl} \tag{4.118}$$

$$\Delta s^{*\mathrm{trial}} = \frac{(s^{*n}+p_u)}{\kappa_h}(-\Delta S_r) \tag{4.119}$$

in which the D_{ijkl}^{en} denotes secant elastic stiffness evaluated at state n.

In the yielding regime ($y^{\mathrm{trial}}\left(\sigma_{ij}^{\prime\mathrm{trial}}, s^{*\mathrm{trial}}, p_c^{\prime}\right) > 0$), the first-order Taylor expansion of the yield function at a trial point is written as follows:

$$y^{\mathrm{new}} = y^{\mathrm{trial}} + \Delta\sigma_{ij}^{\prime\mathrm{corrt}}\frac{\partial y}{\partial\sigma_{ij}^{\prime}}\Big|^{\mathrm{trial}} + \Delta s^{*\mathrm{corrt}}\frac{\partial y}{\partial p_{c(us)}^{\prime}}\frac{\partial p_{c(us)}^{\prime}}{\partial s^{*}}\Big|^{\mathrm{trial}} + \Delta\varepsilon_v^{\mathrm{p}}\frac{p_c^{\prime}}{(\lambda-\kappa)}\frac{\partial y}{\partial p_{c(us)}^{\prime}}\frac{\partial p_{c(us)}^{\prime}}{\partial p_c^{\prime}}\Big|^{\mathrm{trial}} \tag{4.120}$$

Corrective terms to effective stress tensor and modified suction take the following forms:

$$\Delta\sigma_{ij}^{\prime\mathrm{corrt}} = -D_{ijkl}^{en}\Delta\varepsilon_{kl}^{\mathrm{p}} \tag{4.121}$$

$$\Delta s^{*\mathrm{corrt}} = -\frac{(s^{*n}+p_u)}{\kappa_h}\left(-\Delta S_r^{\mathrm{p}}\right) \tag{4.122}$$

Eq. (4.120) can be rewritten using flow rules in Eqs. (4.93-4.94) and the above equations:

$$y^{\mathrm{new}} = y^{\mathrm{trial}} - D_{ijkl}^{en}\Delta\lambda_p\frac{\partial y^{*}}{\partial\chi_{kl}}\frac{\partial y}{\partial\sigma_{ij}^{\prime}}\Big|^{\mathrm{trial}} - \frac{(s^{*n}+p_u)}{\kappa_h}\Delta\lambda_p\frac{\partial y^{*}}{\partial\chi_h}\frac{\partial y}{\partial p_{c(us)}^{\prime}}\frac{\partial p_{c(us)}^{\prime}}{\partial s^{*}}\Big|^{\mathrm{trial}} +$$

$$\frac{p_c^{\prime}}{(\lambda-\kappa)}\Delta\lambda_p\frac{\partial y^{*}}{\partial\chi_v}\frac{\partial y}{\partial p_{c(us)}^{\prime}}\frac{\partial p_{c(us)}^{\prime}}{\partial p_c^{\prime}}\Big|^{\mathrm{trial}} \tag{4.123}$$

The plasticity multiplier $\Delta\lambda_p$ is then obtained by enforcing the yield condition $y^{\mathrm{new}} = 0$ in Eq. (4.123):

$$\Delta\lambda_p = \frac{y^{\mathrm{trial}}}{\left(\frac{\partial y}{\partial\sigma_{ij}^{\prime}}\right)^{T}D_{ijkl}^{en}\frac{\partial y^{*}}{\partial\chi_{kl}}\Big|^{\mathrm{trial}} + \frac{\partial y}{\partial p_{c(us)}^{\prime}}\frac{\partial p_{c(us)}^{\prime}}{\partial s^{*}}\frac{(s^{*n}+p_u)}{\kappa_h}\frac{\partial y^{*}}{\partial\chi_h}\Big|^{\mathrm{trial}} - \frac{\partial y}{\partial p_{c(us)}^{\prime}}\frac{\partial p_{c(us)}^{\prime}}{\partial p_c^{\prime}}\frac{p_c^{\prime}}{(\lambda-\kappa)}\frac{\partial y^{*}}{\partial\chi_v}\Big|^{\mathrm{trial}}} \tag{4.124}$$

which is used to update stress tensor and matric suction through Eqs. (3.153-3.158) in Chapter 3. It is noted that the present investigation is based on infinitesimal strain assumption and focuses on the constitutive behaviour (equivalent to a single integration point). This is the first and essential step in formulating and validating a constitutive model, as has been widely adopted and followed in the literature.

4.3.3. An algorithm for mixed-control loading

An algorithm is developed for mixed-control loading where some components of stress, strain and suction are used to control the loading. An example based on the suction-controlled triaxial test is used to demonstrate the performance of such an algorithm. In this case, net confining pressures and suction are fixed at constant imposed levels of $\bar{\sigma}_{22(\mathrm{i})} = \bar{\sigma}_{33(\mathrm{i})}$ and $s_{(\mathrm{i})}$, respectively. The difference between the imposed and computed quantities can be written as a residual vector as follows:

$$\mathbf{res} = \begin{pmatrix} \bar{\sigma}_{22} \\ \bar{\sigma}_{33} \\ s \end{pmatrix} - \begin{pmatrix} \bar{\sigma}_{22(\mathrm{i})} \\ \bar{\sigma}_{33(\mathrm{i})} \\ s_{(\mathrm{i})} \end{pmatrix} \tag{4.125}$$

Given constant lateral net stress and constant suction imposed, the first-order Taylor expansion of the residual in Eq. (4.125) at the previous state is:

$$\mathbf{res}^{\mathrm{new}} = \mathbf{res}^{\mathrm{previous}} + \begin{pmatrix} \delta\bar{\sigma}_{22} \\ \delta\bar{\sigma}_{33} \\ \delta s \end{pmatrix} \tag{4.126}$$

in which

$$\mathbf{res}^{\mathrm{previous}} = \begin{pmatrix} \bar{\sigma}_{22}^{\mathrm{previous}} \\ \bar{\sigma}_{33}^{\mathrm{previous}} \\ s^{\mathrm{previous}} \end{pmatrix} - \begin{pmatrix} \bar{\sigma}_{22(\mathrm{i})} \\ \bar{\sigma}_{33(\mathrm{i})} \\ s_{(\mathrm{i})} \end{pmatrix} \tag{4.127}$$

is the residual vector computed at the previous state.

The constitutive relationship in Eqs. (4.116-4.117) can be rewritten in the below form of the Voigt notations:

$$\begin{pmatrix} \delta\bar{\sigma}_{11} \\ \delta\bar{\sigma}_{22} \\ \delta\bar{\sigma}_{33} \\ \delta\bar{\sigma}_{12} \\ \delta\bar{\sigma}_{23} \\ \delta\bar{\sigma}_{31} \\ \delta s \end{pmatrix} = \begin{bmatrix} \bar{\Lambda}_{1111} & \bar{\Lambda}_{1122} & \bar{\Lambda}_{1133} & \bar{\Lambda}_{1112} & \bar{\Lambda}_{1123} & \bar{\Lambda}_{1131} & \bar{\Pi}_{11} \\ \bar{\Lambda}_{2211} & \bar{\Lambda}_{2222} & \bar{\Lambda}_{2233} & \bar{\Lambda}_{2212} & \bar{\Lambda}_{2223} & \bar{\Lambda}_{2231} & \bar{\Pi}_{22} \\ \bar{\Lambda}_{3311} & \bar{\Lambda}_{3322} & \bar{\Lambda}_{3333} & \bar{\Lambda}_{3312} & \bar{\Lambda}_{3323} & \bar{\Lambda}_{3331} & \bar{\Pi}_{33} \\ \bar{\Lambda}_{1211} & \bar{\Lambda}_{1222} & \bar{\Lambda}_{1233} & \bar{\Lambda}_{1212} & \bar{\Lambda}_{1223} & \bar{\Lambda}_{1231} & \bar{\Pi}_{12} \\ \bar{\Lambda}_{2311} & \bar{\Lambda}_{2322} & \bar{\Lambda}_{2333} & \bar{\Lambda}_{2312} & \bar{\Lambda}_{2323} & \bar{\Lambda}_{2331} & \bar{\Pi}_{23} \\ \bar{\Lambda}_{3111} & \bar{\Lambda}_{3122} & \bar{\Lambda}_{3133} & \bar{\Lambda}_{3112} & \bar{\Lambda}_{3123} & \bar{\Lambda}_{3131} & \bar{\Pi}_{31} \\ \bar{\Omega}_{11} & \bar{\Omega}_{22} & \bar{\Omega}_{33} & \bar{\Omega}_{12} & \bar{\Omega}_{23} & \bar{\Omega}_{31} & \bar{\Upsilon} \end{bmatrix} \begin{pmatrix} \delta\varepsilon_{11} \\ \delta\varepsilon_{22} \\ \delta\varepsilon_{33} \\ \delta\varepsilon_{12} \\ \delta\varepsilon_{23} \\ \delta\varepsilon_{31} \\ -\delta S_r \end{pmatrix} \tag{4.128}$$

From Eq. (4.128), after some mathematical manipulations, the below expression can be derived:

$$\begin{pmatrix} \delta\bar{\sigma}_{22} \\ \delta\bar{\sigma}_{33} \\ \delta s \end{pmatrix} = \begin{bmatrix} \bar{\Lambda}_{2211} & \bar{\Lambda}_{2212} & \bar{\Lambda}_{2223} & \bar{\Lambda}_{2231} \\ \bar{\Lambda}_{3311} & \bar{\Lambda}_{3312} & \bar{\Lambda}_{3323} & \bar{\Lambda}_{3331} \\ \bar{\Omega}_{11} & \bar{\Omega}_{12} & \bar{\Omega}_{23} & \bar{\Omega}_{31} \end{bmatrix} \begin{pmatrix} \delta\varepsilon_{11} \\ \delta\varepsilon_{12} \\ \delta\varepsilon_{23} \\ \delta\varepsilon_{31} \end{pmatrix} + \begin{bmatrix} \bar{\Lambda}_{2222} & \bar{\Lambda}_{2233} & \bar{\Pi}_{22} \\ \bar{\Lambda}_{3322} & \bar{\Lambda}_{3333} & \bar{\Pi}_{33} \\ \bar{\Omega}_{22} & \bar{\Omega}_{33} & \bar{\Upsilon} \end{bmatrix} \begin{pmatrix} \delta\varepsilon_{22} \\ \delta\varepsilon_{33} \\ -\delta S_r \end{pmatrix} \tag{4.129}$$

Substituting Eq. (4.129) into Eq. (4.126) leads to:

$$\mathbf{res}^{\text{new}} = \mathbf{res}^{\text{previous}} + \begin{bmatrix} \bar{\Lambda}_{2211} & \bar{\Lambda}_{2212} & \bar{\Lambda}_{2223} & \bar{\Lambda}_{2231} \\ \bar{\Lambda}_{3311} & \bar{\Lambda}_{3312} & \bar{\Lambda}_{3323} & \bar{\Lambda}_{3331} \\ \bar{\Omega}_{11} & \bar{\Omega}_{12} & \bar{\Omega}_{23} & \bar{\Omega}_{31} \end{bmatrix} \begin{pmatrix} \delta\varepsilon_{11} \\ \delta\varepsilon_{12} \\ \delta\varepsilon_{23} \\ \delta\varepsilon_{31} \end{pmatrix} +$$

$$\begin{bmatrix} \bar{\Lambda}_{2222} & \bar{\Lambda}_{2233} & \bar{\Pi}_{22} \\ \bar{\Lambda}_{3322} & \bar{\Lambda}_{3333} & \bar{\Pi}_{33} \\ \bar{\Omega}_{22} & \bar{\Omega}_{33} & \bar{Y} \end{bmatrix} \begin{pmatrix} \delta\varepsilon_{22} \\ \delta\varepsilon_{33} \\ -\delta S_r \end{pmatrix} \tag{4.130}$$

The requirement of $\mathbf{res}^{\text{new}} = 0$ in Eq. (4.130) is enforced to obtain the incremental vector of $(\delta\varepsilon_{22} \quad \delta\varepsilon_{33} \quad -\delta S_r)^T$ as:

$$\begin{pmatrix} \delta\varepsilon_{22} \\ \delta\varepsilon_{33} \\ -\delta S_r \end{pmatrix} = \begin{bmatrix} \bar{\Lambda}_{2222} & \bar{\Lambda}_{2233} & \bar{\Pi}_{22} \\ \bar{\Lambda}_{3322} & \bar{\Lambda}_{3333} & \bar{\Pi}_{33} \\ \bar{\Omega}_{22} & \bar{\Omega}_{33} & \bar{Y} \end{bmatrix}^{-1} \left\{ -\mathbf{res}^{\text{previous}} - \begin{bmatrix} \bar{\Lambda}_{2211} & \bar{\Lambda}_{2212} & \bar{\Lambda}_{2223} & \bar{\Lambda}_{2231} \\ \bar{\Lambda}_{3311} & \bar{\Lambda}_{3312} & \bar{\Lambda}_{3323} & \bar{\Lambda}_{3331} \\ \bar{\Omega}_{11} & \bar{\Omega}_{12} & \bar{\Omega}_{23} & \bar{\Omega}_{31} \end{bmatrix} \begin{pmatrix} \delta\varepsilon_{11} \\ \delta\varepsilon_{12} \\ \delta\varepsilon_{23} \\ \delta\varepsilon_{31} \end{pmatrix} \right\} \tag{4.131}$$

The obtained strain and saturation degree increments in Eq. (4.131) are then used to update stress and suction through the semi-implicit algorithm in Section 4.3.2. The residual vector is used to assess the performance of the algorithm for mixed stress-strain control:

$$\left|\frac{res_1}{\bar{\sigma}_{22(\text{i})}}\right| \leq \text{TOLERANCE and } \left|\frac{res_2}{\bar{\sigma}_{33(\text{i})}}\right| \leq \text{TOLERANCE and } \left|\frac{res_3}{s_{(\text{i})}}\right| \leq \text{TOLERANCE} \tag{4.132}$$

with TOLERANCE being a small positive number ($10^{-4} \div 10^{-3}$ is considered acceptable). The use of residual from the previous step in the current step (see Eq. (4.131)), while avoiding iterations, helps obtain reasonable results for small enough increments and also removes issues of error accumulation. The numerical implementation and verification also include the following: (i) quantitative assessments at special conditions (e.g. at the saturated condition when $s = 0$, $S_r = 1$ and $\frac{\Delta q}{\Delta p'} = 3$, at critical state when $\Delta\varepsilon_v^{\text{p}} = 0$, $\Delta S_r^{\text{p}} = 0$ and $\Delta q = 0$ while $\Delta\varepsilon_s^{\text{p}} \neq 0$) (ii) controlling the residuals (see Eq. (4.132)), and (iii) verifications using different approaches (e.g. analytical solution).

In the present approach of numerical implementation, the semi-implicit stress return algorithm is used in conjunction with the algorithm for the mixed-control loading (stress- and strain- controlled) to simulate appropriate loading paths of experimental data.

4.3.4. Numerical verification

In this section, several numerical examples are performed to verify the proposed integration algorithm described in Section 4.3.2 and 4.3.3.

Strain increment sensitivity

The first example focuses on the effect of strain increment size ($\Delta\varepsilon_v$) on its numerical accuracy under drained isotropic compression condition. In this example, the following parameters are used: $\kappa = 0.02$; $\lambda = 0.11$; $\kappa_h = 1.1$; $p'_R = 45.31$ kPa; $\mu = 0.15$ kPa^{-1}; $\xi = 0.39$; $p'_{c0} = 77.32$ kPa; $r = 3.704$; $\beta = 0.05$; $p_b = 80$ kPa. Five numerical simulations are carried out using five volumetric strain increments ($\Delta\varepsilon_v = 2\times10^{-6}; 2\times10^{-5}; 2\times10^{-4}; 2\times10^{-3}; 2\times10^{-2}$) with a constant suction of $s = 100$ kPa. They all are isotropically loaded from the initial net pressure of $\bar{p}_0 = 19.18$ kPa, the specific volume of $v_0 = 1.732$ and saturation degree of $S_{r0} = 0.728$. Responses in $\bar{p}$: v and v: s are plotted in Figure 4.7a and 4.7b, respectively. Also depicted in Figure 4.7b are the relative errors $\left|\frac{s-s_{(i)}}{s_{(i)}}\right|$ between imposed and computed suctions. It can be seen in Figure 4.7a that the algorithm in Section 4.3.3 performs well for small enough increments ($\Delta\varepsilon_v < 2\times10^{-3}$). Larger errors can be seen if the strain increments are high enough. However, the algorithm is stable, given no error accumulation and the steady decrease of error towards the end of the numerical test, despite no iterations were used, thanks to the use of residual control in the algorithm (Eq. (4.131)). Numerical solutions in a suction-controlled test (see Figure 4.7b) helps maintain constant suction of $s = 100$ kPa for strain increment within a reasonable range ($\Delta\varepsilon_v = 2\times10^{-6} \div 2\times10^{-4}$).

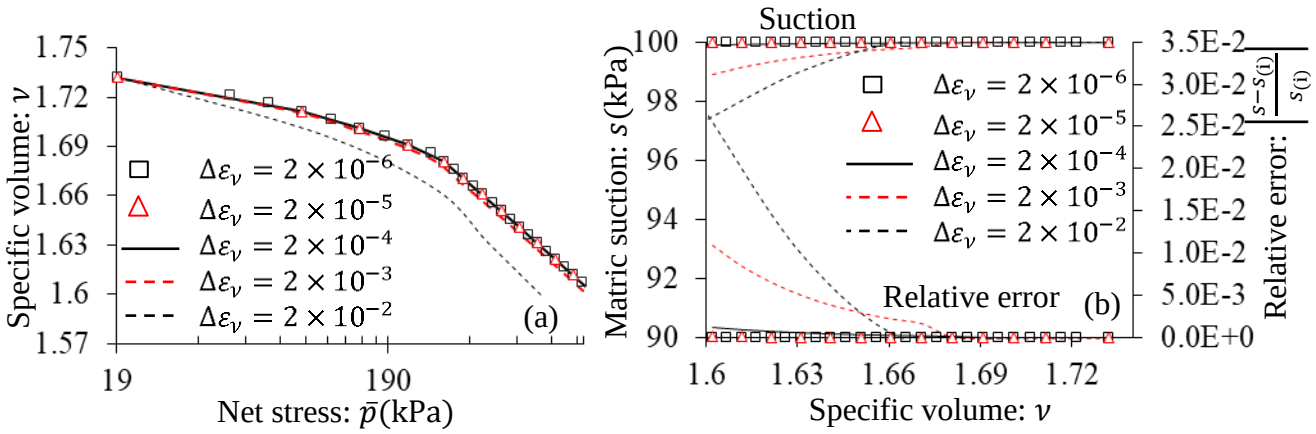

Figure 4.7. Performance of the proposed stress update algorithm under different values of $\Delta\varepsilon_v$ (a) $\bar{p} - v$ and (b) $v - s$, $v - \left|\frac{s-s_{(i)}}{s_{(i)}}\right|$

Verification against semi-analytical and analytical algorithm for isotropic compression condition

The performance of the proposed algorithm in Section 4.3.3 is also verified against a semi-analytical algorithm which uses the semi-implicit stress return algorithm in Section 4.3.2 combined with the analytical enforcement of constant suction condition. This semi-analytical algorithm can be briefly presented as follows.

Given $\Delta\varepsilon_v$ and s, the trial values of effective mean stress $\left(p'^{\text{trial}}\right)$ and modified suction $\left(s^{*\text{trial}}\right)$ in the first step of this algorithm are calculated using the following form:

$$p'^{\text{trial}} = p'^{n} + \Delta p'^{\text{trial}} = p'^{n} + \frac{p'^{n}}{\kappa}\Delta\varepsilon_v \tag{4.133}$$

$$s^{*\text{trial}} = s^{*n} + \Delta s^{*\text{trial}} = s^{*n} + (-s\Delta\varepsilon_v) \tag{4.134}$$

with p'^{n} being effective mean stress at step n

From Eq. (4.124), $\Delta\lambda_p$ in the case of isotropic compression tests takes the following form:

$$\Delta\lambda_p = \frac{y^{\text{trial}}}{\left.\frac{\partial y}{\partial p'}\frac{p'^{n}}{\kappa}\frac{\partial y^*}{\partial \chi_v}\right|^{\text{trial}} + \left.\frac{\partial y}{\partial p'_{c(us)}}\frac{\partial p'_{c(us)}}{\partial s^*}\frac{(s^{*n}+p_u)}{\kappa_h}\frac{\partial y^*}{\partial \chi_h}\right|^{\text{trial}} - \left.\frac{\partial y}{\partial p'_{c(us)}}\frac{\partial p'_{c(us)}}{\partial p'_c}\frac{p'_c}{(\lambda-\kappa)}\frac{\partial y^*}{\partial \chi_v}\right|^{\text{trial}}} \tag{4.135}$$

The new increment of effective mean stress (p') can be computed using $\Delta\lambda_p$ as follows:

$$\Delta p' = \Delta p'^{\text{trial}} + \Delta p'^{\text{corrt}} \tag{4.136}$$

With $\Delta\lambda_p$ obtained, the increment of saturation degree $(-\Delta S_r)$ can be expressed as:

$$-\Delta S_r = \frac{\kappa_h}{(s^{*n}+p_u)}\Delta s^{*\text{trial}} + \Delta\lambda_p \left.\frac{\partial y^*}{\partial \chi_h}\right|^{\text{trial}} \tag{4.137}$$

The effective mean stress or alternatively net stress are then updated using the following equations:

$$p'^{n+1} = p'^{n} + \Delta p' \tag{4.138}$$

$$\bar{p}^{n+1} = p'^{n+1} - S_r^{n+1}s \tag{4.139}$$

where S_r^{n+1} is updated saturation degree thanks to Eq. (4.137).

In this example, $\Delta\varepsilon_v = 2\times10^{-6}$ is used and three different suction levels of $0;\ 25;\ 100$ kPa corresponding to initial conditions of $\bar{p}_0 = 20.64; 19.01; 19.18$ kPa; $v_0 = 1.802; 1.792; 1.732$ and $S_{r0} = 1; 0.768; 0.728$, respectively. The same set of parameters in the previous example is adopted. At various suction levels($s = 0, 25, 100$ kPa), v and S_r are plotted against $\bar{p}$ in Figure 4.8 to present the results obtained using both algorithms. For $s = 0$ the Unloading-Reloading Line (URL) and Normal Compression Line (NCL) are also plotted and considered by an analytical solution for the

case of saturated behaviour. As indicated in Figure 4.8, both numerical and semi-analytical solutions are identical, and they also coincide with the analytical result for the case of saturated behaviour ($s = 0$). These features highlight the numerical stability of the proposed stress return algorithm and the effectiveness of the iterative algorithm to enforce constant suction condition.

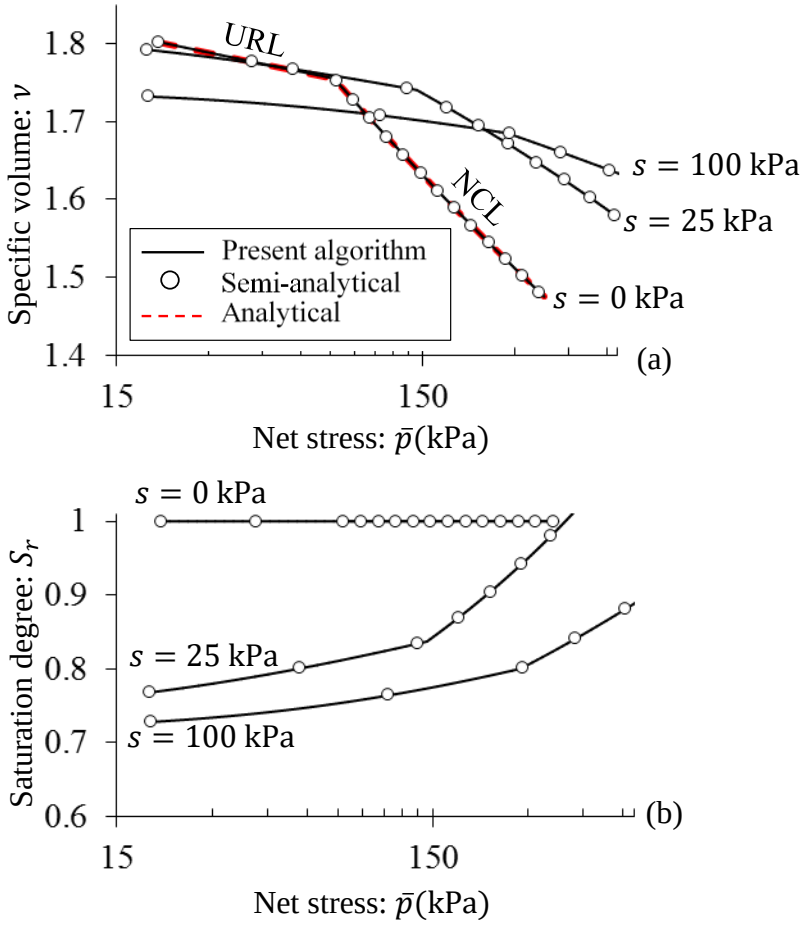

Figure 4.8. Verification of the proposed stress update algorithms in isotropic compressions (a) $\bar{p} - v$ (b) $\bar{p} - S_r$

Verification against the algorithm based on mean effective and deviatoric stresses

For the triaxial shearing tests, the current numerical implementations in this study are based on the tensorial stress (σ'_{ij}-based algorithm). It is now assessed against a counterpart using mean effective and deviatoric stresses (p', q - based algorithm). To do so, an example on the suction-controlled triaxial test is presented using the following model parameters: $\kappa = 0.006$; $\lambda = 0.09$; $M = 1.17$; $G = 7000$ kPa; $\kappa_h = 0.56$; $p'_R = 140.41$ kPa; $\mu = 0.0229$ kPa^{-1}; $\xi = 0.652$; $p'_{c0} = 200$ kPa; $r = 1.818$; $\alpha = 0.5$; $\beta = 0.05$; $p_b = 70$ kPa. In this example, during shearing, the lateral net stress is kept constant at 100 kPa while suctions are fixed at 0, 100, and 300 kPa with $v_0 = 1.576, 1.578, 1.576$, and $S_{r0} = 1, 0.4, 0.2$ respectively. A small axial strain increment of $\Delta\varepsilon_{11} = 10^{-6}$ is used.

Figure 4.9 shows a good match between the two algorithms in terms of deviatoric stress, volumetric strain and saturation degree against the axial strain under a range of suction levels. For the case of zero suction, the behaviour of a critical state model (Collins, 2003) are also sketched in Figures 4.9a and 4.9b, and match well with the numerical results produced by the proposed model. The results in Figure 4.9 again verify the implementation and the capability of the model in handling the transition between saturated and partially saturated conditions.

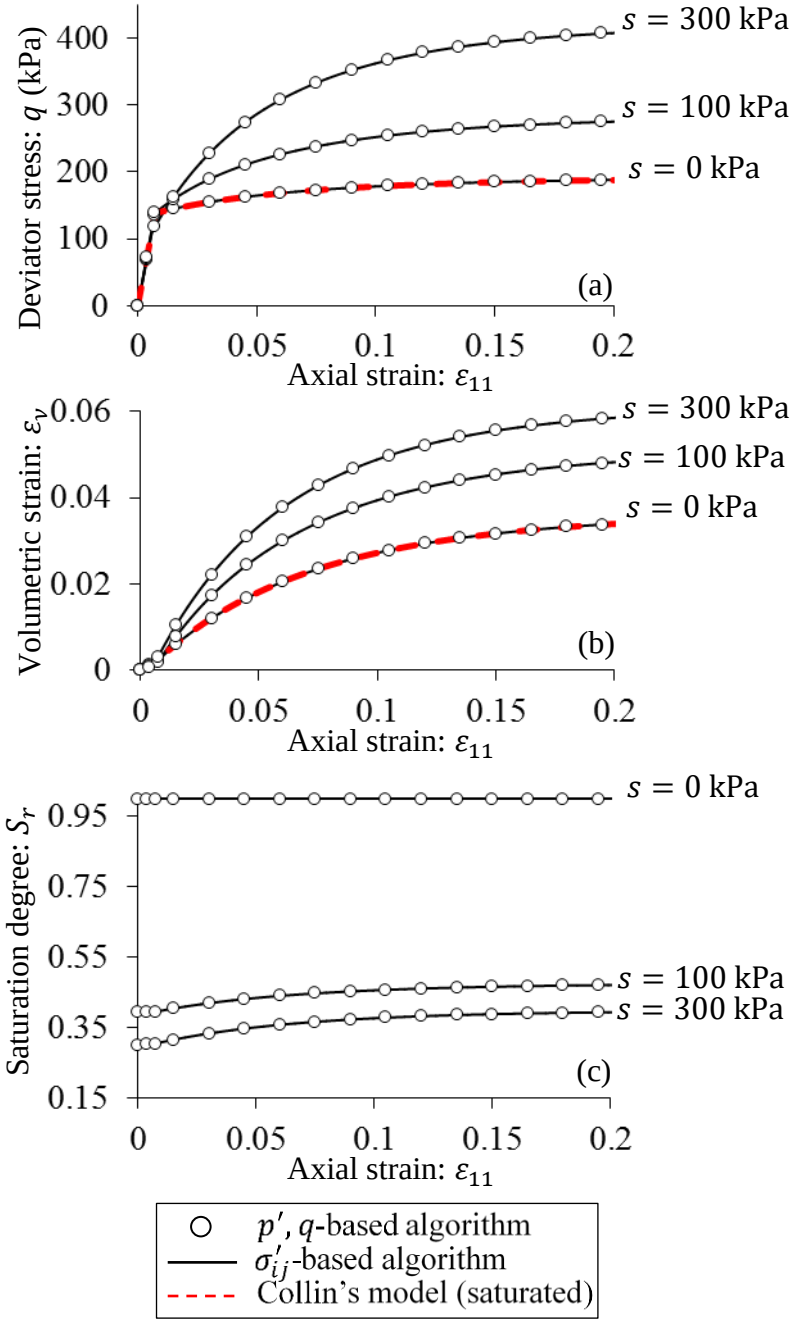

Figure 4.9. Verification of the proposed stress update algorithms in triaxial compressions (a) $\varepsilon_{11} - q$ (b) $\varepsilon_{11} - \varepsilon_v$ and (c) $\varepsilon_{11} - S_r$

4.4. Model parameters

The proposed model possesses 13 parameters categorised into five groups, namely Group 1 ($\kappa, G, \lambda, p'_{c0}, M$), Group 2 ($\kappa_h$), Group 3 ($p'_R, \mu, \xi$), Group 4 ($r, \alpha$) and Group 5 ($\beta, p_b$). This section aims to provide details on the calibration of these model parameters, using a suction-controlled triaxial test on Bourke silt (Uchaipichat, 2005; Uchaipichat & Khalili, 2009). A step by step approach is presented in which parameters in each group are calibrated using relevant sets of experimental data. An assessment of the model behaviour against experimental data, using the calibrated parameters, will then be provided at the end of the Section to demonstrate the effectiveness of the calibration.

In Group 1, parameters κ, G, λ, p'_{c0} and M are calibrated following the same procedure applicable to MCC for saturated soils. Particularly, by fitting the equations of NCL and URL to their experimental counterparts in the saturated state, κ, λ and p'_{c0} can be determined. Based on Eq. (4.3), G is estimated from the average gradients of the $\varepsilon_s - q$ plots obtained from laboratory shear tests. The ratio between effective mean and deviatoric stresses at the ultimate state is used to determine M. For Bourke silt-SCT, $\kappa = 0.006$; $\lambda = 0.09$; $p'_{c0} = 200$ kPa; $M = 1.17$ (Uchaipichat, 2005) and $G = 7000$ kPa are found to match well with the experimental data on the saturated state.

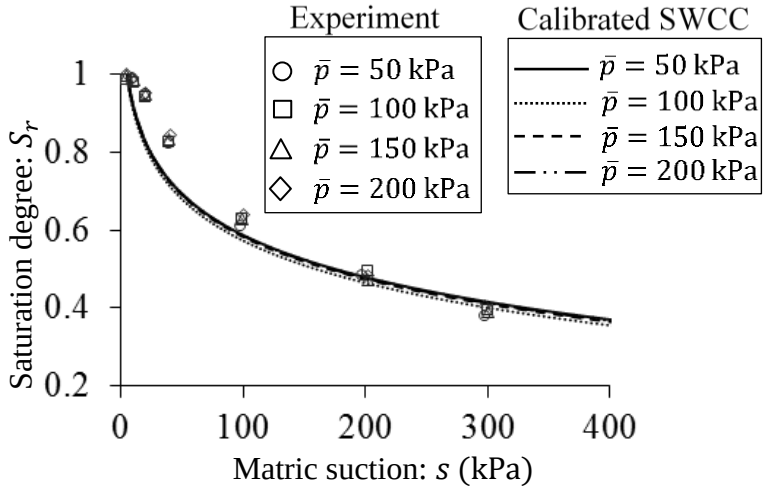

Figure 4.10. Calibration of κ_h based on SWCC obtained from net pressure-controlled tests on Bourke silt (Uchaipichat, 2005; Uchaipichat & Khalili, 2009)

The parameter κ_h (Group 2) governs the s: S_r relationship, and also affect the mechanical behaviour due to the hydro-mechanical coupling (see Eqs. (4.109) and (4.117)). Figure 4.10 shows the best fit to the measured data using $\kappa_h = 0.16$ for drying tests under constant net mean stresses of 50 kPa, 100 kPa, 150 kPa and 200 kPa.

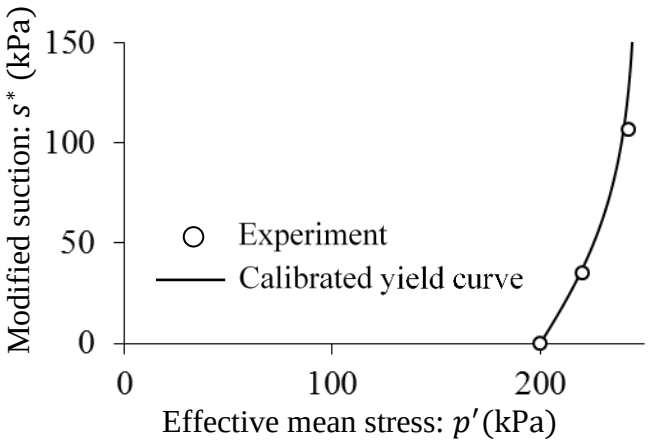

Figure 4.11. Calibration of p'_R, μ and ξ based on suction-controlled isotropic compression tests on Bourke silt (Uchaipichat, 2005; Uchaipichat & Khalili, 2009)

Parameters listed in Group 3 are to control the shape of the initial yield surface in the space of true stress and modified suction. At each level of suction, the model produces higher initial yield stresses and therefore lower rates of saturation degree at lower values of p'_R, ξ and higher values of μ. This is closely linked to the expansion of yield surface when p'_R, ξ get smaller, and μ becomes bigger. The slope of NCL in the stage before yielding is insensitive to changes in these parameters, while that in the yielding stage becomes steeper if p'_R, μ decrease and ξ increases. Furthermore, one should note that different suctions exhibit different effect levels of p'_R, ξ and μ on the model performance. Their effects are less profound at lower suctions for p'_R, ξ and higher suction for μ. It is well matched with the more convergence in yield curves of different ξ and p'_R when a lower suction is imposed, and that of different μ with a higher suction. These features are shown to be good indicators of their significant roles in controlling the soil stiffness and yielding response under hydraulic effects. Especially, these parameters (p'_R, μ and ξ) play significant roles in generating the wetting/drying-induced collapse mechanism. Using a best-fitting least-square procedure, they can be selected to make the LC curve in the $p': s^*$ plane fit with initial yield values of effective mean stress and modified suction provided by isotropic compression tests. Given $\kappa = 0.006;\ \lambda = 0.09;\ p'_{c0} = 200$ kPa in Group 1, the following parameters are chosen for Group 3: $p'_R = 140.41$ kPa; $\mu = 0.0229$ kPa^{-1}; $\xi = 0.652$ to allow the initial $p': s^*$ yield curve to fit well with that from experimental data of Bourke silt-SCT, as illustrated in Figure 4.11.

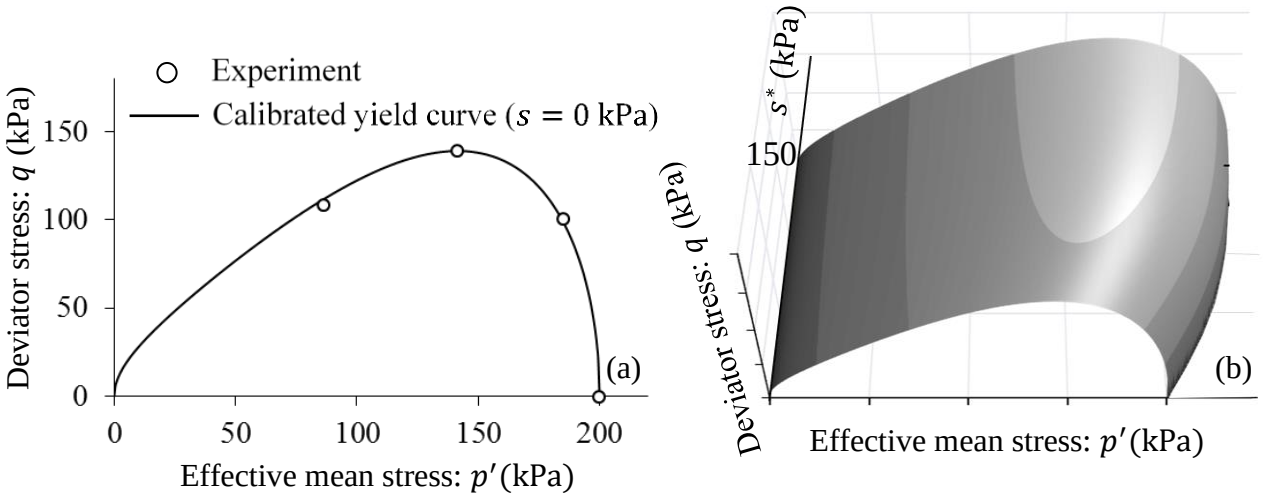

Figure 4.12. Calibration of α based on suction-controlled triaxial tests on Bourke silt (Uchaipichat, 2005; Uchaipichat & Khalili, 2009) (a) $p' - q$ (b) $p' - q - s^*$

Parameters r and α in Group 4 govern the shear strength and dilation. Particularly, the yield surface expands towards the upper right direction in the $p' : q$ space when r decreases. This is consistent with the increase in the initial shear stress with decreasing r, that is stronger at a higher suction. Along with this, at the same shear strain ε_s in the yielding stage, lower values of r imply a more profound dilative behaviour and a smaller saturation degree. This can be explained by the growth of the effective mean stress at the critical state because CSL tends to shift towards NCL in the $p' : v$ plane if r is reduced. As a result, the positive increment of plastic volumetric strain becomes smaller. Reduction in r is physically related to a denser state of soils where the particle rotation is more constrained by interlocking and the shear resistance increases. That results in a more upward movement of the plastic sliding at the inter-particle contact during shearing. On the other hand, the dilation becomes more profound in the saturated state with decreasing α. The sensitivity of the dilative response to the parameter α can be clarified through its main contribution in generating the plastic change of shear strain which significantly affects both direction and magnitude of the non-associated plastic flow vector. This model uses $r = \exp[(N - \Gamma)/(\lambda - \kappa)]$ (Uchaipichat, 2005) as an empirical equation representing the spacing between NCL and CSL in the $p' : v$ plane to estimate r, where N and Γ are reference specific volumes of NCL and CSL under saturated conditions, respectively. With $\kappa = 0.006; \lambda = 0.09$, $N = 2.0472$ and $\Gamma = 1.997$ given in the laboratory (Uchaipichat, 2005), r is estimated as 1.818 for Bourke silt-SCT. Once r is obtained, α can be determined by adjusting it until reaching a best-fit between predictive and measured data of initial yield surface in the $p' : q$ space at $s = 0$ kPa. For example, Figure 4.12a shows a good agreement

between the experimental and theoretical results of Bourke silt-SCT for $\alpha = 0.5$. The calibrated initial yield surface of Bourke silt-SCT in (p', q, s^*) space is depicted in Figure 4.12b.

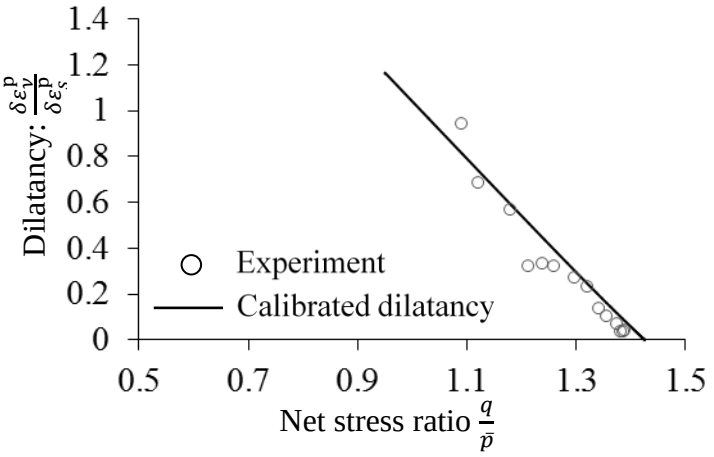

Figure 4.13. Calibration of β based on dilatancy ratio obtained from suction-controlled triaxial tests on Bourke silt under $s = 100\ kPa$ and $\bar{\sigma}_{33} = 100\ kPa$ (Uchaipichat, 2005; Uchaipichat & Khalili, 2009)

Group 5 includes two parameters, β and p_b, both of which are only present in the flow rules (Eqs. (4.78 & 4.80)). Parameter β is a coupling parameter governing the effect of saturation degree on the proportion between $\dot{\varepsilon}_v^p$ and $\dot{\varepsilon}_s^p$, so-called plastic dilatancy ratio, while p_b influences the hydraulic dissipative generalised stress. Reducing p_b increases in the hydraulic energy lost and therefore affects the irrecoverable rate of saturation degree. β can be iteratively calibrated to achieve the best match in terms of the ratio $\dot{\varepsilon}_v^p/\dot{\varepsilon}_s^p$ between the experimental result and its theoretical counterpart obtained from Eqs. (4.78-4.79):

$$\frac{\dot{\varepsilon}_v^p}{\dot{\varepsilon}_s^p} = \frac{\left(p' - \frac{1}{r}p'_{c(us)}\right)\left[(1-\alpha)p' + \frac{\alpha}{r}p'_{c(us)}\right]^2 M^2}{q\left[\left(1-\frac{2}{r}\right)p' + \frac{1}{r}p'_{c(us)}\right]^2} \exp[-\beta(1-S_r)] \tag{4.140}$$

For simplicity, it is assumed that the elastic deformation is very small, and hence the experimentally measured strains are approximately equal to plastic strains (Wong & Wong, 1975). For Bourke silt-SCT, the experimental result of the shear test under $s = 100$ kPa and $\bar{\sigma}_{33} = 100$ kPa is used. As illustrated in Figure 4.13, the numerical results are in good agreement with experimental data for $\beta = 0.05$. After obtaining r and β, p_b can be calibrated using the following equation derived from Eqs. (4.78) and (4.80):

$$p_b = s^* - \frac{[1-\exp[-\beta(1-S_r)]]}{\exp[-\beta(1-S_r)]}\left(p' - \frac{1}{r}p'_{c(us)}\right)\frac{\dot{\varepsilon}_v^p}{(-\dot{S}_r^p)} \tag{4.141}$$

where $\frac{\dot{\varepsilon}_v^{\mathrm{p}}}{(-\dot{s}_r^{\mathrm{p}})} \approx \frac{\dot{\varepsilon}_v}{(-\dot{s}_r)}$ is assumed and variables $(p', s^*, \dot{\varepsilon}_v, \dot{S}_r, S_r)$ are collected from only a single isotropic compression test. Using Eq. (4.141), $p_b = 70$ kPa is obtained using the isotropic loading case with $s = 100$ kPa.

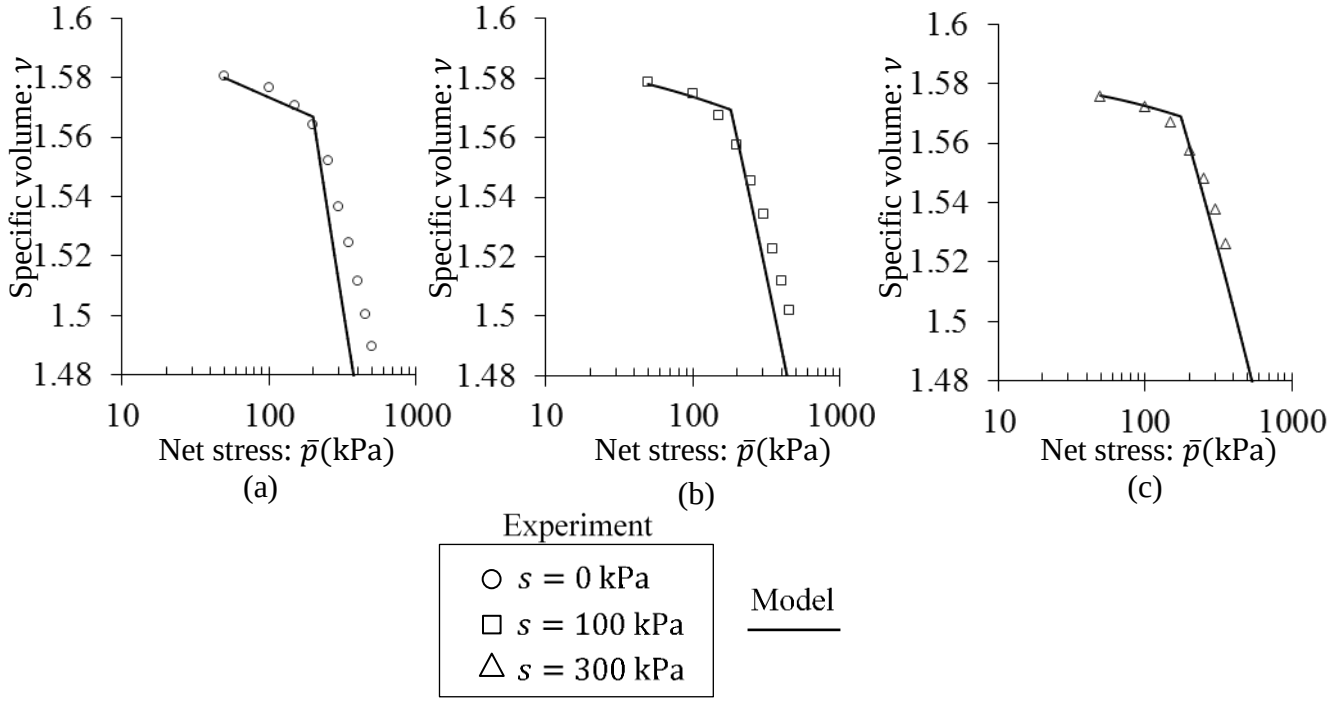

Figure 4.14. Validation with drained isotropic compression tests on Bourke silt (after Uchaipichat, 2005; Uchaipichat & Khalili, 2009) (a) $s = 0$ kPa (b) $s = 100$ kPa (c) $s = 300$ kPa

The calibrated parameters $\kappa = 0.006$; $\lambda = 0.09$; $\kappa_h = 0.16$; $p'_R = 140.41$ kPa; $\mu = 0.0229$ kPa^{-1}; $\xi = 0.652$; $p'_{c0} = 200$ kPa; $r = 1.818$; $\beta = 0.05$ and $p_b = 70$ kPa result in good agreement with experiments on drained isotropic compression test at different suction levels ($s = 0$ kPa; 100 kPa and 300 kPa) (see Figure 4.14).

4.5. Model behaviour and validation

This section is to present several examples to highlight the predictive capacity of the proposed model. The model performance is assessed against experimental results of both isotropic compression and triaxial shear tests under drained and undrained conditions.

4.5.1. Isotropic compression test

The heavily compacted sand-bentonite mixture, constant suction tests (Sun et al., 2009; Sun & Sun, 2012)

In the first example, the drained oedometer test on the heavily compacted sand-bentonite mixture is examined with $p'_{c0} = 550$ kPa (Sun et al., 2009; Sun & Sun, 2012). The following parameters: $\kappa = 0.017;\ \lambda = 0.085; p'_R = 422.38$ kPa; $\mu = 0.0124$ kPa^{-1} and $\xi = 0.357$ are calibrated to best fit the initial yield curve in the $\sigma'_v : s^*$ plane. The data on $s = 600$ kPa is used to obtain $\kappa_h = 0.25; r = 1.299;\ \beta = 0.05$ and $p_b = 70$ kPa. The comparison between the model prediction and measured data at four suction levels of $s = 300$ kPa, 600 kPa, 1200 kPa, and 1500 kPa is illustrated in Figure 4.15.

The results show that the model is able to provide a good match to experimentally observed behaviour. In the elastic regime, the $\sigma'_v : s^*$ stress paths are inside the yield surface (see Figure 4.15d), and no change in the slope of the NCL in the (σ'_v, v) plane is observed (see Figure 4.15c) while in the $(\bar{\sigma}_v, v)$ plane (Figure 4.15a) it is sensitive to the variation of suction. Once the stress path crosses the initial yield surface, the irreversible changes of both specific volume and saturation degree are triggered simultaneously. The initial yield stress is observed to increase when suction increases owing to the characteristic of wetting-induced hardening law in Eq. (4.21). The decrease of the NCL slope with increasing suction is attributed to the hydraulic effect on soil stiffness (see Eq. (4.23)). Furthermore, Figure 4.15b demonstrates that a significant increase in saturation degree is captured, although suction remains unchanged during loading. This is an indication that the mechanical effect on SWCC (Gallipoli et al., 2003; Nuth & Laloui, 2008) is taken into consideration in this model.

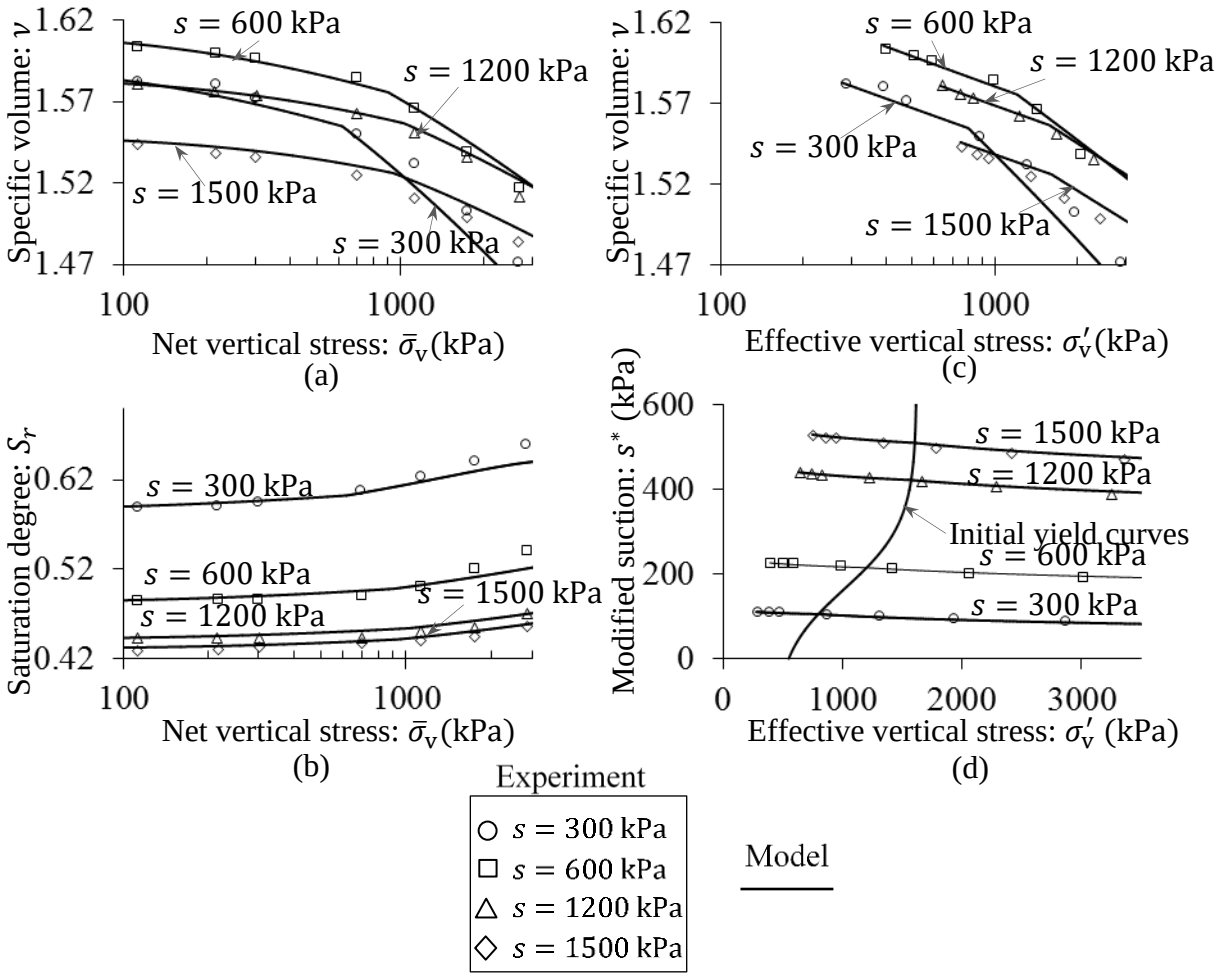

Figure 4.15. Validation with drained oedometer tests on the heavily compacted sand-bentonite mixture (after Sun et al., 2009; Sun & Sun, 2012) (a) $\bar{\sigma}_v - v$ (b) $\bar{\sigma}_v - S_r$ (c) $\sigma'_v - v$ (d) $\sigma'_v - s^*$

Compacted unsaturated expansive clay, constant suction tests (Zhan, 2003)

The drained isotropic compression test on the compacted unsaturated expansive clay (Zhan, 2003) is examined. The calibration of the following parameters is based on the initial yield curve, resulting in $\kappa = 0.015;\ \lambda = 0.05; p'_{c0} = 80$ kPa$; p'_R = 50$ kPa$; \mu = 0.025$ kPa^{-1} and $\xi = 0.3$. The data on $s = 25$ kPa is adopted to determine $\kappa_h = 0.55; r = 2;\ \beta = 0.2$ and $p_b = 70$ kPa. The predicted and measured data at $s = 25$ kPa; 50 kPa; 100 kPa and 200 kPa are illustrated in Figure 4.16. As can be seen, the model can provide a good match to experimental responses, except for some discrepancies at $s = 200$ kPa. In particular, the simultaneous activation in irreversible changes of both volume and saturation degree is well captured. The initial yield stress increases, and the NCL slope decreases when suction increases. Furthermore, saturation degree is observed to significantly increase despite unchanged suction, indicating the model's ability in predicting the mechanical effect on SWCC.

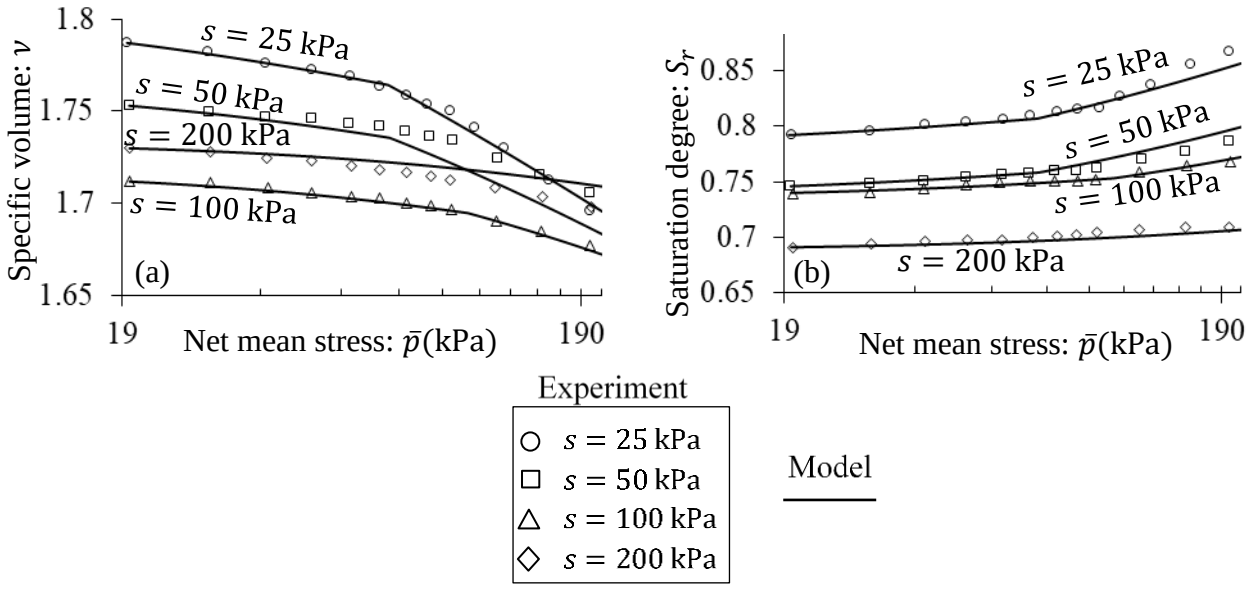

Figure 4.16. Validation with a drained isotropic compression test on compacted unsaturated expansive clay (after Zhan, 2003) (a) $\bar{p} - v$ (b) $\bar{p} - S_r$

Fairbanks silt, constant water content tests (Zhang, 2016)

Next, the undrained isotropic compression test under constant gravimetric water content of $w = 8.3\%$ on Fairbanks silt (Zhang, 2016) is simulated. The parameters for this simulation are taken as follows: $\kappa = 0.006$; $\lambda = 0.026$; $\kappa_h = 0.05$; $p'_R = 206.78$ kPa ; $\mu = 0.0157$ kPa^{-1} ; $\xi = 0.628$; $p'_{c0} = 250$ kPa; $r = 1.5$; $\beta = 0.1$; $p_b = 80$ kPa. In this example, the soil specimen is first loaded from A to B (phase 1) and from B ($\bar{p} = 300$ kPa), an unloading is then conducted ending at point C ($\bar{p} = 100$ kPa; phase 2). After that, phase 3 experiences a reloading along CD until $\bar{p} = 600$ kPa.

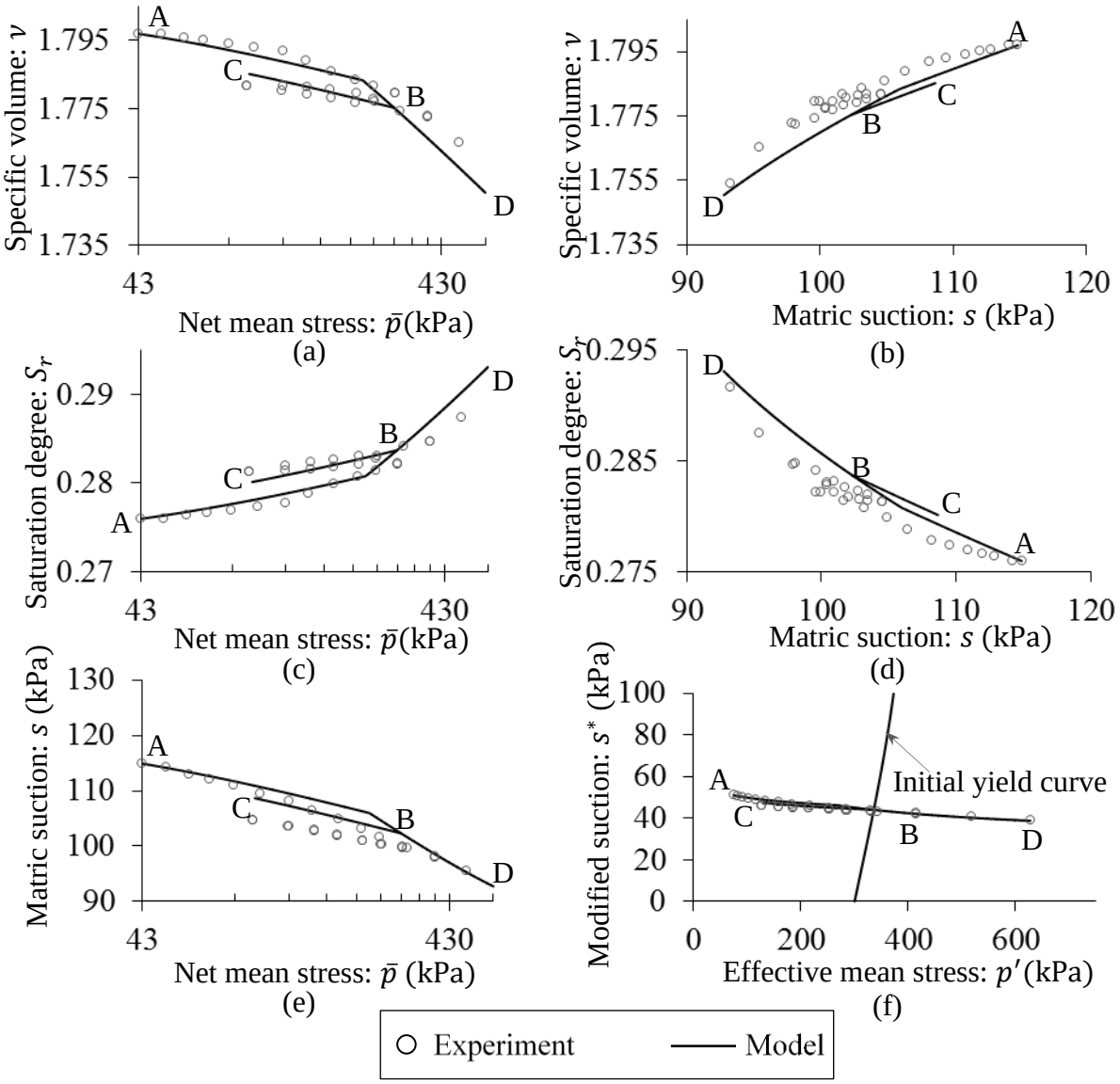

Figure 4.17. Validation with undrained isotropic compression tests on Fairbanks silt at $w = 8.3\%$ (after Zhang, 2016) (a) $\bar{p} - v$ (b) $s - v$ (c) $\bar{p} - S_r$ (d) $s - S_r$ (e) $\bar{p} - s$ (f) $p' - s^*$

As can be seen in Figure 4.17, the whole experimental trends are well reproduced by the model. In phase 1 and 3, together with the reduction in specific volume, the model behaviour exhibits a decrease in matric suction and an increase in saturation degree, and a fairly good prediction of the experimentally measured SWCC can be seen (see Figure 4.17d). In phase 2, a drying response is induced by the unloading process. Both stress-strain and SWCC relationships cannot recover their previous states upon unloading, indicating the ability of the model to produce different responses under wetting and drying. A similar response pattern can also be observed in the case of $w = 9.9\%$, as shown in Figure 4.18. Remarkably, these responses are simulated through the adoption of only a unique yield locus of effective stress and modified suction without using a separate SWCC and

different parameters of drying and wetting processes. This feature represents an advance of the current model compared to others in the literature.

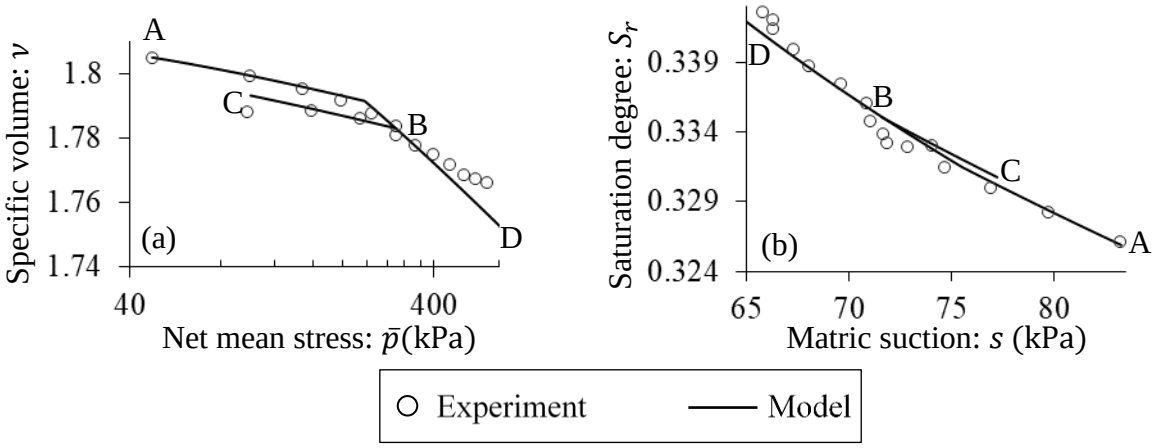

Figure 4.18. Validation with undrained isotropic compression tests on Fairbanks silt at $w = 9.9\%$ (after Zhang, 2016) (a) $\bar{p} - v$ (b) $s - S_r$

Also provided in this test is a sensitivity analysis to investigate the role of parameter β governing the mechanical effects on the wetting-drying difference of SWCC. Figure 4.19 shows cycles of loading from A to B_1, B_2, B_3 and unloading from B_1, B_2, B_3 to C_1, C_2, C_3 using $\beta = 0, 0.1, \text{and } 0.15$, respectively. As depicted in Figure 4.19a, the mechanical behaviour is relatively insensitive to the change of β, facilitating the calibration, while in Figure 4.19b, β has a strong effect on the water retention curves. The change of saturation degree is fully recoverable despite the irrecoverable specific volume if $\beta = 0$, indicating pure mechanical dissipation. When $\beta \neq 0$, the coupled hydro-mechanical dissipation is activated to allow the proposed model to capture the wetting-drying difference during the loading-unloading process, making the current approach distinct from previous studies.

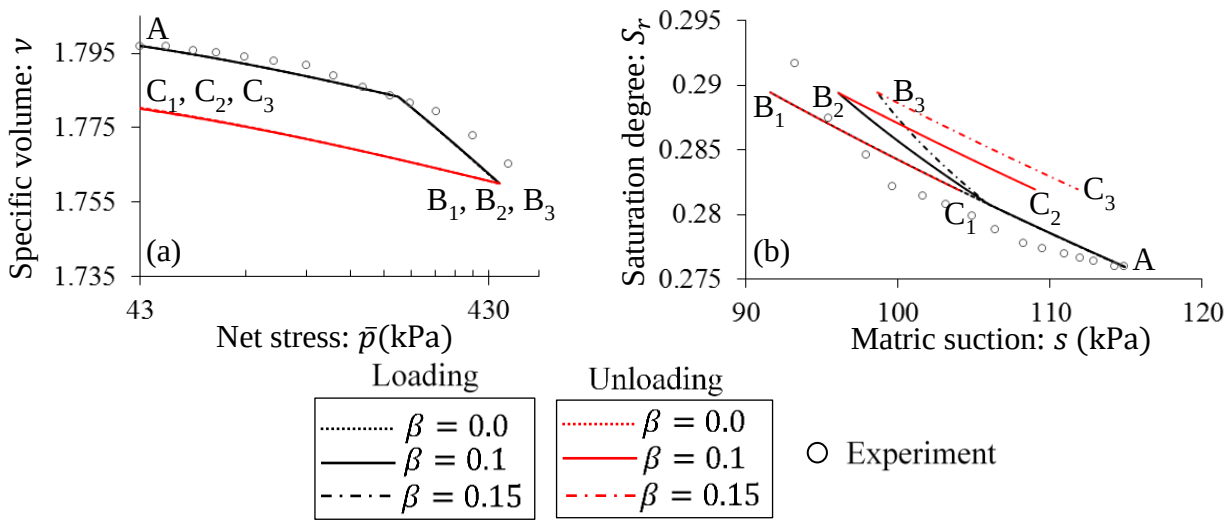

Figure 4.19. Effects of different values of β on the model responses under undrained isotropic compression tests on Fairbanks silt (after Zhang, 2016) (a) $\bar{p} - v$ (b) $s - S_r$

The mixture of Fairbanks silt and Kaolin clay, constant water content tests (Li, 2015)

The numerical prediction under the undrained isotropic compression condition is validated against the experiments on the mixture of Fairbanks silt and Kaolin clay carried out by Li (2015). Three different levels of gravimetric water content are investigated: $w = 11.85\%, 11.99\%$ and 15.91%. The model parameters are: $\kappa = 0.0076$; $\lambda = 0.043$; $\kappa_h = 0.03$; $p'_R = 120$ kPa; $\mu = 0.022$ kPa^{-1}; $\xi = 0.376$; $p'_{c0} = 150$ kPa; $r = 1.5$; $\beta = 0.95$; $p_b = 40$ kPa where $\kappa, \lambda, p'_R, \mu, \xi$ and p'_{c0} are identified using initial yield points obtained from experiments. The calibrations of κ_h, r, β and p_b are based on the experimental loading case of $w = 11.99\%$. Computed and measured results are compared in Figure 4.20. It can be seen that the model predictions agree closely with the experimental data. The variation of the soil response with w is also well-captured. In particular, the initial yield stress and the NCL slope increase with increased gravimetric water content in the net stress space. Lower gravimetric water content corresponding to the higher initial suction exhibits a more profound reduction in suction. The increase in saturation degree is more significant for the higher levels of gravimetric water content. Furthermore, the non-uniqueness of SWCC is observed through its dependence on NCL during loading.

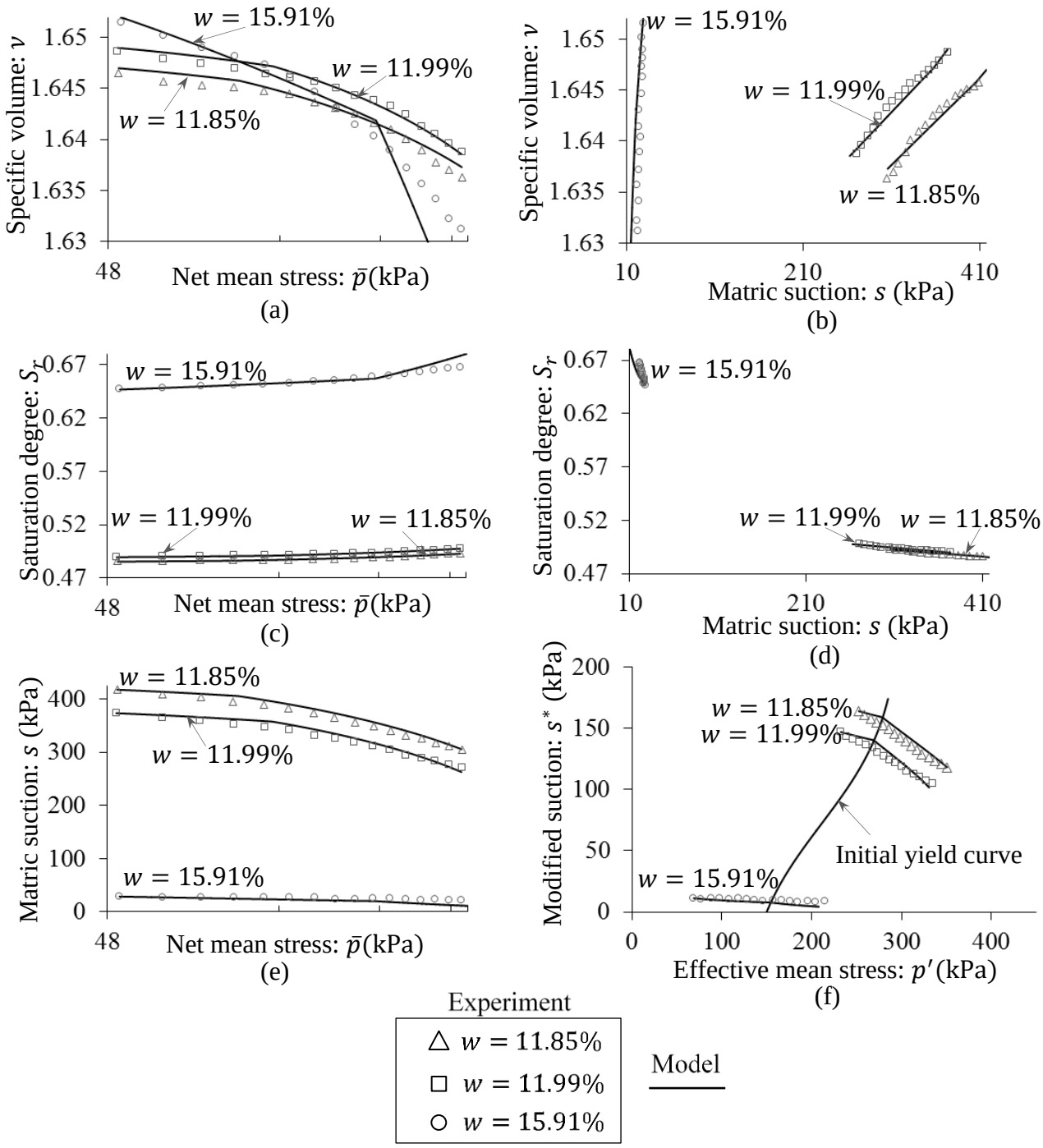

Figure 4.20. Validation with undrained isotropic compression tests on the mixture of Fairbanks silt and Kaolin clay (after Li, 2015) (a) $\bar{p} - v$ (b) $s - v$ (c) $\bar{p} - S_r$ (d) $s - S_r$ (e) $\bar{p} - s$ (f) $p' - s^*$

4.5.2. Triaxial compression tests

Zaoyang clay, constant suction tests (Chen, 2007)

A numerical analysis on the effect of suction on the shear behaviour of the model is conducted through the suction-controlled triaxial shearing test on compacted Zaoyang clay at two levels of suction $s =$ 25 kPa and $s = 100$ kPa (Chen, 2007). The net confining pressure is kept as a constant value of

$\bar{\sigma}_{33} = 50$ kPa during shearing. This simulation uses the following parameters: $\kappa = 0.018; \lambda = 0.11; \kappa_h = 0.9; p'_R = 45.31$ kPa; $\mu = 0.15$ kPa^{-1}; $\xi = 0.39; p'_{c0} = 77.32$ kPa; $r = 3.704$; $\beta = 0.05$; $p_b = 70$ kPa, which are calibrated to best match the experimental results of the suction-controlled isotropic compression test ($s = 25$ kPa and $s = 100$ kPa) as presented in Figure 4.21. The shear test at constant suction $s = 25$ kPa is also adopted to calibrate other constitutive parameters, resulting in $M = 1.29; G = 15000$ kPa and $\alpha = 0.38$.

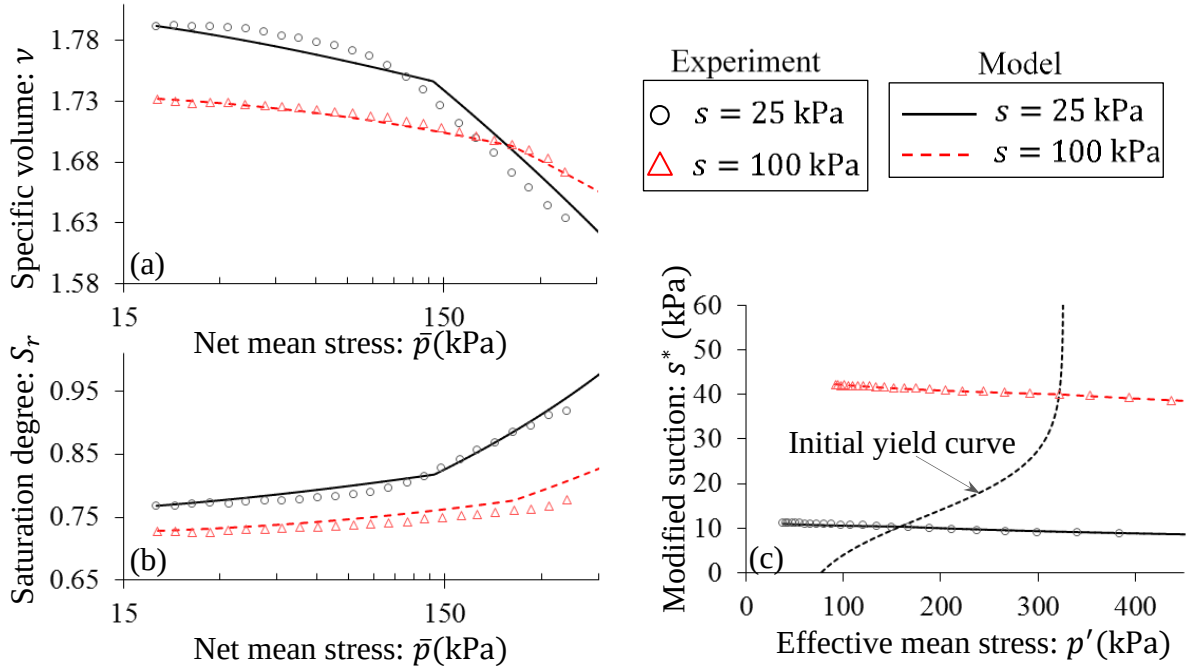

Figure 4.21. Effects of suction on the model responses in suction-controlled isotropic compression test of the compacted Zaoyang clay (after Chen, 2007) (a) $\bar{p} - v$ (b) $\bar{p} - S_r$ (c) $p' - s^*$

As depicted in Figures 4.22a-c, the numerical results show reasonable agreement with the experimental data. In particular, higher suctions tend to produce higher yield shear stresses, as can be explained through the isotropic expansion of yield loci with increasing suction in the p': q space (see Figure 4.22d). Additionally, the model can capture the evolution trend in specific volume and saturation degree during shearing. This feature is shown to be a good indicator of the effect of deviatoric stress/strain on hydraulic behaviour. The effect of suction on dilation behaviour (see Figure 4.22e) can also be reproduced by the model. Although an acceptable match between the model prediction and measured data is achieved, there are observable discrepancies in specific volume and dilatancy ratio at $s = 100$ kPa (see Figure 4.22b). This may be due to the assumption that CSL is unique and the effect of anisotropy on soil response (Stropeit et al., 2008; Al-Sharrad, 2013; Anandarajah, 2008; Hashiguchi & Mase, 2007; Wood & Graham, 1990; Lai et al., 2009; 2016) is overlooked regardless of the hydraulic variation.

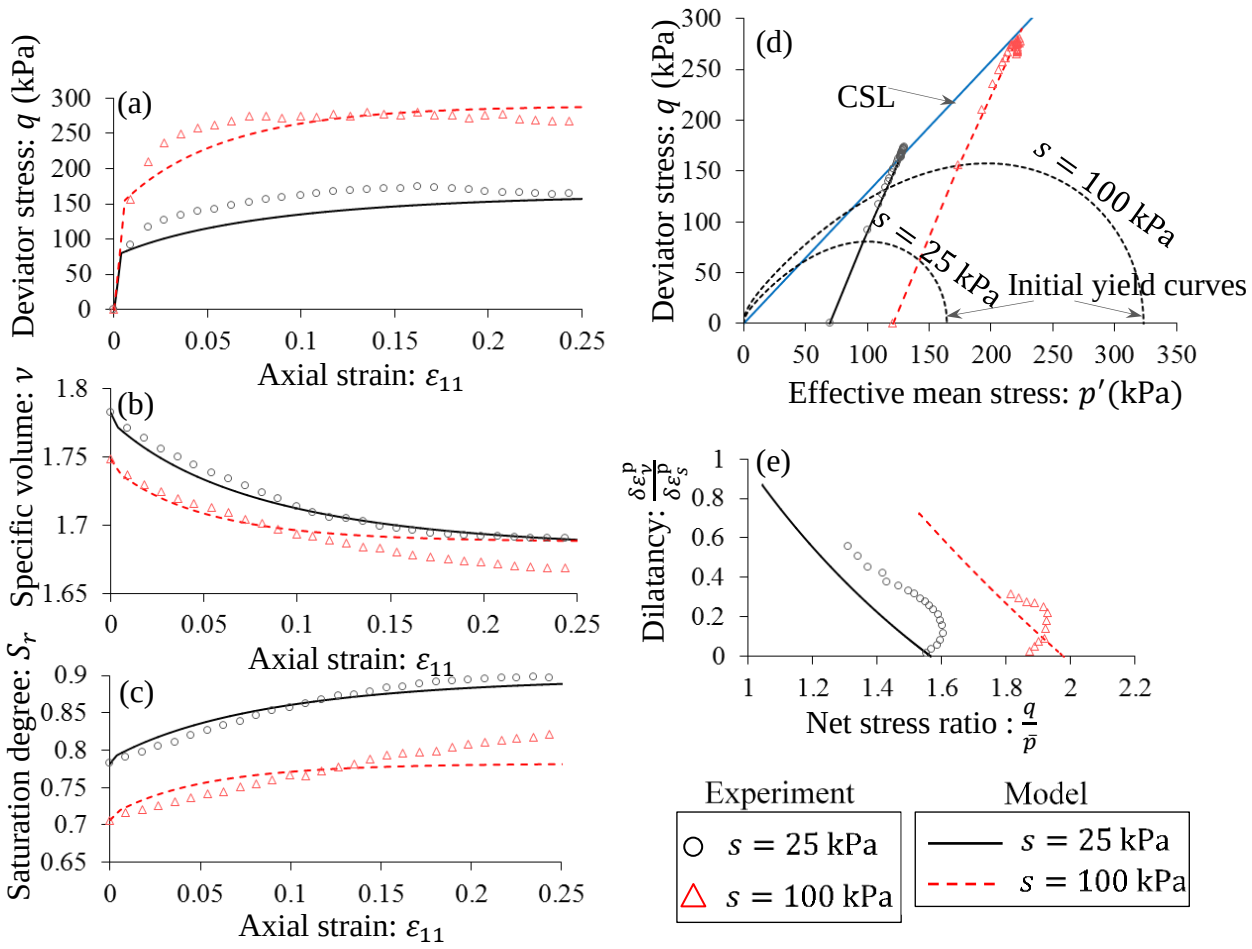

Figure 4.22. Effects of suction on the model response in suction-controlled triaxial compression test on compacted Zaoyang clay (after Chen, 2007) (a) $\varepsilon_{11} - q$ (b) $\varepsilon_{11} - v$ (c) $\varepsilon_{11} - S_r$ (d) $p' - q$ (e) $\frac{q}{\bar{p}} - \frac{\delta\varepsilon_v^p}{\delta\varepsilon_s^p}$

It can be seen in Figure 4.22a that very slight softening responses can be seen while volumetric strain indicates compaction (hardening trend; see Figure 4.22d) and saturation degree increases in this test. However, the softening behaviour, in this case, is minor and may be attributed to the effects of inhomogeneity at the grain scale that are hard or impossible to account for in a continuum model. For example, both grain size and pore size distributions vary in the specimen, resulting in local actions (such as pore collapse and grain rearrangements) that are different across the whole specimen. Due to these local inhomogeneities, the macro response can slightly vary from the overall hardening trend. A continuum model (that is built on the assumption of homogenous deformation at the scale of a Representative Volume Element (REV), well above the grain scale) cannot capture the effects of local inhomogeneities below the RVE scale.

Kurnell sand, constant suction tests (Russell, 2004)

The shear behaviour of the model is next investigated using data obtained from drained triaxial tests on Kurnell sand at $s = 0$ kPa; 100 kPa and 200 kPa with the net confining pressure $\bar{\sigma}_{33} = 50$ kPa (Russell, 2004). This example uses the experimental results of $s = 0$ kPa to calibrate and obtain the following parameters $\kappa = 0.01$; $G = 4300$ kPa; $\lambda = 0.25$; $p'_{c0} = 600$ kPa; $r = 2.5$; $M = 1.28$ and $\alpha = 0.45$. Other parameters: $\kappa_h = 0.004$; $p'_R = 363.31$ kPa; $\mu = 0.0601$ kPa^{-1}; $\xi = 0.6$; $\beta = 0.05$; $p_b = 70$ kPa are calibrated to best fit the test results at $s = 100$ kPa. As depicted in Figure 4.23, the numerical results show reasonable agreement with the experimental data. In particular, higher suctions tend to produce higher yield shear stresses. The model can also give a fairly good prediction of suction-dependent dilation responses (see Figure 4.23b). However, some discrepancies between numerical and experimental data are found at about the peak of shear stress in the case of $s = 100$ kPa and 200 kPa (see Figure 4.23a). This is probably due to the ignorance of strain localisation.

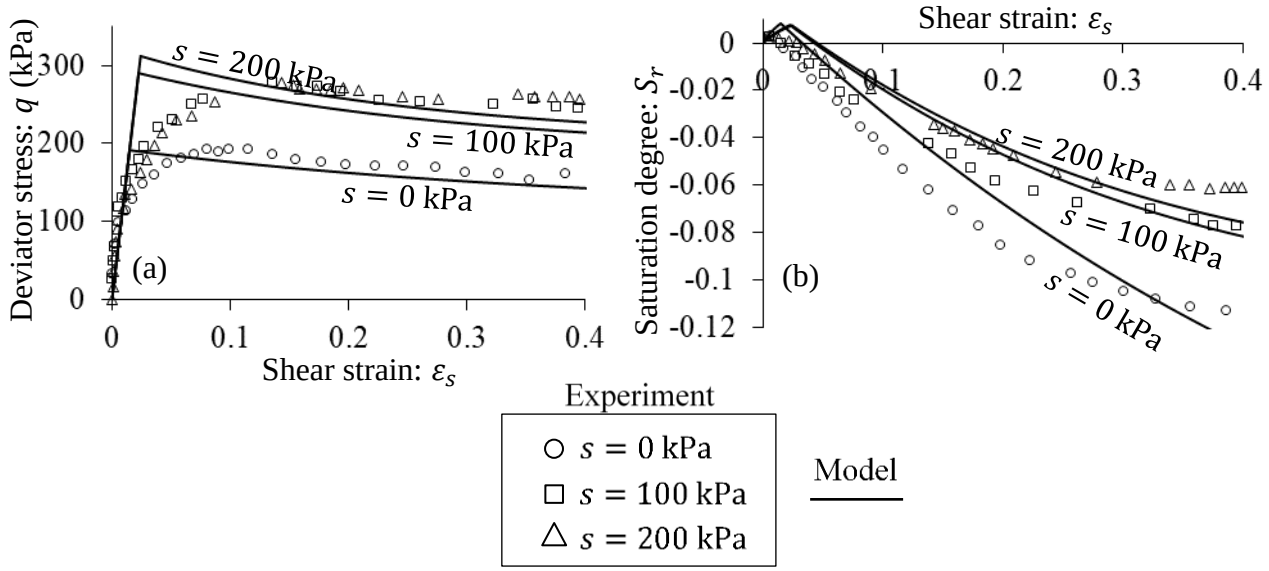

Figure 4.23. Validation with a drained triaxial compression test on the Kurnell sand (after Russell, 2004) (a) $\varepsilon_s - q$ (b) $\varepsilon_s - \varepsilon_v$

Sand-silt-kaolinite mixture, constant water content tests (Maleki & Bayat, 2012)

The model performance is further assessed using the triaxial shearing test on compacted dry sand-silt-kaolinite mixture under the condition of constant gravimetric water content (Maleki & Bayat, 2012). The following model parameters are calibrated using experimental results of $w = 6.1\%$: $\kappa = 0.006$; $\lambda = 0.15$; $M = 1.54$; $G = 7000$ kPa; $\kappa_h = 0.15$; $p'_R = 143.41$ kPa; $\mu = 0.0589$ kPa^{-1}; $\xi = 0.372$; $p'_{c0} = 300$ kPa; $r = 1.85$; $\alpha = 0.55$; $\beta = 0.5$; $p_b = 90$ kPa. The plot presented in

Figure 4.24 is obtained results at two levels of the constant water content of $w = 6.1\%$ and 7.23%, under a net radial stress of $\bar{\sigma}_{33} = 50$ kPa.

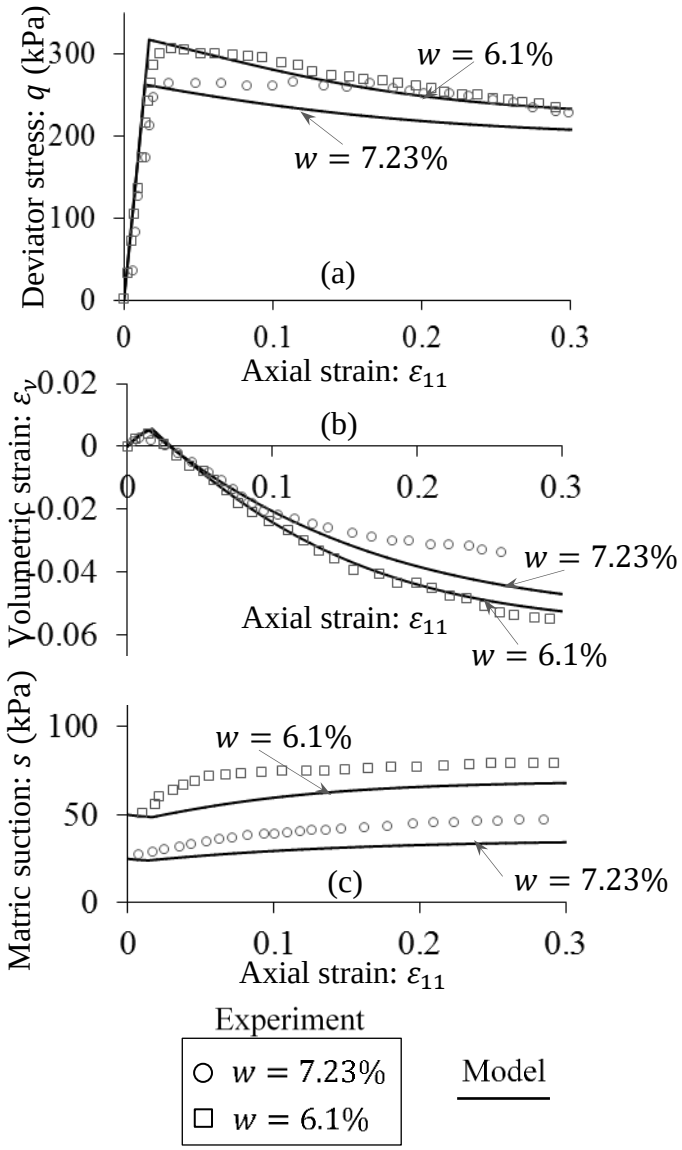

Figure 4.24. Effects of different values of gravimetric water content on the model response under undrained triaxial compression tests on the compacted dry sand-silt-kaolinite mixture (Maleki & Bayat, 2012) (a) $\varepsilon_{11} - q$ (b) $\varepsilon_{11} - \varepsilon_v$ (c) $\varepsilon_{11} - s$

The results in Figure 4.24 show the capability of the model in reproducing the experimental trend drawn from the undrained triaxial compression test. The abrupt slope change in Figure 4.24a is a typical feature and also a limitation of elastoplastic models in capturing the smooth transition from elastic to plastic behaviour. Improvement to capture this smooth transition using sub-loading surface (Salomoni & Fincato, 2012) or a unification of hypo-plastic and elastoplastic theories (Einav, 2012). In this test, a dilation response is observed in which deviatoric stress and volumetric strain initially experience a rapid increase before reaching a peak and then a drop until they become stable at the

critical state, while suction follows the opposite trend. The influence of different gravimetric water contents on the undrained shear behaviour is also reflected in the behaviour of the proposed model. The shear strength is observed to be higher, and the change of suction is more remarkable at lower gravimetric water content. The volumetric strain is more dilative if w decreases.

Bourke silt, constant suction tests (Uchaipichat, 2005; Uchaipichat & Khalili, 2009)

In the next example, the shearing stage of Bourke silt-SCT (Uchaipichat, 2005; Uchaipichat & Khalili, 2009) is used to validate and demonstrate the performance of the model. This test was conducted at three levels of imposed suction $s = 0$ kPa, $s = 100$ kPa and $s = 300$ kPa. The net confining pressure is controlled at $\bar{\sigma}_{33} = 50, 100$ and 150 kPa during shearing. The parameter set of this example, as obtained in Section 4.4, is summarized as follows: $\kappa = 0.006$; $\lambda = 0.09$; $M = 1.17$; $G = 7000$ kPa; $\kappa_h = 0.16$; $p'_R = 140.41$ kPa; $\mu = 0.0229$ kPa^{-1}; $\xi = 0.652$; $p'_{c0} = 200$ kPa; $r = 1.818$; $\alpha = 0.5$; $\beta = 0.05$; $p_b = 70$ kPa. Figures 4.25-4.27 show the comparison between experimental and numerical results on deviatoric stress and volumetric strain plotted against the shear strain. A good match between the results obtained from the numerical analyses and their experimental counterparts can be seen, except some minor discrepancies in the case of $s = 300$ kPa and $\bar{\sigma}_{33} = 150$. These mismatches may be results of using homogeneous assumption, ignoring shear localisation, especially when softening occurs (e.g. $\bar{\sigma}_{33} = 50$ kPa, $s = 0$ kPa). The effects of strain localisation have not yet been considered in this model despite its importance for the failure mechanism of soils (Hashiguchi & Tsutsumi, 2007; Mroginski et al., 2011; Nguyen et al., 2016; Nguyen & Bui, 2020). The readers can refer to Nguyen et al. (2016) and Nguyen & Bui (2020) for issues and treatments for localisation effects at the constitutive level. The current approach will be improved in Chapter 5 to take into account the effects of strain localisation, using the framework proposed in Nguyen & Bui (2020).

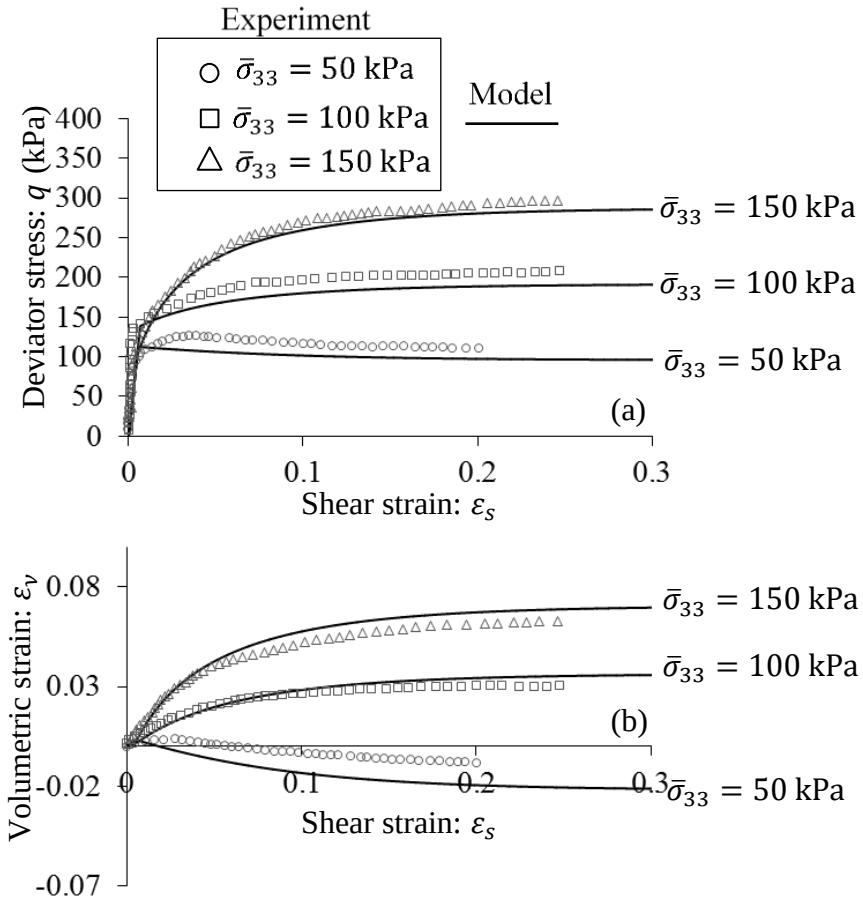

Figure 4.25. Drained triaxial compression tests on Bourke silt at $s = 0$ kPa (after Uchaipichat 2005; Uchaipichat & Khalili, 2009) (a) $\varepsilon_s - q$ (b) $\varepsilon_s - \varepsilon_v$

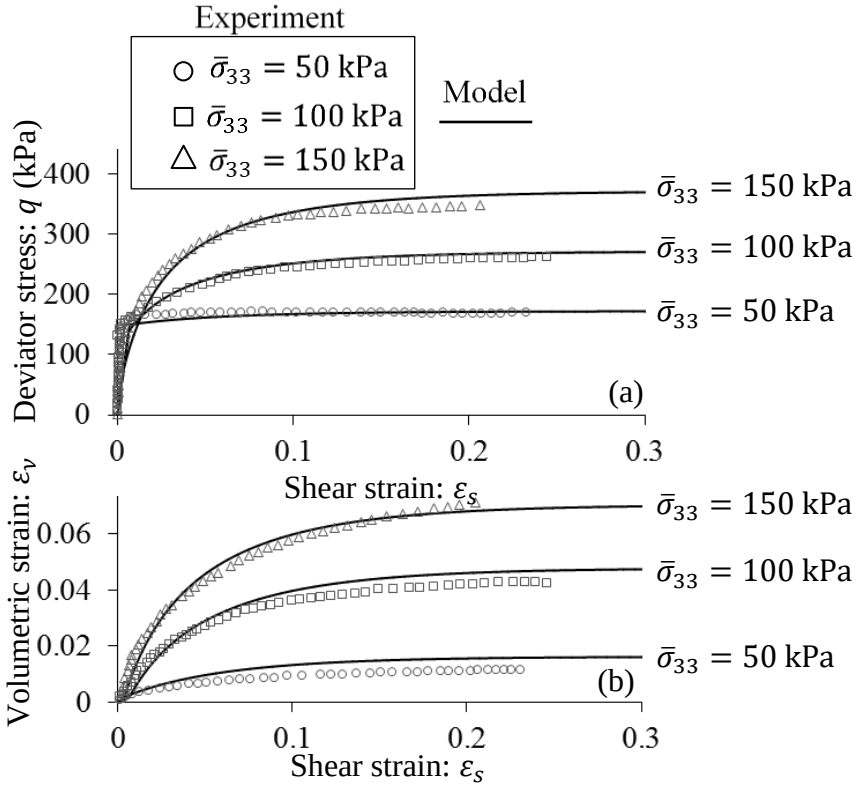

Figure 4.26. Drained triaxial compression tests on Bourke silt at $s = 100$ kPa (after Uchaipichat 2005; Uchaipichat & Khalili, 2009) (a) $\varepsilon_s - q$ (b) $\varepsilon_s - \varepsilon_v$

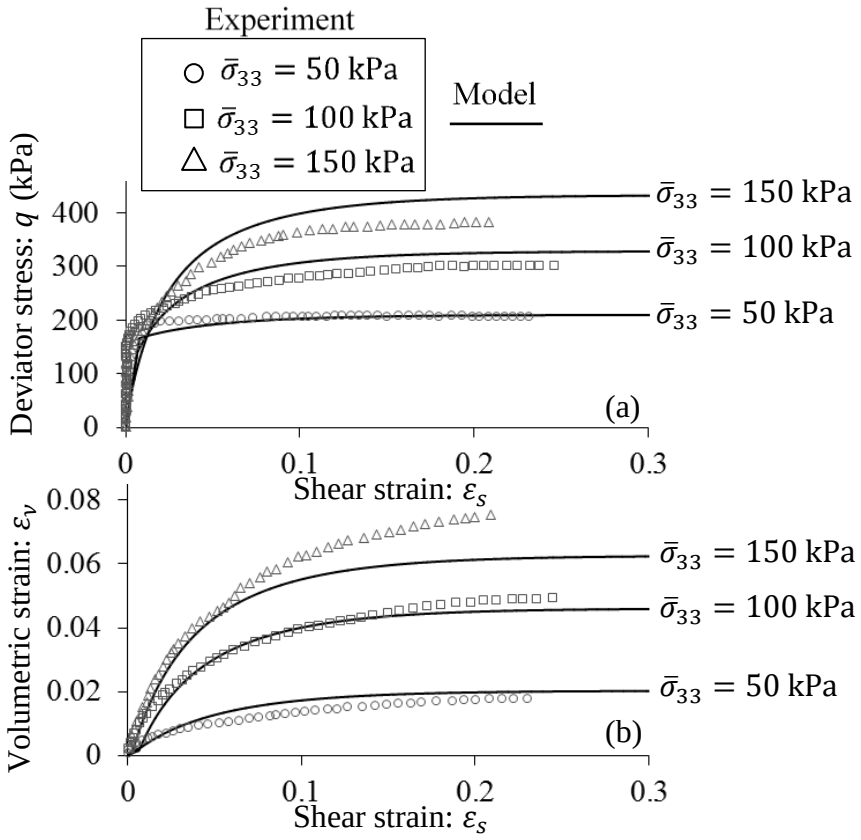

Figure 4.27. Drained triaxial compression tests on Bourke silt at $s = 300$ kPa (after Uchaipichat 2005; Uchaipichat & Khalili, 2009) (a) $\varepsilon_s - q$ (b) $\varepsilon_s - \varepsilon_v$

4.5.3. Model performance under complex loading conditions

Based on the above validation, the proposed model is subjected to a series of combined mechanical-hydraulic loading paths using the same set of parameters for Bourke silt-SCT to explore its performance further. Five loading paths starting at different states are shown in Figure 4.28. In path 1, the soil specimen is isotropically compressed in the saturated state from A ($\bar{p} = 1$ kPa, $v = 1.8, s = 0, S_r = 1$) to B ($\bar{p} = 40$ kPa), C ($\bar{p} = 70$ kPa), D ($\bar{p} = 100$ kPa) and beyond. Path 2 is the drying process at constant net mean stresses of $\bar{p} = 40$ kPa, 70 kPa and 100 kPa from B, C and D to B', C' and D', respectively, to reach $s = 50$ kPa. Another isotropic loading initiated from B' is carried out under constant suction of $s = 50$ kPa in path 3. BB_2, CC_2 and DD_2 are drained shearing loading path 4 when the soil specimen is fully saturated. Path 5 (B'B'$_2$, C'C'$_2$, D'D'$_2$) is the suction-controlled triaxial shearing test at $s = 50$ kPa.

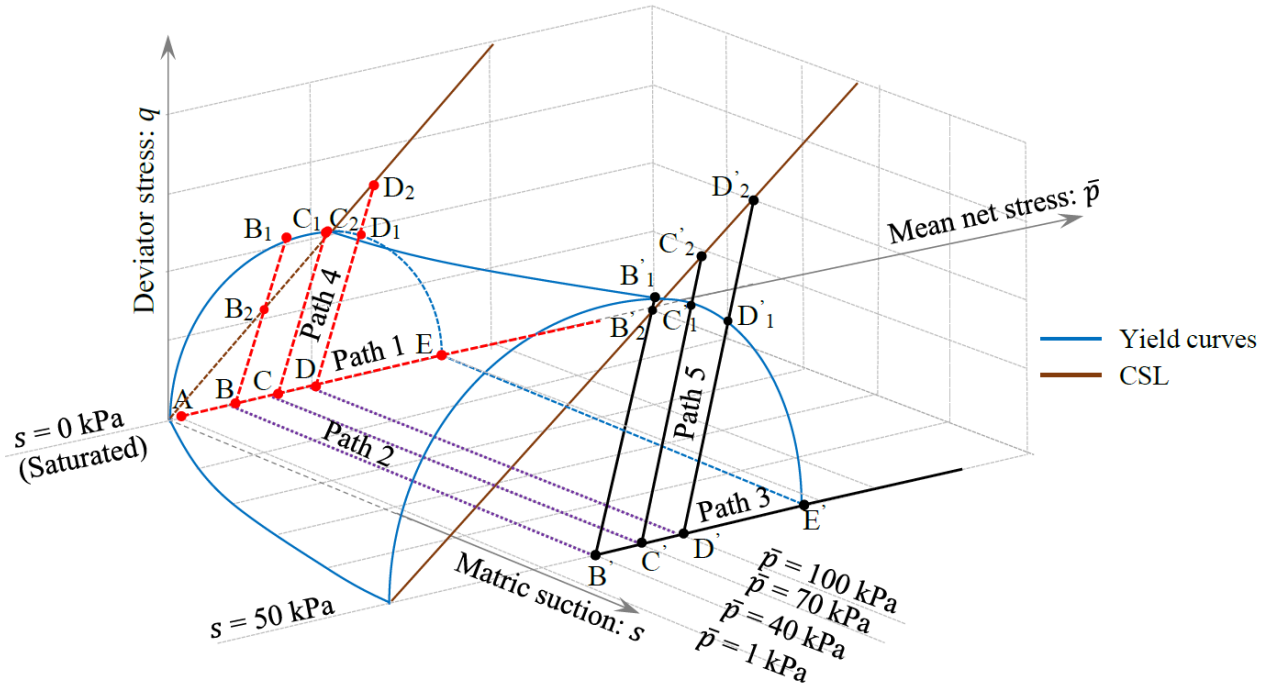

Figure 4.28. Loading and hydraulic paths in $(\bar{p}, q, s)$ space

The numerical results on paths 1,2, and 3 are plotted in Figure 4.29. The shearing stress paths 4 and 5 are illustrated in both the (p', q) and $(\bar{p}, q)$ spaces, as seen in Figure 4.30. Figures 4.31-4.32 plots the deviatoric stress, volumetric strain, saturation degree and dissipation ratios against the axial strain for paths 4 and 5, respectively. Figures 4.29-4.32 demonstrate that the model behaves as expected under the saturated condition where the hydraulic dissipation ratio R_h (hydraulic/total) remains zero during isotropic compression and shearing under $s = 0$ kPa. The water retention curve depicted in Figure 29d shows the variation of saturation from high (at B, C, D) to low (at B', C', D') produced by the model. This demonstrates the capability of the model in capturing a smooth transition from fully saturated to saturated conditions.

As illustrated in Figures 4.30-4.32, the sheared sample first experiences elastic response where early parts of stress paths 4 and 5 are entirely located inside the initial yield surfaces. Plastic response with the activation and development of irrecoverable changes in strain and saturation degree takes place after these paths cross the initial yield surfaces. Coupled hydro-mechanical dissipation dominated by shear dissipation can be seen in Figures 4.31d-f and Figures 4.32d-f. Thereafter, with further shearing, the evolutions of shear stress, volumetric strain and saturation degree gradually stop and attain the steady state at which only the change of shear strain exists. At this state, the dissipation ratios R_v (between volumetric and total) and R_h (between hydraulic and total) approach zero while R_s (shear/total) is equal to 1.

The proper unified forms of yield surface, flow rules and hardening law endow the model with advantages in capturing gradual transitions between hardening, perfect plasticity and softening responses with the changes of net confining pressure and suction. As sketched in Figure 4.31-4.32, the proposed hydro-mechanical coupling can capture different responses, from hardening ($\bar{\sigma}_{33} =$ 100 kPa at $s = 0$ kPa; $\bar{\sigma}_{33} = 70, 100$ kPa at $s = 50$ kPa), to perfect plasticity ($\bar{\sigma}_{33} = 70$ kPa at $s =$ 0 kPa) and softening ($\bar{\sigma}_{33} = 40$ kPa at $s = 0$ kPa; and $\bar{\sigma}_{33} = 40$ kPa at $s = 50$ kPa). To illustrate, during shearing in the yielding stage, the contractive/hardening response involves the increase in deviatoric stress and volumetric strain corresponding to the decrease in the positive value of R_v and the rise in R_s. These features are consistent with what is observed in Figure 4.30 that shearing stress paths first reach initial yield curves (with $p' > \frac{1}{r} p'_{c(us)}$) and then make loading surfaces more expansive before touching CSL. For the response of perfect plasticity, shear strength and volumetric strain are unchanged, whereby $R_v \approx 0$ and $R_s \approx 1$ from the initial yield point to the end of the shearing process. In this case, Figure 4.30 illustrates that the stress path traverses the intersection point between the initial yield curve and CSL at which $p' = \frac{1}{r} p'_{c(us)}$. The softening behaviour follows the opposite trend in $q, \varepsilon_v, S_r, R_v$ and R_s to that of the hardening behaviour. Such a dilative phenomenon is also associated with physical mechanisms observed in Figure 4.30. In this case, after crossing CSL, stress paths keep moving towards reaching yield curves with $p' < \frac{1}{r} p'_{c(us)}$. With further shearing, they then go back and touch CSL to obtain a steady-state where the yield surface is narrowed. Drawing on the above analyses, the more dilative response is observed at lower values of radial stress and suction. The net confining pressure plays a more significant role in controlling the contraction-dilation transition owing to its dominance in the soil skeleton stress.

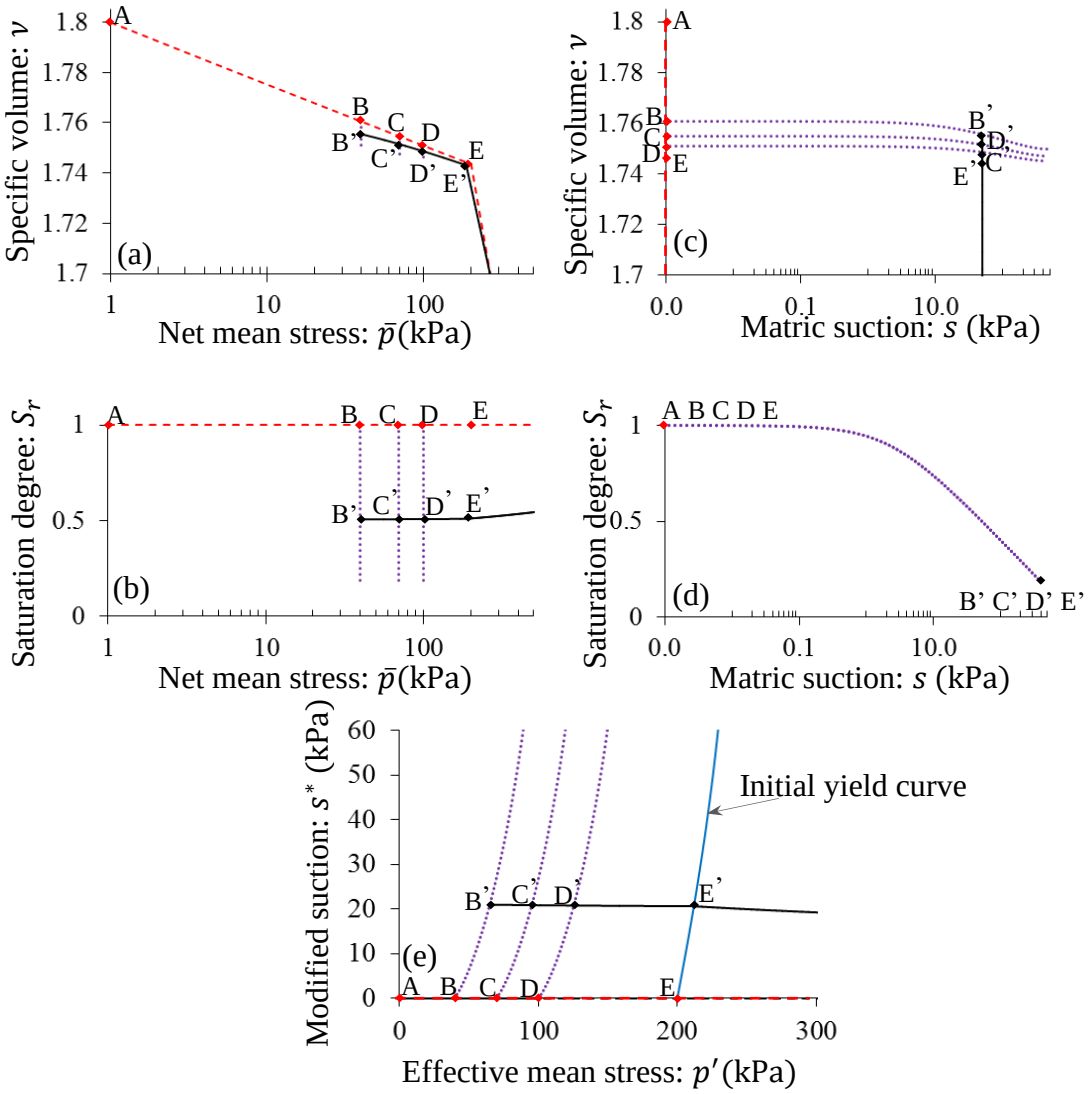

Figure 4.29. The behaviour of the proposed model under load paths 1, 2 and 3 (a) $\bar{p} - \nu$ (b) $s - \nu$ (c) $\bar{p} - S_r$ (d) $s - S_r$ (e) $p' - s^*$

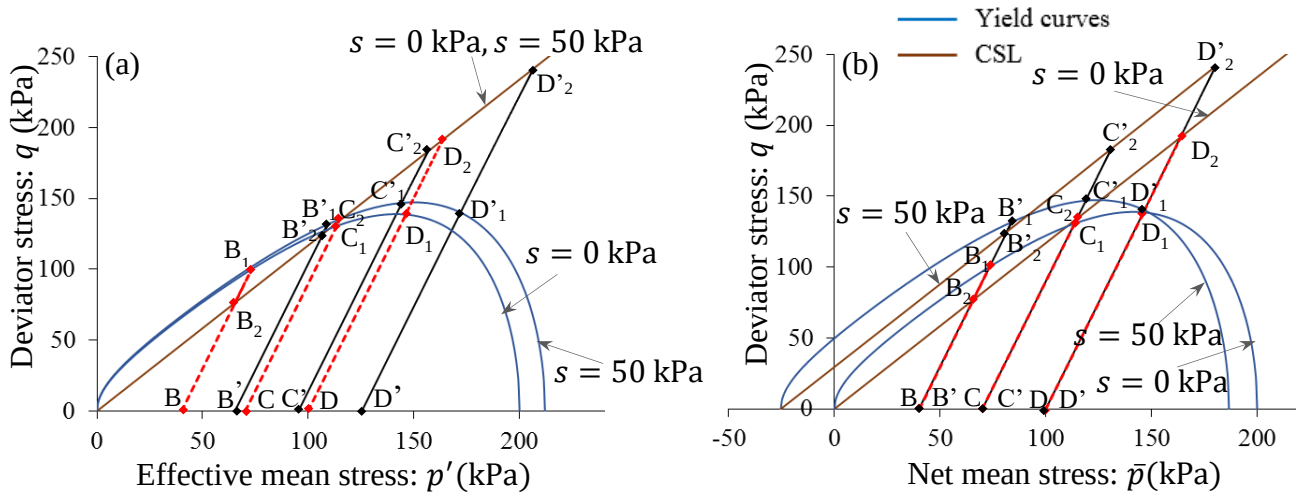

Figure 4.30. Initial yield surface and stress paths of the proposed model under load paths 4 and 5 (a) $p' - q$ (b) $\bar{p} - q$

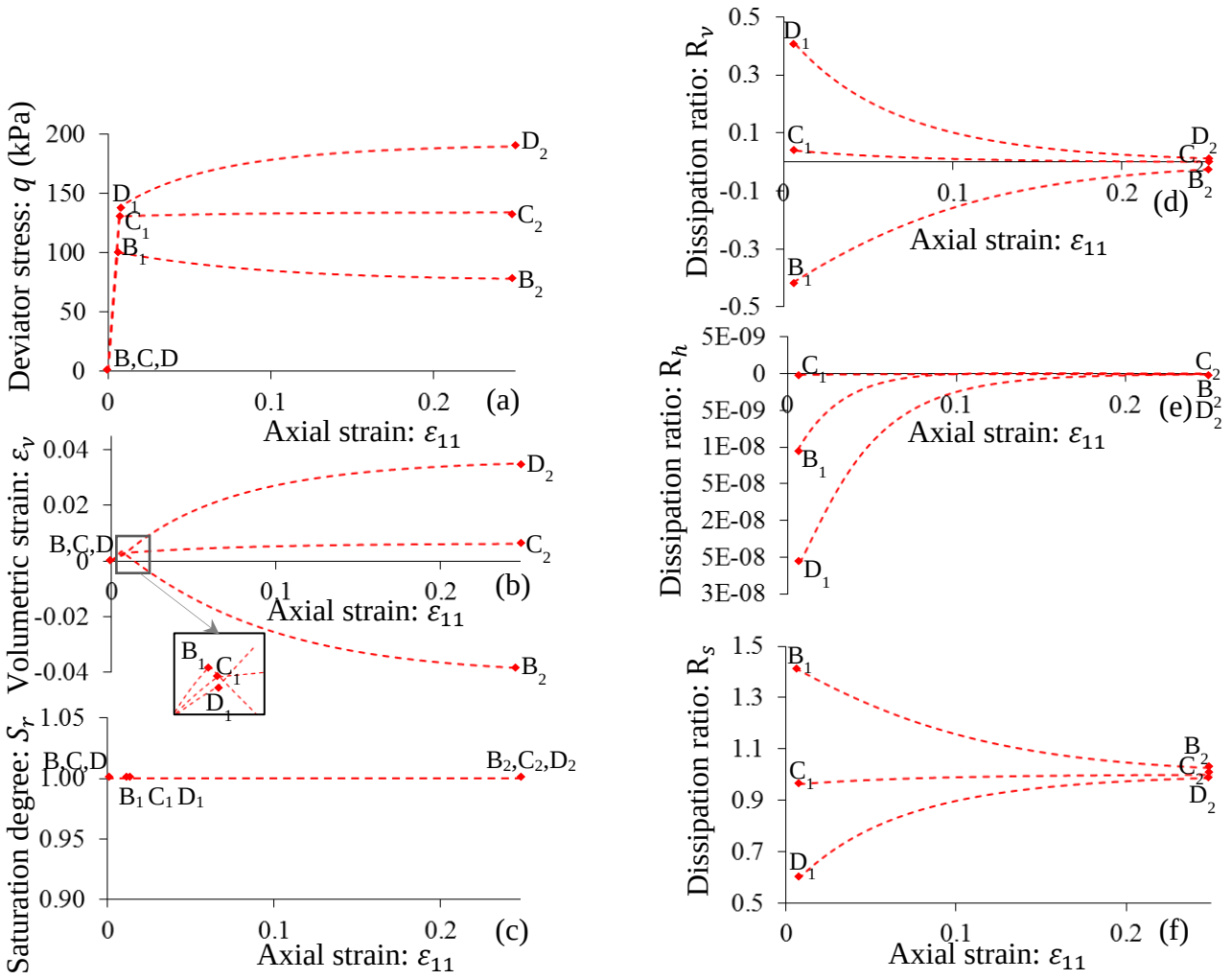

Figure 4.31. The behaviour of the proposed model under load path 4 and $s = 0$ kPa (a) $\varepsilon_{11} - q$ (b) $\varepsilon_{11} - \varepsilon_v$ (c) $\varepsilon_{11} - S_r$ (d) $\varepsilon_{11} - \mathrm{R}_v$ (e) $\varepsilon_{11} - \mathrm{R}_s$ (f) $\varepsilon_{11} - \mathrm{R}_h$

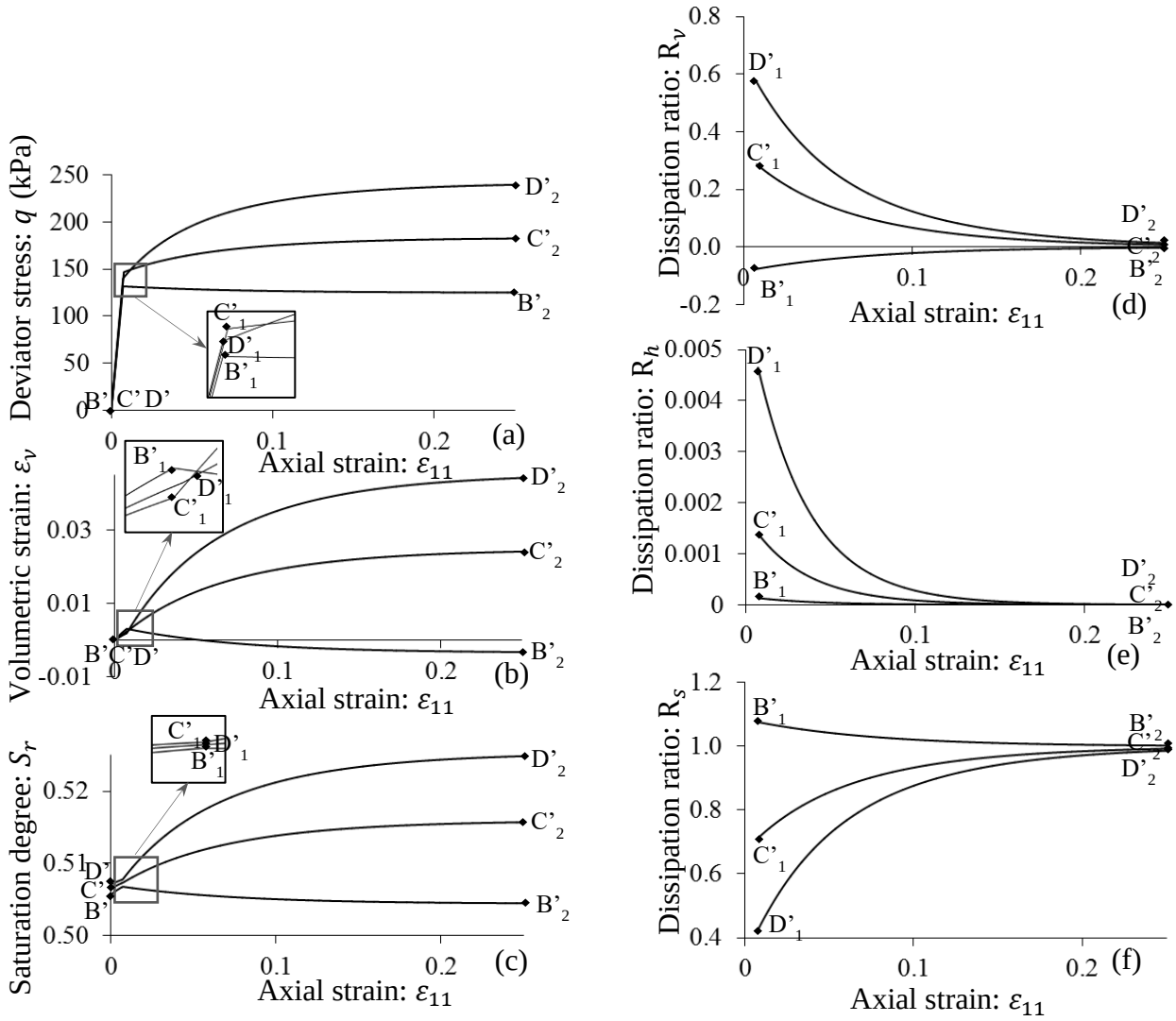

Figure 4.32. The behaviour of the proposed model under load path 5 and $s = 50$ kPa (a) $\varepsilon_{11} - q$ (b) $\varepsilon_{11} - \varepsilon_v$ (c) $\varepsilon_{11} - S_r$ (d) $\varepsilon_{11} - \mathrm{R}_v$ (e) $\varepsilon_{11} - \mathrm{R}_s$ (f) $\varepsilon_{11} - \mathrm{R}_h$

4.6. Closure

In the proposed critical state constitutive model for partially saturated soils derived from the generic thermodynamics-based approach in Chapter 3, the current study strikes a good balance between rigour, simplicity, number of parameters and performance. The rigour in the formulation of the proposed model guarantees thermodynamic admissibility. The obtained model described in equations (4.89-4.94) is simple in its structure given it possesses a single yield surface with effects of both stress and suction, and corresponding evolution laws for plastic strains and irreversible saturation. This leads to strong hydro-mechanical coupling through the simultaneous activation of both hydraulic and mechanical dissipative mechanisms upon yielding, and simplifies the implementation given there is only one yield surface. This continuum scale feature reflects the inseparable nature of the interaction between grain rearrangement and liquid-bridge redistribution at the grain scale while removing the

use of a separate SWCC in the model. Different hydro-mechanical responses obtained in wetting-drying and loading-unloading paths are the consequences of this strong hydro-mechanical coupling in the constitutive structure. This feature makes the current model distinct from existing models for partially saturated soils, which usually disregard or underestimate mechanisms of hydromechanical coupling at the grain level to evaluate how close the constitutive formulations are to given experimental observations of unsaturated soils at the continuum level as discussed in Chapter 2 and hence use multiple yield surfaces. Furthermore, the concept of critical state is well reflected in the model where only the sliding of soil grains governs the whole energy dissipation with the vanishing of the evolutions of shear stress, volumetric strain and saturation degree at the critical state. The model requires only 13 parameters, of which 5 are for a classical Modified Cam Clay model; all of them have been shown in Section 4.4 to be calibrated from standard tests on partially saturated soils. Its efficacy is assessed against a range of experimentally measured behaviour of partially saturated soils, demonstrating the model's predictive capability for a wide range of hydro-mechanical interactions (e.g. hydraulic effects on soil stiffness, dilation, shear strength and mechanical effects on the wetting-drying difference of SWCC). All of the above-mentioned features indicate that the proposed critical state model is able to address a range of requirements for constitutive modelling of partially saturated soils, as reviewed in Chapter 2.

However, it is noted that the proposed critical state model is an example to illustrate the applicability of the generic thermodynamic framework (see Chapter 3) in capturing the coupled hydro-mechanical dissipation of partially saturated soils. Further planned improvements include (i) effects of air-entry suction on yielding, (ii) different forms of NCL under high stresses and more complex loading paths, (iii) anisotropic behaviour, (iv) closed-shape yield surface, and (v) the mechanisms of lower scale grain to grain contacts (e.g. Nguyen & Gan, 2014; Bignonnet et al., 2016; Fang et al., 2017; Nicot & Darve, 2007; Yin et al., 2009) for a mechanism-based expression of effective stress. The incorporation of the mechanisms of localised failure in the constitutive structure discussed and presented in Nguyen & Bui (2020) are also essential. These features will be addressed in future works towards better models for partially saturated soils.

Chapter 5. Meso-macro connection in a mechanism-based approach to constitutive modelling of unsaturated soils under the drained shearing condition

5.1. Introduction

As addressed in Chapter 2, localised failure in geomaterials in general and partially saturated soils in particular results in very different responses in the specimens, with high deformation inside the localisation band and much outside this band. This can be considered as an indispensable mechanism of soil collapse, requiring a new generic constitutive structure taking into account the orientation and thickness of the localisation band (Nguyen et al., 2012, 2014, 2016; Nguyen & Bui, 2020). It is essential to describe intrinsic inelastic mechanisms of the localised failure in variably saturated soils at the meso-macro scale that underpins the macro scale nonlinear responses. In particular, as the assumption on homogeneity in Continuum Mechanics breaks down in post-localisation regime, classical constitutive models for partially saturated soils are no longer valid in this regime. Attempts to capture post-localisation behaviour at the constitutive level are not physically meaningful if not accompanied with enhancements to account for the high strain gradient across the soil sample. A rigorous and systematic thermodynamics-based formulation with two explicitly defined free energy and dissipation potentials (Nguyen & Bui, 2020) is adopted and further developed in this study to correctly describe both pre-and post-localisation responses of partially saturated soils at the constitutive level.

Following the approach of Nguyen & Bui (2020), the kinematics of constitutive structure is enriched, allowing two separate hydro-mechanical responses outside and inside the localisation band to be connected to describe correctly all essential characteristics of the macro behaviour observed in suction-controlled tests on partially saturated soils. Beyond the bifurcation, the material outside the localisation zone is assumed to undergo negligible irreversible deformation, while irreversible behaviour inside this localisation zone is the main source of dissipation of the whole volume element under consideration. This irreversible hydro-mechanical behaviour inside the localisation band is described by a constitutive model for partially saturated soils possessing a single yield surface in stress-suction space governing the interdependence of two evolution rules for plastic strain and irrecoverable saturation degree. These two constitutive relationships are linked by the traction and pore pressure continuity condition across the boundary of the shear band. As a result, this allows to naturally derive a criterion for the onset of localised deformation, taking into account the irreversibility between wetting and drying processes, which has not yet been addressed in the

literature. The effects of mechanical behaviour on SWCC can also be naturally reproduced in the evolution of behaviour inside the localisation region, reflecting the inter-dependence of mechanical and hydraulic dissipations at the grain scale. Furthermore, the proposed framework can be backward compatible with classical constitutive models for responses under homogenous and fully saturated conditions, permitting smooth transitions from diffuse to localised failure and from fully to partially saturated states. The size-dependent behaviour is automatically met for any model derived from the proposed constitutive structure, as the size and orientation of shear band and specimen size are taken into account in the generic formulation. The promising features of this approach are elucidated and the behaviour validated against a range of experimental data obtained from drained tests. Details on the model used for irreversible hydro-mechanical behaviour inside the localisation band have been presented in Chapter 3. It is noted that the generic structure of the proposed approach allows the use of any constitutive models for the behaviour at the mesoscale of the localisation band.

This chapter is organised as follows. In Section 5.2, a general thermomechanical framework is presented to describe fundamental relationships. It is followed by formulations of macro constitutive structures for homogeneous irreversible deformation, the onset of localisation and post-localisation behaviour based on the interactions between the hydromechanical response outside and inside the shear band in Section 5.3. Next, Section 5.4 briefly describes the numerical implementation of this generic framework where bifurcation and two-level stress return algorithms are provided, going with several examples of numerical verification. Identification and calibration of model parameters are then briefly presented in Section 5.5. Sections 5.6 and 5.7 are dedicated to presenting performances of this model, which are validated and investigated through a range of numerical examples.

5.2. A generic thermodynamics-based formulation

A generic thermodynamic approach is described in this section to provide a basis for enhancements to the framework considering two scales for partially saturated soils at the constitutive level.

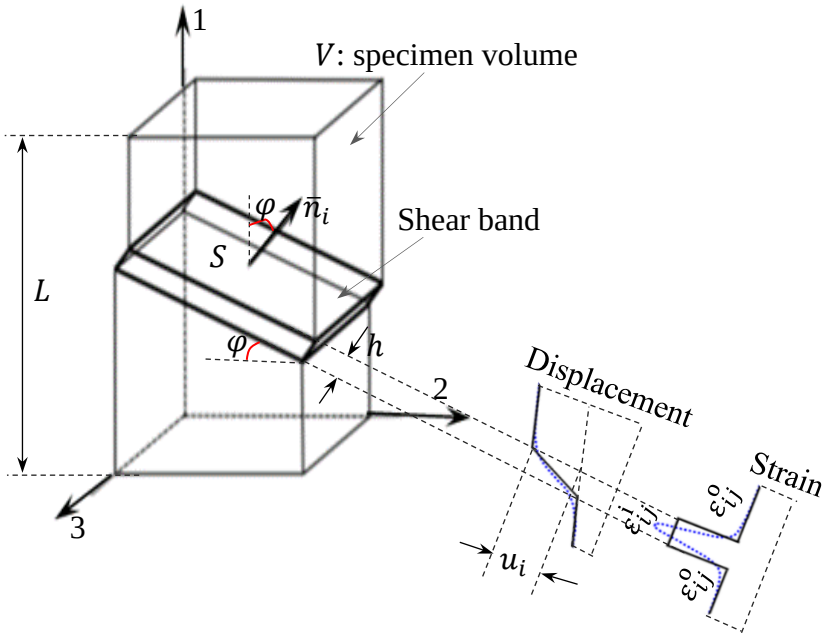

Figure 5.1. A volume element (with volume V) crossed by a finite thickness localisation zone and schematic illustration of displacement and strain profiles in the localised stage of failure.

The key difference between the proposed approach and existing models for partially saturated soils is the details of the shear band. In this framework, only a single tabular shear band is considered for simplicity, although it is acknowledged that the multiple intersecting localisation bands can occur over the sheared specimen (Patil, 2014; Nguyen et al., 2017). As can be seen in Figure 5.1, this band is defined by surface area S, thickness h and normal vector $\bar{n}_i$ representing the orientation. It is embedded within an RVE of arbitrary shape and size with volume V and effective size H' which can be computed from the specimen size and orientation of localisation band through $H' = \frac{V}{S}$.

The volume fraction is introduced as a new parameter capturing the size-dependent behaviour induced by localised failure (Nguyen et al., 2012, 2014, 2016; Nguyen & Bui, 2020):

$$f = \frac{Sh}{V} = \frac{Sh}{SH'} = \frac{h}{H'} \tag{5.1}$$

It is acknowledged that Eq. (5.1) is just an assumption for the sake of simplicity to approximately measure the relative relationship between localised failure and specimen size. Physically, f can vary with loading paths in the post- localisation stage as tackled in (Nguyen & Bui, 2020). However, this feature is not yet considered in the current framework, where f is assumed to be constant.

Given f, the macro strain rate $\dot{\varepsilon}_{ij}$ can be computed as a volume-averaged quantity of strain rates inside $\dot{\varepsilon}^{\mathrm{i}}_{ij}$ and outside $\dot{\varepsilon}^{\mathrm{o}}_{ij}$ the localisation band through the homogenisation as follows (Nguyen et al., 2012):

$$\dot{\varepsilon}_{ij} = (1-f)\dot{\varepsilon}_{ij}^{\mathrm{o}} + f\dot{\varepsilon}_{ij}^{\mathrm{i}} \tag{5.2}$$

The strain rate across the band boundary is not continuous. In this case, a jump between $\dot{\varepsilon}_{ij}^{\mathrm{i}}$ and $\dot{\varepsilon}_{ij}^{\mathrm{o}}$ can be measured from the relative velocity $\dot{u}_i$ between two faces of the localisation band through the following form (Neilsen & Schreyer, 1993) (see Figure 5.1):

$$\dot{\varepsilon}_{ij}^{\mathrm{i}} - \dot{\varepsilon}_{ij}^{\mathrm{o}} = \frac{1}{h}\left(\dot{u}_i \bar{n}_j\right)^{\mathrm{s}} \tag{5.3}$$

From Eqs. (5.2) and (5.3), $\dot{\varepsilon}_{ij}^{\mathrm{o}}$ and $\dot{\varepsilon}_{ij}^{\mathrm{i}}$ can be expressed using primary variables of macro strain rate $\dot{\varepsilon}_{ij}$ and velocity $\dot{u}_i$ as:

$$\dot{\varepsilon}_{ij}^{\mathrm{o}} = \dot{\varepsilon}_{ij} - \frac{f}{h}\left(\dot{u}_i \bar{n}_j\right)^{\mathrm{s}} \tag{5.4}$$

$$\dot{\varepsilon}_{ij}^{\mathrm{i}} = \dot{\varepsilon}_{ij} + \frac{1-f}{h}\left(\dot{u}_i \bar{n}_j\right)^{\mathrm{s}} \tag{5.5}$$

Given the above kinematic enrichment, a generic thermodynamics-based framework is then developed to describe the coupled hydro-mechanical behaviour of partially saturated soils accounting for size effects. The rate of work input $\widetilde{W}$ (Houlsby, 1997; Coussy et al., 2010) (with the tilde sign "$\sim$" representing a pseudo-time-derivative) can be expressed in the form of Bishop's effective stress σ'_{ij} and modified suction s^* as (see Chapter 3):

$$\widetilde{W} = \sigma'_{ij}\dot{\varepsilon}_{ij} + s^*\left(-\dot{S}_r\right) = \left(\sigma_{ij} + sS_r\delta_{ij}\right)\dot{\varepsilon}_{ij} - \bar{\phi}s\dot{S}_r \tag{5.6}$$

where $s^* = \bar{\phi}s$ has been used. In the case of zero air pressure ($p^a = 0$) (assumption iii, Chapter 3) and incompressible solid phase ($\dot{\varepsilon}_{ij}\delta_{ij} = -\dot{\bar{\phi}}$), Eq. (5.6) can be rewritten in the form of total stress σ_{ij} and suction s as:

$$\widetilde{W} = \sigma_{ij}\dot{\varepsilon}_{ij} - s\left(\bar{\phi}\dot{S}_r + S_r\dot{\bar{\phi}}\right) = \sigma_{ij}\dot{\varepsilon}_{ij} + s\left(-\dot{\bar{\phi}}_w\right) \tag{5.7}$$

with $\bar{\phi}_w = \bar{\phi}S_r$ denoting the Lagrangian volumetric water content.

The following energy balance is expressed for the isothermal process (Ziegler, 1983):

$$\widetilde{W} = \widetilde{\Phi} + \Psi \tag{5.8}$$

As previously mentioned in Chapter 2, localised failure induces strong non-homogeneous deformation and saturation within partially saturated soils. In this case, the shear band splits the soil specimen into two separate parts with different responses. Particularly, irrecoverable hydro-mechanical processes can be reasonably assumed to take place within the localisation band, while the behaviour of the surrounding bulk can be reasonably assumed to be recoverable (see Figure 2.31). In

this sense, the Helmholtz free energy of the system can be written considering the configuration of a composite material consisting of two phases as follows:

$$\Psi = (1-f)\Psi^{\mathrm{o}}\left(\varepsilon_{ij}^{\mathrm{o}}, -S_r^{\mathrm{o}}\right) + f\Psi^{\mathrm{i}}\left(\varepsilon_{ij}^{\mathrm{i}}, -S_r^{\mathrm{i}}, \varepsilon_{ij}^{\mathrm{ip}}, -S_r^{\mathrm{ip}}\right) \tag{5.9}$$

in which $\varepsilon_{ij}^{\mathrm{x}}$ and $-S_r^{\mathrm{x}}$ ("x" stands for "i" or "o") are the total strain and saturation degree of the zone "x" with the corresponding Helmholtz energy potential Ψ^{x}. Internal variables $(\varepsilon_{ij}^{\mathrm{ip}}, -S_r^{\mathrm{ip}})$ only appear in Ψ^{i} to indicate that during post-localisation, the energy dissipation process of the whole REV takes place entirely inside the localisation band.

The following form can be obtained after substituting the differential of Eq. (5.9) into Eq. (5.8):

$$\widetilde{W} = \widetilde{\Phi} + (1-f)\left[\frac{\partial\Psi^{\mathrm{o}}}{\partial\varepsilon_{ij}^{\mathrm{o}}}\dot{\varepsilon}_{ij}^{\mathrm{o}} + \frac{\partial\Psi^{\mathrm{o}}}{\partial(-S_r^{\mathrm{o}})}\left(-\dot{S}_r^{\mathrm{o}}\right)\right] + f\left[\frac{\partial\Psi^{\mathrm{i}}}{\partial\varepsilon_{ij}^{\mathrm{i}}}\dot{\varepsilon}_{ij}^{\mathrm{i}} + \frac{\partial\Psi^{\mathrm{i}}}{\partial(-S_r^{\mathrm{i}})}\left(-\dot{S}_r^{\mathrm{i}}\right) + \frac{\partial\Psi^{\mathrm{i}}}{\partial\varepsilon_{ij}^{\mathrm{ip}}}\dot{\varepsilon}_{ij}^{\mathrm{ip}} + \frac{\partial\Psi^{\mathrm{i}}}{\partial\left(-S_r^{\mathrm{ip}}\right)}\left(-\dot{S}_r^{\mathrm{ip}}\right)\right] \tag{5.10}$$

The material responses are assumed to be homogeneous for a unit volume element in each zone outside and inside the shear band. Therefore, the constitutive relationships in Eqs. (3.92-3.94) of Chapter 3 can be used to define the corresponding stress-like variables of each zone as follows:

$$\frac{\partial\Psi^{\mathrm{x}}}{\partial\varepsilon_{ij}^{\mathrm{x}}} = \sigma_{ij}'^{\mathrm{x}} = \sigma_{ij}^{\mathrm{x}} + s^{\mathrm{x}}S_r^{\mathrm{x}}\delta_{ij} \tag{5.11}$$

$$\frac{\partial\Psi^{\mathrm{x}}}{\partial(-S_r^{\mathrm{x}})} = s^{*\mathrm{x}} = \bar{\phi}^{\mathrm{x}}s^{\mathrm{x}} \tag{5.12}$$

where $\sigma_{ij}'^{\mathrm{x}}$, σ_{ij}^{x}, $s^{*\mathrm{x}}$, s^{x} and $\bar{\phi}^{\mathrm{x}}$ are Cauchy effective stress, Cauchy total stress (or Cauchy net stress $\bar{\sigma}_{ij}$ due to $p^a = 0$), modified suction, suction and Lagrangian porosity of zone "x", respectively.

Substituting Eqs. (5.11) and (5.12) into Eq. (5.10) leads to:

$$\widetilde{W} = \widetilde{\Phi} + (1-f)\sigma_{ij}^{\mathrm{o}}\dot{\varepsilon}_{ij}^{\mathrm{o}} + f\sigma_{ij}^{\mathrm{i}}\dot{\varepsilon}_{ij}^{\mathrm{i}} + (1-f)s^{\mathrm{o}}\left(-\dot{\bar{\phi}}_w^{\mathrm{o}}\right) + fs^{\mathrm{i}}\left(-\dot{\bar{\phi}}_w^{\mathrm{i}}\right) + f\left[\frac{\partial\Psi^{\mathrm{i}}}{\partial\varepsilon_{ij}^{\mathrm{ip}}}\dot{\varepsilon}_{ij}^{\mathrm{ip}} + \frac{\partial\Psi^{\mathrm{i}}}{\partial\left(-S_r^{\mathrm{ip}}\right)}\left(-\dot{S}_r^{\mathrm{ip}}\right)\right] \tag{5.13}$$

with $\bar{\phi}_w^{\mathrm{x}} = \bar{\phi}^{\mathrm{x}}S_r^{\mathrm{x}}$ being the Lagrangian volumetric water content associated with region "x".

After substituting Eqs. (5.4-5.5) in the above expression and rearranging it, the following expression can be obtained:

$$\widetilde{W} = \widetilde{\Phi} + \left[(1-f)\sigma_{ij}^{\mathrm{o}} + f\sigma_{ij}^{\mathrm{i}}\right]\dot{\varepsilon}_{ij} - \frac{f(1-f)}{h}\left(\sigma_{ij}^{\mathrm{o}} - \sigma_{ij}^{\mathrm{i}}\right)\left(\dot{u}_i\bar{n}_j\right)^{\mathrm{s}} + (1-f)s^{\mathrm{o}}\left(-\dot{\phi}_w^{\mathrm{o}}\right) + fs^{\mathrm{i}}\left(-\dot{\phi}_w^{\mathrm{i}}\right) + f\left[\frac{\partial\Psi^{\mathrm{i}}}{\partial\varepsilon_{ij}^{\mathrm{ip}}}\dot{\varepsilon}_{ij}^{\mathrm{ip}} + \frac{\partial\Psi^{\mathrm{i}}}{\partial\left(-s_r^{\mathrm{ip}}\right)}\left(-\dot{S}_r^{\mathrm{ip}}\right)\right] \quad (5.14)$$

For suction-controlled (drained) triaxial shear tests, the drainage process is carried out over a long period. The continuity can be usually observed in the relative flow vector of fluid mass between spaces inside and outside the shear band. Therefore, pore pressure can be reasonably assumed to be continuous ($s = s^{\mathrm{i}} = s^{\mathrm{o}}$) across the localisation band (Mroginski et al., 2011; Schiava & Etse, 2006; Borja et al., 2004). With this condition, Eq. (5.14) can be rewritten as:

$$\widetilde{W} = \widetilde{\Phi} + \left[(1-f)\sigma_{ij}^{\mathrm{o}} + f\sigma_{ij}^{\mathrm{i}}\right]\dot{\varepsilon}_{ij} - \frac{f(1-f)}{h}\left(\sigma_{ij}^{\mathrm{o}} - \sigma_{ij}^{\mathrm{i}}\right)\left(\dot{u}_i\bar{n}_j\right)^{\mathrm{s}} + s\left[(1-f)\left(-\dot{\phi}_w^{\mathrm{o}}\right) + f\left(-\dot{\phi}_w^{\mathrm{i}}\right)\right] + f\left[\frac{\partial\Psi^{\mathrm{i}}}{\partial\varepsilon_{ij}^{\mathrm{ip}}}\dot{\varepsilon}_{ij}^{\mathrm{ip}} + \frac{\partial\Psi^{\mathrm{i}}}{\partial\left(-s_r^{\mathrm{ip}}\right)}\left(-\dot{S}_r^{\mathrm{ip}}\right)\right] \quad (5.15)$$

For the comparison purpose, Eq. (5.7) is recalled as follows:

$$\widetilde{W} = \sigma_{ij}\dot{\varepsilon}_{ij} + s\left(-\dot{\phi}_w\right) \quad (5.16)$$

The comparison between Eqs. (5.15) and (5.16) allows obtaining the following relationships:

$$\sigma_{ij} = (1-f)\sigma_{ij}^{\mathrm{o}} + f\sigma_{ij}^{\mathrm{i}} \quad (5.17)$$

$$\left(-\dot{\phi}_w\right) = (1-f)\left(-\dot{\phi}_w^{\mathrm{o}}\right) + f\left(-\dot{\phi}_w^{\mathrm{i}}\right) \quad (5.18)$$

Eqs. (5.17) and (5.18) present the weighted sum of the two stress fields and volumetric water contents inside and outside the shear band to determine macro homogenised stress and volumetric water content.

In this case, the dissipation potential can be obtained as:

$$\widetilde{\Phi} = \frac{f(1-f)}{h}\left(\sigma_{ij}^{\mathrm{o}} - \sigma_{ij}^{\mathrm{i}}\right)\left(\dot{u}_i\bar{n}_j\right)^{\mathrm{s}} - f\left[\frac{\partial\Psi^{\mathrm{i}}}{\partial\varepsilon_{ij}^{\mathrm{ip}}}\dot{\varepsilon}_{ij}^{\mathrm{ip}} + \frac{\partial\Psi^{\mathrm{i}}}{\partial\left(-s_r^{\mathrm{ip}}\right)}\left(-\dot{S}_r^{\mathrm{ip}}\right)\right] \geq 0 \quad (5.19)$$

It can be assumed that the energy dissipation is fully governed by irreversible changes of strain and saturation degree inside the localisation band, given the strain rate $\dot{\varepsilon}_{ij}^{\mathrm{i}}$ (Eq. (5.5)) inside the localisation band and its irreversible part, $\dot{\varepsilon}_{ij}^{\mathrm{ip}}$, are the primary variables governing the inelastic mechanics' behaviour inside this band. This is an assumption that leads to a physically meaningful condition for internal equilibrium and useful constitutive structure (Nguyen & Bui, 2020). Thus, the first term in Eq. (5.19) should vanish:

$$\left(\sigma_{ij}^{\mathrm{o}} - \sigma_{ij}^{\mathrm{i}}\right)\left(\dot{u}_i\bar{n}_j\right)^{\mathrm{s}} = 0 \quad (5.20)$$

Eq. (5.20) must be met for any non-zero velocity jump $\dot{u}_i$. Hence, for a non-trivial solution, the following condition is required:

$$\left(\sigma_{ij}^{\mathrm{o}} - \sigma_{ij}^{\mathrm{i}}\right)\bar{n}_j = 0 \tag{5.21}$$

It can be seen that Eq. (5.21) is the classical traction equilibrium condition across the boundary of the localisation zone, which appears naturally from the proposed thermodynamic formulation.

Given the condition in Eq. (5.21), the dissipation in Eq. (5.19) now reduces to:

$$\widetilde{\Phi} = -f\left[\frac{\partial \Psi^{\mathrm{i}}}{\partial \varepsilon_{ij}^{\mathrm{ip}}}\dot{\varepsilon}_{ij}^{\mathrm{ip}} + \frac{\partial \Psi^{\mathrm{i}}}{\partial\left(-S_r^{\mathrm{ip}}\right)}\left(-\dot{S}_r^{\mathrm{ip}}\right)\right] \geq 0 \tag{5.22}$$

Or,

$$\widetilde{\Phi} = -f\left[\frac{\partial \Psi^{\mathrm{i}}}{\partial \varepsilon_{v}^{\mathrm{ip}}}\dot{\varepsilon}_{v}^{\mathrm{ip}} + \frac{\partial \Psi^{\mathrm{i}}}{\partial \varepsilon_{s}^{\mathrm{ip}}}\dot{\varepsilon}_{s}^{\mathrm{ip}} + \frac{\partial \Psi^{\mathrm{i}}}{\partial\left(-S_r^{\mathrm{ip}}\right)}\left(-\dot{S}_r^{\mathrm{ip}}\right)\right] = f\left[\bar{\chi}_v\dot{\varepsilon}_{v}^{\mathrm{ip}} + \bar{\chi}_s\dot{\varepsilon}_{s}^{\mathrm{ip}} + \bar{\chi}_h\left(-\dot{S}_r^{\mathrm{ip}}\right)\right] \geq 0 \tag{5.23}$$

From Eqs. (5.9) and (5.23), a rate-independent yield criterion can be derived in much the same way as that presented in Chapter 3 with the following generic form of yield function:

$$y = y\left(p'^{\mathrm{i}}, q^{\mathrm{i}}, s^{*\mathrm{i}}, \varepsilon_{v}^{\mathrm{ip}}, \varepsilon_{s}^{\mathrm{ip}}, -S_r^{\mathrm{ip}}\right) \tag{5.24}$$

and flow rules:

$$\dot{\varepsilon}_{v}^{\mathrm{ip}} = \dot{\lambda}_p\frac{\partial y^*}{\partial \chi_v} \tag{5.25}$$

$$\dot{\varepsilon}_{s}^{\mathrm{ip}} = \dot{\lambda}_p\frac{\partial y^*}{\partial \chi_s} \tag{5.26}$$

$$-\dot{S}_r^{\mathrm{ip}} = \dot{\lambda}_p\frac{\partial y^*}{\partial \chi_h} \tag{5.27}$$

The above expressions present a generic form of thermodynamic-based two-scale framework for unsaturated soils, which is able to capture the transition between diffuse ($f = 1$, $\sigma_{ij} = \sigma_{ij}^{\mathrm{o}} = \sigma_{ij}^{\mathrm{i}}$, $\dot{\bar{\phi}}_w = \dot{\bar{\phi}}_w^{\mathrm{o}} = \dot{\bar{\phi}}_w^{\mathrm{i}}$) and localised ($f < 1$, $\sigma_{ij} \neq \sigma_{ij}^{\mathrm{o}} \neq \sigma_{ij}^{\mathrm{i}}$, $\dot{\bar{\phi}}_w \neq \dot{\bar{\phi}}_w^{\mathrm{o}} \neq \dot{\bar{\phi}}_w^{\mathrm{i}}$) stages of failure in a rigorous way. To formulate specific two-scale models based on the above generic formulation, explicitly defined energy and dissipation potentials are needed.

5.3. Constitutive structure

A more comprehensive and correct description of the failure is obtained by capturing the transition from diffuse to localised mode, triggered by a bifurcation point. Following fundamental relationships described in Section 5.2, this section focuses on a constitutive structure that can handle homogeneous

inelastic deformation, the onset of localisation and post-localisation behaviour in the case of constant suction triaxial shear tests (see Figure 5.2).

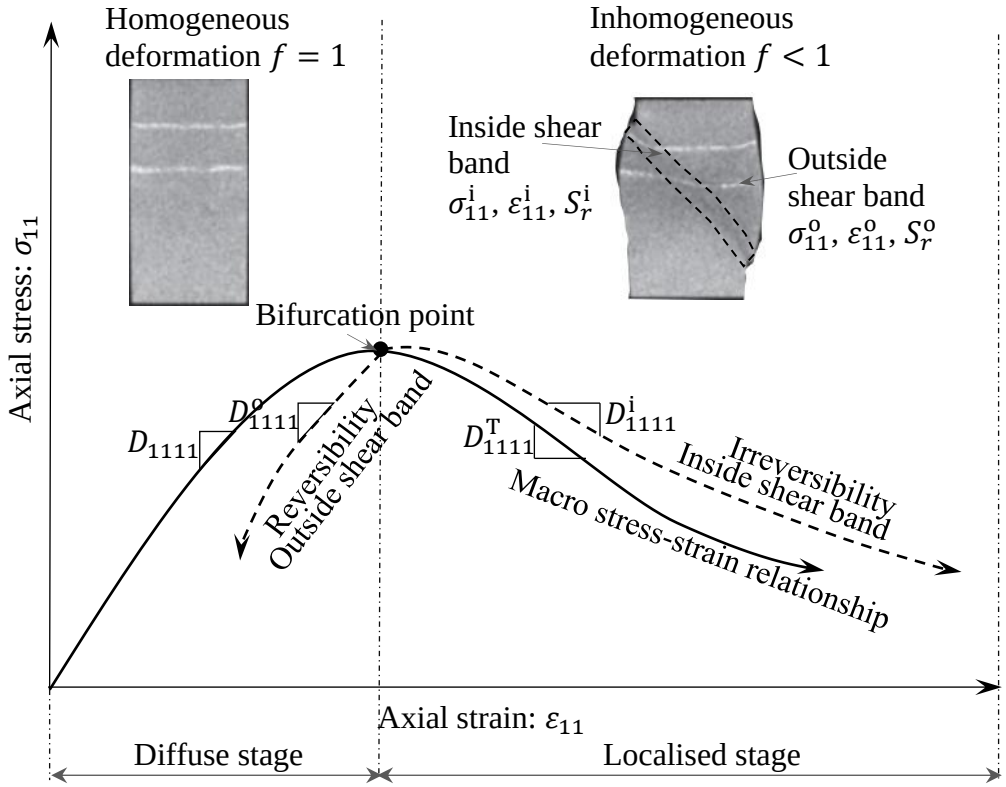

Figure 5.2. Schematic illustration of homogeneous inelastic deformation, the onset of localisation and post-localisation behaviour in the case of axial stress-strain relationship.

5.3.1. Diffuse stage

Before the bifurcation point, materials undergo homogeneous deformation and continuous saturation when $f = 1$. Eqs. (5.2), (5.17) and (5.18) result in a single set of stress-strain and suction-saturation relationships to describe the behaviour of the whole REV. In this case, the generic double-scale formulation in Section 5.2 collapses to the homogeneous one presented in Section 3.3.1 of Chapter 3.

Description of the homogeneous model

To be consistent with the generic thermodynamics-based formulation presented in Section 5.2, the constitutive model used in this stage is almost the same as that proposed in Chapter 4, possessing a good balance between rigour, simplicity, number of parameters and performance. The advantages of this constitutive modelling are that it allows the incorporation of the irreversible degree of saturation and its strong coupling with plastic strain for producing a single critical state yield function and a unique "plastic" multiplier with different evolution rules for internal variables. This is a result of a rigorous thermodynamics-based approach accounting for the interdependence of mechanical and

hydraulic thermodynamic forces and their dependence on all internal variables, in addition to effective stress and suction to reflect the interactions between grain contact sliding and capillary irreversibility at the grain scale. Thanks to these features, this model is able to simulate the simultaneous activation and evolution between yield stress/plastic strain and yield suction/irreversible saturation in a variety of loading and hydraulic conditions without the use of a separate water retention curve and different parameter sets for wetting and drying paths which are usually encountered in many existing constitutive models for partially saturated soils.

An extensive analysis of model performance and dissipation characteristics based on experimental data of partially saturated soils is conducted in Chapter 4 to highlight promising features of the current approach in capturing the dependence of soil stiffness, dilation, shear strength on hydraulic effects (e.g. suction, saturation degree), effects of stress and strain on the wetting-drying difference of SWCC, the smooth transitions between regimes of saturation (capillary, funicular, and pendular), loading (drying, isotropic compression, shearing), dilation (hardening, perfect plasticity, softening). These behavioural features are modelled using only a small number of parameters, all of which can be calibrated from standard tests on partially saturated soils through a systematic procedure.

A minor modification employed to the formulation of the model in Chapter 4, the pressure-dependent elastic moduli of soils is replaced by the pressure-independent one for simplicity thanks to the use of the Helmholtz specific energy potential expressed as follows:

$$\Psi = \frac{E}{6(1-2\varrho)}\left(\varepsilon_v - \varepsilon_v^{\mathrm{p}}\right)^2 + \frac{3}{4}\frac{E}{(1+\varrho)}\left(\varepsilon_s - \varepsilon_s^{\mathrm{p}}\right)^2 + \kappa_h(p_u + s_0^*)\exp\left[\frac{S_{r0}+(-S_r)-(-S_r^{\mathrm{p}})}{\kappa_h}\right] - \left[(-S_r) - \left(-S_r^{\mathrm{p}}\right)\right]p_u + \left(-S_r^{\mathrm{p}}\right)p_b \tag{5.28}$$

where E is the Young modulus; ϱ is the Poisson's ratio.

From Eq. (5.28), constitutive relationships can be obtained as follows:

$$\dot{p}' = \frac{\partial^2\Psi}{\partial(\varepsilon_v)^2} = \frac{E}{3(1-2\varrho)}\left(\dot{\varepsilon}_v - \dot{\varepsilon}_v^{\mathrm{p}}\right) \tag{5.29}$$

$$\dot{q} = \frac{\partial^2\Psi}{\partial(\varepsilon_s)^2} = \frac{3}{2}\frac{E}{(1+\varrho)}\left(\dot{\varepsilon}_s - \dot{\varepsilon}_s^{\mathrm{p}}\right) \tag{5.30}$$

$$\dot{s}^* = \frac{\partial^2\Psi}{\partial(-S_r)^2} = \frac{(s^*+p_u)}{\kappa_h}\left[\left(-\dot{S}_r\right) - \left(-\dot{S}_r^{\mathrm{p}}\right)\right] \tag{5.31}$$

The incremental stress-strain relationship in Eqs. (5.29-5.30) can be rewritten in the tensorial form as:

$$\dot{\sigma}'_{ij} = D^e_{ijkl}\left(\dot{\varepsilon}_{kl} - \dot{\varepsilon}_{kl}^{\mathrm{p}}\right) \tag{5.32}$$

where $D^e_{ijkl} = \frac{E}{2(1+\varrho)}\left(\frac{2\varrho}{1-2\varrho}\delta_{ij}\delta_{kl} + \delta_{ik}\delta_{jl} + \delta_{il}\delta_{jk}\right)$ is the pressure-independent elastic stiffness tensor.

A yield surface in the p': q: s^* space can be derived in the same way as for the model in Chapter 4 as follows:

$$y = \frac{\left(p' - \frac{1}{r}p'_{c(us)}\right)^2}{\left[\left(1-\frac{2}{r}\right)p' + \frac{1}{r}p'_{c(us)}\right]^2} + \frac{(q)^2}{\left[(1-\alpha)p' + \frac{\alpha}{r}p'_{c(us)}\right]^2 M^2} - 1 \leq 0 \tag{5.33}$$

which governs the following evolution rules:

$$\dot{\varepsilon}^{\mathrm{p}}_v = \dot{\lambda}_p \frac{2\left(p' - \frac{1}{r}p'_{c(us)}\right)}{\left[\left(1-\frac{2}{r}\right)p' + \frac{1}{r}p'_{c(us)}\right]^2} \exp[-\beta(1 - S_r)] \tag{5.34}$$

$$\dot{\varepsilon}^{\mathrm{p}}_s = \dot{\lambda}_p \frac{2q}{\left[(1-\alpha)p' + \frac{\alpha}{r}p'_{c(us)}\right]^2 M^2} \tag{5.35}$$

$$-\dot{S}^{\mathrm{p}}_r = \dot{\lambda}_p \frac{2\left(p' - \frac{1}{r}p'_{c(us)}\right)^2}{(s^* - p_b)\left[\left(1-\frac{2}{r}\right)p' + \frac{1}{r}p'_{c(us)}\right]^2}\left[1 - \exp[-\beta(1 - S_r)]\right] \tag{5.36}$$

Further details on the development of this model formulation can be found in Chapter 4. It is noted that $p'_{c(us)}$, in this case, is similar to that given in Eqs. (4.21-4.23), except that $\kappa = 0$ and λ is replaced by the hardening parameter λ'.

$$p'_{c(us)} = p'_R \left[\frac{p'_{c0}\exp\left(\frac{\varepsilon^{\mathrm{p}}_v}{\lambda'}\right)}{p'_R}\right]^{\frac{1}{[(1-\xi)\exp(-\mu s^*)+\xi]}} \tag{5.37}$$

Noting that the minor changes in parameters related to soil stiffness (e.g. E, ϱ, λ') make the model simpler, but do not compromise the model performance.

Constitutive relationship in the diffuse stage

Constitutive relationships in the diffuse regime can be written using Eqs. (3.139-3.140) as follows:

$$\dot{\sigma}'_{ij} = \Lambda_{ijkl}\dot{\varepsilon}_{kl} + \Pi_{ij}\left(-\dot{S}_r\right) \tag{5.38}$$

$$\dot{s}^* = \Omega_{kl}\,\dot{\varepsilon}_{kl} + \Upsilon\left(-\dot{S}_r\right) \tag{5.39}$$

where Λ_{ijkl}, Π_{ij}, Ω_{kl} and Υ take the same form as those in Eqs. (3.141-3.144).

The above expressions are constructed in the same procedure as that illustrated in the preceding chapters (Chapter 3 and 4). Alternatively, the above incremental coupled hydro-mechanical relationships can be rewritten in terms of total stress σ_{ij} (or net stress $\bar{\sigma}_{ij}$ due to $p^a = 0$) and suction s following the same procedure as shown in Eqs. (4.116-4.117).

$$\dot{\sigma}_{ij} = \bar{\Lambda}_{ijkl}\dot{\varepsilon}_{kl} + \bar{\Pi}_{ij}\left(-\dot{S}_r\right) \tag{5.40}$$

$$\dot{s} = \bar{\Omega}_{kl}\,\dot{\varepsilon}_{kl} + \bar{Y}\left(-\dot{S}_r\right) \tag{5.41}$$

For drained triaxial shear tests, suction is fixed at a constant imposed level ($\dot{s} = 0$), allowing Eq. (5.41) to be rewritten as:

$$\left(-\dot{S}_r\right) = (\bar{Y})^{-1}\bar{\Omega}_{kl}\,\dot{\varepsilon}_{kl} \tag{5.42}$$

Substituting the above equation in Eq. (5.40), one gets:

$$\dot{\sigma}_{ij} = \left[\bar{\Lambda}_{ijkl} - (\bar{Y})^{-1}\bar{\Pi}_{ij}\bar{\Omega}_{kl}\right]\dot{\varepsilon}_{kl} = D_{ijkl}\dot{\varepsilon}_{kl} \tag{5.43}$$

with $D_{ijkl} = \bar{\Lambda}_{ijkl} - (\bar{Y})^{-1}\bar{\Pi}_{ij}\bar{\Omega}_{kl}$ being the homogeneous tangent stiffness.

5.3.2. Onset of localisation

The discontinuous bifurcation criterion can be naturally established from the generic framework in Section 5.2 using the continuity of traction across the boundary of the localisation zone. To derive it, this sub-section can start with the internal equilibrium condition in Eq. (5.21) in the following rate form:

$$\left(\dot{\sigma}_{ij}^{\mathrm{o}} - \dot{\sigma}_{ij}^{\mathrm{i}}\right)\bar{n}_j = 0 \tag{5.44}$$

At the onset of localisation, the materials outside and inside the shear band are assumed to follow the same constitutive law associated with the homogeneous tangent stiffness tensor D_{ijkl} (see Eq. (5.43)), leading to:

$$\dot{\sigma}_{ij}^{\mathrm{o}} = D_{ijkl}\dot{\varepsilon}_{kl}^{\mathrm{o}} \tag{5.45}$$

$$\dot{\sigma}_{ij}^{\mathrm{i}} = D_{ijkl}\dot{\varepsilon}_{kl}^{\mathrm{i}} \tag{5.46}$$

Substitution of Eqs. (5.45-5.46) into Eq. (5.44) results in:

$$\left(\dot{\varepsilon}_{kl}^{\mathrm{o}} - \dot{\varepsilon}_{kl}^{\mathrm{i}}\right)D_{ijkl}\bar{n}_j = 0 \tag{5.47}$$

from which and Eq. (5.3), the necessary condition for a discontinuous bifurcation can be obtained as follows:

$$\left(\frac{1}{h}D_{ijkl}\bar{n}_j\bar{n}_l\right)\dot{u}_k = 0 \tag{5.48}$$

For a non-trivial solution, the discontinuous bifurcation condition can be met if the acoustic tensor ($D_{ijkl}\bar{n}_j\bar{n}_l$) has a zero or negative determinant for the loss of ellipticity as follows:

$$\det\left(D_{ijkl}\bar{n}_j\bar{n}_l\right) \leq 0 \tag{5.49}$$

Eq. (5.49) is an extension of the classical discontinuous bifurcation condition (Rudnicki & Rice, 1975) for detecting the emergence of a single tabular shear band in constant suction triaxial shear tests. It implies that the material becomes unstable if a small perturbation in the form of a wave cannot propagate along the normal to the localisation band. This bifurcation condition includes $D_{ijkl} = \bar{\Lambda}_{ijkl} - (\bar{Y})^{-1}\bar{\Pi}_{ij}\bar{\Omega}_{kl}$ with cross-coupling terms (see Eq. (5.43)), reflecting the inter-dependence between mechanical and hydraulic responses inspired from the inseparable nature of grain rearrangement and liquid-bridge redistribution at the micro-scale. Consequently, a path-dependent water retention curve automatically appears, allowing this discontinuous bifurcation criterion to capture the different responses under wetting/drying and mechanical loading paths. This distinguishes the proposed approach from existing ones for partially saturated soils.

Within the discontinuous bifurcation criterion, the matrix form of $\bar{n}_j$ is dependent on the loading paths of experiments. In this sense, examples of how to determine $\bar{n}_j$ in the matrix form for the suction-controlled plane strain biaxial test and tests in a three-dimensional space are illustrated below.

Plane strain biaxial test

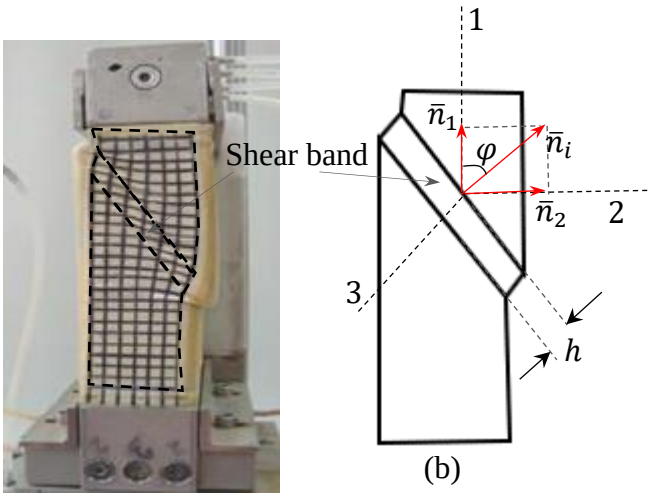

Figure 5.3. (a) Experimental specimen failure (b) Illustration of the direction vector of the localisation band under plane strain condition.

For the plane strain condition, the constitutive relationship in Eq. (5.43) can take the following form of the Voigt notations:

$$\begin{pmatrix} \dot{\sigma}_{11} \\ \dot{\sigma}_{22} \\ \dot{\sigma}_{33} \\ \dot{\sigma}_{12} \end{pmatrix} = \begin{bmatrix} D_{1111} & D_{1122} & D_{1133} & D_{1112} \\ D_{2211} & D_{2222} & D_{2233} & D_{2212} \\ D_{3311} & D_{3322} & D_{3333} & D_{3312} \\ D_{1211} & D_{1222} & D_{1233} & D_{1212} \end{bmatrix} \begin{pmatrix} \dot{\varepsilon}_{11} \\ \dot{\varepsilon}_{22} \\ \dot{\varepsilon}_{33} \\ \dot{\varepsilon}_{12} \end{pmatrix} \tag{5.50}$$

Based on Figure 5.3, the definition of the unit direction vector of the localisation zone is written as:

$$\bar{n}_i = \begin{pmatrix} \bar{n}_1 \\ \bar{n}_2 \end{pmatrix} = \begin{pmatrix} \cos\varphi \\ \sin\varphi \end{pmatrix} \tag{5.51}$$

where φ is the angle between the normal to the localisation band and the vertical axis.

The traction vector $\dot{\bar{t}}_i = \dot{\sigma}_{ij}\bar{n}_j$ acting on the failure plane can be written in the form of the Voigt notations as:

$$\dot{\bar{t}}_i = \begin{pmatrix} \dot{\bar{t}}_1 \\ \dot{\bar{t}}_2 \end{pmatrix} = \begin{bmatrix} \dot{\sigma}_{11} & \dot{\sigma}_{12} \\ \dot{\sigma}_{21} & \dot{\sigma}_{22} \end{bmatrix} \begin{pmatrix} \bar{n}_1 \\ \bar{n}_2 \end{pmatrix} = \begin{pmatrix} \dot{\sigma}_{11}\bar{n}_1 + \dot{\sigma}_{12}\bar{n}_2 \\ \dot{\sigma}_{21}\bar{n}_1 + \dot{\sigma}_{22}\bar{n}_2 \end{pmatrix} = \begin{bmatrix} \bar{n}_1 & 0 & 0 & \bar{n}_2 \\ 0 & \bar{n}_2 & 0 & \bar{n}_1 \end{bmatrix} \begin{pmatrix} \dot{\sigma}_{11} \\ \dot{\sigma}_{22} \\ \dot{\sigma}_{33} \\ \dot{\sigma}_{12} \end{pmatrix} \tag{5.52}$$

The matrix form of $\bar{n}_j$ for the plane strain condition can be derived from the above equation as follows:

$$\bar{n}_i = \begin{bmatrix} \bar{n}_1 & 0 & 0 & \bar{n}_2 \\ 0 & \bar{n}_2 & 0 & \bar{n}_1 \end{bmatrix} = \begin{bmatrix} \cos\varphi & 0 & 0 & \sin\varphi \\ 0 & \sin\varphi & 0 & \cos\varphi \end{bmatrix} \tag{5.53}$$

Tests in three-dimensional space

Regarding the tests in three-dimensional space, the constitutive relationship (Eq. (5.43)) in the form of the Voigt notations can be expressed as:

$$\begin{pmatrix} \dot{\sigma}_{11} \\ \dot{\sigma}_{22} \\ \dot{\sigma}_{33} \\ \dot{\sigma}_{12} \\ \dot{\sigma}_{23} \\ \dot{\sigma}_{31} \end{pmatrix} = \begin{bmatrix} D_{1111} & D_{1122} & D_{1133} & D_{1112} & D_{1123} & D_{1131} \\ D_{2211} & D_{2222} & D_{2233} & D_{2212} & D_{2223} & D_{2231} \\ D_{3311} & D_{3322} & D_{3333} & D_{3312} & D_{3323} & D_{3331} \\ D_{1211} & D_{1222} & D_{1233} & D_{1212} & D_{1223} & D_{1231} \\ D_{2311} & D_{2322} & D_{2333} & D_{2312} & D_{2323} & D_{2331} \\ D_{3111} & D_{3122} & D_{3133} & D_{3112} & D_{3123} & D_{3131} \end{bmatrix} \begin{pmatrix} \dot{\varepsilon}_{11} \\ \dot{\varepsilon}_{22} \\ \dot{\varepsilon}_{33} \\ \dot{\varepsilon}_{12} \\ \dot{\varepsilon}_{23} \\ \dot{\varepsilon}_{31} \end{pmatrix} \tag{5.54}$$

Figure 5.4 demonstrates that the unit direction vector of the localisation zone can be defined using a standard spherical coordinate system as follows:

$$\bar{n}_i = \begin{pmatrix} \bar{n}_1 \\ \bar{n}_2 \\ \bar{n}_3 \end{pmatrix} = \begin{pmatrix} \cos\varphi \\ \sin\varphi\cos\omega \\ \sin\varphi\sin\omega \end{pmatrix} \tag{5.55}$$

with φ representing the zenith angle between the normal to the localisation band and the vertical axis while ω denoting the azimuthal angle in the 23-plane from the 2-axis.

Using Voigt notations, the expression of traction vector $\dot{\bar{t}}_i = \dot{\sigma}_{ij}\bar{n}_j$ in the three-dimensional space can take the following form:

$$\dot{t}_i = \begin{pmatrix} \dot{t}_1 \\ \dot{t}_2 \\ \dot{t}_3 \end{pmatrix} = \begin{bmatrix} \dot{\sigma}_{11} & \dot{\sigma}_{12} & \dot{\sigma}_{13} \\ \dot{\sigma}_{21} & \dot{\sigma}_{22} & \dot{\sigma}_{12} \\ \dot{\sigma}_{31} & \dot{\sigma}_{32} & \dot{\sigma}_{33} \end{bmatrix} \begin{pmatrix} \bar{n}_1 \\ \bar{n}_2 \\ \bar{n}_3 \end{pmatrix} = \begin{pmatrix} \dot{\sigma}_{11}\bar{n}_1 + \dot{\sigma}_{12}\bar{n}_2 + \dot{\sigma}_{13}\bar{n}_3 \\ \dot{\sigma}_{21}\bar{n}_1 + \dot{\sigma}_{22}\bar{n}_2 + \dot{\sigma}_{23}\bar{n}_3 \\ \dot{\sigma}_{31}\bar{n}_1 + \dot{\sigma}_{32}\bar{n}_2 + \dot{\sigma}_{33}\bar{n}_3 \end{pmatrix} =$$

$$\begin{bmatrix} \bar{n}_1 & 0 & 0 & \bar{n}_2 & 0 & \bar{n}_3 \\ 0 & \bar{n}_2 & 0 & \bar{n}_1 & \bar{n}_3 & 0 \\ 0 & 0 & \bar{n}_3 & 0 & \bar{n}_2 & \bar{n}_1 \end{bmatrix} \begin{pmatrix} \dot{\sigma}_{11} \\ \dot{\sigma}_{22} \\ \dot{\sigma}_{33} \\ \dot{\sigma}_{12} \\ \dot{\sigma}_{23} \\ \dot{\sigma}_{31} \end{pmatrix} \tag{5.56}$$

The matrix form of $\bar{n}_j$ for tests in the three-dimensional space can be deduced from Eq. (5.56) as:

$$\bar{n}_i = \begin{bmatrix} \bar{n}_1 & 0 & 0 & \bar{n}_2 & 0 & \bar{n}_3 \\ 0 & \bar{n}_2 & 0 & \bar{n}_1 & \bar{n}_3 & 0 \\ 0 & 0 & \bar{n}_3 & 0 & \bar{n}_2 & \bar{n}_1 \end{bmatrix} =$$

$$\begin{bmatrix} \cos\varphi & 0 & 0 & \sin\varphi\cos\omega & 0 & \sin\varphi\sin\omega \\ 0 & \sin\varphi\cos\omega & 0 & \cos\varphi & \sin\varphi\sin\omega & 0 \\ 0 & 0 & \sin\varphi\sin\omega & 0 & \sin\varphi\cos\omega & \cos\varphi \end{bmatrix} \tag{5.57}$$

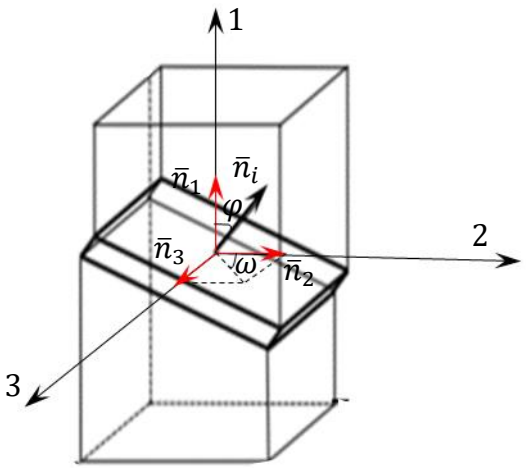

Figure 5.4. Illustration of the direction vector of the localisation band for tests in three-dimensional space.

5.3.3. Localised stage

Beyond the bifurcation point, the material behaviour is inhomogeneous in both inelastic deformation and saturation with $f < 1$. In this stage, for the considered volume element, there are two separate constitutive relationships for the localisation zone and the volume outside that zone. These parts behave under conditions of stress equilibrium with strong variation in strain and saturation across the shear band. The behaviour inside this band is different from the one in the outside zone. Particularly, within the localised band, the material behaves plastically due to a significant movement of soil particles, while the surrounding bulk, of several orders of magnitude in extent, is under elastic

unloading because of a small change in the grain arrangement (see Figure 5.5). It is assumed that the constitutive model for elastic and inelastic behaviour inside and outside the localisation zone remains the same as used for describing the behaviour in the diffuse stage (see Section 5.3.1).

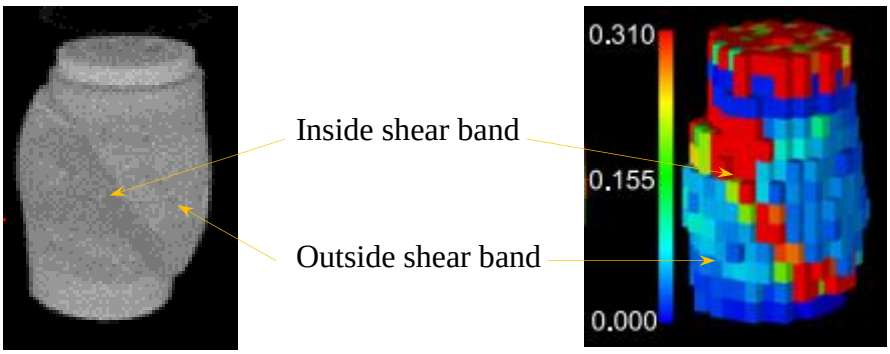

Figure 5.5. Distribution of the incremental shear strain obtained by the DIC analysis at $\varepsilon_{11} = 0.2$ (Higo et al., 2013)

Constitutive relationship outside the shear band

The behaviour of surrounding bulk outside the localisation band is assumed to be recoverable as inconsiderable deformation and saturation within this region are usually observed in experiments. Therefore, from Eqs. (5.9) and (5.11-5.12), the incremental response of a unit volume element outside the localisation band can be expressed in the following form:

$$\dot{\sigma}^{\mathrm{o}}_{ij} + s^{\mathrm{o}}\dot{S}^{\mathrm{o}}_{r}\delta_{ij} + S^{\mathrm{o}}_{r}\dot{s}^{\mathrm{o}}\delta_{ij} = \frac{\partial^2\Psi^{\mathrm{o}}}{\partial\varepsilon^{\mathrm{o}}_{ij}\partial\varepsilon^{\mathrm{o}}_{kl}}\dot{\varepsilon}^{\mathrm{o}}_{kl} + \frac{\partial^2\Psi^{\mathrm{o}}}{\partial\varepsilon^{\mathrm{o}}_{ij}\partial(-\dot{S}^{\mathrm{o}}_{r})}\left(-\dot{S}^{\mathrm{o}}_{r}\right) \tag{5.58}$$

$$s^{\mathrm{o}}\dot{\bar{\phi}}^{\mathrm{o}} + \bar{\phi}^{\mathrm{o}}\dot{s}^{\mathrm{o}} = \frac{\partial^2\Psi^{\mathrm{o}}}{\partial(-\dot{S}^{\mathrm{o}}_{r})\partial\varepsilon^{\mathrm{o}}_{kl}}\dot{\varepsilon}^{\mathrm{o}}_{kl} + \frac{\partial^2\Psi^{\mathrm{o}}}{\partial(-S^{\mathrm{o}}_{r})^2}\left(-\dot{S}^{\mathrm{o}}_{r}\right) \tag{5.59}$$

Due to $\dot{\bar{\phi}}^{\mathrm{o}} = -\delta_{kl}\dot{\varepsilon}^{\mathrm{o}}_{kl}$ (incompressible solid grains) and $\dot{s}^{\mathrm{o}} = 0$ ($s = s^{\mathrm{i}} = s^{\mathrm{o}} = \mathrm{const}$), Eqs. (5.58) and (5.59) can be rewritten as:

$$\dot{\sigma}^{\mathrm{o}}_{ij} - s^{\mathrm{o}}\delta_{ij}\left(-\dot{S}^{\mathrm{o}}_{r}\right) = \frac{\partial^2\Psi^{\mathrm{o}}}{\partial\varepsilon^{\mathrm{o}}_{ij}\partial\varepsilon^{\mathrm{o}}_{kl}}\dot{\varepsilon}^{\mathrm{o}}_{kl} + \frac{\partial^2\Psi^{\mathrm{o}}}{\partial\varepsilon^{\mathrm{o}}_{ij}\partial(-\dot{S}^{\mathrm{o}}_{r})}\left(-\dot{S}^{\mathrm{o}}_{r}\right) \tag{5.60}$$

$$-s^{\mathrm{o}}\delta_{kl}\dot{\varepsilon}^{\mathrm{o}}_{kl} = \frac{\partial^2\Psi^{\mathrm{o}}}{\partial(-\dot{S}^{\mathrm{o}}_{r})\partial\varepsilon^{\mathrm{o}}_{kl}}\dot{\varepsilon}^{\mathrm{o}}_{kl} + \frac{\partial^2\Psi^{\mathrm{o}}}{\partial(-S^{\mathrm{o}}_{r})^2}\left(-\dot{S}^{\mathrm{o}}_{r}\right) \tag{5.61}$$

By combining these above equations, the following constitutive relationship outside the shear band is obtained:

$$\dot{\sigma}^{\mathrm{o}}_{ij} = \left[\frac{\partial^2\Psi^{\mathrm{o}}}{\partial\varepsilon^{\mathrm{o}}_{ij}\partial\varepsilon^{\mathrm{o}}_{kl}} - \left(\frac{\partial^2\Psi^{\mathrm{o}}}{\partial\varepsilon^{\mathrm{o}}_{ij}\partial(-\dot{S}^{\mathrm{o}}_{r})} + s^{\mathrm{o}}\delta_{ij}\right)\left(\frac{\partial^2\Psi^{\mathrm{o}}}{\partial(-S^{\mathrm{o}}_{r})^2}\right)^{-1}\left(\frac{\partial^2\Psi^{\mathrm{o}}}{\partial(-\dot{S}^{\mathrm{o}}_{r})\partial\varepsilon^{\mathrm{o}}_{kl}} + s^{\mathrm{o}}\delta_{kl}\right)\right]\dot{\varepsilon}^{\mathrm{o}}_{kl} = D^{\mathrm{o}}_{ijkl}\dot{\varepsilon}^{\mathrm{o}}_{kl} \tag{5.62}$$

with $D^{\mathrm{o}}_{ijkl} = \frac{\partial^2\Psi^{\mathrm{o}}}{\partial\varepsilon^{\mathrm{o}}_{ij}\partial\varepsilon^{\mathrm{o}}_{kl}} - \left(\frac{\partial^2\Psi^{\mathrm{o}}}{\partial\varepsilon^{\mathrm{o}}_{ij}\partial(-S^{\mathrm{o}}_r)} + s^{\mathrm{o}}\delta_{ij}\right)\left(\frac{\partial^2\Psi^{\mathrm{o}}}{\partial(-S^{\mathrm{o}}_r)^2}\right)^{-1}\left(\frac{\partial^2\Psi^{\mathrm{o}}}{\partial(-\dot{S}^{\mathrm{o}}_r)\partial\varepsilon^{\mathrm{o}}_{kl}} + s^{\mathrm{o}}\delta_{kl}\right)$ being the tangent stiffness tensor outside the shear band.

Constitutive relationship inside the shear band

Using Eqs. (5.9) and (5.11-5.12), the incremental forms of effective stress tensor and modified suction inside the localisation zone can be expressed as:

$$\dot{\sigma}'^{\mathrm{i}}_{ij} = \frac{\partial^2\Psi^{\mathrm{i}}}{\partial\varepsilon^{\mathrm{i}}_{ij}\partial\varepsilon^{\mathrm{i}}_{kl}}\left(\dot{\varepsilon}^{\mathrm{i}}_{kl} - \dot{\varepsilon}^{\mathrm{ip}}_{kl}\right) + \frac{\partial^2\Psi^{\mathrm{i}}}{\partial\varepsilon^{\mathrm{i}}_{ij}\partial(-S^{\mathrm{i}}_r)}\left[\left(-\dot{S}^{\mathrm{i}}_r\right) - \left(-\dot{S}^{\mathrm{ip}}_r\right)\right] \tag{5.63}$$

$$\dot{s}^{*\mathrm{i}} = \frac{\partial^2\Psi^{\mathrm{i}}}{\partial(-S^{\mathrm{i}}_r)\partial\varepsilon^{\mathrm{i}}_{kl}}\left(\dot{\varepsilon}^{\mathrm{i}}_{kl} - \dot{\varepsilon}^{\mathrm{ip}}_{kl}\right) + \frac{\partial^2\Psi^{\mathrm{i}}}{\partial(-S^{\mathrm{i}}_r)^2}\left[\left(-\dot{S}^{\mathrm{i}}_r\right) - \left(-\dot{S}^{\mathrm{ip}}_r\right)\right] \tag{5.64}$$

From Eqs. (5.24-5.27) and (5.63-5.64), following the same procedures demonstrated in the preceding section on the formulation for the homogeneous constitutive relationships (see Eqs. (5.38-5.43)), this sub-section ends up here with the constitutive relationship of the material inside the shear band as:

$$\dot{\sigma}^{\mathrm{i}}_{ij} = \left[\bar{\Lambda}^{\mathrm{i}}_{ijkl} - \left(\bar{Y}^{\mathrm{i}}\right)^{-1}\bar{\Pi}^{\mathrm{i}}_{ij}\bar{\Omega}^{\mathrm{i}}_{kl}\right]\dot{\varepsilon}^{\mathrm{i}}_{kl} = D^{\mathrm{i}}_{ijkl}\dot{\varepsilon}^{\mathrm{i}}_{kl} \tag{5.65}$$

in which $D^{\mathrm{i}}_{ijkl} = \bar{\Lambda}^{\mathrm{i}}_{ijkl} - \left(\bar{Y}^{\mathrm{i}}\right)^{-1}\bar{\Pi}^{\mathrm{i}}_{ij}\bar{\Omega}^{\mathrm{i}}_{kl}$ is the tangent stiffness tensor inside the shear band, which is exactly in the same form as D_{ijkl}, but using Ψ^{i}, $\varepsilon^{\mathrm{i}}_{ij}$, S^{i}_r, σ^{i}_{ij} and s^{i}.

Macro constitutive relationship

These obtained incremental constitutive relationships (see Eqs. (5.62) and (5.65)) can be linked together to construct the formulation representing the incremental macro response of the entire volume element.

Substituting Eqs. (5.62) and (5.65) in the incremental traction continuity condition in Eq. (5.44) gives:

$$\left(D^{\mathrm{o}}_{ijkl}\dot{\varepsilon}^{\mathrm{o}}_{kl} - D^{\mathrm{i}}_{ijkl}\dot{\varepsilon}^{\mathrm{i}}_{kl}\right)\bar{n}_j = 0 \tag{5.66}$$

Eq. (5.66) can be expanded using the kinematic enhancements presented in Eqs. (5.4-5.5) as follows:

$$D^{\mathrm{o}}_{ijkl}\left[\dot{\varepsilon}_{kl} - \frac{f}{h}(\dot{u}_k\bar{n}_l)^{\mathrm{s}}\right]\bar{n}_j - D^{\mathrm{i}}_{ijkl}\left[\dot{\varepsilon}_{kl} + \frac{1-f}{h}(\dot{u}_k\bar{n}_l)^{\mathrm{s}}\right]\bar{n}_j = 0 \tag{5.67}$$

After rearranging the above expression, the incremental displacement jump $\dot{u}_k$ can be obtained as:

$$\dot{u}_k = {C_{ik}}^{-1}\left(D^{\mathrm{o}}_{ijmn} - D^{\mathrm{i}}_{ijmn}\right)\dot{\varepsilon}_{mn}\bar{n}_j \tag{5.68}$$

where

$$C_{ik} = \frac{f}{h}D^{\mathrm{o}}_{ijkl}\bar{n}_l\bar{n}_j + \frac{1-f}{h}D^{\mathrm{i}}_{ijkl}\bar{n}_l\bar{n}_j \tag{5.69}$$

As can be seen in Eq. (5.69), C_{ik} is the localisation or acoustic tensor with a combination of both tangent stiffness tensors outside and inside the localisation band at the constitutive level, bridging both diffuse and localised responses.

From Eqs. (5.4-5.5) and (5.68), the expression of strain rate outside and inside the localisation region can be obtained as:

$$\dot{\varepsilon}^{\mathrm{o}}_{kl} = \dot{\varepsilon}_{kl} - \frac{f}{h}\left[{C_{ik}}^{-1}\left(D^{\mathrm{o}}_{ijmn} - D^{\mathrm{i}}_{ijmn}\right)\dot{\varepsilon}_{mn}\bar{n}_j\bar{n}_l\right]^{\mathrm{s}} \tag{5.70}$$

$$\dot{\varepsilon}^{\mathrm{i}}_{kl} = \dot{\varepsilon}_{kl} + \frac{1-f}{h}\left[{C_{ik}}^{-1}\left(D^{\mathrm{o}}_{ijmn} - D^{\mathrm{i}}_{ijmn}\right)\dot{\varepsilon}_{mn}\bar{n}_j\bar{n}_l\right]^{\mathrm{s}} \tag{5.71}$$

Using Eqs. (5.17), (5.62) and (5.65), the macro stress increment can be determined as the volume-averaged one using incremental stresses inside and outside the shear band through the following form:

$$\dot{\sigma}_{pq} = (1-f)D^{\mathrm{o}}_{pqkl}\dot{\varepsilon}^{\mathrm{o}}_{kl} + fD^{\mathrm{i}}_{pqkl}\dot{\varepsilon}^{\mathrm{i}}_{kl} \tag{5.72}$$

Substituting Eqs. (5.70-5.71) into the above equation and rearranging the obtained expression, one obtains:

$$\dot{\sigma}_{pq} = \left\{(1-f)D^{\mathrm{o}}_{pqmn} + fD^{\mathrm{i}}_{pqmn} - \frac{f(1-f)}{h}{C_{ik}}^{-1}\left(D^{\mathrm{o}}_{ijmn} - D^{\mathrm{i}}_{ijmn}\right)\bar{n}_j\bar{n}_l\left(D^{\mathrm{o}}_{pqkl} - D^{\mathrm{i}}_{pqkl}\right)\right\}\dot{\varepsilon}_{mn} = D^{\mathrm{T}}_{pqmn}\dot{\varepsilon}_{mn} \tag{5.73}$$

in which D^{T}_{pqmn} is the macro tangent stiffness tensor taking the below form:

$$D^{\mathrm{T}}_{pqmn} = \underbrace{(1-f)D^{\mathrm{o}}_{pqmn} + fD^{\mathrm{i}}_{pqmn}}_{\text{upper bound}} - \underbrace{\frac{f(1-f)}{h}{C_{ik}}^{-1}\left(D^{\mathrm{o}}_{ijmn} - D^{\mathrm{i}}_{ijmn}\right)\bar{n}_j\bar{n}_l\left(D^{\mathrm{o}}_{pqkl} - D^{\mathrm{i}}_{pqkl}\right)}_{\text{enhancement}} \tag{5.74}$$

Eq. (5.74) indicates that the macro tangent stiffness tensor consists of two components corresponding to the upper bound solution and an enhancement term accounting for the interaction between responses outside and inside the shear band. This interaction is established thanks to the appearance of orientation and size of the localisation band, allowing the proposed framework to naturally capture the mixed material-structural response and size effect in the post-localisation stage. For $f = 1$ the proposed form of the macro tangent stiffness tensor D^{T}_{pqmn} can automatically become the classical form for homogeneous deformation and saturation D_{ijkl}, capturing the transition between diffuse and localised regimes.

5.4. Numerical implementation

The numerical implementation algorithm of this framework involves three responses: homogenous deformation, the onset of localisation and post-localisation. While the behavioural performance of homogeneous inelastic deformation is numerically implemented following the semi-implicit stress

return algorithm of the classical framework as presented in Chapter 3 (see Eqs. (3.146-3.158)), the algorithms for detecting the onset of bifurcation, the orientation of localisation band, and updating stress and suction in the post-localisation stage are described in this section.

5.4.1. Bifurcation detection algorithm

In this section, two different approaches of bifurcation detection are described; a numerical algorithm and an analytical algorithm. These two algorithms are expected to provide the same solution to determine the onset and orientation of the localisation band during loading.

Numerical algorithm

In the numerical algorithm, to detect the initiation of localised failure, all possible orientations from 0^o to 180^o need to be scanned to determine the corresponding $\bar{n}_j$ at each step from the beginning of the shearing process (Nguyen et al., 2016). Given $\bar{n}_j$ and D_{ijkl} at each step, the determinant of acoustic tensor $\det(D_{ijkl}\bar{n}_j\bar{n}_l)$ is computed. The minimum value of $\det(D_{ijkl}\bar{n}_j\bar{n}_l)$ and the corresponding angle is then checked among scanned angles (Nguyen et al., 2016). The onset of localisation can be detected when the minimisation of $\det(D_{ijkl}\bar{n}_j\bar{n}_l) < 0$ is first satisfied. The angle φ obtained at this point is the final orientation of the shear band used for the rest of the computation. In this approach, the more angles are scanned, the more solutions are accurate.

Analytical algorithm

In this part, an example of an analytical solution for the plane strain biaxial tests is derived to exactly determine the minimisation of acoustic tensor and corresponding orientation of the shear band. In this case, the acoustic tensor can be expanded explicitly in the form of the Voigt notations as:

$$D_{ijkl}\bar{n}_j\bar{n}_l = \begin{bmatrix} \bar{n}_1 & 0 & 0 & \bar{n}_2 \\ 0 & \bar{n}_2 & 0 & \bar{n}_1 \end{bmatrix} \begin{bmatrix} D_{1111} & D_{1122} & D_{1133} & D_{1112} \\ D_{2211} & D_{2222} & D_{2233} & D_{2212} \\ D_{3311} & D_{3322} & D_{3333} & D_{3312} \\ D_{1211} & D_{1222} & D_{1233} & D_{1212} \end{bmatrix} \begin{bmatrix} \bar{n}_1 & 0 \\ 0 & \bar{n}_2 \\ 0 & 0 \\ \bar{n}_2 & \bar{n}_1 \end{bmatrix} =$$

$$\begin{bmatrix} (\bar{n}_1 D_{1111} + \bar{n}_2 D_{1211})\bar{n}_1 + (\bar{n}_1 D_{1112} + \bar{n}_2 D_{1212})\bar{n}_2 & (\bar{n}_1 D_{1122} + \bar{n}_2 D_{1222})\bar{n}_2 + (\bar{n}_1 D_{1112} + \bar{n}_2 D_{1212})\bar{n}_1 \\ (\bar{n}_2 D_{2211} + \bar{n}_1 D_{1211})\bar{n}_1 + (\bar{n}_2 D_{2212} + \bar{n}_1 D_{1212})\bar{n}_2 & (\bar{n}_2 D_{2222} + \bar{n}_1 D_{1222})\bar{n}_2 + (\bar{n}_2 D_{2212} + \bar{n}_1 D_{1212})\bar{n}_1 \end{bmatrix} \tag{5.75}$$

The function of the determinant of localisation tensor in Eq. (5.75) is constructed as follows:

$$\det(D_{ijkl}\bar{n}_j\bar{n}_l) = \{D_{1111}D_{1212}(\bar{n}_1)^4 + D_{1212}D_{2222}(\bar{n}_2)^4 + [D_{1111}(D_{2212} + D_{1222}) + D_{1212}(D_{1112} + D_{1211})](\bar{n}_1)^3\bar{n}_2 + [D_{2222}(D_{1112} + D_{1211}) + D_{1212}(D_{2212} + D_{1222})]\bar{n}_1(\bar{n}_2)^3 + [(D_{1112} + D_{1211})(D_{2212} + D_{1222}) + D_{1111}D_{2222} + (D_{1212})^2](\bar{n}_1\bar{n}_2)^2\} - \{D_{1112}D_{1211}(\bar{n}_1)^4 +$$

$$D_{1222}D_{2212}(\bar{n}_2)^4 + [D_{1112}(D_{2211} + D_{1212}) + D_{1211}(D_{1122} + D_{1212})](\bar{n}_1)^3\bar{n}_2 + [D_{2212}(D_{1122} + D_{1212}) + D_{1222}(D_{2211} + D_{1212})]\bar{n}_1(\bar{n}_2)^3 + [D_{1112}D_{2212} + D_{1222}D_{1211} + (D_{1122} + D_{1212})(D_{2211} + D_{1212})](\bar{n}_1\bar{n}_2)^2\} \quad (5.76)$$

which is then mathematically manipulated to become:

$$\det(D_{ijkl}\bar{n}_j\bar{n}_l) = (D_{1111}D_{1212} - D_{1112}D_{1211})(\bar{n}_1)^4 + (D_{2222}D_{1212} - D_{1222}D_{2212})(\bar{n}_2)^4 + (D_{1111}D_{2212} + D_{1111}D_{1222} - D_{1112}D_{2211} - D_{1211}D_{1122})(\bar{n}_1)^3 n_2 + (D_{2222}D_{1112} + D_{2222}D_{1211} - D_{2212}D_{1122} - D_{1222}D_{2211})\bar{n}_1(\bar{n}_2)^3 + (D_{1112}D_{1222} + D_{1211}D_{2212} + D_{1111}D_{2222} - D_{1122}D_{2211} - D_{1122}D_{1212} - D_{1212}D_{2211})(\bar{n}_1\bar{n}_2)^2 \quad (5.77)$$

Due to properties of the plane strain biaxial tests, Eq. (5.77) can be rewritten as:

$$\det(D_{ijkl}\bar{n}_j\bar{n}_l) = (D_{1111}D_{1212})(\bar{n}_1)^4 + (D_{2222}D_{1212})(\bar{n}_2)^4 + (D_{1111}D_{2222} - D_{1122}D_{2211} - D_{1122}D_{1212} - D_{1212}D_{2211})(\bar{n}_1\bar{n}_2)^2 \quad (5.78)$$

or,

$$\det(D_{ijkl}\bar{n}_j\bar{n}_l) = (D_{1111}D_{1212})(\cos\varphi)^4 + (D_{2222}D_{1212})(\sin\varphi)^4 + (D_{1111}D_{2222} - D_{1122}D_{2211} - D_{1122}D_{1212} - D_{1212}D_{2211})(\cos\varphi\sin\varphi)^2 \quad (5.79)$$

Eq. (5.79) can be rewritten as:

$$\det(D_{ijkl}\bar{n}_j\bar{n}_l) = \frac{1}{4}\{(D_{1111}D_{1212})(1 - \cos2\varphi)^2 + (D_{2222}D_{1212})(1 + \cos2\varphi)^2 + (D_{1111}D_{2222} - D_{1122}D_{2211} - D_{1122}D_{1212} - D_{1212}D_{2211})[1 - (\cos2\varphi)^2]\} \quad (5.80)$$

$\det(D_{ijkl}\bar{n}_j\bar{n}_l)$ is minimum if the following condition is met:

$$\frac{\partial[\det(D_{ijkl}\bar{n}_j\bar{n}_l)]}{\partial(\cos2\varphi)} = \frac{1}{2}[-(D_{1111}D_{1212})(1 - \cos2\varphi) + (D_{2222}D_{1212})(1 + \cos2\varphi) - (D_{1111}D_{2222} - D_{1122}D_{2211} - D_{1122}D_{1212} - D_{1212}D_{2211})\cos2\varphi] = 0 \quad (5.81)$$

Consequently,

$$\cos2\varphi = -\frac{D_{2222}D_{1212} - D_{1111}D_{1212}}{D_{1111}D_{1212} + D_{2222}D_{1212} - (D_{1111}D_{2222} - D_{1122}D_{2211} - D_{1122}D_{1212} - D_{1212}D_{2211})} \quad (5.82)$$

Therefore, from Eqs. (5.80) and (5.82), the bifurcation condition based on the analytical algorithm can be obtained through the following expressions:

$$[\det(D_{ijkl}\bar{n}_j\bar{n}_l)]_{min} = \frac{1}{4}\Big\{(D_{1111}D_{1212})\Big(1 + \frac{D_{2222}D_{1212} - D_{1111}D_{1212}}{D_{1111}D_{1212} + D_{2222}D_{1212} - D_{1111}D_{2222} + D_{1122}D_{2211} + D_{1212} + D_{1212}D_{2211}}\Big)^2 + (D_{2222}D_{1212})\Big(1 -$$

$$\frac{D_{2222}D_{1212}-D_{1111}D_{1212}}{D_{1111}D_{1212}+D_{2222}D_{1212}-D_{1111}D_{2222}+D_{1122}D_{2211}+D_{1122}D_{1212}+D_{1212}D_{2211}}\Big)^2+(D_{1111}D_{2222}-D_{1122}D_{2211}-$$

$$D_{1122}D_{1212}-D_{1212}D_{2211})\Big[1-$$

$$\Big(-\frac{D_{2222}D_{1212}-D_{1111}D_{1212}}{D_{1111}D_{1212}+D_{2222}D_{1212}-D_{1111}D_{2222}+D_{1122}D_{2211}+D_{1122}D_{1212}+D_{1212}D_{2211}}\Big)^2\Big]\Big\}\leq 0 \quad (5.83)$$

5.4.2. Stress return algorithm for post-localisation behaviour

Different from conventional constitutive models, this framework requires a numerical algorithm of two-level stress return procedure (macro and local/localisation zone) to capture inhomogeneous responses in the post-localisation stage (see Figure 5.6). In this algorithm (Nguyen et al., 2016; Nguyen & Bui, 2020), the local level is to bridge the enhanced framework and the classical constitutive behaviour for partially saturated soils, while the macro level is considered as an interface between the proposed framework and BVPs. In particular, the conventional semi-algorithm stress return algorithm (see Section 3.3.3, Chapter 3) can be adopted to update stress and suction inside and outside the localisation band for the local level, using strain and saturation degree increments inside and outside the band obtained from the macro level. For the macro level, the mixed-control loading algorithm (see further details in Chapter 4) is applied to mimic experimental loading conditions involving macro variables (e.g. constant confining pressure and constant suction for the suction-controlled triaxial test), while the traction continuity condition can be enforced to compute the incremental displacement jump for determination of macro tangent stiffness tensor through the following algorithm.

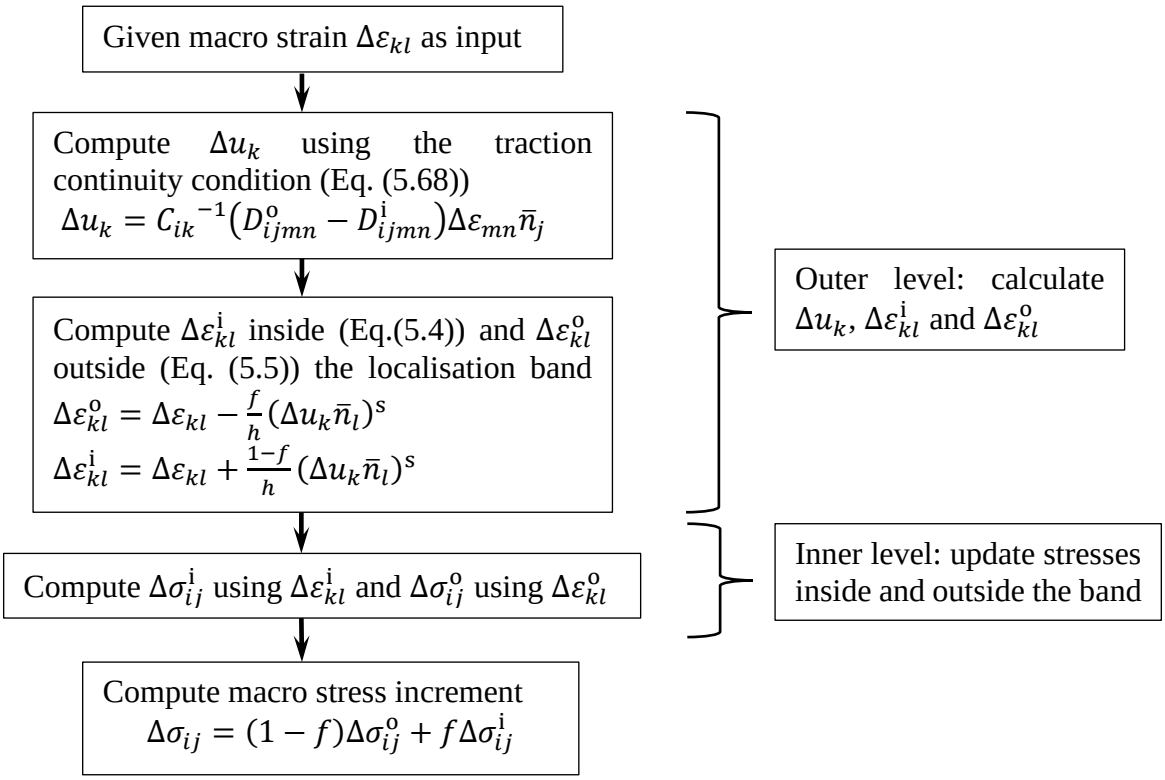

Figure 5.6. A flowchart for stress return algorithm (Nguyen et al., 2016)

Due to numerical error, there is a residual traction vector $\bar{r}_i$ representing the difference between the traction vectors outside ($\bar{t}^{\mathrm{o}}_i = \sigma^{\mathrm{o}}_{ij}\bar{n}_j$) and inside ($\bar{t}^{\mathrm{i}}_i = \sigma^{\mathrm{i}}_{ij}\bar{n}_j$) the discontinuity plane in the following form:

$$\bar{r}_i = \bar{t}^{\mathrm{o}}_i - \bar{t}^{\mathrm{i}}_i = \left(\sigma^{\mathrm{o}}_{ij} - \sigma^{\mathrm{i}}_{ij}\right)\bar{n}_j \tag{5.84}$$

At the previous state, the first-order Taylor expansion of the residual in the above expression can be written as:

$$\bar{r}_i^{\,\mathrm{new}} = \bar{r}_i^{\,\mathrm{previous}} + \left(\delta\sigma^{\mathrm{o}}_{ij} - \delta\sigma^{\mathrm{i}}_{ij}\right)\bar{n}_j \tag{5.85}$$

where $\bar{r}_i^{\,\mathrm{previous}}$ is the residual traction vector at the previous state, taking the form below:

$$\bar{r}_i^{\,\mathrm{previous}} = \left(\delta\sigma^{\mathrm{o,previous}}_{ij} - \delta\sigma^{\mathrm{i,previous}}_{ij}\right)\bar{n}_j \tag{5.86}$$

From Eqs. (5.62) and (5.65), two following local constitutive relationships reflecting the responses inside and outside the localisation zone are written:

$$\delta\sigma^{\mathrm{o}}_{ij} = D^{\mathrm{o}}_{ijkl}\delta\varepsilon^{\mathrm{o}}_{kl} \tag{5.87}$$

$$\delta\sigma^{\mathrm{i}}_{ij} = D^{\mathrm{i}}_{ijkl}\delta\varepsilon^{\mathrm{i}}_{kl} \tag{5.88}$$

in which local strain increments $\delta\varepsilon_{kl}^{\mathrm{o}}$ and $\delta\varepsilon_{kl}^{\mathrm{i}}$ are expressed based on kinematic compatibility conditions in Eqs. (5.4-5.5) as follows:

$$\delta\varepsilon_{kl}^{\mathrm{o}} = \delta\varepsilon_{kl} - \frac{f}{h}(\delta u_k \bar{n}_l)^{\mathrm{s}} \tag{5.89}$$

$$\delta\varepsilon_{kl}^{\mathrm{i}} = \delta\varepsilon_{kl} + \frac{1-f}{h}(\delta u_k \bar{n}_l)^{\mathrm{s}} \tag{5.90}$$

Substituting Eqs, (5.89-5.90) into Eq. (5.85) results in:

$$\bar{r}_i^{\,\mathrm{new}} = \bar{r}_i^{\,\mathrm{previous}} + \left(D_{ijkl}^{\mathrm{o}} - D_{ijkl}^{\mathrm{i}}\right)\delta\varepsilon_{kl}\bar{n}_j - D_{ijkl}^{\mathrm{o}}\frac{f}{h}(\delta u_k \bar{n}_l)^{\mathrm{s}}\bar{n}_j - D_{ijkl}^{\mathrm{i}}\frac{1-f}{h}(\delta u_k \bar{n}_l)^{\mathrm{s}}\bar{n}_j \tag{5.91}$$

To enforce the traction equilibrium condition, $\bar{r}_i^{\,\mathrm{new}} = 0$ in Eq. (5.91) needs to be met, leading to the incremental displacement jump δu_k as:

$$\delta u_k = \left(\frac{f}{h}D_{ijkl}^{\mathrm{o}}\bar{n}_l\bar{n}_j + \frac{1-f}{h}D_{ijkl}^{\mathrm{i}}\bar{n}_l\bar{n}_j\right)^{-1}\left[\bar{r}_i^{\,\mathrm{previous}} + \left(D_{ijkl}^{\mathrm{o}} - D_{ijkl}^{\mathrm{i}}\right)\delta\varepsilon_{kl}\bar{n}_j\right] = {C_{ik}}^{-1}\left[\bar{r}_i^{\,\mathrm{previous}} + \left(D_{ijkl}^{\mathrm{o}} - D_{ijkl}^{\mathrm{i}}\right)\delta\varepsilon_{kl}\bar{n}_j\right] \tag{5.92}$$

The strain increments $\delta\varepsilon_{ij}^{\mathrm{i}}$ and $\delta\varepsilon_{ij}^{\mathrm{o}}$ can be then determined from δu_k before computing stress increments $\delta\sigma_{ij}^{\mathrm{o}}$ and $\delta\sigma_{ij}^{\mathrm{i}}$. Once $\delta\sigma_{ij}^{\mathrm{o}}$ and $\delta\sigma_{ij}^{\mathrm{i}}$ are updated, the macro stress increment can be obtained based on Eq. (5.17) as:

$$\delta\sigma_{ij} = (1-f)\delta\sigma_{ij}^{\mathrm{o}} + f\delta\sigma_{ij}^{\mathrm{i}} \tag{5.93}$$

Solutions of this algorithm are required to satisfy the following criterion:

$$\left|\frac{\bar{r}_1}{\bar{t}_1^{\mathrm{o}}}\right| \leq \mathrm{TOLERANCE} \text{ and } \left|\frac{\bar{r}_2}{\bar{t}_2^{\mathrm{o}}}\right| \leq \mathrm{TOLERANCE} \tag{5.94}$$

5.4.3. Numerical verification

This section is to verify the algorithm of the numerical implementation described in Section 5.4 by performing several numerical examples. In the first example, the numerical accuracy on the algorithm of bifurcation detection in Section 5.4.1 of the suction-controlled biaxial test on Hostun sand at $s = 20$ kPa (Alabdullah, 2010) is verified against an analytical algorithm, adopting the following parameters: $E = 30000$ kPa; $\varrho = 0.25$; $\lambda' = 0.15$; $M = 1.05$; $\kappa_h = 0.88$; $p_R' = 12.41$ kPa; $\xi = 0.652$; $\mu = 0.0629\ \mathrm{kPa}^{-1}$; $p_{c0}' = 1000$ kPa; $r = 1.5$; $\alpha = 0.5$; $\beta = 0.8$; $p_b = 50$ kPa. In Figure 5.7, the results obtained from both algorithms are presented where minimum values of $\det\left(D_{ijkl}\bar{n}_j\bar{n}_l\right)$ and φ are plotted against ε_{11} at two levels of confining pressure: $\bar{\sigma}_{22} = 50$ kPa and $\bar{\sigma}_{22} = 100$ kPa. As illustrated, numerical and analytical solutions are found to agree well, highlighting the numerical stability of the proposed algorithm to detect the onset of localisation.

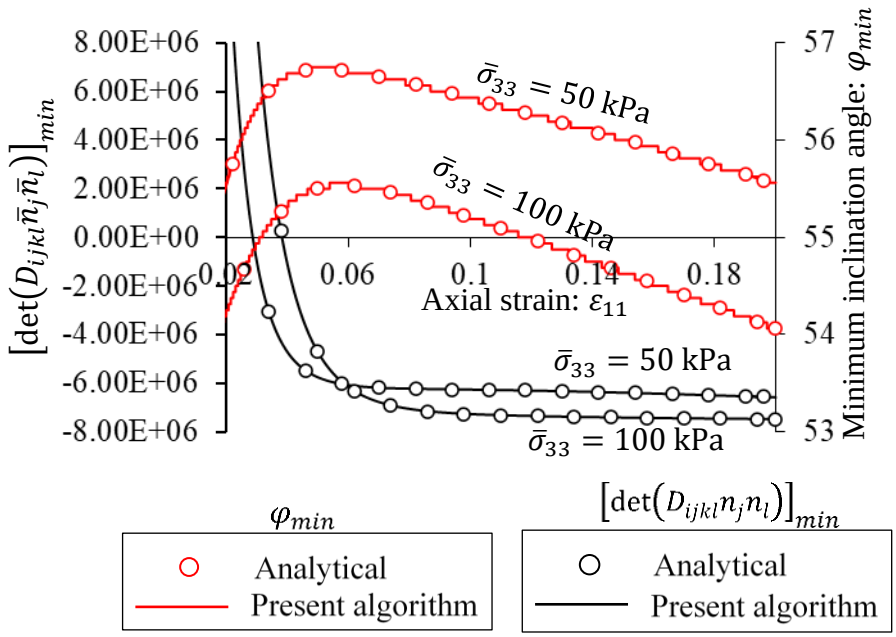

Figure 5.7. Verification of the algorithm for the bifurcation detection in biaxial compressions

Another example based on the drained biaxial test on Hostun sand (Alabdullah, 2010) is conducted to investigate the performance of the proposed two-level algorithm in Section 5.4.2 with $\bar{\sigma}_{22} =$ 50 kPa and $s =$ 20 kPa. This example adopts the same set of parameters in the previous example, adding $h = 24.755\,mm$ and $H' = 55.012\,mm$ for post-localisation behaviour. A comparison between numerical results of the current algorithm of four different axial strain increments ($\Delta\varepsilon_{11} = 1.5 \times 10^{-7}$, 1.5×10^{-6}, 1.5×10^{-5} and 1.5×10^{-4}) is carried out by plotting macro deviatoric stress, volumetric strain, traction and relative error against axial strain in Figures 5.8-5.10. As can be seen, solutions of $\Delta\varepsilon_{11} = 1.5 \times 10^{-7}$, 1.5×10^{-6} and 1.5×10^{-5} are convergent to each other and exhibit small errors. This reveals an adequate performance of the present iterative algorithm in enforcing the traction continuity condition. However, it should be noted that this integration algorithm is unstable for implementations with large strain steps, as seen in the results of $\Delta\varepsilon_{11} = 1.5 \times 10^{-4}$. The present approach is based on infinitesimal strain and limited only to single integration points. In numerical simulations using the Finite Element Method (FEM), or Smoothed Particle Hydrodynamic (SPH), the infinitesimal sizes of strain-like increments cannot always be guaranteed, and hence sub-stepping in combination with this semi-implicit algorithm or full implicit stress return should be used (Nguyen & Bui, 2020). All these algorithms have been tested in Nguyen et al. (2016) and Nguyen & Bui (2020) and can be applied to this model in the future.

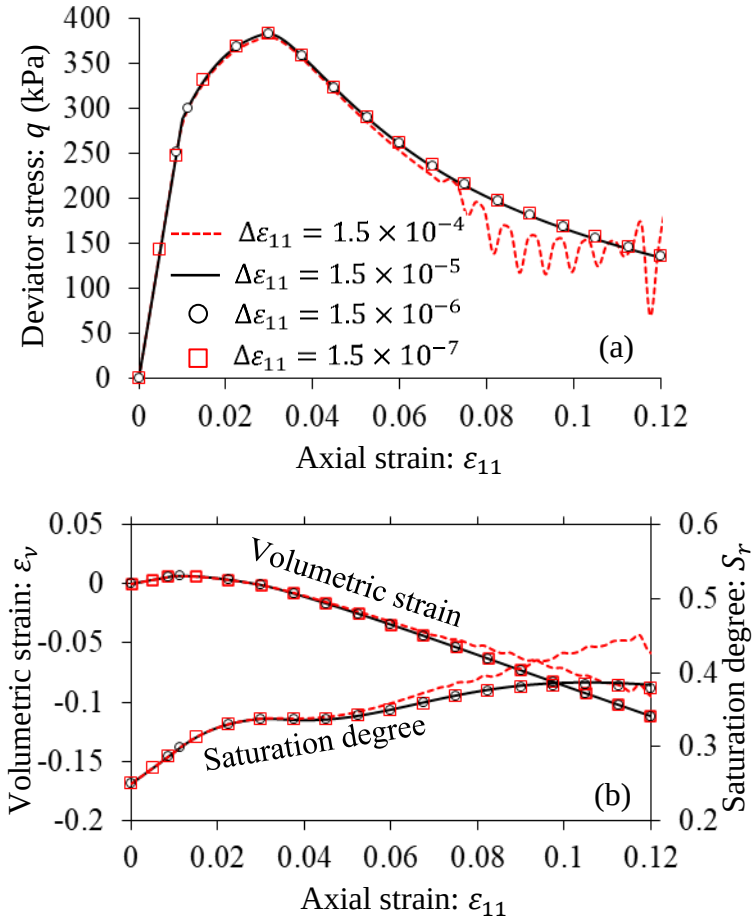

Figure 5.8. Performance of the proposed stress update algorithm under different values of $\Delta\varepsilon_{11}$ (a) $\varepsilon_{11} - q$ (b) $\varepsilon_{11} - \varepsilon_v, S_r$

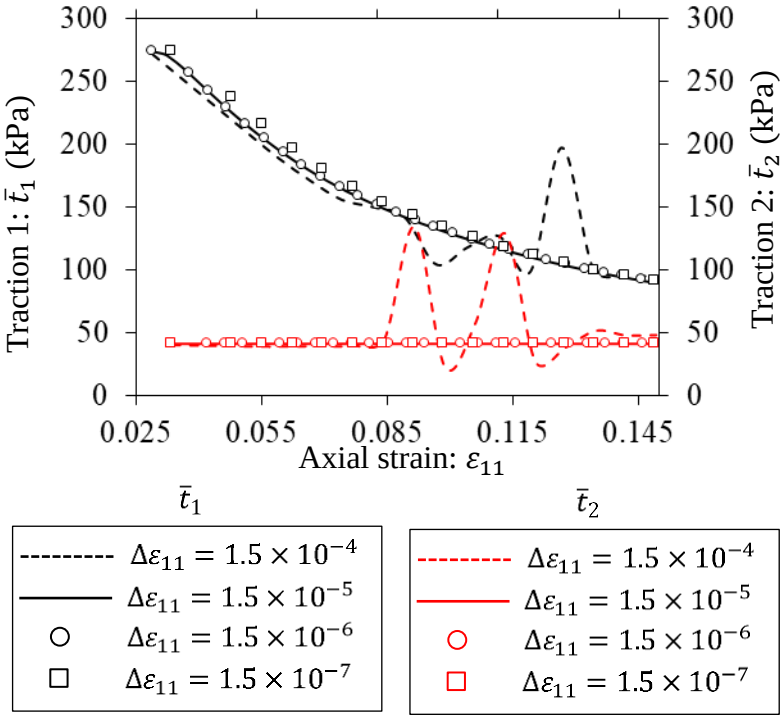

Figure 5.9. Traction of the proposed stress update algorithm under different values of $\Delta\varepsilon_{11}$

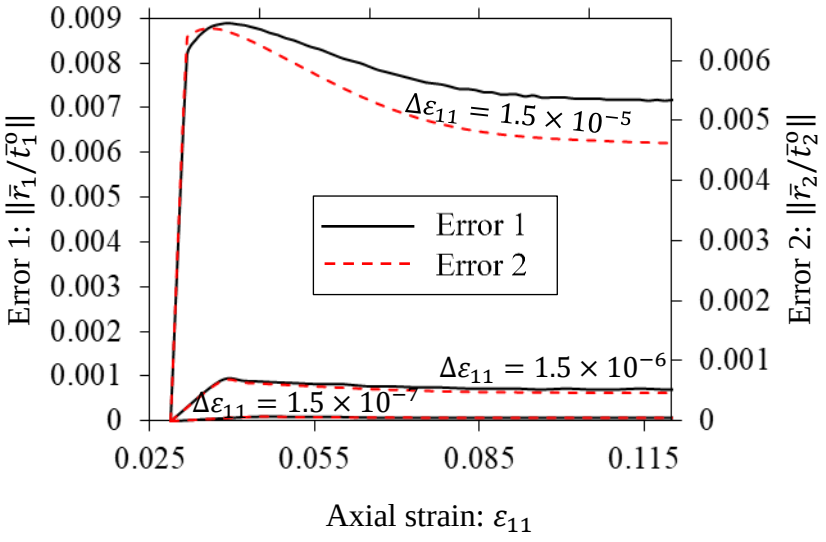

Figure 5.10. The relative error of the proposed stress update algorithm under different values of $\Delta\varepsilon_{11}$

Next, the mixed-control loading algorithm of the two-level stress return procedure is assessed through a simulation on the response of the triaxial shear test on compacted silty (Patil, 2014) in the saturated state. In this example, suction is kept constant at $s = 0$ kPa with $S_{r0} = 1$ while the total lateral pressures are fixed at $\bar{\sigma}_{33} = 200$ kPa and $\bar{\sigma}_{33} = 300$ kPa during shearing. The following parameters

are taken as: $E = 55000$ kPa; $\varrho = 0.25$; $\lambda' = 0.25; M = 1.2$; $\kappa_h = 0.26$; $p'_R = 450$ kPa; $\xi = 0.26; \mu = 0.0055$ kPa^{-1}; $p'_{c0} = 1100$ kPa; $r = 1.5$; $\alpha = 0.85$; $\beta = 0.01$; $p_b = 90$ kPa; $H' = 79.598$ mm and $h = 39.8$ mm. As can been in Figure 5.12, the macro total confining pressures are kept constant, while confining total pressures outside and inside the shear band vary along two separate paths after the bifurcation point. It can also be observed that the $q: p'$path is always a linear line with the slope of $\frac{\Delta q}{\Delta p'} = 3$, although the materials inside and outside the localisation band follow different nonlinear loading paths in the post-localisation regime. These results demonstrate that the proposed mixed-control loading algorithm is accurate in mimicking triaxial loading conditions. Furthermore, S_r keeps unchanged at 1 throughout the loading procedure of the test (see Figure 5.11), indicating the ability of the numerical algorithm in facilitating the transition between saturated and unsaturated conditions.

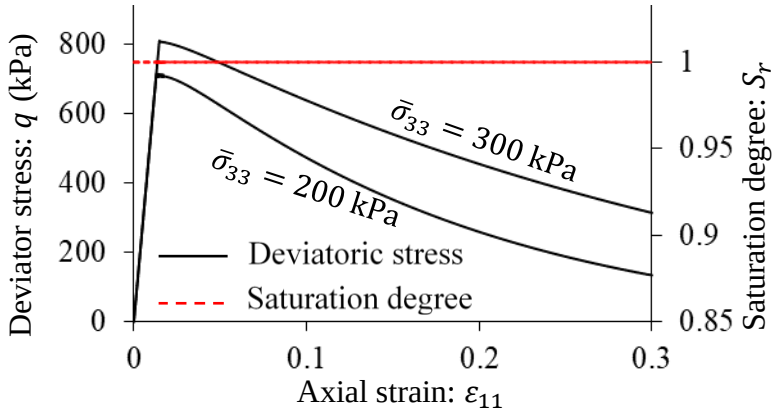

Figure 5.11. Macro performance of the proposed stress update algorithms in triaxial compressions in the saturated state

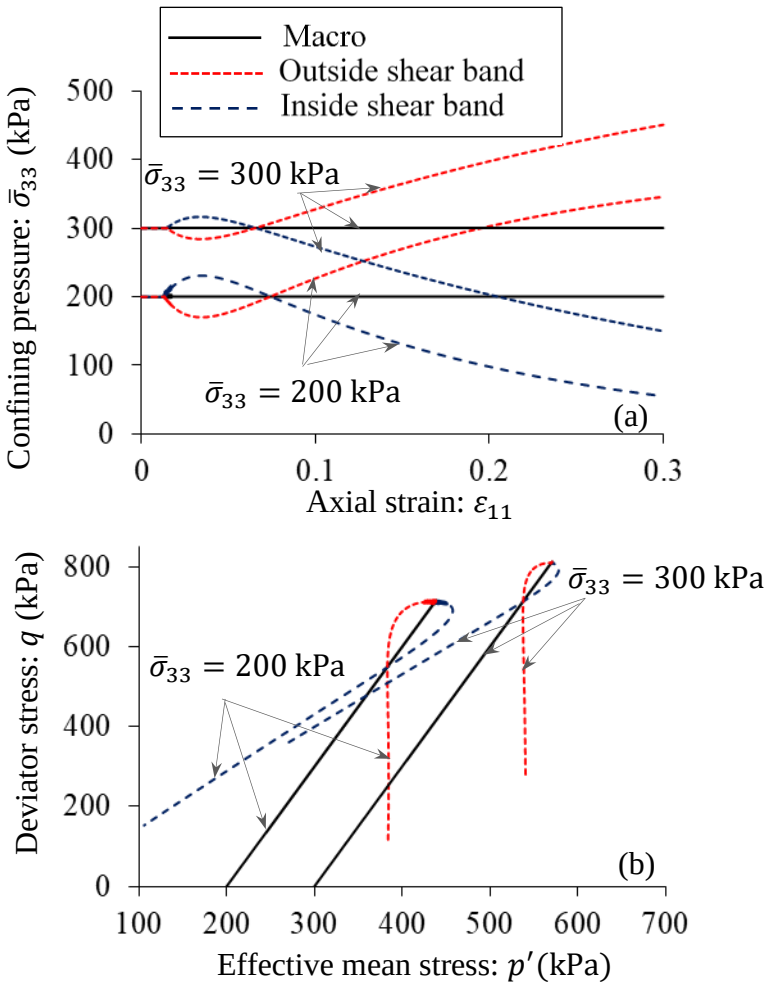

Figure 5.12. Macro and local performances of the proposed stress update algorithms in triaxial compressions in the saturated state (a) $\varepsilon_{11} - \bar{\sigma}_{33}$ and (b) $p' - q$

5.5. Model parameters

As can be seen in Eqs. (5.17-5.18), (5.21), (5.29-5.31) and (5.33-5.37), the proposed model has 15 parameters that can be calibrated following a step by step procedure for relevant experimental data obtained from a series of combined mechanical-hydraulic loading paths. The performance of this calibration approach will be elaborated through an example based on the suction-controlled triaxial shear test on compacted Kaolin soil using specimens with a 100 mm height and 50 mm diameter (Thu, 2006).

5.5.1. Parameters involving diffuse stage

The base model for elastic and inelastic behaviour in the diffuse stage, outside and inside the localisation band has 13 parameters (E, ϱ, κ_h λ', p'_{c0}, p'_R, μ, r, ξ, p_b, β, α and M) which are not

subject to any conditions associated with the model of localised failure. Therefore, these parameters can be calibrated in much similar ways as that of the homogeneous model presented in the preceding chapter (Chapter 4). In particular, experimental results of isotropic compression tests are used to calibrate E, ϱ, λ', p'_{c0}, p'_R, μ, r, ξ, β and p_b by fitting NCLs to their experimental counterparts, while the parameter κ_h can be found to match well with the experimental data of the water retention curve based on drying/wetting tests under the constant net mean stress. By following this calibration procedure, the numerical results of SWCC (drying test under constant net mean stress of $\bar{p} = 100$ kPa, see Figure 5.13a), NCLs (suction-controlled isotropic compression tests at $s = 100$ kPa, 200 kPa, 300 kPa, see Figure 5.13b), are in the best agreement with experimental data in the case of $E = 25000$ kPa; $\varrho = 0.25$; $\lambda' = 0.06$; $\kappa_h = 0.16$; $p'_R = 22$ kPa; $\xi = 0.6$; $\mu = 0.0601$ kPa^{-1}; $p'_{c0} = 300$ kPa; $r = 1.97$; $\beta = 0.05$; $p_b = 70$ kPa. Besides, α and M are associated with the shape of the initial yield surface in the p': q space. Thus, they can be identified by adjusting them until establishing a best match between predicted and measured initial yield curves. For instance, for the suction-controlled triaxial shear test on compacted Kaolin soil (Thu, 2006), data on the initial yield curve in the loading case of $s = 200$ kPa can be used to determine $M = 1.25$ and $\alpha = 0.85$ (see Figure 5.14).

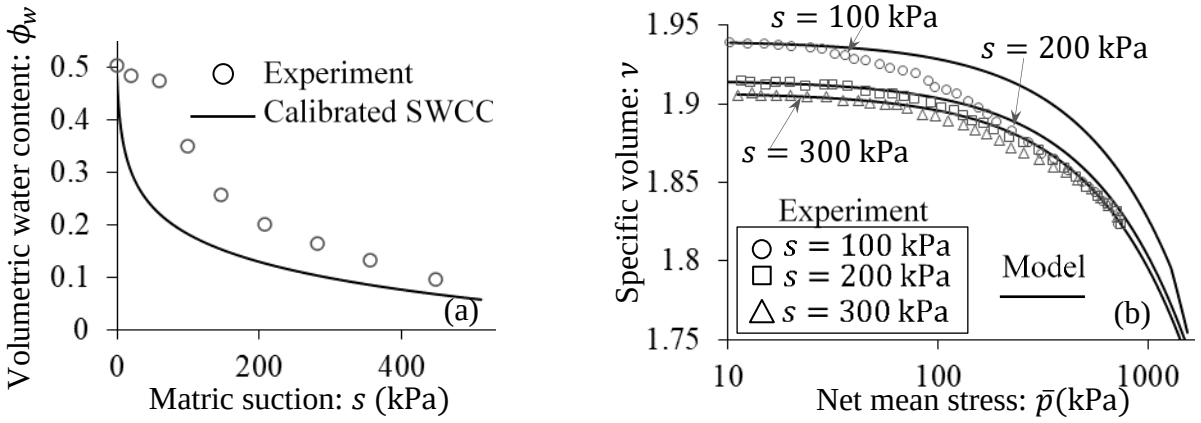

Figure 5.13. (a) Calibration of κ_h based on SWCC obtained from net pressure-controlled tests (b) calibration of E, ϱ, λ', p'_{c0}, r, p'_R, ξ, μ, β and p_b based on suction-controlled isotropic compression tests on Kaolin soil (after Thu, 2006)

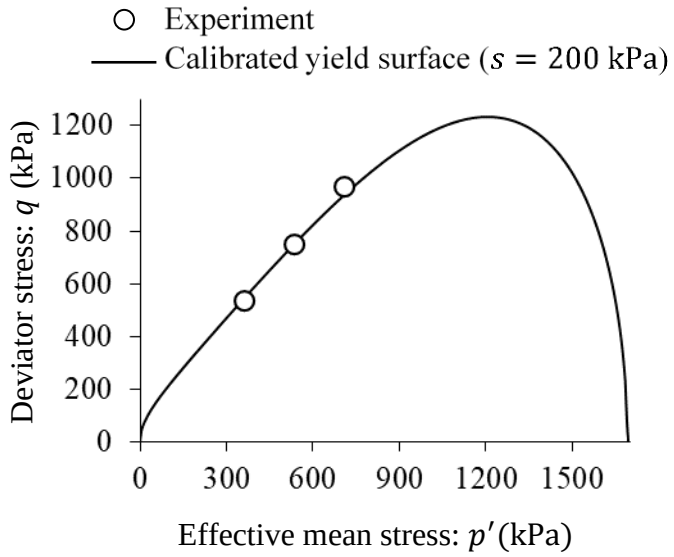

Figure 5.14. Calibration of M and α based on yield surface obtained from suction-controlled triaxial tests on Kaolin soil at $s = 200\ kPa$ (after Thu, 2006)

5.5.2. Size-dependent parameters involving localised stage

In the localised stage, the inhomogeneous deformation and size-dependent behaviour take place within the test specimens. To take this into account, parameters (H', f or h) related to the size of the localisation band and specimen are needed in this approach, apart from parameters of the base model as described earlier. Along with this, an appropriate procedure of calibration is essential to allow this constitutive model to be consistent with the proposed two-scale constitutive approach. In principle, these parameters can be experimentally obtained by making a rough estimation based on experimental shapes of localised failures. In particular, H' can be estimated through the formulation of $H' = Lcos\varphi$ with L denoting the height of the specimen (see Figure 5.1) where φ can be determined approximately through the experimental shape of localised failure (Nguyen et al., 2016). Nevertheless, L and φ change throughout the loading process. Therefore, it is hard to determine an accurate value of H' if experiments do not provide sufficiently the evolutions in L and φ during shearing. On the other hand, physically, the width of shear band h is dependent on the material microstructures and also loading paths (Nguyen et al., 2016; Nguyen & Bui, 2020). The thickness of the localisation band always evolves with deformation during the transition from diffuse to localised failure (Nguyen & Bui, 2020). This evolution of thickness of localisation band has been observed in soils (Ando et al., 2012; Ando, 2013) and also rocks (Verma et al., 2019) using advanced image-based instrumentation. The very thin (or zero thickness) band experimentally observed at the end of the test is the final thickness of this band after this evolution (see Figure 5.15). It is, therefore, not a good representative of the thickness. This evolution should be taken into account if experimental data on the evolution

and correlation with mechanical behaviour are available. However, given the unavailability of such data for partially saturated soils, the evolution of shear band thickness is not taken into account in this model. Instead, an assumed value of shear band thickness, as a representative to reproduce the dissipation and experimentally observed behaviour of the specimen, is used in the model. For these reasons, $H' = 50.46\,mm$ and $f = 0.65$ are chosen in the suction-controlled triaxial shear test on compacted Kaolin soil (Thu, 2006) as an appropriate way to capture the softening response at $s =$ 200 kPa, $\bar{\sigma}_{33} = 100$ kPa as depicted in Figure 5.15.

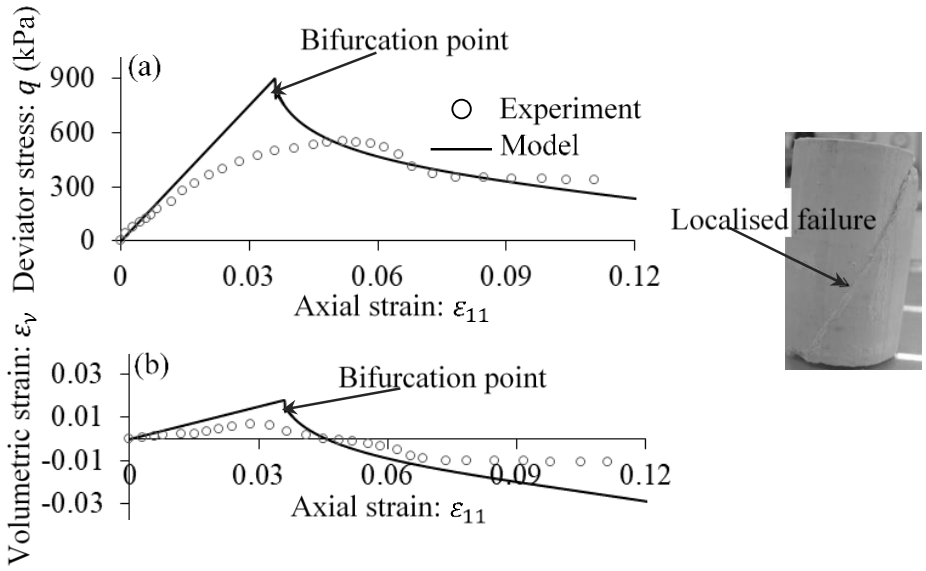

Figure 5.15. Assuming f for the best fit with the softening behaviour ($s = 200\ kPa$, $\bar{\sigma}_{33} = 100\ kPa$) and preventing the unphysical snapbacks in the numerical analysis obtained from suction-controlled triaxial test compression tests on Kaolin soil (after Thu, 2006) (a) $\varepsilon_{11} - q$ (b) $\varepsilon_{11} - \varepsilon_v$

5.6. Model validation

In this section, the prediction capacity of this constitutive model possessing two scales of behaviour is assessed against different experimental results of both triaxial and biaxial shear tests on partially saturated soils under constant suction conditions. The onset and orientation of shear bands are predicted, and shear band geometry (thickness and orientation) along with its hydro-mechanical behaviour are important elements in post-localisation responses of the samples. It is essential to address that the proposed double-scale model for partially saturated soils in this chapter aims at correctly describing and capturing the responses of partially saturated soil samples in both pre-and post-localisation regimes. This is, to the best of my knowledge, an impossible task for existing constitutive models for partially saturated soils. It is noted that the current two-scale model is only

considered as an initial step towards a better and more rigorous approach for modelling localised failures of partially saturated soils involving the size-dependent behaviour that cannot be found in previous studies. At the current stage of research, this study lacks a strong calibration method for parameters related to size-dependent behaviour despite its importance in constitutive modelling due to the lack of available and accessible experimental data providing sufficient data evolving thickness of the localisation band (Nguyen & Bui, 2020).

5.6.1. Hostun sand, biaxial compression test (Alabdullah, 2010)

The model predictions are first validated against the drained biaxial shear test on Hostun sand (Alabdullah, 2010) at two different levels of suction (0 kPa and 20 kPa). In this test, rectangular (prismatic) soil specimens with a width of 100 mm, height of 120 mm and thickness of 40 mm are loaded under confining pressures of $\bar{\sigma}_{22} = 50$ kPa and $\bar{\sigma}_{22} = 100$ kPa. The following model parameters: $E = 30000$ kPa; $\varrho = 0.25$; $\lambda' = 0.15; M = 1.05$; $\kappa_h = 0.88$; $p'_R = 12.41$ kPa; $\xi = 0.652; \mu = 0.0629$ kPa^{-1}; $p'_{c0} = 1000$ kPa; $r = 1.5$; $\alpha = 0.5$; $\beta = 0.8$ and $p_b = 50$ kPa are identified through a calibration procedure based on the experimental results at $\bar{\sigma}_{22} = 50$ kPa. Nonetheless, there are also no clear experimental details on the formation and width of shear bands under various levels of confining pressure and suction in this test. Therefore, parameters related to post-localisation behaviour can be assumed as $H' = 55.012$ mm and $f = 0.45$. It is acknowledged that the selection of these input parameters, mainly based on the curve-fitting technique, is generally arbitrary and has poor linkages with the testing procedures applied. This shortcoming will be addressed in future works. Given this parameter set, a close agreement between the computed and measured results on shear stress and volumetric strain are presented in Figures 5.16a, 5.16b, 5.17a and 5.17b. Furthermore, the band orientations measured in experiments are also reasonably captured by the model, as shown in Figures 5.16c and 5.17c. Nevertheless, there are disparities between numerical and experimental data encountered in the volumetric strain at $s = 20$ kPa. This may be attributed to missing representations of evolution in the band size in the present model, given the proposed approach is based on the assumption of a constant width and inclination angle of the localisation band during shearing.

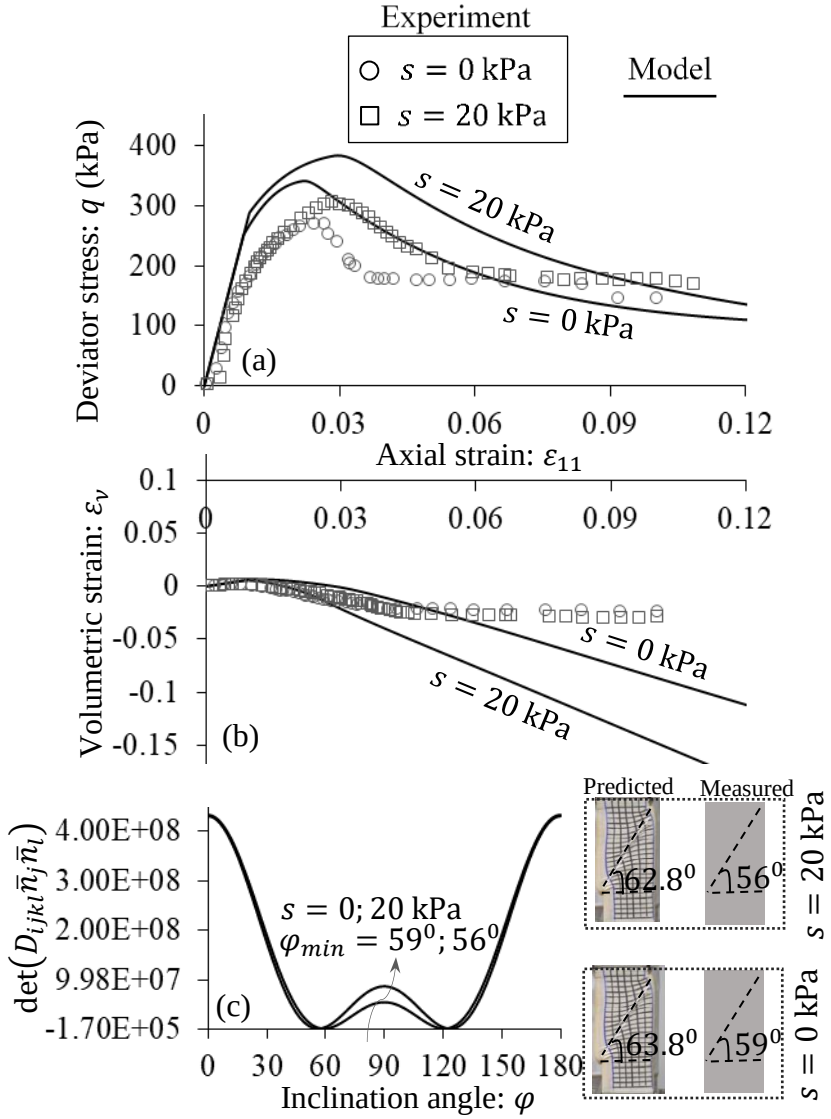

Figure 5.16. Validation with a drained biaxial compression test on Hostun sand at $\bar{\sigma}_{22} = 50$ kPa (after Alabdullah, 2010) (a) $\varepsilon_{11} - q$ (b) $\varepsilon_{11} - \varepsilon_v$ (c) $\varphi - \det(D_{ijkl}\bar{n}_j\bar{n}_l)$ at bifurcation point

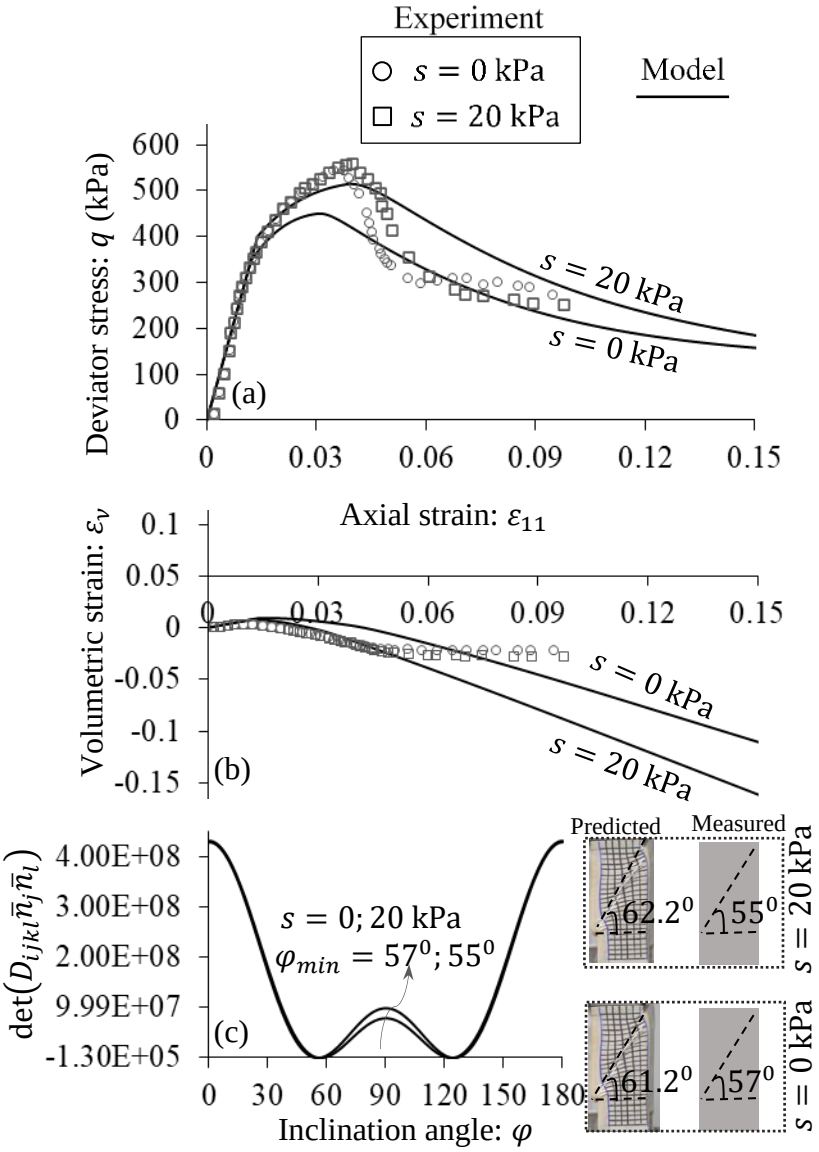

Figure 5.17. Validation with a drained biaxial compression test on Hostun sand at $\bar{\sigma}_{22} = 100$ kPa (after Alabdullah, 2010) (a) $\varepsilon_{11} - q$ (b) $\varepsilon_{11} - \varepsilon_v$ (c) $\varphi - \det(D_{ijkl}\bar{n}_j\bar{n}_l)$ at bifurcation point

5.6.2. Kaolin soil, triaxial compression test (Thu, 2006)

The next example analyses the suction-controlled triaxial shear test on Kaolin soil (Thu, 2006). With calibrated parameters in Section 5.5, the results of model simulations generally are in good agreement with that of experiments on drained triaxial shear test at different suction ($s = 100$ kPa, 200 kPa and 300 kPa) and confining pressures ($\bar{\sigma}_{33} = 200$ kPa and $\bar{\sigma}_{33} = 300$ kPa) levels (see Figures 5.19-5.21), except the results of volumetric strain in the case of $s = 300$ kPa and $\bar{\sigma}_{33} = 300$ kPa (see Figure 5.21b) and inclination angles of the shear band at $s = 200\ kPa$, $\bar{\sigma}_{33} = 100$ kPa (see Figure 5.18).

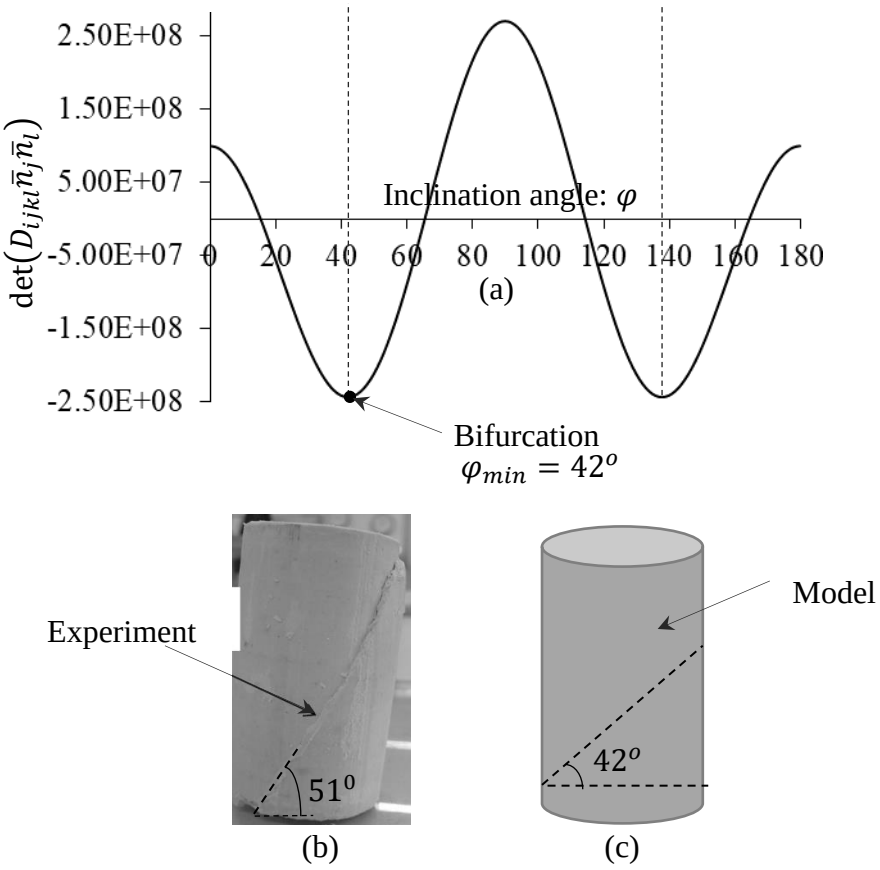

Figure 5.18. The orientation of the shear band obtained from suction-controlled triaxial tests on Kaolin soil (after Thu, 2006) (a) $\varphi - det(D_{ijkl}\bar{n}_j\bar{n}_l)$ at bifurcation point ($s = 200\ kPa$, $\bar{\sigma}_{33} = 100\ kPa$) (b) The measured orientation of shear band ($s = 200\ kPa$, $\bar{\sigma}_{33} = 100\ kPa$) (c) The predicted orientation of shear band ($s = 200\ kPa$, $\bar{\sigma}_{33} = 100\ kPa$)

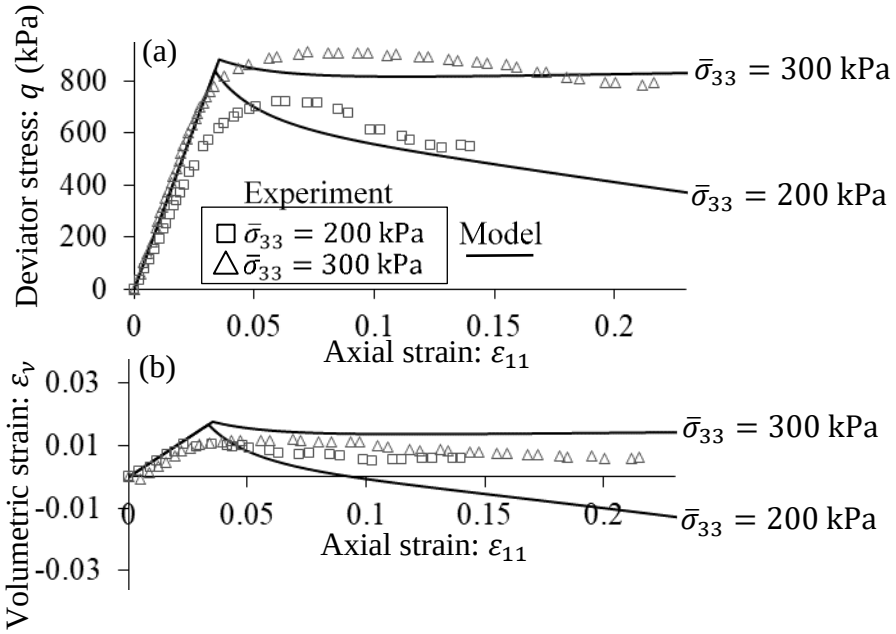

Figure 5.19. Validation with a drained triaxial compression test on Kaolin soil at $s = 100$ kPa (after Thu, 2006) (a) $\varepsilon_{11} - q$ (b) $\varepsilon_{11} - \varepsilon_v$

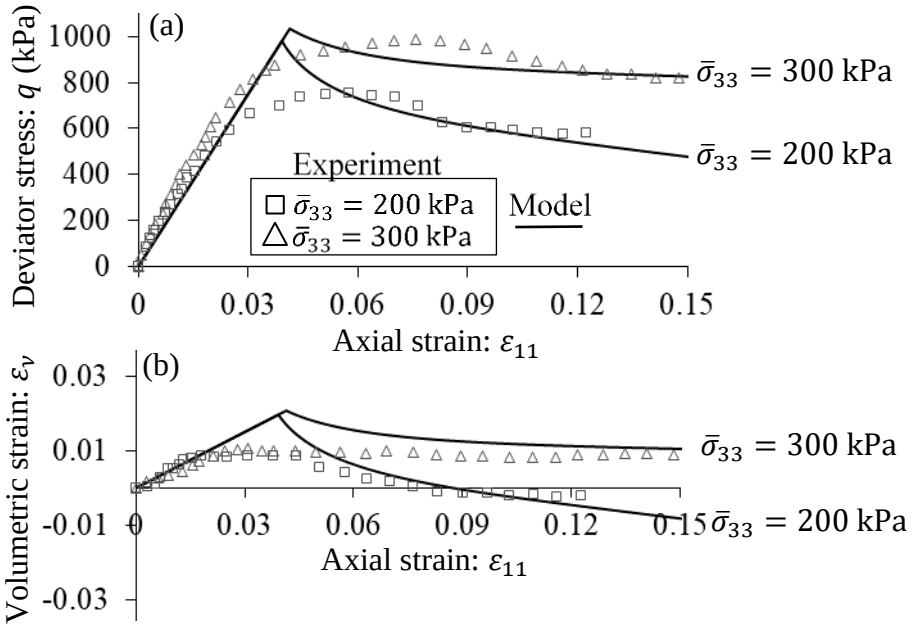

Figure 5.20. Validation with a drained triaxial compression test on Kaolin soil at $s = 200$ kPa (after Thu, 2006) (a) $\varepsilon_{11} - q$ (b) $\varepsilon_{11} - \varepsilon_v$

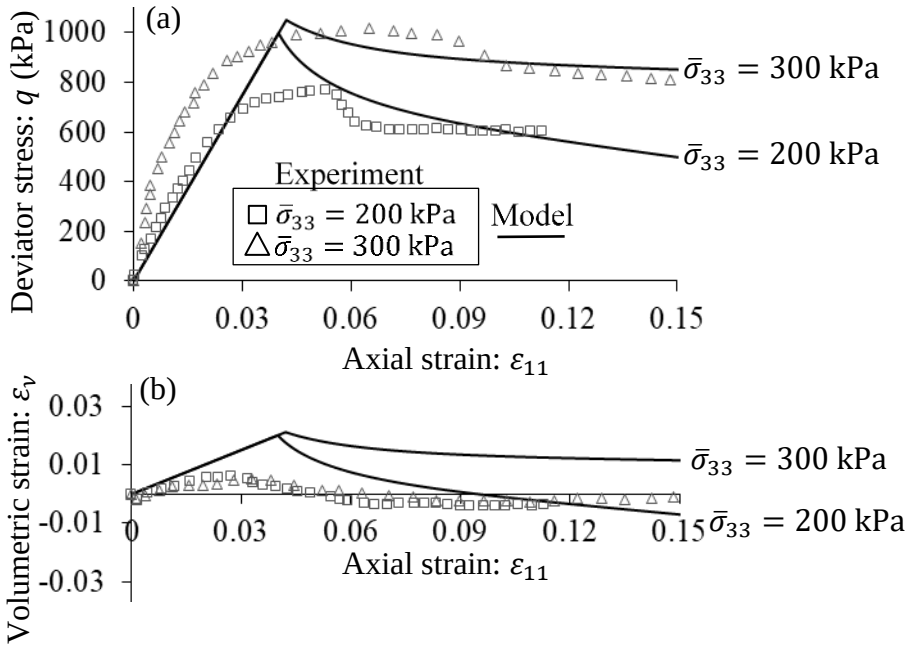

Figure 5.21. Validation with a drained triaxial compression test on Kaolin soil at $s = 300$ kPa (after Thu, 2006) (a) $\varepsilon_{11} - q$ (b) $\varepsilon_{11} - \varepsilon_v$

5.6.3. Compacted silty, triaxial compression test (Patil, 2014)

The model performance is further investigated involving the suction-controlled triaxial shear test on compacted silty sand at four levels of suction $s = 50$ kPa, 250 kPa, 500 kPa and 750 kPa under a constant net confining pressure of $\bar{\sigma}_{33} = 300$ kPa (Patil, 2014). This experiment is conducted on cylindrical specimens of 71.12 mm in diameter and 142.24 mm in height. This simulation adopts the experimental data at $s = 250$ kPa to calibrate the following parameters: $E = 55000$ kPa; $\varrho = 0.25$; $\lambda' = 0.25; M = 1.2;\ \kappa_h = 0.26;\ p'_R = 450$ kPa; $\xi = 0.26; \mu = 0.0055$ kPa^{-1}; $p'_{c0} = 1100$ kPa; $r = 1.5;\ \alpha = 0.85;\ \beta = 0.01;\ p_b = 90$ kPa. For size effects, despite the availability of several experimental data on shapes of localised failure in this test, there is no consensus on measuring it due to the lack of experimental data reflecting its evolution (Nguyen & Bui, 2020). In this sense, h or f is assumed to be a constant at $H' = 79.598$ mm and $f = 0.5$ which can be selected to capture well the experimental softening response and prevent the unphysical snapbacks in the numerical analysis. This is acknowledged as one of the limitations of the present study on strain localisation.

Numerical and experimental results on deviatoric stress and volumetric strain plotted against the axial strain are shown in Figure 5.22. In addition, at various suction levels, the determinant of the acoustic tensor is plotted against the inclination angle of the shear band in Figure 5.23 to investigate the performance of this model in capturing the localised failure patterns observed in experiments. As

illustrated, the computed results reasonably agree with their measured counterparts in the case of $s = 250$ kPa and 500 kPa. However, there is a mismatch between the model prediction and measurement at $s = 50$ kPa because the orientation and thickness of the localisation band are assumed to remain unchanged despite their variation with loading paths in the post-localisation stage (Nguyen & Bui, 2020). Furthermore, the assumption of a single tabular shear band leads to the discrepancy between numerical and experimental data in the case of $s = 750$ kPa where the multiple intersecting localisation bands are experimentally observed (see Figure 5.23d).

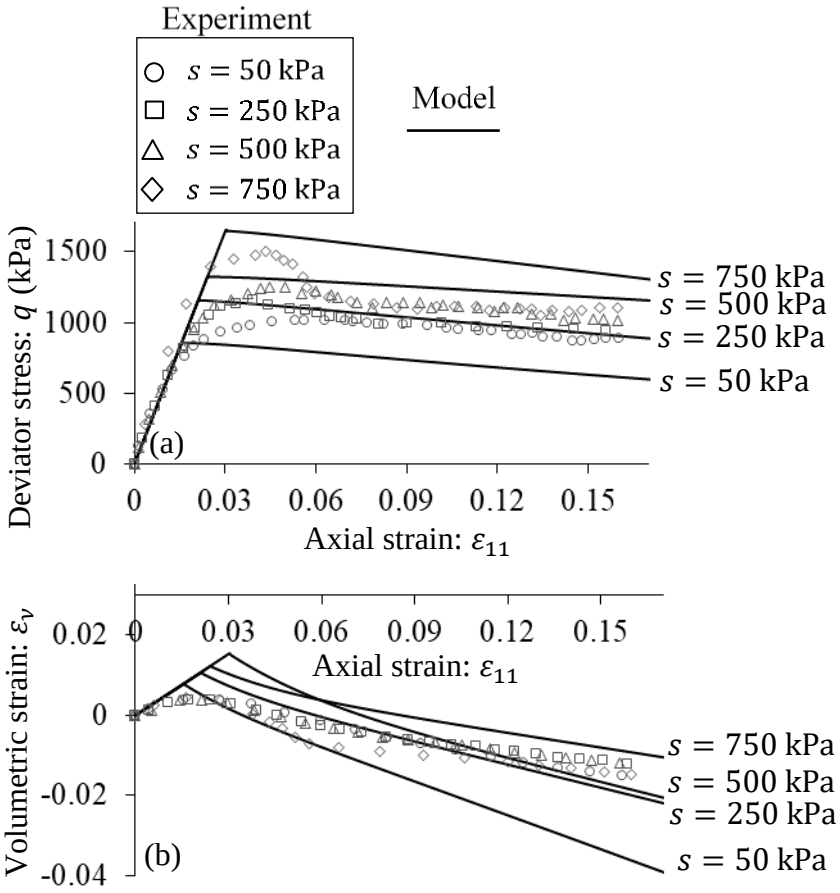

Figure 5.22. Validation with a drained triaxial compression test on compacted silty at $\bar{\sigma}_{33} = 300$ kPa (after Patil, 2014) (a) $\varepsilon_{11} - q$ (b) $\varepsilon_{11} - \varepsilon_v$

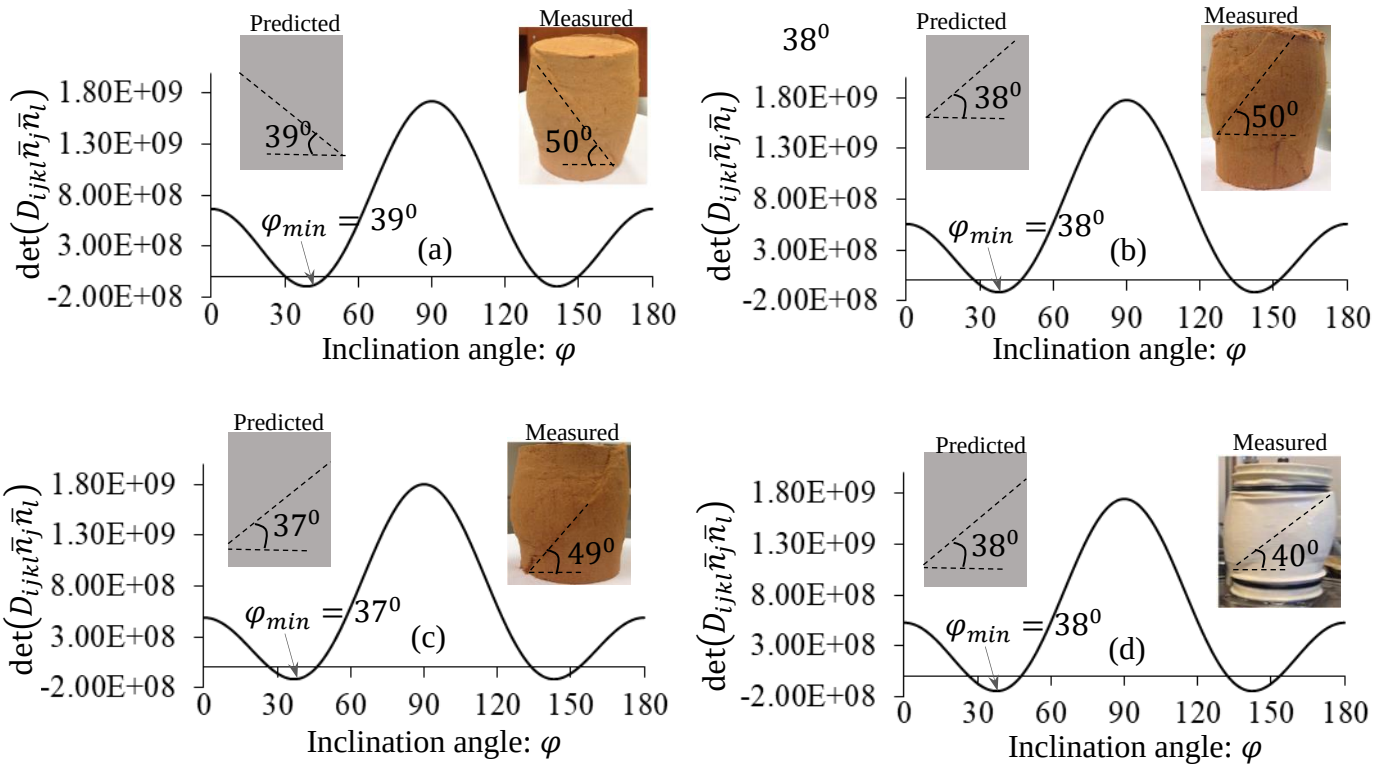

Figure 5.23. Validation with a drained triaxial compression test on compacted silty at bifurcation point at $\bar{\sigma}_{33} = 300$ kPa (after Patil, 2014) (a) $s = 50$ kPa (b) $s = 250$ kPa (c) $s = 500$ kPa (d) $s = 750$ kPa

5.6.4. Kurnell sand, triaxial compression test (Russell, 2004)

The drained triaxial compression test with confining pressure of $\bar{\sigma}_{33} = 50$ kPa under two suction levels of $s = 0$ kPa and 400 kPa (Russell, 2004) is investigated on specimens of Kurnell sand which are cylindrical, 50 mm in diameter and 51 mm in height. Parameters are taken as $E = 11000$ kPa; $\varrho = 0.25$; $\lambda' = 0.3; M = 1.28$; $\kappa_h = 0.16$; $p'_R = 363.31$ kPa; $\xi = 0.6; \mu = 0.0601$ kPa^{-1}; $p'_{c0} = 550$ kPa; $r = 2.5$; $\alpha = 0.65$; $\beta = 0.05$; $p_b = 70$ kPa, which are calibrated to achieve the best fit between the experimental result and its theoretical counterpart at $s = 400$ kPa. Due to the lack of appropriate experimental data for localisation bands, $H' = 35.46$ mm and $f = 0.8$ are assumed in this example to enable the predicted data to agree with measured data in reflecting the softening response and avoid problems of unphysical snapbacks. As can be seen in Figure 5.24, the experimental results are reasonably reproduced by the current model where partially saturated soils ($s = 400$ kPa) are more brittle than fully saturated soils ($s = 0$ kPa).

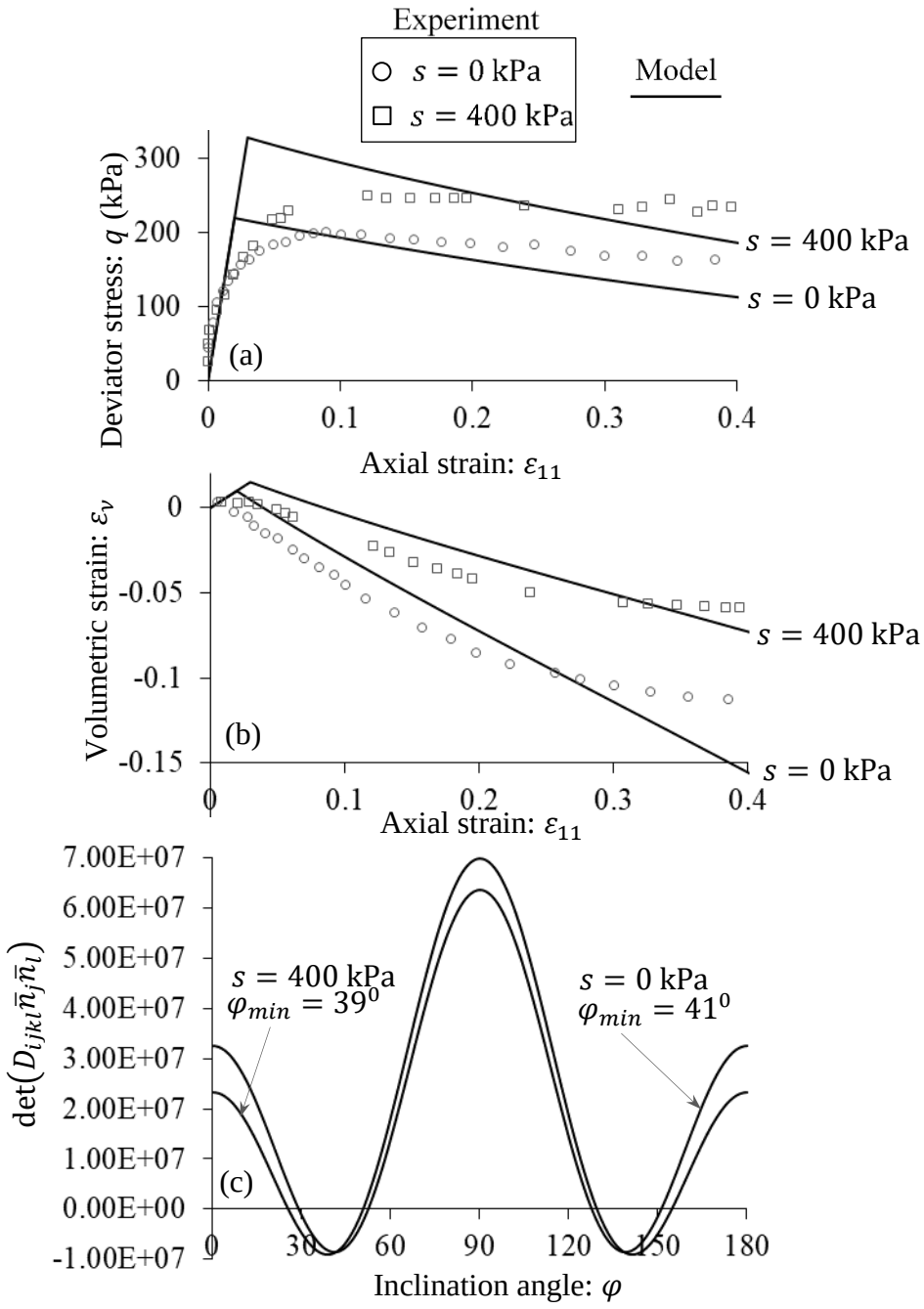

Figure 5.24. Validation with a drained triaxial compression test on Kurnell sand at $\bar{\sigma}_{33} = 50$ kPa (after Russell, 2004) (a) $\varepsilon_{11} - q$ (b) $\varepsilon_{11} - \varepsilon_v$ (c) $\varphi - \det(D_{ijkl}\bar{n}_j\bar{n}_l)$ at bifurcation point

5.7. Predictive model behaviour

In this section, several numerical examples are presented to demonstrate promising features of the proposed approach in simulating post-localisation responses of unsaturated soil samples in the suction-controlled triaxial shear test on Kaolin soil (Thu, 2006).

5.7.1. Onset and orientation of localisation band

The next examples pertain to an analysis of the model behaviour in capturing the effects of strain localisation, with the focus on the onset of localised failure and post-localisation responses using the same parameters in the previous example (see Section 5.5).

Effects of M and α on onset and orientation of localisation band

The bifurcation response of the proposed model ($s = 200$ kPa, $\bar{\sigma}_{33} = 100$ kPa) under the effects of M and α is first explored. For this purpose, a series of numerical simulations are performed for a range of $M = 0.9,\ 1.1,\ 1.25$ and $\alpha = 0.35,\ 0.65,\ 1$, as demonstrated in Figures 5.25 and 5.26, respectively. As depicted in Figures 5.25a and 5.26a, the model produces higher orientations of the localisation band at higher values of M and lower values of α. These features are consistent with what is observed in Figures 5.25b and 5.26b that decreasing M expands the yield surface towards the upper right direction in the $p'{:}\,q$ space, while decreasing α leads to an expansion in the part of the yield curve located on the lower right side and a narrowing in that located on the upper left side of the straight line with the $1{:}\,M$ slope. This observation corresponds to the increase in the initial shear stress when increasing M and decreasing α. The strong sensitivity of the bifurcation response to the parameter α and M can be clarified through their contribution in generating the plastic change of shear strain which significantly affects the tangent stiffness tensor.

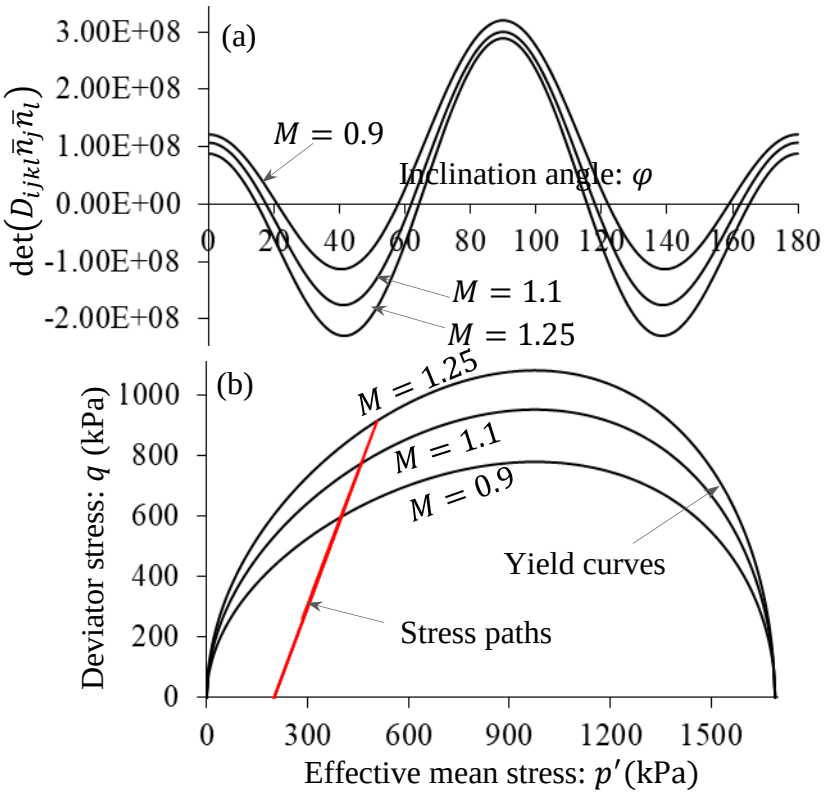

Figure 5.25. Effects of different values of M on the onset of localisation under drained triaxial shear tests on Kaolin soil: (a) $\varphi - det(D_{ijkl}\bar{n}_j\bar{n}_l)$ at bifurcation point (b) $p' - q$

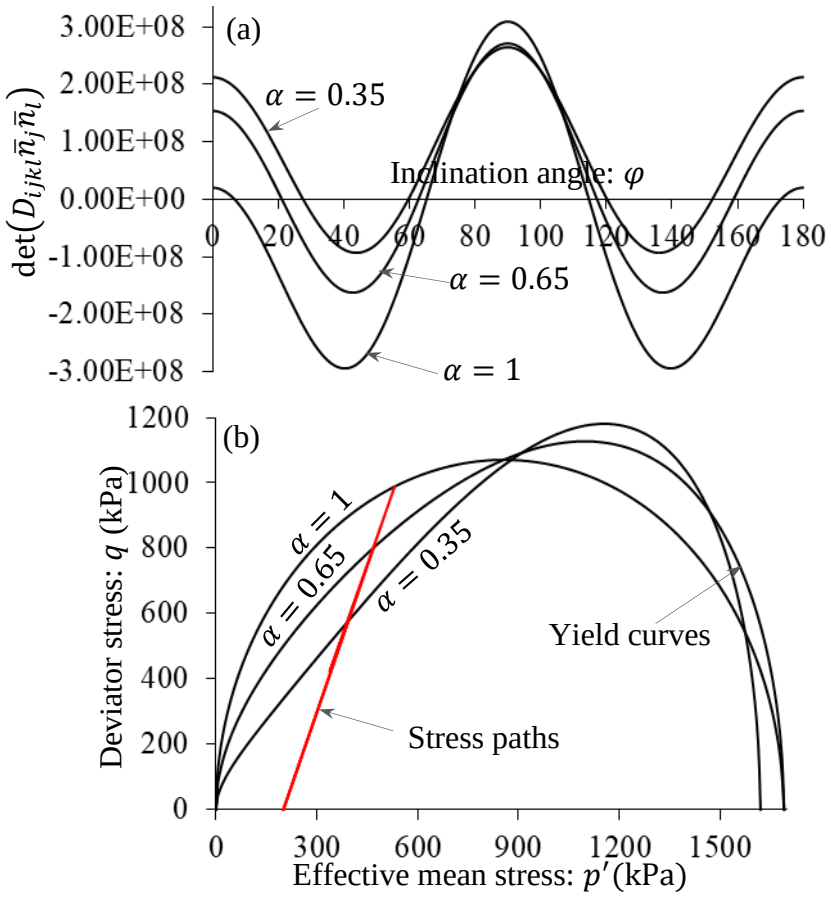

Figure 5.26. Effects of different values of α on the onset of localisation under drained triaxial shear tests on Kaolin soil: (a) $\varphi - det\left(D_{ijkl}\bar{n}_j\bar{n}_l\right)$ at bifurcation point (b) $p' - q$

Effects of suction on onset and orientation of localisation band

A sensitivity analysis on the effect of suction on the bifurcation behaviour of the model is conducted by varying $s = 20$ kPa, 50 kPa and 200 kPa at $\bar{\sigma}_{33} = 100$ kPa. At each level of suction, apart from the $\varepsilon_{11}: q$ and $\varepsilon_{11}: \left[\det\left(D_{ijkl}\bar{n}_j\bar{n}_l\right)\right]_{min}$ results in Figure 5.27a, the variation of the acoustic tensor determinant $\det\left(D_{ijkl}\bar{n}_j\bar{n}_l\right)$ with the band inclination angle at the bifurcation point is also depicted in Figure 5.27b. It can be seen that the orientation of the localisation band increases with increasing suction. This is closely linked to higher initial yield shear stresses due to the expansion of yield surface in the $p': q$ space if suction becomes bigger. Physically, partially saturated soils are stiffer and more brittle because of the development in the shear resistance by vanishing the spatial distribution of water menisci when suction increases.

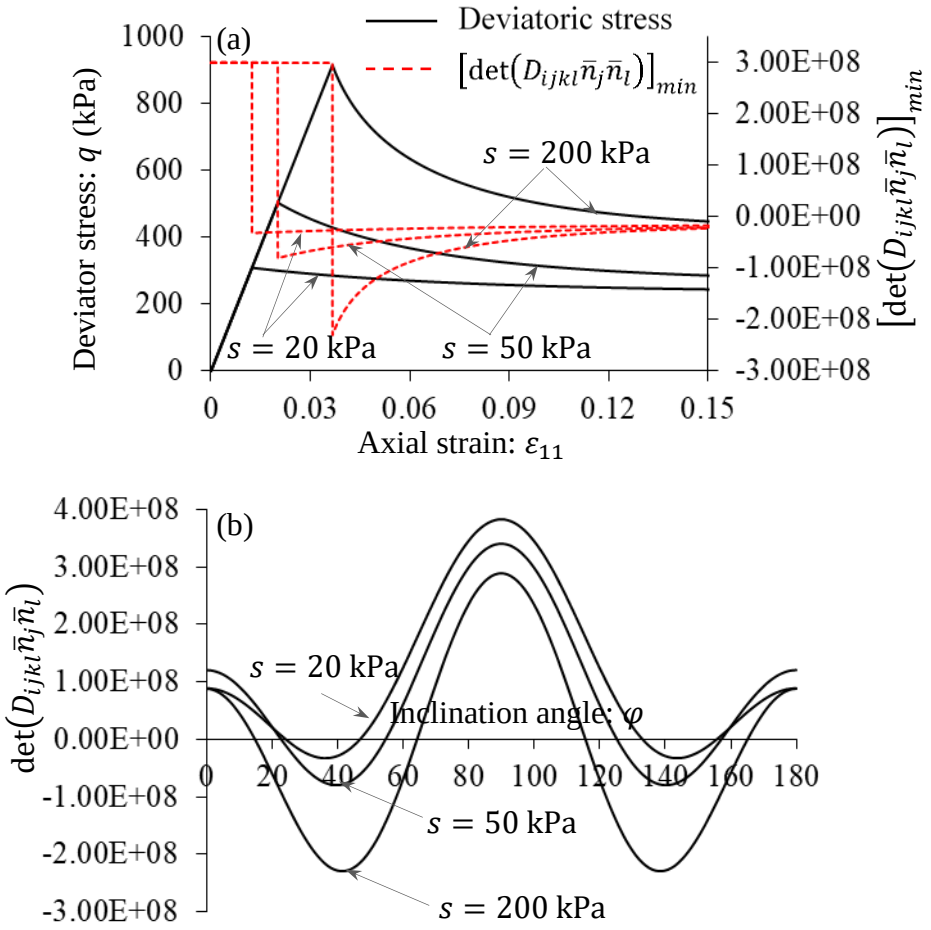

Figure 5.27. Effects of different levels of suction on the onset of localisation under drained triaxial shear tests on Kaolin soil: (a) $\varepsilon_{11} - q, [det(D_{ijkl}\bar{n}_j\bar{n}_l)]_{min}$ (b) $\varphi - det(D_{ijkl}\bar{n}_j\bar{n}_l)$ at the bifurcation point.

Effects of κ_h on onset and orientation of localisation band

As also shown in this section, a parametric study provides an assessment of the effect of varying $\kappa_h = 0.05$, 2 and 7. According to Figure 5.28, increasing κ_h signifies a decrease in the inclination of the localisation band, owing to the corresponding growth in the capillary effect (sS_r) on the soil skeleton stress. As can be seen, κ_h also appears in Eqs. (5.39) for computing the stress increment. Thus, its variation provides different results of the tangent stiffness tensor, reflecting the coupled hydro-mechanical characteristic in the proposed discontinuous bifurcation criterion.

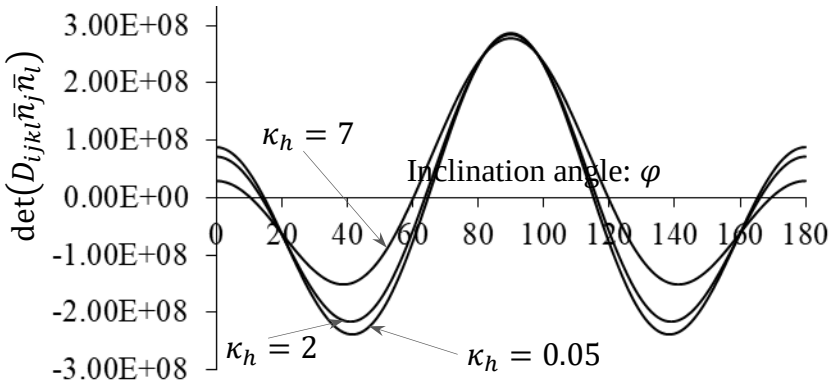

Figure 5.28. Effects of different κ_h on the onset of localisation under drained triaxial shear tests on Kaolin soil

Effects of β on onset and orientation of localisation band

A parametric study is here performed out to investigate the effects of β on the onset of localisation. At different $\beta = 0$, 0.5 and 0.9, $\det(D_{ijkl}n_j n_l)$ is plotted against φ in Figure 5.29. It can be found that the decrease in β reduces the brittleness of the material where φ_{min} increases. This is because the capillary irreversibility is observed to be stronger at a higher β. As can be seen in Eqs. (5.34) and (5.36), β is present in the flow rules for the irrecoverable rate of volumetric strain and saturation degree, and therefore affects the coupled hydro-mechanical energy lost. Furthermore, β governs the influence of saturation degree on the plastic dilatancy ratio $\dot{\varepsilon}_v^{\mathrm{p}}/\dot{\varepsilon}_s^{\mathrm{p}}$ (see Eqs. (5.34-5.35)). The change of saturation degree is purely recoverable despite the occurrence of the plastic change in strain if β is equal to zero. This feature fails to properly reproduce the simultaneous activation and development of both mechanical and hydraulic dissipation. When $\beta \neq 0$, the bi-directional hydro-mechanical dissipation is activated to allow the proposed model to have a better performance in the discontinuous bifurcation condition where the wetting-drying difference is captured during the loading-unloading process. This is an advance as compared with existing bifurcation theories for partially saturated soils.

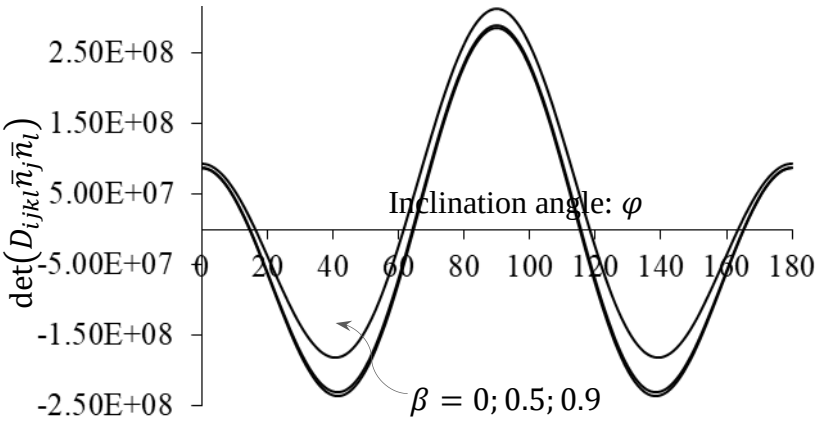

Figure 5.29. Effects of different β on the onset of localisation under drained triaxial shear tests on Kaolin soil (after Thu, 2006)

5.7.2. Post-localisation behaviour

To highlight the predictive capacity of the proposed model in capturing the responses inside and outside the shear band as the underlying ones controlling the macro behaviour in the post-localisation regime, a further example is presented in the case of $s = 200$ kPa. As illustrated in Figure 5.30, at each level of confining pressure ($\bar{\sigma}_{33} = 100$ kPa, 200 kPa, and 300 kPa), the loading paths are first homogeneous in both mechanical and hydraulic responses where the minimum determinant of the acoustic tensor is positive. In this homogeneous stage, there is no difference in stress, volumetric strain and saturation degree between materials inside and outside the localisation zone. Once the localisation is detected, the inhomogeneous changes of both strain and saturation degree are triggered simultaneously. From this point on, a further loading pushes the loading paths inside the localisation band to deviate from the unloading paths outside the band. In conjunction with this, a significant difference in volumetric strain and saturation degree between two local responses (outside and inside the shear band) is reproduced. In this case, volumetric strain and saturation degree of the bulk material exhibit reversible changes while that of the shear band undergo irreversible changes. The combination of these two components results in the averaged macro softening behaviour of the whole unit volume element, which is considered as the material behaviour measured from experiments.

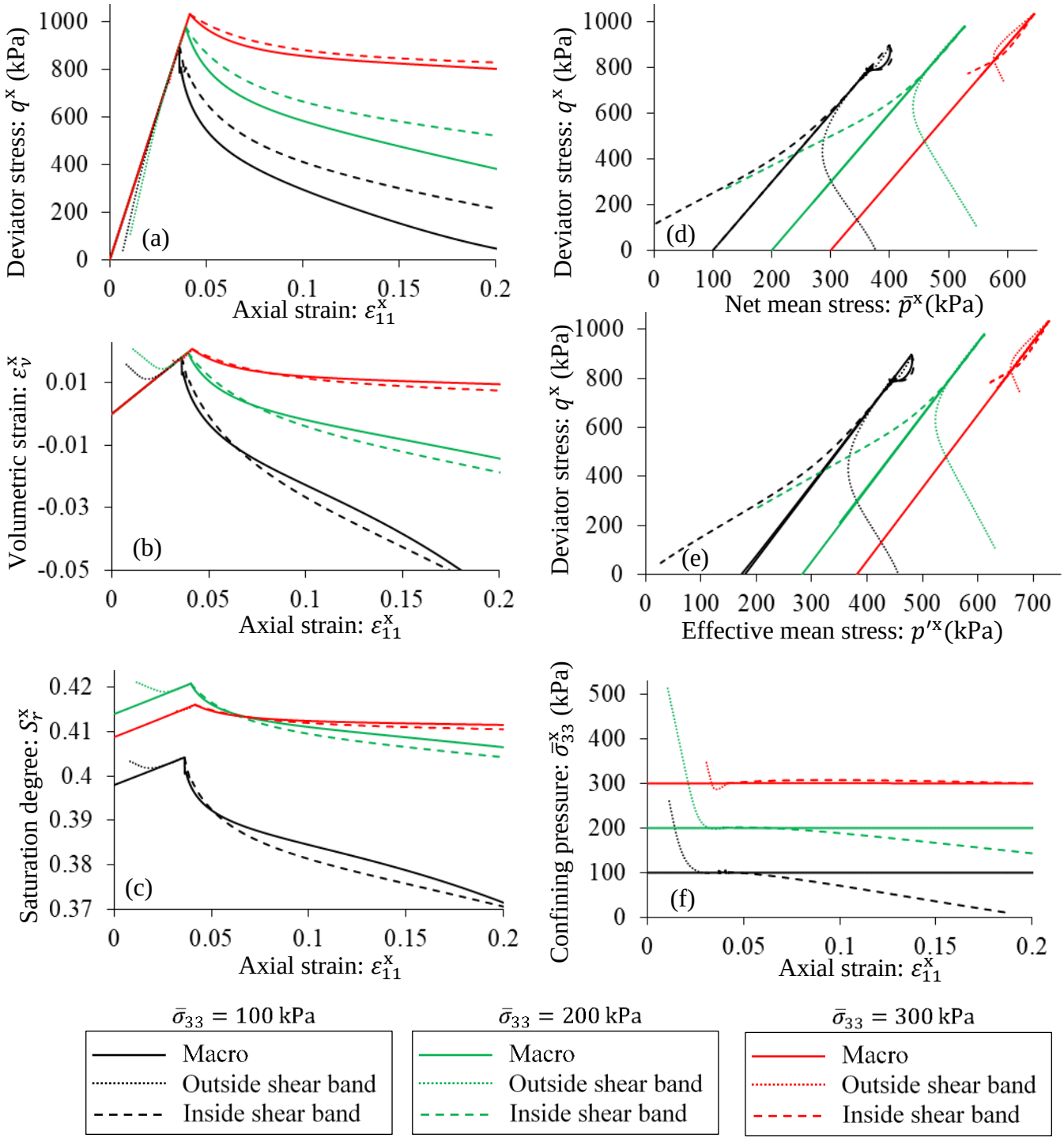

Figure 5.30. Macro behaviour and corresponding response outside and inside the localisation band of the drained triaxial compression test on Kaolin soil at $s = 200$ kPa (a) $\varepsilon_{11}^x - q^x$ (b) $\varepsilon_{11}^x - \varepsilon_v^x$ (c) $\varepsilon_{11}^x - S_r^x$ (d) $\bar{p}^x - q^x$ (e) $p'^x - q^x$ (f) $\varepsilon_{11}^x - \bar{\sigma}_{33}$ ("x" stands for "i" or "o" and also "macro").

5.7.3. Size-dependent behaviour: a parametric study

A parametric study investigating the size-dependent behaviour at the constitutive level is provided by varying $f = 0.4$, 0.6 and 1. In this study, the effects of f on the macro dilation response (q: ε_{11}, ε_v: ε_{11}, S_r: ε_{11}) at $\bar{\sigma}_{33} = 100$ kPa and $s = 200$ kPa are depicted in Figure 5.31. As illustrated, higher deviatoric stresses, higher rates of volumetric strain and saturation degree are produced when f gets higher. This is consistent with the illustration of dissipation energy inside the localisation band in Figure 5.32, where the total energy dissipation scales with the expansion of the reversible unloading zone and the narrowing in the irreversible loading zone when reducing f. Furthermore, the result of this double-scale model coincides with that of the classical model for partially saturated soils by setting $f = 1$ (or $h = H'$), facilitating a transition between homogeneous and inhomogeneous conditions. These scale-effect characteristics are expected to allow the numerical solutions of BVPs to be convergent upon discretisation refinement.

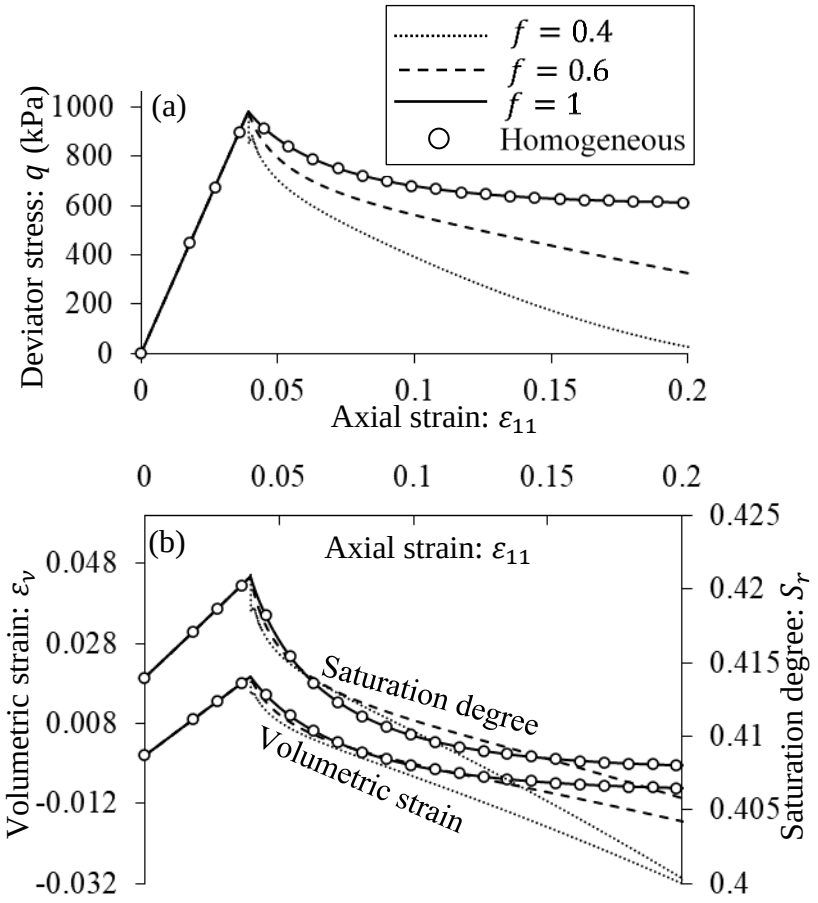

Figure 5.31. Size-dependent behaviour of the drained triaxial compression test on Kaolin soil (a) $\varepsilon_{11} - q$ (b) $\varepsilon_{11} - \varepsilon_v, S_r$

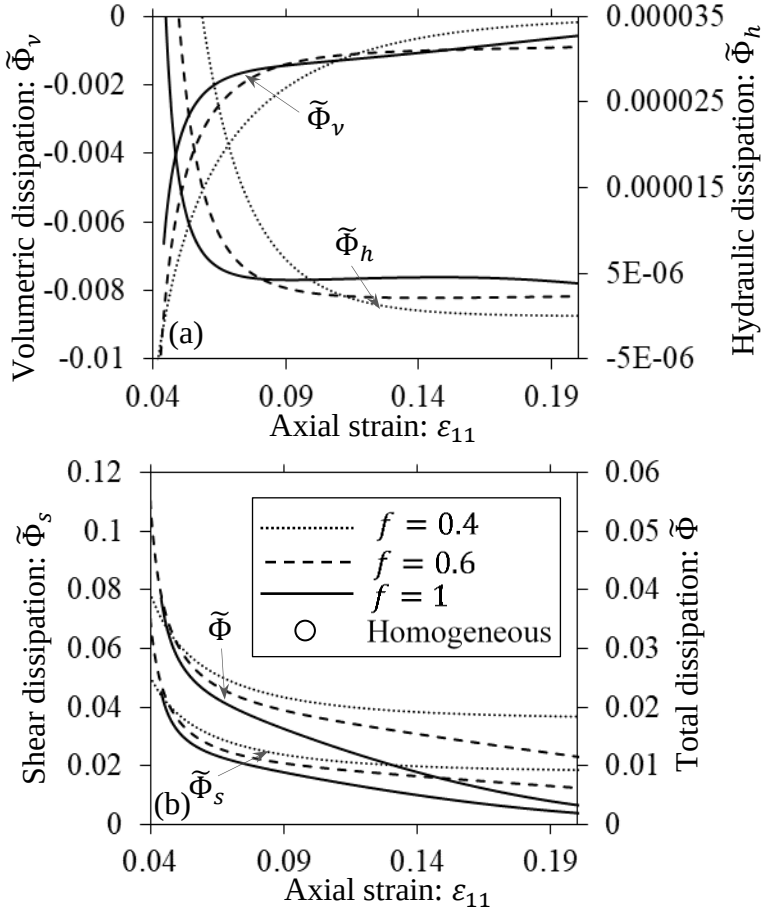

Figure 5.32. Size-dependent behaviour of the drained triaxial compression test on Kaolin soil (a) $\varepsilon_{11} - \tilde{\Phi}_v, \tilde{\Phi}_h$ (b) $\varepsilon_{11} - \tilde{\Phi}, \tilde{\Phi}_s$

5.8. Closure

The motivation of this Chapter is the development of a novel approach to balance rigour, adequacy and simplicity in modelling the post-localisation response of partially saturated soils. This chapter proposes a generic constitutive formulation to handle the transition between homogeneous and localised regimes of failure with orientation and thickness of the shear band to allow capturing the coupled hydro-mechanical response possessing size effects, that is totally overlooked in existing constitutive models for partially saturated soils. For this purpose, the strong inhomogeneous deformation and saturation are reflected through the use of the kinematically enriched approach, which is integrated into a thermodynamics-based two-scale framework reproducing key behavioural features under drained shearing conditions. The whole framework is rigorously derived from two explicitly defined free energy and dissipation potentials taking into account different responses inside (irreversibility) and outside (reversibility) the localisation zone, in conjunction with their interaction under the equilibrium condition of total traction and suction. The behaviour inside the shear band follows the constitutive law of the generic approach in Chapter 3, in which the strong interdependence

of plastic deformation rate and irrecoverable saturation rate is used for the derivation of a single yield surface incorporating the effects of both stress and suction. This automatically leads to a bifurcation criterion and post-localisation behaviour accounting for the wetting-drying difference in the water retention response under the effects of the volume change, which cannot be found in the literature.

Following the general formulation, a specific double-scale constitutive model is proposed for capturing some essential responses observed in suction-controlled triaxial and biaxial shear tests as described in Sections 5.6 and 5.7. This model possesses a small number of identifiable parameters, all of which can be calibrated from standard tests on unsaturated soils considering the effects of strain localisation with details on onset and orientation of the shear band. Its capabilities in predicting the experimental results are investigated through several numerical examples to highlight the applicability of the current approach. Although a good agreement between the numerical and experimental results demonstrates the potential of the generic approach and its derived model, the current study is not yet capable of capturing the post-localisation responses involving (i) multiple intersecting localisation bands (ii) evolution in thickness and orientation of the shear band during shearing (iii) undrained condition and (iv) investigation on the mesh convergence of the numerical solutions of BVPs upon discretisation refinement (v) consistent and rigorous calibration approach for determining parameters related to size-effects due to insufficiency and inadequacy of appropriate experimental data on the thickness and evolution of the shear band.

Chapter 6. Analysis of failure using the Smoothed Particle Hydrodynamics

6.1. Introduction

The review in Chapter 2 has shown the need to develop a robust SPH method for the determination of collapse mechanisms of geomaterials subjected to a wide range of both mechanical loading and saturation cases. In this sense, this chapter develops algorithms for implementation in the mesh-free SPH method to carry out the coupled flow deformation analysis in partially saturated porous media. It is the early stage of studying constitutive modelling of partially saturated soils within the scope of the SPH method. What makes the current approach distinct from other works regarding SPH is its ability to handle the interaction between deformation and fluid flow at both constitutive and structural levels, taking advantages of the generic framework and specific models established beforehand in Chapter 3, 4, 5 and Appendix A. The irrecoverable degree of saturation and its tight interaction with plastic strain is considered for the first time for the coupled dynamic flow-deformation simulation of the SPH method to capture the grain-scale mechanism of hydromechanical coupling. All balance laws and constitutive relationships are solved through a single set of Lagrangian particles following the solid phase motion, making it simple in the numerical implementation.

This chapter is organised as follows. Section 6.2 presents the specific formulation of coupled solid deformation-fluid flow process in partially saturated soils, including both governing and constitutive equations. This is succeeded by an approach for approximate solutions of partial differential equations in Section 6.3, where several fundamental aspects of the SPH method are summarized. In Section 6.4, the numerical algorithm of the proposed SPH approach for two-dimensional (2D) problems is briefly given, along with an example of numerical verification. Various numerical examples are provided towards the end of this chapter (Section 6.5) to demonstrate the capability of the present SPH model in handling the coupling between solid deformation and seepage flow under different loading and hydraulic conditions.

6.2. A mathematical framework of unsaturated flow

This section presents a simple formulation for fully coupled solid deformation-fluid flow in partially saturated deformable porous media to provide the theoretical basis for the present SPH approach. It is derived from the generic framework presented in Chapter 3 by specifying the form of governing equations and constitutive relationships.

6.2.1. Governing equations of seepage flow

This sub-section aims at setting up a specific system of governing equations to describe the flow of water in deformable unsaturated soils. As described in Chapter 3, to describe the coupling between deformation and fluid transport within the deformable body of partially saturated soils, it is essential to develop a coupled hydro-mechanical seepage flow model in a mixed form where governing equations of three phases in porous media are simultaneously solved and tightly linked together through following equations (see Chapter 3).

$$v_i^{ws} = \frac{k_{unsat}K_{sat}}{\phi S_r g}\left(\frac{1}{\rho^w}\frac{\partial s}{\partial x_j}\delta_{ij} + B_i\right) \tag{6.1}$$

$$\frac{D^s S_r}{Dt} = -\frac{k_{unsat}K_{sat}}{g\rho^w\phi}\frac{\partial^2 s}{\partial x_i \partial x_j}\delta_{ij} - \frac{S_r}{\phi}\frac{\partial v_i^s}{\partial x_i} \tag{6.2}$$

$$\frac{D^s v_i^s}{Dt} = \frac{1}{(1-\phi)\rho^s}\left(\frac{\partial \sigma'_{ij}}{\partial x_j} - S_r\frac{\partial s}{\partial x_j}\delta_{ij} + \rho B_i\right) \tag{6.3}$$

$$\frac{D^s \varepsilon_{ij}}{Dt} = \frac{1}{2}\left(\frac{\partial v_i^s}{\partial x_j} + \frac{\partial v_j^s}{\partial x_i}\right) \tag{6.4}$$

$$\frac{D^s \phi}{Dt} = (1-\phi)\frac{\partial v_i^s}{\partial x_i} \tag{6.5}$$

with $k_{unsat} = (S_r)^{\zeta}$

The above-mentioned equations are to present the evolution of both hydraulic (Darcy's seepage velocity (Eq. (6.1)), saturation degree (Eq. (6.2))) and mechanical (solid velocity (Eq. (6.3), strain (Eq. (6.4), porosity (Eq. (6.5)) field variables representing fluid transport through porous media and its interaction with deformation. In this model, it is noted that the motion of the fluid phases is presented with reference to those of the corresponding soil skeleton.

6.2.2. Constitutive relationship

For completeness of this mathematical framework of the coupled flow deformation process of partially saturated soils, the following sub-section provides specific constitutive relationships (e.g. stress-strain, SWCC). In the light of the foregoing discussion in Chapter 2 and 3, the inelastic behaviour of partially saturated soils is experimentally realised through the interdependence between plasticity and hydraulic irreversibility. Its intrinsic nature is the inseparability of mechanical and hydraulic internal variables produced by the hydromechanical interaction at the grain scale. A constitutive model being capable of handling this feature is essentially required for predicting the actual responses of unsaturated soils, and hence is an important element for this numerical analysis. To indicate the flexibility of the generic constitutive approach mentioned in Chapter 3, two different coupled hydro-mechanical models based on Modified Cam-Clay (critical state model) and Drucker-Prager yield criteria as developed in

Chapters 4, 5 and Appendix A, respectively, are adopted in this chapter. The following sub-sections only summarise the key equations and omit the intermediate details of model formulations which can be found in Chapter 4, 5 (Modified Cam-Clay) and Appendix A (Drucker-Prager).

Model based on Modified Cam-Clay yield criterion

The formulation of this Modified Cam-Clay yield criterion is rigorously developed in Chapter 4 and 5. This model uses the state laws for true stresses (see Eqs. (5.28-5.31)) as follows:

$$p' = \frac{E}{3(1-2\varrho)}\left(\varepsilon_v - \varepsilon_v^{\mathrm{p}}\right) \tag{6.6}$$

$$q = \frac{3}{2}\frac{E}{(1+\varrho)}\left(\varepsilon_s - \varepsilon_s^{\mathrm{p}}\right) \tag{6.7}$$

$$s^* = (p_u + s_0^*)\exp\left\{\frac{S_{r0}+[(-S_r)-(-s_r^{\mathrm{p}})]}{\kappa_h}\right\} - p_u \tag{6.8}$$

From Eq. (4.77) or Eq. (5.33), the coupled hydro-mechanical loading function for the Modified Cam-Clay yield criterion is rewritten as:

$$y = \frac{\left(p' - \frac{1}{r}p'_{c(us)}\right)^2}{\left[\left(1-\frac{2}{r}\right)p' + \frac{1}{r}p'_{c(us)}\right]^2} + \frac{(q)^2}{\left[(1-\alpha)p' + \frac{\alpha}{r}p'_{c(us)}\right]^2 M^2} - 1 \leq 0 \tag{6.9}$$

And, its flow rules are given as (see Eqs. (4.78-4.80) or Eqs. (5.34-5.36)):

$$\dot{\varepsilon}_v^{\mathrm{p}} = \dot{\lambda}_p \frac{2\left(p' - \frac{1}{r}p'_{c(us)}\right)}{\left[\left(1-\frac{2}{r}\right)p' + \frac{1}{r}p'_{c(us)}\right]^2}\exp[-\beta(1-S_r)] \tag{6.10}$$

$$\dot{\varepsilon}_s^{\mathrm{p}} = \dot{\lambda}_p \frac{2q}{\left[(1-\alpha)p' + \frac{\alpha}{r}p'_{c(us)}\right]^2 M^2} \tag{6.11}$$

$$-\dot{S}_r^{\mathrm{p}} = \dot{\lambda}_p \frac{2\left(p' - \frac{1}{r}p'_{c(us)}\right)^2}{(s^*-p_b)\left[\left(1-\frac{2}{r}\right)p' + \frac{1}{r}p'_{c(us)}\right]^2}\left[1 - \exp[-\beta(1-S_r)]\right] \tag{6.12}$$

In the above expressions, $p'_{c(us)}$ is the hardening effect dependent upon the hydraulic history of soils associated with the effects of bonding and debonding due to a cementing action, taking the following form (see Eqs. (5.37)):

$$p'_{c(us)} = p'_R\left[\frac{p'_{c0}\exp\left(\frac{\varepsilon_v^{\mathrm{p}}}{\lambda'}\right)}{p'_R}\right]^{\frac{1}{[(1-\xi)\exp(-\mu s^*)+\xi]}} \tag{6.13}$$

Eqs. (6.6-6.13) demonstrate that a single Modified Cam-Clay yield locus is established in a simple form governed by a small number of parameters, delimiting the reversible domain of both mechanical and hydraulic processes. Outstanding features of volumetric response are addressed by the evolution

rules in a comprehensive manner, taking into account all physics of dilation and contraction under the effect of hydraulic irreversibility thanks to the appearance of irreversible saturation. Further details on the model formulation, its dissipation properties, along with implementation algorithms, verification and validation are presented in Chapter 4 and 5.

Model based on Drucker-Prager yield criterion

As presented in Appendix A, the extended Drucker-Prager model for partially saturated soils can be established following the generic approach accounting for thermodynamic kinematic constraints as established beforehand in Chapter 3 through the use of two explicitly defined Helmholtz free energy and dissipation potentials. Its formulation can be summarised as follows.

The constitutive relationship of this model is written as (see Eqs. (A.2-A.4)):

$$p' = \frac{E}{3(1-2\varrho)}\left(\varepsilon_v - \varepsilon_v^{\mathrm{p}}\right) \tag{6.14}$$

$$q = \frac{3}{2}\frac{E}{(1+\varrho)}\left(\varepsilon_s - \varepsilon_s^{\mathrm{p}}\right) \tag{6.15}$$

$$s^* = K_h\left[1 + (-S_r) - \left(-S_r^{\mathrm{p}}\right)\right] \tag{6.16}$$

where K_h is the constant controlling the amount of reversible hydraulic energy (see Appendix A). Eqs. (6.14-6.16) demonstrate that both mechanical and hydraulic constitutive relationships of this model are assumed to be linear in the reversible regime for the sake of simplicity.

From Eqs. (A.26-A.29) in Appendix A, the Drucker-Prager yield criterion for partially saturated soils is demonstrated through the following yield surface (see Figure 6.1):

$$y = q - \mu' p' - c' \leq 0 \tag{6.17}$$

and the evolution rules as follows:

$$\dot{\varepsilon}_v^{\mathrm{p}} = -\dot{\lambda}_p \exp[-\beta(1 - S_r)]\mu' \tag{6.18}$$

$$\dot{\varepsilon}_s^{\mathrm{p}} = \dot{\lambda}_p \tag{6.19}$$

$$-\dot{S}_r^{\mathrm{p}} = -\dot{\lambda}_p \frac{p'}{(s^* - p_b)}\{1 - \exp[-\beta(1 - S_r)]\}\mu' \tag{6.20}$$

in which c' and μ' are functions controlling the size of yield surface and the dilation behaviour to reflect frictional dissipative mechanisms triggered by internal structural changes of soil particles and pore fluids. In this case, c' and μ' can be expressed in an exponential form dependent on the accumulated plastic strain and modified suction (Yerro, 2015; Alonso et al., 2015) as follows:

$$\mu' = \mu'_0 + \omega_\mu s^* \tag{6.21}$$

$$c' = c'_0 \exp\left(-\eta_c \varepsilon_p\right) + c'_m [1 - \exp(-\omega_c s^*)] \tag{6.22}$$

In the above expressions, μ'_0, c'_0 and η_c are parameters of the classical Drucker-Prager yield criterion in the fully saturated state (Nguyen & Bui, 2020); c'_m, ω_μ and ω_c are parameters controlling the hydraulic effects on inelastic behaviour (Yerro, 2015; Alonso et al., 2015); ε_p is the accumulated plastic strain linked with the plastic volumetric and shear strains through constants a_d and b_d, taking the following form (Nguyen & Bui, 2020):

$$\dot{\varepsilon}_p = a_d \dot{\varepsilon}_v^{\mathrm{p}} + b_d \dot{\varepsilon}_s^{\mathrm{p}} = \dot{\lambda}_p \left(a_d \frac{\partial y^*}{\partial \chi_v} + b_d \frac{\partial y^*}{\partial \chi_s} \right) \tag{6.23}$$

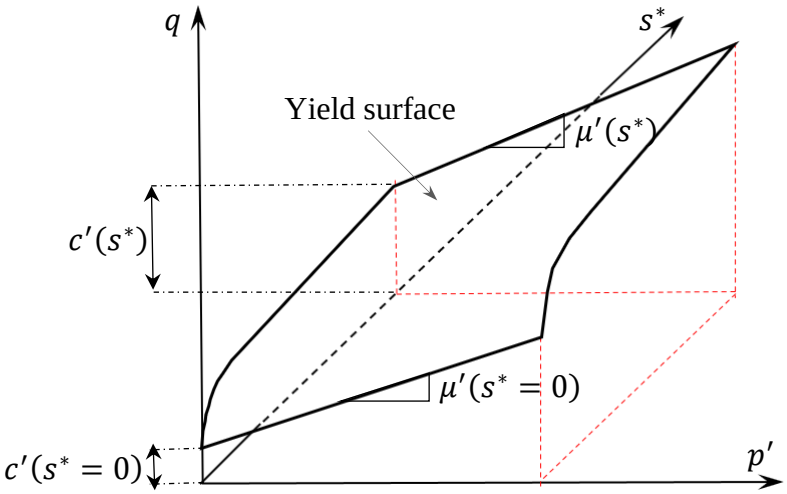

Figure 6.1. Yield surface of model for partially saturated soils based on Drucker-Prager yield criterion in (p', q, s^*) space

The Drucker-Prager model for partially saturated soils presented above in Eqs. (6.14-6.20) can capture the intrinsic interdependence between mechanical and hydraulic internal variables, thanks to the use of a single yield function dependent on stress and suction with a single "plastic" multiplier. The yield function of this model in Eq. (6.17) is represented by a cut-off yield surface in the $p': q: s^*$space, acting as the failure surface of partially saturated soils, as demonstrated in Figure 6.1. It is able to reproduce the increase of initial yield shear stress with increasing suction. The proposed model in Eqs. (6.17-6.20) becomes the classical Drucker-Prager model at $s = 0$ and $S_r = 1$, allowing it to capture the transition from fully to partially saturated states and vice versa.

Discussion

As mentioned earlier, the main concern in this SPH approach is constitutive relationships (stress-strain, suction-saturation degree) to capture the nonlinear inelastic behaviour of unsaturated soils, which serve as the main component in governing the mechanism of soil collapses under effects of

both loading and seepage flow. These two constitutive models (Modified Cam-Clay, Drucker-Prager) (see Eqs. (6.6-6.23)) are used as examples in this chapter to demonstrate this. It is worth noting that the whole formulations of both models are based on the general thermodynamic framework as previously developed in Chapter 3 and hence inherits advantages of this generic approach, realized through the rigour and simplicity in capturing the inseparable nature of the coupling rooting from grain-scale interactions. In these models, using a single yield surface and two flow rules with a single "plastic" multiplier brings benefits to effectively and simply handle the tight interaction between mechanical and hydraulic yielding responses in the numerical implementation at any instant in time without the use of a separate water retention curve, thus removing complicated treatments and simplifying the computational procedure. This feature will be elucidated in Sections 6.4 and 6.5 through several SPH simulations. The thermodynamic admissibility in these models is always guaranteed while underlying dissipative mechanisms are adequately examined (see Chapter 4, Appendix A). This is one of the main distinctions of the present SPH approach compared to existing ones for partially saturated soils.

As can be seen in the results provided in Appendix B, it is apparent that the Modified Cam-Clay model yields better predictions in comparison with the Drucker-Prager model. The main limitation of the constitutive model based on Drucker–Prager yield criterion lies in its incapability of addressing the isotropic compression behaviour and the transition between hardening and softening regimes over the change of loading and saturation conditions, which can be effectively handled by the critical state model (e.g. Modified Cam-Clay) for partially saturated soils. Another deficiency of this model is that the yielding behaviour never takes place towards the positive direction of the effective mean stress axis, as a consequence of the open-shaped failure surface, which can be addressed by adding a hardening cap surface (Kohler & Hofstetter, 2008). Furthermore, the Drucker–Prager yield criterion uses a simple linear relationship between μ' and s^*, although their nonlinear relationship is usually encountered in experiments to describe the dependence of the internal friction on suction and saturation degree. However, noting that the Drucker-Prager model is used in this thesis as only one of typical examples for the derivation of a wide range of models for partially saturated soils from the proposed generic thermodynamics-based approach provided in Chapter 3 to indicate its versatility. Additionally, the advantage of the Drucker–Prager criterion is the simplicity over the Modified Cam-Clay criterion. This is the reason why it has been practically and extensively applied in the field of computational geomechanics in parallel with more sophisticated and adequate Critical State Soil Mechanics models presented in the following formulation.

6.3. Solution approximation using the SPH method

6.3.1. Basic of the SPH method based on the solid phase motion

By passing intermediate details on the mathematical derivation, this section provides a brief summary of the basic SPH formulations where further details can be found in Lucy (1977), Gingold & Monaghan (1977), Monaghan (1992), Bui (2007), Bui & Fukagawa (2008, 2009), Bui et al. (2008, 2011) and Bui & Nguyen (2017;2020). The fundamental of the SPH method is the weighted averaging interpolation process based on the kernel function. Properties of a particle a defined on the spatial coordinate ${x_i}^a$ are studied through its interaction with the neighbouring counterpart b located at the position of ${x_i}^b$ (see Figure 6.2) where i is to represent the coordinate system.

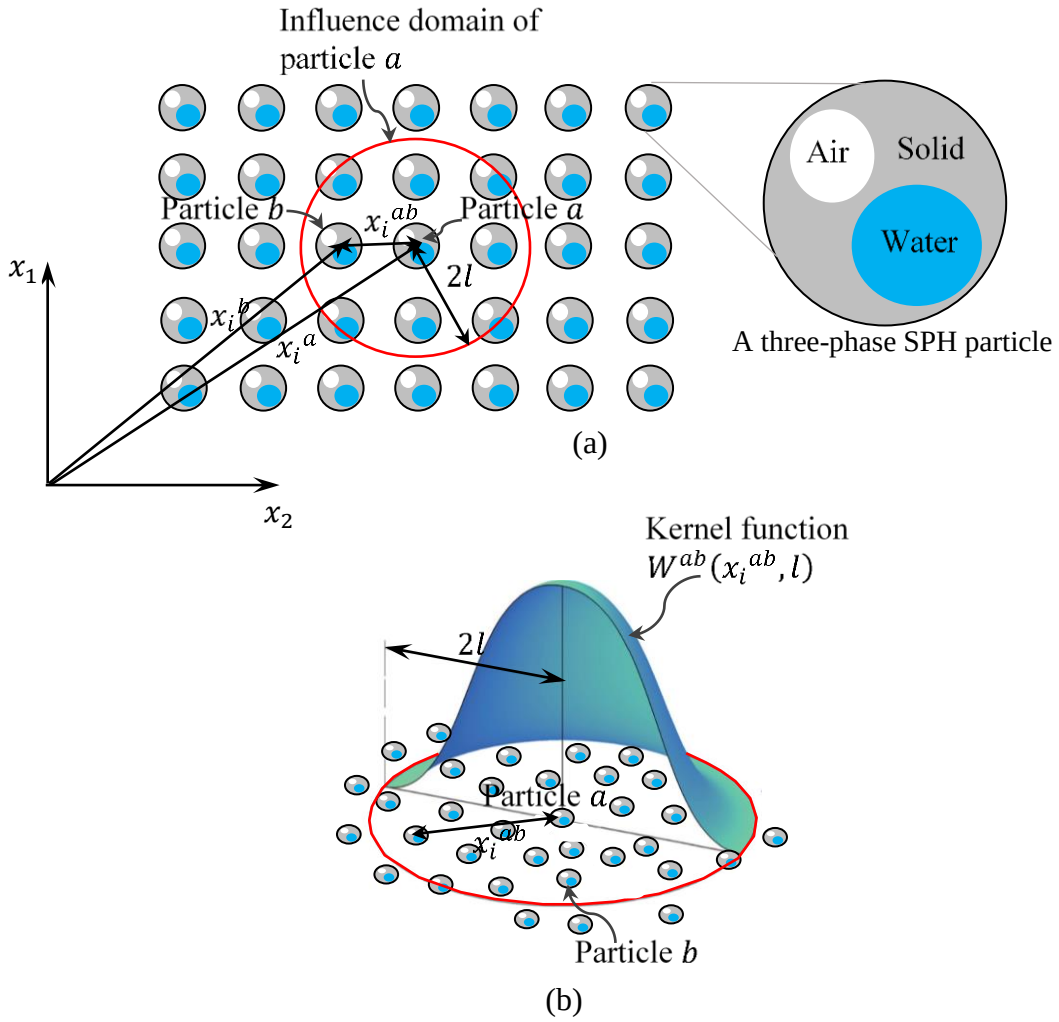

Figure 6.2. (a) Particle interactions in SPH within the influence domain (b) Kernel function

Particle approximation of the field variable following the solid phase motion

The interpolation process of approximating a field variable ψ^a of particle a is a result of the integral representation of the corresponding field variable ψ^b of particle b as follows:

$$\psi^a \approx \int_{\Omega'} \psi^b W^{ab} \, dx_i{}^b \tag{6.24}$$

In Eq. (6.24), $W^{ab}(x_i{}^{ab}, l)$ is the smoothing function of an interpolation domain Ω', expressed in terms of the distance between particles $x_i{}^{ab} = x_i{}^a - x_i{}^b$ and the smoothing length l (see Figure 6.2). In principle, it must be a Dirac Delta Function when l approaches to zero, while satisfying both the normalization condition ($\int_{\Omega'} W^{ab} \, dx_i{}^b = 1$) and the compact support condition ($W^{ab} = 0$ when $|x_i{}^{ab}| > 2l$) accommodating a limited number of "neighbouring" particles in the kernel estimation. The kernel function plays an important role in governing the stability of the computational domain. For the SPH method, Gaussian and Cubic-spline can be seen as the most well-known and widely used kernel functions in the literature (Bui, 2007; Bui & Nguyen, 2020). However, they usually suffer from the issue regarding the paring instability in the numerical simulations where particles clump together (or tensile instability) in the case of a large supporting domain, as a result of the negative Fourier transform of SPH kernel functions for some wave vectors (Dehnen & Aly, 2012). Wendland C2kernel (Wendland, 1995) was found to be more stable than Gaussian and Cubic-spline kernel functions in maintaining the relatively good particle distributions in the large supporting domain, thus removing the tensile instability (Dehnen & Aly, 2012; Bui & Nguyen, 2020). For this reason, the present SPH approach uses the Wendland C2 kernel (Wendland, 1995), which is of the form:

$$W^{ab} = \begin{cases} \frac{7}{4\pi l^2}\left(1 - \frac{1}{2}\frac{|x_i{}^{ab}|}{l}\right)^4 \left(2\frac{|x_i{}^{ab}|}{l} + 1\right) & 0 \le \frac{|x_i{}^{ab}|}{l} < 2 \\ 0 & \frac{|x_i{}^{ab}|}{l} > 2 \end{cases} \tag{6.25}$$

Eq. (6.24) can be discretised onto a finite number of particles N of each kernel interpolation based on the Gaussian quadrature rule in the following form:

$$\psi^a \approx \sum_{b=1}^{N} \left(\frac{m^s}{\bar{\rho}^s}\right)^b \psi^b W^{ab} \tag{6.26}$$

where $(m^s)^b$ and $(\bar{\rho}^s)^b$ are mass and density of the solid phase carried by particle b, respectively. Noting that the mass and density of the solid phase are used in the formulation of particle approximation in Eq. (6.26) because all field variables of the current framework are solved through a single set of SPH particles following the solid phase motion.

Kernel Approximation of first-order function derivatives

The first-order gradient of ψ^a can be approximated using the following integral form:

$$\frac{\partial \psi^a}{\partial {x_i}^a} \approx \int_{\Omega'} \frac{\partial \psi^b}{\partial {x_i}^b} W^{ab} \, d{x_i}^b \tag{6.27}$$

Invoking properties of W^{ab}, the integration by parts of Eq. (6.27) gives:

$$\frac{\partial \psi^a}{\partial {x_i}^a} = \int_{\Omega'} \psi^b \frac{\partial W^{ab}}{\partial {x_i}^a} d{x_i}^b \tag{6.28}$$

From Eq. (6.28), the SPH approximation of $\frac{\partial \psi^a}{\partial {x_i}^a}$ can be obtained by replacing the integral with a summation:

$$\frac{\partial \psi^a}{\partial {x_i}^a} \approx \sum_{b=1}^{N} \left(\frac{m^s}{\rho^s}\right)^b \psi^b \frac{\partial W^{ab}}{\partial {x_i}^a} \tag{6.29}$$

Kernel Approximation of second-order function derivatives

As presented in Section 6.2 of this Chapter, the second-order gradient of suction appears in Eq. (6.2) for computing the rate of saturation degree. In principle, the conventional approach, similar to the Kernel approximation of the first derivative, can be used to numerically approximate this equation (Bui & Nguyen, 2020). Nevertheless, it may lead to a significant numerical instability (Chen et al., 1999) owing to the change in the sign convention of the second-order derivatives of kernel functions. Therefore, a special SPH treatment for approximating the second-order gradient of a scalar function or vector quantities is needed to avoid adopting the second derivatives of the kernel function, that can be found in Monaghan (1992) and Brookshaw (1985). Here, the way given by Brookshaw (1985) is adopted and briefly presented to furnish a basis for approximating the second-order partial derivatives of variables by SPH due to its simplicity and stability (Bui & Nguyen, 2020).

In this approach, to approximate the second-order partial derivative of ψ^a, the second-order Taylor expansion of ψ^b about ${x_i}^a$ can be taken as given below:

$$\psi^b = \psi^a + ({x_i}^b - {x_i}^a)\frac{\partial \psi^a}{\partial {x_i}^a} + \frac{1}{2}({x_i}^b - {x_i}^a)\left({x_j}^b - {x_j}^a\right)\frac{\partial^2 \psi^a}{\partial {x_i}^a \partial {x_j}^a} \tag{6.30}$$

Eq. (6.30) can be rearranged as follows:

$$\frac{\psi^{ba}}{{x_i}^{ba}} = \frac{\partial \psi^a}{\partial {x_i}^a} + \frac{1}{2}{x_j}^{ba}\frac{\partial^2 \psi^a}{\partial {x_i}^a \partial {x_j}^a} \tag{6.31}$$

with $\psi^{ba} = \psi^b - \psi^a$ and ${x_i}^{ba} = {x_i}^b - {x_i}^a$

Eq. (6.31) can be expanded to be an integral form after convolving it with $\frac{\partial W^{ab}}{\partial x_j{}^a} = -\frac{\partial W^{ab}}{\partial x_j{}^b}$:

$$\int_{\Omega'} \frac{\psi^{ba}}{x_i{}^{ba}} \frac{\partial W^{ab}}{\partial x_j{}^a} dx_j{}^b = -\frac{\partial \psi^a}{\partial x_i{}^a} \int_{\Omega'} \frac{\partial W^{ab}}{\partial x_j{}^b} dx_j{}^b - \frac{1}{2} \frac{\partial^2 \psi^a}{\partial x_i{}^a \partial x_j{}^a} \int_{\Omega'} x_j{}^{ba} \frac{\partial W^{ab}}{\partial x_j{}^b} dx_j{}^b \tag{6.32}$$

Based on properties of the smoothing function, integrations by parts can also be applied to the right-hand side of Eq. (6.32), leading to:

$$\frac{\partial^2 \psi^a}{\partial x_i{}^a \partial x_j{}^a} = 2 \int_{\Omega'} \frac{\psi^{ba}}{x_i{}^{ba}} \frac{\partial W^{ab}}{\partial x_j{}^a} dx_j{}^b \tag{6.33}$$

Therefore, the SPH approximation of $\frac{\partial^2 \psi^a}{\partial x_i{}^a \partial x_j{}^a}$ can be deduced from Eq. (6.33) as follows:

$$\frac{\partial^2 \psi^a}{\partial x_i{}^a \partial x_j{}^a} \approx 2 \sum_{b=1}^{N} \left(\frac{m^s}{\bar{\rho}^s}\right)^b \frac{\psi^{ba}}{x_i{}^{ba}} \frac{\partial W^{ab}}{\partial x_j{}^a} \tag{6.34}$$

As can be seen in Eq. (6.34), only the first derivative of the kernel function $\frac{\partial W^{ab}}{\partial x_j{}^a}$ is employed for the Kernel approximation of second-order function derivatives, hence helping to remedy the numerical instability encountered in using the traditional approach accounting for the second derivative of the kernel function.

6.3.2. Solution approximation using the SPH method

In this section, approximate solutions of partial differential equations (Eqs. (6.1-6.5)) are proposed, following the particle discretization scheme given in Eqs. (6.29) and (6.34). The derivation of SPH kernel approximation for field variables is similar to procedures established and illustrated in Bui (2007), Bui & Fukagawa (2008, 2009), Bui et al. (2008, 2011), Bui & Nguyen (2017), Bui & Nguyen (2020) where the relative difference and link between the quantities of particles a and b for a given interacting pair are considered (Bui, 2007).

Darcy seepage velocity

To compute the Darcy seepage velocity, Eq. (6.1) can be represented in the expanded form as:

$$v_i^{ws} = \frac{k_{unsat} K_{sat}}{g \rho^w \phi S_r} \left(\frac{\partial s}{\partial x_j} - s \frac{\partial 1}{\partial x_j}\right) \delta_{ij} + \frac{k_{unsat} K_{sat}}{g \phi S_r} B_i \tag{6.35}$$

The particle discretization method in Eq. (6.29) is adopted to transform Eq. (6.35) into the following approximate form:

$$(v_i^{ws})^a = \left(\frac{k_{unsat} K_{sat}}{g \rho^w \phi S_r}\right)^a \sum_{b=1}^{N} \left(\frac{m^s}{\bar{\rho}^s}\right)^b s^{ba} \frac{\partial W^{ab}}{\partial x_j{}^a} \delta_{ij} + \left(\frac{k_{unsat} K_{sat}}{g \phi S_r}\right)^a B_i \tag{6.36}$$

It is demonstrated in Eq. (6.36) that the above-mentioned SPH approximate solution of Darcy's seepage velocity is dependent on the difference between interacting particles in suction instead of using the summation technique with only suction of neighbouring particles. This treatment helps to make the computational procedure less complicated and the numerical solution more accurate in practice (Bui, 2007; Bui et al., 2008).

Saturation degree rate

From Eq. (6.2), an expanded equation of the saturation degree rate is provided below:

$$\frac{D^s S_r}{Dt} = -\frac{k_{unsat} K_{sat}}{g\rho^w \phi}\frac{\partial^2 s}{\partial x_i \partial x_j}\delta_{ij} - \frac{S_r}{\phi}\left(\frac{\partial v_i^s}{\partial x_i} - v_i^s \frac{\partial 1}{\partial x_i}\right) \tag{6.37}$$

Adopting the SPH approximation approach in Eqs. (6.29) and (6.34) to recast the above equation leading to:

$$\left(\frac{D^s S_r}{Dt}\right)^a = -2\left(\frac{k_{unsat} K_{sat}}{g\rho^w \phi}\right)^a \sum_{b=1}^{N}\left(\frac{m^s}{\bar{\rho}^s}\right)^b \frac{s^{ba}}{{x_i}^{ba}}\frac{\partial W^{ab}}{\partial {x_j}^a}\delta_{ij} - \left(\frac{S_r}{\phi}\right)^a \sum_{b=1}^{N}\left(\frac{m^s}{\bar{\rho}^s}\right)^b (v_i^s)^{ba}\frac{\partial W^{ab}}{\partial {x_i}^a} \tag{6.38}$$

with $s^{ba} = s^b - s^a$

Solid velocity rate

For the solid velocity rate, Eq. (6.3) can be rewritten as:

$$\frac{D^s v_i^s}{Dt} = \frac{\partial}{\partial x_j}\left(\frac{\sigma'_{ij}}{\bar{\rho}^s}\right) + \frac{\sigma'_{ij}}{(\bar{\rho}^s)^2}\frac{\partial \bar{\rho}^s}{\partial x_j} - S_r\left[\frac{\partial}{\partial x_j}\left(\frac{s}{\bar{\rho}^s}\right) + \frac{s}{(\bar{\rho}^s)^2}\frac{\partial \bar{\rho}^s}{\partial x_j}\right]\delta_{ij} + \frac{\rho}{\bar{\rho}^s}B_i \tag{6.39}$$

Using Eq. (6.29), the SPH approximation of Eq. (6.39) can then take the following form:

$$\left(\frac{D^s v_i^s}{Dt}\right)^a = \sum_{b=1}^{N}(m^s)^b\left\{\left[\frac{\sigma'_{ij}}{(\bar{\rho}^s)^2}\right]^b + \left[\frac{\sigma'_{ij}}{(\bar{\rho}^s)^2}\right]^a\right\}\frac{\partial W^{ab}}{\partial {x_j}^a} - (S_r)^a \sum_{b=1}^{N}(m^s)^b\left\{\left[\frac{s}{(\bar{\rho}^s)^2}\right]^b + \left[\frac{s}{(\bar{\rho}^s)^2}\right]^a\right\}\frac{\partial W^{ab}}{\partial {x_j}^a}\delta_{ij} + \left(\frac{\rho}{\bar{\rho}^s}\right)^a B_i \tag{6.40}$$

In the above expression, the SPH approximation of solid velocity rate is based on the interaction in a pair of interacting particles through the summation of their stress and suction. This approximation technique was proved to be more effective in stabilising the numerical solution compared to the treatment used for Darcy seepage velocity and saturation degree rate (Bui, 2007). To handle shock waves and to prevent the unphysical penetration of particles or forming clumps, an artificial viscosity $Д_{ij}^{ab}$ and a repulsive force f_n^{ab} in a state of particles under tension are incorporated into Eq. (6.40), following the approach suggested by Bui et al. (2008). In this case, Eq. (6.40) can be expanded as:

$$\left(\frac{D^s v_i^s}{Dt}\right)^a = \sum_{b=1}^{N}(m^s)^b \left\{\left[\frac{\sigma'_{ij}}{(\bar{\rho}^s)^2}\right]^b + \left[\frac{\sigma'_{ij}}{(\bar{\rho}^s)^2}\right]^a - Д_{ij}^{ab}\delta_{ij} + f_n^{ab}\left(Л_{ij}^a + Л_{ij}^b\right)\right\}\frac{\partial W^{ab}}{\partial {x_j}^a} -$$

$$(S_r)^a \sum_{b=1}^{N}(m^s)^b \left\{\left[\frac{s}{(\bar{\rho}^s)^2}\right]^b + \left[\frac{s}{(\bar{\rho}^s)^2}\right]^a\right\}\frac{\partial W^{ab}}{\partial {x_j}^a}\delta_{ij} + \left(\frac{\rho}{\bar{\rho}^s}\right)^a B_i \qquad (6.41)$$

where δ_{ij} is the Kronecker delta; $Л_{ij}^a$ and $Л_{ij}^b$ are the rotation of the local artificial stress tensor to their principal values. Further details on this treatment can be found in Bui et al. (2008).

Strain rate tensor

The strain rate tensor in Eq. (6.4) can be rewritten as follows:

$$\frac{D^s \varepsilon_{ij}}{Dt} = \frac{1}{2}\left(\frac{\partial v_i^s}{\partial x_j} - v_i^s \frac{\partial 1}{\partial x_j}\right) + \frac{1}{2}\left(\frac{\partial v_j^s}{\partial x_i} - v_j^s \frac{\partial 1}{\partial x_i}\right) \qquad (6.42)$$

Applying the approximation technique (Eq. (6.29)) to each term of the right-hand side in the above equation, one obtains:

$$\left(\frac{D^s \varepsilon_{ij}}{Dt}\right)^a = \frac{1}{2}\sum_{b=1}^{N}\left(\frac{m^s}{\bar{\rho}^s}\right)^b (v_i^s)^{ba}\frac{\partial W^{ab}}{\partial {x_j}^a} + \frac{1}{2}\sum_{b=1}^{N}\left(\frac{m^s}{\bar{\rho}^s}\right)^b \left(v_j^s\right)^{ba}\frac{\partial W^{ab}}{\partial {x_i}^a} \qquad (6.43)$$

with $(v_i^s)^{ba} = (v_i^s)^b - (v_i^s)^a$

The strain rate tensor is approximated in a similar way as for the third term in Eqs. (6.37-6.38) of saturation degree rate using the relative velocities between the investigated particle and all the other particles in the support domain.

Porosity rate

By adopting the approach similar to that for the strain rate tensor and passing intermediate details of mathematical manipulations, the SPH particle discretization of the void fraction rate can be deduced from Eq. (6.5) as:

$$\left(\frac{D^s \phi}{Dt}\right)^a = (1-\phi^a)\sum_{b=1}^{N}\left(\frac{m^s}{\bar{\rho}^s}\right)^b (v_i^s)^{ba}\frac{\partial W^{ab}}{\partial {x_i}^a} \qquad (6.44)$$

which helps to capture effectively the change of porosity induced by the variation between interaction particles in the velocity of the solid constituent.

6.4. Numerical implementation

6.4.1. Brief on SPH algorithms

This sub-section centres on the numerical algorithms of the proposed SPH approach based on Bui (2007), Bui & Fukagawa (2008, 2009), Bui et al. (2008, 2011) and Bui & Nguyen (2017, 2020), in which key features of two-dimensional (2D) problems are briefly presented below. All SPH algorithms discussed here have been implemented in the SPH code provided by A/Prof Ha H. Bui (Monash University), co-supervisor of this thesis, for academic purposes. Only minor changes are needed for the implementation of all models for partially saturated soils in this study. The proposed algorithm is expected to provide a high degree of accuracy with an acceptable simulation time. Further details on the numerical algorithms of SPH and their applicability can be found in the references (Bui, 2007; Bui & Nguyen, 2020).

Initial setup and configuration process: At the start of the computational procedure, spatial domains are constructed through polygons, representing the initial geometry of problems. SPH particles are then uniformly generated inside these polygons, carrying initial physical properties. In this step, it is noted that an appropriate number of particles based on a certain threshold is chosen to guarantee the stability and accuracy of the SPH approximation procedure, depending on specific applications.

Particle approximation: After determining interaction pairs, Eqs. (6.36), (6.38), (6.41), (6.43) and (6.44) are used to compute Darcy's seepage velocity, saturation degree rate, void fraction rate, solid velocity rate and strain tensor rate at time t, respectively.

Time integration: Standard numerical techniques such as the accurate second-order leapfrog, predictor-corrector and Runge-Kutta schemes can be adopted for the numerical integration of the ordinary time-dependent differential governing equations where rates of some field variables (void fraction, solid velocity) as computed beforehand are utilised. Among these methods of time integration, the leapfrog algorithm is usually employed for the SPH method thanks to its advantage in reducing the memory storage required in the computational procedure compared to others (Bui et al., 2008; 2011; Bui & Nguyen, 2017; 2020). Thus, the Leap-Frog algorithm is performed in this study for advancing solid velocity and porosity at a half time step while updating location in a full-time step (see Figure 6.3) as described in the forms below:

$$v_k^s\left(t+\frac{\Delta t}{2}\right)=v_k^s\left(t-\frac{\Delta t}{2}\right)+\Delta t\frac{D^s v_k^s}{Dt}(t) \tag{6.45}$$

$$\phi\left(t+\frac{\Delta t}{2}\right)=\phi\left(t-\frac{\Delta t}{2}\right)+\Delta t\frac{D^s \phi}{Dt}(t) \tag{6.46}$$

$$x_k(t+\Delta t)=x_k(t)+\Delta t v_k^s\left(t+\frac{\Delta t}{2}\right) \tag{6.47}$$

where Δt is the size of each time step which must be controlled at a small enough constant or meet the following Courant-Friedrichs-Levy condition with the use of material sound speed c_s (Bui, 2007; Bui & Nguyen, 2020) to maintain the accuracy and stability of integrated solutions:

$$\Delta t \leq 0.1 \frac{l}{c_s} \tag{6.48}$$

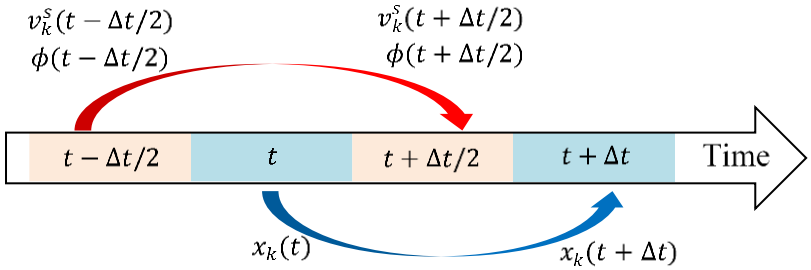

Figure 6.3. Schematic description of the Leap-Frog algorithm for the time integration

Stress return algorithm: Stress and suction are updated using the semi-implicit stress return algorithm presented in Chapter 3, in which increments of strain and saturation degree are computed as follows:

$$\left(\Delta\varepsilon_{ij}\right)^a = \left(\frac{D^s\varepsilon_{ij}}{Dt}\right)^a \Delta t \tag{6.49}$$

$$\left(\Delta S_r\right)^a = \left(\frac{D^s S_r}{Dt}\right)^a \Delta t \tag{6.50}$$

Acknowledging that the numerical implementation of constitutive relationships in this SPH model is limited only to single integration points where a simple algorithm is adopted to make the numerical solutions adequate and acceptable enough in simulating BVPs, requiring the use of small enough sizes of the time step. Thus, further research work is required to enhance the present stress return algorithm. For example, further improvement to the exactness of the scheme for updating stresses and suction with any size of time step can also be obtained through the sub-stepping in combination with this semi-implicit algorithm or full implicit stress return (Nguyen & Einav, 2009).

Boundary treatments: In the literature, several techniques such as ghost particles and virtual particles have been widely used to tackle this problem (Libersky & Petschek, 1991; Takeda et al., 1994; Randles & Libersky, 1996; Morris et al., 1997; Bui, 2007; Bui et al., 2008). These boundary conditions have been proven to be robust and efficient in simulating SPH boundary lines aligned with the axis of the Cartesian coordinate and preventing the penetration of real particles into boundary walls and the Kernel truncation (Bui, 2007; Bui & Nguyen, 2017). A similar approach (Bui, 2007) is taken in this study to flexibly simulate any shape of the wall boundary through the use of polygonal domains.

Particularly, in this approach, walls are treated as polygonal domains of boundary particles a where their field variables $(\psi^{boundary})^a$ can be set to a prescribed value $\psi^{prescribed}$:

$$(\psi^{boundary})^a = \psi^{prescribed} \tag{6.51}$$

or determined by making use of the interpolation process (Bui, 2007; Zhao, 2019) based on information of their real neighbours b (see Figure 6.4):

$$(\psi^{boundary})^a = \frac{\sum_{b=1}^{N}\left(\frac{m^s}{\bar{\rho}^s}\right)^b \psi^b W^{ab}}{\sum_{b=1}^{N}\left(\frac{m^s}{\bar{\rho}^s}\right)^b W^{ab}} \tag{6.52}$$

It is noted that Eqs. (6.51-6.52) are generic forms of boundary condition used in the present SPH model to describe how field variables of boundary particles are defined. Specifications of $\psi^{boundary}$ are identified in specific conditions based on appropriate assumptions.

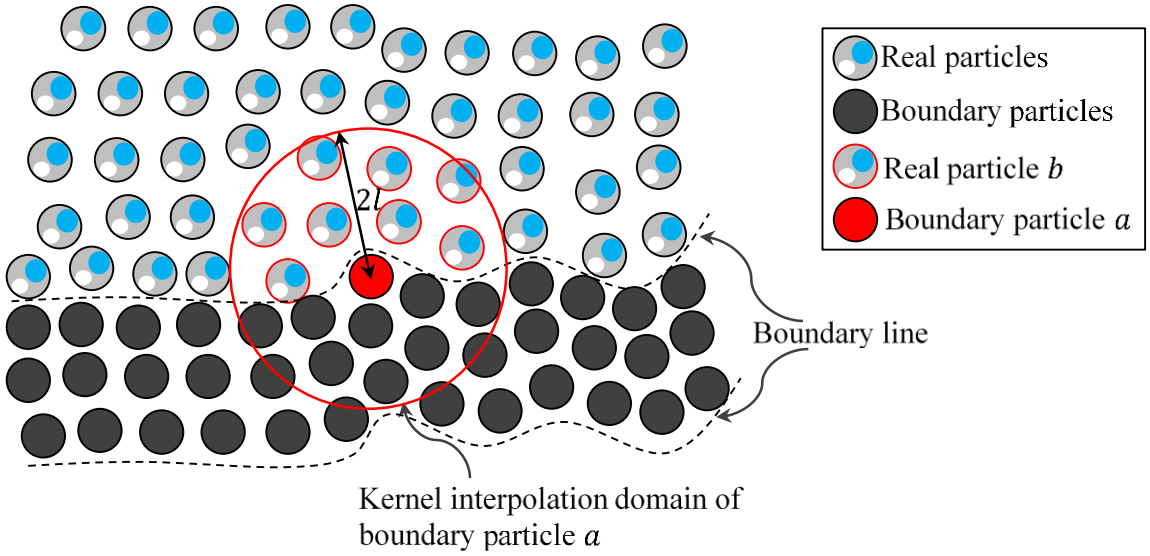

Figure 6.4. Arrangement of boundary and real particles in SPH

For the coupled flow deformation simulation of partially saturated soils, the boundary wall can be defined as a combination of several types of mechanical and hydraulic boundary conditions, which are developed from Eqs. (6.51-6.52) and summarised in Table 6.1 and Table 6.2, respectively. As can be seen in Table 6.1, for rigid boundary condition, the velocities of all boundary particles are kept fixed at zero while their effective stresses are computed to be the same as that of their neighbouring real counterparts through the interpolation process, producing repulsive forces to prevent real particles from penetrating the boundary. The prescribed velocity boundary condition is used to describe the movement of wall boundary induced by external forces (e.g. surcharge loadings, pressures of footing/foundation on soils) where a constant velocity is prescribed to all boundary particles and their

effective stress is interpolated and explained in the same way as for the rigid boundary condition to prevent the penetration of real particles into the boundary wall.

Table 6.1. Mechanical boundary conditions

Rigid boundary condition	$\left(\sigma_{ij}^{\prime boundary}\right)^a = \frac{\sum_{b=1}^{N}\left(\frac{m^s}{\bar{\rho}^s}\right)^b \sigma_{ij}^{\prime b} W^{ab}}{\sum_{b=1}^{N}\left(\frac{m^s}{\bar{\rho}^s}\right)^b W^{ab}}$ $\left(v_i^{s,boundary}\right)^a = 0$
The prescribed velocity boundary condition	$\left(\sigma_{ij}^{\prime boundary}\right)^a = \frac{\sum_{b=1}^{N}\left(\frac{m^s}{\bar{\rho}^s}\right)^b \sigma_{ij}^{\prime b} W^{ab}}{\sum_{b=1}^{N}\left(\frac{m^s}{\bar{\rho}^s}\right)^b W^{ab}}$ $\left(v_i^{s,boundary}\right)^a = v_i^{s,prescribed}$

Table 6.2 shows that two types of boundary condition for the fluid phase are proposed in this SPH model, including impermeable and permeable (pore pressure) boundary conditions. The impermeable one is based on the condition that the suction of particles on the boundary layer is set equal to that of the nearby real particles using the interpolation technique as presented in Eq. (6.52). This is to describe that there is no seepage flow across the boundary where the flow velocity vanishes due to $\frac{\partial s}{\partial x_j} = 0$ or $\sum_{b=1}^{N}\left(\frac{m^s}{\bar{\rho}^s}\right)^b [s^b - (s^{boundary})^a] \frac{\partial W^{ab}}{\partial {x_j}^a} \delta_{ij} = 0$ (see Eqs. (6.35-6.36)). It is noted that the current condition for impermeable boundary does not always strictly satisfy the Neumann condition where the fluid pressure of a boundary particle must be set to that of a real particle in the normal direction across the walls (Shao & Lo, 2003, Bui & Nguyen, 2017). Acknowledging that the current treatment is simple for the ease of implementation and verified to be acceptable in Bui & Fukagawa (2013), requiring further developments. On the other hand, the Dirichlet boundary condition is used to model the pore pressure boundary condition by imposing a constant suction on boundary particles. In the current model, conditions related to flux across the boundary wall are ignored for simplicity, although they are necessary to simulate the coupled flow deformation problems comprehensively. This shortcoming will be tackled in future works.

Table 6.2. Hydraulic boundary conditions

Impermeable boundary condition	$(s^{boundary})^a = \frac{\sum_{b=1}^{N}\left(\frac{m^s}{\bar{\rho}^s}\right)^b s^b W^{ab}}{\sum_{b=1}^{N}\left(\frac{m^s}{\bar{\rho}^s}\right)^b W^{ab}}$

Permeable (pore pressure) boundary condition	$(s^{boundary})^a = s^{prescribed}$

6.4.2. Verification

Verification of the implementation of SPH approximation

To verify the accuracy of the proposed SPH approach, a simple example of the groundwater flow through a rigid soil skeleton is analysed where $v_i^s = 0$, $\phi = \bar{\phi} = const$ and $S_r^{\mathrm{p}} = 0$. In this situation, Eq. (6.2) is simplified to:

$$\frac{D^s S_r}{Dt} = -\frac{k_{unsat} K_{sat}}{g\rho^w \phi} \frac{\partial^2 s}{\partial x_i \partial x_j} \delta_{ij} \tag{6.53}$$

while Eq. (6.16) can be rewritten as follows:

$$\frac{D^s S_r}{Dt} = -\frac{\phi}{K_h} \frac{D^s s}{Dt} \tag{6.54}$$

Substitution of Eq. (6.54) into Eq. (6.53) yields the following relation:

$$\frac{D^s s}{Dt} = \frac{k_{unsat} K_{sat} K_h}{g\rho^w \phi^2} \frac{\partial^2 s}{\partial x_i \partial x_j} \delta_{ij} = C_s \frac{\partial^2 s}{\partial x_i \partial x_j} \delta_{ij} \tag{6.55}$$

For simplicity, in this example, the following assumption is made:

$$C_s = \frac{K_{sat} K_h}{g\rho^w \phi^2} = const \tag{6.56}$$

which is the coefficient of consolidation due to $k_{unsat} = 1$.

Boundary conditions of this problem are all rigid and permeable, with $s^{prescribed} = s^{prescribed(top)}$ for the top wall and $s^{prescribed} = 0$ for three others. In this situation, Eq. (6.55) can be manipulated mathematically by a Fourier transform to obtain the 2D analytical solution (Tracy, 1995), as shown below:

$$\frac{s}{s^{prescribed(top)}} = \frac{4}{L_c} \sum_{i=1}^{\infty} \frac{\sin\left[\frac{(2i-1)\pi}{L_c} x_2\right]}{\left[\frac{(2i-1)\pi}{L_c}\right]} \times \left\{ \frac{\sinh\left[\frac{(2i-1)\pi}{L_c} x_1\right]}{\sinh\left[\frac{(2i-1)\pi}{L_c} H_c\right]} + \right.$$

$$\left. \frac{2}{C_s H_c} \sum_{j=1}^{\infty} \frac{(-1)^j \left(\frac{j\pi}{H_c}\right) C_s}{\left(\frac{(2i-1)\pi}{L_c}\right)^2 + \left(\frac{j\pi}{H_c}\right)^2} \sin\left(\frac{j\pi}{H_c} x_1\right) \exp\left[-\frac{\left(\frac{(2i-1)\pi}{L_c}\right)^2 + \left(\frac{j\pi}{H_c}\right)^2}{C_s} t \right] \right\} \tag{6.57}$$

where x_1 ($0 \le x_1 \le H_c$) and x_2 ($0 \le x_2 \le L_c$) are positions along the vertical and horizontal directions, respectively.

For the purpose of verification, a rectangular soil column being $H_c = 0.6m$ in height and $L_c = 1m$ in width is examined using the following parameters for seepage flow: $\phi = 0.3$, $\rho^w = 1000\ kg/m^3$, $K_{sat} = 16.67 \times 10^{-3} m/s$; $k_{unsat} = 1\ m/s$ and $K_h = 1000\ \mathrm{N/m^2}$ in which an SPH domain is discretised by 6000 particles. Its geometry and boundary conditions corresponding to the solution in Eq. (6.57) are presented in Figure 6.5 with $s^{prescribed(top)} = 500\ \mathrm{N/m^2}$ for the top wall. Figures 6.6 and 6.7 are given to illustrate variations of suction with location ($x_1 = 0.1\ m,\ 0.5\ m$ and $x_2 = 0.1\ m$, $0.5\ m$) at $t = 30s$ and $t = 50s$, computed by both SPH based on the condition of rigid soil skeleton and analytical approaches. As can be seen, there is almost no difference between the results from the two approaches. This feature provides evidence to confirm the accuracy of the present SPH method in performing the simulation of the unsaturated seepage flow through solid earth structures. The same results can be obtained by adopting the normalised SPH approximations for Kernel derivatives. Snapshots of numerical data on suction within the soil column shown in Figures 6.8 indicate the propagation process of drying ($s = 500\ \mathrm{N/m^2}$) along the downward direction from the top surface.

These results are also compared to the numerical solution obtained from the SPH model for the deformable soil skeleton through the use of the constitutive model based on Drucker Prager yield criterion with the following parameters: $E = 10^6\ \mathrm{N/m^2}$; $\varrho = 0.3$; $\mu_0' = 0.5$; $c_0' = 8 \times 10^5\ \mathrm{N/m^2}$; $\eta_c = 0$; $a_d = 0.5$; $b_d = 0.5$; $\omega_\mu = 10^{-7}\ \mathrm{m^2/N}$; $c_m' = 9 \times 10^5\ \mathrm{N/m^2}$; $\omega_c = 7 \times 10^{-7}\ \mathrm{m^2/N}$; $p_b = 10^4 \mathrm{N/m^2}$; $\beta = 0.01$; $\rho^s = 1800\ \mathrm{kg/m^3}$. These parameters are assumed to maintain the elastic deformation of the soil column during the whole infiltration process. This leads to a small displacement of soil structure, allowing consistency with solutions in the case of rigid soil skeleton. As shown in Figures 6.6 and 6.7, the SPH result under the condition of deformable soil skeleton closely agrees with analytical and SPH data obtained by assuming a rigid soil skeleton. These features indicate an acceptable result of numerical implementation in the proposed SPH approach for computing the seepage flow inside deformable porous media despite some discrepancies at $t = 30s$.

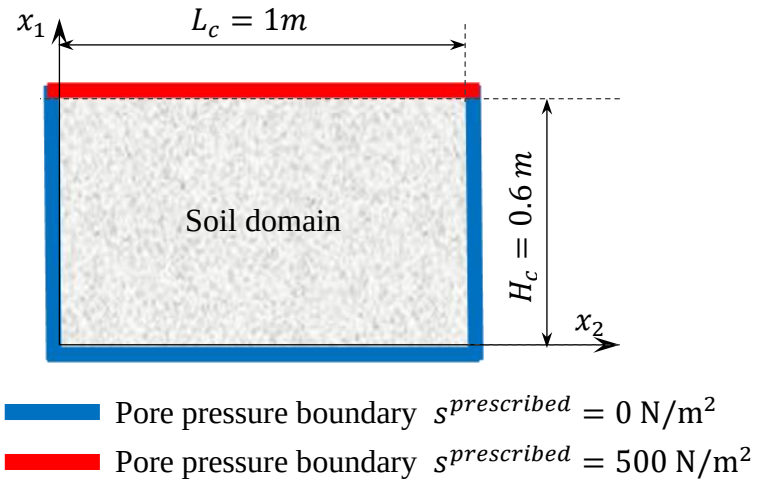

Figure 6.5. Geometrical data used in the numerical analysis

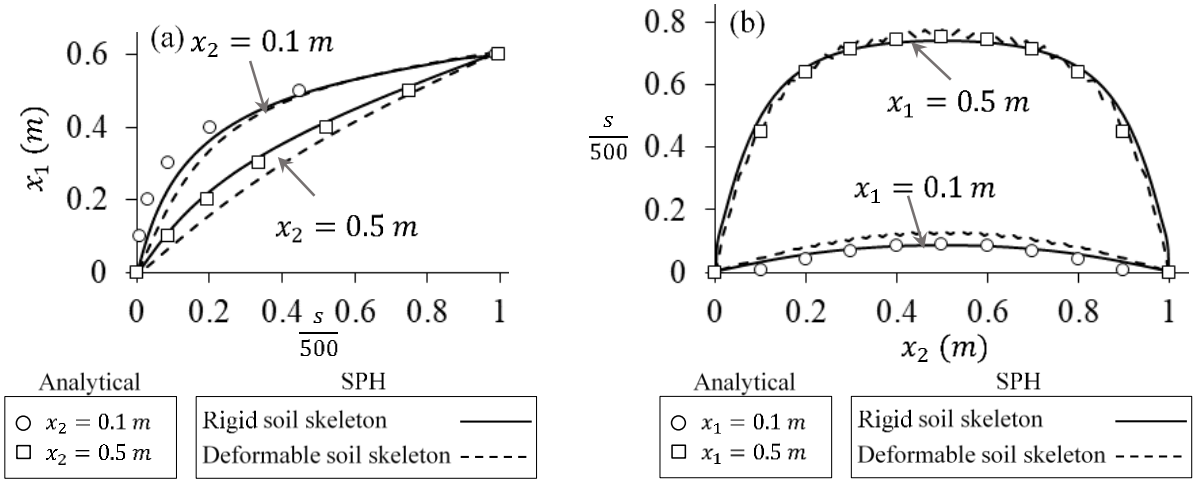

Figure 6.6. Verification of the proposed SPH algorithm using the infiltration test (a) $\frac{s}{500} - x_1$ (b) $x_2 - \frac{s}{500}$ at $t = 30s$

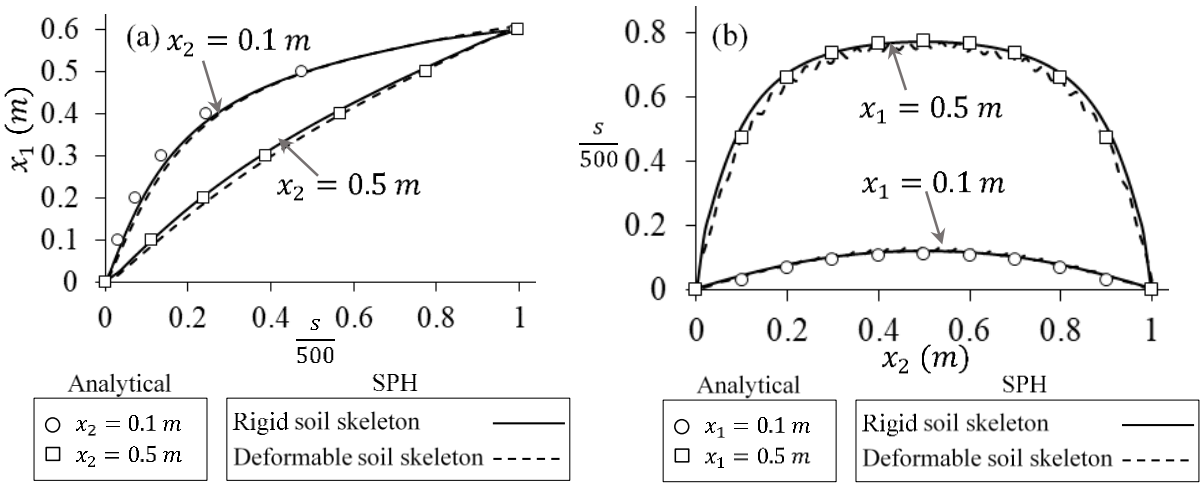

Figure 6.7. Verification of the proposed SPH algorithm using the infiltration test (a) $\frac{s}{500} - x_1$ (b) $x_2 - \frac{s}{500}$ at $t = 50s$

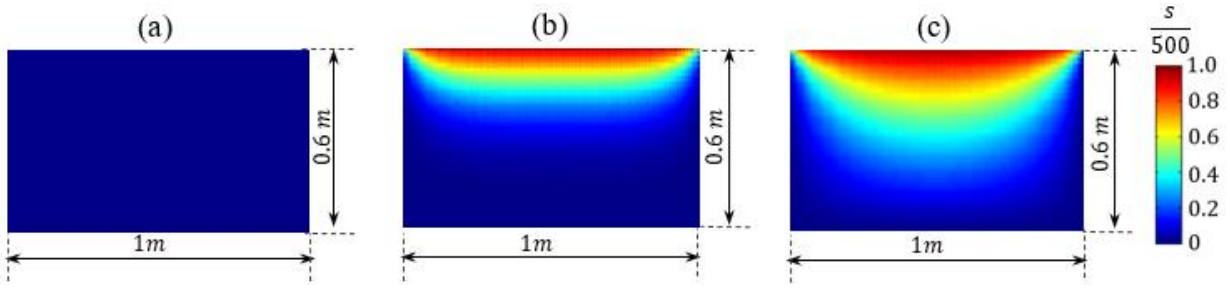

Figure 6.8. The evolution of suction in the soil column during the infiltration process (a) $t = 0s$ (b) $t = 30s$ (c) $t = 50s$

Verification of the implementation of the constitutive model

The proposed SPH approach is next verified through studying collapse mechanisms of a slope under external mechanical loading of footing, being of interest in investigating the stress return algorithm of the constitutive model. The geometry of the example is shown in Figure 6.9. The structure is rigid and impermeable at the bottom and lateral edges. It is subjected to a vertical downward displacement on the top edge of the structure through a prescribed velocity (see Figure 6.9). This SPH analysis is conducted using 5105 particles. In this example, stress and suction are computed through the adoption of Modified Cam-clay yield criterion with the following set of parameters: $E = 2 \times 10^6\ \mathrm{N/m^2}$; $\kappa_h = 0.1$; $\varrho = 0.3$; $M = 0.7$; $\lambda' = 0.5$; $p'_{c0} = 2 \times 10^5\ \mathrm{N/m^2}$; $r = 3$; $\alpha = 0.11$; $p'_R = 1.9 \times 10^5 \mathrm{N/m^2}$; $\xi = 0.65$; $\mu = 0.02\ \mathrm{m^2/N}$; $p_b = 7 \times 10^4 \mathrm{N/m^2}$; $\beta = 0.05$; $\rho^s = 1650\ \mathrm{kg/m^3}$; $\rho^w = 1000\ \mathrm{kg/m^3}$; $\zeta = 2$; $K_{sat} = 9 \times 10^{-4} \mathrm{m/s}$. Figure 6.10 give computed contour data of plastic shear strain at two representative times to demonstrate the evolution of yielding behaviour during loading. As illustrated, the behavioural trend of this test is reasonably captured by the current SPH model where the

localization of plastic shear strain into a narrow band is triggered, initiating from the slope crest under the footing and spreading towards the slope toe to create a slip surface. This phenomenon gives rise to a movement of the soil mass along the slip surface without any boundary deficiency effect. The formation of shear bands goes with a rapid reduction of the shear strength beyond the peak, which is intrinsically linked to the interaction between the rearrangement (sliding and rotation) of soil grains and the disruption of water meniscuses inside shear bands associated with irreversible deformation and saturation. The behaviour of material outside the band is reversible due to the negligible microstructural changes. These features can be seen in Figure 6.11, presenting numerical stress paths at point A (see Figure 6.9), which are compared to the result implemented in a constitutive driver using increments of strains and saturation from the SPH solution. As demonstrated in Figure 6.11, both solutions are identical, highlighting the numerical stability of the proposed stress return algorithm in the current SPH approach.

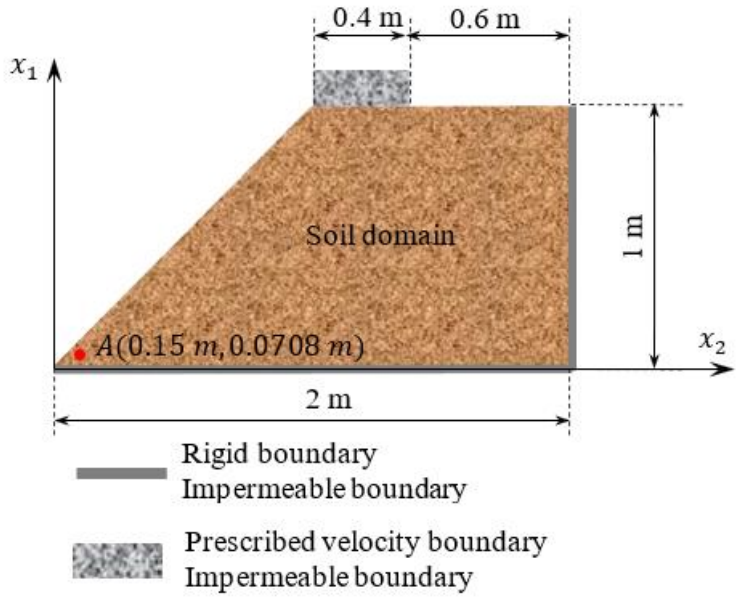

Figure 6.9. Geometrical data used in the numerical analysis

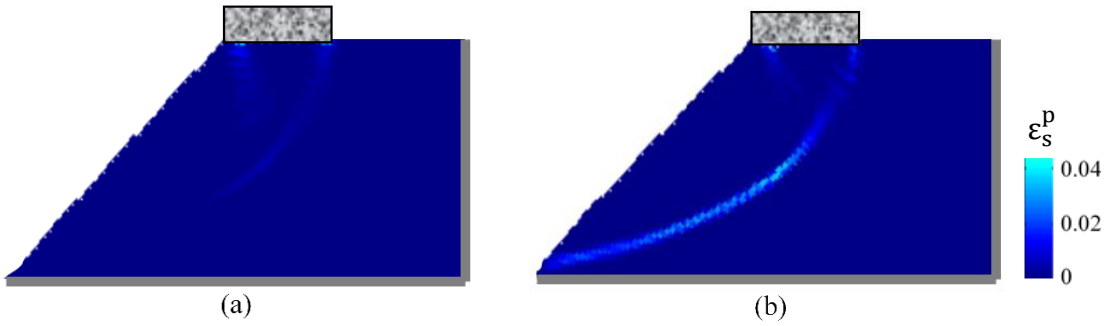

Figure 6.10. Development of plastic shear strain at (a) $t = 0.2\ s$ (b) $t = 0.5\ s$

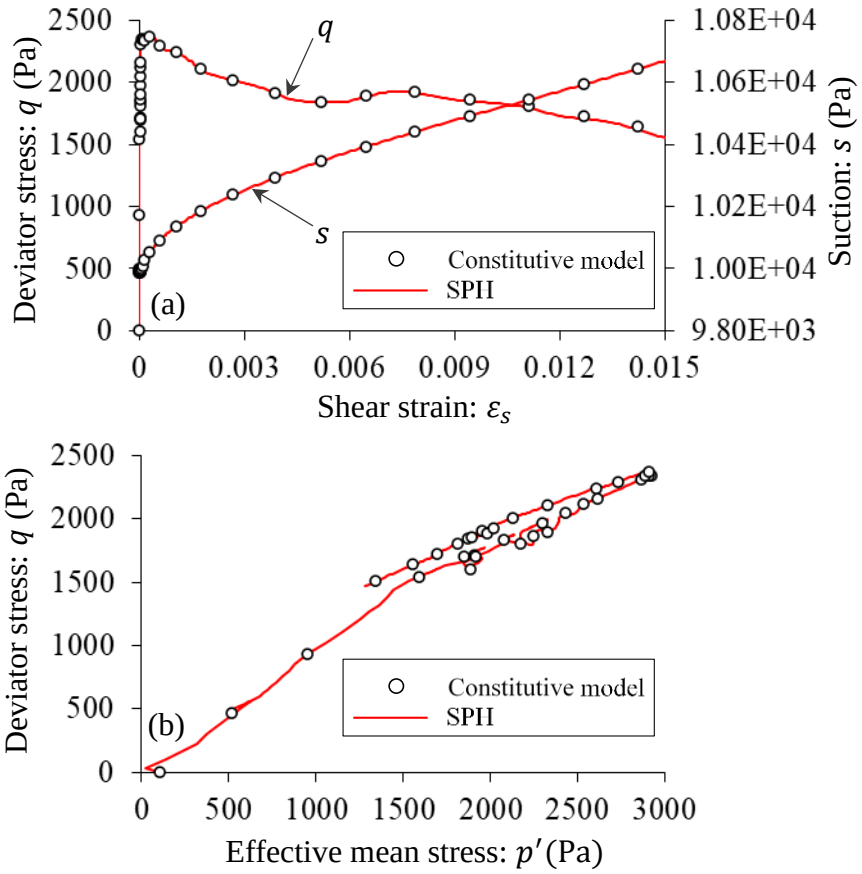

Figure 6.11. Verification of the proposed stress update algorithms of constitutive model based on Modified Cam-Clay yield criterion in SPH for results at point A (a) $\varepsilon_s - q$, $\varepsilon_s - s$ (b) $p' - q$

To verify further the numerical implementation of the constitutive model in SPH, this chapter next examines responses of a partially saturated soils domain loaded with a rigid footing, using the model based on the Drucker-Prager yield criterion. This example is based on a discrete computational domain 4 m long and 2 m wide with 6480 particles, as geometrically represented by Figure 6.12. The top wall is limited within the area of footing in which prescribed velocity and impermeable boundary conditions are adopted to form it. All the remaining boundaries are defined by rigid and impermeable conditions. In this simulation, the following parameters are assumed: $E = 2 \times 10^6$ N/m^2; $K_h = 10^6$ N/m^2; $\varrho = 0.3$; $\mu_0' = 0.1$; $c_0' = 8 \times 10^3$N/m^2; $\eta_c = 0.3$; $a_d = 0.5$; $b_d = 0.5$; $\omega_\mu = 10^{-6}$ m^2/N; $c_m' = 9 \times 10^3$ N/m^2; $\omega_c = 7 \times 10^{-6}$ m^2/N; $p_b = 10^4$N/m^2; $\beta = 0.01$; $\rho^s = 1800$ kg/m^3; $\rho^w = 1000$ kg/m^3; $\zeta = 2$; $K_{sat} = 10^{-4}$m/s. The contours of plastic volumetric strain and irreversible saturation are also plotted in Figure 6.13 to observe the pattern of deformation and seepage flow within the soil structure. This external loading process leads to the loss of strength, then the slope stability is no longer maintained and start to experience localised failures after a period of time. From this point onward, the inelastic response of partially saturated soils is induced by the

initiation of shear bands as well as their propagation determined by the strong interaction between plastic strain and irreversible saturation that cannot be found in existing SPH models. This analysis is to demonstrate how the coupled hydro-mechanical dissipation affects the evolution of strain localisation and then indicate advanced features of the current model compared to others. Especially, the obtained results of numerical analyses show a considerable correspondence with what is usually observed for problems on the load-bearing capacity of footings in the literature (Vesic, 1973; Terzaghi, 1943; Meyerhof 1978; Hanna 1982; Cerato & Lutenegger 2006). This indicates the reasonable implementation of the proposed SPH approach. In particular, the external load makes soil particles move in horizontal and downward directions, thus pushing soil out from beneath the footing. At early stages, the failure process begins with inclined shear bands (BD, CD) initiating from the two lower corners of the rigid footing and then propagates along two other curved bands (DGE, DHF) toward the upper corners of the soil specimen. Two faint localised bands along GI and HK can also be observed. All these bands divide the collapsed structure into three wedge-shaped zones, including Rankin active zone (BCD), Prandtl's radial shear zone (BDGI, CDHK) and Rankin passive zone (EGI, FHK). Figure 6.14 presents a good match between results of SPH and constitutive driver in terms of deviatoric stress, suction, plastic strains and irreversible saturation degree against the shear strain computed at point A. This again confirms the accuracy of numerical implementation in updating stresses and suction.

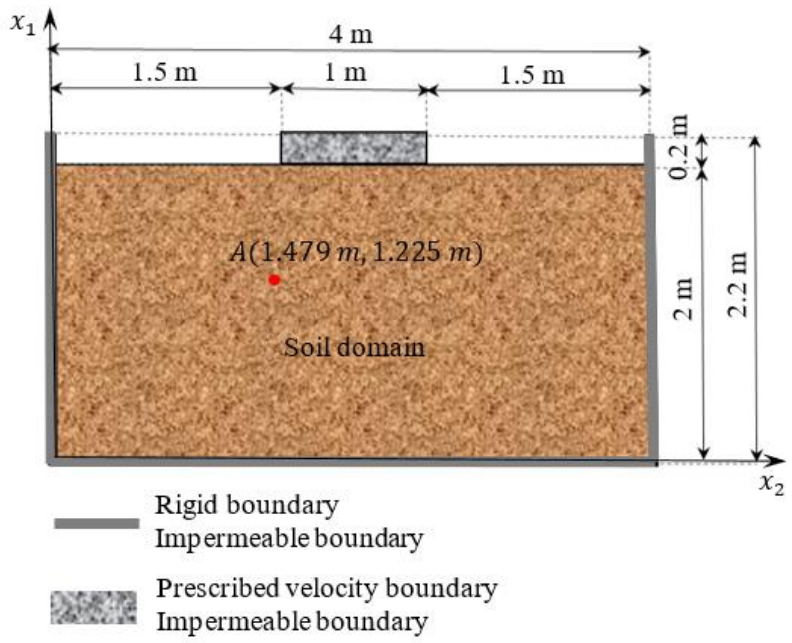

Figure 6.12. Geometrical data used in the numerical analysis

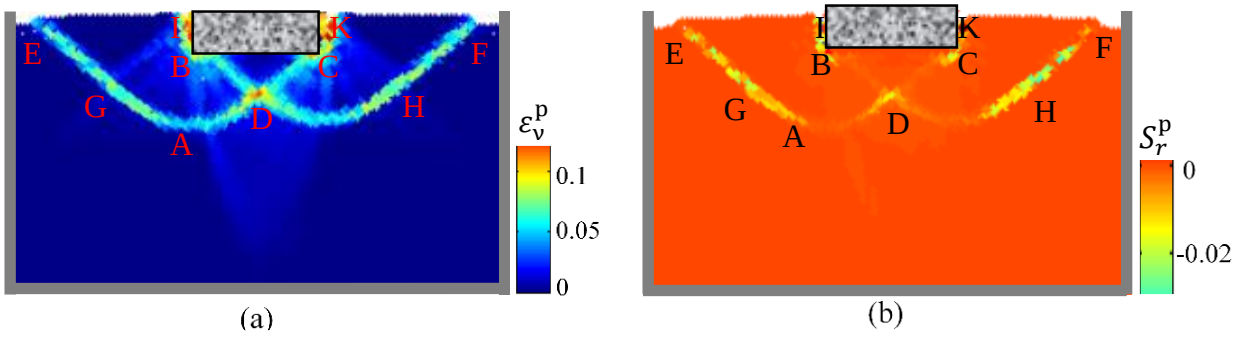

Figure 6.13. (a) Plastic volumetric strain (b) Irreversible saturation at $t = 2\ s$

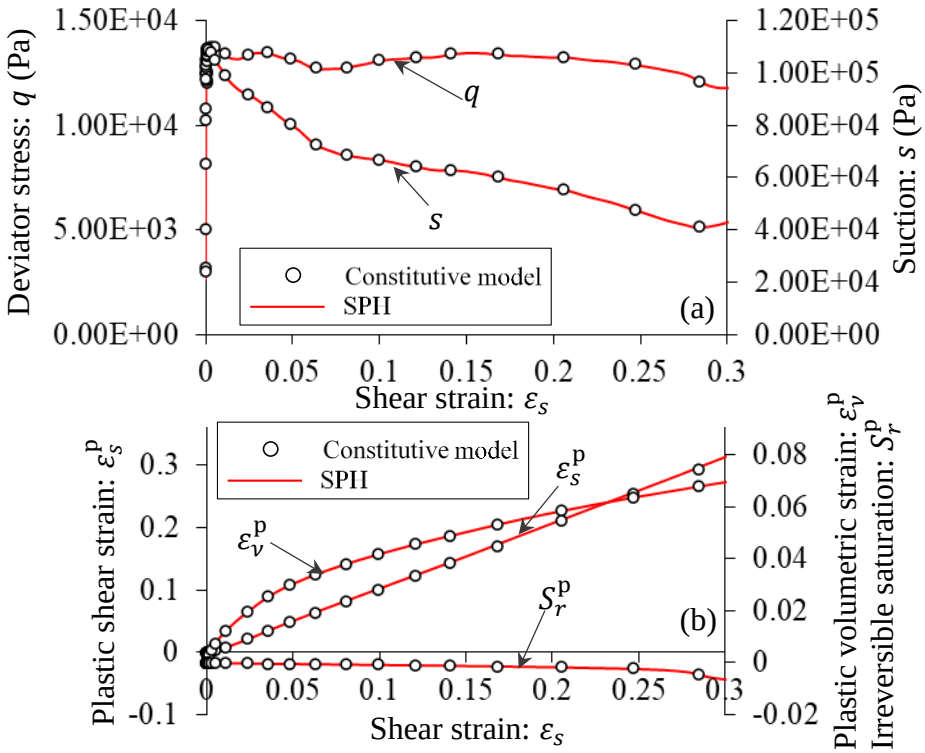

Figure 6.14. Verification of the proposed stress update algorithms of constitutive model based on Drucker-Prager yield criterion in SPH for results at point A (a) $\varepsilon_s - q$, $\varepsilon_s - s$ (b) $\varepsilon_s - \varepsilon_v^p$, $\varepsilon_s - \varepsilon_s^p$, $\varepsilon_s - S_r^p$

6.5. Numerical examples

This section is dedicated to numerical analyses under plane-strain conditions to investigate whether the proposed SPH approach is able to capture key features of the coupled flow deformation problems. Here attention is paid to the coupled hydro-mechanical failure mechanism of partially saturated soils under different loading and hydraulic conditions. This SPH approach focuses on describing simple examples to demonstrate how the tight interaction between mechanical (plastic strain) and hydraulic

(irreversible saturation) internal variables can be incorporated into the constitutive formulation, which is implemented in SPH by means of generic formulations as developed in Chapter 3. It is noted that the expectation of this chapter here is only to provide satisfactory trends of the coupled hydro-mechanical behaviour in terms of BVPs, in lieu of attempting to produce the excellent fits with experimental data at this research stage.

6.5.1. Stability of unsaturated soil slopes subjected to an external load (Suhail et al., 2018)

Based on the test on alluvial soil carried out by Suhail et al. (2018), the next example describes the response of an unsaturated soil embankment under a strip footing placed on the embankment crest using the model based on Modified Cam-Clay yield criterion, with the following material properties: $E = 2 \times 10^6\ \mathrm{N/m^2}$; $\kappa_h = 0.1$; $\varrho = 0.3$; $M = 0.7$; $\lambda' = 0.5$; $p'_{c0} = 2 \times 10^5\ \mathrm{N/m^2}$; $r = 2.5$; $\alpha = 0.11$; $p'_R = 1.9 \times 10^5 \mathrm{N/m^2}$; $\xi = 0.65$; $\mu = 0.02\ \mathrm{m^2/N}$; $p_b = 7 \times 10^4 \mathrm{N/m^2}$; $\beta = 0.05$; $\rho^s = 1650\ \mathrm{kg/m^3}$; $\rho^w = 1000\ \mathrm{kg/m^3}$; $\zeta = 2$; $K_{sat} = 9 \times 10^{-4} \mathrm{m/s}$. It is noted that these parameters are acceptably assumed based on several general soil properties of alluvial soil given by Suhail et al. (2018), and they are not calibrated rigorously due to the lack of appropriate experimental data for yielding behaviour (e.g. isotropic compression tests, triaxial shear tests, wetting/drying tests) as presented in Chapter 4 and 5. This is acknowledged as a limitation of the current study and will be addressed in future works. The embankment geometry is illustrated in Figure 6.15. In this problem, boundary conditions along lateral and bottom edges are rigid and impervious, while a vertical downward velocity on the top edge of the structure is prescribed. A total number of 4152 SPH particles are used to set up the initial numerical domain of this simulation.

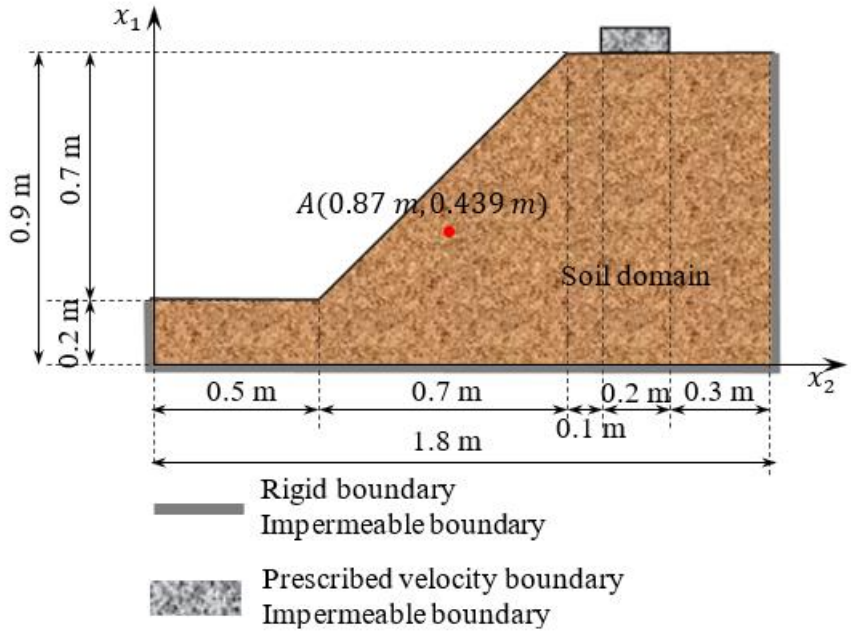

Figure 6.15. Geometrical data of slope used in the numerical analysis

The distribution of the plastic strain and irreversible saturation degree of the numerical analysis at $t = 0.5\ s$ is shown in Figure 6.16 to illustrate the failure mode of this test. It is demonstrated that the major mechanisms triggering the embankment failure are reasonably captured by the current model with the high concentration of plastic strain inside slipping zones (see Figure 6.16a). Furthermore, it can be seen in Figure 6.16b that the irrecoverable saturation degree can be observed inside the localised shear bands but not in the surrounding bulk materials. In particular, a downward movement of particles can be observed under the external loading where soils are pushed out from beneath the footing, causing the loss of soil strength and then slope instability. After a few seconds, two inclined localisation bands initiate from the two lower corners of the foundation, spreading along BD and CD and intersecting at point D. With increasing loads, the shear band CD keeps propagating until reaching the point close to the slope toe and then dominates the failure process, while the band BD stops propagating at the joining point D and nearly disappears at the end of the loading process. Shortly after that, the soil mass above the major localisation band CDE detaches slightly from the undeformed region under this band (see Figure 6.19). Along with this, a dilation response is observed in which deviatoric stress initially experience a rapid increase before reaching a peak, and then a drop as shown through numerical results of stress paths, shear stress-strain, plastic shear strain rate and irreversible saturation rate plotted for point A (see Figure 6.17). Figure 6.17 illustrates that changes in stress, suction, strain, saturation degree and internal variables during shearing activate and develop simultaneously and have effects on one another. This allows capturing the strong coupling between mechanical and hydraulic yielding responses at any instant.

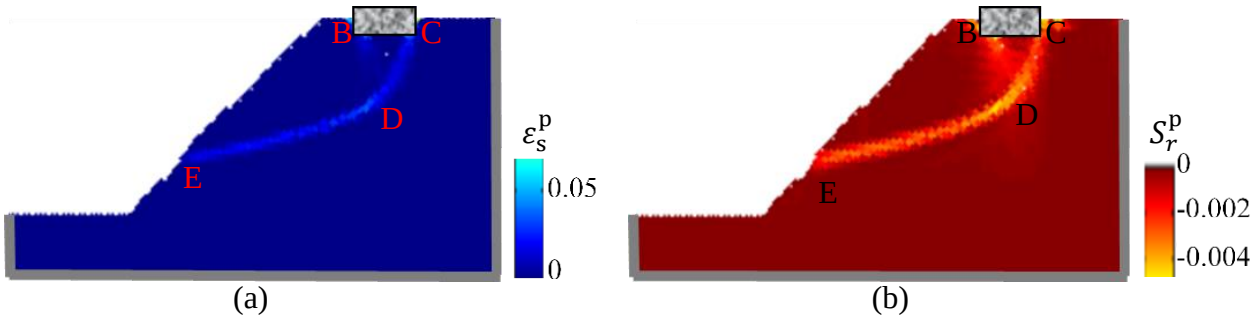

Figure 6.16. (a) Plastic shear strain (b) Irreversible saturation at $t = 0.5\ s$

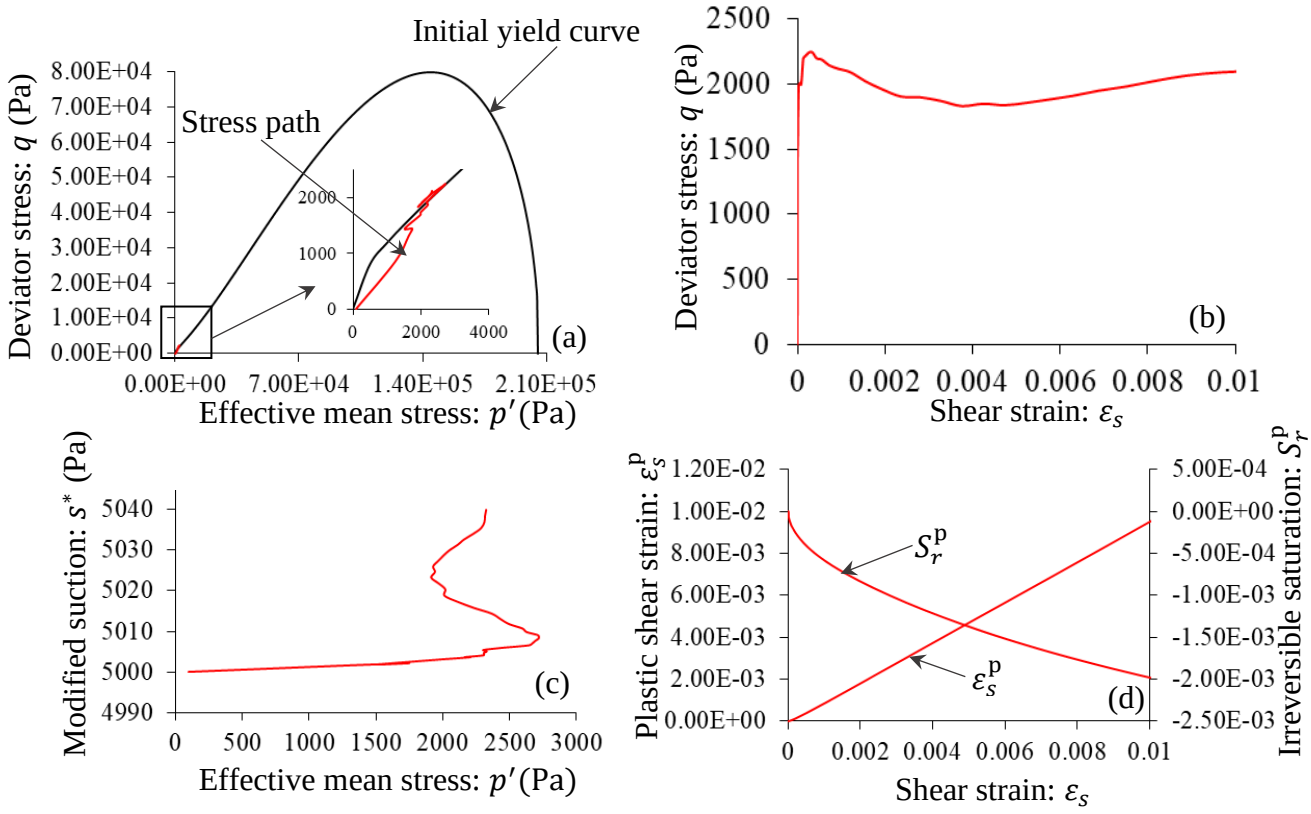

Figure 6.17. (a) Stress path and the yield curve $p' - q$ (b) Shear stress-strain curve $\varepsilon_s - q$ (c) Modified suction-effective mean stress $p' - s^*$ (d) plastic shear strain $\varepsilon_s - \varepsilon_s^p$ and irreversible saturation $\varepsilon_s - S_r^p$ at point A

Figure 6.18 depicts the profiles of suction and Darcy seepage velocity in the soil slope at $t = 0.5\ s$ to describe the behaviour of subsurface seepage flow induced by the deformation of the soil structure owing to the external load. A seepage flow activates and develops inside shear bands within the structure (see Figure 6.18) in parallel with this mechanical process, creating a hydromechanical resonance during the collapse. Figure 6.18b illustrates that Darcy seepage velocity inside shear bands is higher than that of other regions due to the increase in their suction, as demonstrated in Figure 6.18a. The highest change in suction and Darcy's seepage velocity is found to concentrate inside the region

of intense plastic strain (see Figure 6.18), demonstrating that the hydraulic process is one of the driving forces behind the localized failure in partially saturated soils. All the above-mentioned features indicate the ability of the proposed SPH approach to predict the coupled fluid flow caused by the settlement beneath the footing. To illustrate this phenomenon, the movement of particles in the porous packing causes local instabilities propagated to fluid interfaces. As a result, instantaneous jumps between stable configurations cause the discontinuity of water phases such as imbibition or drainage of pore throats and bridge rupture. In addition, this process of grain rearrangement leads to the variation of capillary pressures, which enables liquid bridges to redistribute. These results also demonstrate the inter-dependence of effective stress and suction on others and the rate of all internal variables, reflecting the grain-scale mechanism of hydromechanical coupling thanks to the advantages of the proposed constitutive approach.

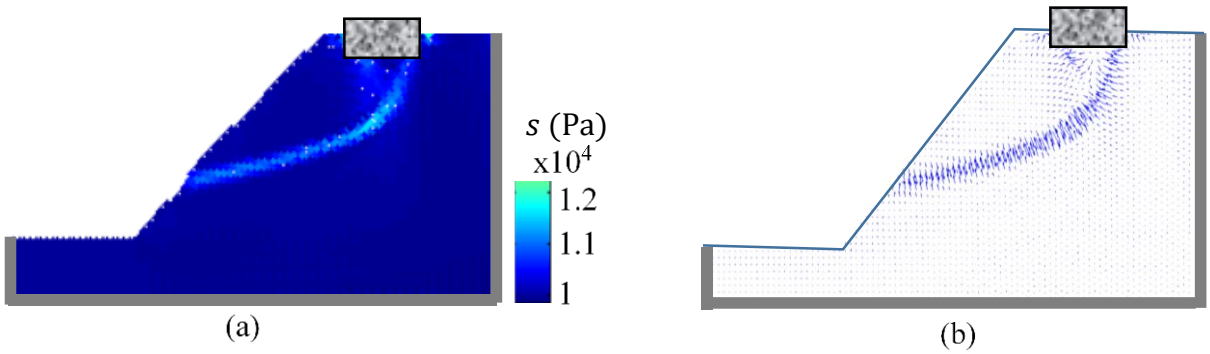

Figure 6.18. (a) Suction (b) Darcy's seepage velocity at $t = 0.5\ s$

To simply validate this simulation, experimental and numerical failure shape are provided in Figure 6.19. Figure 6.19 indicates that the experimental trend on the final slope configuration of this test are reasonably reproduced by the proposed model where the initiation of localisation band takes place in front of the slope crest, and it then propagates towards a point close to the slope toe. Nevertheless, the model predicts a less steep failure plane in comparison with that observed in experiments, although it is noted that this observation is unclear. This discrepancy is acknowledged as a weakness of the proposed approach, which may have arose as a result of simplifying assumptions in the phenomenological description of seepage force. Another reason for this discrepancy may be that the dependence of the deviatoric response on the Lode angle and anisotropic mechanisms are not accounted for in the model. This discrepancy may also come from the use of inadequate calibration procedures and inappropriate input parameters as there is not enough experimental data associated with the inelastic behaviour of partially saturated soils. Furthermore, the current approach does not contain any information related to the width and inclination of the shear band in constitutive

formulations to describe the size-dependent response when localised failures take place within the embankment. These features should be further examined in future studies.

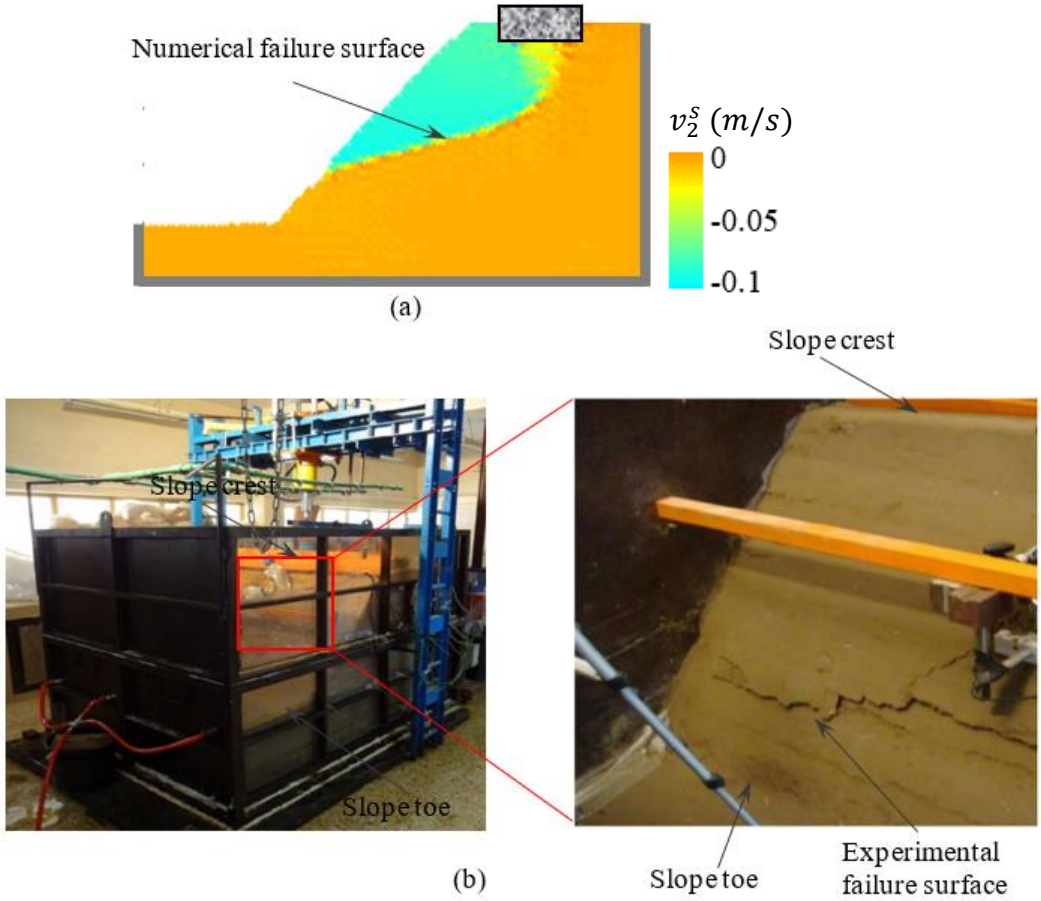

Figure 6.19. (a) Configuration of slope failure in simulation presented by the contour of horizontal solid velocity (b) Configuration of slope failure in the experiment.

Next, a parametric analysis gives results about the influence of the resolution of spatial discretisation on the performance of the proposed model. In SPH, the size of the element is represented by the size of the Kernel supporting domain (Bui & Nguyen, 2020). In this study, different numerical simulations at $l = 0.026\,m$, $0.0271\,m$ and $0.0275\,m$ are investigated at point A (see Figure 6.20). Figure 6.20 demonstrates that there is a significant divergence in shear stress-strain curves of different l. Reducing l causes a rise in shear stress, demonstrating the numerical problem associated with the mesh dependence of the proposed model. This is due to the fact that localisation of deformation in the form of shear bands during material failure leads to the breakdown of the assumption of homogenous deformation used in the current model due to considerable variation of strain and saturation across the shear band involving the size-dependent behaviour (see Chapter 2, 5). The present model does not contain any information related to the width, inclination and evolution of inside shear band (inelastic) in governing formulations and address strain localisation using phenomenological enhancements such

as rate-dependent or nonlocal regularisations. This issue can be addressed by integrating the two-scale model proposed in Chapter 5 into the current SPH-based scheme to warrant the convergence of the numerical results upon discretisation refinement. This is, however, not covered within the scope of this thesis, given it requires much more details about the soil properties and soil tests for these properties, including the evolution of localisation and shear band, all of which could not be found in the literature. This shortcoming is acknowledged and will be addressed in future works.

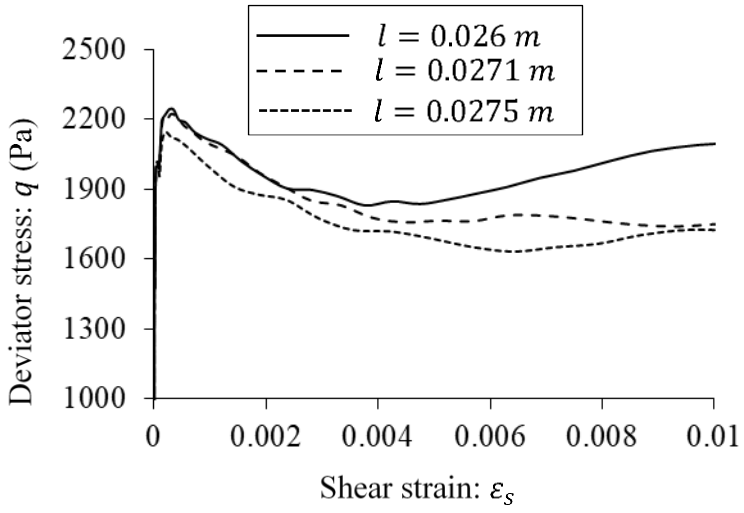

Figure 6.20. Performance of the proposed model under the resolution of spatial discretisation

Also in this problem, a parametric study for examining the effect of coupling parameter β (see flow rules in Eqs. (6.10) and (6.12)) on structural responses are given to indicate the main distinction and advance of the proposed approach in reflecting the interdependence between plastic strain and irreversible saturation degree compared to existing numerical methods for partially saturated soils. In this example, parameters are the same as for the previous simulation, except that β varies ($\beta = 0$; $\beta = 0.1$). It is worth pointing out that the irreversible change of saturation degree is found for numerical simulations at $\beta = 0.1$ (see Figure 6.21b), that cannot be performed when $\beta = 0$ (see Figure 6.21a). As shown in Figure 6.22, shear strength decreases while suction increases with increasing β. These results are shown to be good indicators of a significant role of β in controlling the hydromechanical yielding response of partially saturated soils because it can facilitate the model to manifest the interaction between the hydraulic dissipation in SWCC and the elastoplastic behaviour through the use of a single yield surface dependent on both stress and suction. This is one of the distinguishing features of this SPH solution as compared to existing ones.

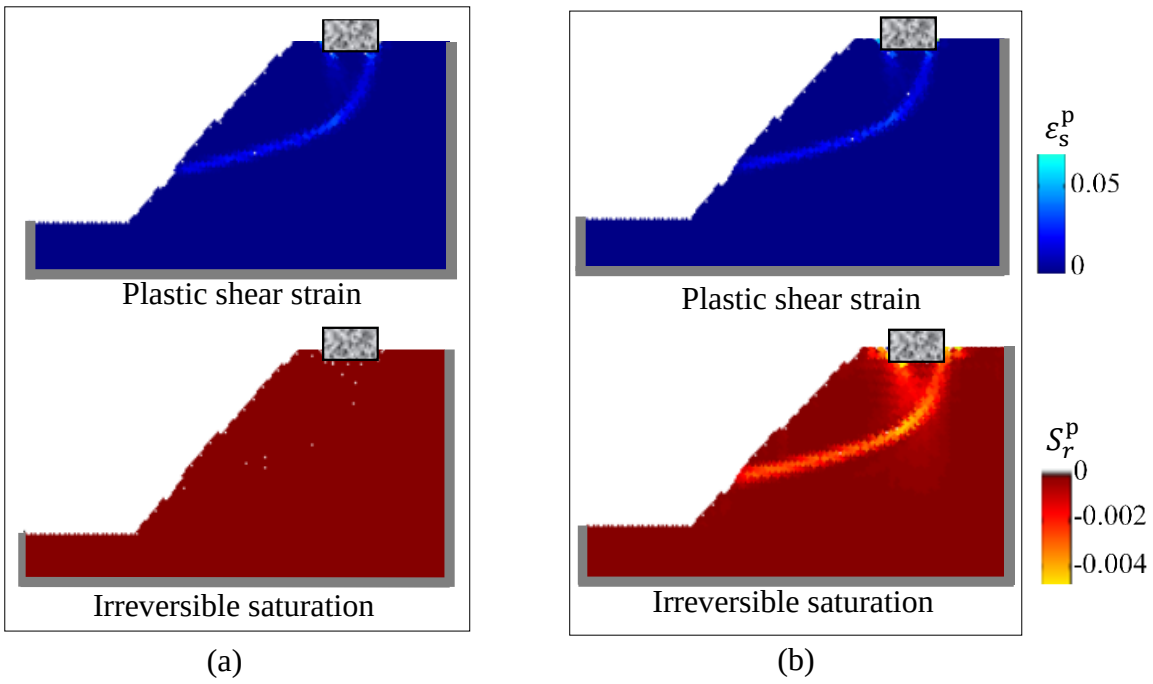

Figure 6.21. Effects of different values of β (a) $\beta = 0$ (b) $\beta = 0.1$ on the model responses at $t = 0.5\ s$

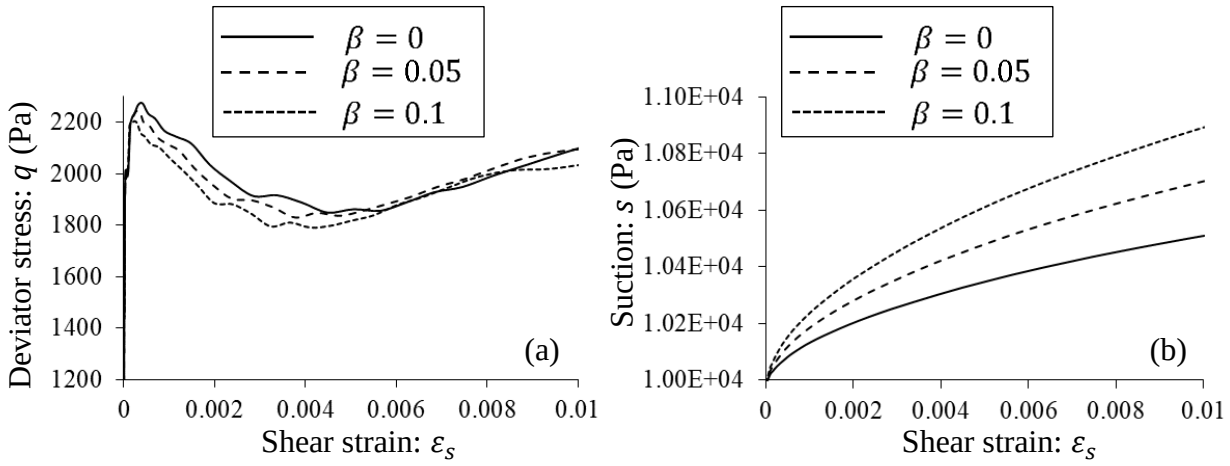

Figure 6.22. Effects of different values of β on the model responses of point A at $t = 0.5\ s$ (a) $\varepsilon_s - q$ (b) $\varepsilon_s - s$

By using the same set of parameters, a parametric study is performed to illustrate the influence of initial suction on the mechanical responses during loading. In this analysis, the results of plastic shear strain (see Figure 6.23) are observed at three levels of initial suction: $s_0 = 5000\ \mathrm{N/m^2}$; $7000\ \mathrm{N/m^2}$ and $20000\ \mathrm{N/m^2}$. Computed data at $t = 0.5\ s$ of these simulations show that the soil structure exhibits a higher resistance when subjected to a higher level of suction, going with a more pronounced and earlier failure mode. The thickness of the shear band remains almost unchanged, but its orientation varies when initial suction changes. The process of localised failure takes place in a relatively

shallower depth measured from the crest at a higher suction. These observations are consistent with behavioural results for partially saturated soils at the constitutive level as investigated beforehand in Chapter 4 and 5, revealing that the current numerical method is able to capture the hydraulic effects on the soil deformation at the structural level. This is due to the significant effect of suction on the change of the Bishop's effective stress. Furthermore, the yield stress increases when suction increases thanks to the use of wetting-induced hardening law in Eq. (6.13).

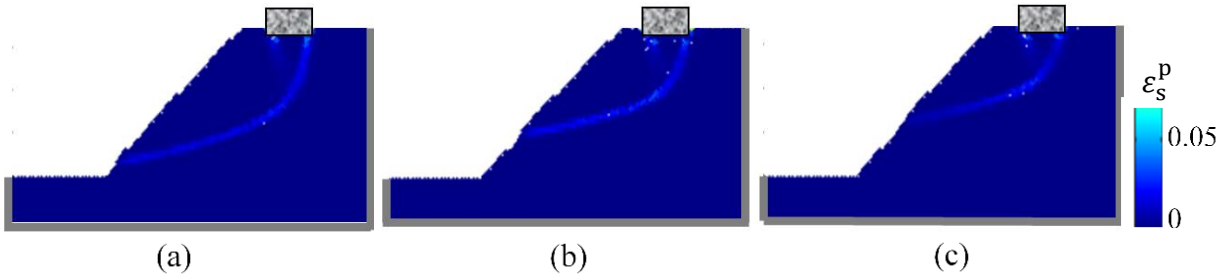

Figure 6.23. Effects of different initial suction levels (a) $s = 5000\ Pa$ (b) $s = 7000\ Pa$ (c) $s = 20000\ Pa$ on the model responses at $t = 0.5\ s$

6.5.2. The wetting-induced slope failure of a partially saturated soil embankment (Kitamura et al., 2017)

Additionally provided is a numerical analysis of BVPs subjected to the external hydraulic pressures to further explore the promising performance of the present approach, with the emphasis on the effect of fluid transport on the mechanical deformation and failure of soil skeleton. In this sense, an infiltration test of a soil embankment made of unsaturated Shirasu soil (Kitamura et al., 2007) is selected to demonstrate the capability of the present approach in capturing the wetting collapse mechanism. In this simulation, the soil structure is subjected to a process of water injection. All the geometrical data of the analysed structure are illustrated in Figure 6.24. Impervious and rigid boundary conditions are applied to the left (EF) and bottom (HG) edges. The hydraulic boundary condition along the horizontal lower surface (EH) of the embankment is permeable with $s^{prescribed} = 2500\ \mathrm{N/m^2}$, while its mechanical constraint is defined by the rigid condition to simulate the infiltration process generated by a water injection placed along EH in the real test. The extended Drucker-Prager model for partially saturated soils is used to represent the stress-strain and water retention responses. To numerically discretise it, this simulation adopts 2840 particles which are characterized by the following parameters (Ando et al., 2015; Xiong et al., 2014; Zhao, 2019): $E = 2 \times 10^6\ \mathrm{N/m^2}$; $K_h = 2 \times 10^4\ \mathrm{N/m^2}$; $\varrho = 0.3$; $\mu_0' = 0.3$; $c_0' = 0\ \mathrm{N/m^2}$; $\eta_c = 0.3$; $a_d = 0.5$; $b_d = 0.5$; $\omega_\mu = 0\ \mathrm{m^2/N}$; $c_m' = 2.3 \times 10^3\ \mathrm{N/m^2}$; $\omega_c = 5 \times 10^{-4}\ \mathrm{m^2/N}$; $p_b = 10^4 \mathrm{N/m^2}$; $\beta = 0.01$; $\rho^s = 2450\ \mathrm{kg/m^3}$; $\rho^w = 1000\ \mathrm{kg/m^3}$; $\zeta = 2$; $K_{sat} = 7.75 \times 10^{-5} \mathrm{m/s}$. In this example, the initial

stresses are assumed to be induced by gravity representing the equilibrium state of the undisturbed body due to the lack of appropriate experimental data. To describe it, the K_0-method is adopted where the vertical stress is determined from a product between the unit weight of soil and its elevation (Bui & Fukagawa, 2013). A product between the earth pressure coefficient K_0 and the vertical stress is used to compute the lateral stresses (Bui & Fukagawa, 2013). Owing to the insufficiency of essential experimental data for describing the soil failure related to the inelastic response, these constants are assumed using appropriate information provided in Ando et al. (2015); Xiong et al. (2014) and Zhao (2019) without the use of a consistent calibration method. It is acknowledged that this feature is a shortcoming of the present work. Therefore, a more rigorous and adequate calibration procedure is required in future works to have a better connection between BVPs and experimental data. Furthermore, according to Alonso et al. (2015), a small-time increment is required in the explicit formulation of the numerical analysis to give stable solutions, leading to very long computational time for the explicit code in the case of low permeability. In this case, to reduce the computational time, the permeability can be artificially increased. Along with this, experimental and numerical times can be comparative using the dimensionless time (Alonso et al., 2015; Yerro, 2015) as: $\bar{t} = \frac{t}{t_f}$ in which t is the real time and t_f is the time to failure (Alonso et al., 2015). It is acknowledged that this approach is just a simple treatment to make the computational time shorter.

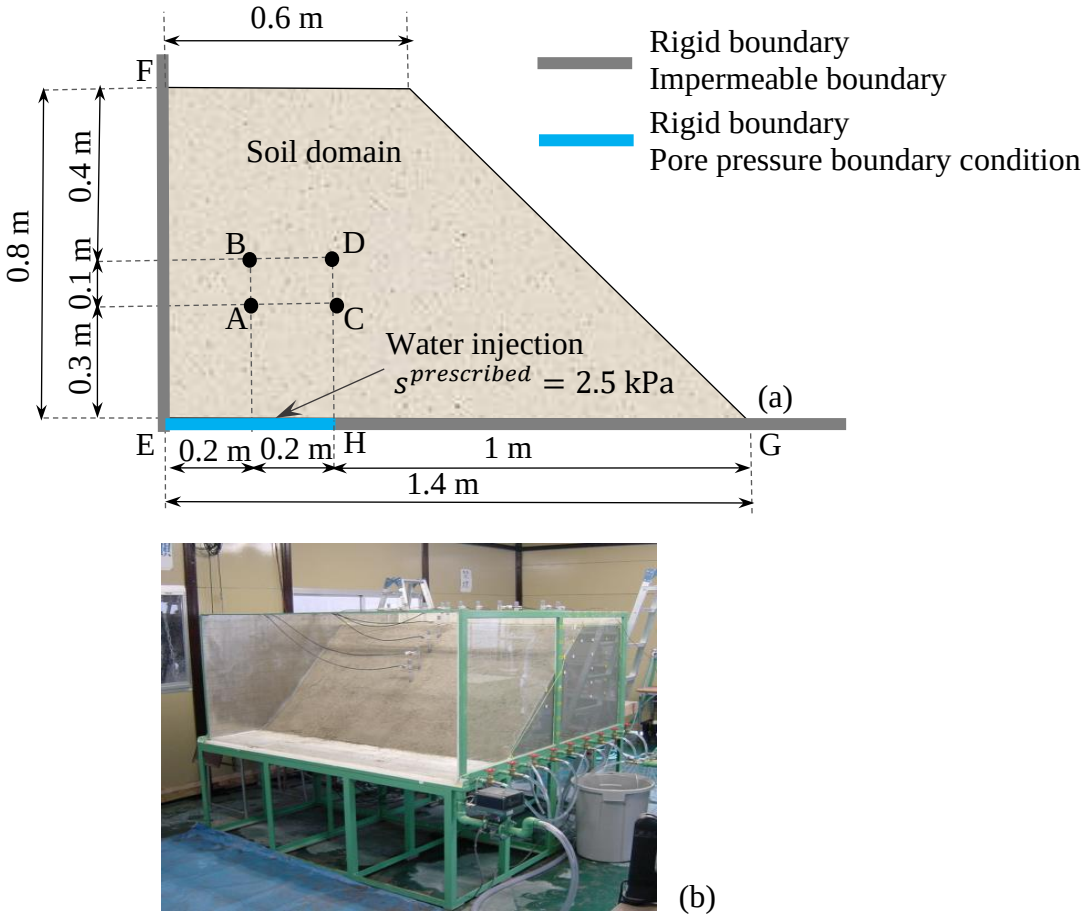

Figure 6.24. Geometrical data used in the numerical analysis (a) Initial geometry for the test (b) Image of testing apparatus.

To figure out how the partially saturated fluid transport and the corresponding progressive failure process take place inside the embankment, contour plots of suction and seepage velocity are illustrated in Figure 6.25 at several time steps ($\bar{t} = 0.167; 0.333;\ 0.5; 0.833;\ 0.983$ and 1). By way of illustration, starting from the bottom edge EH, the coupled hydro-mechanical seepage flow travels in down-to-up or left-to-right directions within the soil structure. The comparison between experimental and numerical results on suction plotted against the dimensionless time at four points A, B, C, D within the slope is shown in Figure 6.26. Figure 6.26 show that the proposed SPH model is capable of providing a good match to experimentally observed behaviour where suction at these points decreases during the infiltration process. However, there are several quantitative mismatches between predicted and measured data in regards to the change in suction at points C and D. This issue may be attributed to the fact that several explicit effects of mechanical field quantities (porosity, stress) on the hydraulic conductivity have not yet been considered in governing equations of seepage flow.

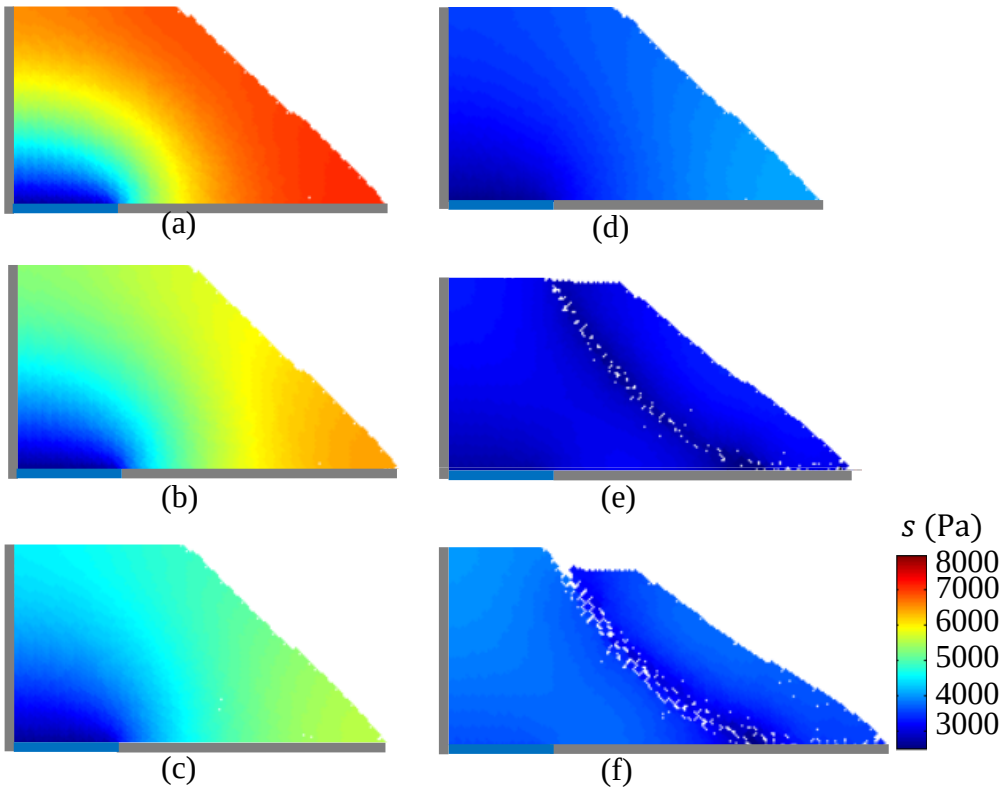

Figure 6.25. The evolution of suction in the slope during the infiltration process at (a) $\bar{t} = 0.167$ (b) $\bar{t} = 0.333$ (c) $\bar{t} = 0.5$ (d) $\bar{t} = 0.833$ (e) $\bar{t} = 0.983$ (f) $\bar{t} = 1$

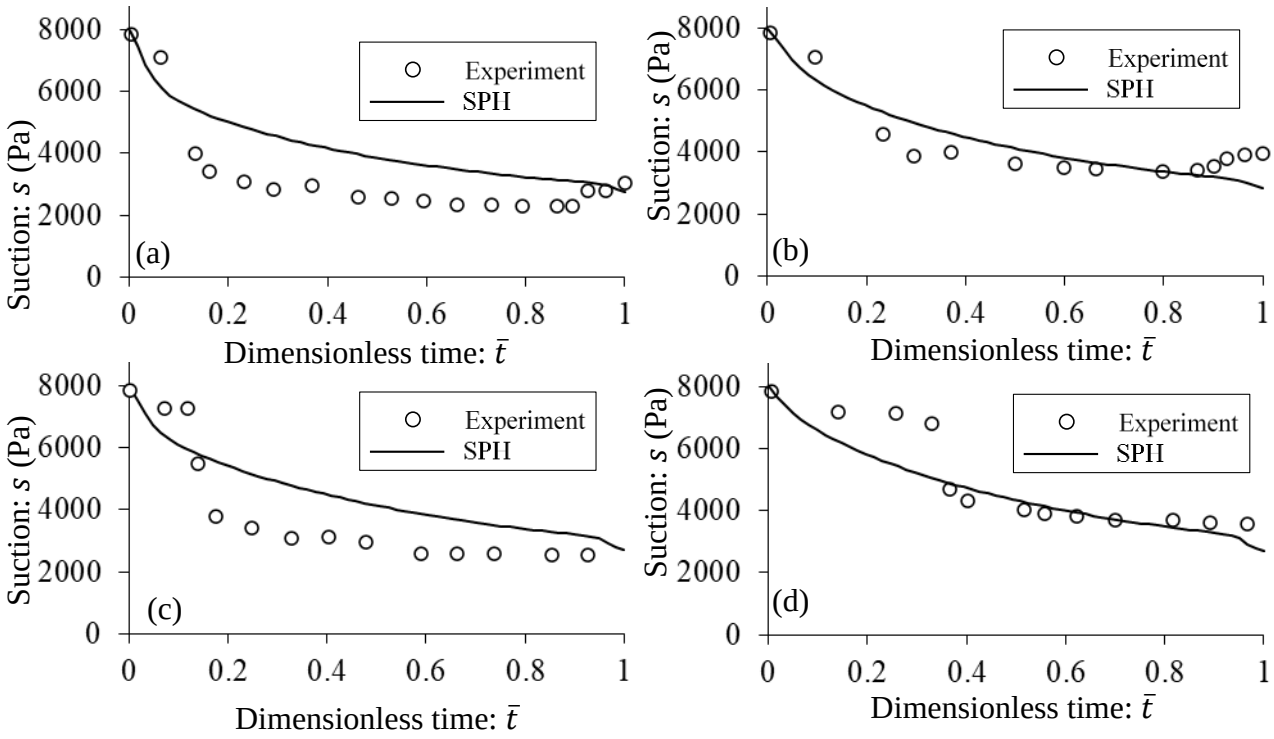

Figure 6.26. Validation with experimental data in terms of suction (after Kitamura et al., 2007) (a) Point A (b) Point B (c) Point C (d) Point D.

Additionally depicted in Figure 6.27 is the contour of plastic shear strain at $\bar{t} = 0.5; 0.95; 0.983$ and 1 to represent the failure mode. Due to the reduction in matric suction during infiltration, slope instability occurs $\Delta\bar{t} = 0.5$ after the beginning of the process of water infiltration, going with a circular arc-shaped shear band which initiates from the slope toe G and then spreads towards the middle of the slope crest. Within this shear band, the simultaneous activation and evolution of plastic deformation and irreversible saturation are observed, describing the inseparable nature of coupled hydro-mechanical behaviour at the grain scale that none of the previous numerical methods for unsaturated soils can address (see Figure 6.28). A complete slip surface is then formed, triggering the global soil collapse. The structure exhibits a progressive detachment of the soil mass above the localisation band from the undeformed region under it until reaching the maximum displacement, reflecting the loss in the soil strength induced by the wetting process. The onset and development of the localisation band create a channel of fluid flow within the slope, readjusting the direction and magnitude of Darcy's seepage velocity (see Figure 6.28b). These features support the view that the wetting-induced collapse mechanism of partially saturated soils can be well captured by the proposed SPH method.

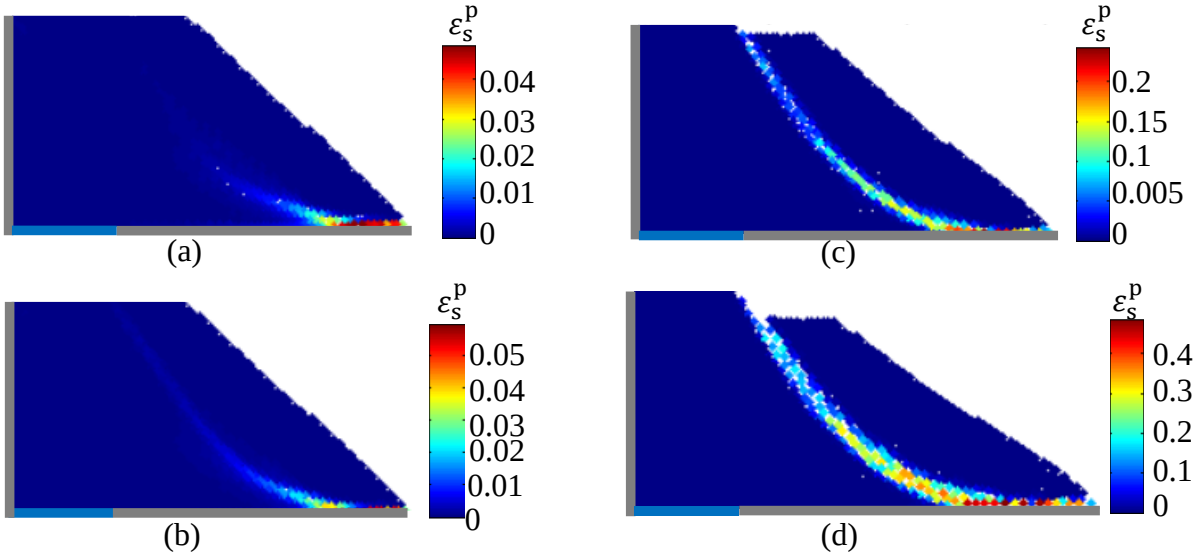

Figure 6.27. The evolution of plastic shear strain in the slope during the infiltration process at (a) $\bar{t} = 0.5$ (b) $\bar{t} = 0.95$ (c) $\bar{t} = 0.983$ (d) $\bar{t} = 1$

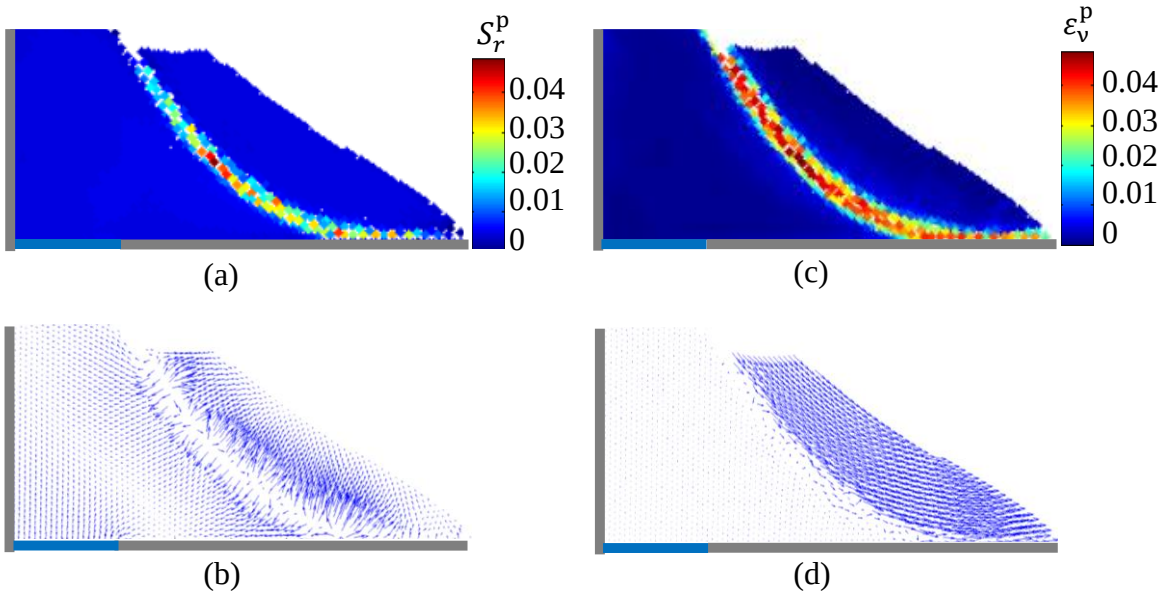

Figure 6.28. (a) Irreversible saturation (b) Darcy's seepage velocity (c) Plastic volumetric strain (d) Solid velocity at $\bar{t} = 1$.

When $\beta = 0$, there is no irreversible saturation and hence no hydraulic dissipation, a pure mechanical dissipation is observed where the irrecoverable change of saturation degree totally vanishes although the soil structure still exhibits the plastic deformation (see Figure 6.29). This is the case of existing SPH models for partially saturated soils, which fail to give a meaningful measure of the simultaneous activation and development of both hydraulic and mechanical yielding responses at any instant in the inelastic regime, even though they yield adequate results matching those of experiments in some cases. The occurrence of irreversible saturation at $\beta \neq 0$ (see Figure 6.28) enables the present approach to capture the inseparable nature of mechanical and hydraulic energy dissipations inspired from microscale interactions between grain contact sliding and capillary irreversibility. It is important to note that plastic strain and irreversible saturation activate and develop simultaneously inside these shear bands during loading (see Figure 6.28), as a result of using the strong coupling approach based on the intrinsic dependence of generalised dissipative stresses on each other and also on internal variables apart from their interactions through the constitutive equations. These obtained results reflect that taking into account the irreversible change of saturation degree, a sign for the wetting-drying difference, is essential for predicting the failure of partially saturated soils. This again confirms the effectiveness of the proposed SPH model in capturing actual mechanisms of the coupled hydro-mechanical yielding behaviour of partially saturated soils and makes it distinct from other SPH models.

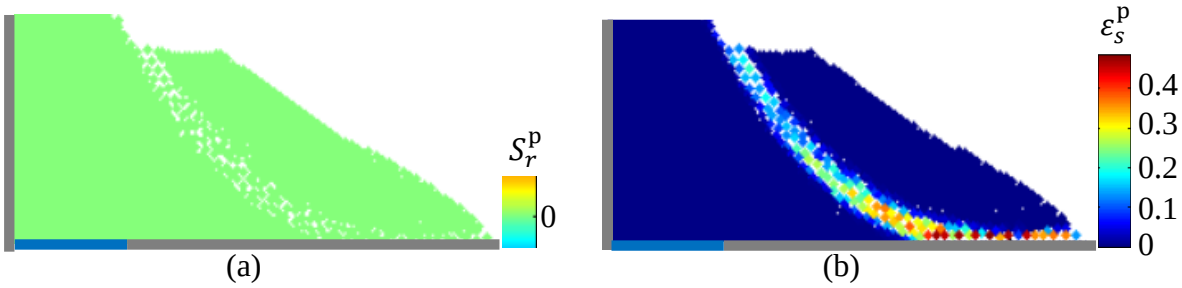

Figure 6.29. (a) Irreversible saturation (b) Plastic shear strain at $\bar{t} = 1$ when $\beta = 0$.

6.6. Closure

This chapter focuses on the development of a simple and rigorous SPH approach to studying the coupled solid deformation/fluid diffusion in deformable partially saturated soils subjected to a wide range of loading and hydraulic boundary conditions for addressing concerns as mentioned in Chapter 1 and 3. This approach is simple in its formulation, given the use of a single Lagrangian layer representing the mix of solid and fluid phases whose field quantities are solved simultaneously. Governing and constitutive equations of this method are rigorously and systematically constructed using the generic approach provided in Chapter 3, 4, 5 and Appendix A, thanks to the specifications of thermodynamic potentials. One of the unique features that distinguishes the proposed SPH model from other existing ones for partially saturated soils is the inclusion of irreversible saturation and its interaction with plastic strain in the constitutive relationships of Modified Cam-Clay and Drucker Prager yield criteria, allowing to reproduce the hydraulic dissipation and thus the hydraulic irreversibility of SWCC. This approach is able to provide the strong hydromechanical coupling reflected in an intrinsic dependence of all thermodynamic forces on stress, suction, internal variables and their rates through a single-yield surface model encapsulating the simultaneous evolution of plastic strains and irrecoverable saturation inspired from the inseparable interaction between grain rearrangement and liquid-bridge redistribution at the grain scale as discussed earlier in Chapters 2,3 and 4. Several numerical examples showing the capability of the proposed approach in simulating the tight coupling between seepage flow and large deformation of partially saturated soils are presented where the strength loss and soil collapse due to both external loading and infiltration processes in some typical tests are reasonably captured.

Notwithstanding, this work is just in an early stage for researching the behaviour of partially saturated soils by the SPH-based scheme. It is geared towards the goal of interpreting mechanisms involving the interdependence between plasticity and hydraulic irreversibility instead of pursuing an excellent match to particular sets of experimentally measured data. It is acknowledged that there is a lack of strong validations of numerical simulation results while the determination of parameters has not

carefully been addressed in the current study with somewhat arbitrary choices, owing to an insufficiency of appropriate experimental evidence for inelastic behavioural features of partially saturated soils. Furthermore, the current SPH model totally ignores details on thickness and orientation of localisation band in constitutive equations and numerical regularization techniques, resulting in the ill-posed boundary problems in the post-localisation regime. The double-scale model for partially saturated soils, as proposed in Chapter 5, can be incorporated into the present SPH approach to remedy this problem. It is, however, not yet adopted in this study, and the realization of this enhancement is left here as future work on the SPH model development.

Chapter 7. Conclusion and future research

7.1. Summary and conclusion

The emphasis of this thesis is placed on the development of new thermodynamics-based approaches and associated constitutive models incorporating better coupling between mechanical (stress-strain) and hydraulic (SWCC) responses in a framework of coupled flow-deformation problem to simulate failure mechanisms of partially saturated soils under different loading and saturation conditions. The key focus is a good balance between rigour, simplicity, number of parameters and performance of all approaches and models.

The basis of the model development is the intrinsic nature of the interaction between grain rearrangement and redistribution of liquid bridges at the grain contacts, which governs the simultaneous activation and evolution of both mechanical and hydraulic yielding responses at the continuum level. This study pursues more rigorous formulations to better reflect these underlying mechanisms in continuum constitutive models through the inseparable relationship between plastic strains and irrecoverable degree of saturation, employed as two key internal variables in thermodynamics-based continuum modelling of partially saturated soils. This is achieved thanks to the dependence of all thermodynamic forces on stress, suction and their rates in a new thermodynamic approach. Alternatively, it has also been shown that the use of constraints in thermodynamic formulations could also be a good and simple way to achieve the goal of having a single loading function with two evolution rules for plastic strain and irrecoverable saturation. The key findings and contribution in this thesis are:

(i) Development of a thermodynamic approach for constitutive modelling of partially saturated soils within the framework of coupled solid deformation-fluid flow in porous media. The key feature that makes this thermodynamic approach distinct from existing ones is the strong coupling between hydraulic and mechanical responses realised in a single yield surface dependent on both stress and suction and two flow rules for the rates of plastic strains and irreversible saturation rates, sharing a single plastic multiplier (see Chapter 3). An alternative option, employing constraints in thermodynamics-based formulations for constitutive models for partially saturated soils, has also been explored and shown promising potential in obtaining models with a single yield surface and two evolution rules for plastic strain and irrecoverable saturation.

(ii) Systematic establishment of a critical state model for partially saturated soils following the generic formulation with a thorough and rigorous investigation of the thermodynamic admissibility and dissipation properties. This model offers good potential for predicting essential experimental features

observed in suction- and water content-controlled tests at low stresses using a small number of parameters, all of which can be calibrated using standard tests through a systematic procedure (see Chapter 4).

(iii) Extension to the general thermodynamics-based approach for constitutive modelling partially saturated soils taking into account strain localisation. This is the first attempt to describe and capture correctly both pre-and post-localisation responses of partially saturated soils at the material level. This approach allows the ability to capture the gradual transition from homogeneous to localised failure, along with a coupled hydro-mechanical discontinuous bifurcation criterion accounting for the difference between wetting and drying. For the first time, the details on the localisation band (thickness, orientation) are incorporated into the constitutive equations to allow modelling the size-dependent behaviour of partially saturated soils under drained conditions (see Chapter 5).

(iv) Implementation of the proposed coupled hydro-mechanical framework in a meshfree scheme (SPH) to examine the potential applicability of the proposed approach to predict water transports and soil collapses in BVPs of three-phase porous media under a wide range of loading and hydraulic conditions. This is the first time that the irrecoverable degree of saturation is taken into account in an SPH-based approach to capture the effects of the wetting-drying difference of SWCC on the coupled flow deformation process of partially saturated soils (see Chapter 6).

These contributions and their corresponding limitations are further discussed in the following sub-sections:

7.1.1. Generic coupled flow deformation framework

This thesis develops a generic hydromechanical framework for the coupled solid deformation-fluid laminar flow within three-phase porous media based on the continuum theory of mixture and plasticity. In this framework, field variables (e.g. seepage force, solid velocity, porosity, saturation degree) following the movement of the solid skeleton are formulated in a simple mixed form by combining basic laws of mass and momentum conservation of all constituents in the mixture. Its constitutive models with coupling between mechanical (stress-strain) and hydraulic responses (SWCC) are formulated on the basis of a generalised thermodynamics-based approach possessing the strong coupling between volumetric, shear and hydraulic dissipation processes. Central to this development is the adoption of a special form of dissipation potential inspired from mechanisms at the grain scale for physical interpretations of the interdependence of thermodynamic forces, internal variables and their rates. In the context of unsaturated soil modelling, this is the first time such a strong coupling is used for coupling irreversible degree of saturation with plastic strain, resulting in

a model with a single yield surface and two flow rules for the irrecoverable degree of saturation and plastic strain. It distinguishes the proposed approach from several other thermodynamics-based approaches, which require more than one yield function due to the decoupling of dissipative stresses from all stresses and suction when adding the internal hydraulic variable.

The proposed thermodynamic approach for constitutive modelling of partially saturated soils enables a more natural evolution of yield surface under coupled hydro-mechanical effects, in lieu of using arbitrary and complicated treatments for the coupled evolution of multiple yield functions as seen in several existing models for partially saturated soils. Thanks to this, the cross-coupling terms of tangent stiffness tensor reflecting the inter-dependence between mechanical and hydraulic responses upon yielding are automatically obtained. As a result, SWCC in this framework has a path-dependence nature governed by hydro-mechanical loading paths of both stress and suction, inducing different responses under wetting/drying and mechanical loading conditions. This feature reflects the inseparable nature of the tight hydromechanical coupling rooting from grain-scale interactions and permits removing the use of a separate water retention curve for inelastic behaviour, as commonly found in many existing studies. The proposed generic formulations for flow through and constitutive models of partially saturated porous media possess versatility for the development of different constitutive models and their implementation for solutions of BVPs involving partially saturated soils through the specifications of seepage force and both energy and dissipation potentials.

It is noted that details associated with underlying mechanisms at the grain scale are not explicitly incorporated into constitutive equations of the current model framework despite their importance for an accurate understanding of the actual responses of partially saturated soils. Microscopic mechanisms are used here only as a means to identify constraints on the interdependence of internal variables (e.g. plastic strain tensor and irreversible saturation degree) in thermodynamics-based continuum modelling where their strong coupling in energy dissipation at the continuum level is the focus of this thesis. The inseparable interaction between grain rearrangement and liquid-bridge redistribution at the microscopic scale is understood as fundamentals for the purpose of clarifying the current selection of Helmholtz specific energy potential and energy dissipation at the macro averaged behaviour over a certain volume element. It is acknowledged that the proposed approaches and models do not possess explicit links between grain-scale processes and their continuum representatives, plastic strain and irrecoverable saturation. These explicit links that require grain-scale modelling and homogenisation are not within the scope of this study. Instead, several simplifying assumptions in the phenomenological descriptions of the essential mechanisms have been used in the current approach. Their appropriateness and validity are the subjects of future study.

7.1.2. Constitutive modelling of partially saturated soils

Following the proposed general thermodynamic approach, a particular constitutive model based on the concept of critical state is constructed. The fundamental of this model is the inelastic responses of partially saturated soils at the critical state where volumetric and hydraulic energy dissipations totally vanish, and the total dissipation is fully governed by shear strain only. Helmholtz specific energy and dissipation potentials are explicitly defined, taking into account some key behavioural features of suction-and water content-controlled triaxial shear tests at low pressures to derive this whole model through a systematic procedure with a small number of assumptions. This leads to the construction of a three-dimensional Modified Cam-Clay family yield surface whose tear-drop shape in p': q: s^* space can be expanded with suction through a simple monotonic function of hardening law. In comparison with the previous unsaturated soil models, this model possesses fewer parameters (13 parameters), all of which can be consistently calibrated through a step-by-step process linked with different experimental loading paths of standard tests.

Various numerical examples are performed to demonstrate that the current approach can offer the capacity to handle fully coupled hydro-mechanical responses of partially saturated soils under a broad range of testing conditions. In particular, this model gives a good performance on the transition between different states (e.g. saturated and partially saturated, isotropic compression and triaxial shear, hardening and softening) and hydromechanical coupling (e.g. effects of suction and saturation degree on soil stiffness, dilation, shear strength and effects of stress and strain on the wetting-drying difference of SWCC). The advantages of the present approach in quantifying the amounts of hydraulic and mechanical energy dissipations and guaranteeing the thermodynamic admissibility are also demonstrated in extensive analyses on coupled hydro-mechanical dissipation characteristics.

However, the present critical state model is acknowledged just as a relatively simple example to emphasize the applicability of the generic framework in capturing the coupled hydro-mechanical dissipation of partially saturated soils. As always, there are shortcomings. For instance, the anisotropic nature of behaviour is not addressed in this model, resulting in the incapacity to reproduce experimental data on distorted or rotated tear-drop shapes of the yield surface (Cui & Delage, 1996; Zhan, 2003). In addition, the model neglects the explicit effect of air entry value on effective stress and the Loading-Collapse curve, which is important to understanding the actual transition between fully and partially saturated states. Another shortcoming lies in the open-shaped yield curve in the p': s^* plane that hinders adequate simulations of hydraulic paths under the constant net stress in some experimental situations because of the indefinite yield limit with suction increase. Furthermore, no attention has been paid to modelling responses of partially saturated soils at high-stress levels,

involving the transition to full-void closure and pressurised saturation. These features lead to some mismatches in simulating experiments, as noted in Chapter 4.

7.1.3. Strain localisation of partially saturated soils

To capture the inhomogeneous deformation induced by the localised failure in partially saturated soils, this thesis proposes a new mechanism-based model to embed essential shear band details (orientation and thickness) in the constitutive relationships. Within this model, two separate hydromechanical responses outside (reversibility) and inside (irreversibility) the localisation band are connected by means of the kinematically enriched approach under drained conditions, all of which appear naturally through rigorous procedures following a thermodynamically consistent approach based on two explicitly defined energy potentials. The model, constructed in this manner, is capable of capturing the transition between pre-and post-localization responses in a physically meaningful way as it can reduce to be identical to a classical constitutive model for homogeneous deformation.

The model also facilitates a natural derivation of the in-built criterion for detecting onset and orientation of the localisation band, accounting for the difference between wetting and drying under various loading and saturation conditions, all of which have not yet been considered in the literature. The irreversible change of saturation degree (a sign for the wetting-drying difference) is taken into account in the discontinuous bifurcation condition. The incorporation of a length scale related to the width of the localisation zone and the size of the volume element (specimen) into the constitutive equations allows this model to describe post-localisation correctly and hence size-dependent behaviour, removing the needs for additional ad hoc regularisations for the numerical analysis of BVPs involving localised failure.

The ability of the proposed double-scale approach in taking the concurrent existence of hydraulic effects (suction, saturation degree) towards mechanical processes (stress, strain, porosity) and vice versa into consideration in the bifurcation criterion and post-localisation behaviour is highlighted to some extents in different verification, validation and parametric studies at the material level. Through a consistent calibration method covering size-effect parameters, a good agreement between predicted and measured data on the orientation of the localisation band and the softening response of several suction-controlled triaxial shear tests are obtained, indicating the potential of this approach.

Although the obtained results demonstrate that considerable progress has been made in modelling the localised failure of partially saturated soils, several weaknesses exist in the current model. For example, the gradual variation of the width of the localisation band during the transition from diffuse to localised failure is ignored, although its dependence on the loading history and the underlying

complicated nonlinear microstructural processes is usually observed in experiments. The proposed approach does not consider the effects of the shape of the volume element and positions of the localisation band in the specimen, given the fact that the formulation assumes idealised conditions to simplify the derivation. Since no consensus has been reached on measuring thickness and inclination angle of the shear band in experiments, a very simple method is used to calibrate the length scale for fitting the experimental data on the softening behaviour. Furthermore, only a single tabular shear band of the localised failure is considered in the current model, making it hard to reproduce the experimental responses related to the appearance of multiple intersecting bands over the sheared specimen (Patil, 2014; Nguyen et al., 2017). All of these deficiencies in the physical definition of the length scale are regarded as possible explanations for mismatches between predicted and measured results in some loading cases, as demonstrated in Chapter 5. On the other hand, the proposed formulation is applicable only to drained conditions of partially saturated soils where strain localisation involving undrained loading paths has not yet been investigated.

7.1.4. Study of Boundary Value Problems

The potential applicability of the proposed continuum approach for simulating the coupled flow deformation process in the solutions of BVPs is investigated using the Smoothed Particle Hydrodynamics. In this implementation, the necessary detailed forms of seepage force and thermodynamic potentials (Helmholtz specific energy, dissipation) are assumed to derive specific solutions of partial differential equations. Two constitutive models for partially saturated soils based on Drucker-Prager and Modified Cam-Clay yield criteria are used, following generic formulations and procedures established in Chapter 3.

This study is expected to represent a significant advancement towards developing a simple but robust SPH-based continuum framework to yield an appropriate reflection of the underlying nature of the grain scale interaction in modelling the coupled hydro-mechanical behaviour of unsaturated soils. In particular, its simplicity is realised through the adoptions of a single set of Lagrangian particles for solving the system of governing differential equations (single-layer approach) and a unique yield locus for updating stress and suction. The promising performance of the proposed approach in handling failure mechanisms of partially saturated soils is demonstrated through a broad range of numerical examples (e.g. verification, validation, parametric study) under different mechanical and hydraulic boundary conditions. Full coupling between fluid flow patterns and large deformations/failures of the solid phase are captured relatively well. It is worth noting here that the developed SPH framework possesses advantages compared to existing ones thanks to the advanced

constitutive models used, with the capacity to tackle the difference in wetting and drying and the simultaneous activation and development of yield stress and suction at any instant in time.

It should be emphasized that this study is only an initial step towards a better strategy for simulating failures of partially saturated soils by the SPH-based framework involving the intrinsic nature of interdependence between plasticity and hydraulic irreversibility. This thesis mainly attempts to develop a rigorous approach with the promising potential of applications in constitutive modelling of partially saturated soils in different deformation and saturation states. In this sense, the current constitutive model is just intended to demonstrate the capacity of the new continuum modelling approach with acceptable trends of behaviour rather than to produce a perfect match with experiments. At this stage, there is a lack of adequate experimental data in existing laboratory or field tests that can provide sufficient details of inelastic responses of partially saturated soils. This brings challenges to the development of a consistent and appropriate calibration procedure to determine parameters associated with yield criteria for reaching a good fit between predictive and measured results. Furthermore, the integration of thickness and orientation of shear band in the constitutive relationships is not considered in the SPH simulations due to the lack of experimental data with sufficient details on the correlation between hydro-mechanical responses and the evolution of localisation bands. Nevertheless, the importance of shear localisation in controlling the actual behaviour of unsaturated soils is acknowledged. The use of rate-dependent or nonlocal regularisations will also be considered in the near future to overcome issues associated with localised failure in the analysis of BVPs involving softening and/or localisations.

7.2. Future research directions

Given the above-mentioned limitations, further works and investigations are required to improve the approach and models developed in this study. For this purpose, several possible research directions are currently being planned for the future as follow up to this project. They are briefly described as follows:

7.2.1. Micromechanical enrichments

Local components for micromechanical responses (e.g. surface tension, contact angle, traction) are missing in the current approach, despite their indispensability in generating actual behaviour of partially saturated soils. This requires further theoretical research to better understand the phenomena at both grain and macro (continuum) scales and their effects on the macro hydro-mechanical behaviour of unsaturated soils (e.g. micro-macro links). As a step towards this, the present thermodynamics-based continuum model can be further enhanced by adding the micromechanics-

based details to constitutive equations. This development can start with a new closed-form work input of the volume element, including particle information (size, shape) and modes of micromechanical interaction (surface tension, contact angle, air-water interfacial area) based on a microscale analysis of conservation equations and thermodynamic statements. This is expected to lead to better forms of stress-like variables (effective stress, hydraulic variables) accounting for the micromechanical aspects. From this, with the use of appropriate energy potentials (Helmholtz specific free energy, dissipation), a corresponding model can be constructed through a procedure similar to the one described in this thesis where the observed microscopic components are automatically accommodated in the constitutive structure.

In an alternative way, a new micromechanics-based approach based on Nguyen & Gan (2014) can be put forward to gain physical insights into bridging both macroscopic and microscopic responses at the constitutive level. In this approach, the material is treated as a composite one possessing two separate phases (scales): localized (micro) and bulk (macro), where several possible contact surface across the volume element are idealized to define the localized phase. The bulk behaviour can follow the constitutive law of the continuum model developed in Chapter 3 and 4, while the response of the localized phase can be represented by grain to grain contact laws of friction and capillary forces, including essential micromechanical details in different saturation and deformation regimes. The interaction between these two phases is then established through an internal equilibrium to maintain the traction continuity across the contact surface, leading to an overall constitutive relationship of the volume element containing both micro and macroscale responses. This planned research is expected to bring in a fruitful way to reproduce the realistic behaviour of partially saturated soils faithfully, in comparison with continuum approaches mapping everything onto a single constitutive relationship.

7.2.2. Improving model behaviour

Another potential direction for future research can involve several further enhancements in the responses of the current critical state model in Chapter 4. In this regard, the main concern is the reconstruction of the loading function to offer a combination of advanced features found in several existing studies to move towards a closer representation of unsaturated soil response. For example, the anisotropic behaviour can be taken into account in the dissipation potential to derive the yield locus in distorted tear-drop shapes to match with some experimental observations closely. The yield curve can also be improved to incorporate the effects of air-entry suction (Sheng et al., 2008; 2011; Khalili et al., 2008; Loret & Khalili, 2000; 2002) to achieve a better reflection on the transition between fully and partially saturated states thanks to the modifications to the equations of effective stress and volume change. In addition, a closed-shape yield surface (Thu et al., 2007b; Sivakumars &

Doran, 2000; Delage & Graham, 1996; Tang & Graham, 2002) is essential to better predict water retention curves of stress-controlled drying tests, requiring several behavioural features observed in these tests to appear in thermodynamic potentials. The hardening law for the loading function still needs further modifications to allow the model to capture yielding responses under more complicated loading paths (Loret & Khalili, 2000; 2002) and high stresses related to the pressurized saturation and the transition to full-void (Mun & McCartney, 2015; 2017; Zhou et al., 2018).

7.2.3. Localisation of deformation

Future study should address the evolution of the thickness of the shear band to complete the description of the current double-scale approach for better predictive capabilities with the general idea rooting from Nguyen & Bui (2020). In this development, the volume fraction f (length scale) representing the width of the localisation zone is inserted into the thermodynamics-based constitutive formulation as an internal variable instead of a constant input parameter. Different constituents for the behaviour inside and outside the localisation zone and the rate-dependent evolution of this zone can be then rigorously constructed using a similar procedure to that given in Chapter 5. Another extension of the current two-scale model for capturing the nested scale nature of the localised failure with multiple shear bands is also needed (Nguyen et al., 2017). To address it, one of the possible improvements is the introduction of multiple length scales and variables (stress, suction, strain, saturation degree) in the current thermodynamics-based size-dependent framework, each of which is defined for a localisation band based on an existing approach for progressive compaction localisation (Nguyen et al., 2017). Furthermore, the size-dependent behaviour under undrained conditions is neglected in this thesis but should be studied in the near future as it could open doors to a more comprehensive understanding and simulation of localised failure of partially saturated soils. Towards this goal, the movement of all three phases (air, water, solid) as one material and thus the mass conservation of fluid phases in the solid matrix motion can be assumed (Borja, 2004), allowing the use of balance laws (mass, momentum) to derive an appropriate condition describing the distribution of suction and saturation degree across the boundary of the shear band. This condition is then incorporated into a thermodynamics-based framework for further steps.

7.2.4. Regularisation to deal with softening and localisation in the analysis of BVPs

The numerical implementation of the current SPH model (Chapter 6) is limited to the homogeneous deformation without the details on the localisation band (orientation, thickness) characterising the post-localisation behaviour, hence leading to the lack of convergence of numerical solutions with respect to the mesh refinement. This problem can be remedied in the future by an implementation of the two-scale model developed in Chapter 5 into the SPH-based scheme presented in Chapter 6, going

with adequate analysis of regularisation effects for the solutions of BVPs. In this analysis, the width of the localisation band (h) is considered as an intrinsic material property where it is presumably fixed during loading and remains the same in all particle discretisation sizes. The effective size of the volume element (H') in this case is defined by the effective size of an SPH particle (size of the Kernel supporting domain) crossed by the shear band, which can vary depending on the resolution of the spatial discretisation. As demonstrated in several publications on the fracture of solids and also soil cracking (Nguyen et al., 2014; 2016; Wang et al., 2019; 2020; Tran et al., 2019), the numerical solutions are expected to converge upon the refinement of the spatial discretisation, thanks to the intrinsic regularisation of the approach. This approach is computationally efficient and can be used to analyse large scale failure, given the fact that SPH particles can be larger than the thickness of the localisation band, thanks to the embedded localisation band in the constitutive structure. For small scale analysis, the size of the SPH particles can be smaller than the thickness of the localisation band, facilitating the application of classical regularisation techniques such as nonlocal/gradient (Pijaudier-Cabot & Bazant, 1987; Chen & Schreyer, 1987; Peerlings et al., 1996) and rate-dependent regularisations (Das et al., 2013; Mir et al., 2018) based on Perzyna's visco-plasticity (Perzyna, 1966; Sluys, 1992; Borst et al., 1993).

References

Abduljauwad, S, Al-Sulaimani, G, Basunbul, I & Al-Buraim, I 1998, 'Laboratory and field studies of response of structures to heave of expansive clay', *Geotechnique*, vol. 48, no. 1, pp. 103-121.

Abed, AA & Vermeer, PA 2009, 'Numerical simulation of unsaturated soil behaviour', *International journal of computer applications in technology*, vol. 34, no. 1, pp. 2-12.

Ahmadi-Adli, M, Huvaj, N & Toker, NK 2017, 'Rainfall-triggered landslides in an unsaturated soil: a laboratory flume study', *Environmental Earth Sciences*, vol. 76, no. 21, p. 735.

Al-Rub, RKA & Darabi, MK 2012, 'A thermodynamic framework for constitutive modeling of time- and rate-dependent materials. Part I: Theory', *International Journal of Plasticity*, vol. 34, pp. 61-92.

Al-Sharrad, M, Gallipoli, D & Wheeler, S 2017, 'Experimental investigation of evolving anisotropy in unsaturated soils', *Geotechnique*, vol. 67, no. 12, pp. 1033-1049.

Al-Sharrad, MA 2013, 'Evolving anisotropy in unsaturated soils: experimental investigation and constitutive modelling', University of Glasgow.

Alabdullah, J 2010, *Testing unsaturated soil for plane strain conditions: A new double-wall biaxial device*, Lehrstuhl für Grundbau, Boden-und Felsmechanik.

Alonso, E 1988, 'Consolidation analysis of patially saturated soils-Apprication to earthdam construction', *Numerical Method in Geomechanics*, vol. 2, pp. 1303-1308.

Alonso, E, Gens, A & Hight, D 1987, 'General report. Special problem soils', in *Proceedings of the 9th European Conference on soil mechanics and foundation engineering, Dublin*, vol. 3, pp. 1087-1146.

Alonso, EE, Gens, A & Josa, A 1990, 'A constitutive model for partially saturated soils', *Geotechnique*, vol. 40, no. 3, pp. 405-430.

Alonso, EE, Pinyol, N & Gens, A 2013, 'Compacted soil behaviour: initial state, structure and constitutive modelling', *Geotechnique*, vol. 63, no. 6, pp. 463-478.

Alonso Pérez de Agreda, E, Yerro Colom, A & Pinyol Puigmartí, NM 2015, 'Recent developments of the Material Point Method for the simulation of landslides', in *IOP conference series: earth and environment*, vol. 26, p. 012003.

AM Marinho, F, Gonzalo Carnero Guzmán, G & Del Gaudio Orlando, P 2016, 'Constant water content compression tests on unsaturated compacted soil with suction measurement using a HCT', *International Journal of Geomechanics*, vol. 16, no. 6, p. D4015008.

Anandarajah, A 2008, 'Multi-mechanism anisotropic model for granular materials', *International Journal of Plasticity*, vol. 24, no. 5, pp. 804-846.

Ando, E 2013, 'Experimental investigation of microstructural changes in deforming granular media using x-ray tomography'.

Andò, E, Hall, SA, Viggiani, G, Desrues, J & Bésuelle, P 2012, 'Grain-scale experimental investigation of localised deformation in sand: a discrete particle tracking approach', *Acta Geotechnica*, vol. 7, no. 1, pp. 1-13.

Ando, Y, Suda, K, Konishi, S & Akagi, H 2015, 'Rigid plastic FE slope stability analysis combined with rain fall water infiltration', *Japanese Geotechnical Society Special Publication*, vol. 1, no. 3, pp. 23-28.

Australian Building Codes Board 2015, 'Landslide Hazards Handbook', https://www.abcb.gov.au/Resources/Publications/Education-Training/Landslide-Hazards

Bachmann, J, Woche, S, Goebel, MO, Kirkham, M & Horton, R 2003, 'Extended methodology for determining wetting properties of porous media', *Water Resources Research*, vol. 39, no. 12.

Balieu, R & Kringos, N 2015, 'A new thermodynamical framework for finite strain multiplicative elastoplasticity coupled to anisotropic damage', *International Journal of Plasticity*, vol. 70, pp. 126-150.

Bandara, S, Ferrari, A & Laloui, L 2016, 'Modelling landslides in unsaturated slopes subjected to rainfall infiltration using material point method', *International journal for numerical and analytical methods in geomechanics*, vol. 40, no. 9, pp. 1358-1380.

Bardenhagen, SG & Kober, EM 2004, 'The generalized interpolation material point method', *Computer Modeling in Engineering and Sciences*, vol. 5, no. 6, pp. 477-496.

Bardet, P & Choucair, W 1991, 'A linearized integration technique for incremental constitutive equations', *International journal for numerical and analytical methods in geomechanics*, vol. 15, no. 1, pp. 1-19.

Bavas, J 2020, 'Emergency declaration revoked for leaking Talgai dam, residents allowed to return', ABC News, https://www.abc.net.au/news/2020-02-16/residents-allowed-to-return-to-area-near-leaking-talgai-dam/11969788.

Bear, J 2013, *Dynamics of fluids in porous media*, Courier Corporation.

Bear, J 2018, *Modeling phenomena of flow and transport in porous media*, vol. 31, Springer.

Bian, H, Shahrour, I & Jia, Y 2017, 'Influence of soil saturation on the free field response of liquefiable soils', *Underground Space*, vol. 2, no. 1, pp. 30-37.

Bianchi, F, Thielmann, M, Mani, R, Or, D & Herrmann, HJ 2016, 'Tensile stress relaxation in unsaturated granular materials', *Granular Matter*, vol. 18, no. 4, p. 75.

Bignonnet, F, Dormieux, L & Kondo, D 2016, 'A micro-mechanical model for the plasticity of porous granular media and link with the Cam clay model', *International Journal of Plasticity*, vol. 79, pp. 259-274.

Biot, MA 1941, 'General theory of three-dimensional consolidation', *Journal of applied physics*, vol. 12, no. 2, pp. 155-164.

Blake, T & Haynes, J 1969, 'Kinetics of liquidliquid displacement', *Journal of colloid and interface science*, vol. 30, no. 3, pp. 421-423.

Blatz, J & Graham, J 2003, 'Elastic-plastic modelling of unsaturated soil using results from a new triaxial test with controlled suction', *Geotechnique*, vol. 53, no. 1, pp. 113-122.

Blonquist Jr, J, Jones, SB, Lebron, I & Robinson, D 2006, 'Microstructural and phase configurational effects determining water content: Dielectric relationships of aggregated porous media', *Water Resources Research*, vol. 42, no. 5.

Bolzon, G, Schrefler, B & Zienkiewicz, O 1996, 'Elastoplastic soil constitutive laws generalized to partially saturated states', *Geotechnique*, vol. 46, no. 2, pp. 279-289.

Borja, RI 2004, 'Cam-Clay plasticity. Part V: A mathematical framework for three-phase deformation and strain localization analyses of partially saturated porous media', *Computer Methods in Applied Mechanics and Engineering*, vol. 193, no. 48-51, pp. 5301-5338.

Borja, RI & White, JA 2010, *Conservation laws for coupled hydro-mechanical processes in unsaturated porous media: theory and implementation*, Lawrence Livermore National Lab.(LLNL), Livermore, CA (United States).

Borst, RDE, Sluyes, LJ, Muhlhaus, HB & Pamin, J 1993, 'Fundamental Issues in Finite Element Analyses of Localisation of Deformation', *Engineering Computations: International Journal for Computer-Aided Engineering*, vol. 10, no.2, pp. 99-121.

Bozkurt, M, Fratta, D & Likos, W 2017, 'Capillary forces between equally sized moving glass beads: an experimental study', *Canadian Geotechnical Journal*, vol. 54, no. 9, pp. 1300-1309.

Brooks, RH & Corey, AT 1964, 'Hydraulic properties of porous media', *Hydrology papers (Colorado State University); no. 3*.

Brookshaw, L 1985, 'A method of calculating radiative heat diffusion in particle simulations', in *Proceedings of the Astronomical society of Australia*, vol. 6, pp. 207-210.

Bruno, AW & Gallipoli, D 2019, 'A coupled hydromechanical bounding surface model predicting the hysteretic behaviour of unsaturated soils', *Computers and Geotechnics*, vol. 110, pp. 287-295.

Bui, HH & Fukagawa, R 2009, 'A first attempt to solve soil-water coupled problem by SPH', *Japanese Terramechanics*, vol. 29, pp.33-38.

Bui, HH & Fukagawa, R 2013, 'An improved SPH method for saturated soils and its application to investigate the mechanisms of embankment failure: case of hydrostatic pore-water pressure', *International journal for numerical and analytical methods in geomechanics*, vol. 37, no. 1, pp. 31-50.

Bui, HH & Fukagawa, R 2008, 'Elasto-plastic large deformation analysis of geomaterial using SPH', *Japanese Terramechanics*, vol. 28, pp.177-182

Bui, HH, Fukagawa, R, Sako, K & Ohno, S 2008, 'Lagrangian meshfree particles method (SPH) for large deformation and failure flows of geomaterial using elastic–plastic soil constitutive model', *International journal for numerical and analytical methods in geomechanics*, vol. 32, no. 12, pp. 1537-1570.

Bui, HH, Fukagawa, R, Sako, K & Wells, JC 2011, 'Slope stability analysis and discontinuous slope failure simulation by elasto-plastic smoothed particle hydrodynamics (SPH)', *Geotechnique*, vol. 61, no. 7, pp. 565-574.

Bui, HH & Nguyen, GD 2017, 'A coupled fluid-solid SPH approach to modelling flow through deformable porous media', *International Journal of Solids and Structures*, vol. 125, pp. 244-264.

Bui, HH & Nguyen, GD 2020 'Smoothed particle hydrodynamics (SPH) and its applications in geomechanics', *Alert Geomaterials Doctoral school on Point based Method in Geomechanics*.

Buisson, M & Wheeler, S 2000, 'Inclusion of hydraulic hysteresis in a new elasto-plastic', *Experimental evidence and theoretical approaches in unsaturated soils*, p. 109.

Buscarnera, G 2010, 'Rainfall Induced Flow Slides: Constitutive Modelling Mechanical Instability and Theoretical Interpretation', Politecnico di Milano.

Buscarnera, G & Einav, I 2012, 'The yielding of brittle unsaturated granular soils', *Geotechnique*, vol. 62, no. 2, pp. 147-160.

Buscarnera, G & Mihalache, C 2014, 'Instability of unsaturated soils: A review of theoretical methods', *Journal of Geo-Engineering Sciences*, vol. 2, no. 1-2, pp. 39-65.

Buscarnera, G & Nova, R 2009, 'An elastoplastic strainhardening model for soil allowing for hydraulic bonding–debonding effects', *International journal for numerical and analytical methods in geomechanics*, vol. 33, no. 8, pp. 1055-1086.

Buscarnera, G & Nova, R 2011, 'Modelling instabilities in triaxial testing on unsaturated soil specimens', *International journal for numerical and analytical methods in geomechanics*, vol. 35, no. 2, pp. 179-200.

Butterfield, R 1979, 'A natural compression law for soils (an advance on e–log p′)', *Geotechnique*, vol. 29, no. 4, pp. 469-480.

Cadoret, T, Mavko, G & Zinszner, B 1998, 'Fluid distribution effect on sonic attenuation in partially saturated limestones', *Geophysics*, vol. 63, no. 1, pp. 154-160.

Callari, C & Abati, A 2009, 'Finite element methods for unsaturated porous solids and their application to dam engineering problems', *Computers & structures*, vol. 87, no. 7-8, pp. 485-501.

Callari, C, Armero, F & Abati, A 2010, 'Strong discontinuities in partially saturated poroplastic solids', *Computer Methods in Applied Mechanics and Engineering*, vol. 199, no. 23-24, pp. 1513-1535.

Callari, C, Auricchio, F & Sacco, E 1998, 'A finite-strain Cam-clay model in the framework of multiplicative elasto-plasticity', *International Journal of Plasticity*, vol. 14, no. 12, pp. 1155-1187.

Carman, PC 1956, 'Flow of gases through porous media'.

Caunce, CM 2010, 'Effective road pavement design for expansive soils in Ipswich'.

Cerato, A & Lutenegger, A 2006, 'Bearing capacity of square and circular footings on a finite layer of granular soil underlain by a rigid base', *Journal of Geotechnical and Geoenvironmental Engineering*, vol. 132, no. 11, pp. 1496-1501.

Chandler, R, Crilly, M, SMITH, M, SMITH, M & BRE 1992, 'A low-cost method of assessing clay desiccation for low-rise buildings', in *Proceedings of the Institution of Civil Engineers-civil engineering*, Thomas Telford-ICE Virtual Library, vol. 92, pp. 82-89.

Chandler, R & Gutierrez, C 1986, 'The filter-paper method of suction measurement', *Geotechnique*, vol. 36, no. 2, pp. 265-268.

Charlier, R, Li, X, Bolle, A, Geiser, F, Laloui, L & Vulliet, L 1997, 'Mechanical behaviour model of an unsaturated sandy silt', in *Proc. of the XIVth Int. Conf. on Soil Mechanics and Foundation Engineering*.

Chateau, X, Moucheront, P & Pitois, O 2002, 'Micromechanics of unsaturated granular media', *Journal of Engineering Mechanics*, vol. 128, no. 8, pp. 856-863.

Chen, J, Beraun, J & Carney, T 1999, 'A corrective smoothed particle method for boundary value problems in heat conduction', *International Journal for Numerical Methods in Engineering*, vol. 46, no. 2, pp. 231-252.

Chen, R 2007, *Experimental study and constitutive modelling of stress-dependent coupled hydraulic hysteresis and mechanical behaviour of an unsaturated soil*, Hong Kong University of Science and Technology (Hong Kong).

Chen, Z & Schreyer, H 1987, 'Simulation of soil-concrete interfaces with nonlocal constitutive models', *Journal of Engineering Mechanics*, vol. 113, no. 11, pp. 1665-1677.

Childs, EC & Collis-George, N 1950, 'The permeability of porous materials', *Proceedings of the Royal Society of London. Series A. Mathematical and Physical Sciences*, vol. 201, no. 1066, pp. 392-405.

Chiu, C & Ng, CWW 2003, 'A state-dependent elasto-plastic model for saturated and unsaturated soils', *Geotechnique*, vol. 53, no. 9, pp. 809-829.

Chiu, CF 2002, 'Behaviour of unsaturated loosely compacted weathered materials'.

Cho, GC & Santamarina, JC 2001, 'Unsaturated particulate materials—particle-level studies', *Journal of Geotechnical and Geoenvironmental Engineering*, vol. 127, no. 1, pp. 84-96.

Collins, I 2003, 'A systematic procedure for constructing critical state models in three dimensions', *International Journal of Solids and Structures*, vol. 40, no. 17, pp. 4379-4397.

Collins, I 2005, 'The concept of stored plastic work or frozen elastic energy in soil mechanics', *Geotechnique*, vol. 55, no. 5, pp. 373-382.

Collins, I & Houlsby, G 1997, 'Application of thermomechanical principles to the modelling of geotechnical materials', *Proceedings of the Royal Society of London. Series A: Mathematical, Physical and Engineering Sciences*, vol. 453, no. 1964, pp. 1975-2001.

Collins, I & Kelly, P 2002, 'A thermomechanical analysis of a family of soil models', *Geotechnique*, vol. 52, no. 7, pp. 507-518.

Collins, IF & Hilder, T 2002, 'A theoretical framework for constructing elastic/plastic constitutive models of triaxial tests', *International journal for numerical and analytical methods in geomechanics*, vol. 26, no. 13, pp. 1313-1347.

Considine, M 1984, 'Soils shrink, trees drink, and houses crack', *ECOS Magazine*, vol. 41, pp. 13-15.

Corey, AT 1957, 'Measurement of water and air permeability in unsaturated soil', *Soil Science Society of America Journal*, vol. 21, no. 1, pp. 7-10.

Coussy, O, Pereira, J-M & Vaunat, J 2010, 'Revisiting the thermodynamics of hardening plasticity for unsaturated soils', *Computers and Geotechnics*, vol. 37, no. 1-2, pp. 207-215.

Crisfield, MA & Tassoulas, JL 1993, 'Non-Linear Finite Element Analysis of Solids and Structures, Volume 1', *Journal of Engineering Mechanics*, vol. 119, no. 7, pp. 1504-1505.

Crouch, RS, Wolf, JP & Dafalias, YF 1994, 'Unified critical-state bounding-surface plasticity model for soil', *Journal of Engineering Mechanics*, vol. 120, no. 11, pp. 2251-2270.

Cruz, JA, Hoyos, LR & Lizcano, A 2012, 'Unsaturated soil response under plane strain conditions using a servo/suction-controlled biaxial apparatus', in *Unsaturated Soils: Research and Applications*, Springer, pp. 31-38.

Cui, Y & Delage, P 1996, 'Yielding and plastic behaviour of an unsaturated compacted silt', *Geotechnique*, vol. 46, no. 2, pp. 291-311.

Cunningham, M, Ridley, A, Dineen, K & Burland, J 2003, 'The mechanical behaviour of a reconstituted unsaturated silty clay', *Geotechnique*, vol. 53, no. 2, pp. 183-194.

d'Onza, F, Gallipoli, D, Wheeler, S, Casini, F, Vaunat, J, Khalili, N, Laloui, L, Mancuso, C, Mašín, D & Nuth, M 2011, 'Benchmark of constitutive models for unsaturated soils', *Geotechnique*, vol. 61, no. 4, pp. 283-302.

Dangla, P & Pereira, J-M 2014, 'A thermodynamic approach to effective stresses in unsaturated soils incorporating the concept of partial pore deformations', *Vadose Zone Journal*, vol. 13, no. 5, pp. 1-11.

Darabi, MK, Al-Rub, RKA & Omidi, O 2018, 'A thermodynamically consistent framework to derive local/nonlocal generalized nonassociative plasticity/viscoplasticity theories', *International Journal of Plasticity*, vol. 110, pp. 19-37.

Darve, F 1994, ‘Stability and uniqueness in geomaterials constitutive modelling’, *Proceedings of Localisation and bifurcation theory for soils and rocks*, Balkema, pp. 73–88.

Darve, F 1994, ‘Liquefaction phenomenon: modelling, stability and uniqueness’, *Proceedings of Verification of numerical procedures for the analysis of soil liquefaction problems*, Arulanandan & Scott, pp. 1305-1319.

Darve, F 1996, ‘Liquefaction phenomenon of granular materials and constitutive stability’, *Engineering computations*, vol. 13, no. 7, pp. 5-28.

Darve, F, Flavigny, E & Rojas, E 1986, ‘A class of incrementally non-linear constitutive relations and applications to clays’, *Computers and Geotechnics*, vol. 2, no. 1, pp. 43-66.

Darve, F, Servant, G, Laouafa, F & Khoa, HDV 2004, ‘Failure in geomaterials: continuous and discrete analyses’, *Computer Methods in Applied Mechanics and Engineering*, vol. 193, no. 27-29, pp. 3057–3085.

Daouadji A, Darve F, Al Gali H, Hicher P, Laouafa F, Lignon S, Nicot F, Nova R, Pinheiro M, Prunier F, Sibille L & Wan R 2010, ‘Diffuse failure in geomaterials: Experiments, theory and modelling’, *International journal for numerical and analytical methods in geomechanics*, vol. 35, no. 16, pp. 1731–1773.

Das, A, Nguyen, GD & Einav, I 2013, 'The propagation of compaction bands in porous rocks based on breakage mechanics', *Journal of Geophysical Research: Solid Earth*, vol. 118, no. 5, pp. 2049-2066.

DE'AN, S, Matsuoka, H, YAO, Y & Ichihara, W 2000, 'An elasto-plastic model for unsaturated soil in three-dimensional stresses', *Soils and Foundations*, vol. 40, no. 3, pp. 17-28.

Dehnen, W & Aly, H 2012, 'Improving convergence in smoothed particle hydrodynamics simulations without pairing instability', *Monthly Notices of the Royal Astronomical Society*, vol. 425, no. 2, pp. 1068-1082.

Delage, P & Graham, J 1996, 'Mechanical behaviour of unsaturated soils: understanding the behaviour of unsaturated soils requires reliable conceptual models', in *PROCEEDINGS OF THE FIRST INTERNATIONAL CONFERENCE ON UNSATURATED SOILS/UNSAT'95/PARIS/FRANCE/6-8 SEPTEMBER 1995. VOLUME 3*.

Desrues, J & Viggiani, G 2004, ‘Strain localization in sand: an overview of the experimental results obtained in Grenoble using stereophotogrammetry’, *International journal for numerical and analytical methods in geomechanics*, vol. 28, no. 4, pp. 279–321.

Dessouky, SH, Oh, J, Ilias, M, Lee, SI & Park, D 2015, 'Investigation of various pavement repairs in low-volume roads over expansive soil', *Journal of Performance of Constructed Facilities*, vol. 29, no. 6, p. 04014146.

Ehlers, W, Graf, T & Ammann, M 2004, 'Deformation and localization analysis of partially saturated soil', *Computer Methods in Applied Mechanics and Engineering*, vol. 193, no. 27-29, pp. 2885-2910.

Einav, I 2007a, 'Breakage mechanics—part I: theory', *Journal of the Mechanics and Physics of Solids*, vol. 55, no. 6, pp. 1274-1297.

Einav, I 2007b, 'Breakage mechanics—Part II: Modelling granular materials', *Journal of the Mechanics and Physics of Solids*, vol. 55, no. 6, pp. 1298-1320.

Einav, I 2012, 'The unification of hypo-plastic and elasto-plastic theories', *International Journal of Solids and Structures*, vol. 49, no. 11-12, pp. 1305-1315.

Einav, I, Houlsby, G & Nguyen, G 2007, 'Coupled damage and plasticity models derived from energy and dissipation potentials', *International Journal of Solids and Structures*, vol. 44, no. 7-8, pp. 2487-2508.

Ergun, S 1952, 'Fluid flow through packed columns', *Chem. Eng. Prog.*, vol. 48, pp. 89-94.

Estabragh, AR & Javadi, AA 2008, 'Critical state for overconsolidated unsaturated silty soil', *Canadian Geotechnical Journal*, vol. 45, no. 3, pp. 408-420.

Fadaei-Kermani, E, Shojaee, S, Memarzadeh, R & Barani, G 2019, 'Numerical simulation of seepage problem in porous media', *Applied Water Science*, vol. 9, no. 4, p. 79.

Fang, H, Zheng, H & Zheng, J 2017, 'Micromechanics-based multimechanism bounding surface model for sands', *International Journal of Plasticity*, vol. 90, pp. 242-266.

Farias, M, Pinheiro, M & Neto, MC 2006, 'An elastoplastic model for unsaturated soils under general three-dimensional conditions', *Soils and Foundations*, vol. 46, no. 5, pp. 613-628.

Farouk, A, Lamboj, L & Kos, J 2004, 'A numerical model to predict matric suction inside unsaturated soils', *Acta Polytechnica*, vol. 44, no. 4.

Fredlund, D 1989, 'The character of the shear strength envelope for unsaturated soils', in *Proceedings of the 12th international conference on soil mechanics and foundation engineering (ICSMFE). The Victor de Mello Volume, Rio de Janeiro*, pp. 142-149.

Fredlund, D, Gan, JK & Gallen, P 1995, 'Suction measurements on compacted till specimens and indirect filter paper calibration technique', *Transportation research record*, vol. 1481, pp. 3-9.

Fredlund, DG & Rahardjo, H 1993, *Soil mechanics for unsaturated soils*, John Wiley & Sons.

Fredlund, DG & Wong, DK 1989, 'Calibration of thermal conductivity sensors for measuring soil suction', *Geotechnical Testing Journal*, vol. 12, no. 3, pp. 188-194.

Fredlund, DG & Xing, A 1994, 'Equations for the soil-water characteristic curve', *Canadian Geotechnical Journal*, vol. 31, no. 4, pp. 521-532.

Gallipoli, D, Grassl, P, Wheeler, S & Gens, A 2018, 'On the choice of stress–strain variables for unsaturated soils and its effect on plastic flow', *Geomechanics for Energy and the Environment*, vol. 15, pp. 3-9.

Gallipoli, D, Wheeler, S & Karstunen, M 2003, 'Modelling the variation of degree of saturation in a deformable unsaturated soil', *Geotechnique*, vol. 53, no. 1, pp. 105-112.

Gan, Y, Maggi, F, Buscarnera, G & Einav, I 2013, 'A particle–water based model for water retention hysteresis', *Géotechnique Letters*, vol. 3, no. 4, pp. 152-161.

Gardner, W 1958, 'Some steady-state solutions of the unsaturated moisture flow equation with application to evaporation from a water table', *Soil science*, vol. 85, no. 4, pp. 228-232.

Geiser, F, Laloui, L & Vulliet, L 2000, 'On the volume measurement in unsaturated triaxial test', in *Unsaturated soils for Asia. Proceedings of the Asian Conference on Unsaturated Soils, UNSAT-ASIA 2000, Singapore, 18-19 May, 2000*, AA Balkema, pp. 669-674.

Gens, A, Sánchez, M & Sheng, D 2006, 'On constitutive modelling of unsaturated soils', *Acta Geotechnica*, vol. 1, no. 3, p. 137.

Ghasemzadeh, H & Amiri, SG 2013, 'A hydro-mechanical elastoplastic model for unsaturated soils under isotropic loading conditions', *Computers and Geotechnics*, vol. 51, pp. 91-100.

Ghasemzadeh, H, Sojoudi, M, Amiri, SG & Karami, M 2017, 'Elastoplastic model for hydro-mechanical behavior of unsaturated soils', *Soils and Foundations*, vol. 57, no. 3, pp. 371-383.

Gholizadeh, E & Latifi, M 2018, 'A coupled hydro-mechanical constitutive model for unsaturated frictional and cohesive soil', *Computers and Geotechnics*, vol. 98, pp. 69-81.

Ghorbani, J, Airey, DW & El-Zein, A 2018, 'Numerical framework for considering the dependency of SWCCs on volume changes and their hysteretic responses in modelling elasto-plastic response of unsaturated soils', *Computer Methods in Applied Mechanics and Engineering*, vol. 336, pp. 80-110.

Gili, J & Alonso, E 2002, 'Microstructural deformation mechanisms of unsaturated granular soils', *International journal for numerical and analytical methods in geomechanics*, vol. 26, no. 5, pp. 433-468.

Gingold, RA & Monaghan, JJ 1977, 'Smoothed particle hydrodynamics: theory and application to non-spherical stars', *Monthly Notices of the Royal Astronomical Society*, vol. 181, no. 3, pp. 375-389.

Goebel, M-O, Bachmann, J, Woche, SK, Fischer, WR & Horton, R 2004, 'Water potential and aggregate size effects on contact angle and surface energy', *Soil Science Society of America Journal*, vol. 68, no. 2, pp. 383-393.

Goetze, E 2020, 'Drought causes buildings to crack, leaving homeowners facing hefty repair bills', ABC news, https://www.abc.net.au/news/2020-01-06/drought-causing-building-cracks-subsidence/11840828

Gray, WG, Schrefler, BA & Pesavento, F 2009, 'The solid phase stress tensor in porous media mechanics and the Hill–Mandel condition', *Journal of the Mechanics and Physics of Solids*, vol. 57, no. 3, pp. 539-554.

Griffiths, D & Lu, N 2005, 'Unsaturated slope stability analysis with steady infiltration or evaporation using elasto-plastic finite elements', *International journal for numerical and analytical methods in geomechanics*, vol. 29, no. 3, pp. 249-267.

Guiamatsia, I & Nguyen, GD 2012, 'A generic approach to constitutive modelling of composite delamination under mixed-mode loading conditions', *Composites science and technology*, vol. 72, no. 2, pp. 269-277.

Guo, P & Stolle, D 2013, 'Coupled analysis of bifurcation and shear band in saturated soils', *Soils and Foundations*, vol. 53, no. 4, pp. 525-539.

Ha, BH 2007, 'Lagrangian mesh-free particle method (SPH) for large deformation and post-failure of geomaterial using elasto-plastic constitutive models'.

Haltas, I & Ulusoy, S 2015, 'Scaling and scale invariance of conservation laws in Reynolds transport theorem framework', *Chaos: An Interdisciplinary Journal of Nonlinear Science*, vol. 25, no. 7, p. 075406.

Hamdhan, I & Schweiger, H 2013, 'Finite element method–based analysis of an unsaturated soil slope subjected to rainfall infiltration', *International Journal of Geomechanics*, vol. 13, no. 5, pp. 653-658.

Hanna, A 1982, 'Bearing capacity of foundations on a weak sand layer overlying a strong deposit', *Canadian Geotechnical Journal*, vol. 19, no. 3, pp. 392-396.

Hashiguchi, K 1995, 'On the linear relations of v–ln p and ln v–ln p for isotropic consolidation of soils', *International journal for numerical and analytical methods in geomechanics*, vol. 19, no. 5, pp. 367-376.

Hashiguchi, K & Mase, T 2007, 'Extended yield condition of soils with tensile yield strength and rotational hardening', *International Journal of Plasticity*, vol. 23, no. 12, pp. 1939-1956.

Hashiguchi, K & Tsutsumi, S 2007, 'Gradient plasticity with the tangential-subloading surface model and the prediction of shear-band thickness of granular materials', *International Journal of Plasticity*, vol. 23, no. 5, pp. 767-797.

Hassanizadeh, SM & Gray, WG 1990, 'Mechanics and thermodynamics of multiphase flow in porous media including interphase boundaries', *Adv. Water Resour*, vol. 13, no. 4, pp. 169-186.

Heinse, R, Jones, SB, Steinberg, SL, Tuller, M & Or, D 2007, 'Measurements and modeling of variable gravity effects on water distribution and flow in unsaturated porous media', *Vadose Zone Journal*, vol. 6, no. 4, pp. 713-724.

Hernquist, L & Katz, N 1989, 'TREESPH-A unification of SPH with the hierarchical tree method', *The Astrophysical Journal Supplement Series*, vol. 70, pp. 419-446.

Hicher, P-Y & Chang, CS 2007, 'A microstructural elastoplastic model for unsaturated granular materials', *International Journal of Solids and Structures*, vol. 44, no. 7-8, pp. 2304-2323.

Higo, Y, Oka, F, Kimoto, S, Sanagawa, T & Matsushima, Y 2011, 'Study of strain localization and microstructural changes in partially saturated sand during triaxial tests using microfocus X-ray CT', *Soils and Foundations*, vol. 51, no. 1, pp. 95-111.

Higo, Y, Oka, F, Sato, T, Matsushima, Y & Kimoto, S 2013, 'Investigation of localized deformation in partially saturated sand under triaxial compression using microfocus X-ray CT with digital image correlation', *Soils and Foundations*, vol. 53, no. 2, pp. 181-198.

Hillel, D 2012, *Soil and water: physical principles and processes*, Elsevier.

Hossain, MA & Yin, J-H 2010, 'Shear strength and dilative characteristics of an unsaturated compacted completely decomposed granite soil', *Canadian Geotechnical Journal*, vol. 47, no. 10, pp. 1112-1126.

Hossain, MA & Yin, J-H 2015, 'Dilatancy and strength of an unsaturated soil-cement interface in direct shear tests', *International Journal of Geomechanics*, vol. 15, no. 5, p. 04014081.

Houlsby, G 1997, 'The work input to an unsaturated granular material', *Geotechnique*, vol. 47, no. 1, pp. 193-196.

Houlsby, G & Puzrin, A 2000, 'A thermomechanical framework for constitutive models for rate-independent dissipative materials', *International Journal of Plasticity*, vol. 16, no. 9, pp. 1017-1047.

Houlsby, GT & Puzrin, AM 2007, *Principles of hyperplasticity: an approach to plasticity theory based on thermodynamic principles*, Springer Science & Business Media.

Houston, SL, Houston, WN & Wagner, A-M 1994, 'Laboratory filter paper suction measurements', *Geotechnical Testing Journal*, vol. 17, no. 2, pp. 185-194.

Hu, R, Chen, Y-F, Liu, H-H & Zhou, C-B 2015, 'A coupled stress–strain and hydraulic hysteresis model for unsaturated soils: thermodynamic analysis and model evaluation', *Computers and Geotechnics*, vol. 63, pp. 159-170.

Hu, R, Liu, H-H, Chen, Y, Zhou, C & Gallipoli, D 2014, 'A constitutive model for unsaturated soils with consideration of inter-particle bonding', *Computers and Geotechnics*, vol. 59, pp. 127-144.

Huang, M & Jia, C-Q 2009, 'Strength reduction FEM in stability analysis of soil slopes subjected to transient unsaturated seepage', *Computers and Geotechnics*, vol. 36, no. 1-2, pp. 93-101.

Idelsohn, S, Oñate, E & Del Pin F 2004, 'The particle finite element method: a powerful tool to solve incompressible flows with free-surfaces and breaking waves', *International Journal for Numerical Methods in Engineering*, vol. 61, no. 7, pp. 964–989.

Irmay, S 1954, 'On the hydraulic conductivity of unsaturated soils', *Eos, Transactions American Geophysical Union*, vol. 35, no. 3, pp. 463-467.

Jeong, S, Lee, K, Kim, J & Kim, Y 2017, 'Analysis of rainfall-induced landslide on unsaturated soil slopes', *Sustainability*, vol. 9, no. 7, p. 1280.

Jiang, G, Chen, W, Liu, X, Yuan, S, Wu, L & Zhang, C 2018, 'Field study on swelling-shrinkage response of an expansive soil foundation under high-speed railway embankment loads', *Soils and Foundations*, vol. 58, no. 6, pp. 1538-1552.

Johari, A & Talebi, A 2019, 'Stochastic analysis of rainfall-induced slope instability and steady-state seepage flow using random finite-element method', *International Journal of Geomechanics*, vol. 19, no. 8, p. 04019085.

Jommi, C 2000, 'Remarks on the constitutive modelling of unsaturated soils', *Experimental evidence and theoretical approaches in unsaturated soils*, pp. 139-153.

Kasangaki, GJ 2012, 'Experimental study of hydro-mechanical behaviour of granular materials', Heriot-Watt University.

Khalili, N, Habte, M & Zargarbashi, S 2008, 'A fully coupled flow deformation model for cyclic analysis of unsaturated soils including hydraulic and mechanical hystereses', *Computers and Geotechnics*, vol. 35, no. 6, pp. 872-889.

Khalili, N & Khabbaz, M 1998, 'A unique relationship for χ for the determination of the shear strength of unsaturated soils', *Geotechnique*, vol. 48, no. 5, pp. 681-687.

Khattab, SA, Al-Sulaifanie, BJ & alarna, Amm 2018, 'Stability of unsaturated soil slopes subjected to external load and rainfall', *International Journal of Geotechnical Engineering*, pp. 1-9.

Kido R, Higo Y, Takamura F 2017, 'Microscopic investigation of progressive changes of pore water distribution in shear band of unsaturated sand under triaxial compression', *Journal of Japan Society of Civil Engineers Ser C (Geosphere Engineering)*, vol. 73, no. 2, pp. 233-247.

Kim, JM 2000, 'A fully coupled finite element analysis of water-table fluctuation and land deformation in partially saturated soils due to surface loading', *International Journal for Numerical Methods in Engineering*, vol. 49, no. 9, pp. 1101-1119.

Kim, MS, Onda, Y, Uchida, T, Kim, JK & Song, YS 2018, 'Effect of seepage on shallow landslides in consideration of changes in topography: case study including an experimental sandy slope with artificial rainfall', *Catena*, vol. 161, pp. 50-62.

Kitamura, R 2007, 'Soil tank test on seepage and failure behaviors of Shirasu slope during rainfall', *Japanese Geotechnical Journal*, vol. 2, no. 3, pp. 149-168.

Kitamura, R, Haruyama, M & Misumi, K 1984, 'Mechanical properties of Shirasu under intermediate and low pressures', *Japanese Geotechnical Journal*, vol. 32, no. 2, pp. 17-21.

Kodikara, J, Jayasundara, C & Zhou, A 2020, 'A generalised constitutive model for unsaturated compacted soils considering wetting/drying cycles and environmentally-stabilised line', *Computers and Geotechnics*, vol. 118, p. 103332.

Kohler, R & Hofstetter, G 2008, 'A cap model for partially saturated soils', *International journal for numerical and analytical methods in geomechanics*, vol. 32, no. 8, pp. 981-1004.

Lai, Y, Jin, L & Chang, X 2009, 'Yield criterion and elasto-plastic damage constitutive model for frozen sandy soil', *International Journal of Plasticity*, vol. 25, no. 6, pp. 1177-1205.
Lai, Y, Liao, M & Hu, K 2016, 'A constitutive model of frozen saline sandy soil based on energy dissipation theory', *International Journal of Plasticity*, vol. 78, pp. 84-113.
Lappalainen, K, Manninen, M, Alopaeus, V, Aittamaa, J & Dodds, J 2009, 'An analytical model for capillary pressure–saturation relation for gas–liquid system in a packed-bed of spherical particles', *Transport in porous media*, vol. 77, no. 1, pp. 17-40.
Lee, LM, Kassim, A & Gofar, N 2011, 'Performances of two instrumented laboratory models for the study of rainfall infiltration into unsaturated soils', *Engineering Geology*, vol. 117, no. 1-2, pp. 78-89.
Lee, R & Fredlund, D 1984, 'Measurement of soil suction using the MCS 6000 sensor', in *Fifth International Conference on Expansive Soils 1984: Preprints of Papers*, Institution of Engineers, Australia, p. 50.
Lei, X, He, S, Chen, X, Wong, H, Wu, L & Liu, E 2020, 'A generalized interpolation material point method for modelling coupled seepage-erosion-deformation process within unsaturated soils', *Advances in Water Resources*, p. 103578.

Lei, X, Wong, H, Fabbri, A, Bui, TA & Limam, A 2016, 'Some general remarks on hyperplasticity modelling and its extension to partially saturated soils', *Zeitschrift für angewandte Mathematik und Physik*, vol. 67, no. 3, p. 64.
Leiba, M 2013, 'Impact of landslides in Australia to December 2011', *Australian Journal of Emergency Management, The*, vol. 28, no. 1, p. 28.
Leong, EC, He, L & Rahardjo, H 2002, 'Factors affecting the filter paper method for total and matric suction measurements', *Geotechnical Testing Journal*, vol. 25, no. 3, pp. 322-333.
Leshchinsky, B, Vahedifard, F, Koo, H-B & Kim, S-H 2015, 'Yumokjeong Landslide: an investigation of progressive failure of a hillslope using the finite element method', *Landslides*, vol. 12, no. 5, pp. 997-1005.
Leventhal, AR & Kotze, GP 2008, 'Landslide susceptibility and hazard mapping in Australia for land-use planning—with reference to challenges in metropolitan suburbia', *Engineering Geology*, vol. 102, no. 3-4, pp. 238-250.
Lewis, RW & Schrefler, BA 1998, *The finite element method in the static and dynamic deformation and consolidation of porous media*, John Wiley.
Li, J & Cameron, D 1996, *Finite element analysis of deep beams in expansive clays*.
Li, J, Cameron, DA & Ren, G 2014, 'Case study and back analysis of a residential building damaged by expansive soils', *Computers and Geotechnics*, vol. 56, pp. 89-99.

Li, J & Guo, L 2017, 'Field investigation and numerical analysis of residential building damaged by expansive soil movement caused by tree root drying', *Journal of Performance of Constructed Facilities*, vol. 31, no. 1, p. D4016003.

Li, L 2015, *Evaluate unsaturated soil behavior using constant water content triaxial tests*, University of Alaska Fairbanks.

Li, X 2003, 'Effective stress in unsaturated soil: a microstructural analysis', *Geotechnique*, vol. 53, no. 2, pp. 273-277.

Li, X 2005, 'Modelling of hysteresis response for arbitrary wetting/drying paths', *Computers and Geotechnics*, vol. 32, no. 2, pp. 133-137.

Li, X 2007a, 'Thermodynamics-based constitutive framework for unsaturated soils. 1: Theory', *Geotechnique*, vol. 57, no. 5, pp. 411-422.

Li, X 2007b, 'Thermodynamics-based constitutive framework for unsaturated soils. 2: A basic triaxial model', *Geotechnique*, vol. 57, no. 5, pp. 423-435.

Li, X 2015, 'Multiscale hydro-mechanical analysis of unsaturated granular materials using bridging scale method', *Engineering Computations: Int J for Computer-Aided Engineering*, vol. 32, no. 4, pp. 935-955.

Li, X, Thomas, H & Fan, Y 1999, 'Finite element method and constitutive modelling and computation for unsaturated soils', *Computer Methods in Applied Mechanics and Engineering*, vol. 169, no. 1-2, pp. 135-159.

Libersky, LD & Petschek, AG 1991, 'Smooth particle hydrodynamics with strength of materials', in *Advances in the free-Lagrange method including contributions on adaptive gridding and the smooth particle hydrodynamics method*, Springer, pp. 248-257.

Likos, WJ 2014, 'Effective stress in unsaturated soil: Accounting for surface tension and interfacial area', *Vadose Zone Journal*, vol. 13, no. 5.

Likos, WJ & Lu, N 2004, 'Hysteresis of capillary stress in unsaturated granular soil', *Journal of Engineering Mechanics*, vol. 130, no. 6, pp. 646-655.

Liu, C & Muraleetharan, KK 2012a, 'Coupled hydro-mechanical elastoplastic constitutive model for unsaturated sands and silts. I: Formulation', *International Journal of Geomechanics*, vol. 12, no. 3, pp. 239-247.

Liu, C & Muraleetharan, KK 2012b, 'Coupled hydro-mechanical elastoplastic constitutive model for unsaturated sands and silts. II: Integration, calibration, and validation', *International Journal of Geomechanics*, vol. 12, no. 3, pp. 248-259.

Liu, E, Lai, Y, Wong, H & Feng, J 2018, 'An elastoplastic model for saturated freezing soils based on thermo-poromechanics', *International Journal of Plasticity*, vol. 107, pp. 246-285.

Liu, G-R & Liu, MB 2003, *Smoothed particle hydrodynamics: a meshfree particle method*, World scientific.

Lloret-Cabot, M, Wheeler, SJ & Sánchez, M 2017, 'A unified mechanical and retention model for saturated and unsaturated soil behaviour', *Acta Geotechnica*, vol. 12, no. 1, pp. 1-21.

Lloret, M 2011, 'Numerical modelling of coupled behaviour in unsaturated soils', *PhD Thesis*.

Loret, B & Khalili, N 2000, 'A three-phase model for unsaturated soils', *International journal for numerical and analytical methods in geomechanics*, vol. 24, no. 11, pp. 893-927.

Loret, B & Khalili, N 2002, 'An effective stress elastic–plastic model for unsaturated porous media', *Mechanics of Materials*, vol. 34, no. 2, pp. 97-116.

Loret, B & Rizzi, E 1999, 'Strain localization in fluid-saturated anisotropic elastic–plastic porous media with double porosity', *Journal of the Mechanics and Physics of Solids*, vol. 47, no. 3, pp. 503-530.

Louati, H, Oulahna, D & de Ryck, A 2015, 'Apparent friction and cohesion of a partially wet granular material in steady-state shear', *Powder Technology*, vol. 278, pp. 65-71.

Louati, H, Oulahna, D & de Ryck, A 2017, 'Effect of the particle size and the liquid content on the shear behaviour of wet granular material', *Powder Technology*, vol. 315, pp. 398-409.

Lourenço, S, Gallipoli, D, Augarde, CE, Toll, DG, Fisher, PC & Congreve, A 2012, 'Formation and evolution of water menisci in unsaturated granular media', *Geotechnique*, vol. 62, no. 3, pp. 193-199.

Lu, N 2008, 'Is matric suction a stress variable?', *Journal of Geotechnical and Geoenvironmental Engineering*, vol. 134, no. 7, pp. 899-905.

Lucy, LB 1977, 'A numerical approach to the testing of the fission hypothesis', *The astronomical journal*, vol. 82, pp. 1013-1024.

Macari, EJ, Hoyos, LR & Arduino, P 2003, 'Constitutive modeling of unsaturated soil behavior under axisymmetric stress states using a stress/suction-controlled cubical test cell', *International Journal of Plasticity*, vol. 19, no. 10, pp. 1481-1515.

Maleki, M & Bayat, M 2012, 'Experimental evaluation of mechanical behavior of unsaturated silty sand under constant water content condition', *Engineering Geology*, vol. 141, pp. 45-56.

Mallikarachchi, H & Soga, K 2019, 'Prediction of Shear Localisation in Granular Materials based on a Critical State Non-coaxial Model', in *E3S Web of Conferences*, EDP Sciences, vol. 92, p. 16006.

Manahiloh, KN & Meehan, CL 2017, 'Determining the soil water characteristic curve and interfacial contact angle from microstructural analysis of X-ray CT images', *Journal of Geotechnical and Geoenvironmental Engineering*, vol. 143, no. 8, p. 04017034.

Mašín, D 2010, 'Predicting the dependency of a degree of saturation on void ratio and suction using effective stress principle for unsaturated soils', *International journal for numerical and analytical methods in geomechanics*, vol. 34, no. 1, pp. 73-90.

Matsuoka, H, Sun, Da, Kogane, A, Fukuzawa, N & Ichihara, W 2002, 'Stress–strain behaviour of unsaturated soil in true triaxial tests', *Canadian Geotechnical Journal*, vol. 39, no. 3, pp. 608-619.

Mbonimpa, M, Aubertin, M, Maqsoud, A & Bussière, B 2006, 'Predictive model for the water retention curve of deformable clayey soils', *Journal of Geotechnical and Geoenvironmental Engineering*, vol. 132, no. 9, pp. 1121-1132.

McKeen, RG 1980, 'Field studies of airport pavements on expansive clay', in *Expansive Soils*, ASCE, pp. 242-261.

McNamara, H 2014, 'An estimate of energy dissipation due to soil-moisture hysteresis', *Water Resources Research*, vol. 50, no. 1, pp. 725-735.

Mehndiratta, S & A. Sawant, V 2017, 'Numerical modelling of mechanical behaviour of partially saturated soils using coupled FEA', *International Journal of Geotechnical Engineering*, vol. 11, no. 5, pp. 452-466.

Menon, S & Song, X 2019, 'Coupled Analysis of Desiccation Cracking in Unsaturated Soils through a Non-Local Mathematical Formulation', *Geosciences*, vol. 9, no. 10, p. 428.

Meyerhof, G 1978, 'Bearing capacity of anisotropic cohesionless soils', *Canadian Geotechnical Journal*, vol. 15, no. 4, pp. 592-595.

Miller, GA, Khoury, CN, Muraleetharan, KK, Liu, C & Kibbey, TC 2008, 'Effects of soil skeleton deformations on hysteretic soil water characteristic curves: Experiments and simulations', *Water Resources Research*, vol. 44, no. 5.

Mills, N 1966, 'Incompressible mixtures of Newtonian fluids', *International Journal of Engineering Science*, vol. 4, no. 2, pp. 97-112.

Mir, A, Nguyen, GD & Sheikh, AH 2018, 'A thermodynamics-based model for brittle to ductile behaviour and localised failure of porous rocks', *International Journal of Solids and Structures*, vol. 152, pp. 161-184.

Monaghan, JJ 1992, 'Smoothed particle hydrodynamics', *Annual review of astronomy and astrophysics*, vol. 30, no. 1, pp. 543-574.

Morland, L 1972, 'A simple constitutive theory for a fluid-saturated porous solid', *Journal of geophysical research*, vol. 77, no. 5, pp. 890-900.

Morris, JP, Fox, PJ & Zhu, Y 1997, 'Modeling low Reynolds number incompressible flows using SPH', *Journal of computational physics*, vol. 136, no. 1, pp. 214-226.

Morrow, NR 1975, 'The effects of surface roughness on contact: angle with special reference to petroleum recovery', *Journal of Canadian Petroleum Technology*, vol. 14, no. 04.

Moscariello, M, Salager, S & Cuomo, S 2016, 'X-ray computed tomography for capillary collapse of loose unsaturated sand', *Procedia Eng*, vol. 158, pp. 33-38.

Mroginski, JL, Etse, G & Vrech, SM 2011, 'A thermodynamical gradient theory for deformation and strain localization of porous media', *International Journal of Plasticity*, vol. 27, no. 4, pp. 620-634.

Mualem, Y 1976, 'A new model for predicting the hydraulic conductivity of unsaturated porous media', *Water Resources Research*, vol. 12, no. 3, pp. 513-522.

Muhlhaus, HB 1986, 'Shear band analysis for granular materials within the framework of Cosserat theory', *Archive of Applied Mechanics*, vol. 59, no. 3, pp. 187-196.

Muhlhaus, HB & Vardoulakis, I 1987, 'The thickness of shear bands in granular materials', *Geotechnique*, vol. 37, no. 3, pp. 271–283.

Mun, W & McCartney, JS 2015, 'Compression mechanisms of unsaturated clay under high stresses', *Canadian Geotechnical Journal*, vol. 52, no. 12, pp. 2099-2112.

Mun, W & McCartney, JS 2017, 'Constitutive model for drained compression of unsaturated clay to high stresses', *Journal of Geotechnical and Geoenvironmental Engineering*, vol. 143, no. 6, p. 04017014.

Muraleetharan, KK, Liu, C, Wei, C, Kibbey, TC & Chen, L 2009, 'An elastoplatic framework for coupling hydraulic and mechanical behavior of unsaturated soils', *International Journal of Plasticity*, vol. 25, no. 3, pp. 473-490.

Muraleetharan, KK & Wei, C 1999, 'Dynamic behaviour of unsaturated porous media: Governing equations using the theory of mixtures with interfaces (TMI)', *International journal for numerical and analytical methods in geomechanics*, vol. 23, no. 13, pp. 1579-1608.

Nagel, F & Meschke, G 2010, 'An elasto-plastic three phase model for partially saturated soil for the finite element simulation of compressed air support in tunnelling', *International journal for numerical and analytical methods in geomechanics*, vol. 34, no. 6, pp. 605-625.

Neilsen, M & Schreyer, H 1993, 'Bifurcations in elastic-plastic materials', *International Journal of Solids and Structures*, vol. 30, no. 4, pp. 521-544.

Ng, A & Small, J 2000, 'Use of coupled finite element analysis in unsaturated soil problems', *International journal for numerical and analytical methods in geomechanics*, vol. 24, no. 1, pp. 73-94.

Ng, CWW, Zhan, LT, Bao, CG, Fredlund, DG & Gong, BW 2003, 'Performance of an unsaturated expansive soil slope subjected to artificial rainfall infiltration', *Geotechnique*, vol. 53, no. 2, pp. 143-157.

Ng, CWW & Zhou, R 2005, 'Effects of soil suction on dilatancy of an unsaturated soil', in *Proceedings of the 16th International Conference on Soil Mechanics and Geotechnical Engineering: Geotechnology in Harmony with the Global Environment*.

Nguyen, CT, Nguyen, GD, Das, A & Bui, HH 2017, 'Constitutive modelling of progressive localised failure in porous sandstones under shearing at high confining pressures', *International Journal of Rock Mechanics and Mining Sciences*, vol. 93, pp. 179-195.

Nguyen, G & Gan, Y 2014, 'A multiphase constitutive modeling framework for unsaturated soil behavior', in *Unsaturated Soils: Research & Applications*, CRC Press, pp. 359-366.

Nguyen, GD 2005, 'A thermodynamic approach to constitutive modelling of concrete using damage mechanics and plasticity theory', Oxford University, UK.

Nguyen, GD & Bui, HH 2020, 'A thermodynamics-and mechanism-based framework for constitutive models with evolving thickness of localisation band', *International Journal of Solids and Structures*, vol. 187, pp. 100-120.

Nguyen, GD & Einav, I 2009, 'The energetics of cataclasis based on breakage mechanics', *Pure and applied geophysics*, vol. 166, no. 10-11, pp. 1693-1724.

Nguyen, GD & Einav, I 2010, 'A stress-return algorithm for nonlocal constitutive models of softening materials', *International Journal for Numerical Methods in Engineering*, vol. 82, no. 5, pp. 637-670.

Nguyen, GD, Einav, I & Guiamatsia, I 2012, 'On the partition of fracture energy in constitutive modelling of quasi-brittle materials', *Engineering Fracture Mechanics*, vol. 79, pp. 225-244.

Nguyen, GD, Korsunsky, AM & Belnoue, JP-H 2015, 'A nonlocal coupled damage-plasticity model for the analysis of ductile failure', *International Journal of Plasticity*, vol. 64, pp. 56-75.

Nguyen, GD, Korsunsky, AM & Einav, I 2014, 'A constitutive modelling framework featuring two scales of behaviour: fundamentals and applications to quasi-brittle failure', *Engineering Fracture Mechanics*, vol. 115, pp. 221-240.

Nguyen, GD, Nguyen, CT, Nguyen, VP, Bui, HH & Shen, L 2016, 'A size-dependent constitutive modelling framework for localised failure analysis', *Computational Mechanics*, vol. 58, no. 2, pp. 257-280.

Nicot, F & Darve, F 2005, 'A multi-scale approach to granular materials', *Mechanics of Materials*, vol. 37, no. 9, pp. 980-1006.

Nicot, F & Darve, F 2007, 'Basic features of plastic strains: from micro-mechanics to incrementally nonlinear models', *International Journal of Plasticity*, vol. 23, no. 9, pp. 1555-1588.

Nonoyama, H, Moriguchi, S, Sawada, K & Yashima, A 2015, 'Slope stability analysis using smoothed particle hydrodynamics (SPH) method', *Soils and Foundations*, vol. 55, no. 2, pp. 458-470.

Nova, R 1989, 'Liquefaction, stability, bifurcations of soil via strain-hardening plasticity', Numerical Methods for the Localisation and Bifurcation of Granular Bodies, *Proceedings of the International Works*, Technical University of Gdansk, pp. 117–132.

Nova, R 1994, ‘Controllability of the incremental response of soil specimens subjected to arbitrary loading programmes’, *Journal of the Mechanical Behavior of Materials*, vol. 5, no. 2, pp. 193–201.

Nuth, M & Laloui, L 2008, 'Advances in modelling hysteretic water retention curve in deformable soils', *Computers and Geotechnics*, vol. 35, no. 6, pp. 835-844.

Oh, S & Lu, N 2015, 'Slope stability analysis under unsaturated conditions: Case studies of rainfall-induced failure of cut slopes', *Engineering Geology*, vol. 184, pp. 96-103.

Oka, F, Kimoto, S, Takada, N, Gotoh, H & Higo, Y 2010, 'A seepage-deformation coupled analysis of an unsaturated river embankment using a multiphase elasto-viscoplastic theory', *Soils and Foundations*, vol. 50, no. 4, pp. 483-494.

Okura, Y, Kitahara, H, Ochiai, H, Sammori, T & Kawanami, A 2002, 'Landslide fluidization process by flume experiments', *Engineering Geology*, vol. 66, no. 1-2, pp. 65-78.

Oliver, J 2012, ‘Strain localization, strong discontinuities and material fracture: Matches and mismatches’, *Computer Methods in Applied Mechanics and Engineering*, vol. 241-244, pp. 323-336.

Oliver, J, Cervera, M & Manzoli, O 1999, ‘Strong discontinuities and continuum plasticity models: the strong discontinuity approach’, *International Journal of Plasticity*, vol. 15, no. 3, pp. 319-351.

Omar, T & Sadrekarimi, A 2015, 'Effect of triaxial specimen size on engineering design and analysis', *International Journal of Geo-Engineering*, vol. 6, no. 1, p. 5.

Oñate, E, Idelsohn, S, Del Pin F & Aubry R 2004, ‘The particle finite element method. an overview’, *International Journal of Computational Methods*, vol. 1, no. 2, pp. 267–307.

Patil, UD 2014, 'Response of unsaturated silty sand over a wider range of suction states using a novel double-walled triaxial testing system'.

Patil, UD, Puppala, AJ, Hoyos, LR & Pedarla, A 2017, 'Modeling critical-state shear strength behavior of compacted silty sand via suction-controlled triaxial testing', *Engineering Geology*, vol. 231, pp. 21-33.

Pedroso, DM & Farias, MM 2011, 'Extended Barcelona basic model for unsaturated soils under cyclic loadings', *Computers and Geotechnics*, vol. 38, no. 5, pp. 731-740.

Peerings, RH, Borst, RDE, Brekelmans, WA & De Vree, JHP 1996, ‘Gradient Enhanced Damage For Quasi-Brittle Materials’, *International Journal for Numerical Methods in Engineering*, vol. 39, no. 19, pp. 3391-3403.

Pereira, J-M & Arson, C 2013, 'Retention and permeability properties of damaged porous rocks', *Computers and Geotechnics*, vol. 48, pp. 272-282.

Perić, D, Zhao, G & Khalili, N 2014, 'Strain localization in unsaturated elastic-plastic materials subjected to plane strain compression', *Journal of Engineering Mechanics*, vol. 140, no. 7, p. 04014050.

Perzyna, P 1966, 'Fundamental problems in viscoplasticity', in *Advances in applied mechanics*, vol. 9, Elsevier, pp. 243-377.

Pham, HQ 2005, 'A volume-mass constitutive model for unsaturated soils'.

Phene, C, Hoffman, G & Rawlins, S 1971, 'Measuring soil matric potential in situ by sensing heat dissipation within a porous body: I. Theory and sensor construction', *Soil Science Society of America Journal*, vol. 35, no. 1, pp. 27-33.

Pijaudier-Cabot, G & Bažant, ZP 1987, 'Nonlocal damage theory', *Journal of Engineering Mechanics*, vol. 113, no. 10, pp. 1512-1533.

Pupazzoni, R 2020, 'Houses are cracking in the dry, hot weather, but when should you start to worry?', ABC news, https://www.abc.net.au/news/2020-01-10/house-cracks-widen-as-unprecedented-drought-dries-soil/11854734.

Puzrin, A & Houlsby, G 2001, 'A thermomechanical framework for rate-independent dissipative materials with internal functions', *International Journal of Plasticity*, vol. 17, no. 8, pp. 1147-1165.

Rahardjo, H, Heng, OB & Choon, LE 2004, 'Shear strength of a compacted residual soil from consolidated drained and constant water content triaxial tests', *Canadian Geotechnical Journal*, vol. 41, no. 3, pp. 421-436.

Randles, P & Libersky, LD 1996, 'Smoothed particle hydrodynamics: some recent improvements and applications', *Computer Methods in Applied Mechanics and Engineering*, vol. 139, no. 1-4, pp. 375-408.

Raveendiraraj, A 2009, 'Coupling of mechanical behaviour and water retention behaviour in unsaturated soils', University of Glasgow.

Ravindran, S, Gratchev, I & Jeng, D 2019, 'Analysis of rainfall-induced landslides in northern New South Wales, Australia', *Australian Geomechanics*, vol. 54, no. 4, pp. 85-99.

Revil, A & Cathles Iii, L 1999, 'Permeability of shaly sands', *Water Resources Research*, vol. 35, no. 3, pp. 651-662.

Richards, B 1992, 'Modeling interactive load-deformation and flow processes in soils, including unsaturated and swelling soils', in *Proc. 6th. Australia-New Zealand Conf. on Geomech.*

Richards, B, Peter, P & Emerson, W 1983, 'The effects of vegetation on the swelling and shrinking of soils in Australia', *Geotechnique*, vol. 33, no. 2, pp. 127-139.

Ridley, A & Burland, J 1993, 'A new instrument for the measurement of soil moisture suction', *Geotechnique*, vol. 43, no. 2, pp. 321-324.

Ridley, AM 1995, 'Discussion on "Laboratory Filter Paper Suction Measurements" by Sandra L. Houston, William N. Houston, and Anne-Marie Wagner', *Geotechnical Testing Journal*, vol. 18, no. 3, pp. 391-396.

Robles, J & Elorza, F 2002, 'A triaxial constitutive model for unsaturated soils', *L. Vulliet, L. Laloui, and B. Schrefler. EPFL Press, Lausanne, Switzerland*, pp. 207-213.

Rohe, A & Vermeer, PA 2014, 'Multiphase modelling of large deformations using mpm: Applications in geotechnics and soil-water transition', Colloquium at University of Padova.

Romero, E & Simms, PH 2008, 'Microstructure investigation in unsaturated soils: a review with special attention to contribution of mercury intrusion porosimetry and environmental scanning electron microscopy', *Geotechnical and Geological engineering*, vol. 26, no. 6, pp. 705-727.

Roscoe, KH & Burland, J 1968, 'On the generalized stress-strain behaviour of wet clay'.

Rudnicki, JW & Rice, J 1975, 'Conditions for the localization of deformation in pressure-sensitive dilatant materials', *Journal of the Mechanics and Physics of Solids*, vol. 23, no. 6, pp. 371-394.

Russell, A & Khalili, N 2006, 'A unified bounding surface plasticity model for unsaturated soils', *International journal for numerical and analytical methods in geomechanics*, vol. 30, no. 3, pp. 181-212.

Russell, AR 2004, 'Cavity expansion in unsaturated soils', University of New South Wales Sydney, Australia.

Russell, AR & Buzzi, O 2012, 'A fractal basis for soil-water characteristics curves with hydraulic hysteresis', *Geotechnique*, vol. 62, no. 3, pp. 269-274.

Rutqvist, J, Ijiri, Y & Yamamoto, H 2011, 'Implementation of the Barcelona Basic Model into TOUGH–FLAC for simulations of the geomechanical behavior of unsaturated soils', *Computers & Geosciences*, vol. 37, no. 6, pp. 751-762.

Salomoni, VA & Fincato, R 2012, 'Retracted: Subloading surface plasticity model algorithm for 3D subsidence analyses above gas reservoirs', *International Journal of Geomechanics*, vol. 12, no. 4, pp. 414-427.

Santagiuliana, R & Schrefler, B 2006, 'Enhancing the Bolzon–Schrefler–Zienkiewicz constitutive model for partially saturated soil', *Transport in porous media*, vol. 65, no. 1, pp. 1-30.

Schiava, R & Etse, G 2006, 'Constitutive modeling and discontinuous bifurcation assessment in unsaturated soils'.

Schnellmann, R, Busslinger, M, Schneider, HR & Rahardjo, H 2010, 'Effect of rising water table in an unsaturated slope', *Engineering Geology*, vol. 114, no. 1-2, pp. 71-83.

Schofield, A & Wroth, P 1968, *Critical state soil mechanics*, McGraw-hill.

Selker J & Or D 2018, 'Soil Hydrology and Biophysics', online book, Oregon State University, https://open.oregonstate.education/soilhydrologyandbiophysics/.

Shao, S & Lo, EY 2003, 'Incompressible SPH method for simulating Newtonian and non-Newtonian flows with a free surface', *Advances in Water Resources*, vol. 26, no. 7, pp. 787-800.

Sharma, RS 1998, 'Mechanical behaviour of unsaturated highly expansive clays', University of Oxford.

Sheng, D 2011, 'Review of fundamental principles in modelling unsaturated soil behaviour', *Computers and Geotechnics*, vol. 38, no. 6, pp. 757-776.

Sheng, D, Fredlund, DG & Gens, A 2008, 'A new modelling approach for unsaturated soils using independent stress variables', *Canadian Geotechnical Journal*, vol. 45, no. 4, pp. 511-534.

Sheng, D, Sloan, S & Gens, A 2004, 'A constitutive model for unsaturated soils: thermomechanical and computational aspects', *Computational Mechanics*, vol. 33, no. 6, pp. 453-465.

Sheng, D, Sloan, SW, Gens, A & Smith, DW 2003, 'Finite element formulation and algorithms for unsaturated soils. Part I: Theory', *International journal for numerical and analytical methods in geomechanics*, vol. 27, no. 9, pp. 745-765.

Shwan, B 2015, 'Experimental and numerical study of the shear strength of unsaturated sand', University of Sheffield.

Sillers, WS & Fredlund, DG 2001, 'Statistical assessment of soil-water characteristic curve models for geotechnical engineering', *Canadian Geotechnical Journal*, vol. 38, no. 6, pp. 1297-1313.

Simms, P & Yanful, E 2004, 'A discussion of the application of mercury intrusion porosimetry for the investigation of soils, including an evaluation of its use to estimate volume change in compacted clayey soils', *Geotechnique*, vol. 54, no. 6, pp. 421-426.

Sivakumar, V 1993, 'A critical state framework for unsaturated soil', University of Sheffield.

Sivakumar, V & Doran, I 2000, 'Yielding characteristics of unsaturated compacted soils', *Mechanics of Cohesive-frictional Materials: An International Journal on Experiments, Modelling and Computation of Materials and Structures*, vol. 5, no. 4, pp. 291-303.

Skinner, A, Hignett, C & Dearden, J 1997, 'Resurrecting the gypsum block for soil moisture measurement', *Australian Viticulture, October/November*.

Sluys, LJ 1992, 'Wave Propagation, Localisation and Dispersion in Softening Solids', PhD thesis, TU Delft.

Soga, K, Alonso, E, Yerro, A, Kumar, K & Bandara, S 2016, 'Trends in large-deformation analysis of landslide mass movements with particular emphasis on the material point method', *Geotechnique*, vol. 66, no. 3, pp. 248-273.

Sołowski, W & Sloan, S 2015, 'Equivalent stress approach in creation of elastoplastic constitutive models for unsaturated soils', *International Journal of Geomechanics*, vol. 15, no. 2, p. 04014041.

Song, X 2014, 'Strain localization in unsaturated porous media'.

Song, X & Borja, RI 2014, 'Mathematical framework for unsaturated flow in the finite deformation range', *International Journal for Numerical Methods in Engineering*, vol. 97, no. 9, pp. 658-682.

Song, X & Khalili, N 2019, 'A peridynamics model for strain localization analysis of geomaterials', *International journal for numerical and analytical methods in geomechanics*, vol. 43, no. 1, pp. 77-96.

Song, X, Wang, K & Ye, M 2018, 'Localized failure in unsaturated soils under non-isothermal conditions', *Acta Geotechnica*, vol. 13, no. 1, pp. 73-85.

Stropeit, K, Wheeler, S & Cui, Y 2008, 'An anisotropic elasto-plastic model for unsaturated soils'.

Sun, D, Matsuoka, H & Xu, Y 2004, 'Collapse behavior of compacted clays in suction-controlled triaxial tests', *Geotechnical Testing Journal*, vol. 27, no. 4, pp. 362-370.

Sun, D, Sheng, D, Cui, H & Sloan, S 2007, 'A density-dependent elastoplastic hydro-mechanical model for unsaturated compacted soils', *International journal for numerical and analytical methods in geomechanics*, vol. 31, no. 11, pp. 1257-1279.

Sun, D, Sun, W & Yan, W 2009, 'Hydraulic and mechanical behaviour of sand-bentonite mixture', in *Proceeding of International Symposium on Unsaturated Soil Mechanics and Deep Geological Nuclear Waste Disposal, Shanghai*, pp. 24-25.

Sun, Da, Sun, W & Xiang, L 2010, 'Effect of degree of saturation on mechanical behaviour of unsaturated soils and its elastoplastic simulation', *Computers and Geotechnics*, vol. 37, no. 5, pp. 678-688.

Sun, W & Sun, Da 2012, 'Coupled modelling of hydro-mechanical behaviour of unsaturated compacted expansive soils', *International journal for numerical and analytical methods in geomechanics*, vol. 36, no. 8, pp. 1002-1022.

Taibi, S, Dumont, M & Fleureau, JM 2009, 'Effect of the interfacial tension and wettability on the behaviour of unsaturated granular media', in *AIP Conference Proceedings*, American Institute of Physics, vol. 1145, pp. 915-918.

Takatsu, Y 2017, 'Modification of the fundamental theorem for transport phenomena in porous media', *International Journal of Heat and Mass Transfer*, vol. 115, pp. 1109-1120.

Takeda, H, Miyama, SM & Sekiya, M 1994, 'Numerical simulation of viscous flow by smoothed particle hydrodynamics', *Progress of theoretical physics*, vol. 92, no. 5, pp. 939-960.

Tamagnini, R 2004, 'An extended Cam-clay model for unsaturated soils with hydraulic hysteresis', *Geotechnique*, vol. 54, no. 3, pp. 223-228.

Tamagnini, R 2005, 'The influence of hydraulic hysteresis on unsaturated soils FE analyses', in *Unsaturated Soils: Numerical and Theoretical Approaches*, Springer, pp. 67-80.

Tamagnini, R & Pastor, M 2004, 'A thermodynamically based model for unsaturated soil: a new framework for generalized plasticity', *Unsaturated Soils. Advances in Testing, Modelling and Engineering Applications*, pp. 121-134.

Tang, GX & Graham, J 2002, 'A possible elastic plastic framework for unsaturated soils with high-plasticity', *Canadian Geotechnical Journal*, vol. 39, no. 4, pp. 894-907.

Tang, Y & Taiebat, H 2015, 'Finite element formulation of unsaturated soil and its application on bearing capacity problems', in.

Tarantino, A 2007, 'A possible critical state framework for unsaturated compacted soils', *Geotechnique*, vol. 57, no. 4, pp. 385-389.

Tarantino, A 2009, 'A water retention model for deformable soils', *Geotechnique*, vol. 59, no. 9, pp. 751-762.

Terazaghi, K 1965, 'Theoretical soil mechanics', *John Wiley and Sons*.

Thomas, H & He, Y 1995, 'Analysis of coupled heat, moisture and air transfer in a deformable unsaturated soil', *Geotechnique*, vol. 45, no. 4, pp. 677-689.

Thu, TM 2006, 'Shear strength and volume change relationship for an unsaturated soil'.

Thu, TM, Rahardjo, H & Leong, E-C 2006, 'Shear strength and pore-water pressure characteristics during constant water content triaxial tests', *Journal of Geotechnical and Geoenvironmental Engineering*, vol. 132, no. 3, pp. 411-419.

Thu, TM, Rahardjo, H & Leong, E-C 2007a, 'Elastoplastic model for unsaturated soil with incorporation of the soil-water characteristic curve', *Canadian Geotechnical Journal*, vol. 44, no. 1, pp. 67-77.

Thu, TM, Rahardjo, H & Leong, E-C 2007b, 'Soil-water characteristic curve and consolidation behavior for a compacted silt', *Canadian Geotechnical Journal*, vol. 44, no. 3, pp. 266-275.

Tindall, JA, Kunkel, JR & Anderson, DE 1999, *Unsaturated zone hydrology for scientists and engineers*, vol. 3, Prentice Hall Upper Saddle River, NJ.

Toll, D & Ong, B 2003, 'Critical-state parameters for an unsaturated residual sandy clay', *Geotechnique*, vol. 53, no. 1, pp. 93-103.

Topp, GC, Davis, JL & Annan, AP 1980, 'Electromagnetic determination of soil water content: Measurements in coaxial transmission lines', *Water Resources Research*, vol. 16, no. 3, pp. 574-582.

Toyota, H, Sakai, N & Nishimura, T 2001, 'Effects of stress history due to unsaturation and drainage condition on shear properties of unsaturated cohesive soil', *Soils and Foundations*, vol. 41, no. 1, pp. 13-24.

Tracy, FT 1995, '1-D, 2-D, and 3-D analytical solutions of unsaturated flow in groundwater', *Journal of hydrology*, vol. 170, no. 1-4, pp. 199-214.

Tran, HT, Wang, Y, Nguyen, GD, Kodikara, J, Sanchez, M & Bui, HH 2019, 'Modelling 3D desiccation cracking in clayey soils using a size-dependent SPH computational approach', *Computers and Geotechnics*, vol. 116, p. 103209.

Uchaipichat, A 2005, *Experimental investigation and constitutive modelling of thermo-hydro-mechanical coupling in unsaturated soils*, University of New South Wales.

Uchaipichat, A 2010, 'Prediction of shear strength for unsaturated soils under drying and wetting processes', *Electronic Journal of Geotechnical Engineering*, vol. 15, pp. 1087-1102.

Uchaipichat, A & Khalili, N 2009, 'Experimental investigation of thermo-hydro-mechanical behaviour of an unsaturated silt', *Geotechnique*, vol. 59, no. 4, pp. 339-353.

Valdes-Parada, FJ, Ochoa-Tapia, JA & Alvarez-Ramirez, J 2009, 'Validity of the permeability Carman–Kozeny equation: A volume averaging approach', *Physica A: Statistical Mechanics and its Applications*, vol. 388, no. 6, pp. 789-798.

Van Genuchten, MT 1980, 'A closed-form equation for predicting the hydraulic conductivity of unsaturated soils', *Soil Science Society of America Journal*, vol. 44, no. 5, pp. 892-898.

Vanapalli, S, Fredlund, D & Pufahl, D 1999, 'The influence of soil structure and stress history on the soil–water characteristics of a compacted till', *Geotechnique*, vol. 49, no. 2, pp. 143-159.

Vanapalli, SK & Oh, WT 2010, 'Mechanics of unsaturated soils for the design of foundation structures', in *Proceedings of the 3rd WSEAS international conference on Engineering mechanics, structures, engineering geology*, World Scientific and Engineering Academy and Society (WSEAS), pp. 363-377.

Vardon, PJ, Wang, B & Hicks, MA 2017, 'Slope failure simulations with MPM', *Journal of Hydrodynamics*, vol. 29, no. 3, pp. 445-451.

Vardoulakis, I 1989, 'Shear-banding and liquefaction in granular materials on the basis of a Cosserat continuum theory', *Ingenieur-Archiv*, vol. 59, pp. 106-13.

Vaunat, J, Merchán, V, Romero, E & Pineda, J 2007, 'Residual strength of clays at high suctions', in *Theoretical and Numerical Unsaturated Soil Mechanics*, Springer, pp. 151-163.

Vaunat, J, Romero, E & Jommi, C 2000, 'An elastoplastic hydromechanical model for unsaturated soils', *Experimental evidence and theoretical approaches in unsaturated soils*, vol. 20, no. 0, p. 0.

Verma, R, Pour, A, Dawidowski, P, Nguyen, G, Bui, H, Karakus, M & Taheri, A 2019, 'Analysing Localisation Behaviour of Rocks using Digital Image Correlation', in *13TH INTERNATIONAL CONFERENCE ON THE MECHANICAL BEHAVIOUR OF MATERIALS*, p. 303.

Vesic, AS 1973, 'Analysis of ultimate loads of shallow foundations', *Journal of Soil Mechanics & Foundations Div*, vol. 99, no. sm1.

Wan, R, Khosravani, S & Pouragha, M 2014, 'Micromechanical analysis of force transport in wet granular soils', *Vadose Zone Journal*, vol. 13, no. 5, pp. 1-12.

Wang, B, Vardon, P & Hicks, M 2018, 'Rainfall-induced slope collapse with coupled material point method', *Engineering Geology*, vol. 239, pp. 1-12.

Wang, J-P, Gallo, E, François, B, Gabrieli, F & Lambert, P 2017, 'Capillary force and rupture of funicular liquid bridges between three spherical bodies', *Powder Technology*, vol. 305, pp. 89-98.
Wang, Y, Bui, HH, Nguyen, GD & Ranjith, P 2019, 'A new SPH-based continuum framework with an embedded fracture process zone for modelling rock fracture', *International Journal of Solids and Structures*, vol. 159, pp. 40-57.
Wang, Y, Tran, HT, Nguyen, GD, Ranjith, PG & Bui, HH 2020, 'Simulation of mixed-mode fracture using SPH particles with an embedded fracture process zone', *International journal for numerical and analytical methods in geomechanics*.
Wei, C & Dewoolkar, MM 2006, 'Formulation of capillary hysteresis with internal state variables', *Water Resources Research*, vol. 42, no. 7.
Wendland, H 1995, 'Piecewise polynomial, positive definite and compactly supported radial functions of minimal degree', *Advances in computational Mathematics*, vol. 4, no. 1, pp. 389-396.
Wheeler, S, Sharma, R & Buisson, M 2003, 'Coupling of hydraulic hysteresis and stress–strain behaviour in unsaturated soils', *Geotechnique*, vol. 53, no. 1, pp. 41-54.
Wheeler, S & Sivakumar, V 1995, 'An elasto-plastic critical state framework for unsaturated soil', *Geotechnique*, vol. 45, no. 1, pp. 35-53.
Wong, H, Morvan, M & Branque, D 2010, 'A 13-parameter model for unsaturated soil based on bounding surface plasticity', *Journal of Rock Mechanics and Geotechnical Engineering*, vol. 2, no. 2, pp. 135-142.
Wong, P & Wong, P 1975, 'Yielding and plastic flow of sensitive cemented clay', *Geotechnique*, vol. 25, no. 4, pp. 763-782.
Wood, DM & Graham, J 1990, 'Anisotropic elasticity and yielding of a natural plastic clay', *International Journal of Plasticity*, vol. 6, no. 4, pp. 377-388.
Xie, J, Uchimura, T, Wang, G, Shen, Q, Maqsood, Z, Xie, C, Liu, J, Lei, W, Tao, S & Chen, P 2020, 'A new prediction method for the occurrence of landslides based on the time history of tilting of the slope surface', *Landslides*, vol. 17, no. 2, pp. 301-312.
Xie, S & Shao, J-F 2006, 'Elastoplastic deformation of a porous rock and water interaction', *International Journal of Plasticity*, vol. 22, no. 12, pp. 2195-2225.
Xiong, X, Shi, Z, Xiong, Y, Peng, M, Ma, X & Zhang, F 2019, 'Unsaturated slope stability around the Three Gorges Reservoir under various combinations of rainfall and water level fluctuation', *Engineering Geology*, vol. 261, p. 105231.
Xiong, X, Shi, ZM, Guan, SG & Zhang, F 2018, 'Failure mechanism of unsaturated landslide dam under seepage loading–Model tests and corresponding numerical simulations', *Soils and Foundations*, vol. 58, no. 5, pp. 1133-1152.

Xiong, Y, Bao, X, Ye, B & Zhang, F 2014, 'Soil–water–air fully coupling finite element analysis of slope failure in unsaturated ground', *Soils and Foundations*, vol. 54, no. 3, pp. 377-395.

Yang, H, Yang, T, Zhang, S, Zhao, F, Hu, K & Jiang, Y 2020, 'Rainfall-induced landslides and debris flows in Mengdong Town, Yunnan Province, China', *Landslides*, pp. 1-11.

Yerro, A, Alonso, E & Pinyol, N 2015, 'The material point method for unsaturated soils', *Geotechnique*, vol. 65, no. 3, pp. 201-217.

Yerro Colom, A 2015, 'MPM modelling of landslides in brittle and unsaturated soils'.

Yin, Z-Y, Chang, CS, Hicher, P-Y & Karstunen, M 2009, 'Micromechanical analysis of kinematic hardening in natural clay', *International Journal of Plasticity*, vol. 25, no. 8, pp. 1413-1435.

Yu, H-S 1998, 'CASM: A unified state parameter model for clay and sand', *International journal for numerical and analytical methods in geomechanics*, vol. 22, no. 8, pp. 621-653.

Zhan, L 2003, 'Field and laboratory study of an unsaturated expansive soil associated with rain-induced slope instability'.

Zhang, B & Muraleetharan, KK 2018, 'Liquefaction of Level Ground Unsaturated Sand Deposits Using a Validated Fully Coupled Analysis Procedure', *International Journal of Geomechanics*, vol. 18, no. 10, p. 04018118.

Zhang, F & Ikariya, T 2011, 'A new model for unsaturated soil using skeleton stress and degree of saturation as state variables', *Soils and Foundations*, vol. 51, no. 1, pp. 67-81.

Zhang, H & Schrefler, B 2004, 'Particular aspects of internal length scales in strain localization analysis of multiphase porous materials', *Computer Methods in Applied Mechanics and Engineering*, vol. 193, no. 27-29, pp. 2867-2884.

Zhang, X 2016, 'Limitations of suction-controlled triaxial tests in the characterization of unsaturated soils', *International journal for numerical and analytical methods in geomechanics*, vol. 40, no. 2, pp. 269-296.

Zhang, X & Li, L 2011, 'Limitations in the constitutive modeling of unsaturated soils and solutions', *International Journal of Geomechanics*, vol. 11, no. 3, pp. 174-185.

Zhang, X, Liu, J & Li, P 2010, 'Determining the shapes of yield curves for unsaturated soils by modified state surface approach', *Journal of Geotechnical and Geoenvironmental Engineering*, vol. 136, no. 1, pp. 239-247.

Zhang, X & Lytton, RL 2009a, 'Modified state-surface approach to the study of unsaturated soil behavior. Part I: Basic concept', *Canadian Geotechnical Journal*, vol. 46, no. 5, pp. 536-552.

Zhang, X & Lytton, RL 2009b, 'Modified state-surface approach to the study of unsaturated soil behavior. Part II: General formulation', *Canadian Geotechnical Journal*, vol. 46, no. 5, pp. 553-570.

Zhang, X & Lytton, RL 2012, 'Modified state-surface approach to the study of unsaturated soil behavior. Part III: Modeling of coupled hydromechanical effect', *Canadian Geotechnical Journal*, vol. 49, no. 1, pp. 98-120.

Zhang, Z 2017, 'A thermodynamics-based theory for thethermo-poro-mechanical modeling of saturated clay', *International Journal of Plasticity*, vol. 92, pp. 164-185.

Zhao, C, Asreazad, S, Li, J & Cai, G 2014, 'Necessary conditions for the critical state of unsaturated soils', in *Unsaturated Soils: Research & Applications*, CRC Press, pp. 201-208.

ZHAO, S 'Numerical Modelling of Strain Localisation and Failure in Dry/unsaturated Soils Using the Smoothed Particle Hydrodynamics Method', Monash University.

Zhou, A-N, Sheng, D, Sloan, SW & Gens, A 2012a, 'Interpretation of unsaturated soil behaviour in the stress–saturation space, I: volume change and water retention behaviour', *Computers and Geotechnics*, vol. 43, pp. 178-187.

Zhou, A-N, Sheng, D, Sloan, SW & Gens, A 2012b, 'Interpretation of unsaturated soil behaviour in the stress–saturation space: II: constitutive relationships and validations', *Computers and Geotechnics*, vol. 43, pp. 111-123.

Zhou, A & Sheng, D 2009, 'Yield stress, volume change, and shear strength behaviour of unsaturated soils: validation of the SFG model', *Canadian Geotechnical Journal*, vol. 46, no. 9, pp. 1034-1045.

Zhou, A & Sheng, D 2015, 'An advanced hydro-mechanical constitutive model for unsaturated soils with different initial densities', *Computers and Geotechnics*, vol. 63, pp. 46-66.

Zhou, A, Wu, S, Li, J & Sheng, D 2018, 'Including degree of capillary saturation into constitutive modelling of unsaturated soils', *Computers and Geotechnics*, vol. 95, pp. 82-98.

Ziegler, H 2012, *An introduction to thermomechanics*, Elsevier.

Zienkiewicz, O 1982, 'Basic formulation of static and dynamic behaviours of soil and other porous media', *Applied mathematics and mechanics*, vol. 3, no. 4, pp. 457-468.

Zienkiewicz, OC, Chan, A, Pastor, M, Paul, D & Shiomi, T 1990, 'Static and dynamic behaviour of soils: a rational approach to quantitative solutions. I. Fully saturated problems', *Proceedings of the Royal Society of London. A. Mathematical and Physical Sciences*, vol. 429, no. 1877, pp. 285-309.

Appendix A. Model based on Drucker Prager yield criterion for partially saturated soils

A.1. Formulation

A.1.1. Helmholtz specific energy potential

The Helmholtz free energy potential can be assumed in the following specific form:

$$\Psi = \frac{E}{6(1-2\varrho)}\left(\varepsilon_v - \varepsilon_v^{\mathrm{p}}\right)^2 + \frac{3}{4}\frac{E}{(1+\varrho)}\left(\varepsilon_s - \varepsilon_s^{\mathrm{p}}\right)^2 + \frac{1}{2}K_h\left[1 + (-S_r) - \left(-S_r^{\mathrm{p}}\right)\right]^2 + \left(-S_r^{\mathrm{p}}\right)p_b \tag{A.1}$$

where E is the Young modulus; ϱ is the Poisson's ratio and K_h is the constant controlling the amount of reversible hydraulic energy.

The state laws for true stresses are obtained from Eq. (A.1) as:

$$p' = \frac{\partial \Psi}{\partial \varepsilon_v} = \frac{E}{3(1-2\varrho)}\left(\varepsilon_v - \varepsilon_v^{\mathrm{p}}\right) \tag{A.2}$$

$$q = \frac{\partial \Psi}{\partial \varepsilon_s} = \frac{3}{2}\frac{E}{(1+\varrho)}\left(\varepsilon_s - \varepsilon_s^{\mathrm{p}}\right) \tag{A.3}$$

$$s^* = \frac{\partial \Psi}{\partial(-S_r)} = K_h\left[1 + (-S_r) - \left(-S_r^{\mathrm{p}}\right)\right] \tag{A.4}$$

Eqs. (A.2) and (A.3) indicate that elastic bulk and shear moduli are independent on the pressure. On the other hand, similar to many existing models for unsaturated soils (Alonso et al., 1990; Sheng et al., 2004; Wheeler et al., 2003), effects of suction and saturation degree on the elastic soil stiffness are assumed to be so insignificant that they can be negligible in this model.

Eq. (A.1) also results in the generalised stresses, as shown below:

$$\bar{\chi}_v = -\frac{\partial \Psi}{\partial \varepsilon_v^{\mathrm{p}}} = \frac{E}{3(1-2\varrho)}\left(\varepsilon_v - \varepsilon_v^{\mathrm{p}}\right) = p' \tag{A.5}$$

$$\bar{\chi}_s = -\frac{\partial \Psi}{\partial \varepsilon_s^{\mathrm{p}}} = \frac{3}{2}\frac{E}{(1+\varrho)}\left(\varepsilon_s - \varepsilon_s^{\mathrm{p}}\right) = q \tag{A.6}$$

$$\bar{\chi}_h = -\frac{\partial \Psi}{\partial\left(-S_r^{\mathrm{p}}\right)} = K_h\left[1 + (-S_r) - \left(-S_r^{\mathrm{p}}\right)\right] - p_b = s^* - p_b \tag{A.7}$$

A.1.2. Dissipation potential, yield function and flow rules

From Eq. (3.115) of Chapter 3, the generic dissipation potential with kinematic constraint equations can be rewritten as:

$$\widetilde{\Phi} = \varphi^v \dot{\varepsilon}_v^{\mathrm{p}} + \varphi^s \dot{\varepsilon}_s^{\mathrm{p}} + \varphi^h\left(-\dot{S}_r^{\mathrm{p}}\right) + \Lambda_1\left(B'\dot{\varepsilon}_v^{\mathrm{p}} + A'\dot{\varepsilon}_s^{\mathrm{p}}\right) + \Lambda_2\left[C'\dot{\varepsilon}_v^{\mathrm{p}} + A'\left(-\dot{S}_r^{\mathrm{p}}\right)\right] \geq 0 \tag{A.8}$$

A single yield function y^* in the space of all thermodynamic forces (χ_v, χ_s, and χ_h) can be derived from the above expression as (see Eq. (3.120)):

$$y^* = A'\chi_v - B'\chi_s - C'\chi_h - A'\varphi^v + B'\varphi^s + C'\varphi^h \leq 0 \tag{A.9}$$

The generic flow rules of plastic strain and irreversible saturation take the following forms (see Eqs. (3.121-3.123):

$$\dot{\varepsilon}_v^{\mathrm{p}} = \dot{\lambda}_p \frac{\partial y^*}{\partial \chi_v} = \dot{\lambda}_p A' \tag{A.10}$$

$$\dot{\varepsilon}_s^{\mathrm{p}} = \dot{\lambda}_p \frac{\partial y^*}{\partial \chi_s} = -\dot{\lambda}_p B' \tag{A.11}$$

$$-\dot{S}_r^{\mathrm{p}} = \dot{\lambda}_p \frac{\partial y^*}{\partial \chi_h} = -\dot{\lambda}_p C' \tag{A.12}$$

For an explicitly defined dissipation potential, specific expressions φ^v, φ^h, φ^s, A', B' and C' in Eqs. (A.8-A.12) are needed and take the following forms:

$$\varphi^v = 0 \tag{A.13}$$

$$\varphi^h = 0 \tag{A.14}$$

$$\varphi^s = c' \tag{A.15}$$

$$A' = -\exp[-\beta(1 - S_r)]\mu' \tag{A.16}$$

$$B' = -1 \tag{A.17}$$

$$C' = \frac{p'}{(s^* - p_b)}\{1 - \exp[-\beta(1 - S_r)]\}\mu' \tag{A.18}$$

where c' and μ' are functions controlling the size of yield surface and the dilation behaviour, taking the following forms:

$$\mu' = \mu'_0 + \omega_\mu s^* \tag{A.19}$$

$$c' = c'_0 \exp\left(-\eta_c \varepsilon_p\right) + c'_m[1 - \exp(-\omega_c s^*)] \tag{A.20}$$

with μ'_0, c'_0 and η_c being parameters of the classical Drucker-Prager yield criterion in the fully saturated state; c'_m, ω_μ and ω_c representing parameters controlling the hydraulic effects on inelastic behaviour; ε_p denoting the accumulated plastic strain whose increment can be expressed as follows:

$$\dot{\varepsilon}_p = a_d \dot{\varepsilon}_v^{\mathrm{p}} + b_d \dot{\varepsilon}_s^{\mathrm{p}} = \dot{\lambda}_p \left(a_d \frac{\partial y^*}{\partial \chi_v} + b_d \frac{\partial y^*}{\partial \chi_s}\right) \tag{A.21}$$

By adopting Eqs. (A.13-A.18), the loading function in the dissipative stress space y^* is obtained from Eq. (A.9) as:

$$y^* = -\exp[-\beta(1 - S_r)]\mu'\chi_v + \chi_s - \frac{p'}{(s^* - p_b)}\{1 - \exp[-\beta(1 - S_r)]\}\mu'\chi_h - c' \leq 0 \tag{A.22}$$

In this model, Ziegler's orthogonality condition (Eqs. (3.97-3.99)) reads:

$$\chi_v = \bar{\chi}_v = p' \tag{A.23}$$

$$\chi_s = \bar{\chi}_s = q \tag{A.24}$$

$$\chi_h = \bar{\chi}_h = s^* - p_b \tag{A.25}$$

Substituting Eqs. (A.23-A.25) into Eq. (A.22), after rearranging the obtained expression, the function of yield surface in true stress space can be established as:

$$y = q - \mu' p' - c' \leq 0 \tag{A.26}$$

From Eqs. (A.10-A.12) and (A.16-A.18), flow rules are formulated as follows:

$$\dot{\varepsilon}_v^{\mathrm{p}} = \dot{\lambda}_p \frac{\partial y^*}{\partial \chi_v} = -\dot{\lambda}_p \exp[-\beta(1 - S_r)]\mu' \tag{A.27}$$

$$\dot{\varepsilon}_s^{\mathrm{p}} = \dot{\lambda}_p \frac{\partial y^*}{\partial \chi_s} = \dot{\lambda}_p \tag{A.28}$$

$$-\dot{S}_r^{\mathrm{p}} = \dot{\lambda}_p \frac{\partial y^*}{\partial \chi_h} = -\dot{\lambda}_p \frac{p'}{(s^* - p_b)}\{1 - \exp[-\beta(1 - S_r)]\}\mu' \tag{A.29}$$

Combining Eqs. (A.27) and (A.28) leads to the following tensorial form:

$$\dot{\varepsilon}_{ij}^{\mathrm{p}} = \dot{\lambda}_p \frac{\partial y^*}{\partial \chi_{ij}} = \dot{\lambda}_p \left(\frac{\partial y^*}{\partial \chi_v} \frac{\partial \chi_v}{\partial \chi_{ij}} + \frac{\partial y^*}{\partial \chi_s} \frac{\partial \chi_s}{\partial \chi_{ij}} \right) \tag{A.30}$$

A.2. Dissipation properties

For the sake of completeness, what follows are detailed analyses of the bi-directional hydro-mechanical dissipation of the proposed model. Of importance to these analyses is to provide formulations for use in the proof of thermodynamic admissibility and connections between individual dissipation mechanisms. By using Ziegler's orthogonality condition in Eqs. (A.23-A.25) and flow rules in Eqs. (A.27-A.29), volumetric, shear and hydraulic parts of the total dissipation rate are written as:

$$\widetilde{\Phi}_v = \chi_v \dot{\varepsilon}_v^{\mathrm{p}} = p' \dot{\varepsilon}_v^{\mathrm{p}} = -p' \dot{\lambda}_p \exp[-\beta(1 - S_r)]\mu' \tag{A.31}$$

$$\widetilde{\Phi}_s = \chi_s \dot{\varepsilon}_s^{\mathrm{p}} = q \dot{\varepsilon}_s^{\mathrm{p}} = q \dot{\lambda}_p \tag{A.32}$$

$$\widetilde{\Phi}_h = \chi_h \left(-\dot{S}_r^{\mathrm{p}}\right) = (s^* - p_b)\left(-\dot{S}_r^{\mathrm{p}}\right) = -\dot{\lambda}_p p' \{1 - \exp[-\beta(1 - S_r)]\}\mu' \tag{A.33}$$

As can be seen in Eqs. (A.31-A.33), the positiveness of $\widetilde{\Phi}_s$ is always guaranteed while $\widetilde{\Phi}_v$ and $\widetilde{\Phi}_h$ are always negative. Noting that the negativeness of volumetric and hydraulic dissipations has nothing to violate the second thermodynamic principle if the total energy lost is guaranteed to be non-negative. This reveals that the restriction of thermodynamic admissibility used here is less stringent to enable the proposed framework to more flexibly generate the full coupling between different

phases of unsaturated soils (Houlsby & Puzrin, 2007). As the dissipation potential is a homogeneous function of degree one in terms of internal variables for the rate-independent material, it can result from a combination of Eqs. (A.31-A.33) as follows:

$$\widetilde{\Phi} = \widetilde{\Phi}_v + \widetilde{\Phi}_s + \widetilde{\Phi}_h = q\dot{\lambda}_p - p'\dot{\lambda}_p \exp[-\beta(1-S_r)]\mu' - \dot{\lambda}_p p'\{1-\exp[-\beta(1-S_r)]\}\mu' = (q - p'\mu')\dot{\lambda}_p \tag{A.34}$$

Substitution Eq. (A.26) into Eq. (A.34), one gets:

$$\widetilde{\Phi} = c'\dot{\lambda}_p \geq 0 \tag{A.35}$$

As can readily be seen in Eq. (A.35), the positiveness of the total dissipation rate is always satisfied for any loading and saturation condition, emphasizing the thermodynamically admissible process of this model. Furthermore, in the above expressions, an explicit link is adequately established between the proportion of energy lost due to plasticity and hydraulic irreversibility. It can be described by the dissipation ratios $\mathrm{R}_v, \mathrm{R}_s, \mathrm{R}_h$ between $\widetilde{\Phi}_v, \widetilde{\Phi}_s, \widetilde{\Phi}_h$ and $\widetilde{\Phi}$ as follows:

$$\mathrm{R}_v = \frac{\widetilde{\Phi}_v}{\widetilde{\Phi}} = -\frac{p'\dot{\lambda}_p \exp[-\beta(1-S_r)]\mu'}{c'\dot{\lambda}_p} = -\frac{p'\exp[-\beta(1-S_r)]\mu'}{c'} \tag{A.36}$$

$$\mathrm{R}_s = \frac{\widetilde{\Phi}_s}{\widetilde{\Phi}} = \frac{q\dot{\lambda}_p}{c'\dot{\lambda}_p} = \frac{q}{c'} \tag{A.37}$$

$$\mathrm{R}_h = \frac{\widetilde{\Phi}_h}{\widetilde{\Phi}} = -\frac{\dot{\lambda}_p p'\{1-\exp[-\beta(1-S_r)]\}\mu'}{c'\dot{\lambda}_p} = -\frac{p'\{1-\exp[-\beta(1-S_r)]\}\mu'}{c'} \tag{A.38}$$

The above expressions allow quantifying how amounts of hydraulic and mechanical energy are expended within the total budget, hence interpreting essential hydro-mechanical responses under the guarantee of thermodynamic admissibility. This feature highlights one of the key differences between our approach and other existing models for partially saturated soils.

A.3. Semi-implicit stress return algorithm

In this subsection, the specification of the semi-implicit stress return algorithm in Chapter 3 is briefly described for this proposed Drucker-Prager model. Under the setting described above in Eqs. (A.2-A.4), the following incremental stress-strain and suction-saturation degree relationships can be written as:

$$\dot{\sigma}'_{ij} = D^e_{ijkl}\left(\dot{\varepsilon}_{kl} - \dot{\varepsilon}^{\mathrm{p}}_{kl}\right) \tag{A.39}$$

$$\dot{s}^* = K_h\left[\left(-\dot{S}_r\right) - \left(-\dot{S}^{\mathrm{p}}_r\right)\right] \tag{A.40}$$

where $D^e_{ijkl} = \frac{E}{2(1+\varrho)}\left(\frac{2\varrho}{1-2\varrho}\delta_{ij}\delta_{kl} + \delta_{ik}\delta_{jl} + \delta_{il}\delta_{jk}\right)$ is the pressure-independent elastic stiffness tensor.

Based on Eqs. (3.146-3.147) and (A.39-A.40), the values of effective stress $\left(\sigma_{ij}^{\prime\mathrm{trial}}\right)$ and modified suction $\left(s^{*\mathrm{trial}}\right)$ at the trial state read:

$$\sigma_{ij}^{\prime\mathrm{trial}} = \sigma_{ij}^{\prime n} + D_{ijkl}^{e}\Delta\varepsilon_{kl} \tag{A.41}$$

$$s^{*\mathrm{trial}} = s^{*n} + K_h(-\Delta S_r) \tag{A.42}$$

In the inelastic regime when $y^{\mathrm{trial}} \geq 0$, the first-order Taylor expansion of the yield function about the elastic trial point can be taken as:

$$y^{\mathrm{new}} = y^{\mathrm{trial}} - D_{ijkl}^{e}\Delta\lambda_p \frac{\partial y^*}{\partial \chi_{kl}}\frac{\partial y}{\partial \sigma_{ij}^{\prime}}\Big|^{\mathrm{trial}} - K_h\Delta\lambda_p \frac{\partial y^*}{\partial \chi_h}\left(\frac{\partial y}{\partial \mu^{\prime}}\frac{\partial \mu^{\prime}}{\partial s^*} + \frac{\partial y}{\partial c^{\prime}}\frac{\partial c^{\prime}}{\partial s^*}\right)\Big|^{\mathrm{trial}} + \Delta\lambda_p\left(a_d\frac{\partial y^*}{\partial \chi_v} + b_d\frac{\partial y^*}{\partial \chi_s}\right)\frac{\partial y}{\partial c^{\prime}}\frac{\partial c^{\prime}}{\partial \varepsilon_p}\Big|^{\mathrm{trial}} \tag{A.43}$$

If $y^{\mathrm{new}} = 0$ is enforced, the following expression of plasticity multiplier can be obtained:

$$\Delta\lambda_p = \frac{y^{\mathrm{trial}}}{\left(\frac{\partial y}{\partial \sigma_{ij}^{\prime}}\right)^T D_{ijkl}^{e}\frac{\partial y^*}{\partial \chi_{kl}}\Big|^{\mathrm{trial}} + \left(\frac{\partial y}{\partial \mu^{\prime}}\frac{\partial \mu^{\prime}}{\partial s^*} + \frac{\partial y}{\partial c^{\prime}}\frac{\partial c^{\prime}}{\partial s^*}\right)K_h\frac{\partial y^*}{\partial \chi_h}\Big|^{\mathrm{trial}} - \frac{\partial y}{\partial c^{\prime}}\frac{\partial c^{\prime}}{\partial \varepsilon_p}\left(a_d\frac{\partial y^*}{\partial \chi_v} + b_d\frac{\partial y^*}{\partial \chi_s}\right)\Big|^{\mathrm{trial}}} \tag{A.44}$$

in which explicit forms of $\frac{\partial y}{\partial \sigma_{ij}^{\prime}}$, $\frac{\partial y}{\partial s^*}$, $\frac{\partial y}{\partial \varepsilon_p}$, $\frac{\partial y}{\partial \mu^{\prime}}$, $\frac{\partial y}{\partial c^{\prime}}$, $\frac{\partial \mu^{\prime}}{\partial s^*}$, $\frac{\partial c^{\prime}}{\partial s^*}$ and $\frac{\partial c^{\prime}}{\partial \varepsilon_p}$ are written as follow:

$$\frac{\partial y}{\partial \sigma_{ij}^{\prime}} = \frac{\partial y}{\partial p^{\prime}}\frac{\partial p^{\prime}}{\partial \sigma_{ij}^{\prime}} + \frac{\partial y}{\partial q}\frac{\partial q}{\partial \sigma_{ij}^{\prime}} = -\mu^{\prime}\frac{\partial p^{\prime}}{\partial \sigma_{ij}^{\prime}} + \frac{\partial q}{\partial \sigma_{ij}^{\prime}} \tag{A.45}$$

$$\frac{\partial y}{\partial \mu^{\prime}} = -p^{\prime} \tag{A.46}$$

$$\frac{\partial y}{\partial c^{\prime}} = -1 \tag{A.47}$$

$$\frac{\partial \mu^{\prime}}{\partial s^*} = \omega_\mu \tag{A.48}$$

$$\frac{\partial c^{\prime}}{\partial s^*} = \omega_c c_m^{\prime}\exp(-\omega_c s^*) \tag{A.49}$$

$$\frac{\partial c^{\prime}}{\partial \varepsilon_p} = -\eta_c c_0^{\prime}\exp\left(-\eta_c\varepsilon_p\right) \tag{A.50}$$

$$\frac{\partial y}{\partial s^*} = -p^{\prime}\omega_\mu - \omega_c c_m^{\prime}\exp(-\omega_c s^*) \tag{A.51}$$

$$\frac{\partial y}{\partial \varepsilon_p} = \eta_c c_0^{\prime}\exp\left(-\eta_c\varepsilon_p\right) \tag{A.52}$$

After obtaining $\Delta\lambda_p$ through Eq. (A.44), Eqs. (3.153-3.158) in Chapter 3 are then applied for updating stress tensor and matric suction.

Appendix B. Validation with a drained triaxial compression test on silty soil (Estabragh & Javadi, 2008)

This Appendix aims to provide simple numerical examples to briefly illustrate the capacity of the proposed constitutive models in capturing the shear behaviour based on drained triaxial tests, apart from many other results presented in Chapter 4 and 5. In particular, the drained triaxial shear test on the silty soil (Estabragh & Javadi, 2008) is used to validate the performance of the present models where results at four levels of imposed suction $s = 0$ kPa; 100 kPa; 200 kPa and 300 kPa are studied to investigate the Modified Cam-Clay model. In this simulation, the net confining pressure remains unchanged at $\bar{\sigma}_{33} = 50$ kPa; 100 kPa; 200 kPa; 300 kPa; 400 kPa during shearing. This simulation uses the following parameters: $E = 100000$ kPa; $\varrho = 0.25$; $\lambda' = 0.08$; $M = 1.33$; $\kappa_h = 0.004$; $p'_R = 363.31$ kPa; $\xi = 0.6$; $\mu = 0.0601$ kPa^{-1}; $p'_{c0} = 550$ kPa; $r = 2$; $\alpha = 0.85$; $\beta = 0.05$ and $p_b = 70$ kPa, which are calibrated by fitting predictive results to their experimental counterparts in the case of $s = 0$ kPa and 100 kPa. On the other hand, another example is given to show the effectiveness of the Drucker-Prager model for capturing the experimental response at different suction levels (100 kPa; 200 kPa) observed in drained triaxial tests on this soil where the net confining pressure is maintained at $\bar{\sigma}_{33} = 50$ kPa (Estabragh & Javadi, 2008). Parameters used in this validation example are listed as follows: $E = 100000$ kPa; $\varrho = 0.25$; $K_h = 2000$ kPa; $\mu'_0 = 0.27$; $c'_0 = 200$ kPa ; $\eta_c = 3$; $a_d = 0.5$; $b_d = 1$; $\omega_\mu = 0.0008$ kPa^{-1} ; $c'_m = 50$ kPa ; $\omega_c = 0.05$ kPa^{-1}; $\beta = 0.05$ and $p_b = 70$ kPa where they are calibrated to make the numerical results fit with testing data under constant suction of $s = 100$ kPa. In Figures B.1-B.5, q and ε_v are plotted against ε_{11} to describe the model validation results. As can be seen, these validation examples are provided to show acceptable agreements between experimental observations and model performances in terms of drained triaxial tests, demonstrating the applicability of both models in reflecting the hydraulic effects on shear stress and volumetric strain. In particular, this model can manifest the shear responses after the initial yield shear stress, where higher yield shear stresses are produced at higher suctions and confining pressures. This is thanks to the gradual expansion of the yield surface towards the positive side of the modified suction axis when suction increases. Nevertheless, it is noted that the numerical volumetric curves are not relatively close to the measured ones in some loading cases despite a reasonable reflection on the experimental trend due to missing details of shear bands related to the size-dependent behaviour in the case of localised failures.

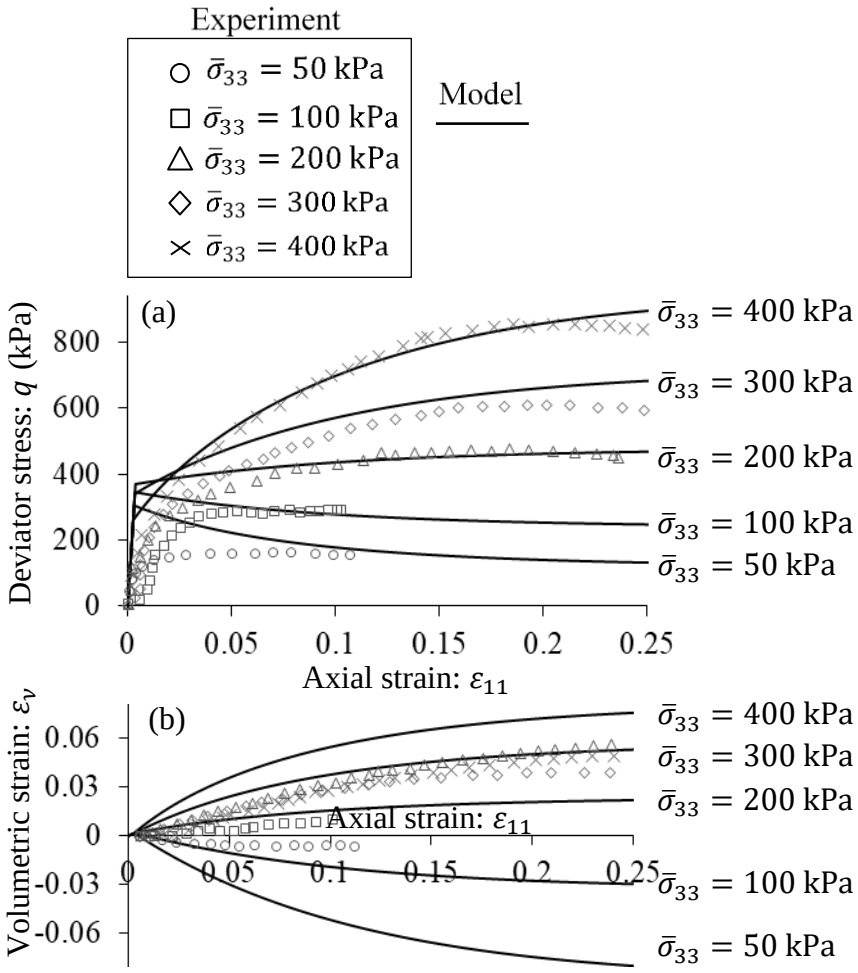

Figure B.1. Validation with a drained triaxial compression test on silty soil at $s = 0$ kPa (after Estabragh & Javadi, 2008) for the extended Modified Cam-Clay model (a) $\varepsilon_{11} - q$ (b) $\varepsilon_{11} - \varepsilon_v$

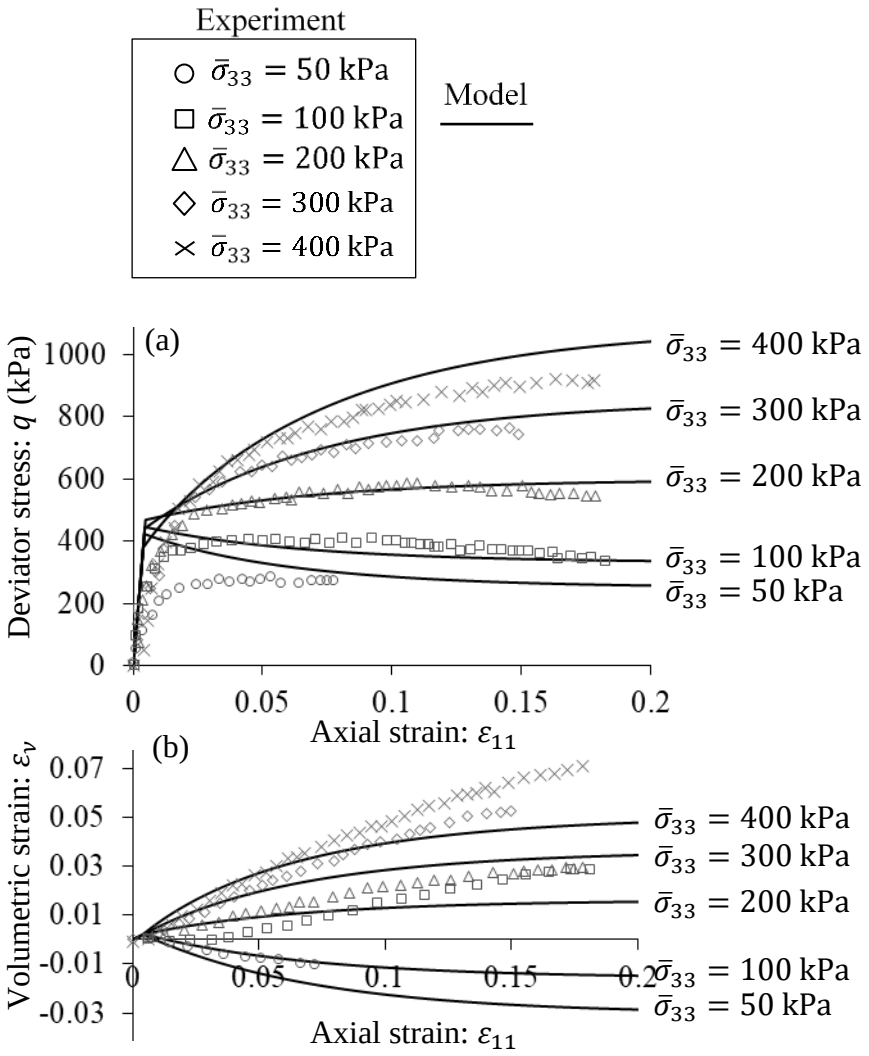

Figure B.2. Validation with a drained triaxial compression test on silty soil at $s = 100$ kPa (after Estabragh & Javadi, 2008) for the extended Modified Cam-Clay model (a) $\varepsilon_{11} - q$ (b) $\varepsilon_{11} - \varepsilon_v$

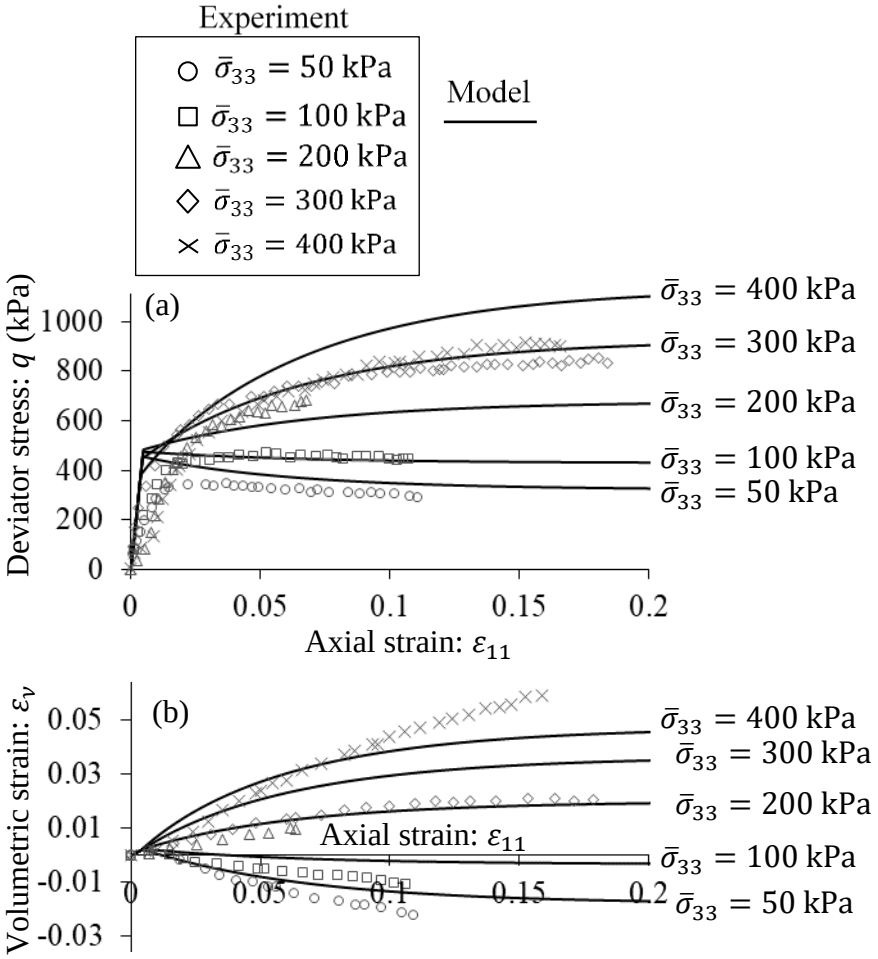

Figure B.3. Validation with a drained triaxial compression test on silty soil at $s = 200$ kPa (after Estabragh & Javadi, 2008) for the extended Modified Cam-Clay model (a) $\varepsilon_{11} - q$ (b) $\varepsilon_{11} - \varepsilon_v$

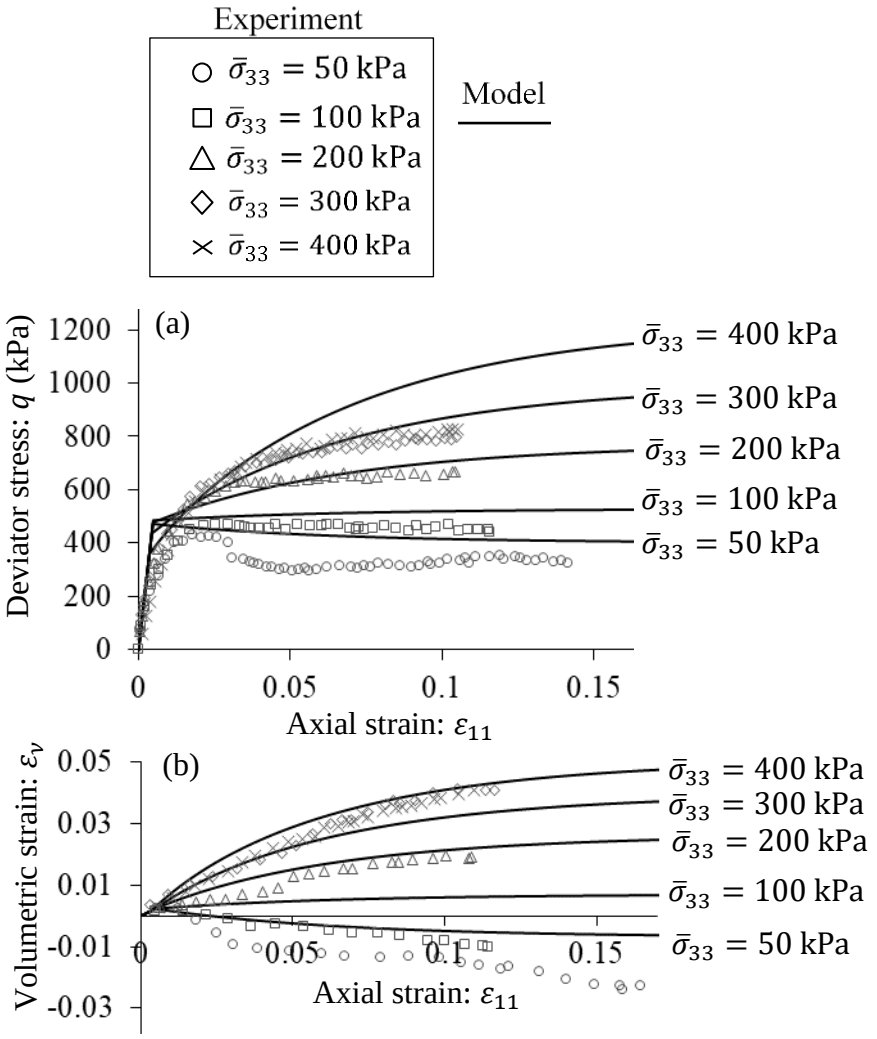

Figure B.4. Validation with a drained triaxial compression test on silty soil at $s = 300$ kPa (after Estabragh & Javadi, 2008) for the extended Modified Cam-Clay model (a) $\varepsilon_{11} - q$ (b) $\varepsilon_{11} - \varepsilon_v$

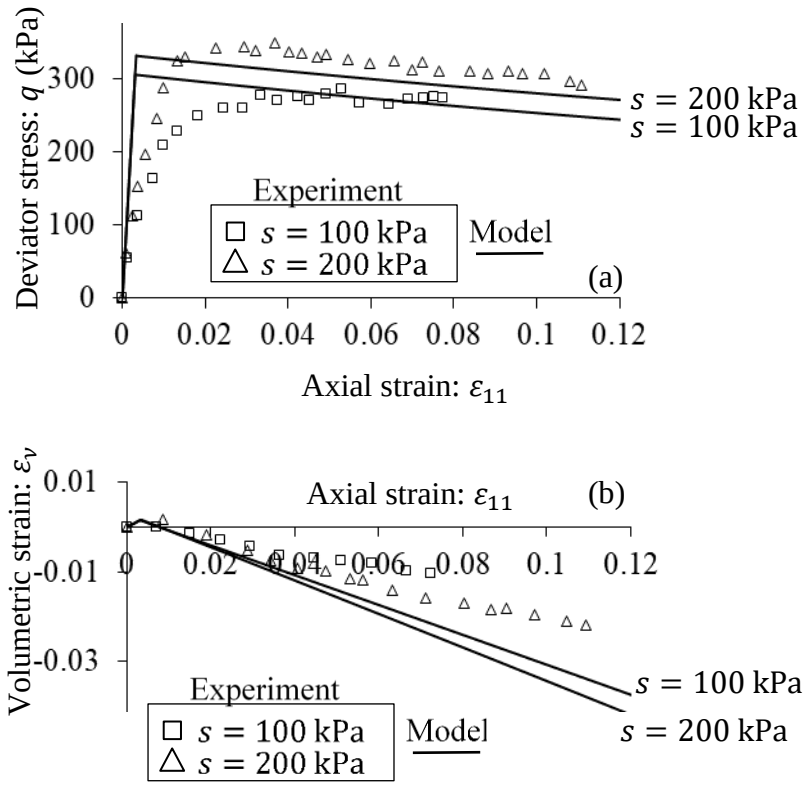

Figure B.5. Validation with a drained triaxial compression test on silty soil at $\bar{\sigma}_{33} = 50$ kPa (after Estabragh & Javadi, 2008) for the extended Drucker-Prager model (a) $\varepsilon_{11} - q$ (b) $\varepsilon_{11} - \varepsilon_v$

Appendix C. Phan, DG, Nguyen, GD, Bui, HH & Bennett, T 2021 'Constitutive modelling of partially saturated soils: Hydro-mechanical coupling in a generic thermodynamics-based formulation', International Journal of Plasticity, vol 136 (https://doi.org/10.1016/j.ijplas.2020.102821).

Statement of Authorship

Title of Paper	Constitutive modelling of partially saturated soils: Hydro-mechanical coupling in a generic thermodynamics-based formulation
Publication Status	☑ Published ☐ Accepted for Publication ☐ Submitted for Publication ☐ Unpublished and Unsubmitted work written in manuscript style
Publication Details	Phan, DG, Nguyen, GD, Bui, HH & Bennett, T 2021 'Constitutive modelling of partially saturated soils: Hydro-mechanical coupling in a generic thermodynamics-based formulation', International Journal of Plasticity, vol 136 (https://doi.org/10.1016/j.ijplas.2020.102821).

Principal Author

Name of Principal Author (Candidate)	Dat G. Phan		
Contribution to the Paper	Conceptualization, Methodology, Software, Validation, Formal analysis, Writing-Original draft preparation		
Overall percentage (%)	70		
Certification:	This paper reports on original research I conducted during the period of my Higher Degree by Research candidature and is not subject to any obligations or contractual agreements with a third party that would constrain its inclusion in this thesis. I am the primary author of this paper.		
Signature		Date	30 Nov 2020

Co-Author Contributions

By signing the Statement of Authorship, each author certifies that:

i. the candidate's stated contribution to the publication is accurate (as detailed above);
ii. permission is granted for the candidate in include the publication in the thesis; and
iii. the sum of all co-author contributions is equal to 100% less the candidate's stated contribution.

Name of Co-Author	Giang D. Nguyen		
Contribution to the Paper	Supervision, Conceptualization, Methodology, Formal analysis, Writing-Reviewing and Editing		
Signature		Date	30 Nov 2020

Name of Co-Author	Ha H. Bui

Contribution to the Paper	Supervision, Conceptualization, Formal analysis, Writing- Reviewing and Editing		
Signature		Date	30 Nov 2020

Name of Co-Author	Terry Bennett		
Contribution to the Paper	Supervision, Conceptualization, Formal analysis, Writing- Reviewing and Editing		
Signature		Date	30 Nov 2020

Please cut and paste additional co-author panels here as required.

International Journal of Plasticity 136 (2021) 102821

Contents lists available at ScienceDirect

International Journal of Plasticity

journal homepage: http://www.elsevier.com/locate/ijplas

Constitutive modelling of partially saturated soils: Hydro-mechanical coupling in a generic thermodynamics-based formulation

Dat G. Phan [a], Giang D. Nguyen [a,*], Ha H. Bui [b], Terry Bennett [a]

[a] School of Civil, Environmental and Mining Engineering, The University of Adelaide, Adelaide, Australia
[b] Department of Civil Engineering, Monash University, Clayton, Australia

ARTICLE INFO

Keywords:
partially Saturated soils
Thermodynamics
Hydro-mechanical coupling
Constitutive modelling
Plasticity
Critical state

ABSTRACT

Hydro-mechanical coupling is a crucial element in constitutive modelling of partially saturated soils, given the dependence of the macro behaviour on the interaction between frictional sliding, grain rearrangement and ruptures of liquid bridges and their redistributions at the grain contacts. The inseparable nature of this interaction requires the interdependence of all internal variables describing the inelastic behaviour of a continuum model. We propose a new generic thermodynamics-based approach to coupling the effects of deformation and saturation in modelling partially saturated soils taking into account the interdependence of all internal variables. This approach allows the derivation of models from only two explicitly defined energy and dissipation potentials, leading to coupled hydro-mechanical behaviour governed by a single yield surface in stress-suction space and two evolution rules for plastic strains and irrecoverable saturation. This coupling provides a path-dependent hydraulic response, reflecting the nature of the hydro-mechanical interactions at the grain scale, while removing the use of a separate Soil Water Characteristic Curve (SWCC). The benefits are the reduction in number of parameters in conjunction with the identification and calibration of all model parameters from standard tests. An extensive experimental validation shows the capabilities of the model and the advantages of the proposed thermodynamics-based approach.

1. Introduction

The majority of geotechnical structures are constructed in soils well above the groundwater table which are normally partially saturated over their entire service life (Wheeler and Sivakumar, 1995; Vanapalli et al., 1999). Thus, geohazards usually involve partially saturated soils and their responses under different loading and hydraulic conditions. A constitutive model being able to predict the soil behaviour under a wide range of both mechanical loading and saturation conditions is essentially needed for the prediction of geotechnical failure involving unsaturated soils. This is a challenge given the complex and coupled hydro-mechanical interactions at the grain scale that govern the macro responses. For example, suction and surface tension along with interfaces between phases at the grain scale have long been recognised as key factors governing the macro responses (Gallipoli et al., 2003; Likos, 2014). They produce the capillary forces exerted by water menisci and affect the grain-to-grain contact behaviour (Gallipoli et al.,

* Corresponding author.
E-mail addresses: giang.nguyen@trinity.oxon.org, g.nguyen@adelaide.edu.au (G.D. Nguyen).

https://doi.org/10.1016/j.ijplas.2020.102821
Received 4 February 2020; Received in revised form 3 July 2020; Accepted 11 July 2020
Available online 28 July 2020

2003; Hoxha et al., 2007; Xie and Shao, 2006). The macro behaviour is therefore governed by the coupled hydro-mechanical mechanism due to the interaction between the two grain scale phenomena, (i) grain sliding and rearrangement, (ii) ruptures of liquid bridge and their redistributions (Bianchi et al., 2016; Mani et al., 2013). These grain-scale phenomena result in observable hydro-mechanical coupling at the continuum level that has been extensively investigated in several suction-controlled (i.e. Alonso, 1987; Cui and Delage, 1996; Wheeler and Sivakumar, 1995; Chen, 2007; Macari et al., 2003) and constant water content triaxial tests (Thu et al., 2006; Marinho et al., 2016; Rahardjo et al., 2004; Maleki and Bayat, 2012; Li, 2015; Zhang, 2016). Particularly, when suction increases, the shear strength (Vaunat et al., 2007; Toyota et al., 2001), yield limit (Alonso et al., 1990; Wheeler and Sivakumar, 1995; Cui and Delage, 1996) and dilatancy (Ng and Zhou, 2005; Cui and Delage, 1996) increases. All of the features described above are accompanied by the volume change associated with irreversible change of saturation (Sharma, 1998; Wheeler et al., 2003), both of which are induced by coupled mechanical and wetting/drying processes. This volume change is considered as one of the most fundamental properties of partially saturated soils (Sheng et al., 2008).

The above key characteristics of partially saturated soil behaviour should be reflected in a constitutive model to capture the transition between partially and fully-saturated conditions (Zhou and Sheng, 2009; Sheng, 2011). For example, the effects of suction on the stress-strain relationships have been addressed in several papers (e.g. Alonso et al., 1990; Wheeler and Sivakumar, 1995; Cui and Delage, 1996; Sun et al., 2000; Stropeit et al., 2008; Blatz and Graham, 2003; Macari et al., 2003). In particular, suction was used in a loading-collapse (LC) yield function to capture the plastic compression due to the wetting-induced collapse behaviour. The normal compression line (NCL) shifts with suction where the compression index was found to decrease (Alonso, 1987; Alonso et al., 1990; Cui and Delage, 1996; Zhang et al., 2009a,b) or increase (Wheeler and Sivakumar, 1995; Matsuoka et al., 2002; Sun et al., 2000, 2004) with increasing suction. However, the link between suction and degree of saturation was missing in these models, making it hard to reproduce the dependence of model responses on different saturation regimes (capillary in fully saturated conditions, funicular at high saturations, pendular at low saturations). For example, cohesion induced by the distributions of liquid bridges between particles are very different in the three saturation regimes (Louati et al., 2015, 2017; Wang et al., 2017). To address this, Zhou et al. (2012a,b) and Zhou and Sheng (2015), used an NCL with soil compression index varying with effective degree of saturation, while Alonso et al. (2013) proposed a NCL dependent on both suction and saturation degree. Wheeler et al. (2003), Tamagnini (2004), Xie and Shao (2006) and Buscarnera and Nova (2009) suggested different hardening constitutive laws governing the coexistence of strain and saturation rates. These studies demonstrate that both suction and saturation degree play an indispensable role in modelling the wetting/drying-induced collapses of partially saturated soils.

Nomenclature

κ	elastic index
λ	slope of NCL in the $\ln\nu : \ln p^{`}$ plane for saturated conditions
λ_{us}	stiffness parameter for partially saturated conditions
$p^{`}_{c0}$	the initial yield pressure under isotropic compression at fully saturated condition
M	slope of CSL
G	shear moduli
N	reference specific volumes of NCL under the saturated condition
Γ	reference specific volumes of CSL under the saturated condition
κ_h	parameter controlling the amount of reversible energy stored in the water menisci
μ	parameter controlling the change of soil stiffness with modified suction
ξ	parameter controlling the maximum soil stiffness
$p^{`}_{R}$	parameter controlling the yield curve
r	spacing ratio
α	parameter governing the strength of the material and non-associativity of the flow rules
β	parameter governing the coupling between saturation and volumetric deformation upon yielding
p_b	parameter controlling the stored irreversible hydraulic energy
p_u	unity pressure
ν	specific volume
ϕ	Lagrangian porosity
ϕ_0	initial Lagrangian porosity
ϕ^n	Lagrangian porosity at step n
w	gravimetric water content
S_r	total saturation degree
S_r^p	irreversible saturation degree
S_{r0}	total saturation degree at initial state
S_r^n	total saturation degree at step n
ε_v	total volumetric strain
ε_v^p	plastic volumetric strain
ε_s	total shear strain
ε_s^p	plastic shear strain
ε_{ij}	total strain tensor
ε_{ij}^p	plastic strain tensor
s	matric suction
s^n	matric suction at step n
s^*	modified suction

(*continued on next page*)

(*continued*)

s_0^*	initial modified suction
s^{*n}	modified suction at step n
$s^{*\text{trial}}$	trial modified suction
$s^{*\text{corrt}}$	corrective modified suction
$\bar{p}$	net mean stress
$\bar{p}^n$	net mean stress at step n
$p^{'}$	Bishop's effective mean stress
χ	effective stress parameter
$p_0^{'}$	Initial Bishop's effective mean stress
$p^{'n}$	effective mean stress at step n
$p^{'\text{trial}}$	trial effective mean stress
$p^{'\text{corrt}}$	corrective effective mean stress
$p_c^{'}$	pre-consolidation stress at the saturated condition
$p_{c(us)}^{'}$	yield stress at the partially saturated condition
$p_{CSL}^{'}$	effective mean stress at the critical state
$\sigma_v^{'}$	Bishop's effective vertical stress
$\bar{\sigma}_v$	net vertical stress
q	shear stress
q_{CSL}	shear stress at the critical state
$\sigma_{ij}^{'}$	effective stress
$\sigma_{ij}^{'n}$	effective stress at step n
$\sigma_{ij}^{'\text{trial}}$	trial effective stress
$\sigma_{ij}^{'\text{corrt}}$	corrective effective stress
$\bar{\sigma}_{ij}$	net stress
$\bar{\sigma}_{ij}^n$	net stress at step n
$\widetilde{W}$	rate of work input
Ψ	Helmholtz specific free energy
$\tilde{\Phi}$	dissipation potential
$\bar{\chi}_v$	thermodynamic conjugates of volumetric plastic strain rate $\dot{\varepsilon}_v^p$
$\bar{\chi}_s$	thermodynamic conjugates of shear plastic strain rate $\dot{\varepsilon}_s^p$
$\bar{\chi}_h$	thermodynamic conjugates of irrecoverable saturation rate $-\dot{S}_r^p$
χ_v	volumetric dissipative generalised stresses
χ_s	shear dissipative generalised stresses
χ_h	hydraulic dissipative generalised stresses
χ_{ij}	dissipative generalised stress tensor
$\tilde{\Phi}_v$	volumetric part of the total dissipation rate
$\tilde{\Phi}_s$	shear part of the total dissipation rate
$\tilde{\Phi}_h$	hydraulic part of the total dissipation rate
R_v	volumetric dissipation ratio
R_s	shear dissipation ratio
R_h	hydraulic dissipation ratio
φ_1^v, φ_2^v	first order homogeneous functions of $\dot{\varepsilon}_v^p$
φ^s	first order homogeneous function of $\dot{\varepsilon}_s^p$
φ^h	first order homogeneous function of $-\dot{S}_r^p$
A, B	functions governing the behaviour of the model
y^*	yield function in generalised stress space (χ_v, χ_s, and χ_h)
y	yield function in true stress space ($p^{'}$, q, and s^*)
y^n	loading function in true stress space at n state
y^{trial}	trial loading function in true stress space
y^{new}	new loading function in true stress space
λ_p	non-negative plasticity-like multiplier
D_{ijkl}^e	pressure-dependent elastic stiffness tensor
D_{ijkl}^{en}	secant elastic stiffness evaluated at state n
$\Lambda_{ijkl}, \Pi_{ij}, \Omega_{kl}, \Upsilon$	terms of the tangent stiffness tensor expressed in terms of $\sigma_{ij}^{'}$ and s^*
$\overline{\Lambda}_{ijkl}, \overline{\Pi}_{ij}, \overline{\Omega}_{kl}, \overline{\Upsilon}$	terms of the tangent stiffness tensor expressed in terms of $\bar{\sigma}_{ij}$ and s
res	residual vector
$\mathbf{res}^{\text{new}}$	new residual vector
$\mathbf{res}^{\text{previous}}$	previous residual vector

The use of a SWCC independent of the volumetric behaviour has been the focus in several models (Thu et al., 2007a; Zhou and Sheng, 2009; Russell and Khalili, 2006) to reflect the effects of degree of saturation and suction on the mechanical behaviour. This kind of SWCC can facilitate the development of the models, despite neglecting its non-uniqueness observed and addressed in several papers (Nuth and Laloui, 2008; Miller et al., 2008; Gallipoli et al., 2003; Vanapalli et al., 1999; Tarantino, 2009; Mašín, 2010; Mbonimpa

et al., 2006). Other models employing a SWCC dependent on volume change to have stronger interactions between hydraulic and mechanical responses have also been proposed (i.e. Buscarnera and Nova, 2009; Chiu and Ng, 2003; Jommi, 2000; Bolzon et al., 1996). Despite their successes in taking into account the hydro-mechanical coupling in the constitutive behaviour of partially saturated soils, the difference in wetting and drying paths was not taken into account in these models.

More complete representations of water retention behaviour, taking into account the irreversibility between wetting and drying processes, has been successfully addressed in several fully coupled hydro-mechanical models (e.g. Gallipoli et al., 2003; Loret and Khalili, 2000, 2002; Wheeler et al., 2003; Hu et al., 2014; Khalili et al., 2008; Muraleetharan et al., 2009; Liu & Muraleetharan, 2011a, b; Sheng et al., 2008; Sun et al., 2007, 2010; Sun and Sun, 2012; Zhou et al., 2012a,b; 2018; Zhou and Sheng, 2015; Lloret-Cabot et al., 2017; Ghorbani et al., 2018; Gholizadeh and Latifi, 2018; Bruno and Gallipoli, 2019; Kodikara et al., 2020). These fully coupled models can capture several important features of the coupled hydro-mechanical behaviour under different loading and saturation conditions, such as irreversible swelling/shrinkage upon wetting/drying, load/deformation-dependency of capillary hysteresis, together with effects of hydraulic hysteresis on shear strength, stiffness, and dilation. Nevertheless, the identification and calibration of several parameters in these models (e.g. Bruno and Gallipoli, 2019; Gholizadeh and Latifi, 2018; Liu & Muraleetharan, 2011a,b; Zhou et al., 2012a,b; 2018) is a challenge for their applications. To capture the wetting-drying difference in the behaviour, several models (e.g. Khalili et al., 2008; Muraleetharan et al., 2009; Liu & Muraleetharan, 2011a,b; Zhou et al., 2018; Sun and Sun, 2012; Kodikara et al., 2020) adopted a separate law for hydraulic hysteresis requiring different sets of parameters for drying and wetting paths. In addition, the hydro-mechanical coupling in some models (e.g. Wheeler et al., 2003; Sheng et al., 2004; Muraleetharan et al., 2009; Sun et al., 2010; Lloret-Cabot et al., 2017; Kodikara et al., 2020) requires the use of multiple yield surfaces, e.g. one mechanical (Loading Collapse; LC) and two hydraulic (Suction Increase/Decrease; SI/SD, usually as horizontal straight lines) with complicated treatments for the coupled evolutions of all yield functions (Wheeler et al., 2003; Sheng et al., 2004). Delage and Graham (1996) and Tang and Graham (2002) found that LC and SI/SD should merge into a single yield locus to capture the micromechanical nature of coupled hydro-mechanical yielding. This issue has been investigated through the combination of drained isotropic compression and drying tests of Sivakumars and Doran (2000) and the extended Barcelona Basic model of Pedroso and Farias (2011). On the other hand, net stress-controlled experiments by Thu et al. (2007b) and Sivakumars and Doran (2000) showed that these widely adopted horizontal straight lines for SI/SD are not reasonable despite their usefulness in constitutive modelling as discussed in several papers (e.g. Delage and Graham, 1996; Robles et al., 2002; Tang and Graham, 2002; Zhang et al., 2009).

The development of thermodynamic-based approaches to constitutive modelling of partially saturated soils have attracted considerable attention in the last 15 years (Sheng et al., 2004; Tamagnini and Pastor, 2005; Uchaipichat, 2005; Santagiuliana and Schrefler, 2006; Li, 2007a,b; Coussy et al., 2010; Buscarnera and Einav, 2012; Dangla and Pereira, 2014; Hu et al., 2015; Lei et al., 2016). The key advantage of such developments is that all essential behavioural characteristics of the considered material can be rigorously incorporated in a thermodynamics-based model, whilst the number of arbitrary assumptions and also model parameters can be reduced without compromising the model performance. The success of such approaches to constitutive modelling has been demonstrated for not only partially unsaturated soils, but a wide range of engineering materials (Buscarnera and Einav, 2012; Liu et al., 2018; Zhang, 2017; Balieu and Kringos, 2015; Nguyen et al., 2015; Lai et al., 2016; Al-Rub and Darabi, 2012; Darabi et al., 2018). Despite the attempts and some successes, full coupling between plasticity and hydraulic irreversibility and their associated hydro-mechanical dissipation properties are usually not adequate in previous thermodynamics-based approaches. In particular, the hydraulic dissipation attributed to the irrecoverable change of saturation degree is overlooked in Tamagnini and Pastor (2005), Uchaipichat (2005), Coussy et al. (2010), Buscarnera and Einav (2012), Dangla and Pereira (2014) and Lei et al. (2016). Consequently, these models cannot naturally capture different responses under wetting and drying paths. Additionally, despite bringing the usefulness, the use of multiple yield surfaces in several models (Sheng et al., 2004; Santagiuliana and Schrefler, 2006; Hu et al., 2015) does not reflect the inseparable nature of the hydro-mechanical interactions at the grain scale, given the dissipative stresses are not dependent on the rates of all internal variables.

In this paper, a new generic thermodynamics-based approach incorporating key characteristics of partially saturated soil behaviour is developed. We aim for the establishment of a rigorous thermodynamics-based approach that leads to a good balance between rigour, simplicity, number of parameters and performance in the derived constitutive models. From the above literature review, this balance has not always been the case in existing models. The proposed thermodynamic formulation is used as a versatile means to connect all essential behavioural characteristics of partially saturated soils, resulting in a single yield surface in stress-suction space and two evolution rules for plastic strains and irrecoverable saturation with a single "plastic" multiplier. This is thanks to the inter-dependence of mechanical and hydraulic dissipations in the proposed dissipation potential, providing a smooth transition between saturated and partially saturated conditions. This coupling naturally induces the effects of mechanical behaviour on the saturation-suction relationship. As a result, models derived from this approach possess an implicitly defined SWCC dependent on the volumetric behaviour, reflecting the hydro-mechanical interactions at the grain scale. This is consistent with suggestions in Wheeler et al. (2003), based on both micro-mechanical reasoning and experiments (e.g. Sharma, 1998; Gallipoli et al., 2003), that the irreversible part of the volumetric strain, arising from the mechanical energy lost due to slippage at inter-particle contacts, results in the translation of the water retention curve. The proposed thermodynamic formulation also helps minimise the number of parameters required, while not compromising the performance of the derived models. The obtained model, formulated under infinitesimal strain assumption, possesses a small number of identifiable parameters, which have clear physical meanings and can be calibrated from standard tests on partially saturated soils. The model performance is assessed and validated against a range of experiments on partially saturated soils.

The outline of this paper is as follows. In section 2, a critical state thermo-mechanical framework for partially saturated soils is described to provide a basis for the development of constitutive models. This is followed by the formulation of a model and its dissipation properties. Section 3 describes the numerical implementation algorithms and their verification. The parameter

identification and determination are presented in Section 4, followed by the validation and demonstration of the capabilities of the proposed model in Section 5.

2. A thermodynamics-based model for partially saturated soils

2.1. A generic thermodynamics-based framework

The experimentally observed behaviour of partially saturated soils requires coupling between internal variables representing the hydro-mechanical behaviour in constitutive modelling. In this section, a generic thermodynamic approach is described to serve as a basis for the interaction between the mechanical and hydraulic responses represented by plastic strain and irrecoverable saturation, respectively. The inseparable nature of this interaction will be reflected in the proposed approach through interdependence of plastic strain and irrecoverable saturation.

Following Houlsby (1997) and Coussy et al. (2010), the rate of work input can be expressed as:

$$\widetilde{W} = (\overline{p} + S_r s)\dot{\varepsilon}_v + q\dot{\varepsilon}_s - \phi s\dot{S}_r = p^{'}\dot{\varepsilon}_v + q\dot{\varepsilon}_s + s^{*}\left(-\dot{S}_r\right) \tag{1}$$

where $\overline{p}$, $p^{'}, q, s, s^{*}, \varepsilon_v, \varepsilon_s, S_r, \phi$ are the net mean stress, effective mean stress, shear stress, matric suction, modified suction, volumetric strain, shear strain, saturation degree and Lagrangian porosity, respectively. It can be seen that the modified suction, $s^{*} = s\phi$ with porosity explicitly representing the effect of volumetric changes on the hydraulic conductivity of bulk fluid, is used as a conjugate of the strain-like variable $-\dot{S}_r$, according to Houlsby (1997), Coussy et al. (2010) and Buscarnera and Einav (2012). It agrees with Lu (2008) and Vaunat et al. (2000) that suction can be considered a stress-like variable. Under geotechnical sign convention (compression positive) and assumption of incompressible solid grains, the volumetric strain can be expressed as $\varepsilon_v = \phi_0 - \phi$, with ϕ_0 being the initial porosity. The triaxial stresses ($p^{'}, q$) and triaxial strains (ε_v, ε_s) can be expressed in terms of Cauchy stress ($\sigma^{'}_{ij}$) and strain tensors (ε_{ij}), respectively (with δ_{ij} being the Kronecker delta).

$$p^{'} = -\frac{1}{3}\sigma^{'}_{kk} \qquad q = \sqrt{\frac{3}{2}\left(\sigma^{'}_{ij} - \frac{1}{3}\sigma^{'}_{kk}\delta_{ij}\right)\left(\sigma^{'}_{ij} - \frac{1}{3}\sigma^{'}_{kk}\delta_{ij}\right)} \tag{2}$$

$$\varepsilon_v = \varepsilon_{kk} \qquad \varepsilon_s = \sqrt{\frac{2}{3}\left(\varepsilon_{ij} - \frac{1}{3}\varepsilon_v\delta_{ij}\right)\left(\varepsilon_{ij} - \frac{1}{3}\varepsilon_v\delta_{ij}\right)} \tag{3}$$

We acknowledge the limitation of the work input (Eq. (1)) in neglecting the work due to moving air-fluid interface in a partially saturated volume element, as explained in Houlsby (1997), the consequence of which is the simplest form of Bishop's effective stress parameter, $\chi = S_r$. Physically, the effective stress here can be understood as the stress at inter-particle contacts related to the deformation and failure of the soil skeleton, governed by both external load and contact-level capillary action. From the micromechanical point of view, there must be two contributions to the capillarity of the average skeleton stress, including suction and surface tension forces along the contours between grains and liquid bridges (Wan et al., 2014; Li, 2003; Likos, 2014), both of which affect the form of Bishop's effective stress parameter χ. The latter still needs further investigation (Likos, 2014) and is not always taken into account in constitutive modelling (Gallipoli et al., 2003; Hu et al., 2014). On the other hand, there have been attempts for phenomenological expressions of effective stress parameter χ, which can be represented as either a function of saturation degree (e.g. Hassanizadeh and Gray, 1990; Muraleetharan and Wei, 1999) or air-entry value (Khalili and Khabbaz, 1998) to capture the transition between fully and partially saturated states. Despite their usefulness demonstrated in Russell and Khalili (2006), Khalili et al. (2008), Loret & Khalili (2002), extensive research on the micromechanical aspects for better forms of Bishop's effective stress parameter χ is still needed (Wan et al., 2014; Li, 2003). This research is therefore not covered within the scope of this study.

Under isothermal conditions, the energy balance is of the form (Ziegler, 1983):

$$\widetilde{W} = \dot{\Psi} + \tilde{\Phi} \tag{4}$$

with $\dot{\Psi}$ being the rate of Helmholtz specific free energy and $\tilde{\Phi} \geq 0$ denoting the energy dissipation. The tilde symbol "~" is used here to indicate the path-dependent nature of the work input and dissipation; only their rates can be defined. For partially saturated soils, the mechanical energy dissipation is attributable to the rearrangement of particles through the sliding/rolling contact, leading to plastic strain (Collins, 2005; Li, 2007a). The pore fluid redistribution is induced by this grain rearrangement, resulting in the formation and/or breakage of water menisci that are associated with irreversible change of saturation (Wheeler et al., 2003; Mani et al., 2013). These two grain scale dissipations activate and develop simultaneously and have mutual effects on each another (Li, 2007a; Hu et al., 2015; Wheeler et al., 2003). For example, during the wetting/drying process, the redistribution of water menisci induce changes of capillary forces between grains and hence their inter-particle contact forces, leading to the rearrangement of particles. Under mechanical loadings, the movement of particles triggers the imbibition/drainage of pore throats and rupture of fluid bridges. Additionally, the change of inter-particle distances induces variation of capillary pressures enabling liquid bridges to redistribute. These coupled hydro-mechanical processes lead to the irreversible deformation and saturation observed at the macro scale. In constitutive modelling of partially saturated soils, the use of irrecoverable saturation degree S_r^p has also been adopted in some papers (Wheeler

et al., 2003; Li, 2007a; Hu et al., 2015). These irreversible strains and strain-like variable (volumetric plastic strain ε_v^p, and deviatoric plastic strain ε_s^p and irrecoverable saturation degree S_r^p) govern the dissipation and hence are used as internal variables controlling the behaviour of the proposed partially saturated soil model. The Helmholtz free energy can assume the following general form:

$$\Psi = \Psi\left(\varepsilon_v, \varepsilon_s, -S_r, \varepsilon_v^p, \varepsilon_s^p, -S_r^p\right) \tag{5}$$

Therefore its rate is:

$$\dot{\Psi} = \frac{\partial \Psi}{\partial \varepsilon_v}\dot{\varepsilon}_v + \frac{\partial \Psi}{\partial \varepsilon_s}\dot{\varepsilon}_s + \frac{\partial \Psi}{\partial(-S_r)}\left(-\dot{S}_r\right) + \frac{\partial \Psi}{\partial \varepsilon_v^p}\dot{\varepsilon}_v^p + \frac{\partial \Psi}{\partial \varepsilon_s^p}\dot{\varepsilon}_s^p + \frac{\partial \Psi}{\partial\left(-S_r^p\right)}\left(-\dot{S}_r^p\right) \tag{6}$$

By substituting Eq. (6) into Eq. (4), we obtain:

$$\widetilde{W} = \frac{\partial \Psi}{\partial \varepsilon_v}\dot{\varepsilon}_v + \frac{\partial \Psi}{\partial \varepsilon_s}\dot{\varepsilon}_s + \frac{\partial \Psi}{\partial(-S_r)}\left(-\dot{S}_r\right) + \frac{\partial \Psi}{\partial \varepsilon_v^p}\dot{\varepsilon}_v^p + \frac{\partial \Psi}{\partial \varepsilon_s^p}\dot{\varepsilon}_s^p + \frac{\partial \Psi}{\partial\left(-S_r^p\right)}\left(-\dot{S}_r^p\right) + \tilde{\Phi} \tag{7}$$

Comparing Eq. (7) with Eq. (1), the following fundamental relationships are obtained:

$$p' = \frac{\partial \Psi}{\partial \varepsilon_v} \tag{8}$$

$$q = \frac{\partial \Psi}{\partial \varepsilon_s} \tag{9}$$

$$s^* = \frac{\partial \Psi}{\partial(-S_r)} \tag{10}$$

and

$$\tilde{\Phi} = -\frac{\partial \Psi}{\partial \varepsilon_v^p}\dot{\varepsilon}_v^p - \frac{\partial \Psi}{\partial \varepsilon_s^p}\dot{\varepsilon}_s^p - \frac{\partial \Psi}{\partial\left(-S_r^p\right)}\left(-\dot{S}_r^p\right) = \overline{\chi}_v\dot{\varepsilon}_v^p + \overline{\chi}_s\dot{\varepsilon}_s^p + \overline{\chi}_h\left(-\dot{S}_r^p\right) \tag{11}$$

in which the generalised stresses $\overline{\chi}_v = -\frac{\partial \Psi}{\partial \varepsilon_v^p}, \overline{\chi}_s = -\frac{\partial \Psi}{\partial \varepsilon_s^p}$ and $\overline{\chi}_h = -\frac{\partial \Psi}{\partial(-S_r^p)}$ are the thermodynamic conjugates to the volumetric plastic strain ε_v^p, shear plastic strain ε_s^p and irrecoverable saturation degree $-S_r^p$, respectively.

On the other hand, for rate-independent behaviour (Houlsby and Puzrin, 2000) the dissipation is a homogeneous function of order one in terms of $\dot{\varepsilon}_v^p$, $\dot{\varepsilon}_s^p$ and $-\dot{S}_r^p$:

$$\tilde{\Phi} = \frac{\partial \tilde{\Phi}}{\partial \dot{\varepsilon}_v^p}\dot{\varepsilon}_v^p + \frac{\partial \tilde{\Phi}}{\partial \dot{\varepsilon}_s^p}\dot{\varepsilon}_s^p + \frac{\partial \tilde{\Phi}}{\partial\left(-\dot{S}_r^p\right)}\left(-\dot{S}_r^p\right) = \chi_v\dot{\varepsilon}_v^p + \chi_s\dot{\varepsilon}_s^p + \chi_h\left(-\dot{S}_r^p\right) \tag{12}$$

where χ_v, χ_s and χ_h are volumetric, shear and hydraulic dissipative generalised stresses, respectively. Comparing Eq. (11) with Eq. (12), a form of Ziegler's orthogonality condition (Ziegler, 1983; Houlsby and Puzrin, 2000; Puzrin and Houlsby, 2001) can be obtained:

$$\chi_v = \overline{\chi}_v \tag{13}$$

$$\chi_s = \overline{\chi}_s \tag{14}$$

$$\chi_h = \overline{\chi}_h \tag{15}$$

In general, for rate-independent models, the dissipation potential $\tilde{\Phi}$ can assume any forms that are first order homogeneous in the rates of internal variables, provided the thermodynamic admissibility is met. We note that explicit representations of grain scale details are missing in this model, given the proposed approach is based on continuum mechanics. It will be addressed in our future works to move towards a better model where micromechanics-based approaches (e.g. Nguyen and Gan, 2014; Bignonnet et al., 2016; Fang et al., 2017; Nicot and Darve, 2007; Yin et al., 2009) can be adopted. In this paper, micro scale mechanisms are used only to obtain constraints on the interactions of internal variables, reflected in the dependence of all thermodynamic forces on stress, suction, plastic strain and irrecoverable saturation and their rates. The inseparable nature of the grain scale hydro-mechanical coupling described earlier requires that χ_v, χ_s, and χ_h be dependent on stress, suction, all internal variables and their rates representing the dissipative processes. Mathematically they can be written as (i stands for v, s, or h):

$$\chi_i = \chi_i\left(p,\ q,\ s^*, \dot{\varepsilon}_v^p, \dot{\varepsilon}_s^p, \dot{S}_r^p\right) \tag{16}$$

Although a decoupling of χ_i from all the rates of internal variables can be used to simplify the formulation as can be seen in several thermodynamics-based models in the literature (Sheng et al., 2004; Li, 2007a,b; Hu et al., 2015; Santagiuliana and Schrefler, 2006), this decoupling at this level leads to the employment of different loading functions to describe the interactions between different dissipative processes. Instead, a tighter coupling between these processes is pursued in this study, in which a special form of first order homogeneous dissipation potential (Collins and Houlsby, 1997; Collins and Kelly, 2002; Collins and Hilder, 2002; Collins, 2003; Einav

et al., 2007) is used to obtain the required form of dissipative generalised stresses in Eq. (16). This generic form of dissipation potential has been used successfully in modelling dissipative processes involving more than one dissipative mechanisms. Examples include coupling plastic strains with breakage (Einav, 2007a,b; Nguyen and Einav, 2009) and damage with plastic strains (Nguyen et al., 2012; Guiamatsia and Nguyen, 2012; Mir et al., 2018). The dissipation potential takes the following generic form:

$$\tilde{\Phi} = \sqrt{(\varphi_1^v)^2 + (\varphi^s)^2 + (\varphi^h)^2} + \varphi_2^v \tag{17}$$

In the above expression, φ_1^v, and φ_2^v are first order homogeneous functions of $\dot{\varepsilon}_v^p$; they are required for the introduction of dilation behaviour in the model. Functions φ^s, and φ^h are first order homogeneous with respect to $\dot{\varepsilon}_s^p$, and $\dot{S}_r^p$, respectively. The specific expressions of these functions (φ_1^v, φ_2^v, φ^s, and φ^h) govern the behaviour of the constitutive model and will be presented in the next subsection.

The dissipative generalised stresses take the following generic forms:

$$\chi_v = \frac{\partial\tilde{\Phi}}{\partial\dot{\varepsilon}_v^p} = \frac{\partial\tilde{\Phi}}{\partial\varphi_1^v}\frac{\partial\varphi_1^v}{\partial\dot{\varepsilon}_v^p} + \frac{\partial\tilde{\Phi}}{\partial\varphi_2^v}\frac{\partial\varphi_2^v}{\partial\dot{\varepsilon}_v^p} = \frac{\varphi_1^v}{\sqrt{(\varphi_1^v)^2 + (\varphi^s)^2 + (\varphi^h)^2}}\frac{\partial\varphi_1^v}{\partial\dot{\varepsilon}_v^p} + \frac{\partial\varphi_2^v}{\partial\dot{\varepsilon}_v^p} \tag{18}$$

$$\chi_s = \frac{\partial\tilde{\Phi}}{\partial\dot{\varepsilon}_s^p} = \frac{\partial\tilde{\Phi}}{\partial\varphi^s}\frac{\partial\varphi^s}{\partial\dot{\varepsilon}_s^p} = \frac{\varphi^s}{\sqrt{(\varphi_1^v)^2 + (\varphi^s)^2 + (\varphi^h)^2}}\frac{\partial\varphi^s}{\partial\dot{\varepsilon}_s^p} \tag{19}$$

$$\chi_h = \frac{\partial\tilde{\Phi}}{\partial(-\dot{S}_r^p)} = \frac{\partial\tilde{\Phi}}{\partial\varphi^h}\frac{\partial\varphi^h}{\partial(-\dot{S}_r^p)} = \frac{\varphi^h}{\sqrt{(\varphi_1^v)^2 + (\varphi^s)^2 + (\varphi^h)^2}}\frac{\partial\varphi^h}{\partial(-\dot{S}_r^p)} \tag{20}$$

Thanks to the properties of first order homogeneous functions, the following equation can be deduced from Eqs. (18-20):

$$\chi_v\dot{\varepsilon}_v^p + \chi_s\dot{\varepsilon}_s^p + \chi_h(-\dot{S}_r^p) = \tilde{\Phi} \tag{21}$$

Thus, the dissipation rate function in Eq. (17) can be written as follows:

$$\tilde{\Phi} = \tilde{\Phi}_v + \tilde{\Phi}_s + \tilde{\Phi}_h \tag{22}$$

where $\tilde{\Phi}_v = \chi_v\dot{\varepsilon}_v^p$, $\tilde{\Phi}_s = \chi_s\dot{\varepsilon}_s^p$ and $\tilde{\Phi}_h = \chi_h(-\dot{S}_r^p)$ are denoted as volumetric, shear and hydraulic parts of the total dissipation rate, respectively. The above properties allow the investigation of dissipation characteristics of any partially saturated models derived from this proposed generic framework, given the explicitly defined dissipation potential (see Eq. (17)). This will be illustrated in sub-section 2.3.

As can be seen in Eqs. (18-20), all dissipative generalised stresses χ_i are dependent on all rates of internal variables, $\dot{\varepsilon}_v^p$, $\dot{\varepsilon}_s^p$, and $-\dot{S}_r^p$. Thanks to this, the degenerate Legendre transformation of the dissipation potential (Puzrin and Houlsby, 2001) leads to a single yield function y^* in generalised stress space (χ_v, χ_s, and χ_h):

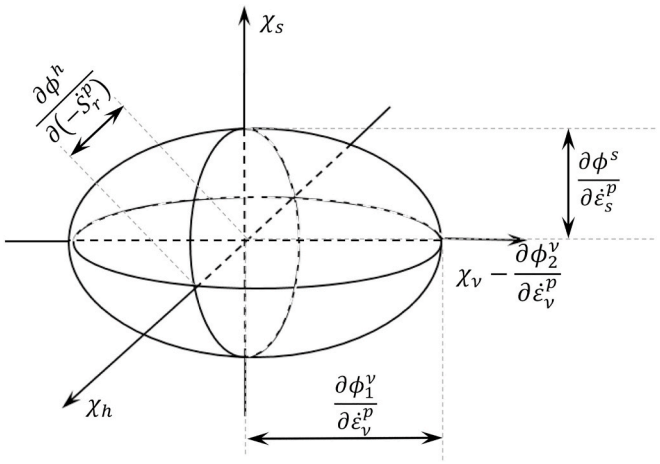

Fig. 1. Geometric representation of yield potential in dissipative stress space.

$$y^* = \frac{\left(\chi_\nu - \frac{\partial \varphi_2^\nu}{\partial \bar{\varepsilon}_\nu^p}\right)^2}{\left(\frac{\partial \varphi_1^\nu}{\partial \bar{\varepsilon}_\nu^p}\right)^2} + \frac{(\chi_s)^2}{\left(\frac{\partial \varphi^s}{\partial \bar{\varepsilon}_s^p}\right)^2} + \frac{(\chi_h)^2}{\left(\frac{\partial \varphi^h}{\partial \left(-\bar{S}_r^p\right)}\right)^2} - 1 \le 0 \tag{23}$$

Eq. (23) represents an ellipsoid as shown in Fig. 1. The role of y^* is similar to that of a plastic potential in classical plasticity theory. Three evolution laws (or flow rules) for the rates of plastic strains and irreversible saturation rates, sharing a single multiplier $\dot{\lambda}_p$ can then be expressed as:

$$\dot{\varepsilon}_\nu^p = \dot{\lambda}_p \frac{\partial y^*}{\partial \chi_\nu} = \dot{\lambda}_p \frac{2\left(\chi_\nu - \frac{\partial \varphi_2^\nu}{\partial \bar{\varepsilon}_\nu^p}\right)}{\left(\frac{\partial \varphi_1^\nu}{\partial \bar{\varepsilon}_\nu^p}\right)^2} \tag{24}$$

$$\dot{\varepsilon}_s^p = \dot{\lambda}_p \frac{\partial y^*}{\partial \chi_s} = \dot{\lambda}_p \frac{2\chi_s}{\left(\frac{\partial \varphi^s}{\partial \bar{\varepsilon}_s^p}\right)^2} \tag{25}$$

$$-\dot{S}_r^p = \dot{\lambda}_p \frac{\partial y^*}{\partial \chi_h} = \dot{\lambda}_p \frac{2\chi_h}{\left(\frac{\partial \varphi^h}{\partial \left(-\bar{S}_r^p\right)}\right)^2} \tag{26}$$

Eqs. (8-10) and (23-26) present a generic form of thermodynamic-based models for partially saturated soils. The specifications of functions φ_1^ν, φ_2^ν, φ^s, and φ^h complete the definition of a specific model. This coupling allows capturing the simultaneous activation and development of both mechanical and hydraulic yielding at any instant without requiring arbitrary and complicated treatments, in comparison with the use of multiple yield surfaces and plastic multipliers (e.g. Wheeler et al., 2003; Sheng et al., 2004; Santagiuliana and Schrefler, 2006). The specifications of both energy and dissipation potentials to formulate a specific constitutive model for partially saturated soils will be described in the next sub-section.

2.2. A constitutive model based on critical state soil mechanics for partially saturated soils

A critical state model is described in this section following the generic formulation in Section 2.1 to serve as an example to indicate its promising performances in simulating suction- and water content-controlled tests at low stresses.

2.2.1. Helmholtz specific energy potential

The Helmholtz specific energy potential can be assumed of the following form:

$$\Psi = \overbrace{\kappa p_0^{'} \exp\left[\frac{\left(\varepsilon_v - \varepsilon_\nu^p\right)}{\kappa}\right]}^{Volumetric\ \ part} + \overbrace{\frac{3}{2}G\left(\varepsilon_s - \varepsilon_s^p\right)^2}^{Shear\ \ part} + \overbrace{\kappa_h\left(p_u + s_0^*\right)\exp\left\{\frac{S_{r0} + \left[\left(-S_r\right) - \left(-S_r^p\right)\right]}{\kappa_h}\right\} - \left[\left(-S_r\right) - \left(-S_r^p\right)\right]p_u + \left(-S_r^p\right)p_b}^{Hydraulic\ \ part} \tag{27}$$

where κ is the elastic index controlling the pressure-dependent elastic behaviour of the model; G is the shear moduli; κ_h is to control the amount of reversible energy stored in the water menisci (Buscarnera and Einav, 2012); $p_u = 1$ kPa is to make the unit consistent and p_b is a parameter controlling the stored irreversible hydraulic energy. Initial values of $p^{'}$, s^* and S_r are denoted as $p_0^{'}$, s_0^* and S_{r0}, respectively.

Eq. (27) indicates that the Helmholtz free energy is a combination of stored energies induced by both mechanical and hydraulic processes. They are produced by the compressed grains which can recover to their previous states (Collins, 2005) and the reversible movement of the air-water interfaces (Wheeler et al., 2003). The last term of Eq. (27), $(-S_r^p)p_b$, represents the irrecoverable hydraulic energy that is stored in the volume element, reflecting the entrapment of fluid menisci in the heterogeneous structure during wetting-drying processes (Wei and Dewoolkar, 2006). It is noted that the Helmholtz free energy potential is of phenomenological form and the elastic behaviour does not possess strong hydro-mechanical coupling, given the focus on the dissipation properties and inelastic behaviour.

Using Eqs. (8)–(10) and (27), the true stresses are:

$$p^{'} = \frac{\partial \Psi}{\partial \varepsilon_\nu} = p_0^{'} \exp\left[\frac{\left(\varepsilon_v - \varepsilon_\nu^p\right)}{\kappa}\right] \tag{28}$$

$$q = \frac{\partial \Psi}{\partial \varepsilon_s} = 3G\left(\varepsilon_s - \varepsilon_s^p\right) \tag{29}$$

$$s^* = \frac{\partial \Psi}{\partial(-S_r)} = (p_u + s_0^*)\exp\left\{\frac{S_{r0} + \left[(-S_r) - \left(-S_r^p\right)\right]}{\kappa_h}\right\} - p_u \tag{30}$$

The generalised stresses can also be obtained from the Helmholtz free energy potential in Eq. (27) as:

$$\overline{\chi}_\nu = -\frac{\partial \Psi}{\partial \varepsilon_\nu^p} = p_0^{'} \exp\left[\frac{\left(\varepsilon_\nu - \varepsilon_\nu^p\right)}{\kappa}\right] = p^{'} \tag{31}$$

$$\overline{\chi}_s = -\frac{\partial \Psi}{\partial \varepsilon_s^p} = 3G\left(\varepsilon_s - \varepsilon_s^p\right) = q \tag{32}$$

$$\overline{\chi}_h = -\frac{\partial \Psi}{\partial\left(-S_r^p\right)} = (p_u + s_0^*)\exp\left\{\frac{S_{r0} + \left[(-S_r) - \left(-S_r^p\right)\right]}{\kappa_h}\right\} - p_u - p_b = s^* - p_b \tag{33}$$

Eq. (28) implies the pressure-dependent elastic soil bulk employing a linear relationship between $\ln\nu$ and $\ln p^{'}$ (Butterfield, 1979; Hashiguchi, 1995; Callari et al., 1998; Collins and Kelly, 2002). Since $s^* = s\phi$, and $\varepsilon_v = \phi_0 - \phi$ (Section 2.1) hydraulic effects on the elastic stiffness are accounted for in the $(p^{'}, s)$ space. However these effects are usually considered insignificant and can be neglected (Alonso et al., 1990; Sheng et al., 2004). Eqs. (28) and (30) can be expanded to forms of net mean stress and suction to expose the interaction between NCL and SWCC. Further details can be found in Appendix A.

2.2.2. Dissipation potential

The nature of grain scale interactions leads to the proposal of a suitable form of dissipation potential (see Eq. (17)) that reflects the hydro-mechanical coupling in the inelastic behaviour of unsaturated soils. Functions φ_1^ν, φ_2^ν, φ^s and φ^h in the dissipation potential (see Eq. (17)) take the below specific forms:

$$\varphi_1^\nu = \frac{1}{\sqrt{\exp[-\beta(1-S_r)]}} A\dot{\varepsilon}_\nu^p \tag{34}$$

$$\varphi_2^\nu = \frac{p_{c(us)}^{'}}{r}\dot{\varepsilon}_\nu^p \tag{35}$$

$$\varphi^s = B\dot{\varepsilon}_s^p \tag{36}$$

$$\varphi^h = \frac{1}{\sqrt{1-\exp[-\beta(1-S_r)]}} \frac{(s^* - p_b)}{\left(p^{'} - \frac{p_{c(us)}^{'}}{r}\right)}\left(-\dot{S}_r^p\right)A \tag{37}$$

The dimensionless parameter β $(0 < \beta \leq 1)$ is used to govern the coupling between saturation and volumetric deformation upon yielding. Its role will be elaborated in Sections 4 and 5.1. Parameter r is defined as "spacing ratio" in the range of 1.5-∞ to control the dilatancy (Crouch et al., 1994; Yu, 1998; Collins and Hilder, 2002; Lai et al., 2016). The evolving threshold pressure $p_{c(us)}^{'}$ can take different forms of evolution laws based on experimentally observed responses at low stresses (e.g. Alonso et al., 1990; Wheeler et al., 2003; Sheng et al., 2008; Tamagnini, 2004; Khalili et al., 2008) or high stresses (Mun and McCartney, 2017; Loret and Khalili, 2002; Alonso et al., 2013; Zhou et al., 2018). We present in this study a relatively simple law that can reproduce experimental trends at low pressures (see further details in Appendix B); any other forms can be used given the generic thermodynamic framework proposed in this study. Function $p_{c(us)}^{'}$ is expressed as a function of s^* and ε_ν^p:

$$p_{c(us)}^{'} = p_R^{'}\left(\frac{p_c^{'}}{p_R^{'}}\right)^{\frac{\lambda-\kappa}{\lambda_{us}-\kappa}} = p_R^{'}\left[\frac{p_{c0}^{'}\exp\left(\frac{\varepsilon_\nu^p}{\lambda-\kappa}\right)}{p_R^{'}}\right]^{\frac{\lambda-\kappa}{\lambda[(1-\xi)\exp(-\mu s^*)+\xi]-\kappa}} \tag{38}$$

The above evolution law is based on the combination of pre-consolidation effective mean pressure for saturated conditions (Collins and Hilder, 2002),

$$p_c^{'} = p_{c0}^{'}\exp\left[\varepsilon_\nu^p / (\lambda - \kappa)\right] \tag{39}$$

and stiffness parameter for partially saturated conditions,

$$\lambda_{us} = \lambda[(1-\xi)\exp(-\mu s^*) + \xi] \tag{40}$$

with λ representing the slope of the virgin compression line in the $\ln\nu : \ln p^{'}$ plane for saturated conditions; $p_{c0}^{'}$ is the initial yield pressure under isotropic compression at fully saturated condition; $p_R^{'}$ denotes the stress parameter controlling the yield curve; ξ is a dimensionless parameter controlling the maximum soil stiffness and μ is a constant related to the change of soil stiffness with modified suction.

Functions A and B in Eqs. (34) and (36-37) govern the behaviour of the model. They are first order homogeneous in terms of $p^{'}$ and

$p'_{c(us)}$ and take the following forms (see details on how to obtain them in Appendices C.1 & C.2):

$$A = \left(1 - \frac{2}{r}\right)p' + \frac{1}{r}p'_{c(us)} \tag{41}$$

$$B = (1-\alpha)Mp' + \frac{\alpha}{r}Mp'_{c(us)} \tag{42}$$

in which α is a parameter governing the strength of the material and non-associativity of the flow rules, via the teardrop shape and convexity near the origin of the yield surface. The slope of the CSL, $M = q_{CSL}/p'_{CSL}$, is also assumed to be unaffected by suction and saturation (Alonso et al., 1990; Al-Sharrad, 2013; Russell and Khalili, 2006; Khalili et al., 2008).

2.2.3. Yield function and flow rules

Using Eqs. (34-37), the yield function in dissipative stress space (Eq. (23)) can be obtained as:

$$y^* = \frac{\left(\chi_\nu - \frac{p'_{c(us)}}{r}\right)^2}{\left[\frac{1}{\sqrt{\exp[-\beta(1-S_r)]}}A\right]^2} + \frac{(\chi_s)^2}{(B)^2} + \frac{(\chi_h)^2}{\left[\frac{1}{\sqrt{1-\exp[-\beta(1-S_r)]}}\frac{(s^*-p_b)}{\left(p' - \frac{p'_{c(us)}}{r}\right)}A\right]^2} - 1 \le 0 \tag{43}$$

Using Eqs. (13-15), (31-33), (41-42) and the orthogonality conditions in the forms $\chi_\nu = \overline{\chi}_\nu = p'$, $\chi_s = \overline{\chi}_s = q$, and $\chi_h = \overline{\chi}_h = s^* - p_b$, we can obtain the yield surface y in true stress space as:

$$y = \frac{\left(p' - \frac{p'_{c(us)}}{r}\right)^2}{A^2} + \frac{(q)^2}{B^2} - 1 = \frac{\left(p' - \frac{1}{r}p'_{c(us)}\right)^2}{\left[\left(1 - \frac{2}{r}\right)p' + \frac{1}{r}p'_{c(us)}\right]^2} + \frac{(q)^2}{\left[(1-\alpha)p' + \frac{\alpha}{r}p'_{c(us)}\right]^2 M^2} - 1 \le 0 \tag{44}$$

As can be seen in Fig. 2, in the $(p' - p'_{c(us)}/r, q)$ plane, the yield function in Eq. (44) is the upper half of an ellipse of radii A and B. The change of its shape towards increasing s^* reflects the effect of suction on shear strength. The ellipse axes coincide with the normal consolidation line (NCL) when $\dot{\varepsilon}^p_\nu = 0$ and critical state line (CSL) when $\dot{\varepsilon}^p_s = 0$, respectively.

In conjunction with this yield surface, the evolution rules in Eqs. (24-26) now become:

$$\dot{\varepsilon}^p_\nu = \dot{\lambda}_p \frac{\partial y^*}{\partial \chi_\nu} = \dot{\lambda}_p \frac{2\left(p' - \frac{1}{r}p'_{c(us)}\right)}{\left[\left(1 - \frac{2}{r}\right)p' + \frac{1}{r}p'_{c(us)}\right]^2} \exp[-\beta(1-S_r)] \tag{45}$$

$$\dot{\varepsilon}^p_s = \dot{\lambda}_p \frac{\partial y^*}{\partial \chi_s} = \dot{\lambda}_p \frac{2q}{\left[(1-\alpha)p' + \frac{\alpha}{r}p'_{c(us)}\right]^2 M^2} \tag{46}$$

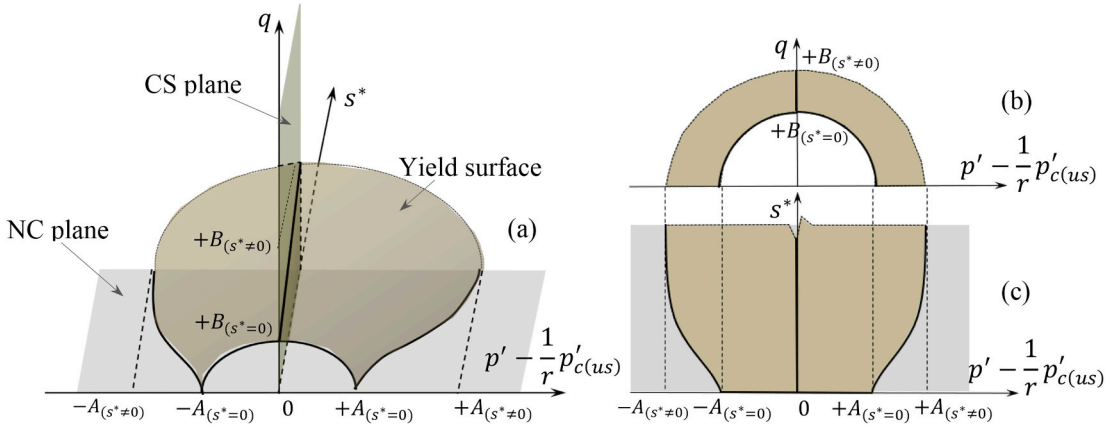

Fig. 2. Yield surface in (a) $\left(p' - \frac{p'_{c(us)}}{r}, q, s^*\right)$ space, (b) $\left(p' - \frac{p'_{c(us)}}{r}, q\right)$ space and (c) $\left(p' - \frac{p'_{c(us)}}{r}, s^*\right)$ space.

$$-\dot{S}_r^p = \dot{\lambda}_p \frac{\partial y^*}{\partial \chi_h} = \dot{\lambda}_p \frac{2\left(p' - \frac{1}{r}p'_{c(us)}\right)^2}{(s^* - p_b)\left[\left(1-\frac{2}{r}\right)p' + \frac{1}{r}p'_{c(us)}\right]^2}[1 - \exp[-\beta(1-S_r)]] \tag{47}$$

As can be seen in Eqs. (45-47), the activation and evolution of both plastic deformation and irrecoverable saturation takes place simultaneously, given the same multiplier $\dot{\lambda}_p$, reflecting the inseparable nature of the hydro-mechanical coupling at the grain scale (Zhang et al., 2009a,b; Delage and Graham, 1996; Tang and Graham, 2002). In particular, the inelastic volumetric response (see Eq. (45)) and evolution of irrecoverable saturation (see Eq. (47)) take into account the coupled hydro-mechanical effects through stresses, volumetric plastic strain, suction and saturation.

The proposed yield surface (see Fig. 3) is identical with the Modified Cam Clay (MCC; see Collins, 2003) model for $r = 2$ and $\alpha = 1$ under saturated condition ($s^* = 0$ and $S_r = 1$), allowing a smooth transition between saturated and partially saturated conditions. The shape of the yield locus reflects the experimental observations of suction-controlled or water content-controlled tests for partially saturated soils: (i) tear-drop shape of the yield surface (see Fig. 3b); (ii) increasing effective yield pressure with modified suction (see Fig. 3c), and (iii) apparent cohesion thanks to $S_r s$ (Jommi, 2000). The above-mentioned features make our approach different from other critical-state-based models for partially saturated soils. A comparison with the Barcelona Basic Model (BBM) (Alonso et al., 1990) is presented in Appendix D. Thanks to the use of the systematic thermomechanical approach, the proposed model has a well-defined structure with a small number of parameters (13 parameters). To highlight this advantage, a comparison on the number of parameters in existing coupled hydro-mechanical models for partially saturated soils is shown in Appendix E.

However, for the sake of simplicity, it is assumed that the partially saturated soil behaves isotropically in both cases of recoverable and irrecoverable deformation/saturation, although the behaviour of wet granular materials can be anisotropic because of highly inhomogeneous textures due to the effects of liquid bridges. We also acknowledge that the proposed model can still be improved to capture the transition between fully and partially saturated states with the effects of air-entry suction (Sheng et al., 2008, 2011; Khalili et al., 2008; Loret and Khalili, 2000, 2002), to have closed-shape yield surface (Thu et al., 2007b; Sivakumar and Doran, 2000; Delage and Graham, 1996; Tang and Graham, 2002), to predict yielding behaviours of more complex experimental loading paths (Loret and Khalili, 2000, 2002), and to simulate NCL with pressurized saturation and the transition to full-void closure at high stresses (Mun and McCartney, 2015, 2017; Zhou et al., 2018).

2.3. Dissipation properties

Using Eq. (22) and Eqs. (45-47), the dissipations due to plastic volumetric deformation, plastic shear deformation and irrecoverable saturation can be expressed as:

$$\tilde{\Phi}_v = \chi_v \dot{\varepsilon}_v^p = p' \dot{\varepsilon}_v^p = \dot{\lambda}_p \frac{2p'\left(p' - \frac{1}{r}p'_{c(us)}\right)}{\left[\left(1-\frac{2}{r}\right)p' + \frac{1}{r}p'_{c(us)}\right]^2}\exp[-\beta(1-S_r)] \tag{48}$$

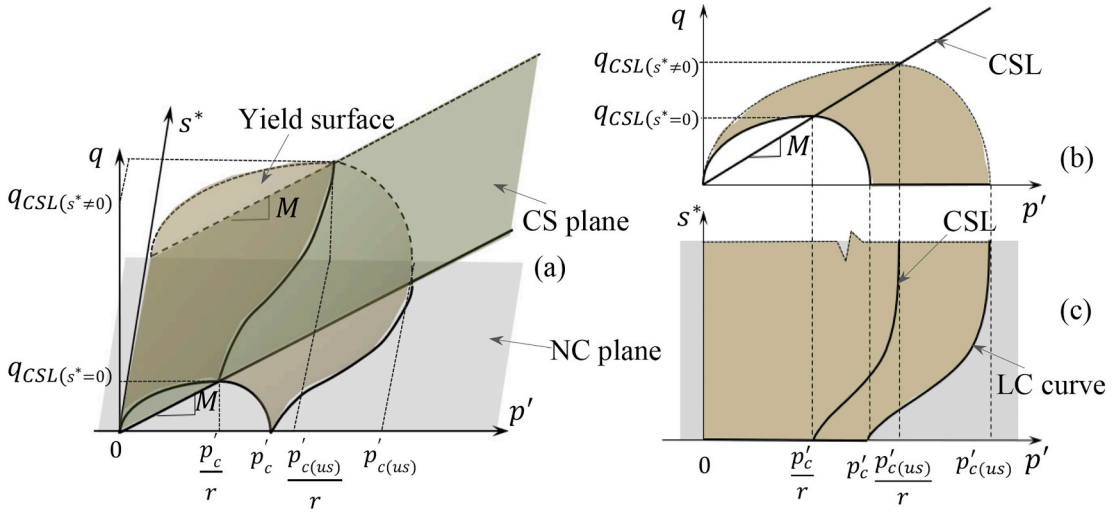

Fig. 3. Yield surface (a) in (p', q, s^*) space; (b) front view (c) top view.

$$\tilde{\Phi}_s = \chi_s \dot{\varepsilon}_s^p = q\dot{\varepsilon}_s^p = \dot{\lambda}_p \frac{2q^2}{\left[(1-\alpha)p^{'} + \frac{q}{r}p_{c(us)}^{'}\right]^2 M^2} \tag{49}$$

$$\tilde{\Phi}_h = \chi_h\left(-\dot{S}_r^p\right) = (s^* - p_b)\left(-\dot{S}_r^p\right) = \dot{\lambda}_p \frac{2\left(p^{'} - \frac{1}{r}p_{c(us)}^{'}\right)^2}{\left[\left(1-\frac{2}{r}\right)p^{'} + \frac{1}{r}p_{c(us)}^{'}\right]^2}\{1 - \exp[-\beta(1-S_r)]\} \tag{50}$$

Utilising Eq. (44) and Eqs. (48-50) allows us to express Eq. (22) in the following form:

$$\tilde{\Phi} = 2\dot{\lambda}_p \left\{1 + \frac{\frac{1}{r}p_{c(us)}^{'}\left(p^{'} - \frac{1}{r}p_{c(us)}^{'}\right)}{\left[\left(1-\frac{2}{r}\right)p^{'} + \frac{1}{r}p_{c(us)}^{'}\right]^2}\exp[-\beta(1-S_r)]\right\} \tag{51}$$

Since $\exp[-\beta(1-S_r)] \leq 1$, we can write:

$$\tilde{\Phi} \geq 2\dot{\lambda}_p \left\{\frac{\left[\left(1-\frac{2}{r}\right)p^{'}\right]^2 + \left(3-\frac{4}{r}\right)\frac{1}{r}p^{'}p_{c(us)}^{'}}{\left[\left(1-\frac{2}{r}\right)p^{'} + \frac{1}{r}p_{c(us)}^{'}\right]^2}\right\}\exp[-\beta(1-S_r)] \tag{52}$$

Given $r \geq 1.5$, the numerator of the bracketed expression in Eq. (52) is always positive, and hence the positiveness of the total dissipation is always guaranteed. However due to dilation, $\tilde{\Phi}_v$ can admit negative values, while $\tilde{\Phi}_s$ and $\tilde{\Phi}_h$ are always positive. From Eqs. (48-51), the dissipation ratios $\mathrm{R}_v, \mathrm{R}_s, \mathrm{R}_h$ between $\tilde{\Phi}_v, \tilde{\Phi}_s, \tilde{\Phi}_h$ and $\tilde{\Phi}$ can be expressed as:

$$\mathrm{R}_v = \frac{\tilde{\Phi}_v}{\tilde{\Phi}} = \frac{p^{'}\left(p^{'} - \frac{1}{r}p_{c(us)}^{'}\right)\exp[-\beta(1-S_r)]}{\left[\left(1-\frac{2}{r}\right)p^{'} + \frac{1}{r}p_{c(us)}^{'}\right]^2 + \frac{1}{r}p_{c(us)}^{'}\left(p^{'} - \frac{1}{r}p_{c(us)}^{'}\right)\exp[-\beta(1-S_r)]} \tag{53}$$

$$\mathrm{R}_s = \frac{\tilde{\Phi}_s}{\tilde{\Phi}} = \frac{\left[\left(1-\frac{2}{r}\right)p^{'} + \frac{1}{r}p_{c(us)}^{'}\right]^2 - \left(p^{'} - \frac{1}{r}p_{c(us)}^{'}\right)^2}{\left[\left(1-\frac{2}{r}\right)p^{'} + \frac{1}{r}p_{c(us)}^{'}\right]^2 + \frac{1}{r}p_{c(us)}^{'}\left(p^{'} - \frac{1}{r}p_{c(us)}^{'}\right)\exp[-\beta(1-S_r)]} \tag{54}$$

$$\mathrm{R}_h = \frac{\tilde{\Phi}_h}{\tilde{\Phi}} = \frac{\left(p^{'} - \frac{1}{r}p_{c(us)}^{'}\right)^2[1 - \exp[-\beta(1-S_r)]]}{\left[\left(1-\frac{2}{r}\right)p^{'} + \frac{1}{r}p_{c(us)}^{'}\right]^2 + \frac{1}{r}p_{c(us)}^{'}\left(p^{'} - \frac{1}{r}p_{c(us)}^{'}\right)\exp[-\beta(1-S_r)]} \tag{55}$$

For $S_r = 1$, we have $\mathrm{R}_h = 0$ indicating purely mechanical dissipation under saturated condition. At critical state where $p^{'} = p_{c(us)}^{'}/r$, volumetric and hydraulic energy dissipations totally vanish, reflecting the fact that the total energy dissipation is fully governed by only the sliding of soil grains. These dissipation properties will be further illustrated using experimental data later in Section 5.3.

3. Numerical implementation

For implementation purpose, the model descriptions can be summarized and rewritten in tensorial form as follows.

The stress-strain and suction-saturation relationships:

$$\dot{\sigma_{ij}} = D_{ijkl}^e(\varepsilon_{kl} - \varepsilon_{kl}^p) \tag{56}$$

$$s^* = (p_u + s_0^*)\exp\left\{\frac{S_{r0} + [(-S_r) - (-S_r^p)]}{\kappa_h}\right\} - p_u \tag{57}$$

where ε_{ij}^p is the plastic strain tensor and D_{ijkl}^e is the pressure-dependent elastic stiffness tensor of the following form:

$$D_{ijkl}^e = \left(\frac{p^{'}}{\kappa} - \frac{2}{3}G\right)\delta_{ij}\delta_{kl} + G\left(\delta_{ik}\delta_{jl} + \delta_{il}\delta_{jk}\right) \tag{58}$$

The yield function and evolution rules:

$$y=\frac{\left(p^{'}-\frac{1}{r}p^{'}_{c(us)}\right)^{2}}{\left[\left(1-\frac{2}{r}\right)p^{'}+\frac{1}{r}p^{'}_{c(us)}\right]^{2}}+\frac{q^{2}}{\left[(1-\alpha)p^{'}+\frac{\alpha}{r}p^{'}_{c(us)}\right]^{2}M^{2}}-1\leq 0 \tag{59}$$

$$\dot{\varepsilon}^{p}_{ij}=\dot{\lambda}_{p}\frac{\partial y^{*}}{\partial\chi_{ij}}=\dot{\lambda}_{p}\left(\frac{\partial y^{*}}{\partial\chi_{\nu}}\frac{\partial\chi_{\nu}}{\partial\chi_{ij}}+\frac{\partial y^{*}}{\partial\chi_{s}}\frac{\partial\chi_{s}}{\partial\chi_{ij}}\right) \tag{60}$$

$$-\dot{S}^{p}_{r}=\dot{\lambda}_{p}\frac{\partial y^{*}}{\partial\chi_{h}}=\dot{\lambda}_{p}\frac{2\left(p^{'}-\frac{1}{r}p^{'}_{c(us)}\right)^{2}}{(s^{*}-p_{b})\left[\left(1-\frac{2}{r}\right)p^{'}+\frac{1}{r}p^{'}_{c(us)}\right]^{2}}[1-\exp[-\beta(1-S_{r})]] \tag{61}$$

where $p^{'}_{c(us)}$ has been defined in Eqs. (38-40), and $\chi_{\nu}=p^{'}$, $\chi_{s}=q$, $\chi_{h}=s^{*}-p_{b}$, and $\frac{\partial y^{*}}{\partial\chi_{\nu}}$ and $\frac{\partial y^{*}}{\partial\chi_{s}}$ are in Eqs. (45) and (46).

3.1. Coupled hydro-mechanical tangent stiffness tensor

From Eqs. (56) and (57), the incremental forms of effective stress tensor $\dot{\sigma}^{'}_{ij}$ and modified suction $\dot{s}^{*}$ can be described as:

$$\dot{\sigma}^{'}_{ij}=D^{e}_{ijkl}(\dot{\varepsilon}_{kl}-\dot{\varepsilon}^{p}_{kl}) \tag{62}$$

$$\dot{s}^{*}=\frac{(s^{*}+p_{u})}{\kappa_{h}}\left[(-\dot{S}_{r})-\left(-\dot{S}^{p}_{r}\right)\right] \tag{63}$$

Using the yield function in Eq. (59), we can write the following consistency condition:

$$\dot{y}=\frac{\partial y}{\partial\sigma^{'}_{ij}}\dot{\sigma}^{'}_{ij}+\frac{\partial y}{\partial p^{'}_{c(us)}}\dot{p}^{'}_{c(us)}=\frac{\partial y}{\partial\sigma^{'}_{ij}}\dot{\sigma}^{'}_{ij}+\frac{\partial y}{\partial p^{'}_{c(us)}}\frac{\partial p^{'}_{c(us)}}{\partial s^{*}}\dot{s}^{*}+\frac{\partial y}{\partial p^{'}_{c(us)}}\frac{\partial p^{'}_{c(us)}}{\partial p^{'}_{c}}\frac{\partial p^{'}_{c}}{\partial\varepsilon^{p}_{\nu}}\dot{\varepsilon}^{p}_{\nu}=0 \tag{64}$$

where explicit forms of $\frac{\partial y}{\partial\sigma^{'}_{ij}}$, $\frac{\partial y}{\partial p^{'}_{c(us)}}$, $\frac{\partial p^{'}_{c(us)}}{\partial p^{'}_{c}}$ and $\frac{\partial p^{'}_{c(us)}}{\partial s^{*}}$ are detailed in Appendix F.

Substituting Eqs. (60-63) in Eq. (64), we get:

$$\frac{\partial y}{\partial\sigma^{'}_{ij}}D^{e}_{ijkl}\left(\dot{\varepsilon}_{kl}-\dot{\lambda}_{p}\frac{\partial y^{*}}{\partial\chi_{kl}}\right)+\frac{\partial y}{\partial p^{'}_{c(us)}}\frac{\partial p^{'}_{c(us)}}{\partial s^{*}}\frac{(s^{*}+p_{u})}{\kappa_{h}}\left[(-\dot{S}_{r})-\dot{\lambda}_{p}\frac{\partial y^{*}}{\partial\chi_{h}}\right]+\frac{\partial y}{\partial p^{'}_{c(us)}}\frac{\partial p^{'}_{c(us)}}{\partial p^{'}_{c}}\frac{p^{'}_{c}}{(\lambda-\kappa)}\dot{\lambda}_{p}\frac{\partial y^{*}}{\partial\chi_{\nu}}=0 \tag{65}$$

Given $\dot{\varepsilon}_{kl}$ and $\dot{S}_{r}$, the multiplier $\dot{\lambda}_{p}$ can be obtained from Eq. (65) in the following form:

$$\dot{\lambda}_{p}=M_{kl}\dot{\varepsilon}_{kl}+H(-\dot{S}_{r}) \tag{66}$$

where

$$M_{kl}=\frac{D^{e}_{ijkl}\frac{\partial y}{\partial\sigma^{'}_{ij}}}{\left(\frac{\partial y}{\partial\sigma^{'}_{ij}}\right)^{T}D^{e}_{ijkl}\frac{\partial y^{*}}{\partial\chi_{kl}}+\frac{\partial y}{\partial p^{'}_{c(us)}}\frac{\partial p^{'}_{c(us)}}{\partial s^{*}}\frac{(s^{*}+p_{u})}{\kappa_{h}}\frac{\partial y^{*}}{\partial\chi_{h}}-\frac{\partial y}{\partial p^{'}_{c(us)}}\frac{\partial p^{'}_{c(us)}}{\partial p^{'}_{c}}\frac{p^{'}_{c}}{(\lambda-\kappa)}\frac{\partial y^{*}}{\partial\chi_{\nu}}} \tag{67}$$

$$H=\frac{\frac{(s^{*}+p_{u})}{\kappa_{h}}\frac{\partial y}{\partial p^{'}_{c(us)}}\frac{\partial p^{'}_{c(us)}}{\partial s^{*}}}{\left(\frac{\partial y}{\partial\sigma^{'}_{ij}}\right)^{T}D^{e}_{ijkl}\frac{\partial y^{*}}{\partial\chi_{kl}}+\frac{\partial y}{\partial p^{'}_{c(us)}}\frac{\partial p^{'}_{c(us)}}{\partial s^{*}}\frac{(s^{*}+p_{u})}{\kappa_{h}}\frac{\partial y^{*}}{\partial\chi_{h}}-\frac{\partial y}{\partial p^{'}_{c(us)}}\frac{\partial p^{'}_{c(us)}}{\partial p^{'}_{c}}\frac{p^{'}_{c}}{(\lambda-\kappa)}\frac{\partial y^{*}}{\partial\chi_{\nu}}} \tag{68}$$

By substituting Eq. (66) into Eqs. (62) and (63), the incremental coupled hydro-mechanical relationships can be written as:

$$\dot{\sigma}^{'}_{ij}=D^{e}_{ijkl}\left\{\dot{\varepsilon}_{kl}-[M_{kl}\dot{\varepsilon}_{kl}+H(-\dot{S}_{r})]\frac{\partial y^{*}}{\partial\chi_{kl}}\right\} \tag{69}$$

$$\dot{s}^{*}=\frac{(s^{*}+p_{u})}{\kappa_{h}}\left\{(-\dot{S}_{r})-[M_{kl}\dot{\varepsilon}_{kl}+H(-\dot{S}_{r})]\frac{\partial y^{*}}{\partial\chi_{h}}\right\} \tag{70}$$

We can rewrite Eqs. (69) and (70) as:

$$\dot{\sigma}'_{ij} = \left[D^e_{ijkl}\left(1 - M_{kl}\frac{\partial y^*}{\partial \chi_{kl}}\right)\right]\dot{\varepsilon}_{kl} + \left(-D^e_{ijkl}H\frac{\partial y^*}{\partial \chi_{kl}}\right)(-\dot{S}_r) = \Lambda_{ijkl}\dot{\varepsilon}_{kl} + \Pi_{ij}(-\dot{S}_r) \tag{71}$$

$$\dot{s}^* = \left[-\frac{(s^* + p_u)}{\kappa_h}\frac{\partial y^*}{\partial \chi_h}M_{kl}\right]\dot{\varepsilon}_{kl} + \left[\frac{(s^* + p_u)}{\kappa_h}\left(1 - H\frac{\partial y^*}{\partial \chi_h}\right)\right](-\dot{S}_r) = \Omega_{kl}\,\dot{\varepsilon}_{kl} + \Upsilon(-\dot{S}_r) \tag{72}$$

in which $\Lambda_{ijkl}, \Pi_{ij}, \Omega_{kl}$ and Υ are terms of the tangent stiffness tensor expressed in terms of σ'_{ij} and s^*:

$$\Lambda_{ijkl} = D^e_{ijkl}\left(1 - M_{kl}\frac{\partial y^*}{\partial \chi_{kl}}\right) \tag{73}$$

$$\Pi_{ij} = -D^e_{ijkl}H\frac{\partial y^*}{\partial \chi_{kl}} \tag{74}$$

$$\Omega_{kl} = -\frac{(s^* + p_u)}{\kappa_h}\frac{\partial y^*}{\partial \chi_h}M_{kl} \tag{75}$$

$$\Upsilon = \frac{(s^* + p_u)}{\kappa_h}\left(1 - H\frac{\partial y^*}{\partial \chi_h}\right) \tag{76}$$

Alternatively, the above incremental coupled hydro-mechanical relationships in Eqs. (71) and (72) can also be expressed in terms of net stress $\overline{\sigma}_{ij}$ and suction s. To do that, the constitutive relationships Eqs. (62) and (63) can be rewritten using Bishop's effective stress ($\sigma'_{ij} = \overline{\sigma}_{ij} + S_r s\delta_{ij}$) and modified suction ($s^* = s\phi$), as:

$$\dot{\overline{\sigma}}_{ij} = \dot{\sigma}'_{ij} - s\dot{S}_r\delta_{ij} - S_r\dot{s}\delta_{ij} \tag{77}$$

$$\dot{s} = \frac{1}{\phi}(\dot{s}^* - s\dot{\phi}) = \frac{1}{\phi}\left(\dot{s}^* + s\delta_{kl}\dot{\varepsilon}_{kl}\right) \tag{78}$$

Substituting Eqs. (71) and (72) in the above equations, we obtain:

$$\dot{\overline{\sigma}}_{ij} = \left[\Lambda_{ijkl} - \frac{S_r\delta_{ij}\,(\overline{\Omega}_{kl} + s\delta_{kl})}{\phi}\right]\dot{\varepsilon}_{kl} + \left[\Pi_{ij} + \left(s - \frac{S_r\Upsilon}{\phi}\right)\delta_{ij}\right]\left(-\dot{S}_r\right) = \overline{\Lambda}_{ijkl}\dot{\varepsilon}_{kl} + \overline{\Pi}_{ij}\left(-\dot{S}_r\right) \tag{79}$$

$$\dot{s} = \left[\frac{(\Omega_{kl} + s\delta_{kl})}{\phi}\right]\dot{\varepsilon}_{kl} + \left(\frac{\Upsilon}{\phi}\right)\left(-\dot{S}_r\right) = \overline{\Omega}_{kl}\,\dot{\varepsilon}_{kl} + \overline{\Upsilon}\left(-\dot{S}_r\right) \tag{80}$$

with $\overline{\Lambda}_{ijkl} = \Lambda_{ijkl} - \frac{S_r\delta_{ij}\,(\overline{\Omega}_{kl}+s\delta_{kl})}{\phi}$; $\overline{\Pi}_{ij} = \Pi_{ij} + \left(s - \frac{S_r\Upsilon}{\phi}\right)\delta_{ij}$; $\overline{\Omega}_{kl} = \frac{(\Omega_{kl}+s\delta_{kl})}{\phi}$ and $\overline{\Upsilon} = \frac{\Upsilon}{\phi}$ expressed in terms of net stress $\overline{\sigma}_{ij}$ and suction s.

As can be seen in Eqs. (71) and (72) (or alternatively, Eqs. (79) and (80)), the cross-coupling terms Π_{ij}, and Ω_{kl} indicate the inter-dependence between mechanical and hydraulic responses. As a consequence, the water retention curve (or SWCC; Eq. (80)) is path-

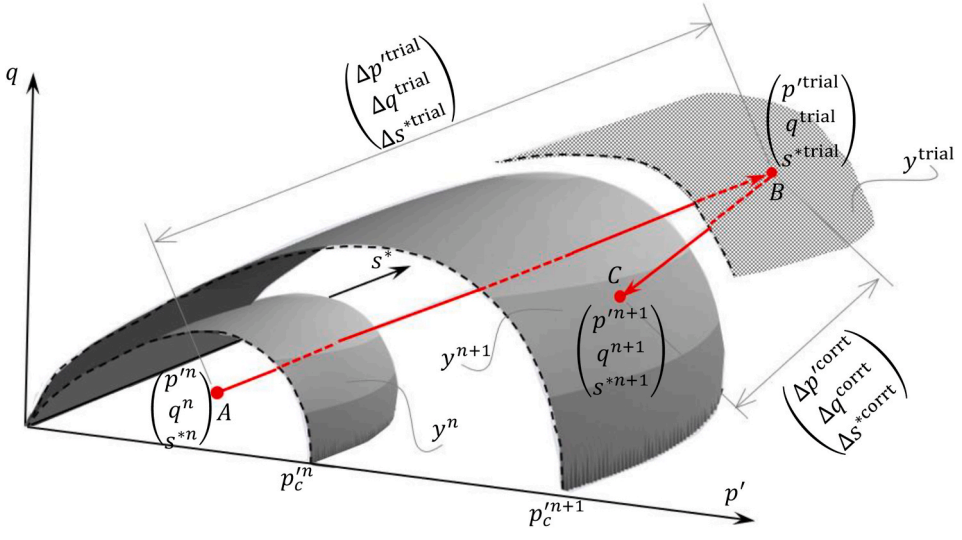

Fig. 4. Schematic representation of the stress update algorithm in three-dimensional space.

dependent, governed by both states (stress, and suction) and hydro-mechanical loading paths. This path-dependence nature of both mechanical and hydraulic responses induces different responses under wetting/drying and mechanical loading conditions, reflecting the inseparable nature of the coupling rooting from grain scale interactions. These are the key characteristics of the proposed model that are advanced from existing models in the literature.

3.2. Semi-implicit stress return algorithm

The semi-implicit stress return algorithm is employed in this constitutive model for the stress and suction update, given the input total strain $\Delta\varepsilon_{kl}$ and saturation degree $(-\Delta S_r)$ increments. This method is to compute and correct trial stress back onto the yield surface if it is located outside of the yield surface (Crisfield, 1993). As illustrated in Fig. 4, in the first step of this algorithm, the values of effective stress $(\sigma_{ij}^{'\text{trial}})$ and modified suction $(s^{*\text{trial}})$ at trial state (see Fig. 4) are calculated from the effective stress tensor $(\sigma_{ij}^{'n})$ and modified suction (s^{*n}) at step n, respectively.

$$\sigma_{ij}^{'\text{trial}} = \sigma_{ij}^{'n} + \Delta\sigma_{ij}^{'\text{trial}} = \sigma_{ij}^{'n} + D_{ijkl}^{en}\Delta\varepsilon_{kl} \tag{81}$$

$$s^{*\text{trial}} = s^{*n} + \Delta s^{*\text{trial}} = s^{*n} + \frac{(s^{*n}+p_u)}{\kappa_h}(-\Delta S_r) \tag{82}$$

in which the D_{ijkl}^{en} denotes secant elastic stiffness evaluated at state n.

If yielding takes place, e.g. $y^{\text{trial}}(\sigma_{ij}^{'\text{trial}}, s^{*\text{trial}}, p_c^{'}) > 0$ (see Fig. 4), a first-order Taylor expansion is applied to the yield function at trial point B (see Fig. 4), resulting in

$$y^{\text{new}} = y^{\text{trial}} + \Delta\sigma_{ij}^{'\text{corrt}}\frac{\partial y}{\partial\sigma_{ij}^{'}}\Big|^{\text{trial}} + \Delta s^{*\text{corrt}}\frac{\partial y}{\partial p_{c(us)}^{'}}\frac{\partial p_{c(us)}^{'}}{\partial s^{*}}\Big|^{\text{trial}} + \Delta\varepsilon_{\nu}^{p}\frac{p_c^{'}}{(\lambda-\kappa)}\frac{\partial y}{\partial p_{c(us)}^{'}}\frac{\partial p_{c(us)}^{'}}{\partial p_c^{'}}\Big|^{\text{trial}} \tag{83}$$

where $\Delta\sigma_{ij}^{'\text{corrt}}$ and $\Delta s^{*\text{corrt}}$ (see Fig. 4) are the corrective terms to effective stress tensor and modified suction, respectively, in the following form, given $\Delta\varepsilon_{kl}$ and $(-\Delta S_r)$ have been applied to move from points A to B (see Fig. 4):

$$\Delta\sigma_{ij}^{'\text{corrt}} = \sigma_{ij}^{'n+1} - \sigma_{ij}^{'\text{trial}} = -D_{ijkl}^{en}\Delta\varepsilon_{kl}^{p} \tag{84}$$

$$\Delta s^{*\text{corrt}} = s^{*n+1} - s^{*\text{trial}} = -\frac{(s^{*n}+p_u)}{\kappa_h}\left(-\Delta S_r^{p}\right) \tag{85}$$

With the use of flow rules in Eqs. (60) and (61), substitution of Eqs. (84) and (85) into Eq. (83) leads to:

$$y^{\text{new}} = y^{\text{trial}} - D_{ijkl}^{en}\Delta\lambda_p\frac{\partial y^{*}}{\partial\chi_{kl}}\frac{\partial y}{\partial\sigma_{ij}^{'}}\Big|^{\text{trial}} - \frac{(s^{*n}+p_u)}{\kappa_h}\Delta\lambda_p\frac{\partial y^{*}}{\partial\chi_h}\frac{\partial y}{\partial p_{c(us)}^{'}}\frac{\partial p_{c(us)}^{'}}{\partial s^{*}}\Big|^{\text{trial}} + \frac{p_c^{'}}{(\lambda-\kappa)}\Delta\lambda_p\frac{\partial y^{*}}{\partial\chi_{\nu}}\frac{\partial y}{\partial p_{c(us)}^{'}}\frac{\partial p_{c(us)}^{'}}{\partial p_c^{'}}\Big|^{\text{trial}} \tag{86}$$

Enforcing the yield condition $y^{\text{new}} = 0$ results in the plasticity multiplier $\Delta\lambda_p$ as:

$$\Delta\lambda_p = \frac{y^{\text{trial}}}{\left(\frac{\partial y}{\partial\sigma_{ij}^{'}}\right)^{T} D_{ijkl}^{en}\frac{\partial y^{*}}{\partial\chi_{kl}}\Big|^{\text{trial}} + \frac{\partial y}{\partial p_{c(us)}^{'}}\frac{\partial p_{c(us)}^{'}}{\partial s^{*}}\frac{(s^{*n}+p_u)}{\kappa_h}\frac{\partial y^{*}}{\partial\chi_h}\Big|^{\text{trial}} - \frac{\partial y}{\partial p_{c(us)}^{'}}\frac{\partial p_{c(us)}^{'}}{\partial p_c^{'}}\frac{p_c^{'}}{(\lambda-\kappa)}\frac{\partial y^{*}}{\partial\chi_{\nu}}\Big|^{\text{trial}}} \tag{87}$$

Once $\Delta\lambda_p$ is obtained, the new increments of effective stress tensor $(\Delta\sigma_{ij}^{'})$ and modified suction (Δs^{*}) can be obtained as follows:

$$\Delta\sigma_{ij}^{'} = \Delta\sigma_{ij}^{'\text{trial}} + \Delta\sigma_{ij}^{'\text{corrt}} \tag{88}$$

$$\Delta s^{*} = \Delta s^{*\text{trial}} + \Delta s^{*\text{corrt}} \tag{89}$$

These increments are then used to update the effective stress tensors and modified suction, or alternatively net stress tensor and matric suction:

$$\sigma_{ij}^{'n+1} = \sigma_{ij}^{'n} + \Delta\sigma_{ij}^{'} \tag{90}$$

$$s^{*n+1} = s^{*n} + \Delta s^{*} \tag{91}$$

$$\overline{\sigma}_{ij}^{n+1} = \sigma_{ij}^{'n+1} - S_r^{n+1}s^{n+1}\delta_{ij} \tag{92}$$

$$s^{n+1} = \frac{s^{*n+1}}{\phi^{n+1}} \tag{93}$$

where ϕ^{n+1} and S_r^{n+1} are updated porosity and saturation degree, respectively.

It is noted that the present investigation is based on infinitesimal strain assumption and focuses on the constitutive behaviour (equivalent to a single integration point). This is the first and essential step in formulating and validating a constitutive model, as has been widely adopted and followed in the literature. In numerical simulations using the Finite Element Method (FEM), or Smoothed Particle Hydrodynamic (SPH), the infinitesimal sizes of strain-like increments cannot always be guaranteed, and hence sub-stepping in combination with this semi-implicit algorithm or full implicit stress return should be used (Nguyen and Einav, 2009). All these algorithms have been tested on different advanced models for geomaterials (Nguyen and Einav, 2009) and can be applied to this unsaturated soil model in the future.

3.3. An algorithm for mixed-control loading

An algorithm is developed for mixed-control loading where some components of stress, strain and suction are used to control the loading. An example based on suction-controlled triaxial test is used to demonstrate the performance of such an algorithm. In this case, net confining pressures and suction are fixed at constant imposed levels of $\overline{\sigma}_{22(\mathrm{i})} = \overline{\sigma}_{33(\mathrm{i})}$ and $s_{(\mathrm{i})}$, respectively. The difference between the imposed and computed quantities can be written as a residual vector as follows:

$$\mathbf{res} = \begin{pmatrix} \overline{\sigma}_{22} \\ \overline{\sigma}_{33} \\ s \end{pmatrix} - \begin{pmatrix} \overline{\sigma}_{22(\mathrm{i})} \\ \overline{\sigma}_{33(\mathrm{i})} \\ s_{(\mathrm{i})} \end{pmatrix} \tag{94}$$

Given constant lateral net stress and constant suction imposed, the first order Taylor expansion of the residual in Eq. (94) at the previous state is:

$$\mathbf{res}^{\mathrm{new}} = \mathbf{res}^{\mathrm{previous}} + \begin{pmatrix} \delta\overline{\sigma}_{22} \\ \delta\overline{\sigma}_{33} \\ \delta s \end{pmatrix} \tag{95}$$

in which

$$\mathbf{res}^{\mathrm{previous}} = \begin{pmatrix} \overline{\sigma}_{22}^{\mathrm{previous}} \\ \overline{\sigma}_{33}^{\mathrm{previous}} \\ s^{\mathrm{previous}} \end{pmatrix} - \begin{pmatrix} \overline{\sigma}_{22(\mathrm{i})} \\ \overline{\sigma}_{33(\mathrm{i})} \\ s_{(\mathrm{i})} \end{pmatrix} \tag{96}$$

is the residual vector computed at the previous state.

The constitutive relationship in Eqs. (79) and (80) can be rewritten in the below form of the Voigt notations:

$$\begin{pmatrix} \delta\overline{\sigma}_{11} \\ \delta\overline{\sigma}_{22} \\ \delta\overline{\sigma}_{33} \\ \delta\overline{\sigma}_{12} \\ \delta\overline{\sigma}_{23} \\ \delta\overline{\sigma}_{31} \\ \delta s \end{pmatrix} = \begin{bmatrix} \overline{\Lambda}_{1111} & \overline{\Lambda}_{1122} & \overline{\Lambda}_{1133} & \overline{\Lambda}_{1112} & \overline{\Lambda}_{1123} & \overline{\Lambda}_{1131} & \overline{\Pi}_{11} \\ \overline{\Lambda}_{2211} & \overline{\Lambda}_{2222} & \overline{\Lambda}_{2233} & \overline{\Lambda}_{2212} & \overline{\Lambda}_{2223} & \overline{\Lambda}_{2231} & \overline{\Pi}_{22} \\ \overline{\Lambda}_{3311} & \overline{\Lambda}_{3322} & \overline{\Lambda}_{3333} & \overline{\Lambda}_{3312} & \overline{\Lambda}_{3323} & \overline{\Lambda}_{3331} & \overline{\Pi}_{33} \\ \overline{\Lambda}_{1211} & \overline{\Lambda}_{1222} & \overline{\Lambda}_{1233} & \overline{\Lambda}_{1212} & \overline{\Lambda}_{1223} & \overline{\Lambda}_{1231} & \overline{\Pi}_{12} \\ \overline{\Lambda}_{2311} & \overline{\Lambda}_{2322} & \overline{\Lambda}_{2333} & \overline{\Lambda}_{2312} & \overline{\Lambda}_{2323} & \overline{\Lambda}_{2331} & \overline{\Pi}_{23} \\ \overline{\Lambda}_{3111} & \overline{\Lambda}_{3122} & \overline{\Lambda}_{3133} & \overline{\Lambda}_{3112} & \overline{\Lambda}_{3123} & \overline{\Lambda}_{3131} & \overline{\Pi}_{31} \\ \overline{\Omega}_{11} & \overline{\Omega}_{22} & \overline{\Omega}_{33} & \overline{\Omega}_{12} & \overline{\Omega}_{23} & \overline{\Omega}_{31} & \overline{Y} \end{bmatrix} \begin{pmatrix} \delta\varepsilon_{11} \\ \delta\varepsilon_{22} \\ \delta\varepsilon_{33} \\ \delta\varepsilon_{12} \\ \delta\varepsilon_{23} \\ \delta\varepsilon_{31} \\ -\delta S_r \end{pmatrix} \tag{97}$$

From Eq. (97), after some mathematical manipulations, we obtain:

$$\begin{pmatrix} \delta\overline{\sigma}_{22} \\ \delta\overline{\sigma}_{33} \\ \delta s \end{pmatrix} = \begin{bmatrix} \overline{\Lambda}_{2211} & \overline{\Lambda}_{2212} & \overline{\Lambda}_{2223} & \overline{\Lambda}_{2231} \\ \overline{\Lambda}_{3311} & \overline{\Lambda}_{3312} & \overline{\Lambda}_{3323} & \overline{\Lambda}_{3331} \\ \overline{\Omega}_{11} & \overline{\Omega}_{12} & \overline{\Omega}_{23} & \overline{\Omega}_{31} \end{bmatrix} \begin{pmatrix} \delta\varepsilon_{11} \\ \delta\varepsilon_{12} \\ \delta\varepsilon_{23} \\ \delta\varepsilon_{31} \end{pmatrix} + \begin{bmatrix} \overline{\Lambda}_{2222} & \overline{\Lambda}_{2233} & \overline{\Pi}_{22} \\ \overline{\Lambda}_{3322} & \overline{\Lambda}_{3333} & \overline{\Pi}_{33} \\ \overline{\Omega}_{22} & \overline{\Omega}_{33} & \overline{Y} \end{bmatrix} \begin{pmatrix} \delta\varepsilon_{22} \\ \delta\varepsilon_{33} \\ -\delta S_r \end{pmatrix} \tag{98}$$

Substituting Eq. (98) into Eq. (95) leads to:

$$\mathbf{res}^{\mathrm{new}} = \mathbf{res}^{\mathrm{previous}} + \begin{bmatrix} \overline{\Lambda}_{2211} & \overline{\Lambda}_{2212} & \overline{\Lambda}_{2223} & \overline{\Lambda}_{2231} \\ \overline{\Lambda}_{3311} & \overline{\Lambda}_{3312} & \overline{\Lambda}_{3323} & \overline{\Lambda}_{3331} \\ \overline{\Omega}_{11} & \overline{\Omega}_{12} & \overline{\Omega}_{23} & \overline{\Omega}_{31} \end{bmatrix} \begin{pmatrix} \delta\varepsilon_{11} \\ \delta\varepsilon_{12} \\ \delta\varepsilon_{23} \\ \delta\varepsilon_{31} \end{pmatrix} + \begin{bmatrix} \overline{\Lambda}_{2222} & \overline{\Lambda}_{2233} & \overline{\Pi}_{22} \\ \overline{\Lambda}_{3322} & \overline{\Lambda}_{3333} & \overline{\Pi}_{33} \\ \overline{\Omega}_{22} & \overline{\Omega}_{33} & \overline{Y} \end{bmatrix} \begin{pmatrix} \delta\varepsilon_{22} \\ \delta\varepsilon_{33} \\ -\delta S_r \end{pmatrix} \tag{99}$$

The requirement of $\mathbf{res}^{\mathrm{new}} = 0$ in Eq. (99) is enforced to obtain the incremental vector of $(\,\delta\varepsilon_{22} \quad \delta\varepsilon_{33} \quad -\delta S_r\,)^T$ as:

$$\begin{pmatrix} \delta\varepsilon_{22} \\ \delta\varepsilon_{33} \\ -\delta S_r \end{pmatrix} = \begin{bmatrix} \overline{\Lambda}_{2222} & \overline{\Lambda}_{2233} & \overline{\Pi}_{22} \\ \overline{\Lambda}_{3322} & \overline{\Lambda}_{3333} & \overline{\Pi}_{33} \\ \overline{\Omega}_{22} & \overline{\Omega}_{33} & \overline{Y} \end{bmatrix}^{-1} \left\{ -\mathbf{res}^{\mathrm{previous}} - \begin{bmatrix} \overline{\Lambda}_{2211} & \overline{\Lambda}_{2212} & \overline{\Lambda}_{2223} & \overline{\Lambda}_{2231} \\ \overline{\Lambda}_{3311} & \overline{\Lambda}_{3312} & \overline{\Lambda}_{3323} & \overline{\Lambda}_{3331} \\ \overline{\Omega}_{11} & \overline{\Omega}_{12} & \overline{\Omega}_{23} & \overline{\Omega}_{31} \end{bmatrix} \begin{pmatrix} \delta\varepsilon_{11} \\ \delta\varepsilon_{12} \\ \delta\varepsilon_{23} \\ \delta\varepsilon_{31} \end{pmatrix} \right\} \tag{100}$$

The obtained strain and saturation degree increments in Eq. (100) are then used to update stress and suction through the semi-

implicit algorithm in Section 3.2. The residual vector is used to assess the performance of the algorithm for mixed stress-strain control:

$$\left|\frac{res_1}{\overline{\sigma}_{22(\mathrm{i})}}\right| \leq \text{TOLERANCE} \text{ and } \left|\frac{res_2}{\overline{\sigma}_{33(\mathrm{i})}}\right| \leq \text{TOLERANCE} \text{ and } \left|\frac{res_3}{s_{(\mathrm{i})}}\right| \leq \text{TOLERANCE} \tag{101}$$

with TOLERANCE being a small positive number ($10^{-4} \div 10^{-3}$ is considered acceptable in our experience). The use of residual from previous step in the current step (see Eq. (100)), while avoiding iterations, helps obtain reasonable results for small enough increments and also removes issues of error accumulation. The numerical implementation and verification also include the following: (i) quantitative assessments at special conditions (e.g. at saturated condition when $s = 0$, $S_r = 1$ and $\frac{\Delta q}{\Delta p} = 3$, at critical state when $\Delta\varepsilon_v^p = 0$, $\Delta S_r^p = 0$ and $\Delta q = 0$ while $\Delta\varepsilon_s^p \neq 0$) (ii) controlling the residuals (see Eq. (101)), and (iii) verifications using different approaches (e.g. analytical solution).

3.4. Numerical verification

In this section, several numerical examples are performed to verify the proposed integration algorithm described in Section 3.2 and 3.3. The first example focuses on the effect of strain increment size ($\Delta\varepsilon_v$) on its numerical accuracy under drained isotropic compression condition. In this example, the following parameters are used: $\kappa = 0.02$; $\lambda = 0.11$; $\kappa_h = 1.1$; $p_R^{'} = 45.31$ kPa; $\mu = 0.15$; $\xi = 0.39$; $p_{c0}^{'} = 77.32$ kPa; $r = 3.704$; $\beta = 0.05$; $p_b = 80$ kPa. Five numerical simulations are carried out using five volumetric strain increments ($\Delta\varepsilon_v = 2\times10^{-6}; 2\times10^{-5}; 2\times10^{-4}; 2\times10^{-3}; 2\times10^{-2}$) with a constant suction of $s = 100$ kPa. They all are isotropically loaded from the initial net pressure of $\overline{p}_0 = 19.18$ kPa, specific volume of $\nu_0 = 1.732$ and saturation degree of $S_{r0} = 0.728$. Responses in $\overline{p} : \nu$ and $\nu : s$ are plotted in Fig. 5a and b, respectively. Also depicted in Fig. 5b are the relative errors $\left|\frac{s-s_{(\mathrm{i})}}{s_{(\mathrm{i})}}\right|$ between imposed and computed suctions. It can be seen in Fig. 5a that the algorithm in Section 3.3 performs well for small enough increments ($\Delta\varepsilon_v < 2\times10^{-3}$). Larger errors can be seen if the strain increments are high enough. However, the algorithm is stable, given no error accumulation and the steady decrease of error towards the end of the numerical test, despite no iterations were used, thanks to the use of residual control in the algorithm (Eq. (100)). Numerical solutions in suction-controlled test (see Fig. 5b) helps maintain constant suction of $s = 100$ kPa for strain increment within a reasonable range ($\Delta\varepsilon_v = 2\times10^{-6} \div 2\times10^{-4}$).

The performance of the proposed algorithm in Section 3.3 is also verified against a semi-analytical algorithm which uses the semi-implicit stress return algorithm in Section 3.2 combined with the analytical enforcement of constant suction condition (see Appendix G). We use $\Delta\varepsilon_v = 2\times10^{-6}$ and three different suction levels of 0; 25; 100 kPa corresponding to initial conditions of $\overline{p}_0 = 20.64; 19.01; 19.18$ kPa; $\nu_0 = 1.802; 1.792; 1.732$ and $S_{r0} = 1; 0.768; 0.728$, respectively. The same set of parameters in the previous example is adopted. At various suction levels ($s = 0, 25, 100$ kPa), ν and S_r are plotted against $\overline{p}$ in Fig. 6 to present the results obtained using both algorithms. For $s = 0$ the Unloading-Reloading Line (URL) and Normal Compression Line (NCL) are also plotted and considered analytical solution for the case of saturated behaviour. As indicated in Fig. 6, both numerical and semi-analytical solutions are identical, and they also coincide with the analytical result for the case of saturated behaviour ($s = 0$). These features highlight the numerical stability of the proposed stress return algorithm, and the effectiveness of the iterative algorithm to enforce constant suction condition.

For the triaxial shearing tests, our numerical implementations in this study are based on the tensorial stress ($\sigma_{ij}^{'}$-based algorithm). It is now assessed against a counterpart using mean effective and deviatoric stresses ($p^{'}, q$ - based algorithm). To do so, an example on the suction-controlled triaxial test is presented using the following model parameters: $\kappa = 0.006$; $\lambda = 0.09$; $M = 1.17$; $G = 7000$ kPa; $\kappa_h = 0.56$; $p_R^{'} = 140.41$ kPa; $\mu = 0.0229$; $\xi = 0.652$; $p_{c0}^{'} = 200$ kPa; $r = 1.818$; $\alpha = 0.5$; $\beta = 0.05$; $p_b = 70$ kPa. In this example, during shearing, the lateral net stress is kept constant at 100 kPa while suctions are fixed at 0, 100, and 300 kPa with $\nu_0 = 1.576$, 1.578, 1.576, and $S_{r0} = 1$, 0.4, 0.2 respectively. A small axial strain increment of $\Delta\varepsilon_{11} = 10^{-6}$ is used. Fig. 7 shows a good match between the two algorithms in terms of deviatoric stress, volumetric strain and saturation degree against the axial strain under a range

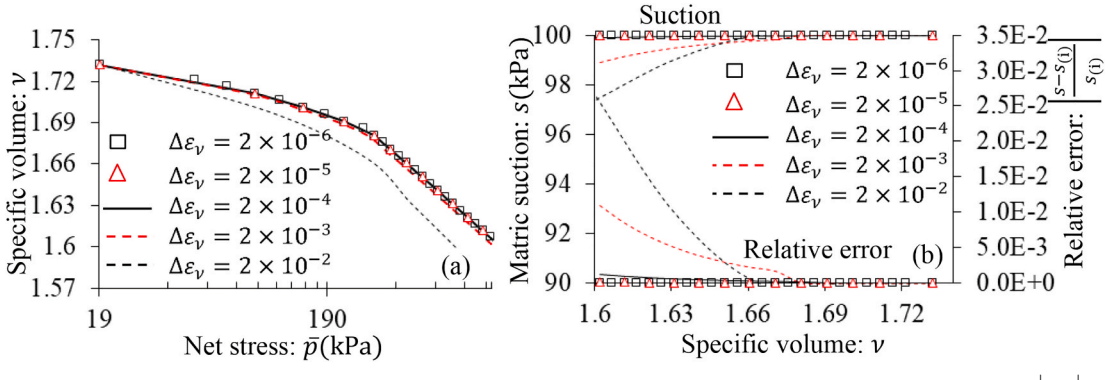

Fig. 5. Performance of the proposed stress update algorithm under different values of $\Delta\varepsilon_v$ (a) $\overline{p} - \nu$ and (b) $\nu - s$, $\nu - \left|\frac{s-s_{(\mathrm{i})}}{s_{(\mathrm{i})}}\right|$.

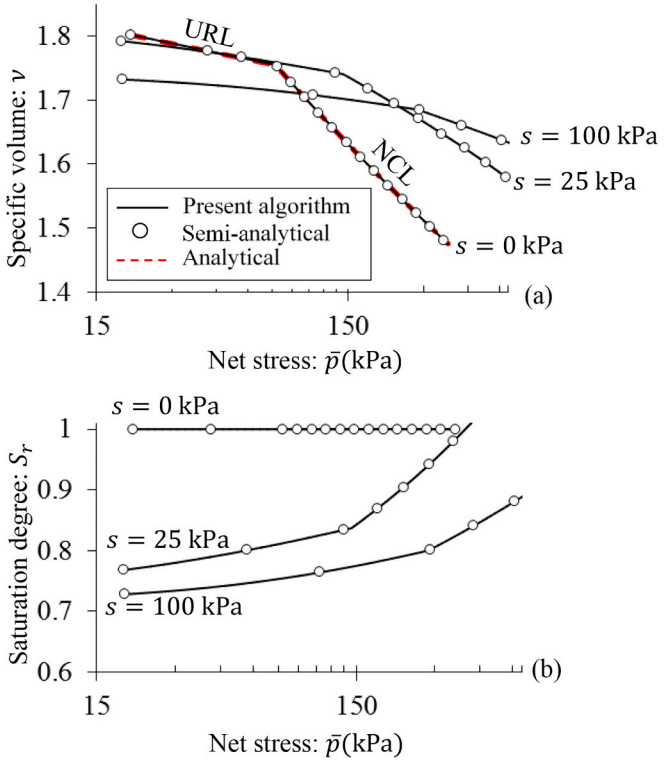

Fig. 6. Verification of the proposed stress update algorithms in isotropic compressions (a) $\bar{p}-\nu$ (b) $\bar{p}-S_r$.

of suction levels. For the case of zero suction, the behaviour of a critical state model (Collins, 2003) are also sketched in Fig. 7a and b, and match well with the numerical results produced by the proposed model. The results in Fig. 7 again verify the implementation and the capability of the model in handling transition between saturated and partially saturated conditions.

4. Model parameters

The proposed model possesses 13 parameters categorised into five groups, namely Group 1 ($\kappa, G, \lambda, p_{c0}^{'}, M$), Group 2 ($\kappa_h$), Group 3 ($p_R^{'}, \mu, \xi$), Group 4 ($r, \alpha$) and Group 5 ($\beta, p_b$). This section aims to provide details on the calibration of these model parameters, using a suction-controlled triaxial test on Bourke silt (Bourke silt-SCT, Uchaipichat, 2005; Uchaipichat and Khalili, 2009). A step by step approach is presented in which parameters in each group are calibrated using relevant sets of experimental data. An assessment of the model behaviour against experimental data, using the calibrated parameters, will then be provided at the end of the Section to demonstrate the effectiveness of the calibration.

In Group 1, parameters κ, G, λ, $p_{c0}^{'}$ and M are calibrated following the same procedure applicable to MCC for saturated soils. Particularly, by fitting the equations of NCL and URL to their experimental counterparts in the saturated state, κ, λ and $p_{c0}^{'}$ can be determined. Based on Eq. (29), G is estimated from the average gradients of the $\varepsilon_s - q$ plots obtained from laboratory shear tests. The ratio between effective mean and deviatoric stresses at ultimate state is used to determine M. For Bourke silt-SCT, $\kappa = 0.006;\ \lambda = 0.09;$ $p_{c0}^{'} = 200$ kPa; $M = 1.17$ (Uchaipichat, 2005) and $G = 7000$ kPa are found to match well with the experimental data on saturated state.

The parameter κ_h (Group 2) governs the $s : S_r$ relationship, and also affect the mechanical behaviour due to the hydro-mechanical coupling (see Eqs. (71) and (79)). Fig. 8 shows the best fit to the measured data using $\kappa_h = 0.16$ for drying tests under constant net mean stresses of 50 kPa, 100 kPa, 150 kPa and 200 kPa.

Parameters listed in Group 3 are to control the shape of the initial yield surface in the space of true stress and modified suction. These parameters ($p_R^{'}, \mu$ and ξ) play significant roles in generating the wetting/drying-induced collapse mechanism. Using a best fitting least-square procedure, they can be selected to make the LC curve in the $p^{'} : s^{*}$ plane fit with initial yield values of effective mean stress and modified suction provided by isotropic compression tests. Given $\kappa = 0.006;\ \lambda = 0.09;\ p_{c0}^{'} = 200$ kPa in Group 1, the following parameters are chosen for Group 3: $p_R^{'} = 140.41$ kPa; $\mu = 0.0229; \xi = 0.652$ to allow the initial $p^{'} : s^{*}$ yield curve to fit well with that from experimental data of Bourke silt-SCT, as illustrated in Fig. 9.

Parameters r and α in Group 4 govern the shear strength. We use $r = \exp[(N-\Gamma)/(\lambda-\kappa)]$ (Uchaipichat, 2005) as an empirical equation representing the spacing between NCL and CSL in the $p^{'} : \nu$ plane to estimate r, where N and Γ are reference specific volumes

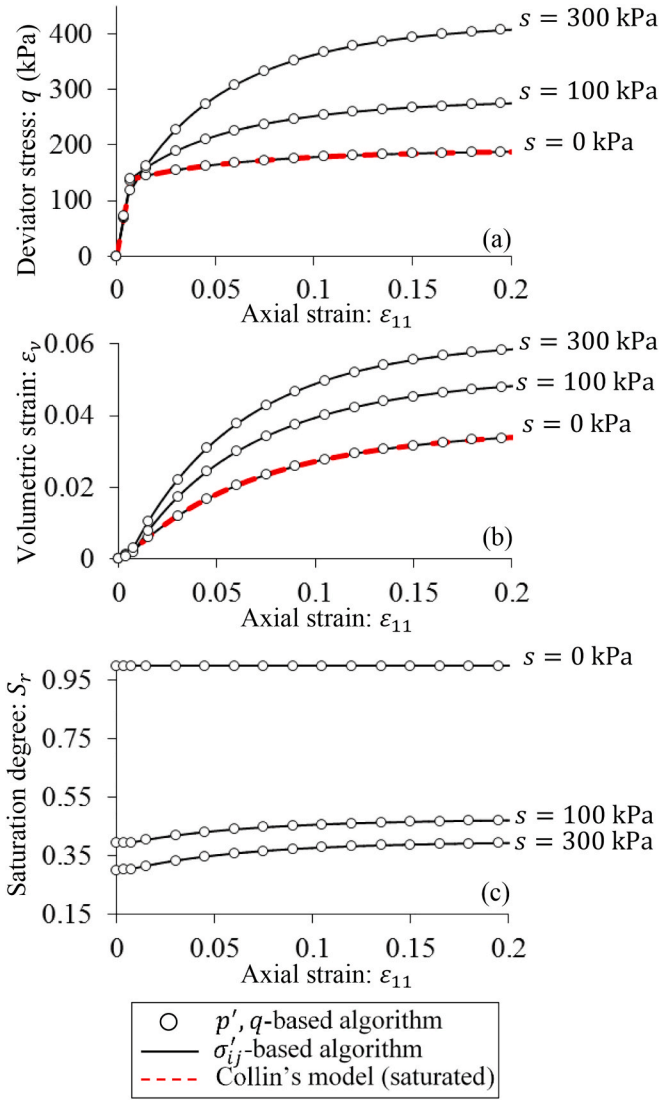

Fig. 7. Verification of the proposed stress update algorithms in triaxial compressions (a) $\varepsilon_{11} - q$ (b) $\varepsilon_{11} - \varepsilon_v$ and (c) $\varepsilon_{11} - S_r$.

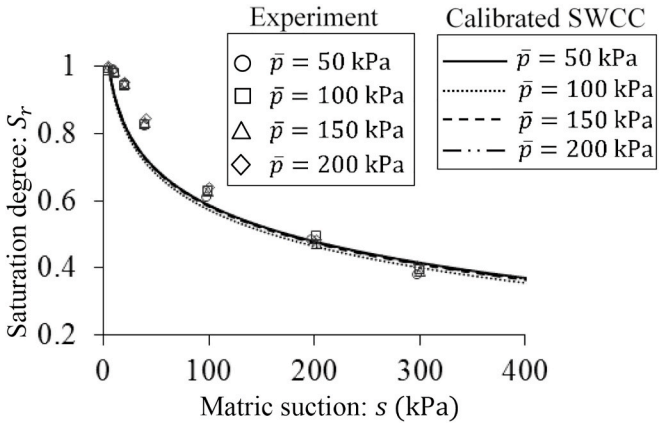

Fig. 8. Calibration of κ_h based on SWCC obtained from net pressure-controlled tests on Bourke silt (Uchaipichat, 2005; Uchaipichat and Khalili, 2009).

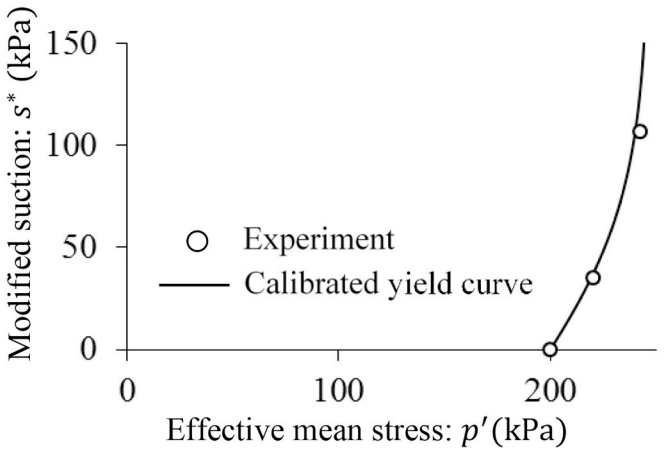

Fig. 9. Calibration of $p_R^{'}, \mu$ and ξ based on suction-controlled isotropic compression tests on Bourke silt (Uchaipichat, 2005; Uchaipichat and Khalili, 2009).

of NCL and CSL under saturated conditions, respectively. With $\kappa = 0.006; \lambda = 0.09, N = 2.0472$ and $\Gamma = 1.997$ given in the laboratory (Uchaipichat, 2005), r is estimated as 1.818 for Bourke silt-SCT. Once r is obtained, α can be determined by adjusting it until reaching a best-fit between predictive and measured data of initial yield surface in the $p^{'} : q$ space at $s = 0$ kPa. For example, Fig. 10a shows a good agreement between the experimental and theoretical results of Bourke silt-SCT for $\alpha = 0.5$. The calibrated initial yield surface of Bourke silt-SCT in $(p^{'}, q, s^{*})$ space is depicted in Fig. 10b.

Group 5 includes two parameters, β and p_b, both of which are only present in the flow rules (Eqs. (45) and (47)). Parameter β is a coupling parameter governing the effect of saturation degree on the proportion between $\dot{\varepsilon}_v^p$ and $\dot{\varepsilon}_s^p$, so-called plastic dilatancy ratio, while p_b influences the hydraulic dissipative generalised stress. Reducing p_b increases in the hydraulic energy lost and therefore affects the irrecoverable rate of saturation degree. We can calibrate β iteratively to achieve the best match in terms of the ratio $\dot{\varepsilon}_v^p / \dot{\varepsilon}_s^p$ between the experimental result and its theoretical counterpart obtained from Eqs. (45) and (46):

$$\frac{\dot{\varepsilon}_v^p}{\dot{\varepsilon}_s^p} = \frac{\left(p^{'} - \frac{1}{r}p_{c(us)}^{'}\right)\left[(1-\alpha)p^{'} + \frac{\alpha}{r}p_{c(us)}^{'}\right]^2 M^2}{q\left[\left(1-\frac{2}{r}\right)p^{'} + \frac{1}{r}p_{c(us)}^{'}\right]^2} \exp[-\beta(1-S_r)] \tag{102}$$

For simplicity, it is assumed that the elastic deformation is very small and hence the experimentally measured strains are approximately equal to plastic strains (Wong and Wong, 1975). For Bourke silt-SCT, the experimental result of shear test under $s =$ 100 kPa and $\overline{\sigma}_{33} = 100$ kPa is used. As illustrated in Fig. 11, the numerical results are in good agreement with experimental data for $\beta = 0.05$. After obtaining r and β, p_b can be calibrated using the following equation derived from Eqs. (45) and (47):

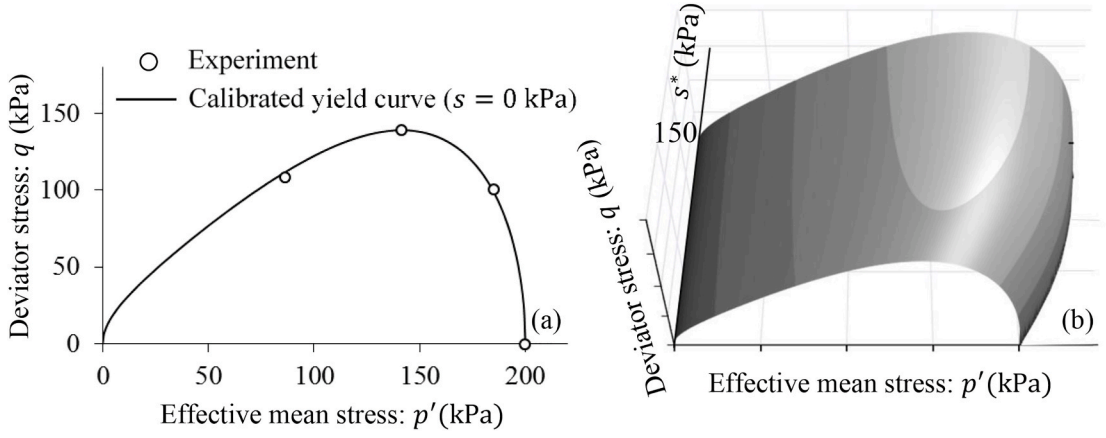

Fig. 10. Calibration of α based on suction-controlled triaxial tests on Bourke silt (Uchaipichat, 2005; Uchaipichat and Khalili, 2009) (a) $p^{'} - q$ (b) $p^{'} - q - s^{*}$.

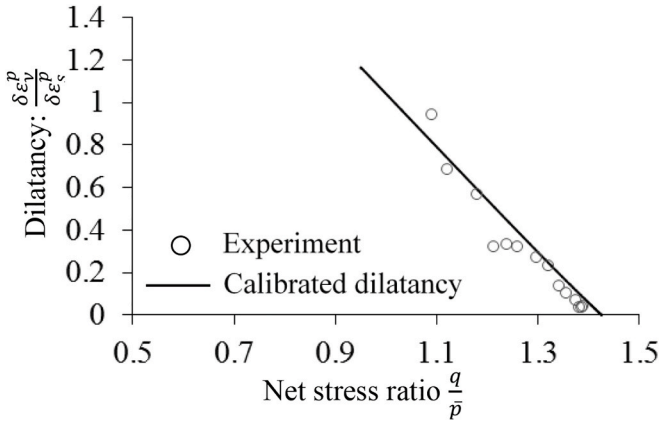

Fig. 11. Calibration of β based on dilatancy ratio obtained from suction-controlled triaxial tests on Bourke silt under $s = 100\ kPa$ and $\bar{\sigma}_{33} = 100\ kPa$ (Uchaipichat, 2005; Uchaipichat and Khalili, 2009).

$$p_b = s^* - \frac{[1-\exp[-\beta(1-S_r)]]}{\exp[-\beta(1-S_r)]}\left(p^{'} - \frac{1}{r}p_{c(us)}^{'}\right)\frac{\dot{\varepsilon}_v^p}{\left(-\dot{S}_r^p\right)} \tag{103}$$

where $\frac{\dot{\varepsilon}_v^p}{\left(-\dot{S}_r^p\right)} \approx \frac{\dot{\varepsilon}_v}{(-\dot{S}_r)}$ is assumed and variables $(p^{'}, s^*, \dot{\varepsilon}_v, \dot{S}_r, S_r)$ are collected from only a single isotropic compression test. Using Eq. (103), $p_b = 70$ kPa is obtained using the isotropic loading case with $s = 100$ kPa.

The calibrated parameters $\kappa = 0.006; \lambda = 0.09; \kappa_h = 0.16; p_R^{'} = 140.41$ kPa; $\mu = 0.0229; \xi = 0.652; p_{c0}^{'} = 200$ kPa; $r = 1.818; \beta = 0.05$ and $p_b = 70$ kPa result in good agreement with experiments on drained isotropic compression test at different suction levels ($s = 0$ kPa; 100 kPa and 300 kPa) (see Fig. 12).

5. Model behaviour and validation

This section is to present several examples to highlight the predictive capacity of the proposed model. The model performance is assessed against experimental results of both isotropic compression and triaxial shear tests under drained and undrained conditions.

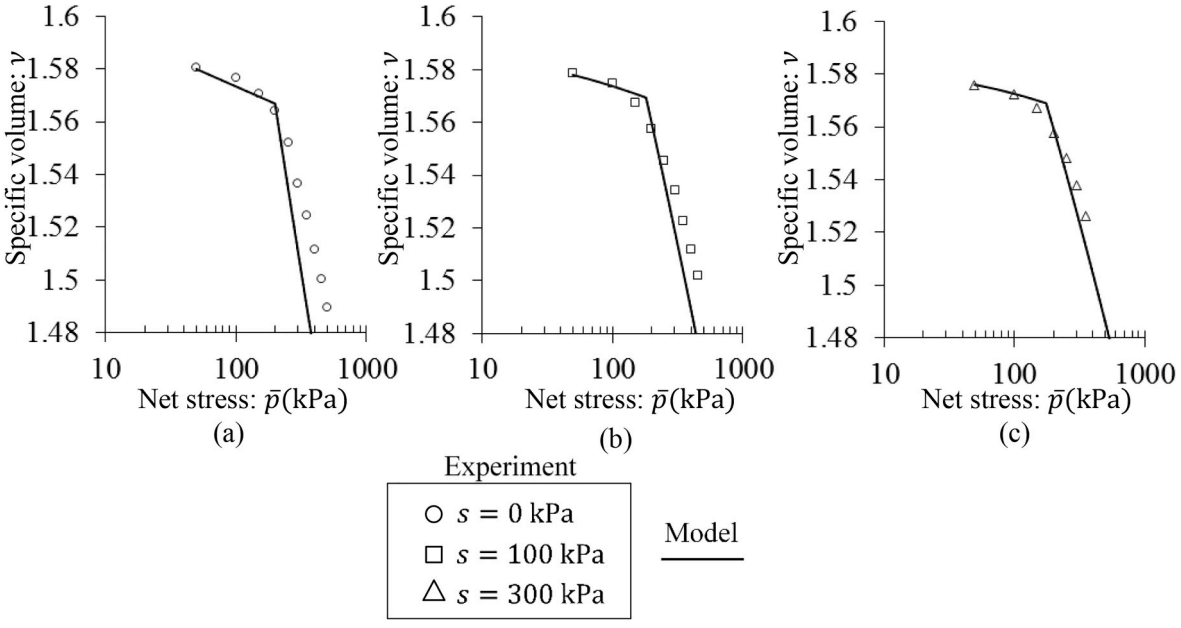

Fig. 12. Validation with drained isotropic compression tests on Bourke silt (after Uchaipichat, 2005; Uchaipichat and Khalili, 2009) (a) $s = 0$ kPa (b) $s = 100$ kPa (c) $s = 300$ kPa.

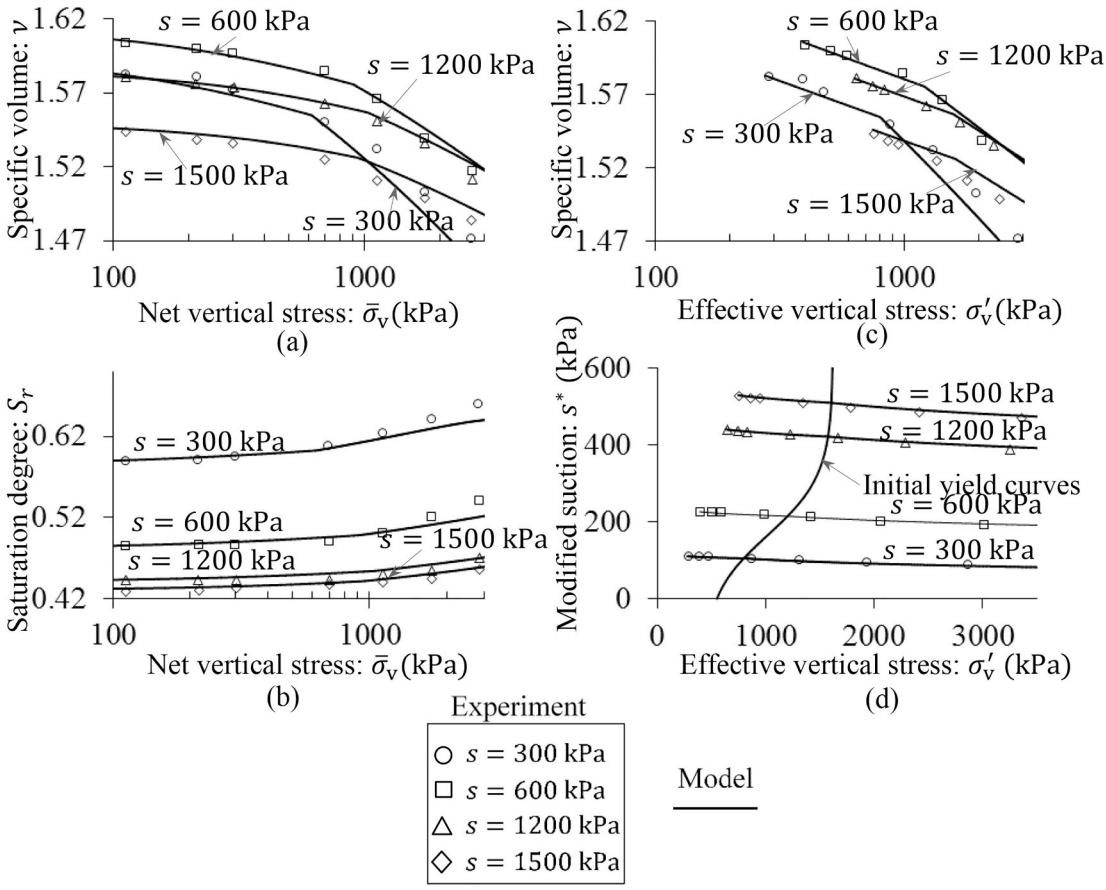

Fig. 13. Validation with drained oedometer tests on heavily compacted sand-bentonite mixture (after Sun et al., 2009; Sun and Sun, 2012) (a) $\bar{\sigma}_v - \nu$ (b) $\bar{\sigma}_v - S_r$ (c) $\sigma'_v - \nu$ (d) $\sigma'_v - s^*$.

5.1. Isotropic compression test

Heavily compacted sand-bentonite mixture, constant suction tests (Sun et al., 2009; Sun and Sun, 2012)

In the first example, we examine the drained oedometer test on heavily compacted sand-bentonite mixture with $p'_{c0} = 550$ kPa (Sun et al., 2009; Sun and Sun, 2012). The following parameters: $\kappa = 0.017$; $\lambda = 0.085$; $p'_R = 422.38$ kPa; $\mu = 0.0124$ and $\xi = 0.357$ are calibrated to best fit the initial yield curve in the $\sigma'_v : s^*$ plane. The data on $s = 600$ kPa is used to obtain $\kappa_h = 0.25$; $r = 1.299$; $\beta = 0.05$ and $p_b = 70$ kPa. The comparison between the model prediction and measured data at four suction levels of $s = 300$ kPa; 600 kPa; 1200 kPa and 1500 kPa is illustrated in Fig. 13.

The results show that the model is able to provide a good match to experimentally observed behaviour. In elastic regime, the $\sigma'_v : s^*$ stress paths are inside the yield surface (see Fig. 13d) and no change in the slope of the NCL in the (σ'_v, ν) plane is observed (see Fig. 13c) while in the $(\bar{\sigma}_v, \nu)$ plane (Fig. 13a) it is sensitive to the variation of suction. Once the stress path crosses the initial yield surface, the irreversible changes of both specific volume and saturation degree are triggered simultaneously. The initial yield stress is observed to increase when suction increases owing to the characteristic of wetting-induced hardening law in Eq. (38). The decrease of the NCL slope with increasing suction is attributed to the hydraulic effect on soil stiffness (see Eq. (40)). Furthermore, Fig. 13b demonstrates that a significant increase in saturation degree is captured although suction remains unchanged during loading. This is an indication that the mechanical effect on SWCC (Gallipoli et al., 2003; Nuth and Laloui, 2008) is taken into consideration in this model.

Fairbanks silt, constant water content tests (Zhang, 2016)

Next, the undrained isotropic compression test under constant gravimetric water content of $w = 8.3\%$ on Fairbanks silt (Zhang, 2016) is simulated. The parameters for this simulation are taken as follows: $\kappa = 0.006$; $\lambda = 0.026$; $\kappa_h = 0.05$; $p'_R = 206.78$ kPa; $\mu = 0.0157$; $\xi = 0.628$; $p'_{c0} = 250$ kPa; $r = 1.5$; $\beta = 0.1$; $p_b = 80$ kPa. In this example, the soil specimen is first loaded from A to B (phase 1), and from B ($\bar{p} = 300$ kPa), an unloading is then conducted ending at point C ($\bar{p} = 100$ kPa; phase 2). Thereafter, phase 3 experiences a reloading along CD until $\bar{p} = 600$ kPa.

As can be seen in Fig. 14, the whole the experimental trends are well reproduced by the model. In phase 1 and 3, together with the

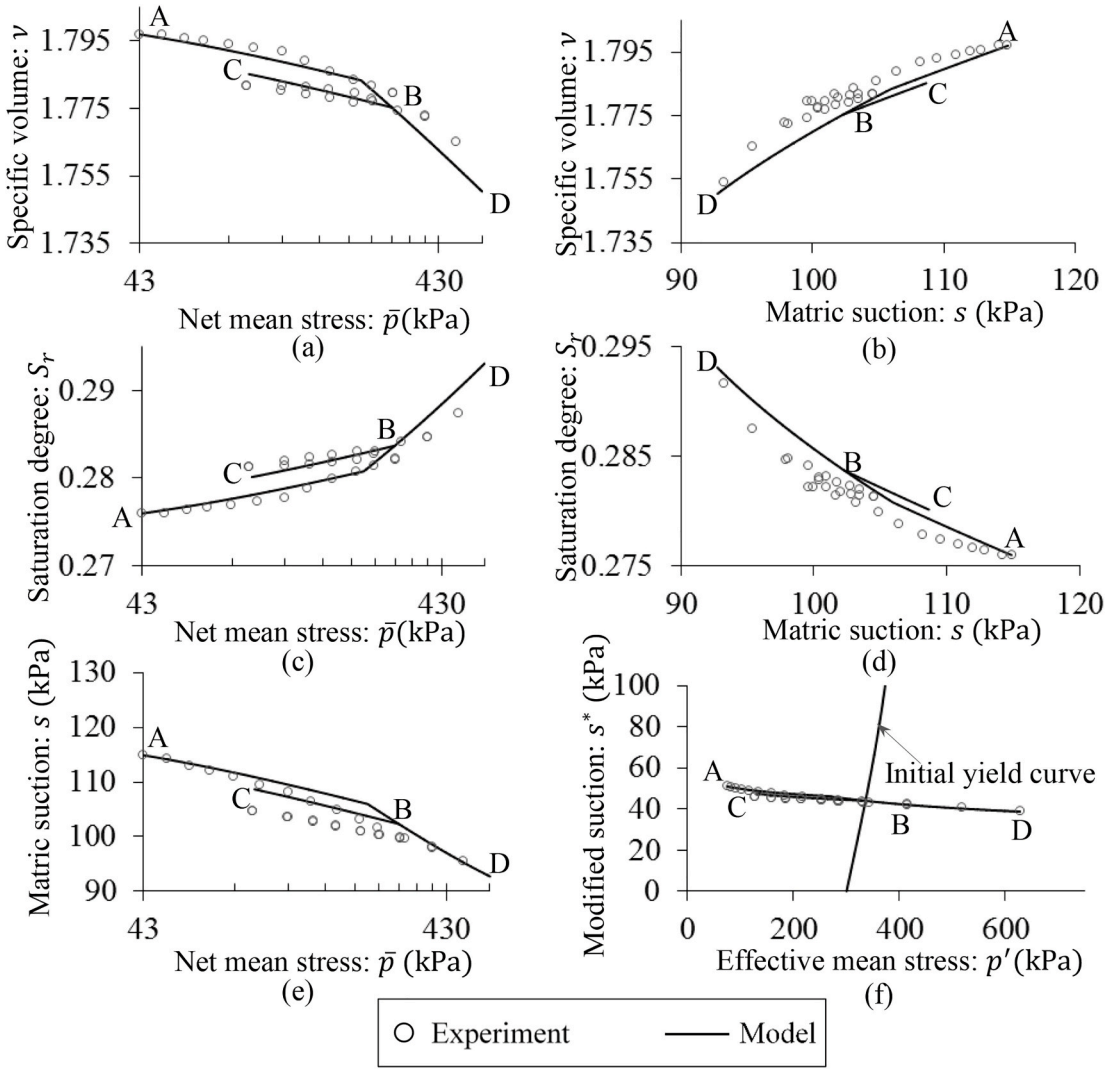

Fig. 14. Validation with undrained isotropic compression tests on Fairbanks silt at $w = 8.3\%$ (after Zhang, 2016) (a) $\bar{p} - \nu$ (b) $s - \nu$ (c) $\bar{p} - S_r$ (d) $s - S_r$ (e) $\bar{p} - s$ (f) $p^{'} - s^{*}$.

reduction in specific volume, the model behaviour exhibits a decrease in matric suction and an increase in saturation degree, and a fairly good prediction of the experimentally measured SWCC can be seen (see Fig. 14d). In phase 2, a drying response is induced by the unloading process. Both stress-strain and SWCC relationships cannot recover their previous states upon unloading, indicating the ability of the model to produce different responses under wetting and drying.

Also provided in this test is a sensitivity analysis to investigate the role of parameter β governing the mechanical effects on the wetting-drying difference of SWCC. Fig. 15 shows cycles of loading from A to B_1, B_2, B_3 and unloading from B_1, B_2, B_3 to C_1, C_2, C_3 using $\beta = 0,\ 0.1,$ and 0.15, respectively. As depicted Fig. 15a the mechanical behaviour is relatively insensitive to change of β, facilitating the calibration, while in Fig. 15b, β has strong effect on the water retention curves. The change of saturation degree is fully recoverable despite the irrecoverable specific volume if $\beta = 0$, indicating pure mechanical dissipation. When $\beta \neq 0$, the coupled hydro-mechanical dissipation is activated to allow the proposed model to capture the wetting-drying difference during the loading-unloading process, making our approach distinct from previous studies.

Mixture of Fairbanks silt and Kaolin clay, constant water content tests (Li, 2015)

The numerical prediction under the undrained isotropic compression condition is validated against the experiments on the mixture of Fairbanks silt and Kaolin clay carried out by Li (2015). Three different levels of gravimetric water content are investigated: $w = 11.85\%,\ 11.99\%$ and 15.91%. The model parameters are: $\kappa = 0.0076$; $\lambda = 0.043$; $\kappa_h = 0.03$; $p_R^{'} = 120$ kPa; $\mu = 0.022$; $\xi = 0.376$; $p_{c0}^{'} = 150$ kPa; $r = 1.5$; $\beta = 0.95$; $p_b = 40$ kPa where $\kappa,\ \lambda,\ p_R^{'}, \mu, \xi$ and $p_{c0}^{'}$ are identified using initial yield points obtained from experiments. The calibrations of κ_h, r, β and p_b are based on the experimental loading case of $w = 11.99\%$. Computed and measured results are compared in Fig. 16. It can be seen that the model predictions agree closely with the experimental data. The variation of the soil

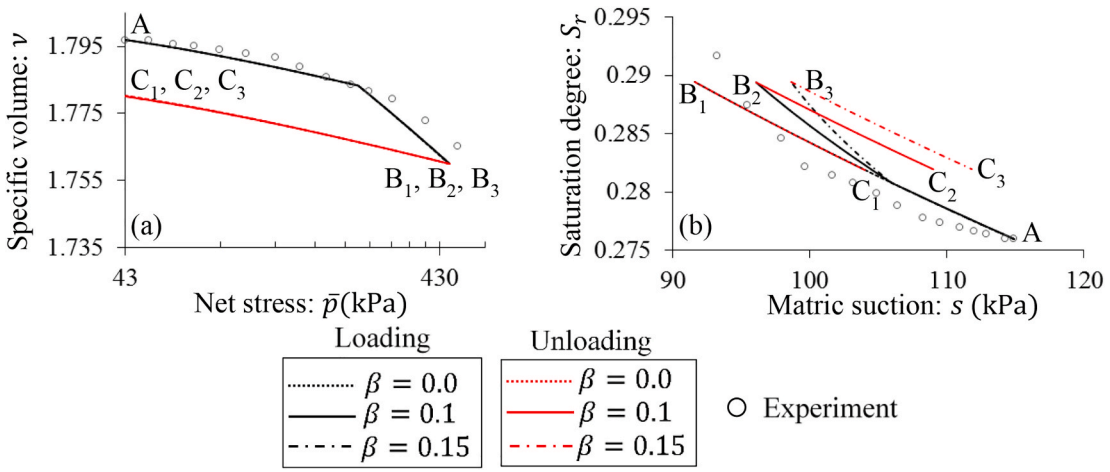

Fig. 15. Effects of different values of β on the model responses under undrained isotropic compression tests on Fairbanks silt (after Zhang, 2016) (a) $\bar{p} - \nu$ (b) $s - S_r$.

response with w is also well-captured. In particular, the initial yield stress and the NCL slope increase with increased gravimetric water content in the net stress space. Lower gravimetric water content corresponding to the higher initial suction exhibits a more profound reduction in suction. The increase in saturation degree is more significant for the higher levels of gravimetric water content. Furthermore, the non-uniqueness of SWCC is observed through its dependence on NCL during loading.

5.2. Triaxial compression tests

Zaoyang clay, constant suction tests (Chen, 2007)

A numerical analysis on the effect of suction on the shear behaviour of model is conducted through the suction-controlled triaxial shearing test on compacted Zaoyang clay at two levels of suction $s = 25$ kPa and $s = 100$ kPa (Chen, 2007). The net confining pressure is kept as a constant value of $\bar{\sigma}_{33} = 50$ kPa during shearing. In this simulation, we use the following parameters: $\kappa = 0.018$; $\lambda = 0.11$; $\kappa_h = 0.9$; $p_R^{'} = 45.31$ kPa; $\mu = 0.15$; $\xi = 0.39$; $p_{c0}^{'} = 77.32$ kPa; $r = 3.704$; $\beta = 0.05$; $p_b = 70$ kPa which are calibrated to best match the experimental results of suction-controlled isotropic compression test ($s = 25$ kPa and $s = 100$ kPa) as presented in Fig. 17. The shear test at constant suction $s = 25$ kPa is also adopted to calibrate other constitutive parameters, resulting in $M = 1.29$; $G = 15000$ kPa and $\alpha = 0.38$.

As depicted in Fig. 18a–c, the numerical results show reasonable agreement with the experimental data. In particular, higher suctions tend to produce higher yield shear stresses, as can be explained through the isotropic expansion of yield loci with increasing suction in the $p^{'} : q$ space (see Fig. 18d). Additionally, the model can capture the evolution trend in specific volume and saturation degree during shearing. This feature is shown to be a good indicator of the effect of deviatoric stress/strain on the hydraulic behaviour. The effect of suction on dilation behaviour (see Fig. 18e) can also be reproduced by the model. Although an acceptable match between the model prediction and measured data is achieved, there are observable discrepancies in specific volume and dilatancy ratio at $s = 100$ kPa (see Fig. 18b). This may be due to the assumption that CSL is unique and the effect of anisotropy on soil response (Stropeit et al., 2008; Al-Sharrad, 2013; Anandarajah, 2008; Hashiguchi and Mase, 2007; Wood and Graham, 1990; Lai et al., 2009, 2016) is overlooked regardless of the hydraulic variation.

It can be seen in Fig. 18a that very slight softening responses can be seen while volumetric strain indicates compaction (hardening trend; see Fig. 18d) and saturation degree increases in this test. However the softening behaviour in this case is minor and may be attributed to the effects of inhomogeneity at the grain scale that are hard or impossible to account for in a continuum model. For example, both grain size and pore size distributions vary in the specimen, resulting in local actions (such as pore collapse and grain rearrangements) that are different across the whole specimen. Due to these local inhomogeneities, the macro response can slightly vary from the overall hardening trend. A continuum model (that is built on the assumption of homogenous deformation at the scale of a Representative Volume Element (REV), well above the grain scale) cannot capture the effects of local inhomogeneities below the RVE scale.

Sand-silt-kaolinite mixture, constant water content tests (Maleki and Bayat, 2012)

The model performance is further assessed using the triaxial shearing test on compacted dry sand-silt-kaolinite mixture under the condition of constant gravimetric water content (Maleki and Bayat, 2012). The following model parameters are calibrated using experimental results of $w = 6.1\%$: $\kappa = 0.006$; $\lambda = 0.15$; $M = 1.54$; $G = 7000$ kPa; $\kappa_h = 0.15$; $p_R^{'} = 143.41$ kPa; $\mu = 0.0589$; $\xi = 0.372$; $p_{c0}^{'} = 300$ kPa; $r = 1.85$; $\alpha = 0.55$; $\beta = 0.5$; $p_b = 90$ kPa. The plot presented in Fig. 19 are obtained results at two levels of constant water content of $w = 6.1\%$ and 7.23%, under a net radial stress of $\bar{\sigma}_{33} = 50$ kPa.

The results in Fig. 19 show the capability of the model in reproducing the experimental trend drawn from the undrained triaxial compression test. The abrupt slope change in Fig. 19a is a typical feature and also limitation of elasto-plastic models in capturing the

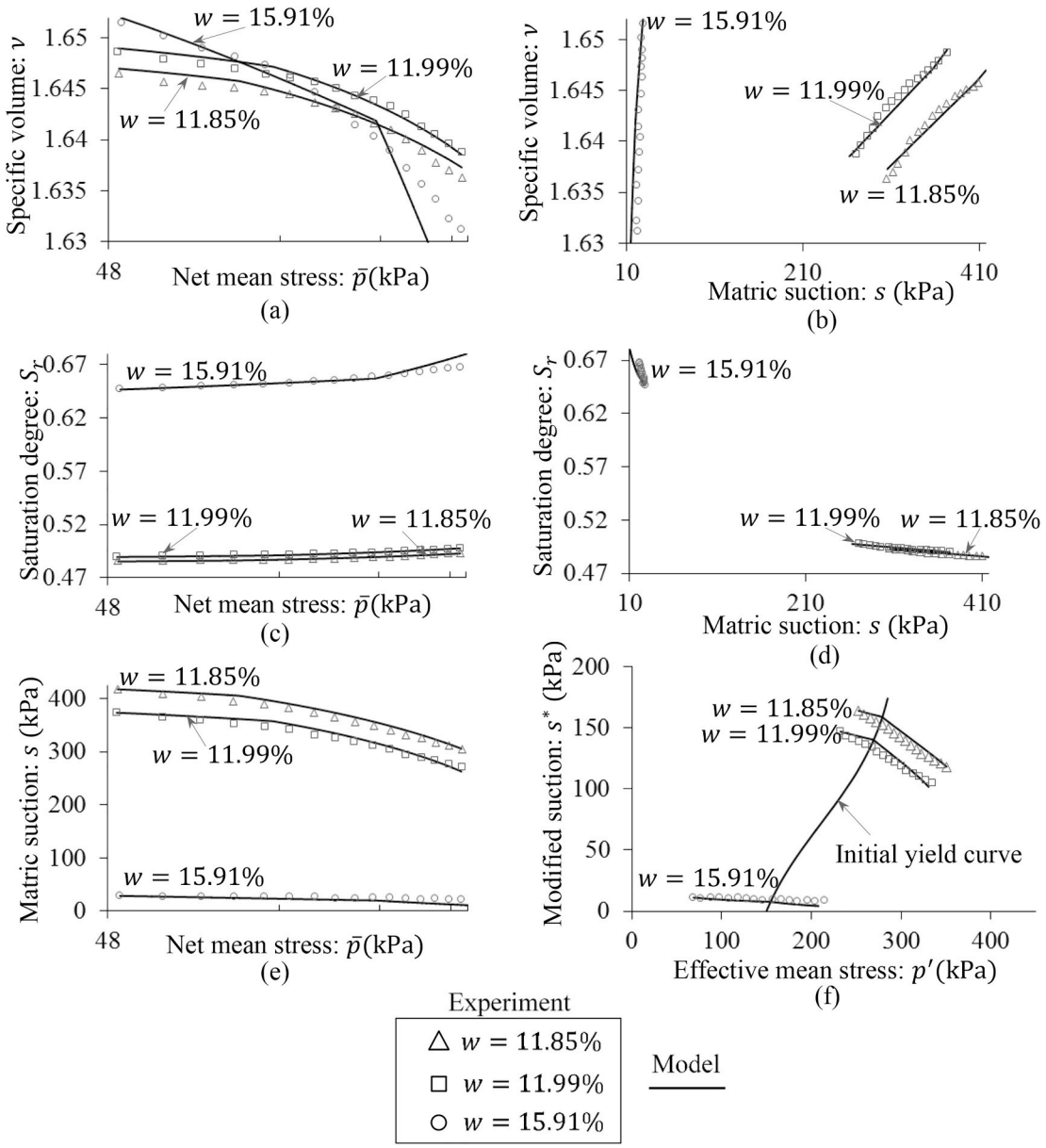

Fig. 16. Validation with undrained isotropic compression tests on the mixture of Fairbanks silt and Kaolin clay (after Li, 2015) (a) $\bar{p}-\nu$ (b) $s-\nu$ (c) $\bar{p}-S_r$ (d) $s-S_r$ (e) $\bar{p}-s$ (f) $p^{'}-s^{*}$.

smooth transition from elastic to plastic behaviour. Improvement to capture this smooth transition using sub-loading surface (Salomoni and Fincato, 2012) or a unification of hypo-plastic and elasto-plastic theories (Einav, 2012). In this test, a dilation response is observed in which deviatoric stress and volumetric strain initially experience a rapid increase before reaching a peak and then a drop until they become stable at the critical state, while suction follows the opposite trend. The influence of different gravimetric water contents on the undrained shear behaviour is also reflected in the behaviour of the proposed model. The shear strength is observed to be higher and the change of suction is more remarkable at lower gravimetric water content. The volumetric strain is more dilative if w decreases.

Bourke silt, constant suction tests (Uchaipichat, 2005; Uchaipichat and Khalili, 2009)

In the next example, the shearing stage of Bourke silt-SCT (Uchaipichat, 2005; Uchaipichat and Khalili, 2009) is used to validate and demonstrate the performance of the model. This test was conducted at three levels of imposed suction $s = 0$ kPa, $s = 100$ kPa and $s = 300$ kPa. The net confining pressure is controlled at $\bar{\sigma}_{33} = 50,\ 100$ and 150 kPa during shearing. The parameter set of this example, as obtained in Section 4, is summarized as follows: $\kappa = 0.006$; $\lambda = 0.09$; $M = 1.17$; $G = 7000$ kPa; $\kappa_h = 0.16$; $p_R^{'} = 140.41$ kPa; $\mu = 0.0229$; $\xi = 0.652$; $p_{c0}^{'} = 200$ kPa; $r = 1.818$; $\alpha = 0.5$; $\beta = 0.05$; $p_b = 70$ kPa. Figs. 20–22 show the comparison between experimental

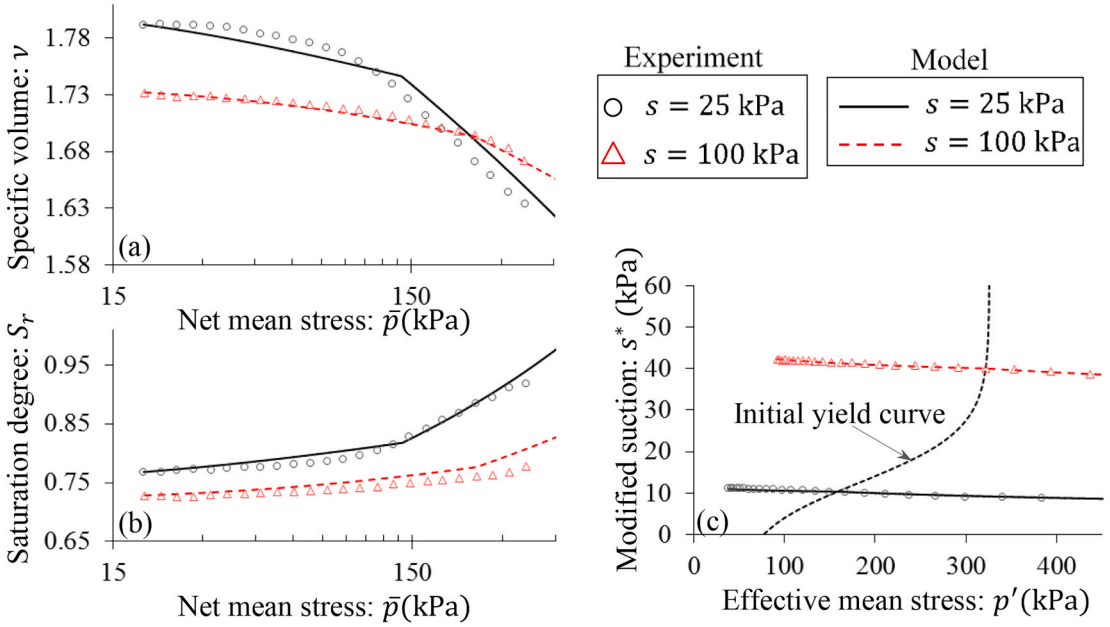

Fig. 17. Effects of suction on the model responses in suction-controlled isotropic compression test of the compacted Zaoyang clay (after Chen, 2007) (a) $\bar{p}-\nu$ (b) $\bar{p}-S_r$ (c) $p^{'}-s^{*}$.

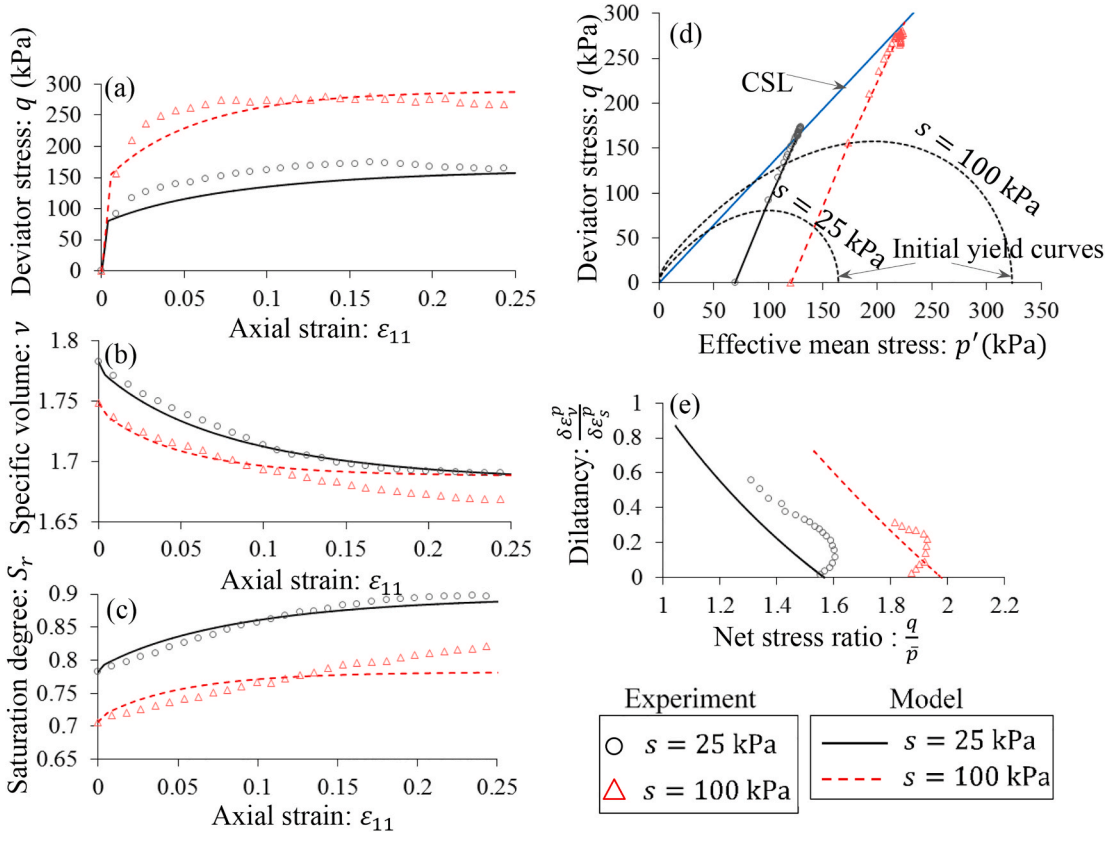

Fig. 18. Effects of suction on the model response in suction-controlled triaxial compression test on compacted Zaoyang clay (Chen, 2007) (a) $\varepsilon_{11}-q$ (b) $\varepsilon_{11}-\nu$ (c) $\varepsilon_{11}-S_r$ (d) $p^{'}-q$ (e) $\frac{q}{\bar{p}}-\frac{\delta\varepsilon_v^p}{\delta\varepsilon_s^p}$.

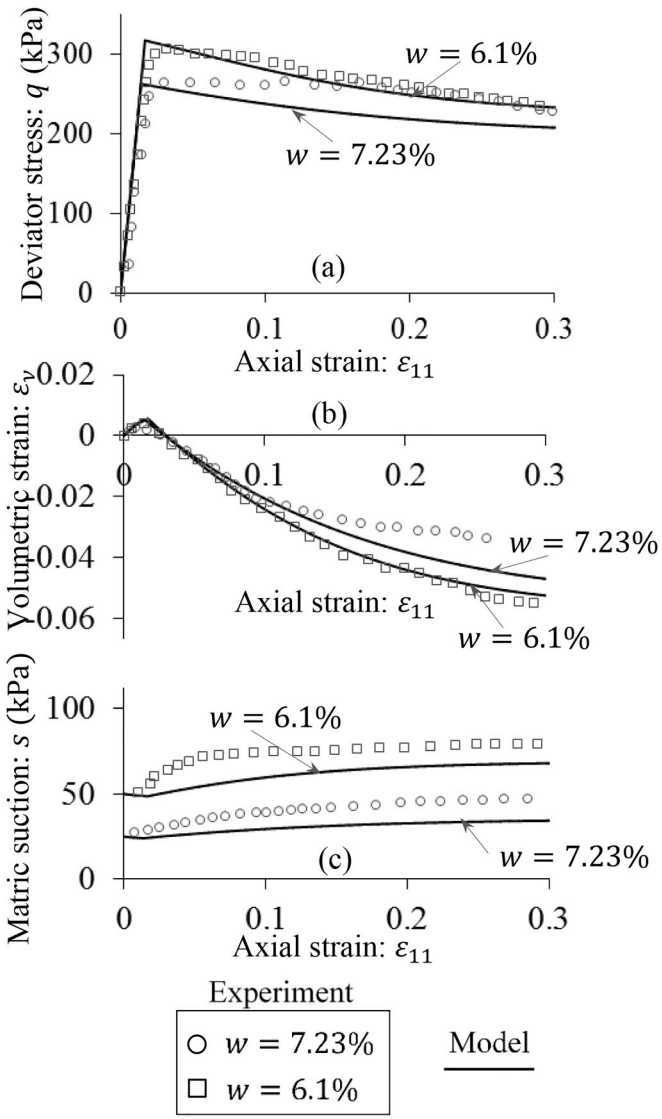

Fig. 19. Effects of different values of gravimetric water content on the model response under undrained triaxial compression tests on compacted dry sand-silt-kaolinite mixture (Maleki and Bayat, 2012) (a) $\varepsilon_{11} - q$ (b) $\varepsilon_{11} - \varepsilon_v$ (c) $\varepsilon_{11} - s$.

and numerical results on deviatoric stress and volumetric strain plotted against the shear strain. A good match between the results obtained from the numerical analyses and their experimental counterparts can be seen, except some minor discrepancies in the case of $s = 300$ kPa and $\bar{\sigma}_{33} = 150$. These mismatches may be results of using homogeneous assumption, ignoring shear localisation especially when softening occurs (e.g. $\bar{\sigma}_{33} = 50$ kPa, $s = 0$ kPa). The effects of strain localisation have not yet been considered in this model despite its importance for the failure mechanism of soils (Hashiguchi and Tsutsumi, 2007; Mroginski et al., 2011; Nguyen et al., 2016; Nguyen and Bui, 2020). The readers can refer to Nguyen et al. (2016) and Nguyen and Bui (2020) for issues and treatments for localisation effects at the constitutive level. The current approach will be improved in the future to take into account the effects of strain localisation, using the framework proposed in Nguyen and Bui (2020).

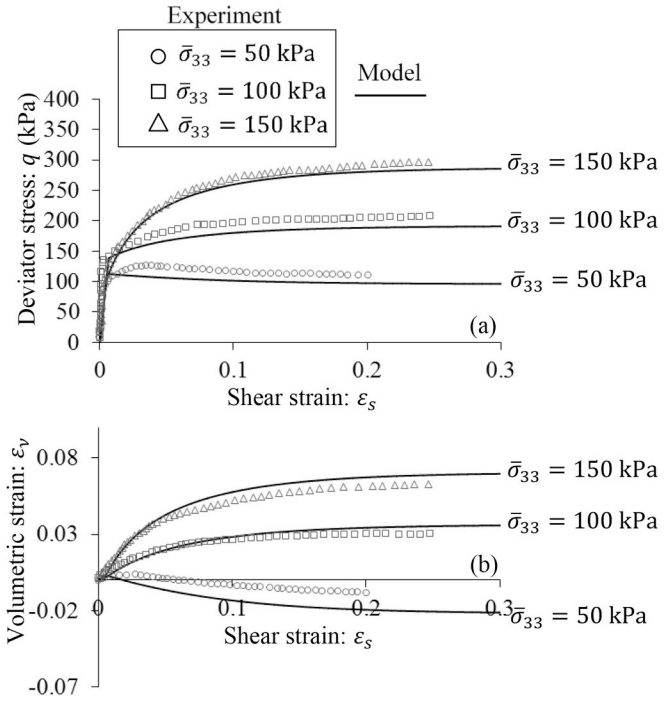

Fig. 20. Drained triaxial compression tests on Bourke silt at $s = 0$ kPa (after Uchaipichat, 2005; Uchaipichat and Khalili, 2009) (a) $\varepsilon_s - q$ (b) $\varepsilon_s - \varepsilon_v$.

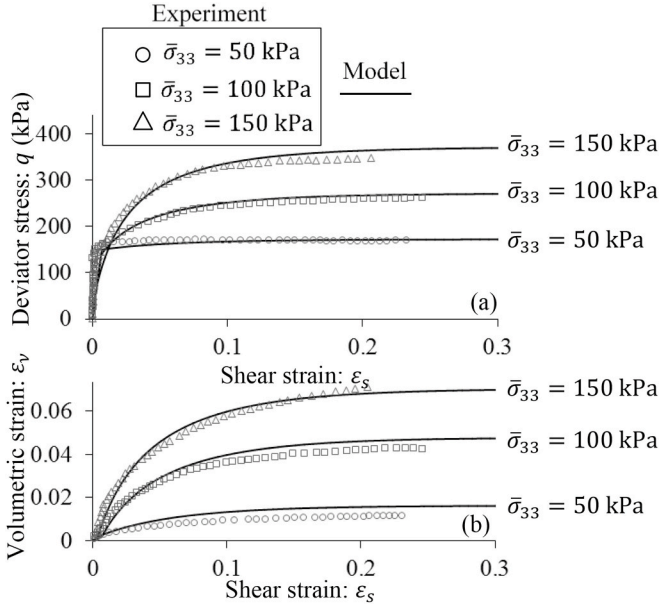

Fig. 21. Drained triaxial compression tests on Bourke silt at $s = 100$ kPa (after Uchaipichat, 2005; Uchaipichat and Khalili, 2009) (a) $\varepsilon_s - q$ (b) $\varepsilon_s - \varepsilon_v$.

5.3. Model performance under complex loading conditions

Based on the above validation, we subject the proposed model to a series of combined mechanical-hydraulic loading paths using the same set of parameters for Bourke silt-SCT to further explore its performance. Five loading paths starting at different states are shown in Fig. 23. In path 1, the soil specimen is isotropically compressed in the saturated state from A ($\bar{p} = 1$ kPa, $\nu = 1.8$, $s = 0$, $S_r = 1$) to B ($\bar{p} = 40$ kPa), C ($\bar{p} = 70$ kPa), D ($\bar{p} = 100$ kPa) and beyond. Path 2 is the drying process at constant net mean stresses of $\bar{p} = 40$ kPa,

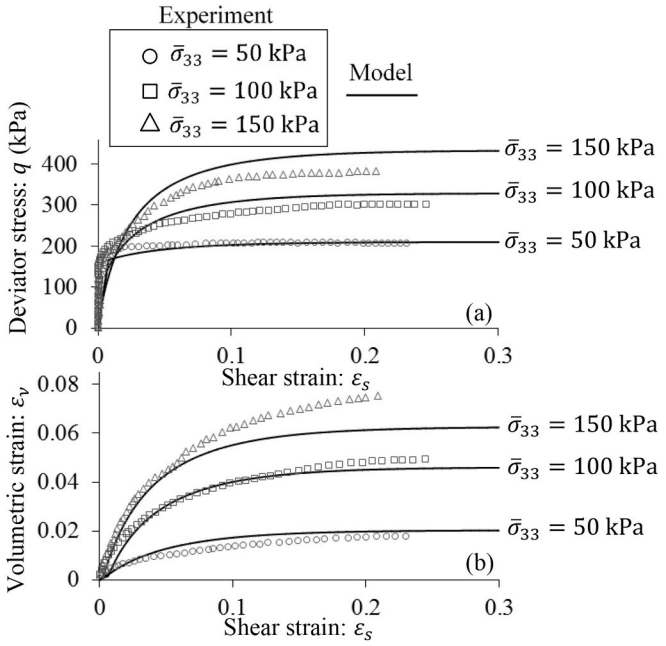

Fig. 22. Drained triaxial compression tests on Bourke silt at $s = 300$ kPa (after Uchaipichat, 2005; Uchaipichat and Khalili, 2009) (a) $\varepsilon_s - q$ (b) $\varepsilon_s - \varepsilon_v$.

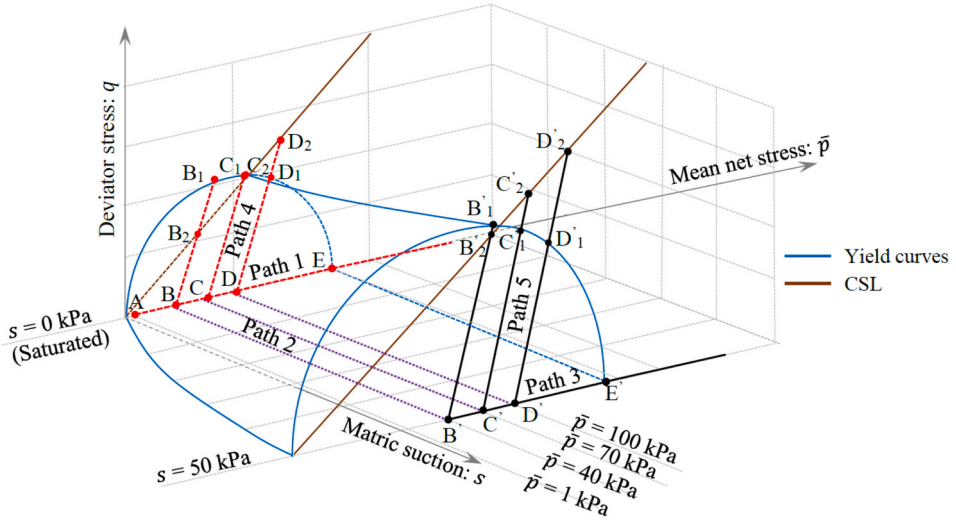

Fig. 23. Loading and hydraulic paths in $(\bar{p}, q, s)$ space.

70 kPa and 100 kPa from B, C and D to B′, C′ and D′, respectively, to reach $s = 50$ kPa. Another isotropic loading initiated from B′ is carried out under constant suction of $s = 50$ kPa in path 3. BB_2, CC_2 and DD_2 are drained shearing loading path 4 when the soil specimen is fully saturated. Path 5 (B'B'$_2$, C'C'$_2$, D'D'$_2$) is the suction-controlled triaxial shearing test at $s = 50$ kPa.

The numerical results on paths 1,2 and 3 are plotted in Fig. 24. The shearing stress paths 4 and 5 are illustrated in both the $(p^{'}, q)$ and $(\bar{p}, q)$ spaces, as seen in Fig. 25. Figs. 26–27 plots the deviatoric stress, volumetric strain, saturation degree and dissipation ratios against the axial strain for paths 4 and 5, respectively. Figs. 24–27 demonstrate that the model behaves as expected under saturated condition where the hydraulic dissipation ratio R_h (hydraulic/total) remains zero during isotropic compression and shearing under $s = 0$ kPa. The water retention curve depicted in Fig. 24d shows the variation of saturation from high (at B, C, D) to low (at B′, C′, D′) produced by the model. This demonstrates the capability of the model in capturing a smooth transition from fully saturated to saturated conditions.

As illustrated in Figs. 25–27, the sheared sample first experiences elastic response where early parts of stress paths 4 and 5 are

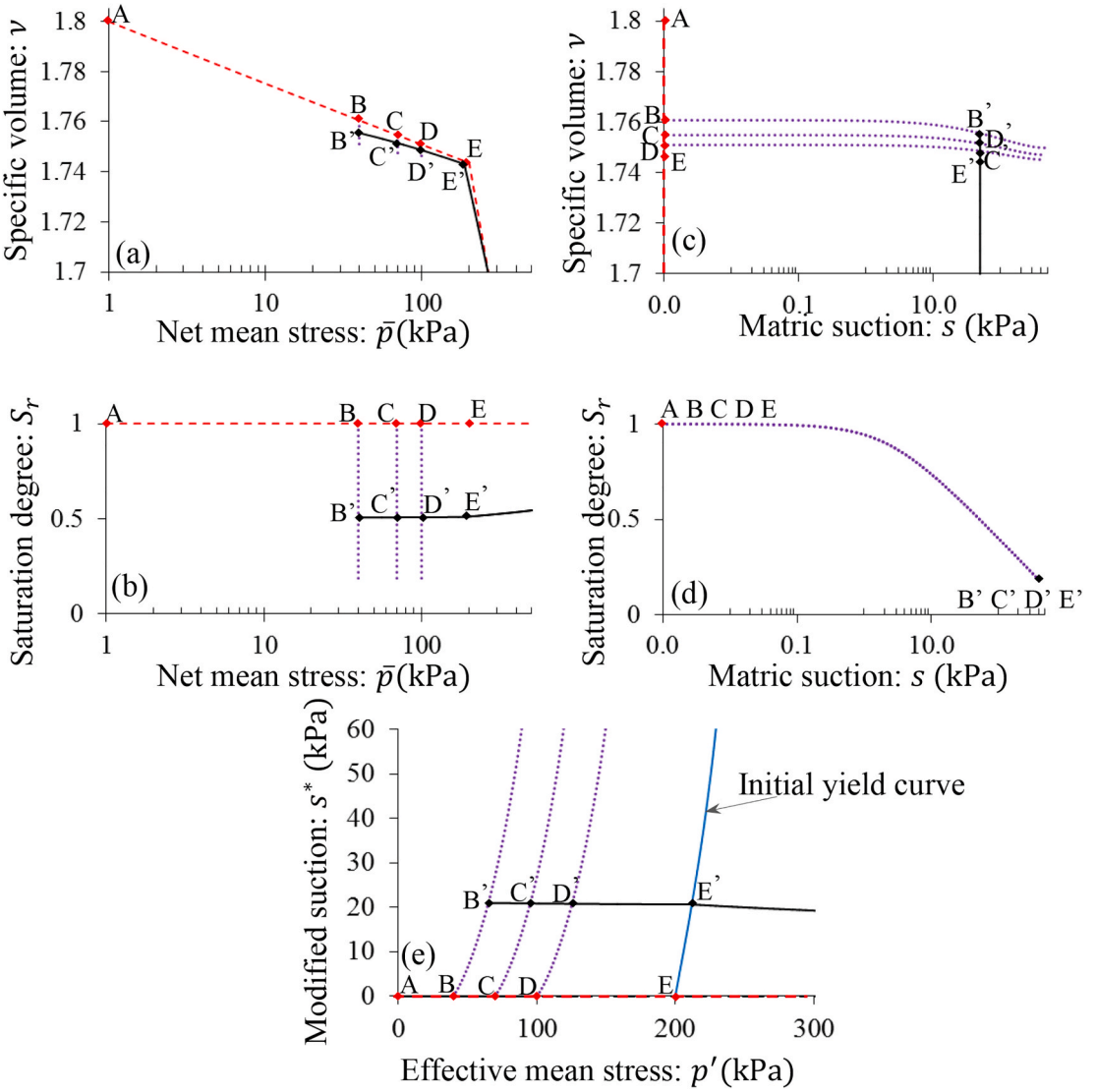

Fig. 24. Behaviour of the proposed model under load paths 1, 2 and 3 (a) $\bar{p}-\nu$ (b) $s-\nu$ (c) $\bar{p}-S_r$ (d) $s-S_r$ (e) $p^{'}-s^{*}$.

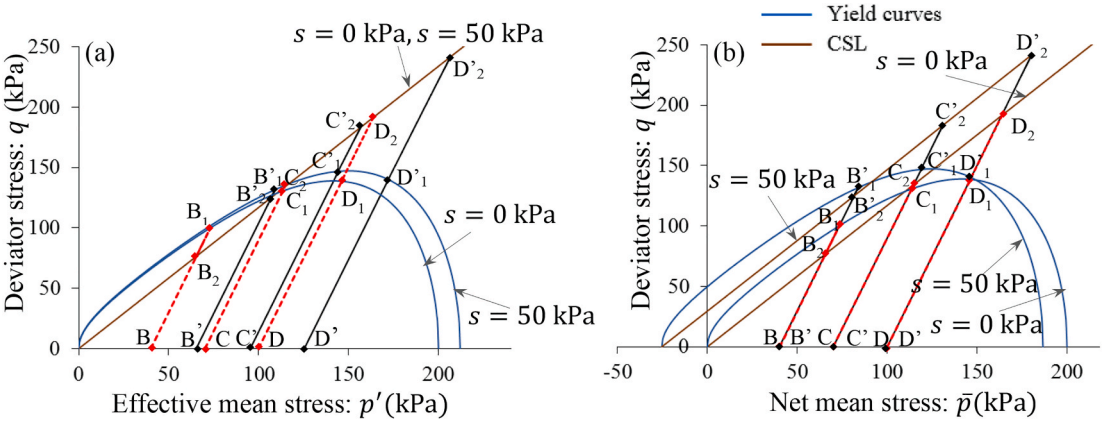

Fig. 25. Initial yield surface and stress paths of the proposed model under load paths 4 and 5 (a) $p^{'}-q$ (b) $\bar{p}-q$.

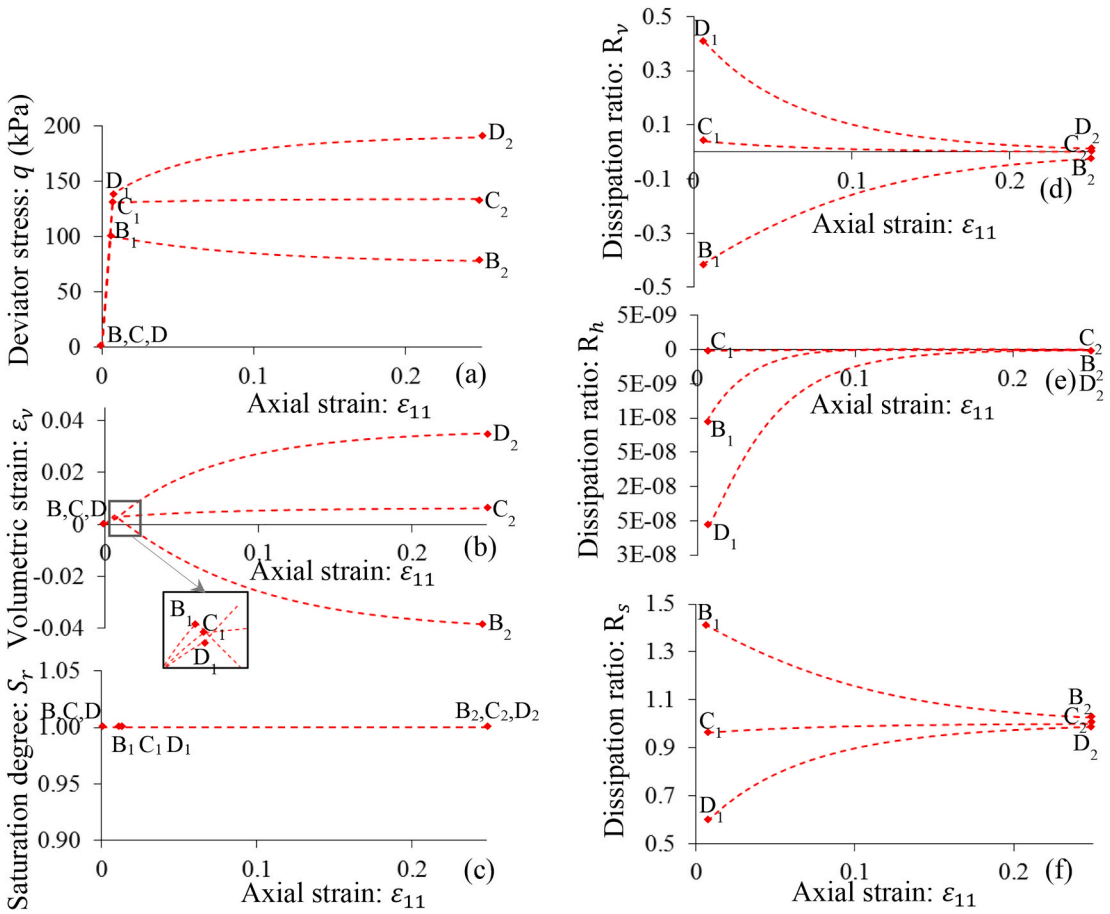

Fig. 26. Behaviour of the proposed model under load path 4 and $s = 0$ kPa (a) $\varepsilon_{11} - q$ (b) $\varepsilon_{11} - \varepsilon_v$ (c) $\varepsilon_{11} - S_r$ (d) $\varepsilon_{11} - \mathrm{R}_v$ (e) $\varepsilon_{11} - \mathrm{R}_s$ (f) $\varepsilon_{11} - \mathrm{R}_h$.

entirely located inside the initial yield surfaces. Plastic response with the activation and development of irrecoverable changes in strain and saturation degree takes place after these paths cross the initial yield surfaces. Coupled hydro-mechanical dissipation dominated by shear dissipation can be seen in Fig. 26d–f and Fig. 27d–f. Thereafter, with further shearing, the evolutions of shear stress, volumetric strain and saturation degree gradually stop and attain the steady state at which only the change of shear strain exists. At this state, the dissipation ratios R_v (between volumetric and total) and R_h (between hydraulic and total) approach zero while R_s (shear/total) is equal to 1. As sketched in Figs. 26–27, the proposed hydro-mechanical coupling can capture different responses, from hardening ($\overline{\sigma}_{33} =$ 100 kPa at $s = 0$ kPa; $\overline{\sigma}_{33} = 70,\ 100$ kPa at $s = 50$ kPa), to perfect plasticity ($\overline{\sigma}_{33} = 70$ kPa at $s = 0$ kPa) and softening ($\overline{\sigma}_{33} = 40$ kPa at $s = 0$ kPa; and $\overline{\sigma}_{33} = 40$ kPa at $s = 50$ kPa).

6. Conclusions

In the proposed generic thermodynamics-based framework for partially saturated soils and a constitutive model derived from it, we strike a good balance between rigour, simplicity, number of parameters and performance. The rigour in the formulation of the proposed generic framework guarantees the thermodynamic admissibility of any models derived from it. The obtained model described in equations (56)–(61) is simple in its structure given it possesses a single yield surface with effects of both stress and suction, and corresponding evolution laws for plastic strains and irreversible saturation. This leads to strong hydro-mechanical coupling through the simultaneous activation of both hydraulic and mechanical dissipative mechanisms upon yielding, and simplifies the implementation given there is only one yield surface. This continuum scale feature reflects the inseparable nature of the interaction between grain rearrangement and liquid-bridge redistribution at the grain scale, while removing the use of a separate SWCC in the model. Different hydro-mechanical responses obtained in wetting-drying and loading-unloading paths are the consequences of this strong

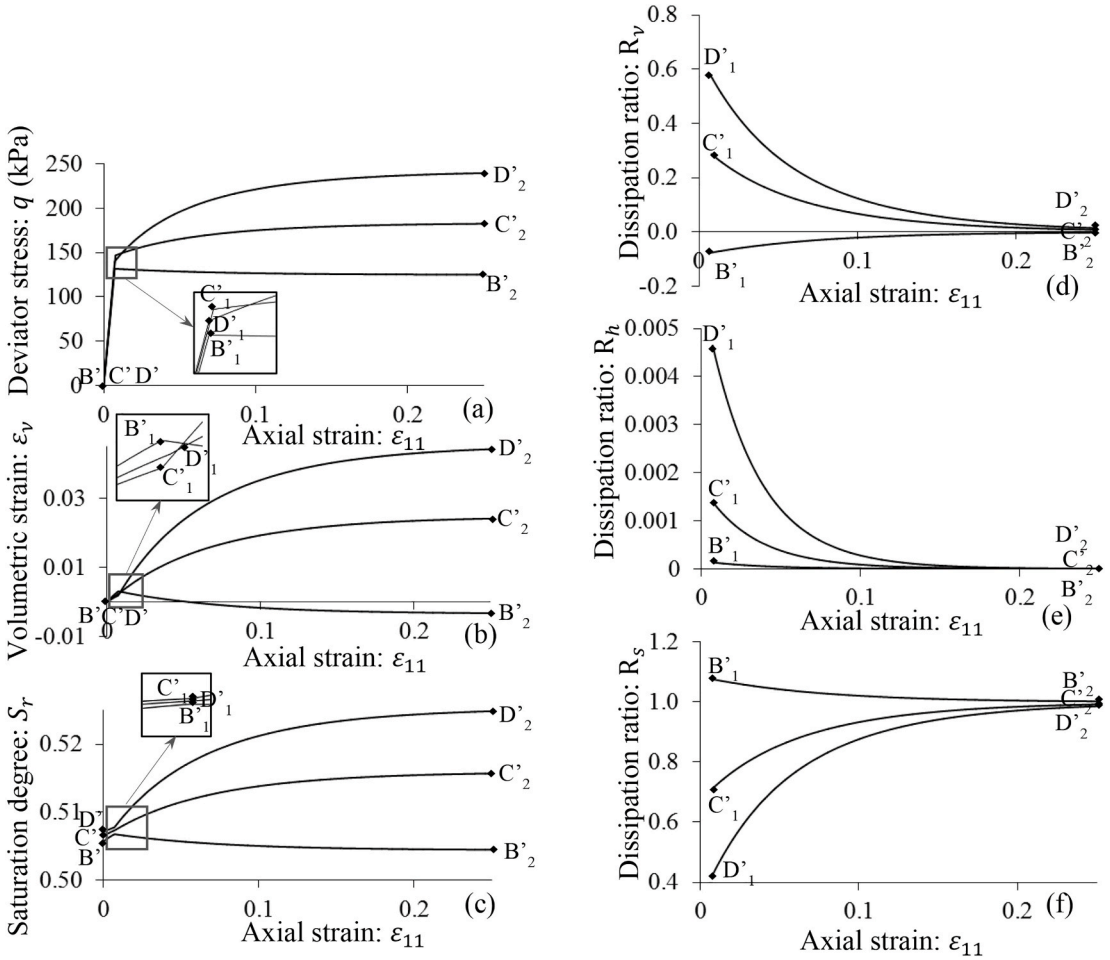

Fig. 27. Behaviour of the proposed model under load path 5 and $s = 50$ kPa (a) $\varepsilon_{11} - q$ (b) $\varepsilon_{11} - \varepsilon_v$ (c) $\varepsilon_{11} - S_r$ (d) $\varepsilon_{11} - R_v$ (e) $\varepsilon_{11} - R_s$ (f) $\varepsilon_{11} - R_h$.

hydro-mechanical coupling in the constitutive structure. The model requires only 13 parameters, of which 5 are for a classical Modified Cam Clay model; all of them have been shown in Section 4 to be calibrated from standard tests on partially saturated soils. Its efficacy is assessed against a range of experimentally measured behaviour of partially saturated soils, demonstrating the model's predictive capability for a wide range of hydro-mechanical interactions (e.g. hydraulic effects on soil stiffness, dilation, shear strength and mechanical effects on the wetting-drying difference of SWCC).

The proposed critical state model is an example to illustrate the applicability of our generic thermodynamic framework in capturing the coupled hydro-mechanical dissipation of partially saturated soils. Further planned improvements include (i) effects of air-entry suction on yielding, (ii) different forms of NCL under high stresses and more complex loading paths, (iii) anisotropic behaviour, (iv) closed-shape yield surface, and (v) the mechanisms of lower scale grain to grain contacts (e.g. Nguyen and Gan, 2014; Bignonnet et al., 2016; Fang et al., 2017; Nicot and Darve, 2007; Yin et al., 2009) for a mechanism-based expression of effective stress. The incorporation of the mechanisms of localised failure in the constitutive structure, discussed and presented in Nguyen and Bui (2020) are also essential. These features will be addressed in our future works towards better models for partially saturated soils.

CRediT authorship contribution statement

Dat G. Phan: Conceptualization, Methodology, Software, Validation, Formal analysis, Writing - original draft. **Giang D. Nguyen:**

Supervision, Conceptualization, Methodology, Formal analysis, Writing - review & editing. **Ha H. Bui:** Supervision, Conceptualization, Formal analysis, Writing - review & editing. **Terry Bennett:** Supervision, Conceptualization, Formal analysis, Writing - review & editing.

Declaration of competing interest

The authors declare that they have no known competing financial interests or personal relationships that could have appeared to influence the work reported in this paper.

Acknowledgements

The authors gratefully acknowledge support from the Australian Research Council via Discovery Projects FT140100408(Nguyen), DP170103793 (Nguyen & Bui), and DP190102779 (Bui & Nguyen).

Appendix H. Supplementary data

Supplementary data to this article can be found online at https://doi.org/10.1016/j.ijplas.2020.102821.

Appendix A. Suction/saturation dependent elasticity

Eqs. (28) and (30) can be expanded as follows:

$$\overline{p} + S_r s = (\overline{p}_0 + S_{r0} s_0)\exp\left[\frac{\left(\varepsilon_v - \varepsilon_v^p\right)}{\kappa}\right] \tag{A.1}$$

$$\phi s = \left\{(p_u + \phi_0 s_0)\exp\left\{\frac{S_{r0} + \left[(-S_r) - \left(-S_r^p\right)\right]}{\kappa_h}\right\} - p_u\right\} \tag{A.2}$$

where $\overline{p}_0$ and s_0 are initial values of mean net stress and suction. From Eqs. (A.1 & A.2), the net mean stress and suction can be expressed as:

$$\overline{p} = \left(\overline{p}_0 + S_{r0} s_0\right)\exp\left[\frac{\left(\varepsilon_v - \varepsilon_v^p\right)}{\kappa}\right] - \frac{S_r}{\phi}\left\{(p_u + \phi_0 s_0)\exp\left\{\frac{S_{r0} + \left[(-S_r) - \left(-S_r^p\right)\right]}{\kappa_h}\right\} - p_u\right\} \tag{A.3}$$

$$s = \frac{1}{\phi}\left\{(p_u + \phi_0 s_0)\exp\left\{\frac{S_{r0} + \left[(-S_r) - \left(-S_r^p\right)\right]}{\kappa_h}\right\} - p_u\right\} \tag{A.4}$$

As can be seen in Eqs. (A.3)-(A.4), both suction and saturation have influence on the change of net stress and hence the elastic stiffness.

Appendix B. hardening law

The form of the employed hardening law is selected based on several experimental observations on NCL in $(p^{'}, \nu)$ of drained isotropic compression tests (e.g. Zhan, 2003; Mun and McCartney, 2017). As demonstrated in Figs. 28 and 29, the hardening law in Eqs. (38)–(40) results in good agreement with experimental data. It is similar to the wetting-induced hardening law proposed in Alonso et al. (1990) which has been shown to be adequate in several models for partially saturated soils (e.g. Alonso et al., 1990; Bolzon et al., 1996; Cui and Delage, 1996; Al-Sharrad, 2013; Sun and Sun, 2012; Macari et al., 2003). However, it is acknowledged that only volume change responses at low stresses were investigated in such cases. Therefore the hardening law represented by Eqs. (38)–(40) is not suitable or even invalid for modelling responses of partially saturated soils under high stress levels (Khalili & Nguyen, personal communication, 29th Nov. 2019), including the transition to void closure and pressurized saturation (Mun and McCartney, 2015, 2017). Fig. 29 shows the responses and the performance of the model using the hardening law (38)–(40) in such cases. We also acknowledge several limitations of drained tests for determining yield curves (Zhang and Li, 2010; Zhang, 2016) and so the inadequacy of the proposed hardening laws in capturing yielding behaviour under more complicated stress paths (Loret and Khalili, 2002).

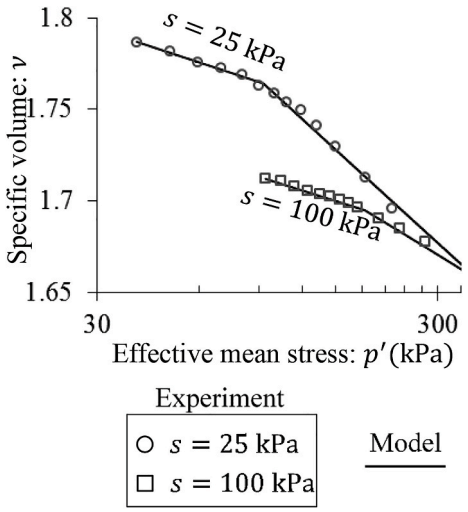

Fig. 28. NCL in $(p^{'},\nu)$ of drained isotropic compression test of the compacted partially saturated expansive clay at $s = 25\ kPa$ and $s = 100\ kPa$ (after Zhan, 2003); $\kappa = 0.015,\ \lambda = 0.05, p_{c0}^{'} = 80\ kPa\ ,\ p_R^{'} = 50\ kPa,\ \mu = 0.025,\ \xi = 0.3$.

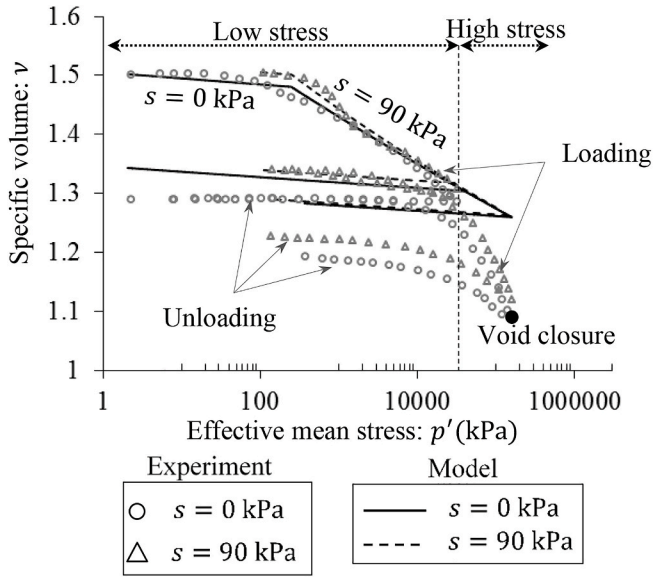

Fig. 29. NCL in $(p^{'},\nu)$ of drained isotropic compression test of the Boulder clay at $s = 0\ \ kPa$ and $s = 90\ \ kPa$ (after Mun and McCartney, 2017); $\kappa = 0.003, \lambda = 0.025,\ p_{c0}^{'} = 250\ kPa,\ p_R^{'} = 300\ \ kPa,\ \mu = -0.005,\ \xi = 0.05$.

Appendix C.1. Functions A and B

We first investigate the dependence of functions A and B on stress-like variables, based on details given in Section 2.1 and 2.2. From Eqs. (17-19), we can write:

$$\chi_\nu - \frac{\partial \varphi_2^\nu}{\partial \dot{\varepsilon}_\nu^p} = \frac{\varphi_1^\nu}{\tilde{\Phi} - \varphi_2^\nu} \frac{\partial \varphi_1^\nu}{\partial \dot{\varepsilon}_\nu^p} \tag{C.1.1}$$

$$\chi_s = \frac{\varphi^s}{\tilde{\Phi} - \varphi_2^\nu} \frac{\partial \varphi^s}{\partial \dot{\varepsilon}_s^p} \tag{C.1.2}$$

Substituting Eqs. (34-36) into Eqs. (C.1.1-C.1.2) yields:

$$\chi_\nu - \frac{p_{c(us)}^{'}}{r} = \frac{A^2 \dot{\varepsilon}_\nu^p}{\tilde{\Phi} - \frac{p_{c(us)}^{'}}{r} \dot{\varepsilon}_\nu^p} \frac{1}{\exp[-\beta(1 - S_r)]} \tag{C.1.3}$$

$$\chi_s = \frac{B^2 \dot{\varepsilon}_s^p}{\tilde{\Phi} - \frac{p'_{c(us)}}{r}\dot{\varepsilon}_v^p} \tag{C.1.4}$$

Invoking Eqs. (13-15), (21) and (31-33), Eqs. (C.1.3-C.1.4) become:

$$p' - \frac{p'_{c(us)}}{r} = \frac{A^2 \dot{\varepsilon}_v^p}{\left(p' - \frac{p'_{c(us)}}{r}\right)\dot{\varepsilon}_v^p + q\dot{\varepsilon}_s^p + (s^* - p_b)\left(-\dot{S}_r^p\right)} \frac{1}{\exp[-\beta(1-S_r)]} \tag{C.1.5}$$

$$q = \frac{B^2 \dot{\varepsilon}_s^p}{\left(p' - \frac{p'_{c(us)}}{r}\right)\dot{\varepsilon}_v^p + q\dot{\varepsilon}_s^p + (s^* - p_b)\left(-\dot{S}_r^p\right)} \tag{C.1.6}$$

The relationship between $-\dot{S}_r^p$ and $\dot{\varepsilon}_v^p$ can be derived from flow rules in Eqs. (45) and (47) as follows:

$$(s^* - p_b)\left(-\dot{S}_r^p\right) = \frac{1 - \exp[-\beta(1-S_r)]}{\exp[-\beta(1-S_r)]}\left(p' - \frac{1}{r}p'_{c(us)}\right)\dot{\varepsilon}_v^p \tag{C.1.7}$$

Substitution of Eq. (C.1.7) into Eqs. (C.1.5-C.1.6), with some mathematical arrangements, one obtains the following functions for A and B:

$$A = \pm\sqrt{\frac{\exp[-\beta(1-S_r)]\left(p' - \frac{p'_{c(us)}}{r}\right)\left[\left(p' - \frac{p'_{c(us)}}{r}\right)\frac{1}{\exp[-\beta(1-S_r)]}\dot{\varepsilon}_v^p + q\dot{\varepsilon}_s^p\right]}{\dot{\varepsilon}_v^p}} \tag{C.1.8}$$

$$B = \pm\sqrt{\frac{q\left[\left(p' - \frac{p'_{c(us)}}{r}\right)\frac{1}{\exp[-\beta(1-S_r)]}\dot{\varepsilon}_v^p + q\dot{\varepsilon}_s^p\right]}{\dot{\varepsilon}_s^p}} \tag{C.1.9}$$

Based on Eq. (C.1.8), the stress derivatives of the function A are written as follows:

$$\frac{\partial A}{\partial p'} = \frac{\left[2\left(p' - \frac{p'_{c(us)}}{r}\right)\dot{\varepsilon}_v^p\right] + \exp[-\beta(1-S_r)]q\dot{\varepsilon}_s^p}{2A\dot{\varepsilon}_v^p} \tag{C.1.10}$$

$$\frac{\partial A}{\partial q} = \frac{\exp[-\beta(1-S_r)]\left(p' - \frac{p'_{c(us)}}{r}\right)\dot{\varepsilon}_s^p}{2A\dot{\varepsilon}_v^p} \tag{C.1.11}$$

$$\frac{\partial A}{\partial p'_{c(us)}} = \frac{2\left(-\frac{1}{r}\right)\left(p' - \frac{p'_{c(us)}}{r}\right)\dot{\varepsilon}_v^p + \left(-\frac{1}{r}\right)\exp[-\beta(1-S_r)]q\dot{\varepsilon}_s^p}{2A\dot{\varepsilon}_v^p} \tag{C.1.12}$$

With Eqs. (C.1.10-C.1.12), the following form can be expressed as:

$$\frac{\partial A}{\partial p'}p' + \frac{\partial A}{\partial q}q + \frac{\partial A}{\partial p'_{c(us)}}p'_{c(us)} = \frac{\left[2\left(p' - \frac{p'_{c(us)}}{r}\right)p'\dot{\varepsilon}_v^p\right] + \exp[-\beta(1-S_r)]p'q\dot{\varepsilon}_s^p}{2A\dot{\varepsilon}_v^p} + \frac{\exp[-\beta(1-S_r)]\left(p' - \frac{p'_{c(us)}}{r}\right)q\dot{\varepsilon}_s^p}{2A\dot{\varepsilon}_v^p}$$
$$+ \frac{2\left(-\frac{1}{r}\right)\left(p' - \frac{p'_{c(us)}}{r}\right)p'_{c(us)}\dot{\varepsilon}_v^p + \left(-\frac{1}{r}\right)\exp[-\beta(1-S_r)]qp'_{c(us)}\dot{\varepsilon}_s^p}{2A\dot{\varepsilon}_v^p} \tag{C.1.13}$$

Or,

$$\frac{\partial A}{\partial p'}p' + \frac{\partial A}{\partial q}q + \frac{\partial A}{\partial p'_{c(us)}}p'_{c(us)} = \frac{2\exp[-\beta(1-S_r)]\left(p' - \frac{p'_{c(us)}}{r}\right)\left[\left(p' - \frac{p'_{c(us)}}{r}\right)\frac{1}{\exp[-\beta(1-S_r)]}\dot{\varepsilon}_v^p + q\dot{\varepsilon}_s^p\right]}{2A\dot{\varepsilon}_v^p} = A \tag{C.1.14}$$

Similarly, we can obtain:

$$\frac{\partial B}{\partial p^{'}}p^{'} + \frac{\partial B}{\partial q}q + \frac{\partial B}{\partial p^{'}_{c(us)}}p^{'}_{c(us)} = B \tag{C.1.15}$$

Eqs. (C.1.14)-(C.1.15) indicate that A and B must be homogeneous functions of degree one of $p^{'}, q$ and $p^{'}_{c(us)}$.

Appendix C.2. Determining functions A and B

We conduct a systematic procedure (Collins, 2003; Collins and Hilder, 2002) to determine specific forms of functions A and B. A and B must be homogeneous functions of degree one in terms of the three defining effective stress variables $p^{'}, q$ and $p^{'}_{c(us)}$ (see Appendix C.1). For simplicity, they are assumed to be in linear forms (Collins and Hilder, 2002):

$$A = a_1 p^{'} + a_2 q + a_3 p^{'}_{c(us)} \tag{C.2.1}$$

$$B = b_1 p^{'} + b_2 q + b_3 p^{'}_{c(us)} \tag{C.2.2}$$

where $a_1, a_2, a_3, b_1, b_2, b_3$ are dimensionless coefficients governing dissipative micromechanical mechanisms. To determine them, let us examine the yielding behaviour of the wet granular material under isotropic compression and decompression where $\dot{\varepsilon}^p_s = 0$ or $q = 0$. In this case, Eq. (C.2.1) can be reduced to the following expression:

$$p^{'} - \frac{1}{r}p^{'}_{c(us)} = \pm A = \pm\left[a_1 p^{'} + a_3 p^{'}_{c(us)}\right] \tag{C.2.3}$$

In Eq. (C.2.3), $p^{'} = p^{'}_{c(us)}$ for the plus sign of the yielding compression and $p^{'} = 0$ for the minus sign of the yielding expansion (see Fig. 2). Employing this, we can deduce from Eq. (C.2.3) that:

$$a_1 = 1 - \frac{2}{r} \text{ and } a_3 = \frac{1}{r} \tag{C.2.4}$$

The coefficient a_2 is determined to be zero by assuming a similarity between deviatoric extension and compression (Uchaipichat, 2005; Collins, 2003). Therefore:

$$A = \left(1 - \frac{2}{r}\right)p^{'} + \frac{1}{r}p^{'}_{c(us)} \tag{C.2.5}$$

Parameters b_1, b_2, b_3 can be identified by examining the yielding response at the critical state where the volumetric strain and saturation degree remain constant (Zhao et al., 2014; Chen, 2007). With $\dot{\varepsilon}^p_v = 0$, if $p^{'}_{CSL}$ and q_{CSL} respectively denote the effective mean and shear stresses at the critical state, Eqs. (44) and (45) are therefore simplified as $(q_{CSL})^2 = B^2$ and $p^{'}_{CSL} = \frac{1}{r}p^{'}_{c(us)}$. With the use of Eq. (C.2.2), these equations lead to:

$$(q_{CSL})^2 = \left[b_1\left(p^{'}_{CSL}\right) + b_2(q_{CSL}) + b_3 r\left(p^{'}_{CSL}\right)\right]^2 \tag{C.2.6}$$

So that,

$$q_{CSL} = \pm\frac{(b_1 + b_3 r)p^{'}_{CSL}}{(1 - b_2)} \tag{C.2.7}$$

Suppose that the compressive (positive) and extensive (negative) shear stresses in Eq. (C.2.7) are similar. Consequently, b_2 is null (Uchaipichat, 2005; Collins, 2003). Furthermore, the uniqueness of CSL with a constant slope M in the $p^{'} : q$ plane is assumed (Russell and Khalili, 2006; Khalili et al., 2008). In this sense, Eq. (C.2.7) provides that:

$$\frac{q_{CSL}}{p^{'}_{CSL}} = M = b_1 + b_3 r \tag{C.2.8}$$

Let us now introduce the dimensionless parameter α $(0 < \alpha \leq 1)$ to enable Eq. (C.2.8) to give:

$$b_1 = (1 - \alpha)M \text{ and } b_3 = \frac{\alpha}{r}M \tag{C.2.9}$$

Consequently,

$$B = (1 - \alpha)Mp^{'} + \frac{\alpha}{r}Mp^{'}_{c(us)} \tag{C.2.10}$$

Appendix D. Comparative study against Barcelona Basic Model (BBM)

A comparison between the proposed model and BBM (Alonso et al., 1990) is carried out regarding the model description. This

comparison is briefly summarized in Table 1. As can be seen, the differences between them are pointed out based on different criteria (i) Methodology (ii) SWCC (iii) Stress-like variables (iv) Strain-like variables (v) Cohesion (vi) Yield surface (vii) Flow rules (viii) Hardening law.

Table 1
Comparison on the model description between the present model and BBM.

Barcelona Basic model (BBM) (see Table 2 for further details)	Present model
(i) Methodology	
Conventional elastoplastic approach	Thermodynamic-based approach
(ii) SWCC (wetting/drying difference, volume-dependent SWCC)	
No	Yes
(iii) Stress-like variables	
Net stress: $\bar{\sigma}_{ij}$ ($\bar{p}$ and q)	Effective stress: σ'_{ij} (p' and q)
Suction: s	Modified suction: s^*
(iv) Strain-like variables	
Strain: ε_{ij}	Strain: ε_{ij}
	Saturation degree: S_r
(v) Cohesion	
$k_s s$	$S_r s$
(vi) Yield surface	
$y_{(LC)} = q^2 - M^2(\bar{p} + k_s s)(\bar{p}_{c(us)} - \bar{p}) \le 0$	$y = \dfrac{\left(p' - \frac{1}{r}p'_{c(us)}\right)^2}{\left[\left(1-\frac{2}{r}\right)p' + \frac{1}{r}p'_{c(us)}\right]^2} + \dfrac{q^2}{\left[(1-\alpha)p' + \frac{\alpha}{r}p'_{c(us)}\right]^2 M^2} - 1 \le 0$
$y_{(SI)} = s - s_c \le 0$	
(vii) Flow rules	
$\dot{\varepsilon}^p_v = \dot{\varepsilon}^p_{v(LC)} + \dot{\varepsilon}^p_{v(SI)} = \dot{\lambda}_{p(LC)} M^2(2\bar{p} + k_s s - \bar{p}_{c(us)}) + \dot{\lambda}_{p(SI)}$	$\dot{\varepsilon}^p_v = \dot{\lambda}_p \dfrac{2\left(p' - \frac{1}{r}p'_{c(us)}\right)}{\left[\left(1-\frac{2}{r}\right)p' + \frac{1}{r}p'_{c(us)}\right]^2} \exp[-\beta(1-S_r)]$
$\dot{\varepsilon}^p_s = \dot{\lambda}_{p(LC)} 2\gamma q$	$\dot{\varepsilon}^p_s = \dot{\lambda}_p \dfrac{2q}{\left[(1-\alpha)p' + \frac{\alpha}{r}p'_{c(us)}\right]^2 M^2}$
	$-\dot{S}^p_r = \dot{\lambda}_p \dfrac{2\left(p' - \frac{1}{r}p'_{c(us)}\right)^2}{(s^* - p_b)\left[\left(1-\frac{2}{r}\right)p' + \frac{1}{r}p'_{c(us)}\right]^2}[1 - \exp[-\beta(1-S_r)]]$
(viii) Hardening law	
$\bar{p}_{c(us)} = \bar{p}_R \left[\dfrac{\bar{p}_{co} \exp\left(\frac{\nu\varepsilon^p_{v(LC)}}{\bar{\lambda}-\bar{\kappa}}\right)}{\bar{p}_R}\right]^{\frac{\bar{\lambda}-\bar{\kappa}}{\bar{\lambda}[(1-\bar{\xi})\exp(-\bar{\mu}s)+\bar{\xi}]-\bar{\kappa}}}$	$p'_{c(us)} = p'_R \left[\dfrac{p'_{c0} \exp\left(\frac{\varepsilon^p_v}{\lambda-\kappa}\right)}{p'_R}\right]^{\frac{\lambda-\kappa}{\lambda[(1-\xi)\exp(-\mu s^*)+\xi]-\kappa}}$
$s_c = (s_{c0} + p_{at})\exp\left(\dfrac{\nu\varepsilon^p_{v(SI)}}{\lambda_s - \kappa_s}\right) - p_{at}$	

Table 2
Definitions of parameters and variables of BBM (Alonso et al., 1990).

k_s	constant controlling the apparent cohesion
$\bar{\kappa}$	slope of URL in the $\nu : \ln\bar{p}$ plane for saturated conditions
$\bar{\lambda}$	slope of NCL in the $\nu : \ln\bar{p}$ plane for saturated conditions
κ_s	elastic stiffness parameter for changes in suction
λ_s	stiffness parameter for changes in suction for virgin states of the soil
γ	parameter controlling the non-associated flow rule
$\bar{\mu}$	parameter controlling the change of soil stiffness with suction
$\bar{\xi}$	parameter controlling the maximum soil stiffness
$\bar{p}_R$	parameter controlling the yield curve
p_{at}	atmospheric pressure
$\bar{p}_{c(us)}$	the yield pressure under isotropic compression at partially saturated condition
$\bar{p}_{c0}$	the initial yield pressure under isotropic compression at fully saturated condition
s_c	hardening parameter of the suction increase yield locus
s_{c0}	the initial hardening parameter of the suction increase yield locus
$y_{(LC)}$	Loading-Collapse yield surface
$y_{(SI)}$	Suction-Increase yield surface
$\varepsilon^p_{v(LC)}$	plastic volumetric strain associated with the Loading-Collapse yield surface

(*continued on next page*)

Table 2 (*continued*)

$\dot{\varepsilon}^{p}_{v(SI)}$	plastic volumetric strain associated with the Suction-Increase yield surface
$\dot{\lambda}_{p(LC)}$	non-negative plasticity-like multiplier of the Loading-Collapse yield surface
$\dot{\lambda}_{p(SI)}$	non-negative plasticity-like multiplier of the Suction-Increase yield surface

As can be seen in the table above, the proposed model has a few notable advances compared to the BBM (i) Thermomechanical rigour (ii) A single yield surface (iii) Saturation degree (iv) inherent SWCC as an integral part of the model (v) Fully coupled hydro-mechanical response taking into account the volume-dependent SWCC (vi) Non-linear increase in cohesion with $S_r s$ (vii) wetting/drying difference.

These features are associated with some main distinctions between the two in terms of parameters as follows: (i) In our hardening laws, parameters κ, λ, $p_R^{'}$, μ and ξ are used for effective stress and modified suction. Therefore, their effects on responses of our model are different from those of the BBM. (ii) r and α are adopted in the present model to provide a more extensive/flexible yielding behaviour in comparison with the BBM. Particular, they allow us to construct the tear-drop shape of the yield surface to mimic a wide variety of experimentally observed initial shear yield surface. (iii) In the BBM, parameter k_s is used to describe the linear increase in cohesion with suction. Instead, the term $S_r s$ in the Bishop's effective stress is to describe the non-linear relationship between cohesion and suction in our model. (iv) Additional parameters κ_h, β and p_b for SWCC are needed for this model which cannot be found in the BBM.

With above-mentioned advances, the present model yields better predictions of the $\varepsilon_s : q$ and $\varepsilon_s : \varepsilon_v$ responses in suction-controlled triaxial shearing test on Speswhite Kaolin at $s = 200$ kPa and $\bar{\sigma}_{33} = 75$ kPa (Raveendiraraj, 2009), as compared to the BBM (see Fig. 30a). Additionally, Fig. 30b demonstrates the ability of our approach to capture the increase in saturation degree during shearing, which cannot be predicted by the BBM.

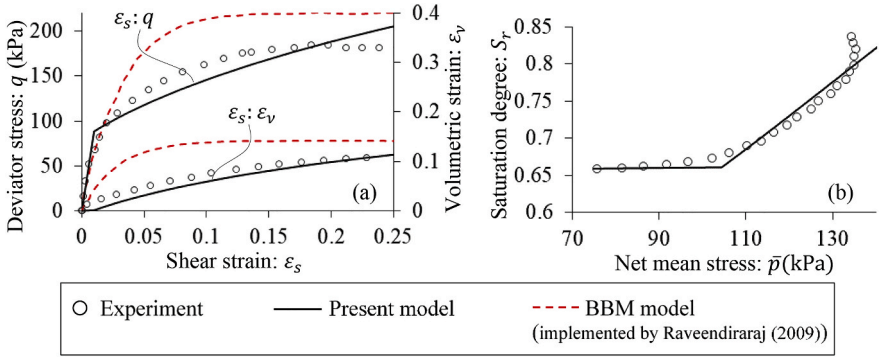

Fig. 30. Drained triaxial compression tests on Speswhite Kaolin at $s = 200$ *kPa* and $\bar{\sigma}_{33} = 75$ *kPa* (after Raveendiraraj, 2009) (a) $\varepsilon_s - q$, $\varepsilon_s - \varepsilon_v$ (b) $\bar{p} - S_r$.$\kappa = 0.01$;$\lambda = 0.3$;$M = 0.889$;$G = 3000$ *kPa*;$\kappa_h = 0.75$;$p_R^{'} = 120$ *kPa*;$\mu = 0.06$;$\xi = 0.6$;$p_{c0}^{'} = 200$ *kPa*;$r = 2.5$;$\alpha = 0.7$;$\beta = 0.005$;$p_b = 70$ *kPa*.

Appendix E. Number of parameters in existing coupled hydro-mechanical models

Table 3
Comparison on the number of parameters in existing coupled hydro-mechanical models.

Model	Number of parameters
Khalili et al. (2008) "A fully coupled flow deformation model for cyclic analysis of unsaturated soils including hydraulic and mechanical hysteresis"	17
Hu et al. (2015) "A coupled stress-strain and hydraulic hysteresis model for unsaturated soils: Thermodynamic analysis and model evaluation"	16
Liu Muraleetharan (2012) "Coupled Hydro-Mechanical Elastoplastic Constitutive Model for Unsaturated Sands and Silts"	32
Ghasemzadeh et al. (2017) "Elastoplastic model for hydro-mechanical behaviour of unsaturated soils"	18
Gholizadeh and Latifi (2018) "A coupled hydro-mechanical constitutive model for unsaturated frictional and cohesive soil"	21
Sun and Sun (2012) "Coupled modelling of hydro-mechanical behaviour of unsaturated compacted expansive soils"	13
Muraleetharan et al. (2009) "An elastoplatic framework for coupling hydraulic and mechanical behaviour of unsaturated soils"	12 (isotropic behaviour only)
Bruno and Gallipoli (2019) "A coupled hydromechanical bounding surface model predicting the hysteretic behaviour of unsaturated soils"	12 (isotropic behaviour only)

Appendix F. Derivatives of the yield function

The derivatives of the yield function in Eq. (59) with respect to effective stress takes the following explicit form:

$$\frac{\partial y}{\partial \sigma_{ij}^{'}} = \frac{\partial y}{\partial p^{'}} \frac{\partial p^{'}}{\partial \sigma_{ij}^{'}} + \frac{\partial y}{\partial q} \frac{\partial q}{\partial \sigma_{ij}^{'}} \tag{F.1}$$

in which,

$$\frac{\partial y}{\partial p^{'}}=\frac{2\left(p^{'}-\frac{1}{r}p^{'}_{c(us)}\right)}{\left[\left(1-\frac{2}{r}\right)p^{'}+\frac{1}{r}p^{'}_{c(us)}\right]^{2}}-\frac{2\left(1-\frac{2}{r}\right)\left(p^{'}-\frac{1}{r}p^{'}_{c(us)}\right)^{2}}{\left[\left(1-\frac{2}{r}\right)p^{'}+\frac{1}{r}p^{'}_{c(us)}\right]^{3}}-\frac{2(1-\alpha)q^{2}}{\left[(1-\alpha)p^{'}+\frac{\alpha}{r}p^{'}_{c(us)}\right]^{3}M^{2}} \tag{F.2}$$

$$\frac{\partial y}{\partial q}=\frac{2q}{\left[(1-\alpha)p^{'}+\frac{\alpha}{r}p^{'}_{c(us)}\right]^{2}M^{2}} \tag{F.3}$$

$\frac{\partial y}{\partial p^{'}_{c(us)}}$ is written as follows:

$$\frac{\partial y}{\partial p^{'}_{c(us)}}=\frac{2\left(-\frac{1}{r}\right)\left(p^{'}-\frac{1}{r}p^{'}_{c(us)}\right)}{\left[\left(1-\frac{2}{r}\right)p^{'}+\frac{1}{r}p^{'}_{c(us)}\right]^{2}}-\frac{2\left(\frac{1}{r}\right)\left(p^{'}-\frac{1}{r}p^{'}_{c(us)}\right)^{2}}{\left[\left(1-\frac{2}{r}\right)p^{'}+\frac{1}{r}p^{'}_{c(us)}\right]^{3}}-\frac{2\left(\frac{\alpha}{r}\right)q^{2}}{\left[(1-\alpha)p^{'}+\frac{\alpha}{r}p^{'}_{c(us)}\right]^{3}M^{2}} \tag{F.4}$$

From Eq. (38), the derivative of $p^{'}_{c(us)}$ with respect to $p^{'}_{c}$ and s^{*} are expressed as:

$$\frac{\partial p^{'}_{c(us)}}{\partial p^{'}_{c}}=\left[\frac{\lambda-\kappa}{\lambda((1-\xi)\exp(-\mu s^{*})+\xi)-\kappa}\right]\left(\frac{p^{'}_{c}}{p^{'}_{R}}\right)^{\frac{\lambda-\lambda((1-\xi)\exp(-\mu s^{*})+\xi)}{\lambda((1-\xi)\exp(-\mu s^{*})+\xi)-\kappa}} \tag{F.5}$$

$$\frac{\partial p^{'}_{c(us)}}{\partial s^{*}}=p^{'}_{R}\left(\frac{p^{'}_{c}}{p^{'}_{R}}\right)^{\frac{\lambda-\kappa}{\lambda((1-\xi)\exp(-\mu s^{*})+\xi)-\kappa}}\ln\left(\frac{p^{'}_{c}}{p^{'}_{R}}\right)\frac{(\lambda-\kappa)\lambda(1-\xi)\mu\exp(-\mu s^{*})}{\left[\lambda((1-\xi)\exp(-\mu s^{*})+\xi)-\kappa\right]^{2}} \tag{F.6}$$

Appendix G. Semi-analytical algorithm for simulating suction-controlled isotropic compression test

Given $\Delta\varepsilon_{v}$ and s, the trial values of effective mean stress ($p^{'\mathrm{trial}}$) and modified suction ($s^{*\mathrm{trial}}$) in the first step of this algorithm are calculated using the following form:

$$p^{'\mathrm{trial}}=p^{'n}+\Delta p^{'\mathrm{trial}}=p^{'n}+\frac{p^{'n}}{\kappa}\Delta\varepsilon_{v} \tag{G.1}$$

$$s^{*\mathrm{trial}}=s^{*n}+\Delta s^{*\mathrm{trial}}=s^{*n}+(-s\Delta\varepsilon_{v}) \tag{G.2}$$

with $p^{'n}$ being effective mean stress at step n

From Eq. (87), $\Delta\lambda_{p}$ in the case of isotropic compression tests takes the following form:

$$\Delta\lambda_{p}=\frac{y^{\mathrm{trial}}}{\left.\frac{\partial y}{\partial p^{'}}\frac{p^{'n}}{\kappa}\frac{\partial y^{*}}{\partial\chi_{v}}\right|^{\mathrm{trial}}+\left.\frac{\partial y}{\partial p^{'}_{c(us)}}\frac{\partial p^{'}_{c(us)}}{\partial s^{*}}\frac{(s^{*n}+p_{u})}{\kappa_{h}}\frac{\partial y^{*}}{\partial\chi_{h}}\right|^{\mathrm{trial}}-\left.\frac{\partial y}{\partial p^{'}_{c(us)}}\frac{\partial p^{'}_{c(us)}}{\partial p^{'}_{c}}\frac{p^{'}_{c}}{(\lambda-\kappa)}\frac{\partial y^{*}}{\partial\chi_{v}}\right|^{\mathrm{trial}}} \tag{G.3}$$

The new increment of effective mean stress ($p^{'}$) can be computed using $\Delta\lambda_{p}$ as follows:

$$\Delta p^{'}=\Delta p^{'\mathrm{trial}}+\Delta p^{'\mathrm{corrt}} \tag{G.4}$$

With $\Delta\lambda_{p}$ obtained, the increment of saturation degree ($-\Delta S_{r}$) can be expressed as:

$$-\Delta S_{r}=\frac{\kappa_{h}}{(s^{*n}+p_{u})}\Delta s^{*\mathrm{trial}}+\Delta\lambda_{p}\left.\frac{\partial y^{*}}{\partial\chi_{h}}\right|^{\mathrm{trial}} \tag{G.5}$$

The effective mean stress or alternatively net stress are then updated using following equations:

$$p^{'n+1}=p^{'n}+\Delta p^{'} \tag{G.6}$$

$$\overline{p}^{n+1}=p^{'n+1}-S_{r}^{n+1}s \tag{G.7}$$

where S_{r}^{n+1} is updated saturation degree thanks to Eq. (G.5)

References

Al-Rub, R.K.A., Darabi, M.K., 2012. A thermodynamic framework for constitutive modeling of time-and rate-dependent materials. Part I: theory'. Int. J. Plast. 34, 61–92. https://doi.org/10.1016/j.ijplas.2012.01.002.

Al-Sharrad, M.A., 2013. Evolving Anisotropy in Unsaturated Soils: Experimental Investigation and Constitutive Modelling. University of Glasgow.

Alonso, E., 1987. Special problem soils: general report. In: Proc. 9th Euro. Conf. SMFE, vol. 3, pp. 1087–1146. *1987*, AA Balkema.

Alonso, E., Pinyol, N., Gens, A., 2013. Compacted soil behaviour: initial state, structure and constitutive modelling. Géotechnique 63 (6), 463. https://doi.org/10.1680/geot.11.P.134.

Alonso, E.E., Gens, A., Josa, A., 1990. A constitutive model for partially saturated soils. Géotechnique 40 (3), 405–430. https://doi.org/10.1680/geot.1990.40.3.405.

Anandarajah, A., 2008. Multi-mechanism anisotropic model for granular materials. Int. J. Plast. 24 (5), 804–846. https://doi.org/10.1016/j.ijplas.2007.07.012.

Balieu, R., Kringos, N., 2015. A new thermodynamical framework for finite strain multiplicative elastoplasticity coupled to anisotropic damage. Int. J. Plast. 70, 126–150. https://doi.org/10.1016/j.ijplas.2015.03.006.

Bianchi, F., Thielmann, M., Mani, R., Or, D., Herrmann, H.J., 2016. Tensile stress relaxation in unsaturated granular materials. Granul. Matter 18 (4), 75. https://doi.org/10.1007/s10035-016-0673-6.

Bignonnet, F., Dormieux, L., Kondo, D., 2016. A micro-mechanical model for the plasticity of porous granular media and link with the Cam clay model. Int. J. Plast. 79, 259–274. https://doi.org/10.1016/j.ijplas.2015.07.003.

Blatz, J., Graham, J., 2003. Elastic-plastic modelling of unsaturated soil using results from a new triaxial test with controlled suction. Géotechnique 53 (1), 113–122. https://doi.org/10.1680/geot.2003.53.1.113.

Bolzon, G., Schrefler, B., Zienkiewicz, O., 1996. Elastoplastic soil constitutive laws generalized to partially saturated states. Géotechnique 46 (2), 279–289. https://doi.org/10.1680/geot.1996.46.2.279.

Bruno, A.W., Gallipoli, D., 2019. A coupled hydromechanical bounding surface model predicting the hysteretic behaviour of unsaturated soils. Comput. Geotech. 110, 287–295. https://doi.org/10.1016/j.compgeo.2019.02.025.

Buscarnera, G., Einav, I., 2012. The yielding of brittle unsaturated granular soils. Géotechnique 62 (2), 147–160. https://doi.org/10.1680/geot.10.P.118.

Buscarnera, G., Nova, R., 2009. An elastoplastic strainhardening model for soil allowing for hydraulic bonding–debonding effects. Int. J. Numer. Anal. Methods GeoMech. 33 (8), 1055–1086. https://doi.org/10.1002/nag.756.

Butterfield, R., 1979. A natural compression law for soils (an advance on e-logp'). Géotechnique 29, 469–480.

Callari, C., Auricchio, F., Sacco, E., 1998. A finite-strain Cam-clay model in the framework of multiplicative elasto-plasticity. Int. J. Plast. 14 (12), 1155–1187. https://doi.org/10.1016/S0749-6419(98)00050-3.

Chen, R., 2007. Experimental Study and Constitutive Modelling of Stress-dependent Coupled Hydraulic Hysteresis and Mechanical Behaviour of an Unsaturated Soil. Hong Kong University of Science and Technology, Hong Kong.

Chiu, C., Ng, C., 2003. A state-dependent elasto-plastic model for saturated and unsaturated soils. Géotechnique 53 (9), 809–829. https://doi.org/10.1680/geot.2003.53.9.809.

Collins, I., 2003. A systematic procedure for constructing critical state models in three dimensions. Int. J. Solid Struct. 40 (17), 4379–4397. https://doi.org/10.1016/S0020-7683(03)00226-9.

Collins, I., 2005. The concept of stored plastic work or frozen elastic energy in soil mechanics. Géotechnique 55 (5), 373–382. https://doi.org/10.1680/geot.2005.55.5.373.

Collins, I., Houlsby, G., 1997. Application of thermomechanical principles to the modelling of geotechnical materials. Proc. R. Soc. Lond. Ser. A: Math. Phys. Eng. Sci. 453 (1964), 1975–2001. https://doi.org/10.1098/rspa.1997.0107.

Collins, I., Kelly, P., 2002. A thermomechanical analysis of a family of soil models. Géotechnique 52 (7), 507–518. https://doi.org/10.1680/geot.2002.52.7.507.

Collins, I.F., Hilder, T., 2002. A theoretical framework for constructing elastic/plastic constitutive models of triaxial tests. Int. J. Numer. Anal. Methods GeoMech. 26 (13), 1313–1347. https://doi.org/10.1002/nag.247.

Coussy, O., Pereira, J.-M., Vaunat, J., 2010. Revisiting the thermodynamics of hardening plasticity for unsaturated soils. Comput. Geotech. 37 (1–2), 207–215. https://doi.org/10.1016/j.compgeo.2009.09.003.

Crisfield, M.A., 1993. Non-linear Finite Element Analysis of Solids and Structures, vol. 1. Wiley, New York.

Crouch, R.S., Wolf, J.P., Dafalias, Y.F., 1994. Unified critical-state bounding-surface plasticity model for soil. J. Eng. Mech. 120 (11), 2251–2270. https://doi.org/10.1061/(ASCE)0733-9399(1994)120:11(2251).

Cui, Y., Delage, P., 1996. Yielding and plastic behaviour of an unsaturated compacted silt. Géotechnique 46 (2), 291–311. https://doi.org/10.1680/geot.1996.46.2.291.

Dangla, P., Pereira, J.-M., 2014. A thermodynamic approach to effective stresses in unsaturated soils incorporating the concept of partial pore deformations. Vadose Zone J. 13 (5) https://doi.org/10.2136/vzj2013.06.0110.

Darabi, M.K., Al-Rub, R.K.A., Omidi, O., 2018. A thermodynamically consistent framework to derive local/nonlocal generalized nonassociative plasticity/viscoplasticity theories'. Int. J. Plast. 110, 19–37. https://doi.org/10.1016/j.ijplas.2018.06.006.

Delage, P., Graham, J., 1996. Mechanical behaviour of unsaturated soils: understanding the behaviour of unsaturated soils requires reliable conceptual models. In: Proceedings of the First International Conference on Unsaturated Soils/UNSAT'95/Paris/France/6-8 Septemeber 1995, vol. 3.

Einav, I., Houlsby, G.T., Nguyen, G.D., 2007. Coupled damage and plasticity models derived from energy and dissipation potentials. Int. J. Solid Struct. 44 (7–8), 2487–2508.

Einav, I., 2007a. Breakage mechanics—part I: theory'. J. Mech. Phys. Solid. 55 (6), 1274–1297. https://doi.org/10.1016/j.jmps.2006.11.003.

Einav, I., 2007b. Breakage mechanics—Part II: modelling granular materials. J. Mech. Phys. Solid. 55 (6), 1298–1320. https://doi.org/10.1016/j.jmps.2006.11.004.

Einav, I., 2012. The unification of hypo-plastic and elasto-plastic theories. Int. J. Solid Struct. 49 (11–12), 1301–1315. https://doi.org/10.1016/j.ijsolstr.2012.02.003.

Fang, H., Zheng, H., Zheng, J., 2017. Micromechanics-based multimechanism bounding surface model for sands. Int. J. Plast. 90, 242–266. https://doi.org/10.1016/j.ijplas.2017.01.011.

Gallipoli, D., Gens, A., Sharma, R., Vaunat, J., 2003. An elasto-plastic model for unsaturated soil incorporating the effects of suction and degree of saturation on mechanical behaviour. Géotechnique 53 (1), 123–136. https://doi.org/10.1680/geot.2003.53.1.123.

Ghasemzadeh, H., Sojoudi, M., Amiri, S.G., Karami, M., 2017. Elastoplastic model for hydro-mechanical behavior of unsaturated soils. Soils Found. 57 (3), 371–383. https://doi.org/10.1016/j.sandf.2017.05.005.

Gholizadeh, E., Latifi, M., 2018. A coupled hydro-mechanical constitutive model for unsaturated frictional and cohesive soil. Comput. Geotech. 98, 69–81. https://doi.org/10.1016/j.compgeo.2017.11.010.

Ghorbani, J., Airey, D.W., El-Zein, A., 2018. Numerical framework for considering the dependency of SWCCs on volume changes and their hysteretic responses in modelling elasto-plastic response of unsaturated soils. Comput. Methods Appl. Mech. Eng. 336, 80–110. https://doi.org/10.1016/j.cma.2018.03.008.

Guiamatsia, I., Nguyen, G.D., 2012. A generic approach to constitutive modelling of composite delamination under mixed-mode loading conditions. Compos. Sci. Technol. 72 (2), 269–277. https://doi.org/10.1016/j.compscitech.2011.11.012.

Hashiguchi, K., 1995. On the linear relations of V–lnp and lnv–lnp for isotropic consolidation of soils. Int. J. Numer. Anal. Methods GeoMech. 19, 367–376.

Hashiguchi, K., Mase, T., 2007. Extended yield condition of soils with tensile yield strength and rotational hardening. Int. J. Plast. 23 (12), 1939–1956. https://doi.org/10.1016/j.ijplas.2007.07.011.

Hashiguchi, K., Tsutsumi, S., 2007. Gradient plasticity with the tangential-subloading surface model and the prediction of shear-band thickness of granular materials. Int. J. Plast. 23 (5), 767–797. https://doi.org/10.1016/j.ijplas.2006.08.005.

Hassanizadeh, S.M., Gray, W.G., 1990. Mechanics and thermodynamics of multiphase flow in porous media including interphase boundaries. Adv. Water Resour. 13 (4), 169–186. https://doi.org/10.1016/0309-1708(90)90040-B.

Houlsby, G., 1997. The work input to an unsaturated granular material. Géotechnique 47 (1), 193–196. https://doi.org/10.1680/geot.1997.47.1.193.

Houlsby, G., Puzrin, A., 2000. A thermomechanical framework for constitutive models for rate-independent dissipative materials. Int. J. Plast. 16 (9), 1017–1047. https://doi.org/10.1016/S0749-6419(99)00073-X.
Hoxha, D., Giraud, A., Homand, F., Auvray, C., 2007. Saturated and unsaturated behaviour modelling of Meuse–Haute/Marne argillite. Int. J. Plast. 23 (5), 733–766. https://doi.org/10.1016/j.ijplas.2006.05.002.
Hu, R., Chen, Y.-F., Liu, H.-H., Zhou, C.-B., 2015. A coupled stress–strain and hydraulic hysteresis model for unsaturated soils: thermodynamic analysis and model evaluation. Comput. Geotech. 63, 159–170. https://doi.org/10.1016/j.compgeo.2014.09.006.
Hu, R., Liu, H.-H., Chen, Y., Zhou, C., Gallipoli, D., 2014. A constitutive model for unsaturated soils with consideration of inter-particle bonding. Comput. Geotech. 59, 127–144. https://doi.org/10.1016/j.compgeo.2014.03.007.
Jommi, C., 2000. Remarks on the Constitutive Modelling of Unsaturated Soils', *Experimental Evidence and Theoretical Approaches in Unsaturated Soils*, pp. 139–153.
Khalili, N., Habte, M., Zargarbashi, S., 2008. A fully coupled flow deformation model for cyclic analysis of unsaturated soils including hydraulic and mechanical hystereses. Comput. Geotech. 35 (6), 872–889. https://doi.org/10.1016/j.compgeo.2008.08.003.
Khalili, N., Khabbaz, M., 1998. A unique relationship for χ for the determination of the shear strength of unsaturated soils. Géotechnique 48 (5), 681–687. https://doi.org/10.1680/geot.1998.48.5.681.
Kodikara, J., Jayasundara, C., Zhou, A.N., 2020. A generalised constitutive model for unsaturated compacted soils considering wetting/drying cycles and environmentally-stabilised line. Comput. Geotech. 118, 103332. https://doi.org/10.1016/j.compgeo.2019.103332.
Lai, Y., Jin, L., Chang, X., 2009. Yield criterion and elasto-plastic damage constitutive model for frozen sandy soil. Int. J. Plast. 25 (6), 1177–1205. https://doi.org/10.1016/j.ijplas.2008.06.010.
Lai, Y., Liao, M., Hu, K., 2016. A constitutive model of frozen saline sandy soil based on energy dissipation theory. Int. J. Plast. 78, 84–113. https://doi.org/10.1016/j.ijplas.2015.10.008.
Lei, X., Wong, H., Fabbri, A., Bui, T.A., Limam, A., 2016. Some general remarks on hyperplasticity modelling and its extension to partially saturated soils. Z. Angew. Math. Phys. 67 (3), 64. https://doi.org/10.1007/s00033-016-0646-y.
Li, L., 2015. Evaluate Unsaturated Soil Behavior Using Constant Water Content Triaxial Tests. University of Alaska Fairbanks.
Li, X., 2003. Effective stress in unsaturated soil: a microstructural analysis. Géotechnique 53 (2), 273–277. https://doi.org/10.1680/geot.2003.53.2.273.
Li, X., 2007a. Thermodynamics-based constitutive framework for unsaturated soils. 1: Theory. Géotechnique 57 (5), 411–422. https://doi.org/10.1680/geot.2007.57.5.411.
Li, X., 2007b. Thermodynamics-based constitutive framework for unsaturated soils. 2: a basic triaxial model. Géotechnique 57 (5), 423–435. https://doi.org/10.1680/geot.2007.57.5.423.
Likos, W.J., 2014. Effective stress in unsaturated soil: accounting for surface tension and interfacial area. Vadose Zone J. 13 (5) https://doi.org/10.2136/vzj2013.05.0095.
Liu, C., Muraleetharan, K.K., 2011a. Coupled hydro-mechanical elastoplastic constitutive model for unsaturated sands and silts. I: formulation'. Int. J. GeoMech. 12 (3), 239–247. https://doi.org/10.1061/(ASCE)GM.1943-5622.0000146.
Liu, C., Muraleetharan, K.K., 2011b. Coupled hydro-mechanical elastoplastic constitutive model for unsaturated sands and silts. II: integration, calibration, and validation. Int. J. GeoMech. 12 (3), 248–259. https://doi.org/10.1061/(ASCE)GM.1943-5622.0000147.
Liu, E., Lai, Y., Wong, H., Feng, J., 2018. An elastoplastic model for saturated freezing soils based on thermo-poromechanics. Int. J. Plast. 107, 246–285. https://doi.org/10.1016/j.ijplas.2018.04.007.
Lloret-Cabot, M., Wheeler, S.J., Sánchez, M., 2017. A unified mechanical and retention model for saturated and unsaturated soil behaviour. Acta Geotechnica 12 (1), 1–21. https://doi.org/10.1007/s11440-016-0497-x.
Loret, B., Khalili, N., 2000. A three-phase model for unsaturated soils'. Int. J. Numer. Anal. Methods GeoMech. 24 (11), 893–927. https://doi.org/10.1002/1096-9853(200009)24:11<893::AID-NAG105>3.0.CO;2-V.
Loret, B., Khalili, N., 2002. An effective stress elastic–plastic model for unsaturated porous media. Mech. Mater. 34 (2), 97–116. https://doi.org/10.1016/S0167-6636(01)00092-8.
Louati, H., Oulahna, D., de Ryck, A., 2015. Apparent friction and cohesion of a partially wet granular material in steady-state shear. Powder Technol. 278, 65–71. https://doi.org/10.1016/j.powtec.2015.03.011.
Louati, H., Oulahna, D., De Ryck, A., 2017. Effect of the particle size and the liquid content on the shear behaviour of wet granular material. Powder Technol. 315, 398–409. https://doi.org/10.1016/j.powtec.2017.04.030.
Lu, N., 2008. Is matric suction a stress variable? J. Geotech. Geoenviron. Eng. 134 (7), 899–905. https://doi.org/10.1061/(ASCE)1090-0241(2008)134:7(899).
Macari, E.J., Hoyos, L.R., Arduino, P., 2003. Constitutive modeling of unsaturated soil behavior under axisymmetric stress states using a stress/suction-controlled cubical test cell. Int. J. Plast. 19 (10), 1481–1515. https://doi.org/10.1016/S0749-6419(02)00018-9.
Maleki, M., Bayat, M., 2012. Experimental evaluation of mechanical behavior of unsaturated silty sand under constant water content condition. Eng. Geol. 141, 45–56. https://doi.org/10.1016/j.enggeo.2012.04.014.
Mani, R., Kadau, D., Herrmann, H.J., 2013. Liquid migration in sheared unsaturated granular media. Granul. Matter 15 (4), 447–454. https://doi.org/10.1007/s10035-012-0387-3.
Marinho, F.A.M., Gonzalo Carnero Guzmán, G., Del Gaudio Orlando, P., 2016. Constant water content compression tests on unsaturated compacted soil with suction measurement using a HCT. Int. J. GeoMech. 16 (6), D4015008. https://doi.org/10.1061/(ASCE)GM.1943-5622.0000609.
Mašín, D., 2010. Predicting the dependency of a degree of saturation on void ratio and suction using effective stress principle for unsaturated soils. Int. J. Numer. Anal. Methods GeoMech. 34 (1), 73–90. https://doi.org/10.1002/nag.808.
Matsuoka, H., Sun, Da, Kogane, A., Fukuzawa, N., Ichihara, W., 2002. Stress–strain behaviour of unsaturated soil in true triaxial tests'. Can. Geotech. J. 39 (3), 608–619. https://doi.org/10.1139/t02-031.
Mbonimpa, M., Aubertin, M., Maqsoud, A., Bussière, B., 2006. Predictive model for the water retention curve of deformable clayey soils. J. Geotech. Geoenviron. Eng. 132 (9), 1121–1132. https://doi.org/10.1061/(ASCE)1090-0241(2006)132:9(1121).
Miller, G.A., Khoury, C.N., Muraleetharan, K.K., Liu, C., Kibbey, T.C., 2008. Effects of soil skeleton deformations on hysteretic soil water characteristic curves: experiments and simulations. Water Resour. Res. 44 (5) https://doi.org/10.1029/2007WR006492.
Mir, A., Nguyen, G.D., Sheikh, A.H., 2018. A thermodynamics-based model for brittle to ductile behaviour and localised failure of porous rocks. Int. J. Solid Struct. 152, 161–184. https://doi.org/10.1016/j.ijsolstr.2018.06.025.
Mroginski, J.L., Etse, G., Vrech, S.M., 2011. A thermodynamical gradient theory for deformation and strain localization of porous media. Int. J. Plast. 27 (4), 620–634. https://doi.org/10.1016/j.ijplas.2010.08.010.
Mun, W., McCartney, J.S., 2015. Compression mechanisms of unsaturated clay under high stresses. Can. Geotech. J. 52 (12), 2099–2112. https://doi.org/10.1139/cgj-2014-0438.
Mun, W., McCartney, J.S., 2017. Constitutive model for drained compression of unsaturated clay to high stresses. J. Geotech. Geoenviron. Eng. 143 (6), 04017014 https://doi.org/10.1061/(ASCE)GT.1943-5606.0001662.
Muraleetharan, K.K., Liu, C., Wei, C., Kibbey, T.C., Chen, L., 2009. An elastoplatic framework for coupling hydraulic and mechanical behavior of unsaturated soils. Int. J. Plast. 25 (3), 473–490. https://doi.org/10.1016/j.ijplas.2008.04.001.
Muraleetharan, K.K., Wei, C., 1999. Dynamic behaviour of unsaturated porous media: governing equations using the theory of mixtures with interfaces (TMI). Int. J. Numer. Anal. Methods GeoMech. 23 (13), 1579–1608. https://doi.org/10.1002/(SICI)1096-9853(199911)23:13<1579::AID-NAG58>3.0.CO;2-.
Ng, C.W.W., Zhou, R., 2005. Effects of soil suction on dilatancy of an unsaturated soil. In: Proceedings of the International Conference on Soil Mechanics and Geotechnical Engineering, vol. 16. AA Balkema Publisshers, p. 559.
Nguyen, G.D., Bui, H.H., 2020. A thermodynamics-and mechanism-based framework for constitutive models with evolving thickness of localisation band. Int. J. Solid Struct. https://doi.org/10.1016/j.ijsolstr.2019.05.022 (in press).

Nguyen, G.D., Einav, I., 2009. The energetics of cataclasis based on breakage mechanics. Pure Appl. Geophys. 166 (10–11), 1693–1724. https://doi.org/10.1007/s00024-009-0518-x.
Nguyen, G.D., Einav, I., 2010. A stress-return algorithm for nonlocal constitutive models of softening materials. Int. J. Numer. Methods Eng. 82 (5), 637–670. https://doi.org/10.1002/nme.2790.
Nguyen, G.D., Korsunsky, A.M., Belnoue, J.P.-H., 2015. A nonlocal coupled damage-plasticity model for the analysis of ductile failure. Int. J. Plast. 64, 56–75. https://doi.org/10.1016/j.ijplas.2014.08.001.
Nguyen, G.D., Einav, I., Guiamatsia, I., 2012. On the partition of fracture energy in constitutive modelling of quasi-brittle materials. Eng. Fract. Mech. 79, 225–244. https://doi.org/10.1016/j.engfracmech.2011.11.002.
Nguyen, G.D., Nguyen, C.T., Nguyen, V.P., Bui, H.H., Shen, L., 2016. A size-dependent constitutive modelling framework for localised failure analysis. Comput. Mech. 58 (2), 257–280. https://doi.org/10.1007/s00466-016-1293-z.
Nguyen, G., Gan, Y., 2014. A multiphase constitutive modeling framework for unsaturated soil behavior. In: Unsaturated Soils: Research & Applications. CRC Press, pp. 359–366.
Nicot, F., Darve, F., 2007. Basic features of plastic strains: from micro-mechanics to incrementally nonlinear models. Int. J. Plast. 23 (9), 1555–1588. https://doi.org/10.1016/j.ijplas.2007.01.010.
Nuth, M., Laloui, L., 2008. Advances in modelling hysteretic water retention curve in deformable soils. Comput. Geotech. 35 (6), 835–844. https://doi.org/10.1016/j.compgeo.2008.08.001.
Pedroso, D.M., Farias, M.M., 2011. Extended Barcelona basic model for unsaturated soils under cyclic loadings. Comput. Geotech. 38 (5), 731–740. https://doi.org/10.1016/j.compgeo.2011.02.004.
Puzrin, A., Houlsby, G., 2001. A thermomechanical framework for rate-independent dissipative materials with internal functions. Int. J. Plast. 17 (8), 1147–1165. https://doi.org/10.1016/S0749-6419(00)00083-8.
Rahardjo, H., Heng, O.B., Choon, L.E., 2004. Shear strength of a compacted residual soil from consolidated drained and constant water content triaxial tests. Can. Geotech. J. 41 (3), 421–436. https://doi.org/10.1139/t03-093.
Raveendiraraj, A., 2009. Coupling of Mechanical Behaviour and Water Retention Behaviour in Unsaturated Soils. University of Glasgow. https://eleanor.lib.gla.ac.uk/record=b2663780.
Robles, J., Elorza, F., Vulliet, L., Laloui, L., Schrefler, B., 2002. A Triaxial Constitutive Model for Unsaturated Soils. EPFL Press, Lausanne, Switzerland, pp. 207–213.
Russell, A., Khalili, N., 2006. A unified bounding surface plasticity model for unsaturated soils. Int. J. Numer. Anal. Methods GeoMech. 30 (3), 181–212. https://doi.org/10.1002/nag.475.
Salomoni, V.A., Fincato, R., 2012. Retracted: subloading surface plasticity model algorithm for 3D subsidence analyses above gas reservoirs. Int. J. GeoMech. 12 (4), 414–427. https://doi.org/10.1061/(ASCE)GM.1943-5622.0000124.
Santagiuliana, R., Schrefler, B., 2006. Enhancing the Bolzon–Schrefler–Zienkiewicz constitutive model for partially saturated soil. Transport Porous Media 65 (1), 1–30. https://doi.org/10.1007/s11242-005-6083-6.
Sharma, R.S., 1998. Mechanical Behaviour of Unsaturated Highly Expansive Clays. University of Oxford.
Sheng, D., 2011. Review of fundamental principles in modelling unsaturated soil behaviour. Comput. Geotech. 38 (6), 757–776. https://doi.org/10.1016/j.compgeo.2011.05.002.
Sheng, D., Fredlund, D.G., Gens, A., 2008. A new modelling approach for unsaturated soils using independent stress variables. Can. Geotech. J. 45 (4), 511–534. https://doi.org/10.1139/T07-112.
Sheng, D., Sloan, S., Gens, A., 2004. A constitutive model for unsaturated soils: thermomechanical and computational aspects. Comput. Mech. 33 (6), 453–465. https://doi.org/10.1007/s00466-003-0545-x.
Sivakumar, V., Doran, I., 2000. Yielding characteristics of unsaturated compacted soils', *Mechanics of Cohesive-frictional Materials*. Int. J. Exp. Model. Comput. Mater. Struct. 5 (4), 291–303. https://doi.org/10.1002/(SICI)1099-1484(200005)5:4<291::AID-CFM95>3.0.CO;2-D.
Stropeit, K., Wheeler, S., Cui, Y., 2008. An Anisotropic Elasto-Plastic Model for Unsaturated Soils.
Sun, D., Matsuoka, H., Yao, Y.-P., Ichihara, W., 2000. An elasto-plastic model for unsaturated soil in three-dimensional stresses. Soils Found. 40 (3), 17–28. https://doi.org/10.3208/sandf.40.3_17.
Sun, D., Matsuoka, H., Xu, Y., 2004. Collapse behavior of compacted clays in suction-controlled triaxial tests'. Geotech. Test J. 27 (4), 362–370. https://doi.org/10.1520/GTJ11418.
Sun, D., Sheng, D., Cui, H., Sloan, S., 2007. A density-dependent elastoplastic hydro-mechanical model for unsaturated compacted soils. Int. J. Numer. Anal. Methods GeoMech. 31 (11), 1257–1279. https://doi.org/10.1002/nag.579.
Sun, D., Sun, W., Yan, W., 2009. Hydraulic and mechanical behaviour of sand-bentonite mixture. In: Proceeding of International Symposium on Unsaturated Soil Mechanics and Deep. Geological Nuclear Waste Disposal, Shanghai, pp. 24–25.
Sun, Da, Sun, W., Xiang, L., 2010. Effect of degree of saturation on mechanical behaviour of unsaturated soils and its elastoplastic simulation. Comput. Geotech. 37 (5), 678–688. https://doi.org/10.1016/j.compgeo.2010.04.006.
Sun, W., Sun, Da, 2012. 'Coupled modelling of hydro-mechanical behaviour of unsaturated compacted expansive soils. Int. J. Numer. Anal. Methods GeoMech. 36 (8), 1002–1022. https://doi.org/10.1002/nag.1036.
Tamagnini, R., 2004. An extended Cam-clay model for unsaturated soils with hydraulic hysteresis. Géotechnique 54 (3), 223–228. https://doi.org/10.1680/geot.2004.54.3.223.
Tamagnini, R., Pastor, M., 2005. A thermodynamically based model for unsaturated soil: a new framework for generalized plasticity. In: Unsaturated Soils. Advances in Testing, Modelling and Engineering Applications. Balkema, Leiden, pp. 121–134.
Tang, G.X., Graham, J., 2002. A possible elastic plastic framework for unsaturated soils with high-plasticity. Can. Geotech. J. 39 (4), 894–907. https://doi.org/10.1139/t02-024.
Tarantino, A., 2009. A water retention model for deformable soils. Géotechnique 59 (9), 751–762. https://doi.org/10.1680/geot.7.00118.
Thu, T.M., Rahardjo, H., Leong, E.-C., 2006. Shear strength and pore-water pressure characteristics during constant water content triaxial tests. J. Geotech. Geoenviron. Eng. 132 (3), 411–419. https://doi.org/10.1061/(ASCE)1090-0241(2006)132:3(411).
Thu, T.M., Rahardjo, H., Leong, E.-C., 2007a. Elastoplastic model for unsaturated soil with incorporation of the soil-water characteristic curve. Can. Geotech. J. 44 (1), 67–77. https://doi.org/10.1139/t06-091.
Thu, T.M., Rahardjo, H., Leong, E.-C., 2007b. Soil-water characteristic curve and consolidation behavior for a compacted silt. Can. Geotech. J. 44 (3), 266–275. https://doi.org/10.1139/t06-114.
Toyota, H., Sakai, N., Nishimura, T., 2001. Effects of stress history due to unsaturation and drainage condition on shear properties of unsaturated cohesive soil. Soils Found. 41 (1), 13–24. https://doi.org/10.3208/sandf.41.13.
Uchaipichat, A., 2005. Experimental Investigation and Constitutive Modelling of Thermo-Hydro-Mechanical Coupling in Unsaturated Soils. University of New South Wales.
Uchaipichat, A., Khalili, N., 2009. Experimental investigation of thermo-hydro-mechanical behaviour of an unsaturated silt. Géotechnique 59 (4), 339–353. https://doi.org/10.1680/geot.2009.59.4.339.
Vanapalli, S., Fredlund, D., Pufahl, D., 1999. The influence of soil structure and stress history on the soil-water characteristics of a compacted till. Géotechnique 49 (2), 143–159. https://doi.org/10.1680/geot.1999.49.2.143.
Vaunat, J., Cante, J., Ledesma, A., Gens, A., 2000. A stress point algorithm for an elastoplastic model in unsaturated soils. Int. J. Plast. 16 (2), 121–141. https://doi.org/10.1016/S0749-6419(99)00033-9.
Vaunat, J., Merchán, V., Romero, E., Pineda, J., 2007. Residual strength of clays at high suctions. In: Theoretical and Numerical Unsaturated Soil Mechanics. Springer, pp. 151–163. https://doi.org/10.1007/3-540-69876-0_17.

Wan, R., Khosravani, S., Pouragha, M., 2014. Micromechanical analysis of force transport in wet granular soils. Vadose Zone J. 13 (5) https://doi.org/10.2136/vzj2013.06.0113.
Wang, J.-P., Gallo, E., François, B., Gabrieli, F., Lambert, P., 2017. Capillary force and rupture of funicular liquid bridges between three spherical bodies. Powder Technol. 305, 89–98. https://doi.org/10.1016/j.powtec.2016.09.060.
Wei, C., Dewoolkar, M.M., 2006. Formulation of capillary hysteresis with internal state variables. Water Resour. Res. 42, 7. https://doi.org/10.1029/2005WR004594.
Wheeler, S., Sharma, R., Buisson, M., 2003. Coupling of hydraulic hysteresis and stress–strain behaviour in unsaturated soils. Géotechnique 53 (1), 41–54. https://doi.org/10.1680/geot.2003.53.1.41.
Wheeler, S., Sivakumar, V., 1995. An elasto-plastic critical state framework for unsaturated soil. Géotechnique 45 (1), 35–53. https://doi.org/10.1680/geot.1995.45.1.35.
Wong, P., Wong, P., 1975. Yielding and plastic flow of sensitive cemented clay. Géotechnique 25 (4), 763–782. https://doi.org/10.1680/geot.1975.25.4.763.
Wood, D.M., Graham, J., 1990. Anisotropic elasticity and yielding of a natural plastic clay. Int. J. Plast. 6 (4), 377–388. https://doi.org/10.1016/0749-6419(90)90009-4.
Xie, S., Shao, J.-F., 2006. Elastoplastic deformation of a porous rock and water interaction. Int. J. Plast. 22 (12), 2195–2225. https://doi.org/10.1016/j.ijplas.2006.03.002.
Yin, Z.-Y., Chang, C.S., Hicher, P.-Y., Karstunen, M., 2009. Micromechanical analysis of kinematic hardening in natural clay. Int. J. Plast. 25 (8), 1413–1435. https://doi.org/10.1016/j.ijplas.2008.11.009.
Yu, H.-S., 1998. CASM: a unified state parameter model for clay and sand. Int. J. Numer. Anal. Methods GeoMech. 22 (8), 621–653. https://doi.org/10.1002/(SICI)1096-9853(199808)22:8<621::AID-NAG937>3.0.CO;2-8.
Zhan, L., 2003. Field and Laboratory Study of an Unsaturated Expansive Soil Associated with Rain-Induced Slope Instability. Hong Kong University of Science and Technology.
Zhang, X., 2016. Limitations of suction-controlled triaxial tests in the characterization of unsaturated soils. Int. J. Numer. Anal. Methods GeoMech. 40 (2), 269–296. https://doi.org/10.1002/nag.2401.
Zhang, X., Li, L., 2010. Limitations in the constitutive modeling of unsaturated soils and solutions. Int. J. GeoMech. 11 (3), 174–185. https://doi.org/10.1061/(ASCE)GM.1943-5622.0000076.
Zhang, X., Liu, J., Li, P., 2009. Determining the shapes of yield curves for unsaturated soils by modified state surface approach. J. Geotech. Geoenviron. Eng. 136 (1), 239–247. https://doi.org/10.1061/(ASCE)GT.1943-5606.0000196.
Zhang, X., Lytton, R.L., 2009a. Modified state-surface approach to the study of unsaturated soil behavior. Part I: basic concept. Can. Geotech. J. 46 (5), 536–552. https://doi.org/10.1139/T08-136.
Zhang, X., Lytton, R.L., 2009b. Modified state-surface approach to the study of unsaturated soil behavior. Part II: general formulation. Can. Geotech. J. 46 (5), 553–570. https://doi.org/10.1139/T08-137.
Zhang, Z., 2017. A thermodynamics-based theory for thethermo-poro-mechanical modeling of saturated clay. Int. J. Plast. 92, 164–185. https://doi.org/10.1016/j.ijplas.2017.03.007.
Zhao, C., Li, J., Cai, G., Asreazad, S., 2014. Necessary Conditions for the Critical State of Unsaturated Soils. Unsaturated Soils: Research & Applications, p. 177. https://doi.org/10.13140/2.1.1579.2328.
Zhou, A., Sheng, D., Sloan, S.W., Gens, A., 2012a. Interpretation of unsaturated soil behaviour in the stress–saturation space, I: volume change and water retention behaviour. Comput. Geotech. 43, 178–187. https://doi.org/10.1016/j.compgeo.2012.04.010.
Zhou, A., Sheng, D., Sloan, S.W., Gens, A., 2012b. Interpretation of unsaturated soil behaviour in the stress–saturation space: II: constitutive relationships and validations. Comput. Geotech. 43, 111–123. https://doi.org/10.1016/j.compgeo.2012.02.009.
Zhou, A., Sheng, D., 2009. Yield stress, volume change, and shear strength behaviour of unsaturated soils: validation of the SFG model. Can. Geotech. J. 46 (9), 1034–1045. https://doi.org/10.1139/T09-049.
Zhou, A., Sheng, D., 2015. An advanced hydro-mechanical constitutive model for unsaturated soils with different initial densities. Comput. Geotech. 63, 46–66. https://doi.org/10.1016/j.compgeo.2014.07.017.
Zhou, A., Wu, S., Li, J., Sheng, D., 2018. Including degree of capillary saturation into constitutive modelling of unsaturated soils. Comput. Geotech. 95, 82–98. https://doi.org/10.1016/j.compgeo.2017.09.017.
Ziegler, H., 1983. An Introduction to Thermomechanics. North-Holland.

Appendix D. Phan, DG, Nguyen, GD, Bui, HH & Bennett, T 2020 'A thermodynamics-based formulation for coupled hydro-mechanical behaviour of unsaturated soils', The 16th International Association for Computer Methods and Advances in Geomechanics, IACMAG 2021, Turin May 5th-8th.

Statement of Authorship

Title of Paper	A thermodynamics-based formulation for coupled hydro-mechanical behaviour of unsaturated soils
Publication Status	☑ Published ☐ Accepted for Publication ☐ Submitted for Publication ☐ Unpublished and Unsubmitted work written in manuscript style
Publication Details	Phan, DG, Nguyen, GD, Bui, HH & Bennett, T 2020 'A thermodynamics-based formulation for coupled hydro-mechanical behaviour of unsaturated soils', The 16th International Association for Computer Methods and Advances in Geomechanics, IACMAG 2021, Turin May 5th-8th.

Principal Author

Name of Principal Author (Candidate)	Dat G. Phan		
Contribution to the Paper	Conceptualization, Methodology, Software, Validation, Formal analysis, Writing-Original draft preparation		
Overall percentage (%)	70		
Certification:	This paper reports on original research I conducted during the period of my Higher Degree by Research candidature and is not subject to any obligations or contractual agreements with a third party that would constrain its inclusion in this thesis. I am the primary author of this paper.		
Signature		Date	30 Nov 2020

Co-Author Contributions

By signing the Statement of Authorship, each author certifies that:

i. the candidate's stated contribution to the publication is accurate (as detailed above);
ii. permission is granted for the candidate in include the publication in the thesis; and
iii. the sum of all co-author contributions is equal to 100% less the candidate's stated contribution.

Name of Co-Author	Giang D. Nguyen		
Contribution to the Paper	Supervision, Conceptualization, Methodology, Formal analysis, Writing-Reviewing and Editing		
Signature		Date	30 Nov 2020

Name of Co-Author	Ha H. Bui

Contribution to the Paper	Supervision, Conceptualization, Formal analysis, Writing- Reviewing and Editing		
Signature		Date	30 Nov 2020

Name of Co-Author	Terry Bennett		
Contribution to the Paper	Supervision, Conceptualization, Formal analysis, Writing- Reviewing and Editing		
Signature		Date	30 Nov 2020

Please cut and paste additional co-author panels here as required.

A thermodynamics-based formulation for coupled hydro-mechanical behaviour of unsaturated soils

Dat G. Phan[1], Giang D. Nguyen[1,*], Ha H. Bui[2], Terry Bennett[1]

[1] School of Civil, Environmental and Mining Engineering, University of Adelaide, Australia

[2] Department of Civil Engineering, Monash University, Australia

[*] Corresponding author: g.nguyen@adelaide.edu.au

Abstract The nonlinear behaviour of unsaturated soils is governed by the fully coupled hydro-mechanical phenomenon due to the irrecoverable movement of particles and fluids. It is usually accounted for in constitutive modeling using separate evolution rules for plastic deformation and saturation, linked with two yield conditions for stress and suction. In this paper, a new generic thermodynamics-based approach is developed to provide a more rigorous way to capture these underlying mechanisms. A special form of dissipation potential leading to strong inter-dependence of mechanical and hydraulic internal variables is used for the derivation of a single yield surface. A specific critical state model using a small number of identifiable parameters is derived from the proposed formulation. Its capabilities in predicting the drained and undrained experimental results are investigated to highlight the applicability of our approach.

Keywords: Unsaturated soils, constitutive modelling, thermodynamics, coupled hydro-mechanical

1 Introduction

An intrinsic nature of unsaturated soil behaviour is the hydro-mechanical coupling due to interactions between grain rearrangement and liquid-bridge redistribution. It is reflected at the continuum level through the effects of suction on strength and volumetric behaviour, and capillary hysteresis, which have been observed in several drained and undrained tests. There have been several attempts and some successes to develop constitutive models for unsaturated soils to capture these experimentally observed characteristics in the last 30 years. Particularly, the suction-dependent mechanical responses have been investigated in many models without the soil water characteristic curve (SWCC) (e.g. Alonso et al., 1990). In some others, the hydraulic influence through a SWCC is added (e.g. Thu et al., 2007a) to distinguish the effects of different saturation regimes on the mechanical behaviour. However the effects of mechanical behaviour on hydraulic responses, represented by the SWCC, were not accounted for in these models. The non-uniqueness of SWCC has been well recognised (e.g. Nuth & Laloui, 2008; Tarantino, 2009) and was taken into account in Buscarnera and Nova (2009). However,

this study neglects the wetting-drying difference in the behaviour which has been successfully addressed in several models. For example, Khalili et al. (2008) adopts a separate law of hydraulic hysteresis in which each drying and wetting path possesses different parameters. Others (e.g. Wheeler et al., 2003) employ the multiple yield surface (Loading Collapse (LC), Suction Increase/Decrease (SI/SD)). Nevertheless, according to Delage and Graham (1996), the micromechanical nature of coupled hydro-mechanical yielding should be represented by a unique yield locus. Furthermore, net stress-controlled experiments (Thu et al., 2007b) indicate the irrationality of horizontal straight lines for SI/SD curves adopted in these models.

In this paper, a generic thermodynamics-based approach is developed to describe the interdependence of plastic strain and irrecoverable saturation, as two key internal variables of an unsaturated model. The proposed approach brings benefits in minimizing the number of arbitrary assumptions and model parameters. It uses a single yield surface in stress-suction space with two evolution rules for plastic strains and irrecoverable saturation. The whole model is derived from two explicitly defined free energy and dissipation potentials, and can address the lack of hydraulic dissipation in some earlier thermodynamics-based models (e.g. Buscarnera & Einav, 2012). The interaction between mechanical and hydraulic yielding responses can be captured with a small number of parameters. The promising features of this approach are elucidated through a specific critical state model whose performances are validated against a range of experimental data obtained from drained and undrained tests.

2 A generic thermodynamics-based formulation

The rate of work input can be expressed as:

$$\widetilde{W} = (\bar{p} + S_r s)\dot{\varepsilon}_v + q\dot{\varepsilon}_s - \phi s\dot{S}_r = p'\dot{\varepsilon}_v + q\dot{\varepsilon}_s + s^*\left(-\dot{S}_r\right) = \dot{\Psi} + \widetilde{\Phi} \tag{1}$$

where $\bar{p}, p', q, s, s^*, \varepsilon_v, \varepsilon_s, S_r, \phi$ are the net mean stress, effective mean stress, shear stress, matric suction, modified suction, volumetric strain, shear strain, saturation degree and porosity, respectively. The Helmholtz free energy is assumed as a function of strains and saturation. Therefore, its rate $\dot{\Psi}$ takes form:

$$\dot{\Psi} = \frac{\partial \Psi}{\partial \varepsilon_v}\dot{\varepsilon}_v + \frac{\partial \Psi}{\partial \varepsilon_s}\dot{\varepsilon}_s + \frac{\partial \Psi}{\partial(-S_r)}\left(-\dot{S}_r\right) + \frac{\partial \Psi}{\partial \varepsilon_v^p}\dot{\varepsilon}_v^p + \frac{\partial \Psi}{\partial \varepsilon_s^p}\dot{\varepsilon}_s^p + \frac{\partial \Psi}{\partial(-S_r^p)}\left(-\dot{S}_r^p\right) \tag{2}$$

From Eqs. (1) and (2), the following relationships are obtained:

$$p' = \frac{\partial \Psi}{\partial \varepsilon_v}, \quad q = \frac{\partial \Psi}{\partial \varepsilon_s}, \quad s^* = \frac{\partial \Psi}{\partial(-S_r)} \tag{3}$$

and,

$$\bar{\chi}_v = -\frac{\partial \Psi}{\partial \varepsilon_v^p}, \quad \bar{\chi}_s = -\frac{\partial \Psi}{\partial \varepsilon_s^p}, \quad \bar{\chi}_h = -\frac{\partial \Psi}{\partial(-S_r^p)} \tag{4}$$

in which $\bar{\chi}_v, \bar{\chi}_s$ and $\bar{\chi}_h$ are the thermodynamic conjugates to plastic volumetric strain $\dot{\varepsilon}_v^p$, plastic shear strain $\dot{\varepsilon}_s^p$ and irreversible saturation degree $-\dot{S}_r^p$, respectively.
For rate-independent behavior, the dissipation potential $\widetilde{\Phi}$ is a homogeneous function of order one in terms of $\dot{\varepsilon}_v^p$, $\dot{\varepsilon}_s^p$ and $\dot{S}_r^p$:

$$\widetilde{\Phi} = \sqrt{(\phi_1^v)^2 + (\phi^s)^2 + (\phi^h)^2} + \phi_2^v \tag{5}$$

where ϕ_1^v, ϕ_2^v; ϕ^s and ϕ^h are first order homogeneous functions of $\dot{\varepsilon}_v^p$; $\dot{\varepsilon}_s^p$ and $\dot{S}_r^p$, respectively. From Eq. (5), the volumetric (χ_v), shear (χ_s) and hydraulic (χ_h) dissipative generalised stresses take the following forms:

$$\chi_v = \frac{\partial \widetilde{\Phi}}{\partial \dot{\varepsilon}_v^p}, \quad \chi_s = \frac{\partial \widetilde{\Phi}}{\partial \dot{\varepsilon}_s^p}, \quad \chi_h = \frac{\partial \widetilde{\Phi}}{\partial (-\dot{s}_r^p)} \tag{6}$$

The degenerate Legendre transformation of Eq. (5) leads to a single yield function y^* in the space of $\chi_v, \chi_s,$ and χ_h

$$y^* = \frac{\left(\chi_v - \frac{\partial \phi_2^v}{\partial \dot{\varepsilon}_v^p}\right)^2}{\left(\frac{\partial \phi_1^v}{\partial \dot{\varepsilon}_v^p}\right)^2} + \frac{(\chi_s)^2}{\left(\frac{\partial \phi^s}{\partial \dot{\varepsilon}_s^p}\right)^2} + \frac{(\chi_h)^2}{\left(\frac{\partial \phi^h}{\partial (-\dot{s}_r^p)}\right)^2} - 1 \leq 0 \tag{7}$$

Three flow rules, sharing a single multiplier $\dot{\lambda}_p$, can then be expressed as:

$$\dot{\varepsilon}_v^p = \dot{\lambda}_p \frac{\partial y^*}{\partial \chi_v}, \quad \dot{\varepsilon}_s^p = \dot{\lambda}_p \frac{\partial y^*}{\partial \chi_s}, \quad -\dot{S}_r^p = \dot{\lambda}_p \frac{\partial y^*}{\partial \chi_h} \tag{8}$$

Eqs. (3), (7) and (8) present a generic form of thermodynamic-based models for unsaturated soils. Further details on the above generic formulation and its features from which unsaturated soils model can be defined using explicitly defined energy and dissipation potentials can be found in Phan et al. (2020). The following Section provides an example of such unsaturated soil models formulated based on the above generic formulation.

3 A critical state model for unsaturated soils based on thermodynamics

The Helmholtz free energy potential can assume the following specific form (Phan et al., 2020):

$$\begin{aligned} \Psi = \kappa p_0' \, exp\left[\frac{\left(\varepsilon_v - \varepsilon_v^p\right)}{\kappa}\right] + \frac{3}{2} G\left(\varepsilon_s - \varepsilon_s^p\right)^2 \\ + \kappa_h (p_u + s_0^*) \, exp\left\{\frac{S_{r0} + \left[(-S_r) - \left(-S_r^p\right)\right]}{\kappa_h}\right\} \\ - \left[(-S_r) - \left(-S_r^p\right)\right] p_u + \left(-S_r^p\right) p_b \end{aligned} \tag{9}$$

where κ is the elastic index; G is the shear moduli; κ_h is to control the amount of reversible energy stored in the water menisci (Buscarnera & Einav, 2012); $p_u = 1$ kPa and p_b is a parameter controlling the stored irreversible hydraulic energy; p'_0, s^*_0 and S_{r0} are initial values of p', s^* and S_r, respectively.

For an explicitly defined dissipation potential, functions ϕ_1^v, ϕ_2^v, ϕ^s and ϕ^h in Eq. (5) are needed, and take the following forms (Phan et al, 2020):

$$\phi_1^v = \frac{1}{\sqrt{\mathrm{e}^{-\beta(1-S_r)}}}\left[\left(1-\frac{2}{r}\right)p' + \frac{1}{r}p'_{c(us)}\right]\dot{\varepsilon}_v^p \tag{10}$$

$$\phi_2^v = \frac{p'_{c(us)}}{r}\dot{\varepsilon}_v^p \tag{11}$$

$$\phi^s = \left[(1-\alpha)Mp' + \frac{\alpha}{r}Mp'_{c(us)}\right]\dot{\varepsilon}_s^p \tag{12}$$

$$\phi^h = \frac{1}{\sqrt{1-\mathrm{e}^{-\beta(1-S_r)}}}\frac{(s^*-p_b)}{\left(p'-\frac{p'_{c(us)}}{r}\right)}\left[\left(1-\frac{2}{r}\right)p' + \frac{1}{r}p'_{c(us)}\right]\left(-\dot{S}_r^p\right) \tag{13}$$

in which β ($0 < \beta \leq 1$) is to govern the hydro-mechanical coupling, α is a parameter governing the strength of the material, r is defined as "spacing ratio" to control the dilatancy (Collins & Hilder, 2002), M is the slope of the critical state line. $p'_{c(us)}$ is hardening law based on drained tests at low stresses which takes the following form:

$$p'_{c(us)} = p'_R\left[\frac{p'_{c0}\,exp\left(\frac{\varepsilon_v^p}{\lambda-\kappa}\right)}{p'_R}\right]^{\frac{\lambda-\kappa}{\lambda((1-\xi)exp(-\mu s^*)+\xi)-\kappa}} \tag{14}$$

with λ being the slope of the normal compression line (NCL) at $s = 0$ kPa; p'_{c0} being the initial yield mean pressure at $s = 0$ kPa; p'_R, ξ and μ being parameters controlling the change of soil stiffness and yield stress.

Using Eqs. (3) and (9), the following constitutive relationships are obtained:

$$p' = \frac{\partial\Psi}{\partial\varepsilon_v} = p'_0\mathrm{e}^{\left(\frac{\varepsilon_v-\varepsilon_v^p}{\kappa}\right)} \tag{15}$$

$$q = \frac{\partial\Psi}{\partial\varepsilon_s} = 3G\left(\varepsilon_s - \varepsilon_s^p\right) \tag{16}$$

$$s^* = \frac{\partial\Psi}{\partial(-S_r)} = (p_u + s_0^*)\,\mathrm{e}^{\left\{\frac{S_{r0}+\left[(-S_r)-\left(-S_r^p\right)\right]}{\kappa_h}\right\}} - p_u \tag{17}$$

Adopting Eqs. (7), (9), (10-13) and Ziegler's orthogonality conditions in the forms $\chi_v = \bar{\chi}_v = -\frac{\partial \Psi}{\partial \varepsilon_v^p} = p'$, $\chi_s = \bar{\chi}_s = -\frac{\partial \Psi}{\partial \varepsilon_s^p} = q$, and $\chi_h = \bar{\chi}_h = -\frac{\partial \Psi}{\partial (-S_r^p)} = s^* - p_b$, we can obtain the yield surface y in true stress space as:

$$\frac{\left(p' - \frac{1}{r}p'_{c(us)}\right)^2}{\left[\left(1-\frac{2}{r}\right)p' + \frac{1}{r}p'_{c(us)}\right]^2} + \frac{(q)^2}{\left[(1-\alpha)p' + \frac{\alpha}{r}p'_{c(us)}\right]^2 M^2} - 1 \leq 0 \tag{18}$$

The evolution rules in Eq. (8) can be expressed as follows:

$$\dot{\varepsilon}_v^p = \dot{\lambda}_p \frac{\partial y^*}{\partial \chi_v} = \dot{\lambda}_p \frac{2\left(p' - \frac{1}{r}p'_{c(us)}\right)}{\left[\left(1-\frac{2}{r}\right)p' + \frac{1}{r}p'_{c(us)}\right]^2} \mathrm{e}^{-\beta(1-S_r)} \tag{19}$$

$$\dot{\varepsilon}_s^p = \dot{\lambda}_p \frac{\partial y^*}{\partial \chi_s} = \dot{\lambda}_p \frac{2q}{\left[(1-\alpha)p' + \frac{\alpha}{r}p'_{c(us)}\right]^2 M^2} \tag{20}$$

$$-\dot{S}_r^p = \dot{\lambda}_p \frac{\partial y^*}{\partial \chi_h} = \dot{\lambda}_p \frac{2\left(p' - \frac{1}{r}p'_{c(us)}\right)^2}{(s^* - p_b)\left[\left(1-\frac{2}{r}\right)p' + \frac{1}{r}p'_{c(us)}\right]^2} \left[1 - \mathrm{e}^{-\beta(1-S_r)}\right] \tag{21}$$

For $r = 2$ and $\alpha = 1$ the proposed model in Eqs. (18-21) becomes Modified Cam Clay at $s = 0$ and $S_r = 1$, allowing it to capture the transition from fully to partially saturated behaviour, and vice versa. Further details on the model formulation, its characteristics a dissipation properties, along with implementation algorithms and verification are presented in our forth coming paper (Phan et al., 2020).

5 Validation with experiments

5.1 Drained tests

Firstly, the drained isotropic compression test on the compacted unsaturated expansive clay (Zhan, 2003) is examined. The calibration of the following parameters is based on the initial yield curve, resulting in $\kappa = 0.015$; $\lambda = 0.05$; $p'_{c0} = 80$ kPa; $p'_R = 50$ kPa; $\mu = 0.025$ and $\xi = 0.3$. The data on $s = 25$ kPa is adopted to determine $\kappa_h = 0.55$; $r = 2$; $\beta = 0.2$ and $p_b = 70$ kPa. The predicted and measured data at $s = 25$ kPa; 50 kPa; 100 kPa and 200 kPa are illustrated in Fig. 1. As can be seen, the model can provide a good match to experimental responses, except some discrepancies at $s = 200$ kPa. In particular, the simultaneous activation in irreversible changes of both volume and saturation degree are well captured. The initial yield stress increases and the NCL slope decreases when suction increases. Furthermore, saturation degree is observed to significantly increase despite unchanged suction, indicating the model's ability in predicting the mechanical effect on SWCC.

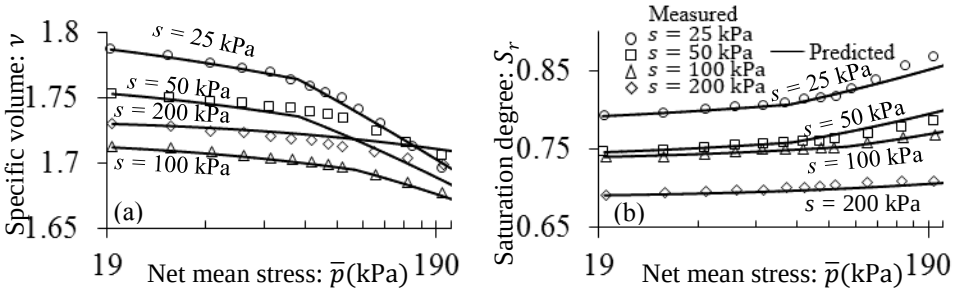

Fig. 1 Drained isotropic compression test on compacted unsaturated expansive clay (after Zhan, 2003) (a) $\bar{p}$: v (b) $\bar{p}$: S_r

The shear behaviour of model is investigated using data obtained from drained triaxial tests on Kurnell sand at $s = 0$ kPa; 100 kPa and 200 kPa with the net confining pressure $\bar{\sigma}_{33} = 50$ kPa (Russell, 2004). We use the experimental results of $s = 0$ kPa to calibrate and obtain the following parameters $\kappa = 0.01$; $G = 4300$ kPa; $\lambda = 0.25$; $p'_{c0} = 600$ kPa; $r = 2.5$; $M = 1.28$ and $\alpha = 0.45$. Other parameters: $\kappa_h = 0.004$; $p'_R = 363.31$ kPa; $\mu = 0.0601$; $\xi = 0.6$; $\beta = 0.05$; $p_b = 70$ kPa are calibrated to best fit the test results at $s = 100$ kPa. As depicted in Fig. 2, the numerical results show reasonable agreement with the experimental data. In particular, higher suctions tend to produce higher yield shear stresses. The model can also give a fairly good prediction of suction-dependent dilation responses (see Fig. 2b).

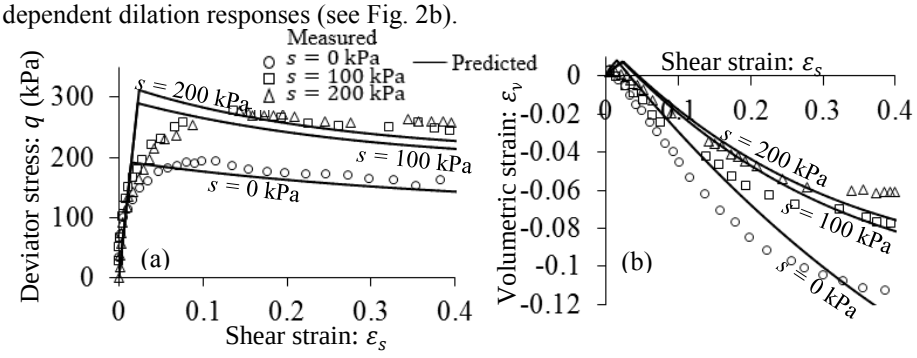

Fig. 2 Drained triaxial compression test on the Kurnell sand (after Russell, 2004) (a) ε_s: q (b) ε_s: ε_v

5.2 Undrained tests

The undrained isotropic compression test with water content $w = 9.9\%$ on Fairbanks silt (Zhang, 2016) is investigated in three phases: loading AB (phase 1), unloading from BC (phase 2) and reloading CD (phase 3). Parameters are : $\kappa = 0.006$; $\lambda = 0.026$; $\kappa_h = 0.05$; $p'_R = 206.78$ kPa; $\mu = 0.0157$; $\xi = 0.628$; $p'_{c0} = 250$ kPa; $r = 1.5$; $\beta = 0.1$; $p_b = 80$ kPa. As can be seen in Fig. 3, the experimental trends of NCL and SWCC are

reasonably reproduced by the model. Particularly, matric suction and specific volume decrease while saturation degree increases in phase 1 and 3. Upon unloading in phase 2, both stress-strain and SWCC relationships cannot recover their previous states, indicating the ability of the model to perform the wetting-drying difference.

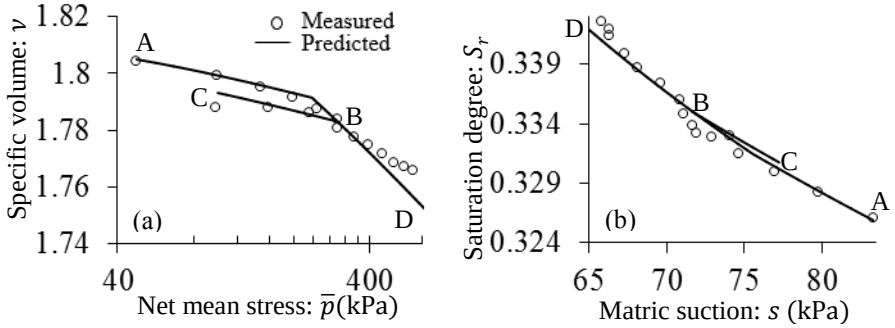

Fig. 3 Undrained isotropic compression test of the Fairbanks silt at $w = 9.9\%$ (after Zhang, 2016) (a) $\bar{p}: v$ (b) $s: S_r$

6 Conclusions

This study focuses on the development of a new generic thermo-mechanical approach for coupled hydro-mechanical behavior in modelling unsaturated soils. This approach allows the derivation of constitutive models possessing a single yield function and three evolution laws for $\dot{\varepsilon}_v^p$, $\dot{\varepsilon}_s^p$ and $-\dot{S}_r^p$ to reproduce the macro behavior generated by the interactions between grain contact sliding and capillary irreversibility at the grain scale. Its benefit is the reduction in the number of parameters and the identification and calibration of all parameters based on standard tests. Following the general formulation, an example of a critical state constitutive model is proposed for capturing some essential features of unsaturated soil responses under drained and undrained triaxial loading conditions. Good agreement between the numerical and experimental results demonstrates the potential of the generic approach and its derived model.

Acknowledgements The authors gratefully acknowledge support from the Australian Research Council via Discovery Projects FT140100408 (Nguyen), DP170103793 (Nguyen & Bui), and DP190102779 (Bui & Nguyen).

7 References

Alonso, E.E., Gens, A. and Josa, A. (1990). A constitutive model for partially saturated soils. *Géotechnique* 40(3), 405-430.

Buscarnera, G. & Einav, I. (2012). The Yielding of Unsaturated Granular Materials, in *Unsaturated Soils: Research and Applications*. Springer, 23-29.

Buscarnera, G. & Nova, R. (2009). An elastoplastic strain hardening model for soil allowing for hydraulic bonding–debonding effects. *International Journal for Numerical and Analytical Methods in Geomechanics* 33(8), 1055-1086.

Collins, I.F. & Hilder, T. (2002). A theoretical framework for constructing elastic/plastic constitutive models of triaxial tests. *International Journal for Numerical and Analytical Methods in Geomechanics* 26(13), 1313-1347.

Delage, P. & Graham, J. (1996). Mechanical behaviour of unsaturated soils: Understanding the behaviour of unsaturated soils requires reliable conceptual models', in *Proceedings of The First International Conference on Unsaturated Soils*/UNSAT'95/Paris/France/6-8 Septemeber 1995. Volume 3.

Khalili, N., Habte, M. and Zargarbashi, S. (2008). A fully coupled flow deformation model for cyclic analysis of unsaturated soils including hydraulic and mechanical hystereses. *Computers and Geotechnics* 35(6), 872-889.

Nuth, M. and Laloui, L. (2008). Advances in modelling hysteretic water retention curve in deformable soils. *Computers and Geotechnics* 35(6), 835-844.

Phan, D.G., Nguyen, G.D., Bui, H.H., Bennett, T. (2020). Constitutive modelling of partially saturated soils: hydro-mechanical coupling in a generic thermodynamics-based formulation. *submitted*.

Russell, A.R. (2004). Cavity expansion in unsaturated soils. *PhD Thesis*, University of New South Wales.

Tarantino, A. (2009), A water retention model for deformable soils, *Géotechnique* 59(9), 751-762.

Thu, T.M., Rahardjo, H., and Leong, E.-C. (2007a). Elastoplastic model for unsaturated soil with incorporation of the soil-water characteristic curve. *Canadian Geotechnical Journal* 44(1), 67-77.

Thu, T.M., Rahardjo, H., and Leong, E.-C. (2007b). Soil-water characteristic curve and consolidation behavior for a compacted silt. *Canadian Geotechnical Journal* 44(3), 266-275.

Wheeler, S., Sharma, R., and Buisson, M. (2003). Coupling of hydraulic hysteresis and stress–strain behaviour in unsaturated soils. *Géotechnique* 53(1), 41-54.

Zhan, L. (2003). Field and laboratory study of an unsaturated expansive soil associated with rain-induced slope instability. *PhD thesis*, Hong Kong University of Science and Technology.

Zhang, X. (2016). Limitations of suction-controlled triaxial tests in the characterization of unsaturated soils', *International Journal for Numerical and Analytical Methods in Geomechanics* 40(2), 269-296.